NASA
National Aeronautics and
Space Administration

THE PRINCETON UNIVERSITY CONFERENCE

PARTIALLY IONIZED AND URANIUM PLASMAS

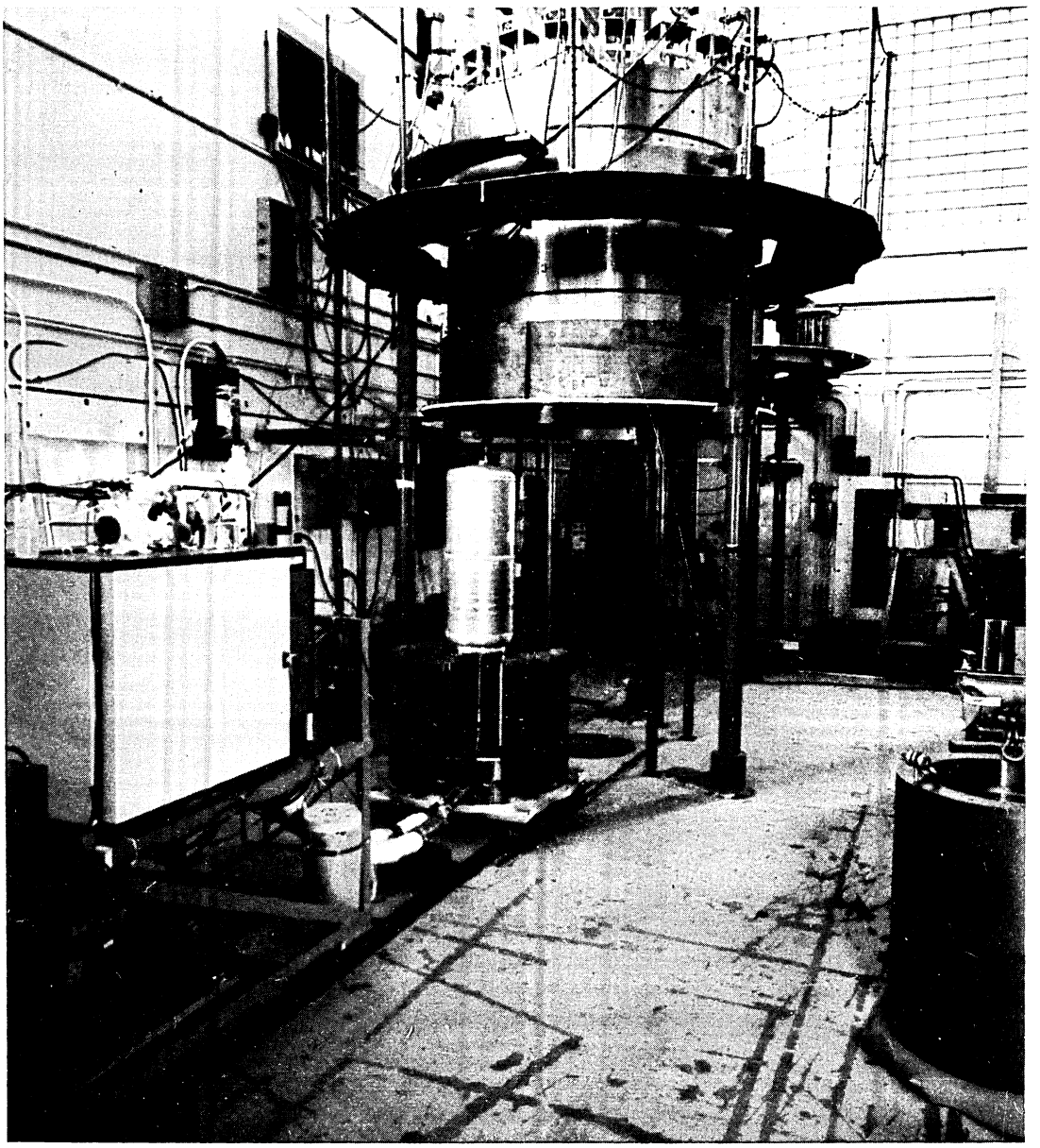

Proceedings of
The Princeton University Conference

on

PARTIALLY IONIZED PLASMAS
including the THIRD SYMPOSIUM ON URANIUM PLASMAS

Edited by

M. Krishnan

Department of Aerospace and Mechanical Sciences
Princeton University

Papers delivered at the One Hundred Thirty Third Meeting
of the Princeton University Conference on June 10-12, 1976

September 1976

Published by
National Aeronautics and Space Administration
Washington, D.C.

PREFACE

The Princeton University Conference on Partially Ionized Plasmas including the Third Symposium on Uranium Plasmas has been undertaken with the support of the Research Division of the National Aeronautics and Space Administration. It has the enthusiastic sponsorship of Mr. F. Carl Schwenk, who is Director of the Research Division and Dr. Karlheinz Thom, Manager of the Plasma Program.

The Conference is being held at a time of ferment in this field especially regarding the possibilities for nuclear pumped lasers. Fundamentals of both electrically and fission generated plasmas have been studied for a considerable time and will be reported at the Conference. Research in gaseous fuel reactors using uranium hexaflouride will be described and their and other partially ionized plasma applications will be discussed.

The members of the Conference Committee are listed on the following page. Their willingness to serve is acknowledged and greatly appreciated. Mr. F. Carl Schwenk is thanked for his luncheon speech entitled FUTURE POWER SYSTEMS IN SPACE and Dr. Theodore B. Taylor, Chairman of the Board of the International Research and Technology Corporation is thanked for his challenging dinner talk NUCLEAR POWER RISKS AND SAFEGUARDS.

The preparation of the papers for this Conference and their presentation are greatly appreciated and the attendance and participation of many prominent workers in the field are recognized as essential to the success of the Conference.

The administrative assistance of the Princeton University Conference Staff and The Aerospace Systems Laboratory is gratefully acknowledged.

Conference Co-Directors:

J. Preston Layton

Jerry Grey

September 1976

LIST OF CONFERENCE COMMITTEE MEMBERS

Conference Chairman
Robert G. Jahn, Dean
School of Engineering & Applied Sciences
Princeton University

Conference Co-Directors
J. Preston Layton
The Aerospace Systems Laboratory
Princeton University

Jerry Grey
Consultant

Conference Editor
M. Krishnan
Department of Aerospace & Mechanical Sciences
Princeton University

Technical Program Committee
Karlheinz Thom, Chairman
Research Division
NASA Headquarters

Kenn Clark
Princeton University

Herbert H. Helmick
Los Alamos Scientific Laboratory

Frank Hohl
NASA Langley Research Center

S. H. Lam
Princeton University

Thomas S. Latham
United Technologies Research Center

Richard T. Schneider
University of Florida

Woldemar von Jaskowsky
Princeton University

Herbert Weinstein
Illinois Institute of Technology

TABLE OF CONTENTS

TABLE OF CONTENTS (Continued)

TABLE OF CONTENTS (Continued)

Welcome

Robert G. Jahn
Princeton University

It is my great pleasure to welcome you all here to this conference on Partially Ionized Plasmas including the Third Symposium on Uranium Plasmas. It is a particular pleasure first of all because I see so many close personal friends and colleagues involved in the program and in the audience; colleagues from both other academic institutions and the industrial sector, and especially our very good body of friends from the space agency. I also find it a particularly happy occasion to welcome you here because of the quality of the program that has been assembled by Karl Thom and his committee. From what could have been a very disparate and polyglot specturm of topics, they have put together a meeting of great interest and considerable coherence. I am looking forward to participating in it as much as I possibly can.

Then, too, it is a meeting which covers a field that we here at the School of Engineering and Applied Science have identified as one of those relatively few areas in which we are going to attempt to have something to say. This has been the case for many years. A significant number of our faculty and a corresponding cadre of research staff and graduate students have worked in the areas that are the concern of this conference for many years, and you will hear from some of them during the course of the meeting.

Also, this subject we are discussing over the next few days is a particularly appropriate one to be aired in an academic institution. It is not a field that has enjoyed by any stretch of the imagination the priorities and the high pressure of some other research activities in this country. We certainly do not compete with the big programs of controlled fusion, defense systems, etc. Notwithstanding, it is an area which has been ripe for good scholarship, for careful and leisurely work, the joy of exploring side avenues and checking allowed alternative possibilities and seeing some substance begin to grow out of this nebulous domain in which we began many years ago. I have the sense right now that the field is coming ripe for some very significant developments out of the basic science, and I hope we see some of that coming to fruition here in the next two or three days.

In addition to satisfaction in the meeting and my hope that you will all share our interest in this program, I hope you will have some fun while you are here and take the opportunity to enjoy our campus and our town and to see the various technical activities here within the school. Thank you all for coming.

Purpose

J. P. Layton
Princeton University

During the past several years a number of new avenues of research on partially ionized plasmas have opened, particularly in the area of fissioning and fission-fragment excited plasmas and in nuclear pumped lasers. Important progress has also been made in the science and technology of uranium hexafluoride cavity reactors. This conference will review past accomplishments, survey current research, and examine future growth of the science, technology and applications in these interesting and potentially important topic areas. Workshop discussions will concentrate on the status in the various areas of this field, including the identification of new research tasks.

As I have observed the field over some period of time, fission plasmas have not received the broad fundamental attention which they deserve. Considerable ground work has been laid, and it is to be hoped that in publishing the proceedings of this conference and in future papers, theses, and articles in archive journals that the topic of fission plasmas and other partially-ionized plasmas will begin to receive the attention that is warranted by the kinds of applications which appear to be offered in a number of future technologies.

Some fields suffer from too much physics. I am not sure that, even with some tongue in cheek, I can offer the fusion field as suffering in that way, but perhaps. Sometimes engineers over-react by rushing in to development efforts involving industry spending of tremendous sums without an adequate technology base or bonifide applications. So far work in fission plasmas hasn't erred in either of those directions, and I hope that it can be kept from such errors. As I have seen research here in the academic thicket at Princeton for 25 years, a much closer working relationship between practitioners in the basic sciences and those employing the engineering approach is highly desirable. Engineers also have to get a broader understanding of their overall responsibilities in bringing new technologies into use than they have had in the past.

I have been a missionary for systems analysis, particularly of the broad and parametric sort, for a number of years and have found there are a lot more savages than there are missionaries. However the way to nirvana is undoubtedly as hard on the savages as it is on the missionaries. It is my purpose to urge the need to pursue the overall topic of partially ionized plasmas from both basic science and technology standpoints, but it also needs to be tied together in an analytical way from the systems and applications viewpoints. It is hoped that this field will move toward its applications with better balance than has been evident in many fields involving sophisticated science, high technology and expensive developments.

I offer Figure 1 as presenting an essential

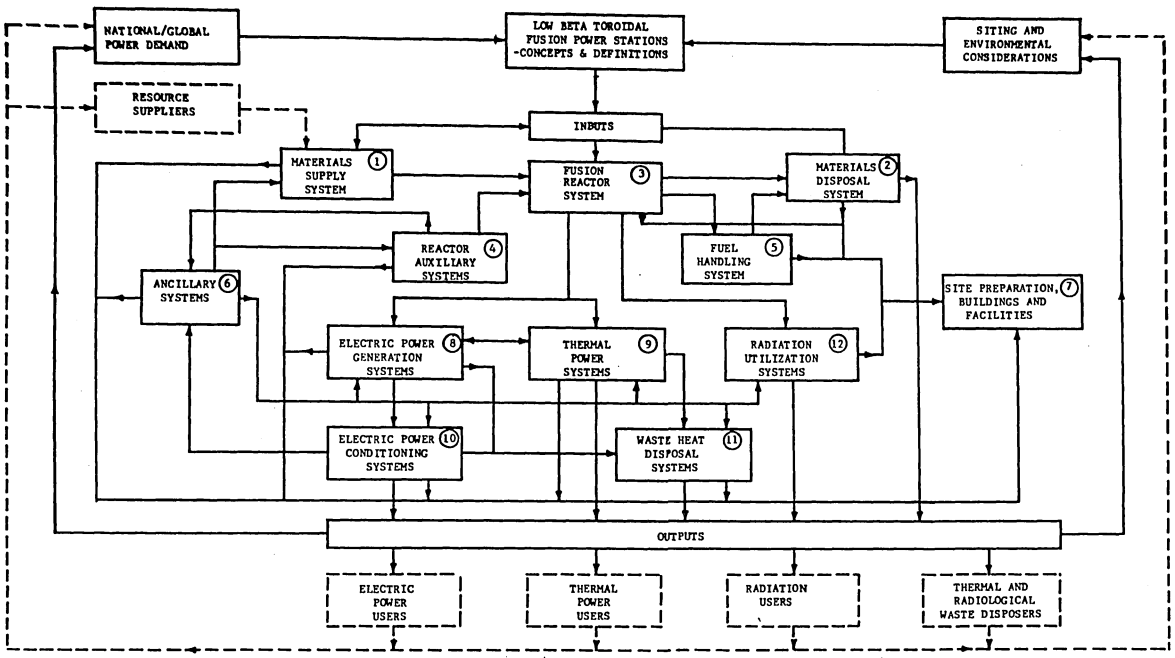

Figure 1 General Purpose Block Diagram for Tokamak Fusion Power Stations

message in how to consider an overall system. This is a sheet that we made up in The Aerospace Systems Laboratory (TASL) here at Princeton when we were undertaking the parametric systems analysis of fusion power stations. It attempts to identify an economically and environmentally viable station as the whole system. The point is that the fusion reactor system at the center has to derive inputs from and is dependent on the concept and definition of all the other systems that make up the station, as well as on the demand and other considerations to provide outputs of value to prospective users. This approach needs to be applied to partially ionized plasma systems at the same time that basic feasibility is being resolved to assist in planning the research and technology programs and in identifying the economic applications.

Methodologies are available for reducing the block diagram of Figure 1 to an overall parametric systems analysis basis. The TASL approach to the analysis of nuclear fusion systems is shown in Figure 2. The interdependence and interaction

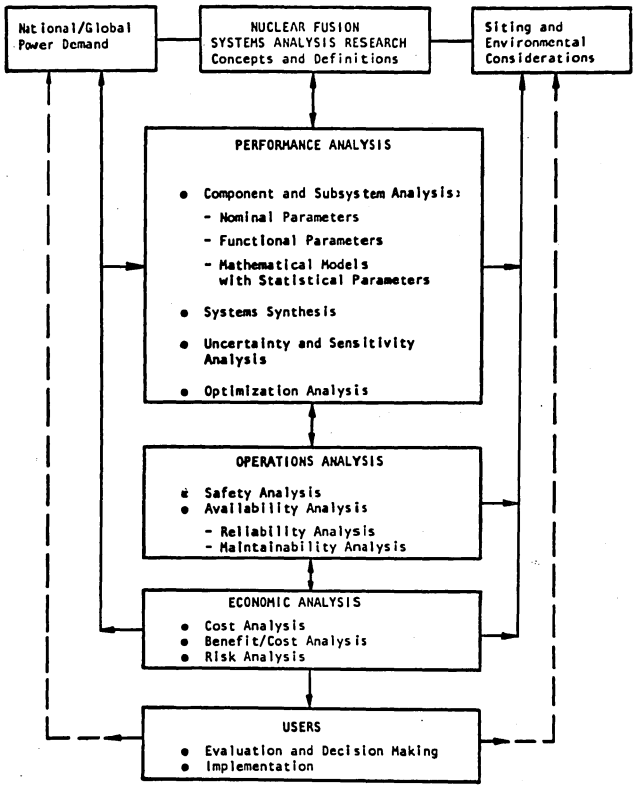

Figure 2 TASL Approach to the Analysis of Nuclear Fusion Systems

between the three primary analytical concerns - performance, operations and economics are indicated as well as the feedback to the power demand and other considerations such as the environment in the concepting and definition of the overall system and its components.

Figure 3 shows how the parametric performance of a typical thermodynamic system can be handled by preparing physically based mathematical models

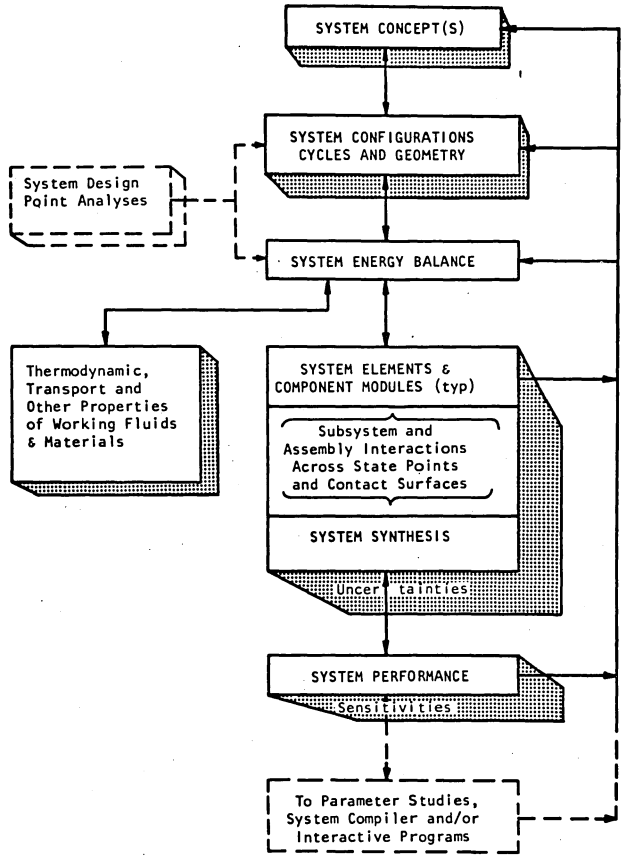

Figure 3 TASL Approach to the Parametric Performance Analysis of a Typical Thermodynamic System

for computer analysis and relating them to reality by reference to existing point designs. Any analysis of future technology is essentially uncertain and therefore probabilistic. A method for handling uncertainty in parametric systems analysis is presented in Figure 4. Although the amount of data required is substantial such an analytical process is ultimately necessary to provide proper benefit/cost and risk analyses needed by a decision maker before proceeding with large scale and very expensive developments. Fortunately, the entire process does not need to be activated at the outset since much can be, and needs to be, learned from simple and partial analyses while the basis for the final analysis is being established.

I will not at this time belabor these points by a more detailed discussion. My purpose was to argue that much work lies ahead - conceptual, analytical and experimental before major systems based on partially ionized phasmas are realized. It is the purpose of this conference to examine where the field stands at the present time and to project a course for the future.

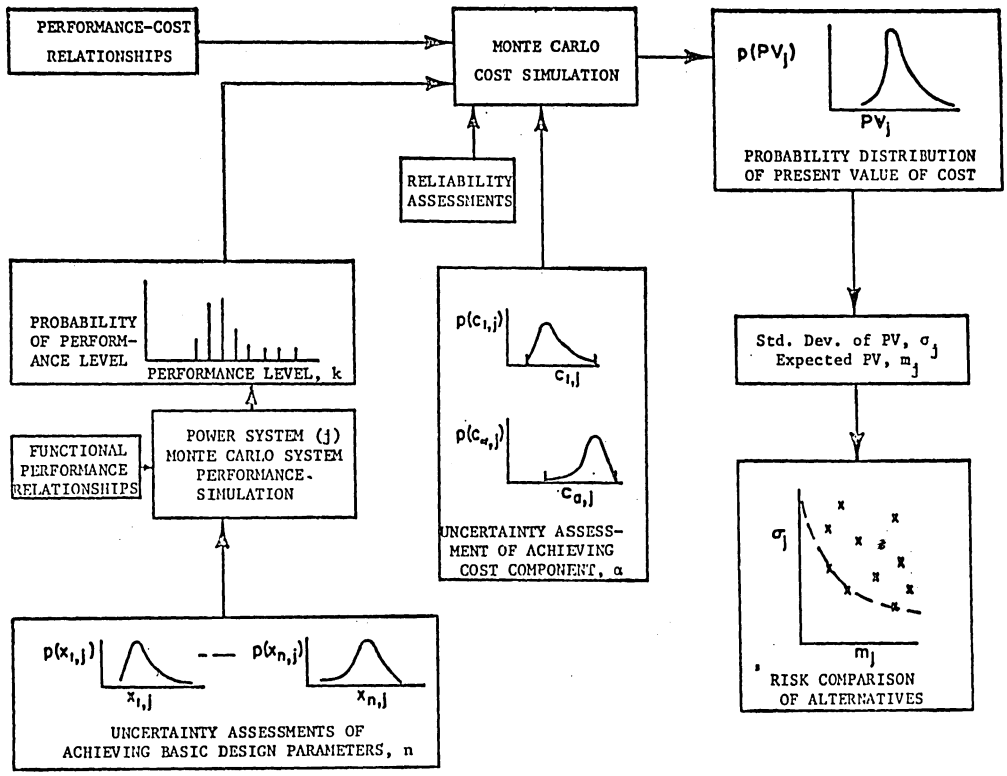

Figure 4 Method of Handling Uncertainty in Parametric Systems Analysis

Background

Jerry Grey
Consultant

This conference has two major branches of effort: one is in electrically-generated plasmas and one is in fission-generated plasmas. These are the subjects of the first two sessions. A third area, not covered at this conference, is combustion-generated plasmas (seeded or not) which have been principally considered for MHD systems.

Although the electrically-generated and fission-generated plasma technologies have enormously disparate backgrounds, as Dean Jahn mentioned earlier, the modern concepts dealt with in this conference both started about the same time: the late '40's and early '50's. The first paper on fission-generated plasmas was published by Shepherd and Cleaver in 1951, although there was considerable discussion before that time in the '40's. In that field, incidentally, the most extensive literature coverage appeared in the first two symposia on uranium plasmas, of which this one is the third. Those two volumes, both of which came out in the early part of this decade, constitute an excellent background in the field.

In electrically-generated plasmas, there is an enormous electrical engineering literature, dealing primarily with switching arcs. Classical texts such as Cobine were published some time ago. The modern science and technology of the subject of this conference, partially ionized dense plasmas, came about with the proliferation of thermal arcjets which occurred sometime in the '50's. There was a major growth in that field in the late '50's and early '60's.

In each of these two primary branches there were two major-sub-branches, giving four almost different topics to discuss. In the fission area, there are the open-cycle concept and the closed-cycle concept. In electric generation, we have steady and pulsed generation of plasmas.

Looking first at electrically-generated plasmas, in the steady state area, I will deal only with relatively modern developments. The first real push was in the commercial applications of resistance-heated gases. Although induction heating technology existed at that time, the companies in the field such as Giannini, Thermal Dynamics, Humphreys, and Linde were principally concerned with commercializing this new science and technology as rapidly as possible using resistance-heated plasma devices. There was a fair amount of growth in the fields of plasma spraying, welding, and cutting (replacing oxy-acetylene torches), and also in the development of an effective research tool for those who wanted to study very high temperature partially ionized plasmas.

The most advanced work in this field was done principally in the testing area, and the most elaborate tools for generating and studying steady state arc-heated plasmas were those developed for simulation of atmospheric reentry, which was one of the key technical problems in the rapidly-growing space program. The only way one could simulate reentry was to generate the equivalent stagnation temperatures, and the best way to do this was with a controlled atmosphere using electrically-heated gases. Some elaborate wind tunnel facilities were built up at WPAFB, AEDC, Ames and other centers, culminating in the enormous 50-megawatt electric tunnel developed and built at Wright Field in the late '60's. These facilities still exist; they are still quite actively used and continue to develop.

During this time, also, there was considerable interest in continuous arc-jet capabilities for space propulsion. Here AVCO was the spearhead, although some early work was done by Giannini and a number of other laboratories, including NASA and the Air Force. There is a current resurgence of interest in thermal arcjets for propulsion, despite their relatively low efficiency compared to some of the others, and whether or not this develops is a matter for resolution in the near future.

Most of the work on these steady state plasma generators was done in gases. Air was particularly useful for the simulation of reentry, but a lot of work was done in nitrogen in the commercial arc-jets and also in wind tunnels, as well as argon and helium for convenience in basic research. For propulsion, hydrogen was the principal gas.

During this time, however, there was some interest in developing higher conductivities by the use of potassium and other seeds. There was also a fair body of work in the alkaline metals, lithium in particular, at Los Alamos and Langley. Toward the end of this era the development of inductively-heated plasmas, particularly useful for simulating fission plasmas, began to accelerate.

In the pulsed plasma area, the early technology was developed by Winston Bostick at Stevens Institute of Technology in his plasmoid experiments. A propulsion effort at Republic Aviation formed the early engineering phase of these devices, but by far the bulk of the technology and the literature was developed here at Princeton under Dr. Jahn's direction.

In the fission-generated plasma area, all the early work was propulsion oriented. The concept of a new high-thrust, high-specific

impulse rocket technology for space flight was the motivating factor. The open cycle was earliest; preliminary work was directed at some form of containment, or separation of the fissioning plasma material from the propellant; that is, uranium is a poor propellant and hydrogen is a good one, and so one would like to generate energy in the uranium and exhaust only the hydrogen.

The earliest studies were based principally on stabilized vortex separation; e.g., theoretical analyses by Kerrebrock, Meghreblian, Rosenzweig, Easton and Johnson, and Grey, The effort began to expand significantly only with the introduction of the coaxial reactor concept, which Weinstein and Ragsdale suggested in an American Rocket Society paper around 1960. The program then grew rapidly under Frank Rom's direction at NASA's Lewis Laboratory, extending to a number of laboratories around the country. These studies were reviewed in a comprehensive series of papers, mainly by Rom and Ragsdale, in the mid-'60's and early '70's.

The principal effort continues to remain in fluid mechanics and heat transfer: the basic problems of containment and how to heat the propellant fluid without burning up the walls of the rocket engine and nozzle. These are covered in a survey paper by Herb Weinstein.

The early studies were mainly cold flow simulation, which led to the spherical geometry that has been examined in most detail. Hot-flow simulations used induction heated plasmas, which simulate the active heating of a plasma while it is simultaneously being cooled by the propellant, modeling the open-cycle system more effectively. These studies were done by the TAFA division of Humphreys. Ward Roman brings this effort up to date by describing the current United Technologies Research Center program.

There were extensive and extremely capable heat transfer studies performed, particularly in the radiation field, principally by United Technologies and Lewis researchers. They developed an extensive and basically new technology in dense plasma radiation characteristics. The current approach is to be all-inclusive, to look at all the possible energy contributions, as is described in a paper by Smith, Smith and Stoenescu.

One of the key elements in absorbing radiated heat transfer in hydrogen in certain important ranges of the spectrum was by seeding the gas with tungsten or graphite particles. A number of capable studies, both theoretical and experimental, were done in this field, the experimental work mainly by Chester Lonzo at Lewis in the mid-'50's, and most of the theoretical work at United Technologies. There were also significant contributions by Georgia Tech and the University of Florida.

There was fairly extensive study in the nucleonic area. Nucleonic criticality was one of the essential elements. The early cavity reactor studies by George Safonov in the early '50's were rudimentary, but the essential consideration of nucleonic criticality was extended rapidly by such people as Carroll Mills at Los Alamos. There was extensive experimental simulation of the plasma core system by Kunze and his collaborators at Idaho in the mid to late '60's, using uranium foils distributed throughout a cavity to simulate the hydrogen plasma, which gave some substance to the nucleonic calculations.

The first basic problem with the fissioning plasma-core system, aside from the question of fundamental feasibility, was that all of the concepts were too big. To get nuclear criticality in a plasma core, it was necessary to use dimensions of the order of several meters as well as very high pressures, giving rise to systems of enormous mass.

The second basic problem was that as the volume got bigger, so much energy was deposited in the walls and in the solid structure that it couldn't all be absorbed by the inflowing propellant. It was necessary to have some external method of "dumping" the excess energy. A radiator was first suggested by Meghreblian around 1960, and then as the systems concepts matured, it appeared that radiation of external heat was going to be necessary.

Two relatively recent developments attempted to cure these problems. The first was Hyland's concept, published in 1970. Instead of depending totally on the plasma core itself for criticality, Hyland placed some solid fuel elements in the reflectors which surrounded the cavity to generate a substantial fraction of the total reactor energy. This allowed him to shrink his reactor down to a dimension of somewhat less than a meter and made the system look a little more practical. However, it aggravated the second problem; that is, even more heat was now generated in the solid material, and therefore much more energy had to be extracted by external systems. A method for utilizing that external energy, developed by Layton and Grey some time ago, is the dual mode concept which Stanley Chow discusses in his paper.

The major efforts in plasma-core technology terminated with the demise of the NASA nuclear program in 1973. The feasibility of neither the open cycle nor the closed cycle concepts had yet been developed; that is, the basic feasibility of containment and ability to operate as a system. The remaining work in the field, which is the subject of this conference, has been supported primarily by NASA's research division.

The other basic approach to plasma-core utilization was the closed cycle. The concept of using a completely closed containment system to hold the uranium plasma and separate it from the hydrogen was actively pursued by McLafferty's

group at United Technologies. This idea of using a fused silica container surrounding the plasma region and transmitting energy totally by radiation from the plasma region to the hydrogen was an obvious outgrowth of the problems associated with the hydrodynamic and other containment problems of the coaxial flow concept. The basic problem was radiation heating in the fused silica and how to avoid it. One approach, stabilization of the vortex flow necessary to produce a convective separation of the hot gases from the vortex, saw a great deal of excellent fluid dynamics research, as well as the radiative heat transfer work cited earlier. Recent studies in these areas are reported by Krascella, by Blue and Roberts, and by Levy.

In addition to the two basic coaxial-flow and closed-cycle ("light-bulb") concepts, there are also a number of other approaches. The magnetic and electric body-force containment concept was studied very early, by Gross and others. The idea of using MHD-driven vortices was examined by Romero and several others. There was serious consideration for some time of the plasma core reactor as a source for MHD power. Principal studies were by Rosa, and more recently by J. R. Williams at Georgia Tech. There is currently a resurgence of interest in this application.

This leads us into the next phase: what is going on today and what areas are most fruitful for exploration? First of all, there seems to be a renewal of interest in the whole propulsion/power application for fission plasmas and for electric propulsion. Schwenk provides an introduction to and a summary of that subject.

A major recent effort has been the use of fission-generated energy for stimulating lasers. There are a number of papers on this topic. There is also a major effort underway in uranium hexafloride utilization as a research tool, the subject of another series of papers.

There are a host of potential new applications. The energy crisis fostered the dragging out of all the old dogs to take a new look at them and see if there are any new applications. There are some interesting new applications in space, as discussed in detail in several papers. These will be elaborated upon in the workshop sessions, which have the purpose of setting the stage for a whole new era of partially ionized plasma research and applications based upon the growing interest and the active research effort that is going on today in a number of new directions.

ADDITIONAL COMMENT BY CARL SCHWENK

Since 1973 our program has become more basic. That has been an advantage to us. We have given the idea of the UF_6 plasma a lot more attention because of several factors. It might just be the most useful form of a fissioning gas, and it certainly is a lot easier to work with. In addition to the experimental advantages it gives, it may also be a very attractive energy source.

ON THE EMISSION MECHANISM IN HIGH CURRENT HOLLOW CATHODE ARCS*

M. Krishnan+
Princeton University
Princeton, New Jersey

Abstract

Large (2 cm-diameter) hollow cathodes have been operated in a magnetoplasmadynamic (MPD) arc over wide ranges of current (0.25 to 17 kA) and mass flow (10^{-3} to 8 g/sec), with orifice current densities and mass fluxes encompassing those encountered in low current steady-state hollow cathode arcs. Detailed cathode interior measurements of current and potential distributions show that maximum current penetration into the cathode is about one diameter axially upstream from the tip, with peak inner surface current attachment up to one cathode diameter upstream of the tip. The spontaneous attachment of peak current upstream of the cathode tip is suggested as a criterion for characteristic hollow cathode operation. This empirical criterion is verified by experiment.

Cathode cavity conduction processes are commented on briefly; the emission processes at the cathode surface are examined in some detail. It is shown that thermionic emission cannot account for the observed current in such MPD discharges. Field emission from micro-spots moving rapidly over the cathode surface is shown to be a possible primary emission mechanism in such cathodes. Possible enhancement of the emission due to the photoelectric effect is also investigated. From order-of-magnitude considerations, it appears that a form of field-enhanced photoelectric emission can account for most of the observed current in the MPD hollow cathode, thus suggesting a possible novel emission mechanism for other hollow cathodes. The emission model preferred has not been experimentally verified.

I. Introduction

Since the early part of this century, the precise nature of the electron emission from cathode surfaces in arc discharges has been the subject of considerable theoretical and experimental investigation. Despite this effort, in many types of arcs, satisfactory theories do not exist for the cathode surface electron emission processes. One such poorly understood arc is the hollow cathode arc.

Hollow cathodes were first used to advantage by Paschen[1] as early as 1916 in spectroscopic studies where such cathodes were shown to be capable of simultaneously providing high electron number density and relatively low temperature ions and neutrals in an essentially field-free cathode cavity. More recently, hollow cathodes have been used as electron emitters in advanced ion thrusters where they exhibit longer lifetimes than oxide coated or liquid metal cathodes.[2] As sources of dense, highly ionized plasma, hollow cathodes have also been investigated at the Oak Ridge National Laboratory and at the Massachusetts Institute of Technology. These researchers point out the important features of a hollow cathode discharge:[3]

(a) the discharge creates a very pure external plasma (low contamination by cathode material,) dense, ($n_e \sim 10^{13}$-10^{14} cm^{-3}) and highly ionized (up to 95%);

(b) the cathode enjoys a reasonably long lifetime, despite high current densities and high cathode wall temperatures (> 2500°K).

An important part of hollow cathode research dealt with the study of the noise oscillations of the discharge[4], since it was interesting to evaluate the possibilities of using hollow cathode arcs as a source of quiet plasma for experimental work on wave propagation. Hollow cathodes were also studied extensively in Europe in the nineteen sixties [5,6]. Large hollow cathodes are currently finding applications in high power lasers[7] and in the production of high power neutral beams for plasma heating in controlled thermonuclear fusion reactors.

Despite the fairly exhaustive studies conducted at these various research establishments on the influence of the various parameters (geometry, gas flow rate, current, external pressure, axial magnetic field strength, electrode temperature, etc.) on the performance of the hollow cathode discharge as an efficient source of dense, highly ionized plasma and as an efficient, long lived electron emitter, the physics of processes inside the cathode cavity are still poorly understood. One major reason for this lack of understanding is that the typical cathode dimensions of most of these researches are so small (0.1 to 0.3 cm. inner diameter) as to preclude detailed diagnostic probing of the cavity interior. Such diagnostic probing is essential to identify the dominant physical processes of emission, ionization and conduction inside the hollow cathode cavity. In the few instances where large hollow cathodes have been used, the high energy levels of a steady-state arc discharge are in themselves not conducive to the use of simple diagnostics.

There is therefore a strong motivation for the detailed diagnostic study of a large diameter hollow cathode in a relatively low energy environment. The MPD arc facility at Princeton (Fig. 1.) is ideally suited to such an endeavor for two reasons:

(a) the large cavity dimensions permit the detailed study of the plasma by probing, photographic and spectroscopic observations.

(b) the total energy content of pulsed, quasi-steady MPD discharges is low enough to permit the use of small diagnostic probes of simple construction, with no cumbersome heat shielding required.

This paper describes the results of detailed measurements made inside the cavity of large (2-cm-diameter) hollow cathodes, over a wide range of

*This work supported by NASA Grant NGL-31-001-005.

+Now at Mason Laboratory, Yale Univ., New Haven, CT.

currents and mass flows as stated above. In section II the experimental apparatus and diagnostic techniques are briefly described. Section III summarizes the major experimental results. Section IV begins an analysis of the cathode surface emission processes by examining thermionic emission. In section V field emission from the cathode surface is discussed. The third possible emission mechanism, photoelectric emission, is examined in section VI, followed by a summary in section VII.

II. Experimental Apparatus

The quasi-steady MPD accelerator with a hollow cathode is shown schematically in Fig. 1. Argon propellant (at feed rates from 10^{-3} to 16 g/sec) is injected into the discharge chamber through a fast-acting solenoid valve fed from a high pressure reservoir. The gas can enter the discharge chamber either through the hollow cathode, or through six outer injectors set in the insulating plexiglas backplate, or through both.

Current to the discharge is supplied as a fast risetime (< 5 μsec) flat-top pulse typically of 1 msec duration by an 84 station LC-ladder network.[8] Charged typically to 4 kV, this 35 kJ network (with a total capacitance of 2.2 mfd) provides, when discharged through a variable impedance[9] in series with the accelerator, currents from as low as 0.25 kA up to 17 kA.

The cylindrical arc chamber is 12.7 cm in diameter and 5.1 cm deep. The hollow cathode is located on axis, screwed into an insulating circular plexiglas backplate. The coaxial annular aluminum anode, displaced slightly downstream from the cathode tip, has an i.d. of 10.2 cm, an outer barrel diameter of 18.8 cm, and a thickness of 1 cm. The particular hollow cathode dimensions and geometry are noted in the subsequent text where appropriate.

The plasma formed in the discharge chamber during every (∿ 1 msec) firing of the discharge exhausts into a glass bell jar vacuum tank with an i.d. of 45 cm, 76 cm long, evacuated to some 10^{-3} torr prior to each discharge by a mechanical pump. A probe carriage mounted inside the tank, controllable in two dimensions from outside the tank, allows detailed probing both inside and outside the hollow cathode.

The self-induced magnetic field everywhere within and about the hollow cathode is measured by an induction coil with an i.d. of 0.05 cm and an o.d. of 0.3 cm, wound from 350 turns of #44 magnet wire. The magnetic probe signal, proportional to dB/dt, is passively integrated through a 10 msec RC integrator and displayed on a Tektronix 551 oscilloscope. At very low currents, the rather low magnetic field signal from the integrator is boosted by a Tektronix AM502 differential amplifier, with gain selection from 10^2-10^5, before being read on the oscilloscope.

A single Langmuir probe, consisting of a cylindrical tungsten wire 0.025 cm in diameter, imbedded in a quartz tube of o.d. 0.02 cm with only the end face of the tungsten exposed to the plasma, is used to measure plasma floating potentials.

In addition to spectral photography of the discharge with interference filters, emission spectra from the hollow cathode discharge were obtained using a Steinheil GH glass prism spectrograph which recorded radiation over the spectral interval from 4200 Å to 6200 Å.

III. The Search for Hollow Cathode Operation in Large Hollow Cathodes

1. Uninsulated Hollow Cathodes

In the first phase of the experiments, the hollow cathode was uninsulated, so that current attachment could occur on the outer cylindrical surface, face, or inner cavity of the cathode. The purpose of these experiments was to determine whether hollow cathode operation, with preferential current attachment inside the cathode cavity, could be obtained in large hollow cathodes in an MPD arc. For typical MPD discharge currents of kiloamperes, the orifice diameter of the cathode (∿ 1 cm) was chosen such that two arbitrary scaling parameters, a mass flux m/s and a current density J/s, where s is the cathode orifice area, were comparable to typical mass fluxes and current densities in low current, steady-state hollow cathode arcs. A typical uninsulated cathode is shown in Fig. 2a. The cavity dimensions are noted on the figure.

With this hollow cathode, when argon gas was injected both from inside and outside the hollow cathode to the discharge, current attachment occurred predominantly from the face and outer surface of the cathode, with no visible plasma formation inside the hollow cathode, as shown in Fig. 3. Fig. 3a shows the camera perspective used in photographing the 16 kA, 12 g/sec discharge through a 4880 Å Ar II narrow bandwidth interference filter. Fig. 3b shows clearly that the luminous regions of the discharge are outside the hollow cathode cavity, while the cavity itself appears quite dark.

Even when gas was injected solely through the hollow cathode, magnetic field measurements revealed that there was negligible current attachment inside the cathode cavity. Fig. 4 shows enclosed current streamlines in and about the hollow cathode cavity derived from the magnetic field measurements for a current of 29 kA, at a mass flow of 0.3 g/sec. The figure shows that a mere 3% of the 29 kA discharge penetrates the cavity under these operating conditions.

These early experiments indicated that merely installing large hollow cathodes in an MPD arc does not guarantee significant current attachment inside the cavity, accompanied by formation of a stable cavity plasma. A careful search was therefore required to identify specific operating conditions under which the discharge would spontaneously emanate from within the cavity. To facilitate this search, it was decided to insulate the face and outer surface of the hollow cathode, thereby forcing the current to attach inside the cavity. Under conditions of 'forced' plasma formation within the cavity, controlled variation of three key independent variables, cathode geometry, mass flow rate, and discharge current, might then lead to the empirical identification of necessary conditions for characteristic hollow cathode operation in MPD arcs. The validity of such empirical criteria, if identified, could easily be tested by removing the insulation of the hollow cathode; to observe whether, under these specified operating conditions, the discharge now preferentially emanates from the cavity interior,

in spite of the available external conducting surface.

2. Insulated Hollow Cathodes

a. Effects of Cathode Geometry Changes. In the first series of experiments with fully insulated hollow cathodes, two of the independent variables, current and mass flow, were fixed, and the effects of cathode geometry changes on the cavity discharge were examined. For all insulated cathodes, gas was injected only through the hollow cathode to the discharge, with the outer injector orifices sealed.

The first question to be answered was whether by forcing current attachment inside the cavity, a stable discharge could be maintained in these large cathodes. Current and potential distributions were measured inside the cavity of hollow cathode HC VIII, shown in Fig. 2e, and were found to be quasi-steady and azimuthally symmetric. The surface current distribution, for J=7 kA, $\dot{m}$=4 g/sec, was determined by translating the magnetic probe axially upstream from the cathode tip at a radius of 0.8 cm, with the 0.3 cm-diameter probe touching the cathode inner surface. This surface current distribution, drawn normalized by the enclosed current at the cathode tip, is shown as the dashed curve in the upper half of Fig. 5. For reference, HC VIII is shown in cross-section at the top of the figure.

The surface current density profile, deduced from the enclosed current profile[9], is shown as the heavy line in the upper half of Fig. 5. It should be noted that the peak current density (> 1 kA/cm^2 at this operating condition), occurs at the cathode tip.

The lower half of Fig. 5 shows floating potentials on the hollow cathode axis obtained using the Langmuir probe. The potential profile shows that coincident with the region of high current density current attachment is a region of weak axial potential gradient, < 10 V/cm.

To obtain further information on the physical processes occurring in the hollow cathode, a few near-infrared spectrograms of the discharge were recorded using another insulated cathode, designated HCI, shown in Fig. 2b. The near infrared spectral region contains a number of strong neutral argon lines which are more readily identifiable than those neutral lines in the visible part of the spectrum, since the latter tends to be dominated by ionized argon and impurity lines. Fig. 6 compares the spectral interval from 6500 Å to 8600 Å for the uninsulated hollow cathode in the 29 kA, 0.3 g/sec discharge with that for the fully insulated cathode, HCI, at 7 kA and 4 g/sec. Both spectrograms were recorded looking directly upstream into the cavity along the axis. Fig. 6a shows that the distribution of radiance of the spectral lines does not reflect any of the cathode geometric features despite the measured 0.8 kA (see Fig. 4) attaching inside the cavity for this 29 kA, 0.3 g/sec condition. The AI lines are barely discernible inside the cavity and there is no continuum radiation.

In dramatic contrast, the spectrum of the fully insulated cathode discharge shows a sharply defined continuum in the cavity with AI and AII lines brightly superimposed on it (Fig. 6b). There is very little radiation recorded beyond the cavity at this exposure, with a high level of radiant flux emanating from the cavity.

Having satisfactorily obtained a quasi-steady azimuthally symmetric discharge inside large hollow cathodes by forcing the current to attach inside the cavity, the effects of cathode geometry variations could now be examined. Some of the many cathode configurations examined are shown in Fig. 2b, c, d, e, f, g and h. As shown in the figure, different tip geometries as well as different inner electrode shapes were examined. In particular, the conical configurations, Fig. 2f, g, may be considered as steps in the transition from a hollow cathode with a cylindrical cavity to a solid electrode with a flat face.

Despite these many drastic changes in cathode geometry, the measured current and potential distributions inside the cavity of these hollow cathodes, at fixed current, 7 kA, and mass flow, 4 g/sec, are all nearly identical to those shown for cathode HC VIII in Fig. 5. The characteristic features of high current, high mass flow hollow cathode operation that emerge from these studies are described elsewhere[10] in detail. They can be summarized as follows:

(a) For all insulated configurations, the discharge current attaches to the downstream portion of the cavity with a peak surface current density at the cathode tip in excess of 1 kA/cm^2. The region over which 80% of the current attaches is 0.6 cm long, coincident with a weak central axial electric field of less than 10 V/cm.

(b) measured radial profiles of floating potential inside the cavity indicate that the bulk of the potential drop occurs near the inner cathode wall, while the cavity interior is nearly field-free.

Due to the insensitivity of the details of the current and potential distributions inside the hollow cathode cavity to changes in cavity geometry at fixed high values of current and mass flow, it was decided to select one particular cathode that was most amenable to diagnostics, and to study this cathode for wide variations in the other two independent variables, current and mass flow. The cathode design selected, designated HC XII, is shown in Fig. 2h.

b. Effects of Current and Mass Flow. For the fixed cathode geometry HC XII, current and potential distributions inside the cavity were measured over as wide a range of currents and mass flows as possible[9] with the given experimental facility. Local measurements of magnetic field and floating potential inside the cavity were made for currents from as low as 0.25 kA up to 17 kA, with mass flows from 10^{-3} up to 16 g/sec.

Fig. 7 shows the surface current density profiles, obtained from magnetic field measurements[9], at various mass flows from 5 x 10^{-3} up to 0.4 g/sec in HC XII, with the current in all cases fixed at 0.25 kA. From these current density distributions, three characteristic features emerge:

(a) As the argon mass flow is reduced from 0.4 g/sec to 0.1 g/sec, the peak in the surface current density moves from 0.3 cm to 1.9 cm upstream of the cathode orifice. Over this same range in mass flow, the length of the

cathode (measured from the end) over which 80% of the input current is found to attach to the surface, increases from 0.7 to 2.2 cm.

(b) Correspondingly, the current attachment at the surface becomes more diffuse, leading, for a fixed current, to a drop in the peak current density.

(c) Further reduction in mass flow from 10^{-1} g/sec to 5×10^{-3} g/sec causes the peak in the current distribution to move downstream towards the open end of the cavity.

Fig. 8 shows surface current density profiles for a fixed, higher current of 0.9 kA and mass flows from 5×10^{-3} g/sec to 8 g/sec. Here, just as at 0.25 kA, the current density peak moves first upstream from the cavity end and the current attachment becomes more diffuse as the mass flow is reduced, from 8 to 6.6×10^{-2} g/sec. Again, still further reduction in mass flow, from 6.6×10^{-2} to 5×10^{-3} g/sec, causes the peak current density to then move downstream towards the cavity end. However, the maximum peak penetration at the higher current is only 0.9 cm, compared to a maximum peak penetration of 1.9 cm at the lower current of 0.25 kA.

Fig. 9 shows similar surface current density distributions for a high current of 4.7 kA. At this high current, unlike at the lower currents, the current density distributions are observed to be quite insensitive to changes in mass flow. For all mass flows, the peak current density occurs between 0 and 0.3 cm from the cavity end, and, in all cases 80% of current attachment to the surface occurs over a length of 0.9 cm from the cavity end.

The data presented in the preceeding three figures may be cross-plotted to demonstrate the effect of discharge current on the cavity current distributions as shown in Fig. 10. Here, for a fixed mass flow of 0.2 g/sec, the surface current distributions are plotted for three currents. These distributions are shown normalized by the peak current density in each case to facilitate their comparison on a linear scale. The figure shows that as current is increased from 0.25 to 4.7 kA, the peak current density moves nearer the cavity end, while current attachment occurs over shorter cathode channel lengths. To examine whether this trend continues to still higher currents, the surface current distribution was measured for a current of 17 kA. This distribution, also shown in Fig. 10, shows that the peak current density occurs still nearer the cathode tip with a shorter cathode length (0.8 cm from the orifice) used for 90% current attachment to the surface.

The length of the cathode cavity over which 90% of current attachment to the surface occurs is defined as the active zone length of the cavity. Fig. 11 summarizes the surface current density measurements by graphing active zone length against mass flow rate, with discharge current as a parameter. The surface current density distributions, characterized by an active zone length, are seen to be most sensitive to changes in mass flow at the lowest current (0.25 kA), becoming least sensitive at the highest current (4.7 kA). The maximum penetration of current into the hollow cathode decreases as the current is increased from one cathode diameter at 0.25 kA to approximately one-tenth of the cathode diameter at 4.7 kA.

The experiments described above reveal significant changes in surface current conduction with changes in current and mass flow. To obtain a more comprehensive picture of the energy deposition patterns inside the volume of the cathode cavity, these surface measurements were supplemented by complete maps of magnetic field and floating potential throughout the volume of the cathode cavity.

Fig. 12 shows, on a cross-sectional view of cathode HCXII, contours of constant current and constant floating potential at a fixed current of 0.25 kA for mass flows of 0.4 g/sec (upper part of figure) and 0.1 g/sec (lower part of figure). At this current of 0.25 kA, Fig. 7 shows that these mass flows represent extremes in the penetration of current into the cathode cavity.

For both mass flows, the equipotential lines are approximately radial in the bulk of the cavity plasma, implying a negligible radial field in the volume of the cavity. In addition, the potentials show a weak axial field of less than 4 V/cm. Since the cathode itself is the zero volt equipotential in both cases, all the radial equipotential contours must bend parallel to the surface somewhere close to it before leaving the cavity. If the potentials bend within the debye sheath separating surface from quasi-neutral plasma, high radial fields ($\sim 10^6$ V/cm) would exist at the surface. The implications of such fields for surface emission processes are discussed later.

From the intersecting grid of current and potential lines, the power density, $\underline{j}\cdot\underline{E}$, in any volume segment of the plasma can be easily determined. The results of this computation are graphed in Fig. 13a, b which show power density as a function of axial position within the cavity, with radius as a parameter. For both mass flows it is observed that the power density profiles near the surface are qualitatively similar to the current density profile measured at the same radial position. Furthermore, in both cases the power density profile retains its form well into the plasma, thus corroborating the significant difference in cavity current penetration inferred earlier from the surface current density measurements.

In summary, by forcing the current to attach inside the hollow cathode cavity, the search for hollow cathode operation in large hollow cathodes in the MPD arc has revealed that the current attaches to the surface in one of two characteristic distributions of surface current density:

(a) At high currents, high mass flows or at very low mass flows, the peak current density occurs at or very near the cathode tip and the bulk of current attachment to the surface occurs within a limited axial region upstream of the cathode tip. This mode of current conduction is characterized as forced current attachment inside the cavity.

(b) For lower currents, at intermediate mass flows, the peak current density occurs measurably upstream of the cathode tip, and a longer length of cathode surface is utilized for current attachment, resulting in more diffuse current conduction at the surface. The spontaneous attachment of current at a point upstream of the cathode tip might be construed as being truly characteristic of

hollow cathode operation, wherein physical processes peculiar to the cavity determine the particular choice of location along the inner cathode surface from which most of the current is conducted.

The first of the above two hypotheses has already been tested in the early experiments with uninsulated hollow cathodes. As shown in Figs 3 and 4, when the current is high (7 kA) then for both mass flows of 6 g/sec and 0.3 g/sec, there is negligible current attachment within the cavity, the bulk of current prefering to attach to the exposed face and outer surface of the hollow cathode. Since there is negligible spontaneous cavity current attachment under these conditions, it is evident that upon insulating the face and outer surface of the cathode, at similar conditions of high current (4.7 kA) and mass flows (4 g/sec and 0.4 g/sec), the current is being forced to attach inside the cathode cavity, with a "forced" current density distribution as shown in Fig. 9. The test of hypothesis b) above, is described in the next section.

3. Characteristic Hollow Cathode Operation

An empirical criterion for characteristic hollow cathode operation in an MPD arc is that the peak surface current density spontaneously occur upstream of the cathode tip along the inner cylindrical surface, as for example, at J=0.25 kA, $\dot{m}$=0.1 g/sec, in Fig. 7. To test this criterion, the insulation on the face and outer surface of cathode HC XII was completely removed, and at the same operating condition of J=0.25 kA, $\dot{m}$=0.1 g/sec, the surface current distribution inside the cavity for this uninsulated cathode was measured. This distribution is shown as the heavy line in Fig. 14a. Also shown in the figure as a dashed line is the measured surface current distribution for the insulated version of the same cathode at the same current and mass flow. The two distributions are normalized by the peak current density in either case. The strong similarity between the two distributions demonstrates that, when the current and mass flow inside the cathode are properly adjusted for a given cathode geometry, the discharge does prefer to run from within the cavity interior in spite of the available external conducting surface.

To supplement the current measurements inside the cavity, photographs of the discharge were also taken for the uninsulated cathode at J=0.25 kA, $\dot{m}$=0.1 g/sec. A typical photograph, taken without any spectral filtering and time-integrated over the discharge duration, is shown in Fig. 14b. The radiance outside the cavity is so low at this exposure that the cathode is not visible at all. To provide a sense of perspective, the discharge was first photographed as in Fig. 14b and then, illuminated by a spot lamp, the discharge chamber was imaged on the same film, using different camera settings. A typical double exposure is shown in Fig. 14c. Figs. 14b, c, show that the discharge radiance emanates predominantly from the cathode cavity interior, with a marked absence of radiance from outside the cavity. This is in sharp contrast to the picture obtained with an uninsulated cathode at much higher current (16 kA) and cathode mass flow (6 g/sec), in which the cavity itself is observed to be quite dark (Fig. 3). Finally, in Fig. 14b it is observed that the downstream 0.8 cm of the cathode cavity appears darker than the region upstream of it. The lowering of intensity of radiance in this region is consistent with the lower surface current density measured in this region (Fig. 14a) and the correspondingly lower volumetric energy deposition (Fig. 13b).

In summary, the spontaneous occurrence of a peak current density upstream of the cathode tip, and the strong similarity between the cavity current distributions for the insulated and uninsulated cathode is deemed strong evidence for the conclusion that this type of surface current distribution, and the values of current and mass flow at which it occurs, are indeed characteristic of hollow cathode conduction for the given geometry.

From the experimental results presented above, interesting dependencies have been revealed of the cathode cavity conduction patterns on both mass flow and current for a fixed cathode geometry. These measurements were not made in sufficient detail to enable the construction of a detailed analytical model of the cathode conduction and emission processes. Furthermore, certain physical parameters germane to the construction of such models, such as electron number density, temperature, state of ionization of the plasma, heavy particle temperatures, etc., have not been directly measured in this work. The approach, therefore, is semi-empirical, but nevertheless useful insofar as it discriminates between several candidate models and thus defines specific directions in which further research might be conducted.

A phenomenological conduction model, consistent with all of the measured current distributions, is described in detail elsewhere.[11] In brief, the mean free path, λ^*, for escape through the cathode orifice of energetic electrons in the distribution tail, is identified as a characteristic conduction dimension. When λ^* is very short or very long relative to the cavity diameter, conduction is electric field dominated, occurring mostly from the cathode tip. When λ^* is roughly one cathode diameter, the resultant axial conductivity gradient opposes the field gradient, thus moving peak current attachment up to one diameter upstream of the tip.

This paper focuses on emission processes at the MPD hollow cathode surface. Three major possible emission mechanisms are investigated: thermionic, pure field, and photoelectric emission. We begin with thermionic emission.

IV. Thermionic Emission

1. Uniform Thermionic Emission

The emitted thermionic current density at a metal surface is given by the Richardson-Dushmann equation:

$$j_{th} = AT^2 \exp(-\frac{e\varphi}{kT}) \qquad (1)$$

where A = 60 A/cm^2 °K^2 for tungsten, T is the cathode surface temperature and φ, the work function, is about 4.5 e.v. for pure tungsten. Fig. 15 is a graph of thermionic current density versus cathode surface temperature for the tungsten hollow cathode. Also shown on the figure are typical measured average surface current densities, $\langle j_s \rangle$, for the range of arc current from 0.25 to 4.7 kA. From these current densities and the Richardson emission curve, it is clear that hollow cathode surface temperatures of order 3200 °K or greater are required

if thermionic emission is to be the major source of electrons in the discharge. For currents greater than 4.7 kA, the maximum thermionic emission, corresponding to the boiling point of tungsten, is still not sufficient to account for the total emitted current at the cathode surface. For the lower currents of 0.25 and 0.9 kA, the cathode, if hot enough, could provide the necessary emission current density. It is therefore instructive to estimate the temperature rise at the hollow cathode surface due to the discharge at these operating conditions.

The discharge is assumed to provide a constant flux, F_o, of heat radially to the cathode surface. The heat is assumed to flow purely radially inside the cathode and the cathode wall is assumed to be infinite in radial thickness. The problem can then be treated as one-dimensional heat conduction in a semi-infinite slab with a constant flux, F_o, incident upon it. The solution of the appropriate heat diffusion equation is standard.[12] We shall save space here by simply showing a sketch of the problem (below) and quoting the result:

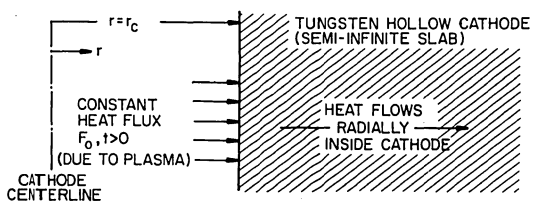

BOUNDARY CONDITIONS: $t=o$ $T(r>r_c)=O$ $t>o$ $\text{FLUX} = \frac{dT}{dr} = F_o$ $T(r=\infty)=O$

The temperature anywhere in the cathode is then given by:[12]

$$T(r,t)=\frac{2F_o}{K}\left[\left(\frac{\chi t}{\pi}\right)^{\frac{1}{2}}\exp\left\{\frac{-(r-r_c)^2}{4\chi t}\right\}-\frac{(r-r_c)}{2}\operatorname{erfc}\left\{\frac{(r-r_c)}{2\sqrt{\chi t}}\right\}\right], \quad r > r_c \qquad (2)$$

where K is the thermal conductivity of tungsten and χ is its thermal diffusivity.

The temperature at the cathode surface ($r = r_c$) is

$$T(r_c,t) = \frac{2F_o}{K}\left(\frac{\chi t}{\pi}\right)^{1/2} \qquad (3)$$

Typically, the MPD hollow cathode takes about 10^{-4} sec to reach a quasi-steady state. For thermionic emission to be significant, the surface temperature should therefore rise to temperatures of order 3000°K or greater in this time. For this time scale, and for characteristic values of the physical constants K and χ, Eq. 3 reads:

$$T(r_c,t) = (2.2 \times 10^{-2})\ F_o \qquad (°K)$$

where F_o is in units of cal/cm^2-sec.

Typically the energy flux to the cathode in an arc discharge is only about 10% of the total energy in the discharge. The rest is distributed among anode heating, gas heating, gas flow power, radiated power and frozen flow power. We shall, however, assume that all the power in the discharge goes into the cathode surface and thereby obtain an estimate of the extreme upper limit to the temperature rise at the cathode surface.

For the higher current of 0.9 kA, with a measured terminal voltage of roughly 40 V, the total discharge power is:

$$P_{TOTAL} = 8.6 \times 10^3 \text{ cal/sec}$$

Experiments have shown that the plasma inside the hollow cathode forms over a length of typically one cathode diameter. The surface area of the cathode which is directly heated by the plasma is therefore:

$$S = \pi \times D \times D = 11.3 \text{ cm}^2$$

where D is the cathode inner diameter of 1.9 cm. The average heat flux to the surface, F_o, is thus:

$$F_o = \frac{P_{TOTAL}}{S} = 7.6 \times 10^2 \text{ cal/cm}^2\text{-sec}$$

For this value of F_o, Eq. 3 gives a temperature rise at the cathode surface of only 17°K. Also, Eq. 2 shows that, on the time scale of 10^{-4}sec, heat has not diffused more than 0.2 cm into the cathode. Since the cathode wall is 0.6 cm thick, our earlier assumption of the cathode as a semi-infinite slab is justifiable. At the higher current of 4.7 kA, with a terminal voltage around 120 v, the surface flux, F_o, is a factor of 15 higher than at 0.9 kA. Even so, Eq. 3 then gives a maximum cathode surface temperature rise of only 260°K.

This simple analysis shows therefore that due to the short duration of the MPD discharge, the cathode is not significantly heated by the discharge. Uniform thermionic emission in the MPD hollow cathode is therefore not likely as the major source of electrons. There is, however, the possibility that the cathode surface is not heated uniformly but in localized spots distributed over the surface. The electrons emitted from these local hot spots could be scattered rapidly to appear to cover the whole surface; since the magnetic field measurements were made at a distance of 0.15 cm away from the surface, due to the 0.3 cm dimension of the probe itself, the probe could have measured only a "smoothed out" current density near the surface. However, this possibility can be negated by a very simple analysis as follows in the next subsection.

2. Thermionic Emission from Localized Hot Spots

Let the number of local hot spots be N. Let the area of each hot spot be A. The average current density of each spot is therefore:

$$\langle j_{SPOT} \rangle = J/NA \qquad A/\text{cm}^2$$

where J is the total discharge current. Now in general when a current j_e of electrons is emitted from a spot, the ion current, j_i, returning to that spot along the field lines is smaller than j_e. This is especially true in an arc where the sheath drop is low (typically 10-20 v), for then the ionization efficiency of the emitted electrons is quite low thus producing a smaller ion current than the emitted electron current.[13] This return ion current density when multiplied by a voltage drop across the sheath gives the flux, F_{SPOT}, incident upon each spot. In arcs in general, the ratio (j_i/j_e) varies from as low as 10^{-3} up to 1.[13,14] For our purposes here, we choose the highest possible value so as to maximize the heat input to the cathode spot. The maximum flux, F_{SPOT}, for a typical sheath drop of 40 volts (a large estimate

for MPD operating conditions) is therefore:

$$F_{SPOT,max.} = \frac{J}{NA} \times \frac{40}{4.2} \text{ cal/cm}^2\text{-sec}$$

Now the largest possible value of J/NA if the emission is thermionic is about 700 A/cm^2, corresponding to the boiling point of tungsten from Fig. 15. With this maximum value of J/NA, the flux into the spot becomes:

$$F_{SPOT,max.} = 7 \times 10^3 \text{ cal/cm}^2\text{-sec}$$

With this flux, Eq. 3 yields a maximum temperature rise at the spot of only 150°K.

It is therefore clear that whether the heat from the discharge is assumed to cover the cathode surface uniformly or to heat any number of localized spots distributed over the surface, the discharge energy is not sufficient to heat any portion of the cathode surface to temperatures above about 500°K, assuming thermionic emission alone is present. If, however, the maximum spot density is not limited to the rather low thermionic values but is several orders of magnitude higher, as for example, with field emission, then the incident power density to the spot can in fact be high enough to cause melting of the individual spots. This point is discussed in the next section. Here we conclude that thermionic emission alone is not likely to provide the measured current in the MPD hollow cathode.

V. Field Emission

On the basis of his pioneering work on electrostatic probe theory, Langmuir[14] recognized that if there is a large number of positive ions in the probe debye sheath, it is possible to pull electrons out of the metal by lowering the potential barrier. Mackeown[15] conducted a detailed theoretical investigation of Langmuir's hypothesis. His major contribution to the theory was the inclusion of the effect of wall-emitted electrons on the sheath, giving rise to Mackeown's equation of bipolar space charge movement:[15]

$$\mathcal{X}_c^2 = 7.6 \times 10^5 \, V_s^{\frac{1}{2}} \{j_+ (\frac{m_+}{m_-})^{\frac{1}{2}} - j_-\}, \; [v^2/cm^2] \quad (4)$$

where $\mathcal{X}_c$ is the cathode surface electric field and V_s the potential drop across the sheath. In 1928 Fowler and Nordheim published a classic study of electron emission in intense electric fields.[16] Their emission equation is:[16]

$$j_e = j_- = 1.54 \times 10^{-6} \mathcal{X}_c^2 / \varphi \exp\{-6.8 \times 10^7 \varphi^{\frac{3}{2}} / \mathcal{X}_c\}, \; [A/cm^2] \quad (5)$$

where φ is the work function of the metal, already referred to earlier. Wasserab[17] carried out a theoretical investigation using Eqs. 4 and 5 for a mercury arc. He emphasizes that if the total current density, $j = j_+ + j_-$, is known, then j_+ and j_- are each uniquely determined by the two equations, for a specified cathode drop V_s and work function, φ. The result of his graphical evaluation[17] is shown in Fig. 16 for a rather low work function of φ = 2v. The figure may be interpreted as follows: with small values of j there is no adequate field for significant electron emission. j_+ therefore varies proportionally to j. At large current desntities, j_+ is practically constant since, when dealing with extreme fields, ($\sim 10^6$ V/cm), a small alteration of j_+ produces a large alteration in j_-, therefore j_- is proportional to j.

By considering the energy balance and the slight ionization ability of the cathode emitted electrons as mentioned above (see Compton[13]), Wasserab proves the condition,

$$q = (j_-/j_+) \gg 1$$

If, for example, we make q = 10, then, from Fig. 16 we observe that even with the small work function of 2v the field emission mechanism is possible only for current densities >10^7 A/cm^2. In the spirit of an optimistic estimate of the total current density requirement for uniform field emission, we might assume that q is as large as unity; i.e. the ion and electron currents to the cathode surface are equal. Then, Fig. 16 shows that total surface current densities of order 10^6 A/cm^2 are still required according to Wasserab's model, for pure field emission at this low work function of 2v. Such current densities are three orders of magnitude larger than the highest measured surface current densities in the MPD hollow cathode, (see Fig. 9). The work function used in the above calculations must be considered as being very low, even taking into account the eventual influence of oxide layers on the tungsten surface. With more realistic values of φ, (φ = 3.5 to 4.5v) it has been shown[9] that still higher current densities are required for field emission than those quoted above for φ = 2v.

It is therefore clear that for pure field emission from the cold MPD hollow cathode, high fields (> 10^6 V/cm) and high current densities >10^6 A/cm^2 are required. With debye sheaths of order 10^{-5}cm in thickness and sheath drops of order 10-20 volts, the necessary high electric fields are certainly possible at the hollow cathode surface. However, the high current densities require that the emission be localized into many spots distributed over the active surface of the cathode. As mentioned earlier, these intense local sources of electrons, if they existed, could not be detected by the magnetic field probe due to its size and distance from the cathode surface. Also, the uniform grayish appearance of the cathode active surface could be accounted for by a rapid, random movement of the spots all over the active surface during the discharge. Such a movement could be caused, for example, by smoothing out of the metal surface due to bombardment of ions returning along the field lines to the spot. The resultant lowering of the local electric field might cause the spot to wander to a region of higher electric field, and so on. Apart from ion bombardment smoothing, the surface of the spot could possibly be smoothed by local melting. Consider for example the case $j_+ = j_- = 10^6$ A/cm^2. Such an ion current density incident upon the spot, falling through a sheath potential of about 20v, will cause the temperature of the spot to reach the melting point of tungsten within less than 30 μsec, according to Eq. 3 above. Such local melting might cause the local electric field to drop considerably and hence cause the emission site to wander to an unheated region where the surface is still rough. Meanwhile the molten spot may solidify and be roughened again by random ion bombardment, thus maintaining the chain of spot movement.

We conclude here that whereas conditions in the MPD hollow cathode might be appropriate to cold field emission, such a mechanism does impose stringent requirements on the nature of the emission sites and is practically impossible to verify experimentally.

VI. Photoelectric Emission

Although photoelectric cathode emission has been recognized as being important in glow discharges for many years, and has been discussed extensively by Loeb[18] and others, it appears to have received scant attention in the literature on high pressure arc discharges. In particular, in hollow cathode discharges, the efficient confinement of radiant energy by the cathode cavity intuitively suggests the possibility of photoelectric enhancement of the surface emission. It is surprising, therefore, that to the best of our knowledge, no quantitative estimates of the photoelectric emission have been reported for hollow cathodes, particularly in situations where thermionic, pure field, Schottky and other secondary emission processes have all been shown to be inapplicable.[19] In the following, a rudimentary analysis of the radiation processes inside the MPD hollow cathode leads to the conclusion that under certain conditions it is possible for photoelectric emission to account for more than 45% of the observed cathode current. This stresses the need for a careful experimental study of photoemission at the surface of MPD hollow cathodes and suggests that photoelectric emission cannot be lightly dismissed from cnsideration as a primary emission mechanism in hollow cathode discharges.

1. Maximum Photoelectric Yield

The maximum possible vacuum photoelectric yield at the MPD hollow cathode surface is estimated as follows: First the simplifying assumption is made that all of the energy in the radiation field inside the cavity arises from a single resonant electronic transition from the first excited state to the neutral or ion ground state of argon. This assumption is reasonable for a near LTE argon plasma in which the resonant energy gap for the neutral atom (ArI) or singly charged ion (ArII), ∿10v, is much larger than that for the higher excited transitions. Two cases are considered: a weakly ionized plasma at low currents[9] in which all the radiant energy is assumed carried by 11.6v resonant photons of ArI, and a strongly ionized plasma at high currents[9] in which 17.1v ArII resonant photons are assumed to carry all the energy in the radiation field. An upper bound to the resonant quantum flux in either of these cases incident on the cathode inner surface can be obtained by assuming that all of the energy in the cavity discharge is in fact in the radiation field (and neglecting end losses). If this maximum possible quantum flux is multiplied by a maximum quantum yield at the surface (ejected electrons/incident quantum), one then estimates the maximum primary photoelectric current at the cathode surface.

The value of the quantum yield depends on the energy of the incident quantum, and is quite sensitive to the angle of incidence and the orientation of the electric field vector of the incident quantum. It has been shown experimentally[20] that light obliquely incident on a photosurface consisting of a liquid sodium-potassium alloy yields a much larger photocurrent (higher quantum efficiency) when the electric vector is contained in the plane of incidence than when it is directed normal to that plane. The ratio of photocurrents for the two polarizations is a function of the angle of incidence and reaches a maximum of about 60 for 60° incidence. The magnitude of this effect for ultraviolet light incident upon a tungsten surface is not precisely known but must be accounted for by proper averaging procedures in any detailed analysis of photoemission in the MPD hollow cathode. For our purposes here, in order to estimate the maximum possible photoelectric yield, we assume the highest reported yield for tungsten in the wavelength range of interest (700-1000 Å). This value, = 0.2, was measured[21] from a tungsten surface contaminated by oxide films, absorbed gases, etc., not unlike the MPD hollow cathode surface.

Table I below, shows the upper bounds of the vacuum photocurrent densities for the lowest current (0.25 kA) at a mass flow of 0.1 g/sec and for the highest current (4.7 kA) at a mass flow of 0.1 g/sec., respectively. For comparison, the second column of the table shows the measured average surface current density at both of these operating conditions.

Table I
Comparison of Calculated Photo-Current Density with Measured Surface Current Density in Hollow Cathode

Operating Conditions	Type of Plasma	Maximum Possible Vacuum Photoelectric Current Density, A/cm^2	Measured Average Surface Current Density, A/cm^2
$\frac{J}{m}$ 0.25 kA 0.1 g/sec	Weakly Ionized All Ar I 2-level Atomic System	7.6	22
$\frac{J}{m}$ 4.7 kA 0.1 g/sec	Strongly Ionized All Ar II 2-level Atomic System	387	830

From Table I it is evident that if all of the power in the cathode region of the MPD hollow cathode arc is incident upon the tungsten surface as high energy resonant quanta, then the resulting photoelectric current could account for between 25 and 50% of the total discharge current. Thus far in the calculation we have not considered the effect of the cathode surface electric field on the emission. The presence of a strong (∿10^6V/cm) electric field at the cathode surface can change the photoemission characteristics.[22] In effect, the field can, under certain circumstances, cause an electron in an excited state within the conduction band of the metal to tunnel through the surface potential barrier and be emitted as a photo-electron. This has the net effect of increasing the quantum yield from the vacuum photoelectric yield generally measured experimentally and used in our calculation above.

In principle, it appears possible therefore, that if a significant fraction of the power in the cathode region in the MPD hollow cathode is incident upon the cathode surface as high energy quanta, then a field enhanced photoelectric effect can account for all of the measured surface current. The task that now remains is to investigate the collisional and radiative processes occurring in the volume of the hollow cathode plasma in order to determine what fraction of the power in the cathode region does in fact reach the cathode surface as high energy

radiation quanta. This is done in the next two subsections.

2. Estimate of Net Fraction of Cathode Region Power Available to the Radiation Field

In the MPD hollow cathode, since most of the current is carried by electrons, the ohmic power $\vec{j}\cdot\vec{E}$, is invested primarily in the electrons. The electrons then transfer, by elastic and inelastic collisions, some of this invested power to the heavy particles. The flow out of the cathode orifice of heavy particles heated by electron elastic scattering, of hot electrons themselves, of radiation, and also of heavy particles in excited states ("frozen" flow power losses) represents a fraction of the cathode region power that cannot be introduced into the surface as radiation. When these individual "orifice loss" components are estimated for different hollow cathode operating conditions and added together,[9] it is found that only 10 to 15% of the cathode region power leaves via the orifice; the majority of the power can therefore be introduced into the radiation field inside the cavity, thus justifying one of the assumptions made in the previous subsection.

3. Integrated Line Intensity in the Hollow Cathode

We have assumed earlier that all of the power in the cathode region is contained in a single optical transition, for either the weakly ionized Ar I plasma or the strongly ionized Ar II plasma. It remains to be shown, therefore, that the integrated line intensity from the resonant optical electronic transition in an Ar I or an Ar II plasma at specified densities and temperatures can, in fact, be as large as the total power in the cathode region of the MPD hollow cathode plasma. This is done as follows:

For the two operating conditions listed in Table I, the absorption coefficient at line center, k_o, is evaluated using:[23]

$$k_o = \frac{2}{\Delta\nu_D}\left(\frac{\ell n 2}{\pi}\right)^{\frac{1}{2}}\left(\frac{\lambda_o^2}{8\pi}\right)\left(\frac{g_2}{g_1}\right) A_{21} N_1 \qquad (6)$$

Here λ_o is the wavelength at line center (in this case the wavelength of the resonant transition); g_2 and g_1 are the statistical weights of the resonant and ground state, respectively; A_{21} is the Einstein coefficient for the resonant transition, and N_1 is the number density of atoms or ions in the ground state. In writing k_o in the form of Eq. 6, it has been assumed that the number density of atoms or ions in the resonant state is much lower than that in the ground state. Also, other processes that could contribute to the broadening of the absorption line have been neglected in comparison with Doppler broadening. When collisional broadening is important, the value of k_o can be considerably less than that given by Eq. 6. However, even when the damping ratio is 1, that is to say when collisional broadening and Doppler broadening are equally important, the value of k_o is still as high as 32% of its pure Doppler broadened value.[23] For typical MPD hollow cathode conditions the damping ratio is in fact quite small[9] ($\sim 10^{-3}$). We may therefore retain the analytically simple form of Eq. 6 and estimate k_o quite accurately under these conditions. The values obtained are shown in Table II, below.

Table II[9]
Absorption Coefficient at Line Center, k_o

Type of Plasma	k_o
0.25 kA, 0.1 g/sec All Ar I Plasma $\lambda_o \simeq 1067$Å, $T_o \sim 2300$°K	2×10^3
4.7 kA, 0.1 g/sec All Ar II Plasma $\lambda_o \simeq 723$Å, $T_o \sim 4.6 \times 10^4$°K	5.4×10^2

From Table II, the large values of k_o, for a cathode cavity dimension of 1 cm, indicate that the resonance radiation is very effectively trapped within the cavity plasma. The spectral radiance of the resonant radiation at line center, $I_\nu(\nu_o)$, can therefore be approximated by the blackbody radiance, $B_\nu(\nu_o)$, at the given frequency and at the temperature of the electrons, T_e. The total intensity of the resonant line radiation is then given by:

$$I_{TOT} = \int_o^\infty I_\nu d\nu \simeq B_\nu(\nu_o) \times W \times \Delta\nu_D \quad [W/cm^2] \qquad (7)$$

where $\Delta\nu_D$ is the Doppler half-width of the line and W is the equivalent width of the line defined as the width (given in Doppler half-widths) of that frequency interval of the nearby black-body spectrum necessary to radiate the same total energy as the spectral line in question. Equation 7 may now be used to estimate the equivalent width of the resonant line necessary for this single line to radiate, as a black-body, a total power equal to the cathode region power in the MPD hollow cathode. The results of this calculation, detailed elsewhere,[9] are presented in Table III, where the equivalent width, W, and the quantity $W \times \Delta\nu_D$, which expresses the equivalent width in angstrom units, are given for two different electron temperatures, for each of the two operating conditions already referred to above.

Table III
Equivalent Width for Single Line to Radiate Total Cathode Region Power[9]

Type of Plasma	Electron Temperature T_e, e.v.	W	$W \times \Delta\nu_D$ Å
0.25 kA 0.1 g/sec weakly ionized	1.5 2	650 93	3.8 0.54
4.7 kA 0.1 g/sec strongly ionized	4 5	72 27	1.3 0.53

Table III shows that the necessary equivalent widths for a single line to radiate the total cathode region power into the cathode surface are quite sensitive to T_e. At $T_e = 1.5$ e.v. for the 0.25 kA weakly ionized plasma,[9] and $T_e = 4$ e.v. for the 4.7 kA strongly ionized plasma,[9] the necessary equivalent widths are observed to be 3.8 and 1.3 Å, respectively. At first glance these widths seem unreasonably large. However, resonance broadening of spectral lines can lead to very large line widths, particularly in high density plasmas[24,25] Recent measurements [26] of the half-width of the 1235.8 Å resonance line of Krypton behind a Mach 12 shock at conditions of neutral density, $N_o \sim 10^{18}$cm^{-3}, $N_e \sim 10^{16}$cm^{-3}, and $T_e = 1$ e.v., show that the reso-

nance line is 10 to 20 Å wide. These post-shock plasma conditions are not unlike those in the MPD hollow cathode and hence the equivalent widths required from Table III are quite plausible.

The equivalent width of a spectral line has also been numerically evaluated to an accuracy of four significant figures by Jansson and Korb.[27] They present a table of values of W for different values of damping ratio, a, and the product $k_o \ell$, where ℓ is a characteristic dimension (cathode cavity radius in our case). For an estimated value of $a \sim 10^{-3}$ in the MPD hollow cathode, the data of Jansson and Korb[27] were used to plot a graph of W versus $k_o \ell$, shown in Fig. 17. Also shown in the figure is a graph of W versus $k_o \ell$ for a higher damping ratio of unity.

As shown in Fig. 17, the equivalent widths of the resonance lines of Ar I and Ar II, when the damping ratio is 10^{-3}, for values of $k_o \ell$ given in Table II are roughtly 10 to 20. From Table III, the equivalent widths necessary for these resonance lines to radiate all of the cathode region power are between 650 and 93 for the Ar I plasma, at temperatures between 1.5 and 2 e.v.; for the Ar II plasma, they are between 72 and 27 for temperatures between 4 and 5 e.v., respectively. The agreement even to only a factor of 10 between the equivalent widths obtained by the above two different approaches is close enough to underscore the possible importance of the photoelectric effect in the MPD hollow cathode. At higher neutral densities and lower heavy particle temperatures than those assumed in the calculations above, which are quite likely under some operating conditions, the damping ratio may be quite a bit larger than 10^{-3}. As an example of the effect of a higher damping ratio on the equivalent width, the data of Ref. (27) have been plotted for a damping ratio of unity in Fig. 17. Now it is observed that at the $k_o \ell$ appropriate to the Ar I or the Ar II plasma, equivalent widths of 10^2 or greater are possible. From Table III this would then mean that the total cathode region power could be radiated in the resonance line at temperatures lower than those discussed above.

The significance of the above calculations is that in the MPD hollow cathode, due to the imprisonment of the resonance radiation, the intensity of the resonance lines can be built up to their maximum possible equilibrium value, given by the Planck function, thus giving rise to a sufficiently high flux of high energy quanta to the cathode surface with a resulting photoelectrically emitted current which is of the same order of magnitude as the observed discharge current. Photoelectric emission thus is a possible uniform primary emission mechanism in hollow cathode discharges.

Summary

Large hollow cathodes in a variety of configurations have been successfully operated in high current MPD arcs without the assistance of auxiliary heating, low work function inserts, or external keeper electrodes. By examining current and potential distributions inside the hollow cathode cavity over a wide range of currents and mass flows, an empirical criterion for characteristic hollow cathode operation has been identified. Thermionic emission has been shown to contribute negligibly to the emitted current in these MPD hollow cathode arcs. Field emission from micro-spots on the cathode surface, and also a form of field-enhanced photoelectric emission, have been suggested as the primary emission mechanisms in such cathodes.

Acknowledgement

The author is grateful to Professor Robert G. Jahn for valuable advice in preparing this paper. Helpful discussions were also held with Dr. Kenn Clark, Professor S. H. Lam, Professor R. B. Miles, Mr. Michael Campbell and Mr. W. F. von Jaskowsky.

References

1. Paschen, F., Ann. d. Physik 50, 1916, p. 901.

2. Byers, D.C., "Performance of Various Oxide Magazine Cathodes in Kaufman Thrusters," NASA TN D-5074, 1968.

3. Lidsky, L.M., Rothleder, S.D., Rose, D.J., Yoshikawa, A., Michelson, C. and Mackin, Jr., R. J., "Highly Ionized Hollow Cathode Discharge," J. of Applied Physics, Vol. 33, No. 8, 1962.

4. Keen, B.E. and Aldridge, R.V., "Low Frequency Wave-Mixing in a Magnetoplasma," Phys. Lett. A 29 (5), 1969 p. 225.

5. Day, B.P., Fearn, D.G., and Burton, G.F., "Ion Engine Development at the Royal Aircraft Establishment, Farnborough," RAE Tech Rep. 71102, 1971.

6. Delcroix, J.L., Minoo, H. and Trindade, A.R., "Etude de decharges a cathode creuse en regime d'arc," Rev. Roum. Phys. 13(5), 1968, p. 401.

7. Jolly, J., "Argon Ion Laser Using Hollow Cathode and Graphite Confining Structure," Proceedings of 1st International Conference on Hollow Cathode Discharges and Their Applications, 1971, p. 20.

8. DiCapua, M.S., Ph.D. thesis, Princeton University, AMS Department 1971.

9. Krishnan, M., Ph.D. thesis, Princeton University, AMS Department, 1976.

10. Krishnan, M., vonJaskowsky, W.F., Clark, K.E. and Jahn, R.G., paper #75-395 presented at AIAA XIth Electric Propulsion Conference, New Orleans, Louisiana, March 1975.

11. Krishnan, M., Jahn, R.G., vonJaskowsky, W.F., and Clark, K.E., paper # 76-984 to be presented at the AIAA XIIth Electric Propulsion Conference, Key Biscayne, Florida, Nov. 1976.

12. Carslaw, H.S. and Jaeger, J.C., Conduction of Heat in Solids, 2nd Ed., Oxford, Clarendon Press, 1959.

13. Compton, K.T., "On the Theory of the Mercury Arc", Phys. Rev. 37, 1931, p. 1077.

14. Langmuir, I., "Uber Feldemission", Gen. Elec. Rev. 26, 1923, p. 735.

    Langmuir, I. and Mott-Smith, H. "Uber Feldemission," Gen. Elec. Rev. 27, 1927, p. 449.

15. Mackeown, S.S., "The Cathode Drop in An Electric Arc," Phys. Rev. 34, 1929, p. 611.

16. Fowler, R.H. and Nordheim, L.W., "Electron Emission in Intense Electric Fields", Proc. Roy. Soc. London A119, 1928, p. 173.

17. Wasserab, T., "Zur Theorie des Quecksilber-Kathodenflecks", Z. Physik 130, 1951, p. 311.

18. Loeb, L.B., Basic Processes of Gaseous Electronics, Univ. of California Press, Cambridge University Press, 1955.

19. Kojadinovic, H. and Minoo, H., "La Region Cathodique D'un Arc A Cathode Creuse En Regime Pulse," Laboratoire De Physique Des Plasmas, Universite de Paris - Sud, Centre D-Orsay, Rapport Internelle, Dec. 1974.

20. Garbuny, M., Optical Physics, Academic Press, New York, 1965, pp. 395-397.

21. Wheaton, J.E.G., "Photoelectric Yield of Tungsten", J. Opt. Soc. Am., 54, 1964, p. 287.

22. Williams, R., Semiconductors and Semimetals, Vol. 6, eds. R.K. Willardson and A. Beer, Academic Press, 1970, p. 97.

23. Mitchell, A.C.G., and Zemansky, M.W., Resonance Radiation and Excited Atoms, Cambridge University Press, 1961.

24. Suckewer, S., Licki, J., Mizera, B. and Zelazny, P., "Study of Various Methods for Determination of the Plasma Temperature in the MHD Generator Duct," translated from the Russian in "Electricity from MHD" IAEA, Vol. IV, Vienna, 1968, pp. 2179-2194.

25. Kulander, J.L., "Curves of Growth for Non-Equilibrium Gases", J.Q.S.R.T., Vol. 8, 1968, pp. 1319-1340.

26. Carls, H.H. and Zuzak, W.W., "Measurement of the Vacuum Ultraviolet Radiation from a Shock Heated Krypton Plasma", J.Q.S.R.T., Vol. 11, 1961 pp. 1135-1141.

27. Jansson, P.A. and Korb, C.L., "A Table of Equivalent Widths of Isolated Lines with Combined Doppler and Collision Broadened Profiles", Vol. 8, 1968, pp. 1399-1409.

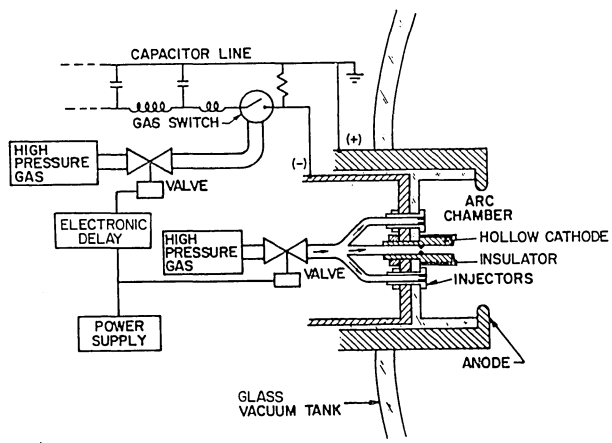

Fig. 1 Hollow Cathode Discharge Apparatus

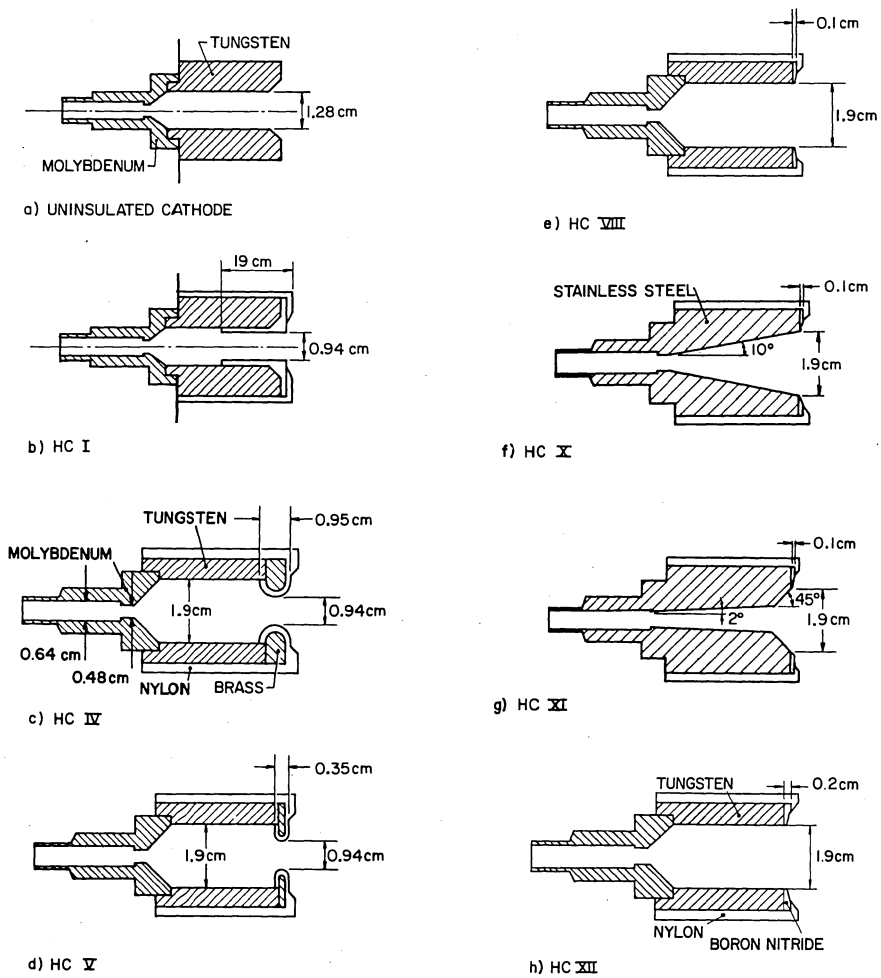

Fig. 2 Hollow Cathode Configurations

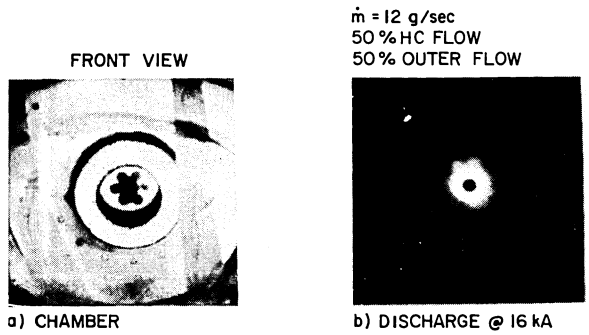

Fig. 3 Discharge Through 4800 Å AII Filter

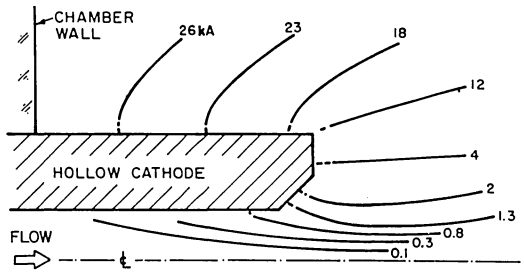

Fig. 4 Enclosed Current Contours; $\dot{m}$ = 0.3 g/sec

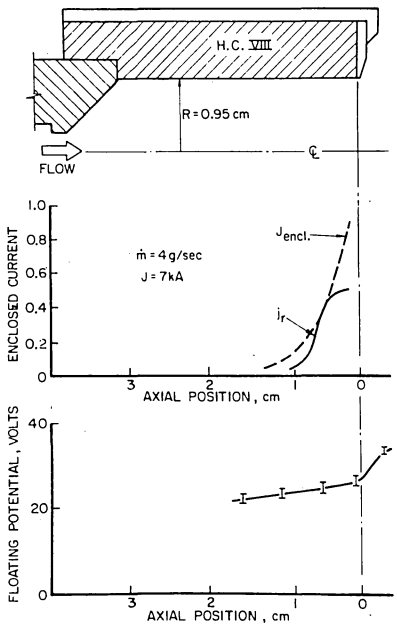

Fig. 5 Current and Potential Distribution in H.C. VIII

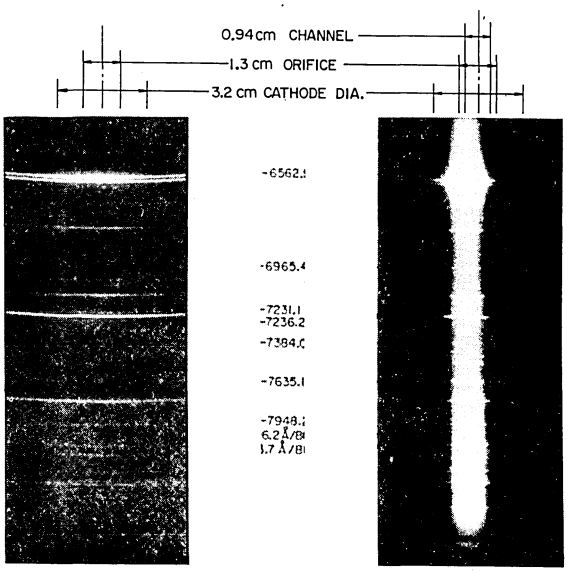

Fig. 6 Spectra of Hollow Cathode Discharge

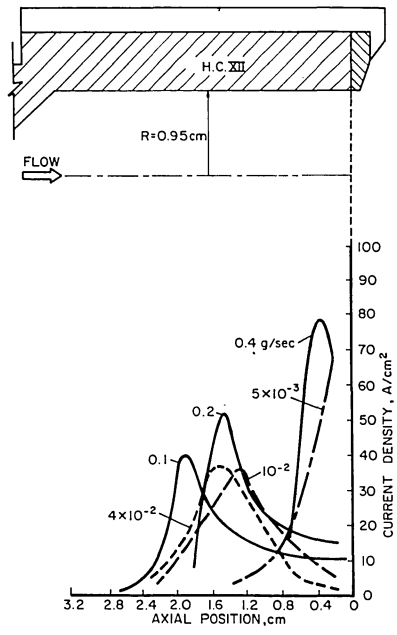

Fig. 7 Current Density Profiles, 0.25 kA

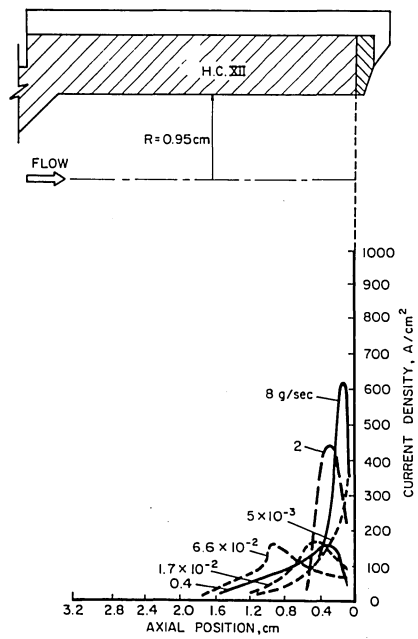

Fig. 8 Current Density Profiles, 0.9 kA

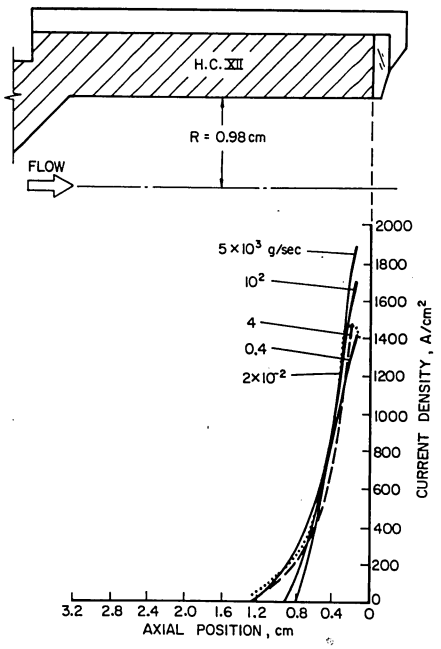

Fig. 9 Current Density Profiles, 4.7 kA

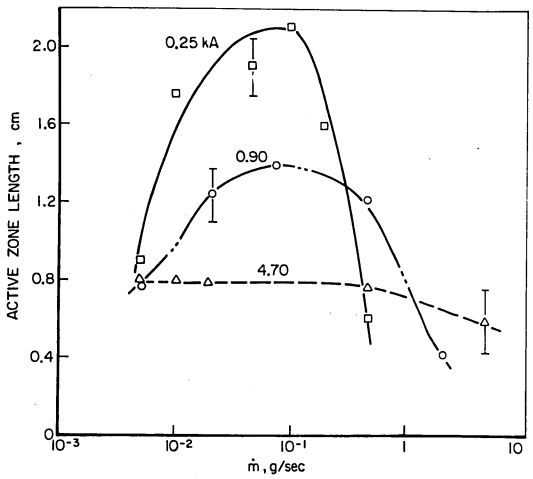

Fig. 11 Active Zone Length

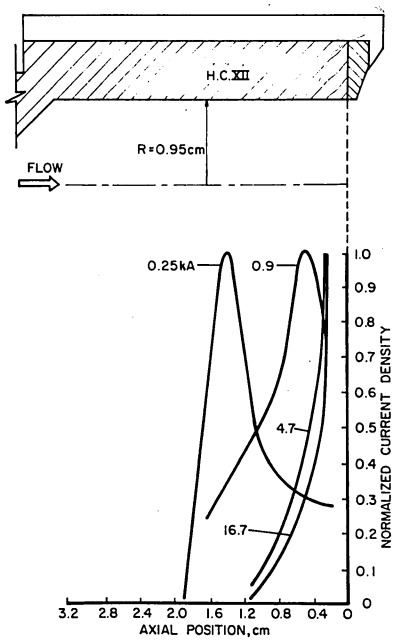

Fig. 10 Current Density Distributions, 0.2 g/sec

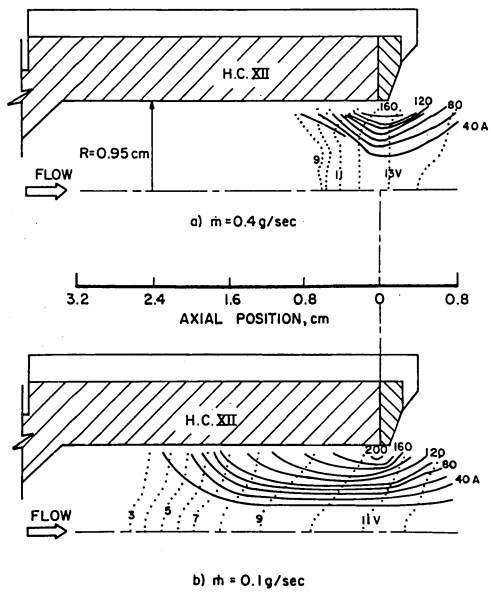

Fig. 12 Enclosed Current and Potential Profiles, 0.25 kA

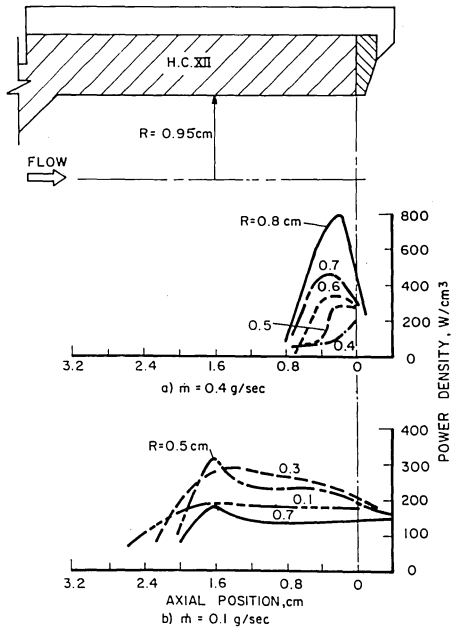

Fig. 13 Power Density Profiles, 0.25 kA

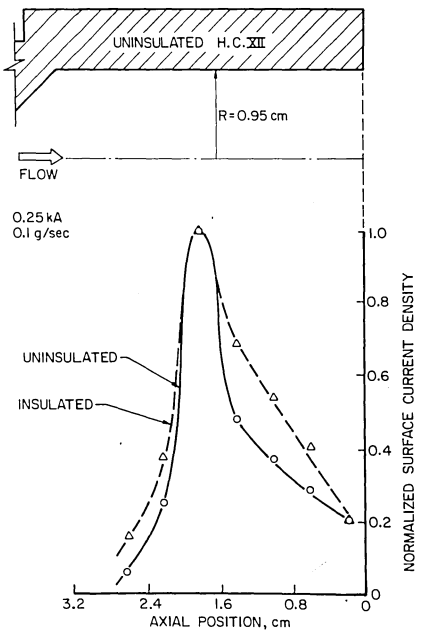

a) Current Density Distributions

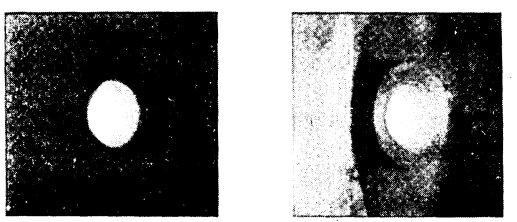

b) DISCHARGE RADIANCE c) DOUBLE EXPOSURE

Fig. 14 Uninsulated Hollow Cathode, J=0.25 kA, $\dot{m}$=0.1 g/sec

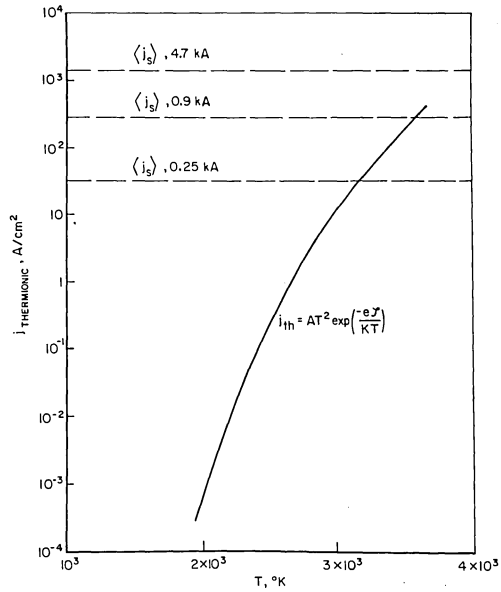

Fig. 15 Thermionic Emission, Tungsten

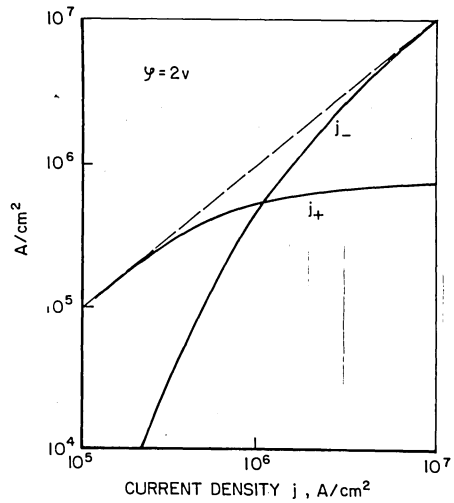

Fig. 16 J_- and J_+ as Functions of $J = J_+ + J_-$, Ref. (17)

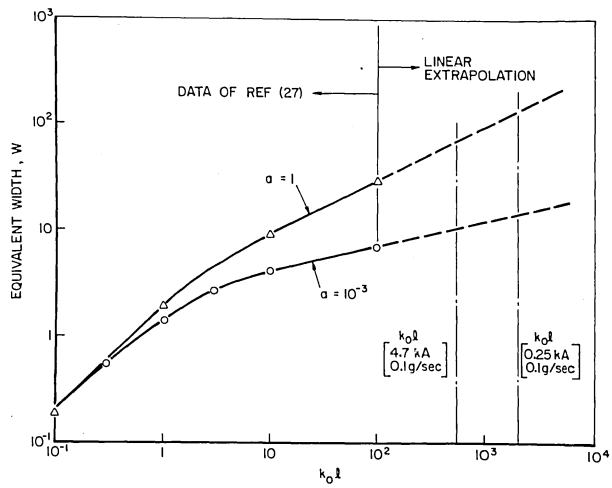

Fig. 17 Equivalent Width for a Voigt Contour, Ref. (27)

DISCUSSION

J. L. MASON: How dependent is your electrodynamic flow modelling on the fluid dynamic modelling, the turbulent flow modelling - do you have to make some assumptions regarding the velocity distributions, for example, and are such assumptions really important to your development of the electrodynamic flow modelling?

M. KRISHNAN: I have not solved the analytical problem owing to the complex nonlinear coupling of electrodynamics with the fluid dynamics inside such a discharge. But we did do an experiment in which flow to the hollow cathode was cut off altogether, and different ambient prefill pressures of argon (corresponding to analytically estimated flow static pressures for each mass flow) were set in the discharge vessel. The surface current distributions measured with ambient gas in the cathode were very similar to those measured at the same current with different mass flows through the cathode. We thus tentatively conclude that it is in fact the static pressure component of the flowing gas in the hollow cathode that is predominantly responsible for establishing the current conduction pattern. Thus fluid dynamics appear to be relatively unimportant to the electrodynamics in such discharges.

J. F. DAVIS: Is it possible that at high pressures, large numbers of argon atoms arrive at the cathode surface as molecules and that therefore self-absorption of vacuum ultra-violet photons is hindered?

M. KRISHNAN: The pressure inside the cathode cavity varies from as low as $\sim 10^{-3}$ torr up to ~ 100 torr. Even at the higher pressures, the cathode plasma is a hot plasma and I would therefore say that there are not a significant fraction of molecules in this discharge.

M. CAMPBELL: The temperatures estimated in such a plasma are around 20,000°K at which molecures cannot exist in any significant fraction.

A SCALING LAW FOR ENERGY TRANSFER BY INELASTIC ELECTRON-MOLECULE COLLISIONS IN MIXTURES

George K. Bienkowski
Princeton University
Princeton, N. J.

Abstract

The equation governing the electron energy distribution in the presence of a spatially uniform electric field in a weakly ionized gas has been reformulated into an integral equation for the logarithmic slope of the distribution function. For gas mixtures in which the dominant electron energy-loss mechanism is by vibrational excitation of the molecules, this equation is suitable for approximate analysis and exact numerical solution by iteration. Super-elastic collisions are easily included in this formulation, and do not seriously effect the convergence of the numerical scheme. The approximate analytical results are only qualitatively correct, but suggest appropriate parameters which correlate the exact numerical results very well. The distribution function as well as certain gross properties such as net energy transfer into vibration, mean energy, and drift velocity depend primarily on a single non-dimensional parameter involving only E/N and the cross sections. This parameter can be physically interpreted as the energy gained from the field between successive inelastic collisions divided by the typical inelastic energy loss per collision. Results for mixtures of CO, He, and N_2 are presented and shown to correlate most of the properties.

I. Introduction

A common and very effective way to transfer energy preferentially into vibrational states is by electron impact in a gas discharge. Many practical infra-red lasers, such as CO and CO_2 depend critically on this process. The analysis of the performance of such a device depends critically on these electron impact excitation rates. Nighan[1] has shown that using a Boltzmann distribution based on the mean electron energy can lead to erroneous results. The determination of the correct electron energy distribution function is therefore critical to the analysis and design of electrically excited molecular lasers.

In most laser codes the electron distribution effects the results directly through the excitation rates:

$$k_{i\to j} \sim N_i n_e \int_0^\infty S_{ij}(\varepsilon) f_e(\varepsilon)\varepsilon d\varepsilon \qquad (1)$$

where N_i is the number density of the molecule in i'th state, n_e the electron number density, $S_{ij}(\varepsilon)$ the inelastic cross section for the i to j transition by electron impact at energy ε, and $f_e(\varepsilon)$ is the electron distribution function. When quasi-steady results are desired the significant parameter becomes the net power into vibration which is:

$$P_{vib} \sim N n_e \int_0^\infty (\overline{S_v \Delta\varepsilon}) f_e(\varepsilon)\varepsilon d\varepsilon \qquad (2)$$

where

$$\overline{S_v \Delta\varepsilon} = \sum_i \left(\frac{N_i}{N}\right) \sum_j S_{ij}(\varepsilon)\varepsilon_{ij} \qquad (3)$$

and N is the gas number density, while ε_{ij} is the energy exchange in the $i \to j$ collision. In either case the results are sensitive to the behavior of the distribution function, because the most relevant cross sections tend to be relatively sharply peaked at precisely the energy where the distribution function is varying most rapidly. The variation of the distribution function in turn is dominated by the behavior of precisely those cross sections.

In most previous work[2,3] the electron distribution function is computed for a specific electric field (E/N) and gas mixture under the assumption that only the excitations from the ground state are important in determining this distribution. For lasing situations where a large number of higher vibrational states may be appreciably populated this assumption may need to be relaxed. This has been recognized before and some calculations estimating the effect of higher vibrational level populations and super-elastic collisions have been published.[1,4] The techniques used have generally relied on modification of techniques developed for zero vibrational temperature and become progressively more difficult to apply as the vibrational temperature becomes large. In addition most of the previous calculations have been made for specific mixtures and presented as examples with no scaling laws proposed. Judd[5] showed that the mean electron energy $\bar{u}$ acts as a normalization parameter independent of mixture ratio for the prediction of rates in CO_2-N_2-He mixtures. Unfortunately to find this parameter for a specific mixture ratio one must essentially do the entire calculation or at least determine a cross plot of $\bar{u}$ versus the mixture ratio for the specific gases considered.

This paper re-formulates the equation for the electron energy distribution function in a way that suggests natural scaling parameters that can be computed a priori, and is amenable to numerical computation over a very wide range of vibrational temperatures.

II. Basic Assumptions and Formulation

Formulation

A standard spherical expansion (up to second term) for the electron distribution function, in a spatially homogeneous weakly ionized gas leads to

the equation for the spherically symmetric part f_0 as presented by Nighan[1]:

$$-\mu(\varepsilon)\frac{df_0(\varepsilon)}{d\varepsilon} = \sum_s \sum_i \sum_j \delta_i^s \int_\varepsilon^{\varepsilon+\varepsilon_{ij}^s} \xi\, S_{ij}^s(\xi) f_0(\xi) d\xi \qquad (4)$$

where

$$\mu(\varepsilon) \equiv \frac{(E/N)^2}{3} \frac{\varepsilon}{\left[\sum_s \delta^s Q_{ms}(\varepsilon)\right]} . \qquad (5)$$

The symbols previously defined which depend on species have been superscripted with the letter s. $Q_{ms}(\varepsilon)$ is the electron-molecule momentum exchange cross section for species s, δ_i^s is the ratio N_i^s/N while $\delta^s = N^s/N = \sum_i N_i^s/N$. For convenience $f_0(\varepsilon)$ can be normalized in such a way that

$$\int_0^\infty f_0(\varepsilon) \sqrt{\varepsilon}\, d\varepsilon = 1. \qquad (6)$$

The second term $f_1(\varepsilon)$ is directly related to the derivative of f_0 and leads to the drift velocity. f_1 must remain small with respect to f_0 in order for the entire procedure to be justified.

Equation (4) can be changed to a pure integral equation by considering the negative of the logarithmic slope of f_0 as the new variable

$$B(\varepsilon) = -\frac{d\, \ell n\, f_0(\varepsilon)}{d\varepsilon} \qquad (7)$$

The incorporation of detailed balance on the molecular level (with no degeneracies)

$$(\varepsilon + \varepsilon_{ij})\, S_{ij}(\varepsilon + \varepsilon_{ij}) = \varepsilon S_{ji}(\varepsilon); \quad (j > i) \qquad (8)$$

leads to the equation

$$\mu(\varepsilon)B(\varepsilon) = \sum_s \sum_i \sum_{j>i} \int_\varepsilon^{\varepsilon+\varepsilon_{ij}^s} \left[\delta_i^s \exp\left(\int_\xi^\varepsilon B(\eta)d\eta\right) - \delta_j^s \exp\left(\int_{\xi-\varepsilon_{ij}^s}^\varepsilon B(\eta)d\eta\right)\right] \xi S_{ij}^s(\xi) d\xi \qquad (9)$$

This equation is suitable both for some approximate analysis and for numerical integral iteration. The equation is essentially exact within the standard assumptions of slight ionization level, two term spherical expansion, and small mass ratio of electrons to neutrals. Any successful analysis of Eq. (9) is going to require either complete knowledge of all the cross sections and population levels, or additional approximations and simplifications. Since the former is not available we propose certain simplifications that will retain the essential features of the problem and are not drastically inconsistent with the expected cross section behavior.

Additional Approximations

No experimental and only limited theoretical results[6] for electron-impact cross sections with vibrationally excited molecules exist. Since in a laser related situation some estimate of the effect of these collisions is better than complete neglect, the following simple assumption is used. The excitation process from level i to i+n is in all respects equivalent to the excitation process from level 0 to level n; i.e., the inelastic cross sections and their associated energy losses depend on the level difference n, but not the identity of the levels:

$$S_{i,i+n}(\varepsilon) \to S_n(\varepsilon) = S_{on}(\varepsilon)$$
$$\varepsilon_{i,i+n} \to \varepsilon_n = n\, \varepsilon_{ol} \qquad (10)$$

The assumption on the energy losses involves essentially the neglect of anharmonicity and its direct effect on Equation (9) is not expected to be serious. The assumption about the cross sections is much more difficult to justify and is undoubtedly not true in detail, the general level of the cross sections is, however, consistent with Chen's results[6] for N_2 even though the energy dependence is not correct.

Incorporating the assumptions (10) with Eq. (9) reduces the double sum (over i and j) into a single one over n = j-i. The resulting equation is:

$$\mu(\varepsilon)B(\varepsilon) = \sum_s \delta^s \sum_n \int_\varepsilon^{\varepsilon+n\varepsilon_{ol}^s} \left[\exp\left(\int_\xi^\varepsilon B(\eta)d\eta\right) - \sigma_n^s \exp\left(\int_{\xi-n\varepsilon_{ol}^s}^\varepsilon B(\eta)d\eta\right)\right] \xi\, S_n^s(\xi) d\xi \qquad (11)$$

where

$$\sigma_n^s = \sum_{j=n}^\infty \delta_j^s/\delta^s \qquad (12)$$

The effect of the vibrational (and electronic) level populations now enters the problem solely through the parameter σ_n^s. In a situation where vibrational excitation is dominant and the lowest levels can be approximated by a Boltzmann distribution function at an equivalent vibrational temperature T_{vo} based on the 0 to 1 population ratio, σ_n^s becomes $\exp(-n\varepsilon_{ol}^s/kT_{vo})$. For typical lasing situations in CO where the "plateau" region of the vibrational level distribution is 10^{-2} to 10^{-3} of the ground state vibrational population this approximation is a very good one. Within these assumptions Equation (11) can serve as the starting point for deducing effects of mixtures through the parameters δ^s and S_n^s, and the effect of elevated vibrational energy through σ_n^s as determined by the parameter T_{vo}.

III. Approximate Solutions

Vibrational Collisions

In the region of energies where vibrational-excitation collisions are dominant, the characteristic range of integration on the right-hand side of Eq. (11) is ε_o a typical vibrational energy spacing. Now the logarithmic slope B is assumed to be approximately constant over an energy range ε_o and also large enough so that integrals from $\varepsilon + \varepsilon_o$ to $\varepsilon + 2\varepsilon_o$ can be neglected compared to integration from ε to $\varepsilon + \varepsilon_o$. These assumptions incorporated into Eq. (11) lead to an approximate

equation for $\beta = \varepsilon_0 B$:

$$\beta^2 = M(\varepsilon)(1-e^{-\beta})\left(1-R\left(\beta, \frac{\varepsilon_0}{kT_{vo}}\right)e^{\beta-\frac{\varepsilon_0}{kT_{vo}}}\right) \quad (13)$$

where

$$M(\varepsilon) = \frac{3Q_m(\varepsilon)\, S_V(\varepsilon+\tilde{\varepsilon})\varepsilon_0^2}{(E/N)^2} \quad (14)$$

and

$$Q_m = \sum_s \delta^s Q_{ms} \text{ and } S_V = \sum_{s,n} \delta^s S_n^s \quad (15)$$

while $\tilde{\varepsilon}$ is an energy value between 0 and ε_0 which defines an average value of S_V. Formally $\tilde{\varepsilon}$ is defined by the relation:

$$\int_0^1 S_V(\varepsilon+\varepsilon_0 x)(\varepsilon+\varepsilon_0 x)e^{-\beta x}dx = S_V(\varepsilon+\tilde{\varepsilon})\varepsilon\int_0^1 e^{-\beta x}dx \quad (16)$$

The parameter $R(\beta,\varepsilon_0/kT_{vo})$ can again be formally defined as

$$\int_0^1 \sum_s \delta^s \sum_n S_n^s\, (\varepsilon+\varepsilon_0 x)\sigma_n^s e^{\beta n\varepsilon_0^s} 1(\varepsilon+\varepsilon_0 x)e^{-\beta x}dx = R\left(\beta, \frac{\varepsilon_0}{kT_{vo}}\right)e^{\left(\beta-\frac{\varepsilon_0}{kT_v}\right)}\varepsilon S_V(\varepsilon+\tilde{\varepsilon})\int_0^1 e^{-\beta x}dx \quad (17)$$

$R(\beta, \varepsilon_0/kT_{vo}) \sim S_1(\varepsilon+\tilde{\varepsilon})/S_V(\varepsilon+\tilde{\varepsilon})$ when $\beta << \varepsilon_0/kT_{vo}$ and the whole term is negligible for $\varepsilon_0/kT_{vo} >> 1$. When β is near ε_0/kT_{vo}, $R(\beta, \varepsilon_0/kT_{vo})$ approaches unity and clearly represents a detailed balance between vibrationally exciting and super-elastic collisions. Equation (13) can be solved for any number of approximate representation of $R(\beta,\varepsilon_0/kT_{vo})$ but the number of assumptions already incorporated in its derivation do not warrant anything but the simplest solution. The term involving $R(\beta, \varepsilon_0/kT_V)$ is assumed to be negligible except when $\beta \approx \varepsilon_0/kT_{vo}$ at which point $\beta = \varepsilon_0/kT_V$ is the appropriate solution. The results of this simple approximation are shown in Figure 1 with $\tilde{\varepsilon} = \varepsilon_0/2$. The approximate solution for β varies linearly with the parameter $M(\varepsilon)$ when $M(\varepsilon) << 1$ and as $\sqrt{M(\varepsilon)}$ when $M(\varepsilon) >> 1$.

Electronic Collisions

The approximate solution above did not explicitly depend on the fact that the dominant inelastic processes were vibrational excitation. The assumption that the logarithmic slope is approximately constant over the characteristic energy range ε_0 (the typical energy loss), however, makes the approximation inappropriate in the energy range where electronic collisions are dominant. A reasonable approximation can be obtained provided the cross sections in this energy range can be approximated by a simple step function followed by a slow $1/\varepsilon$ decay.

$$S_e(\varepsilon) = 0 \qquad \varepsilon < \varepsilon_m$$
$$= \frac{\varepsilon_m S_e(\varepsilon_m)}{\varepsilon} \qquad \varepsilon \geq \varepsilon_m \quad (18)$$

Substitution of Eq. (18) into Eq. (11) together with the assumption that $\varepsilon_m B(\varepsilon_m) >> 1$ leads to the following approximate solution for $\beta_e = \varepsilon_m B\ (\varepsilon)$:

$$\beta_e \approx \frac{\beta_m}{\sqrt{\hat{\varepsilon}}} \qquad \varepsilon > \varepsilon_m$$

$$\frac{\hat{\varepsilon}\beta_m}{\beta_e} \approx \frac{1-e^{-\hat{\varepsilon}\beta_m}}{1-e^{-\hat{\varepsilon}\beta_m}-\beta_m\left(\ell n\hat{\varepsilon}+Ei\ (-\beta_m)-Ei(-\hat{\varepsilon}\beta_m)\right)} \qquad \varepsilon<\varepsilon_m \quad (19)$$

where

$$\hat{\varepsilon} = \varepsilon/\varepsilon_m \text{ and } \beta_m = \frac{\sqrt{3Q_m(\varepsilon_m)S_e(\varepsilon_m)}}{(E/N)}\varepsilon_m \quad (20)$$

The function Ei(x) is the standard exponential integral

$$Ei(x) = \int_{-\infty}^{x} e^t \frac{dt}{t} \quad (21)$$

The result for $\hat{\varepsilon}\beta_m >> 1$ (a reasonable approximation within the expected range of validity) is shown in Figure 1.

Basic Parameters

Aside from the obvious parameter ε_0/kT_{vo} which measures the importance of super-elastic vibrational collisions, the electric field E/N appears in a non-dimensional grouping of the form involving a characteristic inelastic energy loss and the square root of the product of the momentum and inelastic cross sections. In the region of dominant vibrational collisions this modified E/N parameter appears to be $1/\sqrt{M(\varepsilon)}$, while for electronic excitation region, the parameter is $1/\beta_m$. In either regime the parameter can be viewed as the ratio of energy gained from the field by electrons of energy ε between two successive inelastic collisions to the characteristic energy loss for the relevant inelastic process. The generalized parameter is therefore $E\,\ell(\varepsilon)/\varepsilon_c$ where ε_c is obviously chosen either as ε_0 for vibrational collisions or ε_m for the electronic excitation process. The only parameter requiring explanation is the length scale $\ell(\varepsilon)$. Under the assumption of a random walk of the electrons with many elastic energy-conserving collisions between successive inelastic collisions $\ell(\varepsilon) \sim \sqrt{N_c(\varepsilon)}\ \lambda_m(\varepsilon)$ where N_c is the number of elastic collisions between two inelastic collisions and λ_m the momentum mean free path is the characteristic distance between elastic collisions. N_c in turn can be considered to be λ_V/λ_m. Substitution of simple formulas for the mean free paths in terms of the cross sections leads to the result:

$$\frac{E\,\ell(\varepsilon)}{\varepsilon_c} \sim \frac{1}{\sqrt{M(\varepsilon)}} \text{ for vibrational excitation}$$
$$\sim \frac{1}{\beta_m} \text{ for electronic excitation} \quad (22)$$

Indeed while certain aspects of the approximate solutions shown in Figure 1 are certainly of doubtful accuracy the relevance of the energy ratio $E\ell/\varepsilon_c$ is physically obvious and should be the principal parameter determining the local behavior of the distribution function. Figure 2 in fact shows that while the approximate solutions are not qualitatively correct, the parameters mentioned above do a very

good job of correlating a very large number of exact numerical solution for many mixtures of CO, N_2, and He (see Section V).

V. Numerical Solution

Basic Procedure

Equation (11) is amenable to straightforward iteration as a numerical scheme of solution. Considering Eq. (11) in the form

$$B(\varepsilon) = K(B(\varepsilon),\varepsilon) \tag{23}$$

where K is an integral operator, an iteration scheme of the form

$$B^{(n)}(\varepsilon) = \left[K(B^{n-1}(\varepsilon),\varepsilon) + xB^{(n-1)}\right]/(1+x) \tag{24}$$

is used. Iteration is continued until

$$\left|K\left(B^{(n-1)}(\varepsilon),\varepsilon\right) - B^{(n-1)}\right| < aB^{(n-1)} \tag{25}$$

where a is a specified accuracy.

The procedure is insensitive to the choice of x as long as B never approaches $1/kT_{VO}$ and generally takes 5 to 10 iterations. This remains true as long as the parameter $\eta_V = NkT_{VO}\sqrt{(3Q_mS_V)_{max}}/E < \sim .9$.

For low fields and high vibrational temperature $\eta_V > .9$ and the super-elastic collisions practically balance the vibrationally exciting collision in the energy range where the vibrational cross sections are high. The operator K becomes very sensitive to small errors and the convergence of the iteration process given by Eq. (24) becomes strongly dependent on the value of x. Since the major part of the problem comes from that region of energy space where the local $B(\varepsilon)$ is very close to $1/kT_{VO}$, an additional stabilization scheme is introduced to dampen large fluctuations in this energy range. The scheme is operative only when successive iterants on $B(\varepsilon)$ lie on opposite sides of a specified thin strip about $1/kT_{VO}$ $(1/kT_{VO} \pm \gamma)$. The final approach to the converged solution is therefore unaffected by this procedure. Additionally, tests have been performed where x is reduced to zero once the solution has approached within a required accuracy, and further iteration has not indicated any instability.

Solutions have been obtained for many cases where $\eta_V > .9$ with values of x varying between about 2 and 5. The number of iterations to convergence is higher than for the $\eta_V < .9$ situation but generally 12 to 15 are sufficient.

Calculations

All the calculations reported in Section VI were performed with the accuracy, a, set at 10^{-3}, on an IBM 360-91 computer. Each iteration takes from .1 to .2 seconds depending on the number of species, cross sections, and energy points used. A check on the validity of the results is provided by an overall energy balance. This was found to be always satisfied to better than 1%.

A series of calculations were performed for several mixture ratios of CO-He, CO-N_2, and CO-N_2-He, for a number of (E/N)'s. The energy range was generally from ε_ℓ=0 to ε_u=19, with spacing $\Delta\varepsilon$=.05 up to ε=5.0 and $\Delta\varepsilon$=.25 for ε=5.0 to ε_u=19.0. For the range of E/N's used the upper limit on the energy ε_u did not influence the solution in the relevant energy region as long as $\varepsilon_u > 10$. The vibrational cross sections for CO were taken from Schulz[7] and Boness and Schulz[8]. A single electronic-excitation cross section with a threshold of 6 volts and magnitude of 10^{-16} cm^2, as used by Nighan[1], was used for CO. The nitrogen vibrational cross sections were taken from Schulz[7] and Boness and Schulz[8] while electronic and ionization cross sections were taken from Engelhardt, Phelps, and Risk[9]. The momentum cross sections were taken from Hake and Phelps[10] for CO, from Engelhardt, et al.[9] for N_2, and from Frost and Phelps[11] for He.

VI. Results and Conclusions

Scaling Parameters

As suggested by the approximate solution the local logarithmic slope should be primarily dependent upon the parameter $M(\varepsilon)$ within the range where vibrational collisions are dominant. The results of all of the runs were thus plotted as $\beta = -\varepsilon_0 \, d\,\ell n\, f/d\varepsilon$ versus $M(\varepsilon)$ with ε_0 chosen as the mole fraction averaged vibrational spacing,

$$\varepsilon_0 = \sum_s \delta^s \varepsilon_{01}^s \tag{26}$$

A summary of the results is shown in Figure 2 together with the approximate solution. As might be expected the correlation is best at high values of the slope β and poorest at low values. In addition there is noticeable separation between the results where the cross section is rising with increasing energy from those where it is falling. The correlation is, however, in general better than is the quantitative agreement with the approximate solution. The results suggest that scaling of the local behavior of the distribution function from one mixture to another and one E/N to another can be accomplished by examining the $M(\varepsilon)$ parameter, within the energy range where vibrational collisions are dominant.

Carbon Monoxide-Helium Mixtures

The desired results such as $f(\varepsilon)$ and its various moments must of course depend on the shape of the cross sections as well as some characteristic value of $M(\varepsilon)$. In order to test the correlating value of the parameter $M(\varepsilon)$ without too much influence of different cross section shapes, a series of calculations for mixtures of CO and Helium were performed for identical values of the parameter

$$\alpha = E/\left(N\varepsilon_0\sqrt{(Q_mS_V)_{max}}\right) = 1/\sqrt{M(\varepsilon)_{max}} \tag{27}$$

but different mixture ratios (from 100% CO to 5% CO) and E/N's. The results for the distribution function are shown in Figure 3 for two different α's. While there is some spread of the results the parameter appears to be a very good measure of the effectiveness of the electric field. If the results had been plotted for common values of E/N rather than α no apparent correlation would exist as E/N

for 100% CO has to be about 8 times larger than for 5% CO in order to achieve similar behavior. The fraction of the input power going into vibration is shown in Figure 4 as a function of the parameter α. The correlation is extremely good and indicates that $\alpha \gtrsim 1$ is a good indicator where energy begins to go into electronic states. All of the results for $T_{vo} < 1500$ are virtually indistinguishable from the results without super-elastic collisions, but begin to deviate significantly for higher vibrational temperature. As can be seen from the curve for $T_{vo} = 5000°K$, high vibrational temperature produces a reduction of energy into vibration at a fixed α. A more detailed examination of the fractional power into each process involving ($\Delta v = 1$, 2, 3, ... etc.) change in vibrational energy also shows a remarkably good correlation with the parameter α.

The equivalent electron temperature or 2/3 the mean electron energy has generally been considered a useful indicator of the state of the electron gas in a discharge and has been previously used as a correlation parameter for CO_2 mixtures.[5] Figure 5 shows this effective electron energy versus the parameter α for two different vibrational temperatures and different mixtures of CO-He. The correlation is again remarkably good and suggest that the mean energy would also correlate the results as in CO_2. The parameter α, however, is a much more useful scaling parameter as it can be computed simply from given quantities such as E/N, cross sections, and species concentrations. It can be used in preliminary design of experiments by predicting the required change in the electric field to maintain similarity of electron-vibrational pumping under changes of mixture ratios of the gas constituents.

The parameter α appears to be an adequate correlating parameter for CO-He mixtures since the shape of the cross section product $Q_m(\varepsilon)S_v(\varepsilon+\varepsilon_o/2)$ is only very mildly dependent on the mixture. The product $(Q_m S_v)_{max}$ is therefore an adequate measure of the local slope B over the entire relevant energy range rather than simply at the point of maximum slope. If this parameter is to be useful over a wider range of mixture gases including other vibrationally active species, the effect of cross section shape must be included.

Carbon Monoxide, Nitrogen, and Helium Mixtures

In order to assess the importance of the cross section shape in the correlation, a series of calculations for CO-N_2 and CO-N_2-He mixtures were performed. The effect of cross section shape can be primarily represented by the location of the peak ε_p and a half-width δ, as can be seen from some sample plots of the product of the cross sections in Figure 6. Note that in spite of the far greater structure in the vibrational cross sections for N_2, the product $(Q_m S_v)$ is not very different in gross behavior from CO-He results, and the major features can be fitted fairly well by the expression

$$Q_m S_v = (Q_m S_v)_{max} \exp(-((\varepsilon-\varepsilon_p)/\delta)^2) \qquad (28)$$

Since the distribution function $f(\varepsilon)$ involves an integral over the slope $\beta(\alpha(\varepsilon))$, any correlation for f is going to necessarily involve the cross section shape parameters ε_p and δ. The normalization of f further complicates the problem. A relatively simple correlation can be obtained, however, by noting that for a large part of the range of parameters

$$\beta \sim M(\varepsilon) \sim \frac{1}{\alpha^2} e^{-\left(\frac{\varepsilon-\varepsilon_p}{\delta}\right)^2} \qquad (29)$$

Since the slope normalized by δ is more convenient for integration, a new parameter

$$\alpha^* = \frac{\varepsilon_o}{\delta}\alpha = \frac{E/N}{\sqrt{\varepsilon_o \delta}\sqrt{(Q_m S_v)_{max}}} \qquad (30)$$

becomes a more useful measure of the effect of the electric field, and f can be shown to be

$$f = f_n F(\alpha^*, x) \qquad (31)$$

where $x = (\varepsilon-\varepsilon_p)/\delta$. f_n can be estimated a number of different ways, but the most convenient is

$$f_n = \frac{1}{\sqrt{\varepsilon_p - x_o\delta}\,\varepsilon_p} \qquad (32)$$

where x_o is the location of the peak of $\sqrt{\varepsilon}\, f(\varepsilon)$ and can be either estimated using the correlation for β or more simply taken as a constant.

Figure 7 shows f/f_n versus x for two different values of α^* for several mixtures. The correlation within the region of vibrational excitation is remarkable. The curves separate substantially at higher values of x where electronic excitation is important. This is not surprising as the electronic cross sections will certainly not scale with the parameter α^*, and are clearly different for N_2 and CO. Figure 8 shows the fraction of the input power going into vibrational excitation versus the parameter α^*. While there is a noticeable difference when N_2 is included, a ± 10% correlation can still be achieved over a significant range of α^*. Similar plots versus E/N for different mixtures would show no apparent correlation. Figure 8 can be used directly in preliminary design of discharges for laser applications. Scaling from one mixture to another by changing E/N to keep α^* constant will preserve similarity of the power input into vibration.

Figure 9 shows the mean electron energy $\bar{\varepsilon}$ normalized by ε_p, and the drift velocity V_D normalized by

$$V_N = \sqrt{\frac{2e\varepsilon_p}{m}}\sqrt{\frac{S_{v,max}}{Q_{m,max}}} \qquad (33)$$

versus the parameter α^*. Both quantities correlate very well for $\alpha^* < 1$. While the drift velocity is correlated to within about ± 10% over the range of α^* shown, the mean energy shows a substantial systematic spread for $\alpha^* > 1$. While a complete explanation of this effect has not yet been obtained, the much greater dependence of the mean energy on the high energy portion of the distribution function suggests that the difference in electronic cross sections is primarily responsible. Work is in progress to incorporate the electronic cross sections into an additional non-dimensional parameter that will correlate the behavior at high α^*.

Summary of Conclusions

Reformulation of the equation for the electron distribution function into an integral equation for the logarithmic slope has led to both approximate analytic solutions and numerical results by iteration with super-elastic collisions included. The major results of this approach have been the following:

1) Within the region of dominant vibrational excitation the local logarithmic slope is primarily dependent upon the local product of the momentum and total vibrational cross sections ($Q_m S_V$) multiplied by a characteristic energy loss squared (ε_0^2) and divided by $(E/N)^2$. This suggests a scaling law for mixtures and with respect to the field E/N.

2) Super-elastic collisions play little role in the major results until $\varepsilon_0/kT_{V0} < 2$. For sufficiently low electric field and high kT_{V0} the super-elastics produce a local equilibrium with vibrational states in the energy range where vibrational cross sections are high. This reduces the net energy going into vibration and produces the previously observed raising of the "tail" of the distribution function.

3) For mixtures involving only one vibrationally active species correlation of the distribution function and its important moments can be achieved by the parameter α (Eq. 27) based on the peak of the cross section product alone. This is possible because the cross section shape is little changed with mixture ratio.

4) For more varied mixtures such as $CO-N_2-He$ the parameter can be conveniently modified to α^* (Eq. 30) and the results have to be appropriately normalized by parameters involving the cross section shape parameters ε_p and δ. The correlation for the distribution function, vibrational pumping and drift velocity is quite good, while for the mean electron energy the correlation fails for $\alpha^* > 1$. This is probably a direct result of the much greater dependence of the mean energy on the high energy portion of the distribution function where electronic collisions are dominant.

VII. Acknowledgements

This work was performed under Air Force Office of Scientific Research Contract No. F44620-73-C-0059.

References

[1] W. L. Nighan, Phys. Rev. A2, 1989 (1970).
[2] W. L. Nighan, Appl. Phys. Lett. 20, 96 (1972).
[3] M. L. Hamilton, J. J. Kennedy, and T. J. Falk, U.S.A.F. Weapons Lab. Report AWL-TR-73-158, (Sept. 1973).
[4] F. T. Wu, W. M. Yu, and E. A. Lundstrom, Appl. Phys. Lett. 25, 463 (1974).
[5] O. P. Judd, VIII International Quantum Electronics Conference (Abstracts) p. 76, June 1974. Also in Los Alamos Informal Report LA-5562-MS, April 1974.
[6] J. C. Y. Chen, J. Chem. Phys. 40, 3513 (1964).
[7] G. J. Schulz, Phys. Rev. 135, A988 (1974).
[8] M. J. W. Boness and G. J. Schulz, Phys. Rev. A8, 2883 (1973).
[9] A. G. Engelhardt, A. V. Phelps, and C. G. Risk, Phys. Rev. 135, A1566 (1964).
[10] R. D. Hake and A. V. Phelps, Phys. Rev. 158, 70 (1967).
[11] L. S. Frost and A. V. Phelps, Phys. Rev. 127, 1621 (1962).

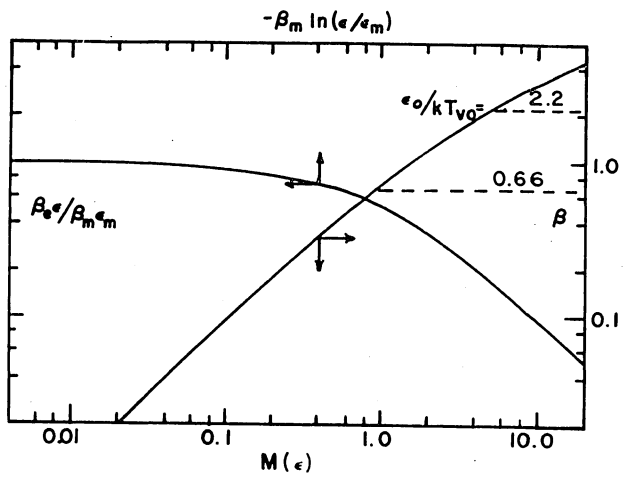

Figure 1. Approximate Local Solutions for the Logarithmic Slope.

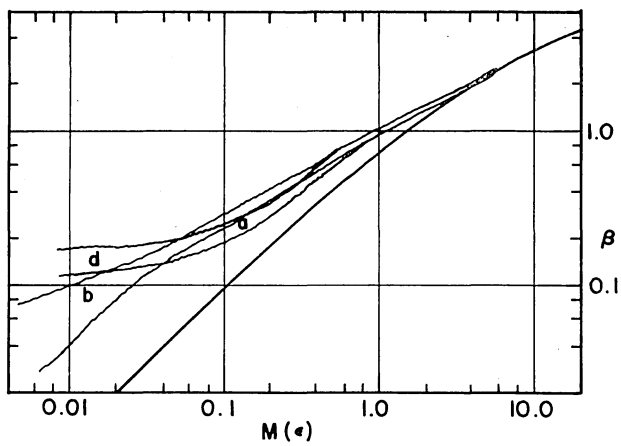

Figure 2. Correlation of Numerical Results for the Logarithmic Slope. a. In the energy range where vibrational cross section is decreasing with energy. b. In the energy range where vibrational cross section is increasing with energy. d. In the energy range where electronic cross section has dominant effect. ⟸ Analytic solution from Figure 1.

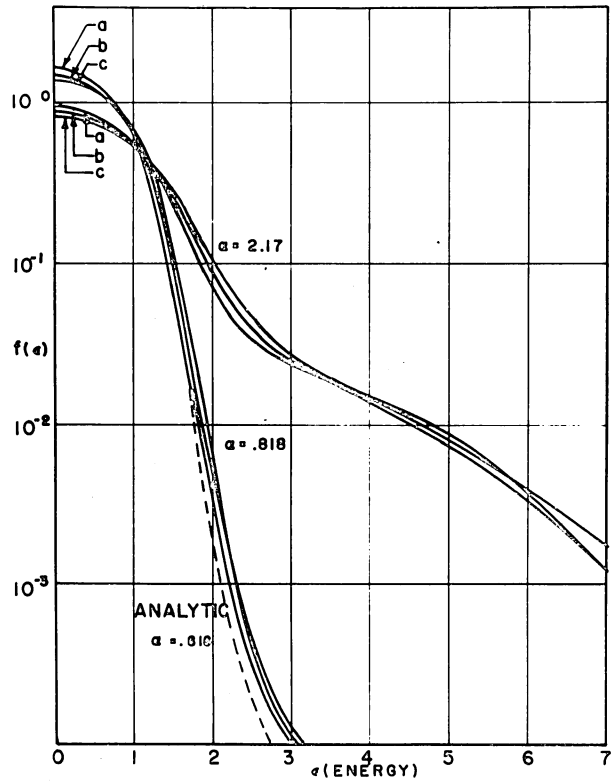

Figure 3. Numerical Results for the Distribution Function in CO-He Mixtures at T_{vo} = 1500°K. a. 5% CO-95% He mixture. b. 50% CO-50% He mixture. c. 100% CO gas.

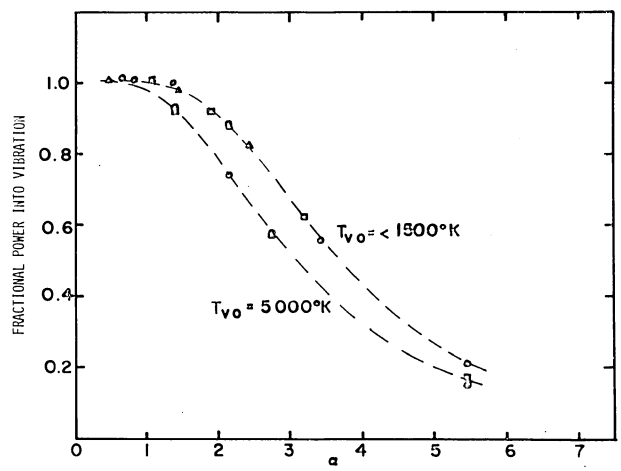

Figure 4. Fraction of Power going into Vibrational States in CO-He Mixtures. ⊡ 5% CO-95% He mixture. △ 50% CO-50% He mixture. ⊙ Pure CO gas.

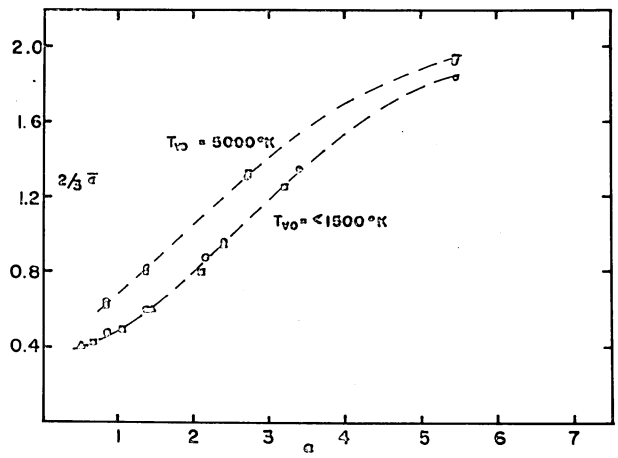

Figure 5. The Effective Electron Temperature (2/3 $\bar{\varepsilon}$) in CO-He Mixtures. ⊡ 5% CO-95% He mixture. △ 50% CO-50% He mixture. ⊙ Pure CO gas.

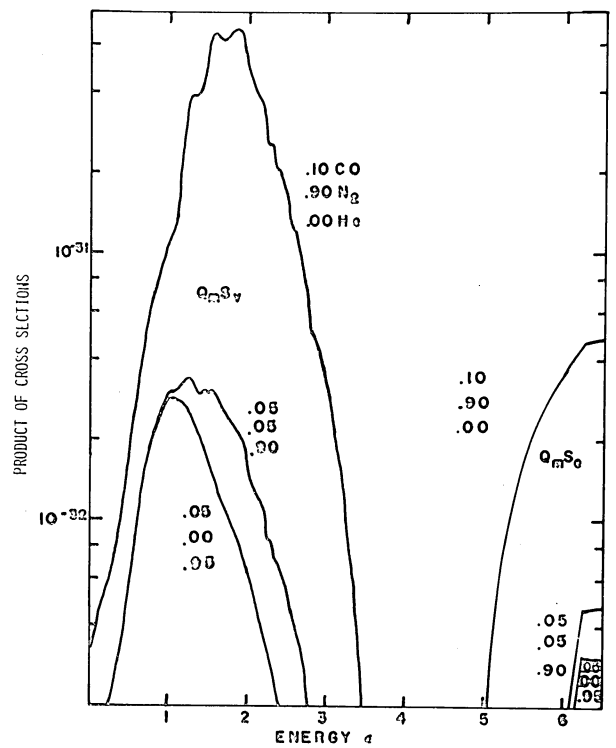

Figure 6. The Product of Elastic and Inelastic Cross Sections versus Energy in CO-N_2-He Mixtures.

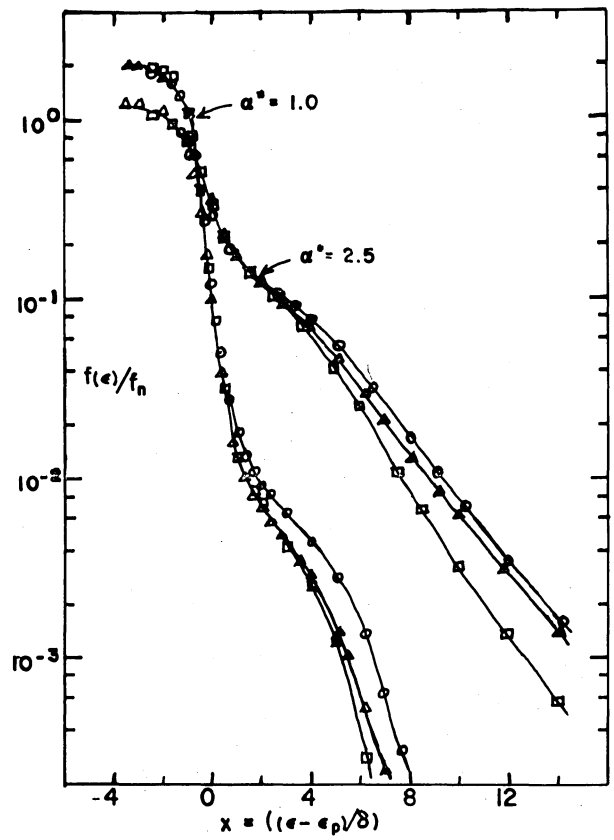

Figure 7. The Distribution Function in CO-N_2-He Mixtures at Two Values of α^*. ⊙ 5% CO-95% He. △ 10% CO-90% N_2. ⊡ 5% CO-5% N_2-90% He.

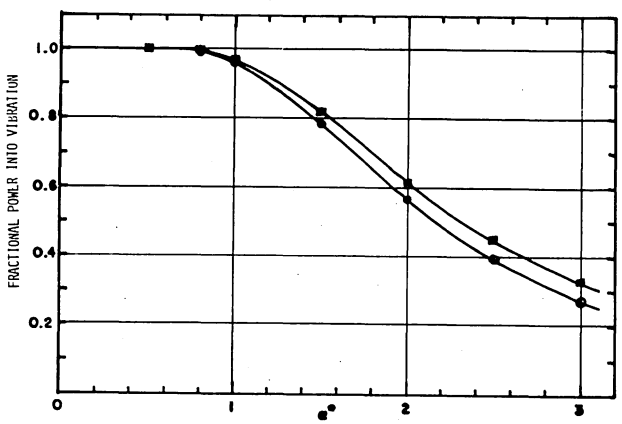

Figure 8. Fraction of Input Power going into Vibrational Excitation. ■ 5% CO-5%N_2 90% He and 10% CO-90%N_2. ○ 5% CO-95% He.

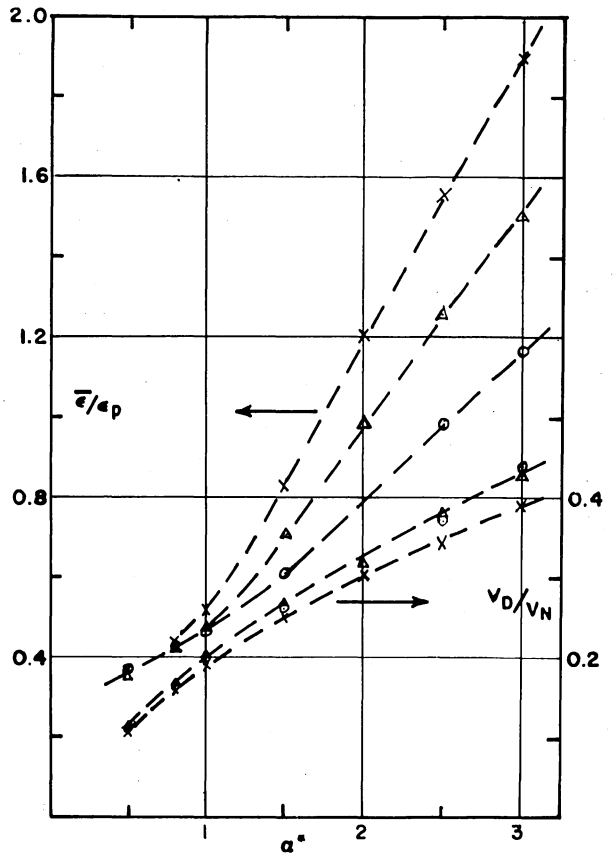

Figure 9. Mean Energy and Drift Velocity in CO-N_2-He Mixtures. ⊙ 10% CO-90% N_2. △ 5% CO-5% N_2-90% He. x 5% CO+.95% He.

DISCUSSION

D. A. McARTHUR: How much does your method depend on the cross-section displaying a very narrow width?

G. K. BIENKOWSKI: I have primarily been motivated to do this for vibrational processes. For laser applications, one is interested in narrow widths because that is how one is transmitting the energy into vibrations preferentially. I mentioned briefly an approximate solution. I also looked in the energy range where electronic transitions are taking place. If one can go to the other limit where the cross-section is relatively flat at the threshold and is relatively flat over other regions, one can use a somewhat different approximation and also come up with a similar result, and there would now be also a correlation for a relatively flat cross-section wherein the correlation would depend somehow on the level of the cross-secton, and presumably the energy would have something to do with the threshold energy. The specific correlation I discussed here does depend on the fact that one has a relatively high cross-section over a relatively narrow range of energy. Therefore almost the entire process locally is determined by what is happening locally and the slope is very high. So one does not have to go very far away from that region to produce essentially the main part of where the distribution function is varying.

PULSER-SUSTAINER GLOW DISCHARGE OPERATION IN STATIC CARBON MONOXIDE LASER MIXTURES

Daryl J. Monson and Craig M. Lee
Ames Research Center, NASA, Moffett Field, California 94035

Abstract

Theoretical studies show that efficient operation of CO electric-discharge supersonic lasers requires discharge methods that allow separate control of electron density, n_e, and reduced electric field, E/N (or electron energy). To date, external ionization by an electron beam has been successfully demonstrated in these lasers. Other promising (but unproven) possibilities include ultraviolet photoionization, ionization by nuclear reaction products, and a high repetition rate series of controlled avalanche ionization pulses (i.e., pulser-sustainer). We wish to report here successful operation of the pulser-sustainer concept in large-volume static room temperature CO laser mixes. (The concept has previously been demonstrated in small-volume static CO_2 laser mixes.) High voltage pulses and ultraviolet sparks at 33 kHz combined with a separate low voltage sustainer electric field produce spatially uniform plasmas in a 3.0 liter volume. Completely independent control of n_e and E/N is demonstrated. The tests are preliminary to testing of the concept in supersonic flow. Results include for several pure gases and mixtures the following measurements: cathode-fall voltage; self-sustaining E/N; recombination rate coefficient; average plasma n_e; average discharge input power; and the maximum discharge energy loading without arcing. Modifications being made to the system to allow higher pressures and energy loadings without arcing, and to allow operation in supersonic flow are discussed.

I. Introduction

The CO electric-discharge supersonic laser shows great promise for both high efficiency and power.[1] To achieve this, however, will require discharge methods which uncouple the plasma production from the process of adding energy to the gas. In particular, desirable discharge methods will combine an external ionization source with a low-voltage sustainer electric field which "tunes" the electrons to an energy sufficiently high for efficient vibrational excitation of CO but not high enough for electronic excitation or additional ionization. (Self-sustaining discharges operate at high electric fields which produce all three effects.) To date, external ionization by an electron beam has been successfully demonstrated in this laser.[2] Other promising, though unproven, possibilities include ultraviolet photoionization,[3] ionization by nuclear reaction products,[4] and the pulser-sustainer method.[5,6]

We wish to report in this paper operation of the pulser-sustainer method in large-volume static room temperature CO laser mixes. The tests are preliminary to testing of the concept in supersonic flow. Basically, the method applies two discharges to the gas. The first fast high-voltage pulse creates a uniform plasma between the electrodes using only a small amount of energy. Then, the second low-voltage sustainer discharge adds energy to the gas during the recombination period following the ionizing pulse. Reilly[5] first applied the method in slowly-flowing CO_2 laser mixes using a single ionizing pulse. Then Hill[6] extended the method potentially to continuous operation by using a string of ionizing pulses at a high-repetition rate such that only a small amount of recombination occurred between pulses. He demonstrated the method in 0.3-ℓ-volume static CO_2 laser mixes for a period extending to one traversal time through a subsonic flow device (i.e., 1 msec).

The test setup used here for CO laser mixes is similar to that used by Hill and will be described in Section II. The results of the tests will be described in Section III, and the conclusions of this study will be given in Section IV.

II. Experimental Apparatus

The electrode geometry used in this study is sketched in Fig. 1. The electrodes are located transversely across a supersonic channel, although for purposes of the present tests the channel was blanked off and filled with static CO laser mixes at room temperature. The electrodes are separated by 5.5 cm with a discharge volume of 3.0 ℓ. (This is an order of magnitude larger than for Hill's initial tests.) The electrodes are aluminum with sand-blasted surfaces and edges that are rounded but do not conform to a Rogowski profile. Two rows of ten UV spark pins each are located 10 cm respectively up and downstream of the main electrodes. (Hill located spark pins behind a porous cathode.) A high-repetition-rate high-voltage pulse forming network[7] is connected to both the spark pins and the main anode. The pulser contains a 0.002-μF capacitor charged to 23 kV. A fast-rise-time quenching spark gap switches the charged capacitor into the gas at a repetition rate of 33 kHz. Because the spark pins are pointed and the downstream ones are closely spaced from ground, they break down a fraction of a microsecond before the main electrodes. This produces a background of low-level preionization for uniform plasma production in the discharge volume. (Each pin is coupled through a 0.00005-μF capacitor so that most of the pulse energy goes into the main discharge.) Finally, a charged 15-μF sustainer capacitor is used as a constant-voltage pumping source during recombination. A large inductor is placed in series with the sustainer capacitor to isolate it from the ionizing pulses.

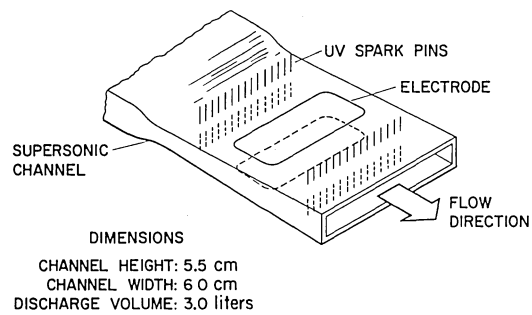

Fig. 1 Sketch of the CO pulser-sustainer discharge laser.

The blanked-off test channel was outgassed and pumped out to 5 μ pressure before commercial grade gases were loaded into it for testing. The impurity level for the tests is estimated at about 200 ppm, with about half coming from the gas bottle and half from the residual outgassing in the plexiglas channel. Sustainer voltages were measured with a Tektronix high-voltage probe and sustainer currents with a Pearson current probe, and both were recorded with an oscilloscope camera.

III. Results and Discussion

Results will first be presented of cathode-fall voltage measurements made in CO, N_2, He, and Ar alone and in various combinations of interest for CO electric-discharge lasers. Then measurements of self-sustaining discharge reduced electric field, E/N, will be presented for these same gases. Finally, measurements of the important operating characteristics of a pulser-sustainer glow discharge in these gases will be presented and discussed.

The total voltage across a glow discharge consists of the drop across the thin cathode-fall layer plus the drop across the positive column. Only the positive column is usable for exciting a laser gas, with the cathode fall serving only to liberate electrons from the cathode to keep the discharge operating. For normal laser geometries, the cathode fall voltage is a small fraction of the positive column voltage and can safely be ignored. However, for the closely-spaced transverse electrode geometry and subatmospheric pressures of the present tests, the cathode-fall voltage is a significant fraction of the total voltage and must therefore be accurately known if the positive column voltage is to be computed. Unfortunately, published values[8] of cathode-fall voltages for pure gases are sparse and for mixtures do not exist. Accordingly, we measured cathode-fall voltages in our test setup for several gases and mixtures. This was performed by the traditional method of striking a DC glow discharge across the electrodes, and then reducing the pressure to a low value (less than 1 torr) until the positive column voltage was negligible and the measured voltage reached a minimum.

The cathode-fall voltage measurements are presented in Fig. 2. They are plotted against the mole fraction of CO in the indicated mixtures. The values range between 200-400 V. Notice that for CO in N_2 or Ar, the voltage gradually decreases with the fraction of CO from the high value for CO to the lower values for the other two gases. For CO in He, however, the voltage stays up close to the value for CO even for very small fractions of CO. Notice, also, that our measured results for pure gases are considerably higher than the published values in Cobine.[8] This is not surprising, however, since Cobine points out that the results one obtains are highly dependent on gas purity and cathode surface condition. We established that our results for pure He were sensitive to gas purity by observing that the cathode-fall voltage increased from its initial value after several minutes in the plexiglas channel. (This is consistent with the previously discussed results for small fractions of CO in He.) The same test with the other gases showed no voltage change with time. Except for He, we feel the main reason for our higher cathode-fall voltages is the oxide layer on our electrodes compared to the pure aluminum surfaces reported in Cobine. The condition of our cathode surface is closer to current laser practice, however.

We had some doubts that the cathode-fall voltage results measured in a DC discharge at low pressure would apply to a pulser-sustainer discharge at much higher pressure. Accordingly, we performed a test for most of the gases in Fig. 2 where we operated a short burst of the pulser with the sustainer voltage turned down to a low value. Although we had some problem reading the voltages accurately at low values due to interaction between the pulser and the sustainer, we observed that at sustainer voltages above the values given in Fig. 2 the plasma remained conducting, whereas below those values the current was zero. We are thus confident that the values given in Fig. 2 are accurate cathode-fall voltages for our pulser-sustainer tests.

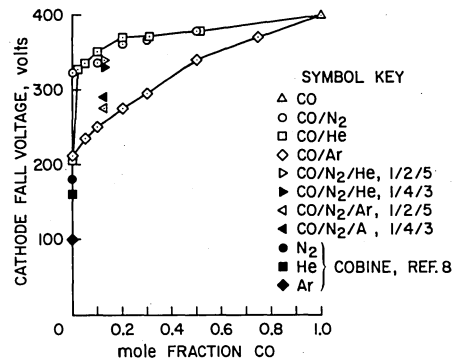

Fig. 2 Cathode-fall voltages for CO gas mixes and aluminum cathode.

Having established the cathode-fall voltages, we proceeded to measure the self-sustaining E/N for many of the same gases and mixtures. We did this to establish the upper limits on sustainer voltage for pulser-sustainer operation, and also to establish at what average electron energies self-sustaining discharges operate for these mixtures. The tests were performed by applying single high-voltage pulses to the gas to create a plasma, and then raising the voltage on a small 1-μF sustainer capacitor to the point where the measured peak voltage across the gas reached an asymptotic value. The cathode-fall voltages in Fig. 2 were then subtracted from the measured maximum voltages.

The results for self-sustaining E/N are shown in Fig. 3. They are plotted against the mole fraction of CO in the indicated mixtures. We feel our results may be somewhat low since we experienced

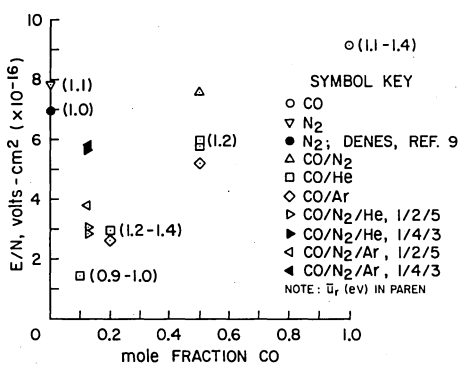

Fig. 3 Self-sustaining E/N for CO gas mixtures.

premature corona breakdown from the anode to our spark pins at the highest sustainer voltages. For cases where two points are given, they represent measurements at two widely different pressures in order to verify the pressure independence of the results. The only measured published value we could find to compare with was from Denes and Lowke[9] for pure N_2. Our value is slightly higher and agrees with Denes and Lowke's value when they deliberately added a small amount of H_2O to their gas to increase the electron dissociative attachment rate. Thus our fairly high impurity level (about 200 ppm) may account for our high N_2 result. For a few of the mixes, the estimated average electron energy is shown in parentheses beside the data point. These were obtained from computer solutions of the electron distribution function.[10,11] The results consistently indicate self-sustaining discharge electron energies slightly above 1 eV. Since efficient vibrational excitation of CO occurs at an energy of 0.5-0.7 eV,[10] this verifies the statement that we made in the introduction that self-sustaining discharges operate at voltages too high for efficient operation of CO lasers.

Following measurement of the cathode-fall voltages and self-sustaining electric fields, we performed pulser-sustainer discharge tests in many of the same gases at the test conditions previously stated in Section II. The procedure we used was to turn on a burst of the pulser lasting 150 μsec, and then raise the sustainer voltage to a point just below the arc-formation limit. This represents about 6 pulses at the stated repetition rate and approximately simulates one flow traversal time through the discharge when the laser is operated with supersonic flow. A typical oscilloscope voltage and current trace from such a test is shown in Fig. 4. For this example, about 90 kW of discharge power is being added to the gas. Notice that the current trace takes about two pulses to build up to a full value because of the inductor in series with the sustainer capacitor. The inductor also causes the slow rise of current after each re-ionizing pulse and the corresponding drop in the discharge voltage. A smaller inductor will speed up the recovery of the voltage and current, but it cannot be made so small that the pulser current is shunted into the sustainer capacitor. The voltage droop observed during the burst is caused by depletion of the 15-μF sustainer capacitor energy. (Future tests will use a 1200-μF capacitor bank to allow testing to 1 msec without a voltage droop.)

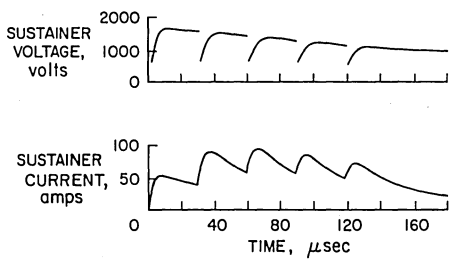

Fig. 4 Current and voltage traces for power loading in 50 torr 1/2/5, $CO/N_2/He$.

A summary of the pulser-sustainer test results for the various gas mixtures is given in Table 1. Results are quoted for each mixture at the pressure that gave the maximum energy loading. Also, mixtures are listed in order of increasing energy loading. The results shown for positive column discharge power are computed by subtracting the cathode-fall voltages in Fig. 2 from the measured voltages.

Consider the results for discharge power and energy loading for CO in He listed in Table 1. The results clearly show a trend of both increasing power and energy loading as the fraction of CO is decreased. The maximum power of 115 kW and energy loading of 0.14 eV/CO molecule both occur for 5% CO. Large fractions of He seem to effectively suppress arcing and allow discharge operation at considerably higher pressures and powers. Also because the fraction of CO is lower, the energy loading per CO molecule also goes up. Computer studies[1] show that an energy loading above 0.1 eV/CO molecule is generally required for these lasers to "turn on," and 0.5 eV/CO molecule is required for them to reach their maximum efficiency. The present results show that we have exceeded threshold for mixtures with less than 10% CO, but that we are still considerably below the desired energy loading.

Replacing part of the CO in a mixture by N_2 is seen to have a desirable effect from Table 1. The presence of N_2 allows operation at considerably higher pressure and power without arcing. Our highest measured power of 171 kW was achieved in the 2.5% CO, 2.5% N_2, 95% He mix. Notice that the energy loading with N_2 is only up slightly, however.

Compare the sustainer E/N and corresponding electron energies listed in Table 1 with the self-sustaining values given in Fig. 3. The present values are observed to be much lower, thus verifying that we have achieved independent control of n_e and E/N. The values achieved for electron energy are actually slightly lower than the optimum range of 0.5-0.7 eV desired.[10]

The average electron densities achieved were computed from the measured currents and computed drift velocities[11,12] for some of the mixtures. They are listed in Table 1. The values range from $2\text{-}4\times10^{11}$ cm^{-3} with the highest values being for mixes with low fractions of CO. This compares with 2×10^{11} cm^{-3} achieved by Hill[6] in his pulser-sustainer tests.

Finally, electron-ion recombination rate coefficients were computed for many of the mixes from the measured decay rate of the sustainer current after the last pulse. The values listed in Table 1 all fall slightly less than 10^{-7} cm^3 sec^{-1}. These values agree with measurements by Douglas-Hamilton[13] in CO where the impurity level was not carefully controlled (as in our case), but our values are about a factor of 5 lower than those measured by Center[14] where the impurities were very carefully controlled. We see a weak trend of increasing rate coefficient with decreasing fraction of CO, but this may be entirely due to the increasing pressure level.[14]

The results of this paper show that we have achieved the energy loading "threshold" for one gas exchange time in the CO supersonic laser but that we are still well short of the maximum desired. We are presently making several design changes that should allow us to operate at higher pressures, voltages and energy loadings without arcing. The most important of these is that we are making new electrodes with edges that conform to a Rogowski profile. (We have noticed in our present tests

that when we arc, breakdown invariably occurs at the electrode edge.) Also, we are increasing the number and decreasing the diameter of our spark pins to provide more UV light for pre-ionization. Finally, we plan on operating our pulser at a higher voltage, a higher repetition rate, and cutting down its circuit inductance in order to achieve higher peak currents (and therefore higher electron densities) in each pulse.

Beyond the above changes, the only way for us to get higher energy loadings with supersonic flow is to increase the gas residence time in the discharge. This can be done by making the discharge longer in the flow direction or replacing He by Ar to slow down the gas. To check out this last idea, we replaced He by Ar for a few of the mixtures listed in Table 1. The result was that we had arc formation at all useful pressures and energy loadings. Thus, Ar does not appear desirable for CO pulser-sustainer discharges. This is in contrast to e-beam CO supersonic lasers which operate best with Ar.[2]

Although the present results are only for static gases, we plan next to try the pulser-sustainer concept in supersonic flow. There we expect our biggest problem will be "blowing out" of the discharge downstream. In order to solve this expected problem, we plan on trying two solutions. First, we are going to recess our electrodes behind dielectric grids similar to those successfully used by Tulip and Seguin[15] in a flowing CO_2 laser. This does two things for us. It presents a smooth surface to the flow while we retain shaped electrodes, and it traps a static low-density plasma behind the grids above the electrodes to hopefully help keep the discharge stationary. (We have tried out grids over our electrodes in a static gas and they don't seem to affect the glow stability.) Second, we plan on trying a resistive anode[16] to try to keep the discharge spread out over the electrodes.

IV. Conclusions

We have demonstrated operation of a pulser-sustainer glow discharge in static 3.0-ℓ-volume CO laser mixtures for times simulating one gas exchange through a supersonic laser. Completely independent control of n_e and E/N is achieved. Electron densities in the range of $2\text{-}4\times10^{11}$ cm^{-3} and average electron energies in the range of 0.4-0.5 eV are attained. This is slightly below the range of electron energies that efficiently excites the CO laser. A maximum discharge power of 171 kW is loaded into the gas at a pressure of 221 torr. This represents an energy loading of 0.16 eV/diatomic molecule for one gas exchange time and exceeds the "turn on" value of 0.1 eV/CO molecule for this laser. It is still short of the desired value of 0.5 eV/CO molecule, however. Best discharge operation is shown to occur for low fractions of CO in He. Replacing part of the CO with N_2 allows higher pressure and higher power operation without arcing. It is observed that Rogowski-shaped electrodes will be necessary to achieve higher pressures and energy loadings without arcing. Mixtures with Ar rather than He fail to produce a good discharge at any useful condition. Cathode-fall voltages between 200-400 V are measured, depending on the mixture. These are slightly higher than classical values for an aluminum cathode. Electron-ion recombination coefficients in the range $0.4\text{-}1.0\times10^{-7}$ cm^3 sec^{-1} are measured. These compare favorably with past measurements in gases with similar impurity levels. Finally, self-sustaining discharges are shown to operate at electron energies exceeding 1 eV, which exceeds the range for efficient vibrational excitation of CO. This establishes the need for discharge methods such as the pulser-sustainer which can operate at a lower electron energy.

References

[1]Monson, D. J., "Potential Open- and Closed-Cycle System Efficiencies for the CO, Supersonic, Electric-Discharge Laser," NASA TM X-62,438, 1975.

[2]Jones, T. G., Byron, S. R., Hoffman, A. L., O'Brien, B. B., and Lacina, W. B., "Electron-Beam-Stabilized CW Electric Discharge Laser in Supersonically Cooled $CO/N_2/Ar$ Mixtures," AIAA Paper No. 74-562. Presented at the AIAA 7th Fluid and Plasma Dynamics Conference, Palo Alto, Calif., June 1974.

[3]Lind, R. C., Wada, J. Y., Dunning, G. J. and Clark, Jr., W. M., "A Long-Pulse High-Energy CO_2 Laser Pumped by an Ultraviolet-Sustained Electric Discharge," *IEEE Journal of Quantum Electronics*, Vol. QE-10, No. 10, Oct. 1974, pp. 818-821.

[4]McArthur, D. A., and Tollefsrud, P. B., "Measurement of Optical Gain in CO Gas Excited Only by Fission Fragments." *IEEE Journal of Quantum Electronics*, Vol. QE-12, No. 4, April 1976, pp. 244-253.

[5]Reilly, J. P., "Pulser-Sustainer Electric-Discharge Laser," *Journal of Applied Physics*, Vol. 43, No. 8, Aug. 1972, pp. 3411-3416.

[6]Hill, A. E., "Continuous Uniform Excitation of Medium-Pressure CO_2 Laser Plasmas by Means of Controlled Avalanche Ionization," *Applied Physics Letters*, Vol. 22, No. 12, June 1973, pp. 670-673.

[7]Austin, W. E., "Test and Development of a High Repetition Rate Pulse Forming Network," NASA CR-137,638, 1975.

[8]Cobine, J. D., *Gaseous Conductors*, Dover Publications, Inc., New York, NY, 1958.

[9]Denes, L. J., and Lowke, J. J., "V-I Characteristics of Pulsed CO_2 Laser Discharges," *Applied Physics Letters*, Vol. 23, No. 3, Aug. 1973, pp. 130-132.

[10]Nighan, W. A., "Electron Energy Distributions and Collision Rates in Electrically Excited N_2, CO, and CO_2," *Physics Review A*, Vol. 2, No. 5, Nov. 1970, pp. 1989-2000.

[11]Proctor, W. A., Private Communication, May 1974.

[12]Long, Jr., W. H., Bailey, W. F., and Garscadden, A., "Electron Drift Velocities in Molecular-Gas-Rare-Gas Mixtures," *Physics Review A*, Vol. 13, No. 1, Jan. 1976, pp. 471-475.

[13]Douglas-Hamilton, D. H., *Record of the 11th Symposium on Electron, Ion, and Laser Beam Technology*, edited by R. F. M. Thornley (San Francisco Press, San Francisco, Calif., 1971), p. 591. See also, Avco Everett Research Laboratory Research Report No. 343, 1972 (unpublished).

[14]Center, R. E., "Electron-Ion Recombination Measurements in CO at High Pressures," *Journal of Applied Physics*, Vol. 44, No. 8, Aug. 1973, pp. 3538-3542.

[15]Tulip, J., and Seguin, H. J. J., "High-Pressure Glow Discharge Using a Differentially Pumped Cathode," *Applied Physics Letters*, Vol. 27, No. 1, July 1975, pp. 15-17.

[16]Bélanger, P. A., Tremblay, R., Boivin, J., and Otis, G., "Atmospheric Pressure CO_2 Pulsed Laser with Semiconducting Plastic Electrodes," *Canadian Journal of Physics*, Vol. 50, No. 22, 1972, pp. 2753-2755.

Table 1 Summary of plasma characteristics for pulser-sustainer glow discharge operation in static CO laser mixtures

Mix $CO/N_2/He$	Optimum Pressure (torr)	E/N (10^{-16} V cm^2)	Electron Energy (eV)	Electron Density (10^{11} cm^{-3})	Recombination Rate Coefficient (10^{-7} cm^3 sec^{-1})	Discharge Power (kW)		Energy Loading (eV per diatomic molecule)
						Total	Positive Column	
1/0/0	22	2.6	0.5	2.2	0.4	72	52	0.03
0/1/0	30	2.0	0.7	3.2	0.5	97	74	0.03
1/0/1	36	1.7	0.4	2.3	0.7	82	61	0.03
1/2/5	50	1.1	-	-	-	88	66	0.04
1/0/4	60	0.9	0.5	3.4	0.6	90	64	0.05
1/0/9	79	0.9	0.4	3.4	0.8	113	86	0.11
1/1/18	101	0.9	-	-	-	152	123	0.13
1/0/19	160	0.6	-	3.8	1.0	138	115	0.14
1/1/38	221	0.5	-	-	-	200	171	0.16

DISCUSSION

J. LAUDENSLAGER: I have a couple of questions on your UV pre-ionization. It is experimentally evident that things like that work in helium but not in argon. Do you feel that the mechanism for this pre-ionization is the ionization in the volume of the gas or photo excitation of the electrons at the surface of the electrodes?

D. M. MONSON: We have operated this device with dielectric grids over recessed electrodes where they are shielded from the UV, and we get the same performance then as we do when the electrodes are exposed to UV.

J. LAUDENSLAGER: Do you feel that you are ionizing the CO?

D. M. MONSON: I think we are ionizing the impurities. We feel that most of our impurities in the static tests arise from the plexiglass chamber which is pumped down to about 5 microns, and therefore continues outgassing. So we inevitably have hydrocarbons. We estimate about 100 parts per million of impurities. So these tests do have a seed gas in the mixture.

J. LAUDENSLAGER: Do you have any feeling for why the argon system doesn's work: it is because the photon energy is lower or perhaps the de-ionization time of argon is much greater?

D. M. MONSON: Perhaps we are not photo-ionizing enough in the argon to create the initial glow. We can operate at very low densities in argon, but when we go to useful pressure ranges, arcing sets in right away.

PLASMA RESEARCH IN ELECTRIC PROPULSION AT COLORADO STATE UNIVERSITY

Paul J. Wilbur and Harold R. Kaufman
Departments of Mechanical Engineering and Physics
Colorado State University
Fort Collins, Colorado 80523

Abstract

The effect of electron bombardment ion thruster magnetic field configurations on the uniformity of the plasma density and the ion beam current density are discussed. The optimum configuration is a right circular cylinder which has significant fields at its outer radii and one end but is nearly field free within the cylinder and at the extraction grid end. The production and loss of the doubly charged ions which effect sputtering damage within thrusters are modeled and the model is verified for the mercury propellant case. Electron bombardment of singly charged ions is found to be the dominant double ion production mechanism. The low density plasma ($\sim 10^6$ elec/cm^3) which exists in the region outside of the beam of thrust producing ions which are drawn from the discharge chamber is discussed. This plasma is modeled by assuming the ions contained in it are generated by a charge exchange process in the ion beam itself. The theoretical predictions of this model are shown to agree with experimental measurements.

Introduction

Ion thrusters hold a promising position in the space propulsion program because of their high exhaust velocity capability. Applications for these devices which are of current interest range from low total impulse satellite stationkeeping missions through the higher total impulse comet rendezvous and out-of-ecliptic primary propulsion missions.

The basic cylindrical thruster is shown schematically in Figure 1. Its operation can be understood by recognizing that electrons are produced within the region bounded by the cathode pole piece and baffle and that they are drawn from this region toward the anode through the aperture adjacent to the baffle. The $\sim$30V potential difference across the baffle aperture, which is maintained by the anode, accelerates these electrons to sufficiently high energies that they can effect ionization of propellant which has been fed into the chamber by the mechanism of electron bombardment. The magnets shown in Figure 1 establish a magnetic field of the order of 50 gauss between the anode and cathode pole pieces which has a typical line of force like the critical field line shown. The bulk of the high energy electrons (primary electrons) coming through the baffle aperture reside within the region defined by the surface of revolution of this critical field line and the screen grid and this is therefore the region within the discharge plasma where the bulk of the ions are produced. As the primary electrons have collisions they lose energy and they, together with the electrons knocked from the atoms, combine to form an electron group having a Maxwellian distribution. The low energy Maxwellian electrons are then collected by the anode. Ions are free to drift around the discharge chamber under the influence of minor electric field and diffusive forces until they hit a conducting surface and are neutralized or until they drift into the vicinity of the grids and are extracted from the discharge chamber at a high velocity thereby producing thrust. Ion extraction is accomplished by a large electrostatic field established between the two grids and the velocity of the thrust producing ions can therefore be controlled by simply adjusting the net potential difference through which the ion falls in passing from the discharge chamber to the ion beam potential (typically of order 1000V).

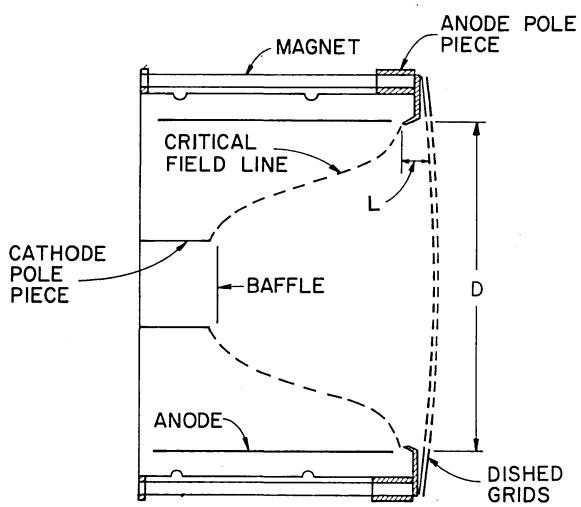

Fig. 1 Divergent Magnetic Field Thruster Schematic

The typical mercury discharge chamber plasma[1] has an electron density of 10^{11} cm^{-3} and a neutral density of 10^{12} cm^{-3}. The electrons have the two group composition mentioned with primary electrons consitituting of the order of 10% of the total. Primary electrons have an energy near 30eV while Maxwellian electrons generally have a temperature near 5eV.

One additional component not shown in Figure 1 which is essential to ion thruster operation is the neutralizer. This device which is located downstream of the grids simply emits electrons which are drawn into the ion beam to effect charge and current neutrality of the beam plasma. Thrusters are generally classified by the diameter of the beam they produce (D) and thrusters which produce beams from 5 cm to 1.5 m in diameter have been tested. The testing discussed here has however been conducted on 15 cm diameter thrusters only. The dishing of the accelerating grids shown in Figure 1 is employed to insure the grids will deflect in a predictable manner and hence not short

under the influence of thermal loads from the discharge chamber plasma.

The low-thrust nature of ion thrusters necessitates long operating times to achieve mission objectives and this necessitates long component lifetimes. The downstream (accelerator) grid is a crucial component subject to life-limiting erosion as a result of charge-exchange ion sputtering[2]. This erosion process occurs when a high velocity propellant ion exiting the grids captures an electron from a nearby low velocity neutral propellant atom. The result of the process is a fast moving neutral and a slow ion. The ion is frequently drawn back into the accelerator grid because its velocity is insufficient to enable it to escape the adverse electric field and the resulting impact on the accelerator grid causes the sputtering damage. The rate of sputter damage is directly proportional to the ion current density from the thruster and because it is generally highest on the centerline, grid erosion is also greatest on the centerline. Since the thrust of the device is directly proportional to ion current the longest lifetime will be achieved in the thruster operating at a given thrust level which has the most uniform radial beam ion current density profile. A thruster having a uniform ion current density beam should then operate and produce thrust as the accel grid erodes uniformly.

Cusped Magnetic Field Thruster[3]

The flatness of an ion beam current density profile is frequently defined as the ratio of average-to-peak current density--a quantity referred to as the flatness parameter (F). Divergent magnetic field ion thrusters like the one shown in Figure 1 have flatness parameters near 0.5 while a value of unity would be ideal. It has been argued that this quantity is low for the divergent thruster because of neutral propellant atom proceeding from the upstream to downstream ends of the thruster is much more likely to be ionized if it is near the thruster centerline than it is if it is near the outer radius. This condition exists because atoms passing near the centerline are exposed to ionizing electron region defined by the critical field line all the way from the baffle to the grids while those with trajectories near the outer radii would be exposed over the distance "L" identified on Figure 1.

The cusped magnetic field thruster of Figure 2 is designed to increase the path length of propellant atoms through the ionizing electron region at the outer radii thereby increasing the ion beam flatness parameter and hence the lifetime of the grids. As indicated by Figure 2, this is accomplished through the addition of a center pole piece and the installation of magnets to produce a north-south-north pole configuration as one proceeds from the cathode to center to anode pole pieces. This produces magnetic lines of force like those suggested by the dotted lines joining the pole pieces and suggests the increase in the length "L" suggested by Figure 2. A second (rear) anode has also been added to this thruster to facilitate uniform electron collection--this rear anode is designed so it can be moved axially during thruster operation to vary the characteristics of the discharge chamber plasma.

Iron filings maps showing lines of force for

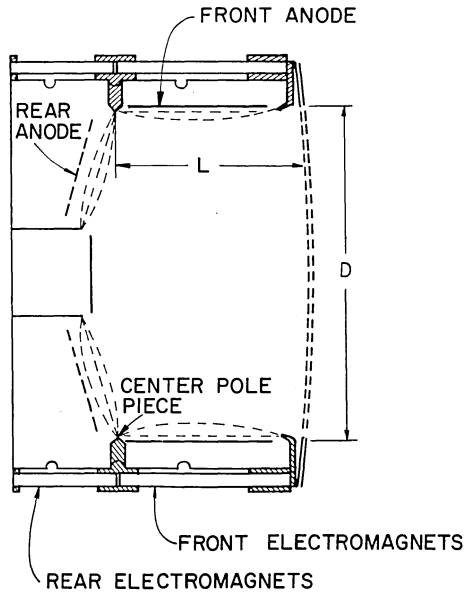

Fig. 2 Cusped Magnetic Field Thruster Schematic

the cusped and divergent magnetic field configurations are shown in Figure 3 for the 15 cm diameter

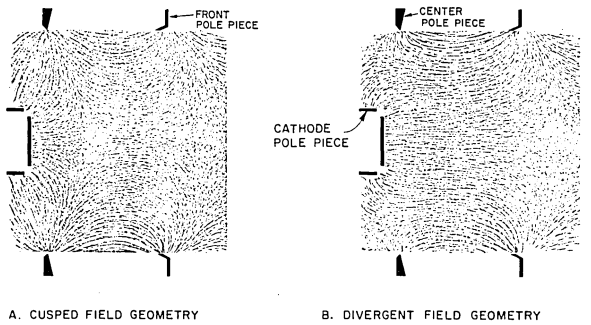

Fig. 3 Iron Filings Maps

thrusters used in this test. Actually the divergent field map shown was obtained using the cusped field thruster operating in the north-north-south pole configuration, but the field shape is essentially the same as that observed in a thruster not having the center pole piece.

Langmuir probe measurements were made throughout the discharge chambers of the cusped and divergent field thrusters when mercury propellant was being used. These data were then analyzed using the two electron group theory of Strickfaden and Geiler[4]. Using Maxwellian electron temperatures, primary electron energies and densities of these species the frequency of occurrence of ionizing collisions (ν) was calculated at each probing location. Figures 4 and 5 present constant collision frequency contour lines obtained from such an analysis for the cusped and divergent field geometries respectively. The contour lines have

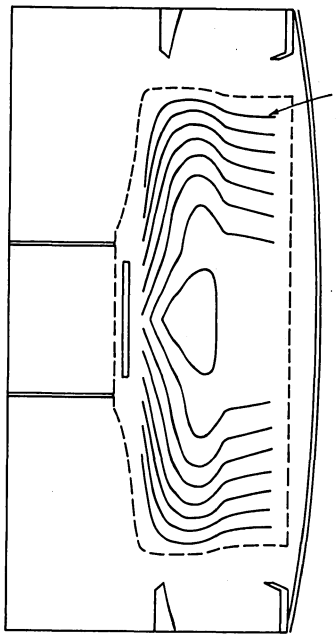

—— NORMALIZED COLLISION FREQUENCY CONTOUR

---- ION PRODUCTION REGION BOUNDARY

Fig. 4 Collision Frequency Contour Map (Cusped Field Thruster)

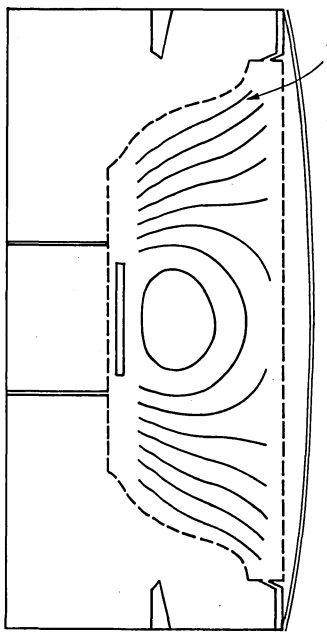

—— NORMALIZED COLLISION FREQUENCY CONTOUR

----- ION PRODUCTION REGION BOUNDARY

Fig. 5 Collision Frequency Contour Map (Divergent Field Thruster)

been normalized with respect to the maximum collision frequency calculated for each configuration and the innermost lines represent the contours on which the collision frequency is 90% of the maximum. The outermost lines are contours corresponding to 20% of the maximum. The dotted lines define the region in which theory suggests the bulk of the ionizing reactions (~95%) occur.

Both the iron filings maps of Figure 3 and the collision frequency contours of Figures 4 and 5 suggest the change to the cusped magnetic field configuration should result in a more uniform ion density profile in the thruster because it facilitates more uniform radial profiles of the ion production rate. Figure 6 shows normalized ion beam

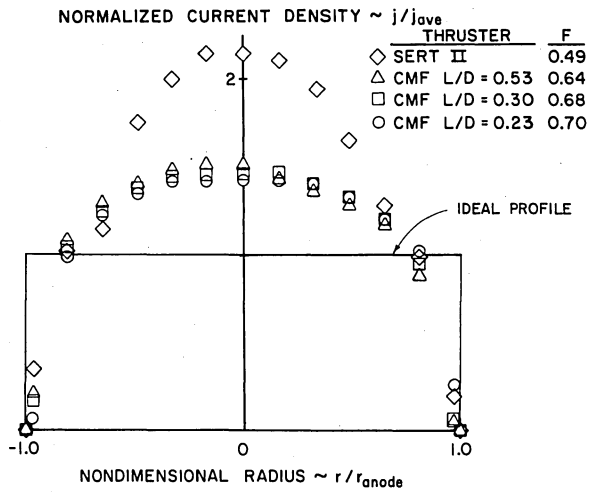

Fig. 6 Current Density Profiles

current density profiles measured using a Faraday probe. The profiles are for a divergent field thruster (designated SERT II for Solar Electric Rocket Test II) and three cusped magnetic field thrusters (CMF) each having different lengths (L). The flatness parameter (F) and the current density curves themselves both show that the cusped field thruster produces much flatter profiles. The variation in the length of the cusped field thruster is observed to have a small effect of the ion beam flatness, but other performance considerations such as the energy cost of producing the ions (discharge loss) suggest the cusped field thruster having the length-to-diameter ratio of 0.3 is preferred.

Re-examination of Figures 3A and 4 suggest that the ion beam profile could be flattened more in the cusped field thruster if the penetration of the magnetic field into the discharge chamber could be reduced to effect a more uniform ionizing collision frequency over the chamber. This reduction in magnetic field penetration is the objective of the multipole magnetic field configuration.

Multipole Magnetic Field Thruster

A sketch of the 15-cm diameter multipole thruster is shown in Figure 7. The magnetic polarity of the pole pieces alternates, giving the overall field shape shown in Figure 8. (Different numbers of pole pieces were used to investigate the

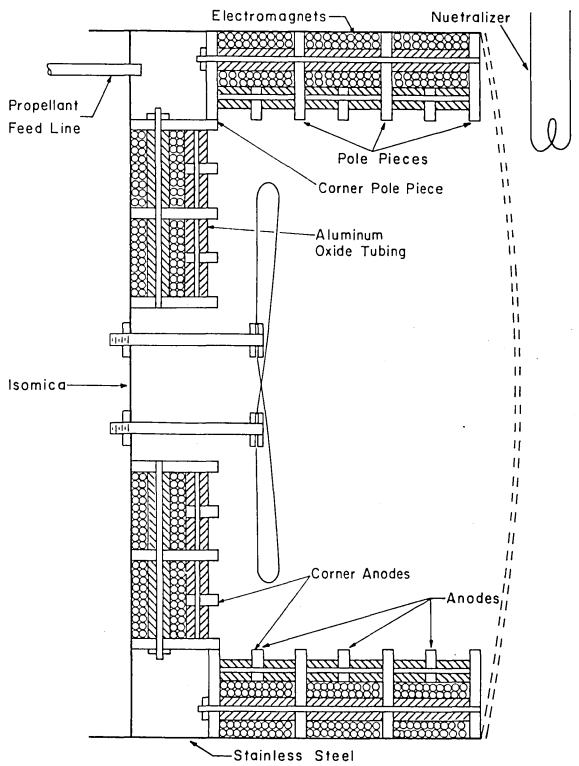

Fig. 7 Multipole Magnetic Field Thruster Schematic

effects of discharge chamber length. Figure 7 shows 4 side or cylindrical pole pieces, while Figure 8 shows 7.) Anodes are located between pole pieces so that the energetic electrons must pass through the fringe magnetic field to reach the anodes. Because these fringe fields extend only a short distance into the discharge chamber, most of the chamber has a very low field strength. This low field strength, of course, results in a uniform distribution of ionizing electrons, hence a uniform plasma density. The refractory wire loop near the center of the chamber serves as the source of ionizing electrons in this thruster which is presently not equipped with the baffle/cathode pole piece arrangement shown for the divergent field thruster of Figure 1.

The multipole thruster can be considered a logical extension of the cusped field design to more pole pieces, inasmuch as the pole pieces are fabricated in a similar manner from sheets of soft ion, with electromagnets used between adjacent pole pieces. But this multipole design is also related to that of Moore[5] and Ramsey[6], primarily in the large number of pole pieces used and the general discharge chamber shape. Moore and Ramsey, however, used permanent magnets as pole pieces with

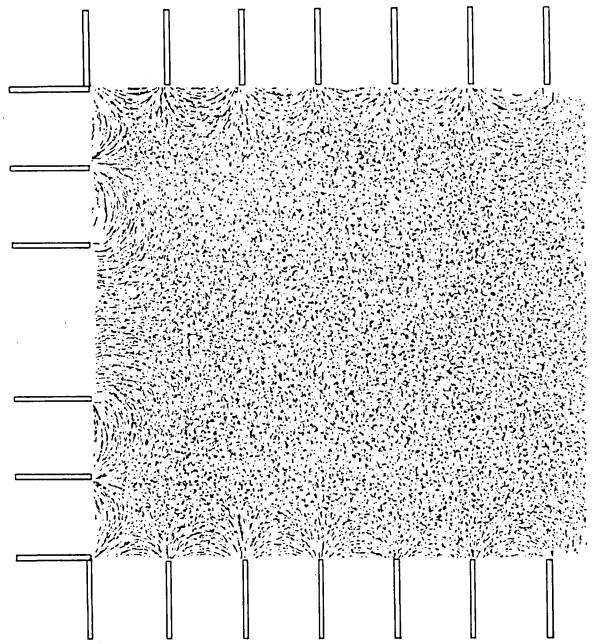

Fig. 8 Iron Filings Map (Multipole Thruster)

the magnetization direction either towards or away from the center of the discharge chamber. If permanent magnets were used in the multipole thruster studied herein, they would replace the electromagnets between pole pieces, rather than become the pole pieces.

Performance of a 5.1 cm long discharge chamber operating on argon is shown in Figure 9 in terms of

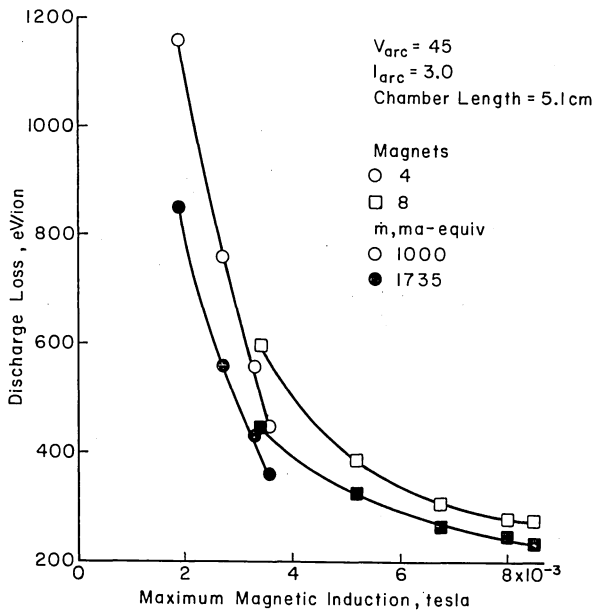

Fig. 9 Effect of Magnetic Field Intensity on Discharge Loss

beam ion energy cost (discharge loss) as a function of magnetic induction measured at a location near the pole pieces. V_{arc} is the voltage difference between the emitter wire and the anodes and I_{arc} is the cathode emission current. The propellant flow rate ($\dot{m}$) is expressed in milliamps in accordance with the convenient convention of assigning one electronic charge to each neutral atom entering the chamber. The use of eight electromagnets resulted in curves in Figure 9 that did not quite match those obtained with four at the same magnetic induction. The trend of decreased discharge loss with increased magnetic field strength, though, is clear. The higher magnetic field is presumably more efficient because it is more effective in containing energetic electrons. A simplified model of electron containment is indicated in Figure 10(a),

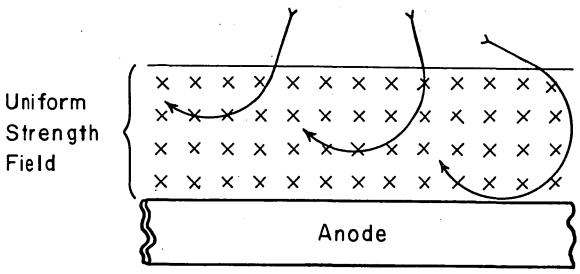

(a) Simplified Deflection Configuration

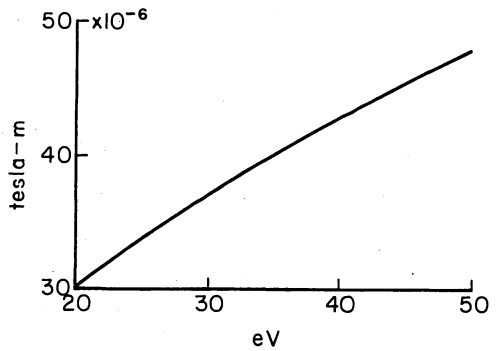

(b) Required Flux per Unit Anode Length as a Function of Electron Energy

Fig. 10 Electron Interaction with Fringe Magnetic Field above Anode

with the fringe field represented by a region with uniform field strength above the anode. Picking a direction of motion for the electron such that the electron has the deepest penetration of this fringe field, it is evident from Figure 10(a) that this penetration corresponds to two electron cyclotron radii. The electron cyclotron radius r_c (in m) is given by

$$r_c = 3.37 \times 10^{-6}\sqrt{E_e}\ /B,$$

where E_e is the electron energy in eV and B is the magnetic field in Tesla. This equation can be rewritten as

$$2r_cB = 6.74 \times 10^{-6}\sqrt{E_e}\ ,$$

where $2r_c$ is depth of the fringe field above the anode and B is the magnetic field in this region. The produce $2r_cB$ can be thought of as the number of flux lines per unit anode length, and is plotted against electron energy in Figure 10(b). The distribution of these flux lines with distance from the anode is not important. For example, half the field strength extending twice as far from the anode would have the same effectiveness in deflecting electrons. This conclusion is also valid for the more realistic case of field strength varying with distance from the anode, which can be shown for increments of deflection angle instead of circular electron orbits. For a varying magnetic-field strength, the integral of magnetic field strength

$$\int_{\text{anode}}^{B\approx 0} \bar{B} \times d\bar{\ell}$$

is the proper quantity to use in place of $2r_cB$. In this case the integration is carried out to the first point of negligible field strength ($B\approx 0$).

The fringe field integral was evaluated numerically and was found to vary with location in the discharge chamber. The largest departures from mean values were found at the two corner anodes. As shown in Figure 11 for the eight magnet configuration at 10 amperes magnet current, the magnetic

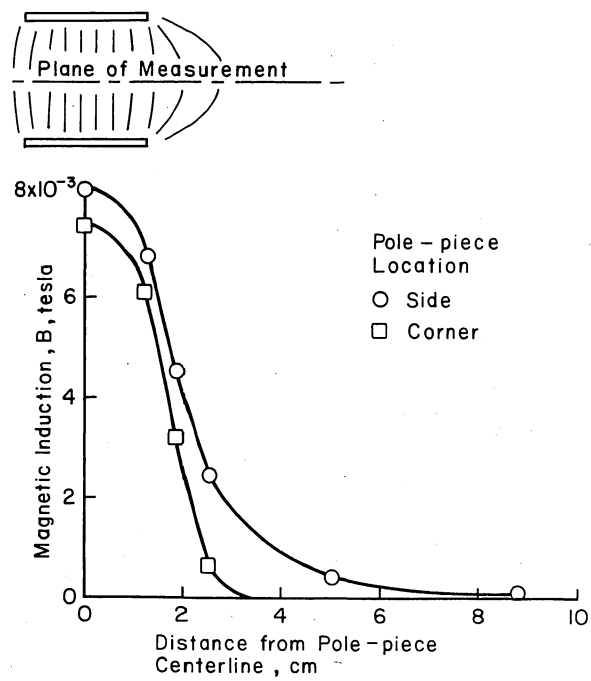

Fig. 11 Magnetic Field Between Pole Pieces

field drops to near zero field strength much faster in the corner than in the side location (typical of the rest of the chamber). This more rapid drop is due to the interference of the two corner fields.

In fact, integration from a location flush with the inside edges of the pole pieces yielded 88 x 10^{-6} Tesla-meters (88. Gauss-cm) for the side location, and only 42 x 10^{-6} Tesla-meters for the corner location.

The variation of discharge losses with magnet current is shown in Figure 12 for the eight-magnet

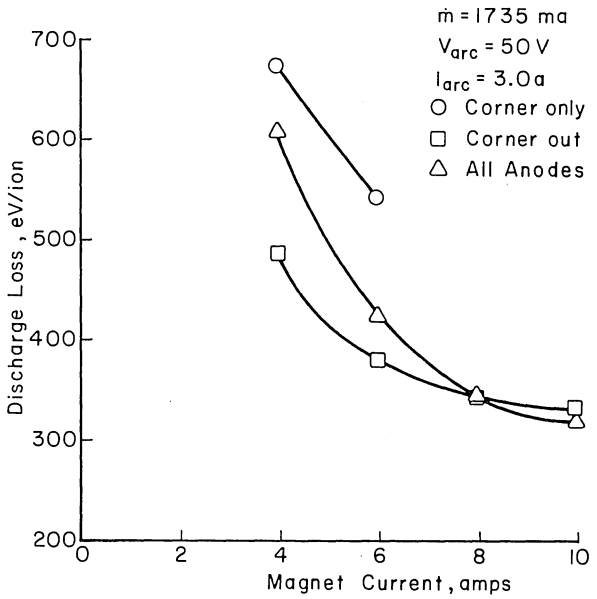

Fig. 12 Variation of Discharge Ion with Magnet Current for Different Anode Configurations (Argon Propellant)

configuration with different anode configurations. Operation with corner anodes alone gave the poorest performance at low magnet currents, while operation was not possible with this configuration at higher currents. The exclusion of the corner anodes gave the best performance at low magnet currents, but resulted in little difference at higher currents.

The data of Figure 12 are consistent with electron loss to corner anodes being the major limiting factor in multipole chamber performance. Further, the fringe field above the corner anodes at 10 amperes is sufficient to give good containment of ionizing electrons. From Figure 11, the fringe field integral at this location was found to be 42 x 10^{-6} Tesla-meters at 10 amperes. For a 50 volt discharge (and about 50 eV primary electrons), Figure 10(b) indicates an integral of 48 x 10^{-6} Tesla-meters should be adequate. The experimental and theoretical values of fringe field integral are thus in good agreement. There are other factors involved in discharge losses, however. Additional tests have shown a slow decrease in losses occurs for additional field strength increases until the integral is about twice the theoretical value given in Figure 10(b). Design for fringe field integrals somewhat above the theoretical value is therefore recommended.

In the tests described above, all anodes were flush with the inside edges of the pole pieces (see Figure 7). The containment of electrons can be equalized for all anodes by changing the field strength of corner pole pieces. A simpler approach, though, is to use the same magnetic field design for all pole pieces and to recess the corner anodes. The electrons are then required to go a short distance beyond the inside edges of the pole pieces to reach the anodes. It was found in additional tests that an anode recess equal to 10 percent of the pole-piece spacing gave a fringe field integral at the corner anodes that was about equal to the same integral elsewhere in the chamber. A discharge chamber with corner anodes recessed in this manner has been tested and found to perform well. Tests with argon, xenon and mercury propellants are presently being conducted to determine the ion beam flatness parameter of this thruster; preliminary data suggest flatter ion beams than those observed in the cusped field thruster.

Discharge Chamber Model

The need for long thruster lifetimes dictates the need for low erosion rates on surfaces exposed to the thruster discharge plasma as well as on the accelerator grid. The plasma contituent which appears to cause the bulk of the erosion on these interior surfaces is the doubly charged ion which is frequently present in significant numbers and which obtains twice as much energy as a singly charged ion passing through the same sheath potential to a collision with a surface. The objective of this model was the prediction of doubly charged ion densities as a function of thruster design and operating parameters. The analysis and verification have been carried out for a mercury plasma.

In order to develop a model for determining the double ion density in the discharge chamber only those ionic and atomic species which were considered significant in determining the double ion density were included. The significant species were selected as those which have substantial electron impact cross sections of formation over the electron energy range of interest so that large numbers of these excited atoms or ions will be produced. These states also have sufficiently long effective lifetimes so that they can participate in production processes before they decay. Only those reactions which lead directly or indirectly to the production of double ions were included.

Figure 13 is a discharge chamber reaction

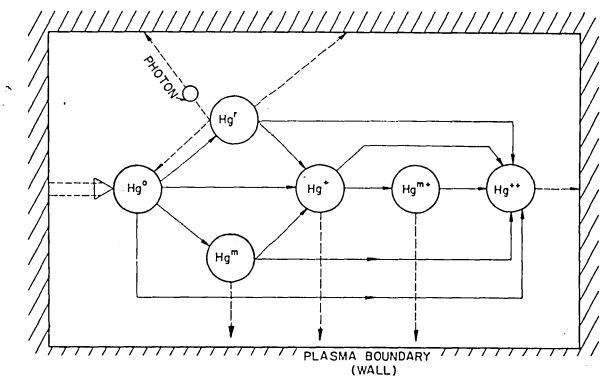

Fig. 13 Discharge Chamber Reaction Schematic

schematic showing these dominant species and the reactions in which each specie can participate. The symbols used represent the following species:

- Hg^o - neutral ground state mercury
- Hg^m - metastable neutral mercury (6^3P_0 and 6^3P_2 states)
- Hg^r - resonance state neutral mercury (6^3P_1 and 6^1P_1 states)
- Hg^+ - singly ionized ground state mercury
- Hg^{m+} - singly ionized metastable mercury ($6^2D_{3/2}$ and $6^2D_{5/2}$ states)
- Hg^{++} - doubly ionized ground state mercury

The arrows in Figure 13 indicate the various interaction routes considered in the analysis. Three different types of reactions are indicated in this figure. The first type of reaction occurs when an electron interacts with an atom or ion producing a more highly excited specie. This reaction is indicated in Figure 13 by an arrow going from one specie to another more highly excited specie (e.g. the production of double ions from singly charged ground state ions). The production of a more highly excited specie also represents a loss mechanism for the less excited specie. The reverse reaction in which, for example, an ion captures an electron is neglected because of its low probability.

The second type of process considered is that of an atom or ion going to a plasma boundary. Such a boundary could be either the discharge chamber wall on which the atom or ion would be de-excited or it could be a grid aperture in which case the atom or ion would be extracted from the discharge region and replaced by an atom from the propellant feed system. In either case this represents a loss rate for any of the excited states. These losses to the boundary are indicated in Figure 13 by the dotted lines to the wall of the chamber. The large arrow back to the neutral ground state represents the resupply of neutral ground state atoms either from the walls or from the propellant supply system.

A third type of reaction shown in Figure 13 is relevant only to the two resonance states. The resonance states differ from metastable states in that they have a very short lifetime before they de-excite spontaneously by emitting a photon of light. However, the energy of this photon is such that it is readily absorbed by a nearby neutral ground state atom producing another resonance state atom. Since the transport time of the photon is small compared to the excited state lifetime the excited state can be considered to exist continuously. Eventually the photon can diffuse to a boundary where it will be lost; this is equivalent to the loss of a resonance state atom.

By equating the production and loss rates of each specie on the basis that equilibrium exists one can solve for the density of each specie of Figure 13 in terms of the plasma properties, the volume and surface area of the region in which ionization takes place and the ionization and excitation cross sections for the reactions. The model was set up so this could be accomplished on the digital computer using a plasma described in terms of average values of primary electron energy and density and average values of Maxwellian electron temperature and density. The details of the model are described in References 7 and 8.

In order to verify the model, several thrusters of different sizes and plasma characteristics were operated while simultaneous measurements of discharge plasma properties and the double and single ion composition of the thrust beam drawn from the thruster were made. Typical plasma property information obtained in a 15 cm dia divergent field thruster are shown in Figure 14. In order to

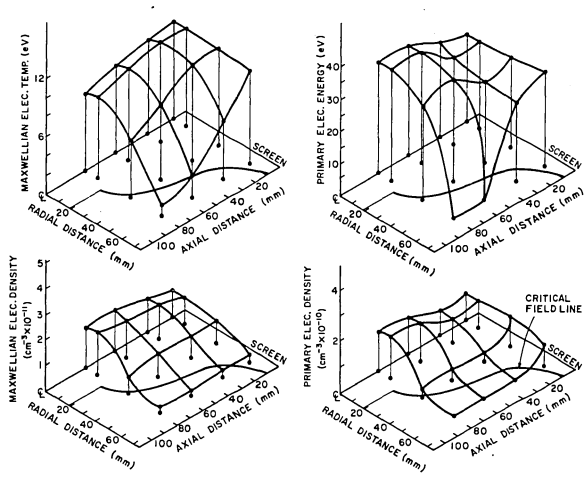

Fig. 14 Typical Plasma Properties

orient these plots, an ion extraction grid (screen) and the critical field line are identified. Plasma property data like that of Figure 14 were averaged using weighting factors determined to be appropriate for this analysis and double ion concentrations were calculated from these input data. Figure 15 shows a typical comparison of the measured and calculated double-to-single ion density ratio. The variable on the abscissa in this plot, propellant utilization, is the ratio of propellant that is drawn from the truster as ion current to the total propellant input to the device. The two plots shown were based on data from thrusters which used two different types of ion accelerating grid systems. The theoretical data of Figure 15 show good agreement with the theory and therefore confirm the model's validity.

Detailed examination of the model shows that single ion production via the intermediate metastable and resonance states is appreciable but that double ions are produced primarily by electron bombardment of singly charged ground state ions at normal thruster operating conditions. On the basis of this latter observation one can develop a simpler model considering only the singly charged ionic ground state to doubly charged ionic route for double ion production. The doubly charged ion density (n_{++}--m^{-3}) is then given by the following equation for a region of uniform plasma properties:

$$n_{++} = n_e^2 \frac{V}{A} \left\{ \frac{n_{pr}}{n_e} v_{pr}(\varepsilon_{pr}) \sigma_+^{++}(\varepsilon_{pr}) + \frac{n_{mx}}{n_e} \int_{E=0}^{\infty} \sigma_+^{++}(E) v_{mx}(E) \left[\frac{dn_{mx}}{n_{mx}} \right] \right\} \Big/ \left\{ T_{mx} e(1+n_{pr}/n_{mx})/m_i \right\}^{\frac{1}{2}}$$

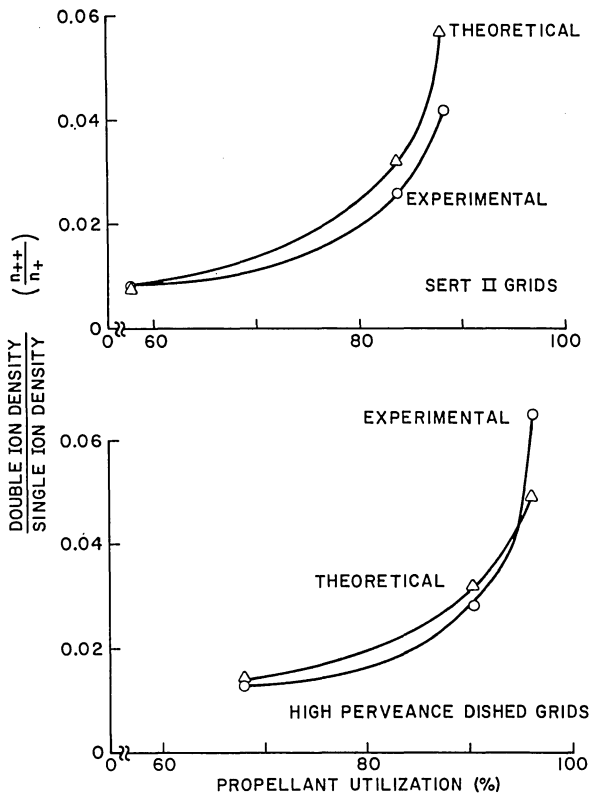

Fig. 15 Double-to-Single Ion Density -- Comparison of Theory and Experiment

where $n_e = n_{pr} + n_{mx}$ is the total electron density --m^{-3}

n_{pr} is the primary electron density--m^{-3}

n_{mx} is the Maxwellian electron density--m^{-3}

V is the volume of the ionizing electron region--m^3

A is the surface area of the ionizing electron region--m^2

$v_{pr}(\xi_{pr})$ is the velocity of primary electron having an energy ξ_{pr}-m/sec

$\sigma_+^{++}(E)$ is the cross section for the singly-to-doubly ionized transition at an energy E - m^2

$v_{mx}(E)$ is the velocity of electrons at energy E - m/sec

(dn_{mx}/n_{mx}) is the Maxwellian distribution function

T_{mx} is the Maxwellian electron temperature-eV

e is the electronic charge constant - 1.6×10^{-19} coul

m_i is the mass of an ion - kg

and Reference 8 contains the required cross sections and a plot of the solution of the integral appearing in this equation as a function of Maxwellian electron temperature.

This equation suggests that the double ion density can be reduced most readily by reducing the electron density. In order to maintain other thruster performance parameters this reduction should be accompanied by an equal increase in the volume-to-surface area ratio. Because electron density is a squared term and volume-to-surface area is a linear one the net effect is a decrease in double ion density.

Charge Exchange Plasma

Depending upon the point at which the charge exchange process occurs between ions and neutrals in the beam, the slow ion which is produced may be able to leave the beam plasma with an energy of a few eV rather than being drawn back into the grids. These then constitute the charge-exchange plasma that surrounds the ion beam and thruster. A typical plot of plasma density against radial distance (downstream of the thruster) is shown in Figure 16. The Debye distance is typically less

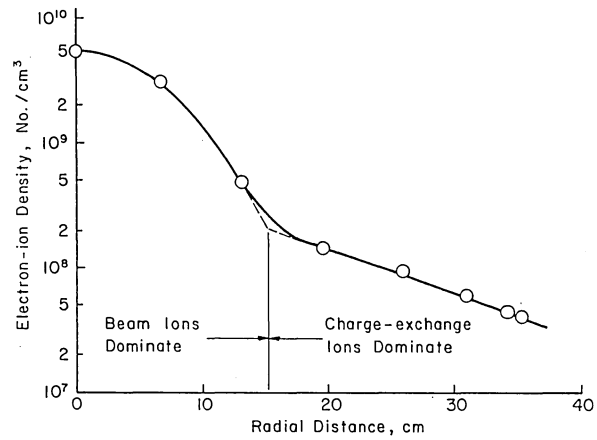

Fig. 16 Separation of Plasma into Ion-beam and Charge-Exchange Regions

than 1 mm in the ion beam, so the electron and ion densities are essentially equal in Figure 16. The central hump represents the beam of high energy (~1000 eV) ions, while the more uniform region farther out is dominated by low velocity charge-exchange ions. Because the charge-exchange ion density decreases slowly with increasing distance, a significant plasma density can exist near much of an electrically propelled spacecraft. This can present a serious problem for the solar array from which operating power is obtained in that the trend is towards higher array voltages for higher electrical efficiency, and this increases the tendency for the array to interact adversely with the charge-exchange plasma.

A typical survey of plasma density near a thruster resulted in the map of Figure 17. The dashed line shows the approximate boundary between the ion beam and the surrounding charge-exchange plasma, with the location of this boundary determined by plots similar to Figure 16. The electron density (n_e) within the ion beam where the plasma potential is V obeys the "barometric" equation

$$n_e = n_{e,ref} \exp[-eV/kT_e],$$

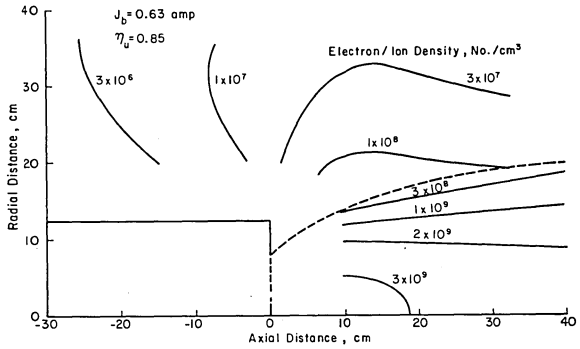

Fig. 17 Map of Electron/Ion Density Near Thruster

which was introduced by Sellen et al.[9] and verified by Ogawa et al.[10, 11]. $n_{e,ref}$ in this equation is the electron density at a location where the potential is defined as zero and T_e is the electron temperature. Agreement with this equation means that contours of constant ion density are also equipotential contours. Further, the electric field direction is such that charge-exchange ions are accelerated toward regions of lower plasma density.

The total production rate of charge-exchange ions $\dot{N}_{ce}$ can be calculated from the efflux of ions and neutrals, together with the charge-exchange cross section. Assuming for simplicity that all the ions leave along the axis of the accelerator system, free molecular flow for neutrals gives a total production rate of

$$\dot{N}_{ce} = \frac{2J_b^2 (1-\eta_u)\, \sigma_{ce}}{\pi r_b \eta_u e^2 \bar{v}_o} ,$$

where J_b is the ion beam current in amperes, η_u is the propellant utilization, σ_{ce} is the charge-exchange cross section in m^2, r_b is the radius of the accelerator system (ion beam) in m, e is the magnitude of the electronic charge in coulombs, and $\bar{v}_o$ is the average neutral velocity ($\sqrt{8kT_o/m_o}$) in m/sec.

A simple isotropic model can be obtained by assuming that the charge-exchange ions are distributed uniformly in all directions from an effective source downstream of the thruster. This effective source is assumed to be one beam radius downstream of the accelerator system, although the exact location will not be important at the usual radial distance of a solar array. To simplify the model for plasma density, the minimum ion velocity for a stable plasma sheath,[12]

$$v = \sqrt{KT_e/m_i} ,$$

is used in place of the more complicated self-consistent solution for charge-exchange ion velocity. (The charge-exchange ion velocity outside of the ion beam depends on the local plasma potential, but the plasma potential is determined by ion density, which depends on ion velocity.) The plasma density n_{ce} at a radius R from the effective source then becomes

$$n_{ce} = \frac{1.49 \times 10^{32} J_b^2 (1-\eta_u)\, \sigma_{ce}\, A}{r_b R^2\, \eta_u \sqrt{T_o T_e}}$$

where T_o and T_e are the neutral and electron temperatures in °K and A is the atomic weight of the propellant atoms. With the further substitutions of 500°K for T_o, 58,000 °K (5 eV) for T_e, 200.6 for the A of mercury, and $6 \times 10^{-19} m^2$ for σ_{ce} of mercury at 1000 eV, the plasma density becomes

$$n_{ce} = \frac{3.3 \times 10^{12} J_b^2 (1-\eta_u)}{r_b R^2 \eta_u}$$

The densities measured along a radius normal to the ion beam direction should agree best with the isotropic model since charge-exchange ions have free access to that direction and yet it is well away from the beam ion trajectories. The theoretical variations of plasma density from the preceding equation are shown in Figure 18 together with

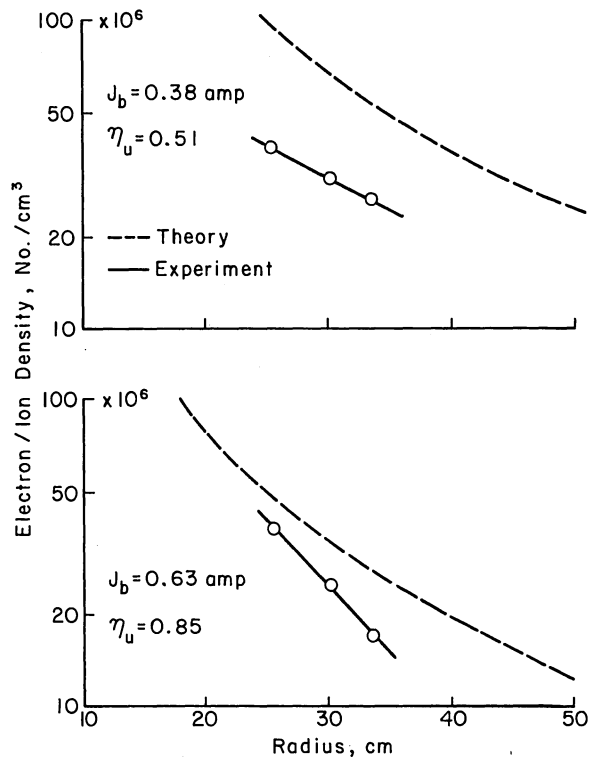

Fig. 18 Comparison of Theoretical and Experimental Electron/Ion Densities Normal to Ion-beam. Axial Position 7.5 cm Downstream of 15 cm Thruster.

experimental data. The agreement between the two is good for a plasma process. The simplifying assumptions were conservative in nature (that is, tending to give higher plasma densities), so the theory was expected to give higher densities than the experimental data.

The charge-exchange plasma is not distributed

isotropically at a given radius. No ions are initially directed in the upstream hemisphere. Only the electric fields surrounding the ion beam serve to deflect charge-exchange trajectories into this upstream direction. Experimental plasma potential measurements showed that the electric field outside the beam was nearly antiparallel to the beam direction. Using this observation, together with the additional observation that the electron temperature outside of the beam is about half that inside the beam, the plasma density at an angle (θ) between 90 and 180 degrees from the beam direction can be derived as

$$n_{ce} = n_{ce,\ 90} \exp\ [-ctn^2\theta],$$

where $n_{ce,\ 90}$ is the plasma density obtained from the isotropic model for the same radius R. This theoretical angular variation is compared in Figure 19 with experimental data for the same radial distance. The theoretical density is shown as

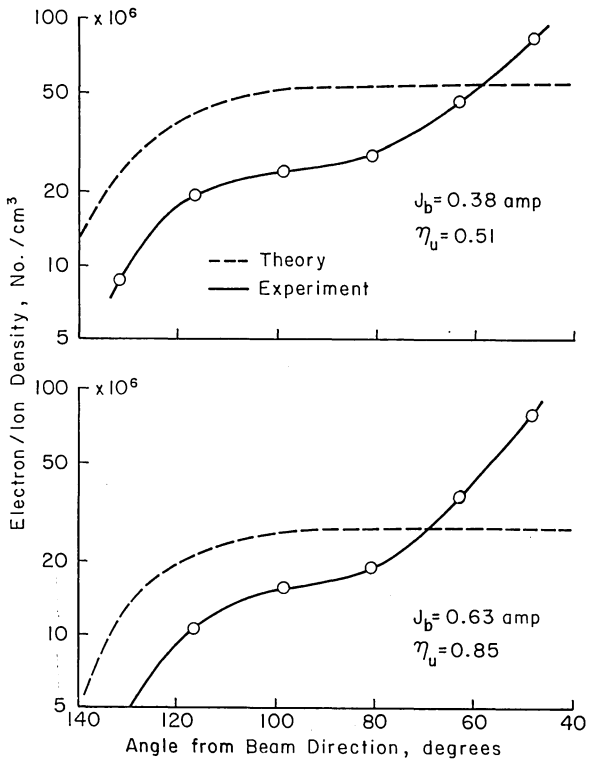

Fig. 19 Comparison of Theoretical and Experimental Electron/Ion Densities at 34 cm Radius and 7.5 cm Downstream of 15 cm Thruster.

uniform for angles less than 90 degrees in Figure 19. This is because no deflection of initial trajectory direction is necessary to reach these directions. The experimental data should be larger than theoretical density at a small enough angle with beam direction because beam ions which will be included in the experimental measurements are not considered in the model. This failing of the model is not a problem because the upstream direction is the one of most interest for interactions of thrusters with solar arrays and other spacecraft components.

The charge-exchange plasma model described above is sufficiently accurate for a qualitative estimate of interaction effects. More exact estimates, though, will require tests of the specific spacecraft configuration. Examples of the limitations of this model were obtained recently using cones downstream of the thruster. It was hoped that these cones would collect most of the charge-exchange ions and thereby greatly decrease the plasma density upstream of the thruster. The experimental reduction was much less than expected. It appeared that the charge-exchange ions negotiated trajectories around the ends of the cones far easier than would be expected from the angle variation predicted by the model presented above.

References

1. Wilbur, P. J., "Hollow Cathode Restartable 15 cm Diameter Ion Thruster," NASA CR-134532, December 1973, pp. 9-11.

2. Kerslake, W. R., "Charge-exchange Effects on the Accelerator Impingement of an Electron-Bombardment Ion Rocket," NASA TN D-1657, May 1963.

3. Beattie, J. R. and P. J. Wilbur, "15 cm Cusped Magnetic Field Mercury Ion Thruster Research," AIAA Paper 75-429, March 1975.

4. Strickfaden, W. B. and K. L. Geiler, "Probe Measurements of the Discharge in an Operating Electron Bombardment Engine," AIAA Journal, Vol. 1, No. 8, pp. 1815-1823, August 1963.

5. Moore, R. D., "Magneto-Electrostatically Contained Plasma Ion Thruster," AIAA Paper No. 69-620 (1969).

6. Ramsey, W. D., "12-cm Magneto-Electrostatic Containment Mercury Ion Thruster Development," J. Spacecraft and Rockets, Vol. 9, pp. 318-321, (1972).

7. Peters, R. R. and P. J. Wilbur, "Double Ion Production in Mercury Thrusters," AIAA Paper 75-398, March 1975.

8. Peters, R. R. "Double Ion Production in Mercury Thruster," NASA CR-135019, April 1976.

9. Sellen, J. M., Jr., Bernstein, W., and Kemp, R. F., Rev. Sci. Instr., Vol. 36, pp. 316-322, (1965).

10. Ogawa, H. S., Cole, R. K., and Sellen, J. M., Jr., AIAA Paper No. 69-263, (1969).

11. Ogawa, H. S., Cole, R. K., and Sellen, J. M., Jr., AIAA Paper No. 70-1142, (1970).

12. Bohm, D., in "The Characteristics of Electrical Discharges in Magnetic Fields," (A. Guthrie and R. K. Wakerling, eds.), pp. 77-86, McGraw-Hill Book Co., 1949.

DISCUSSION

J. P. LAYTON: Where does the lifetime situation stand now with respect to the kind of applications that are starting to look attractive?

P. J. WILBUR: For thruster applications, lifetimes of critical components like the cathode, in excess of 20,000 hours have been demonstrated in the laboratory. Thrusters have been tested over 10,000 hours, and tests are in progress now which extend beyond that. For other applications, we have a broad-beam ion source here which we use for other purposes like ion milling and machining functions and sputtering functions. The lifetimes there can be far in excess of those associated with spacecraft because we can use carbon grids and they have very long lifetimes associated with them. Lifetimes are adequate for ground-based applications, and I feel that they are adequate for most missions as well.

J. P. LAYTON: Is enough now known about these to scale them to any size or power level?

P. J. WILBUR: Tests have been run on thrusters which range in size from 5 cm in diameter to 1½ meters in diameter. There is a wealth of knowledge available on scaling. While analytical modelling has been moderately successful, the empirical approach to designing these thrusters is quite well developed.

J. P. LAYTON: How are the efficiencies of these thrusters at the lower effective jet velocities?

P. J. WILBUR: The efficiencies are still good. Typically the potentials that we are accelerating the ions through are of order 1000 volts now and we can get efficiencies of around 70%.

W. F. von JASKOWSKY: I was intrigued by your statement in the abstract that your model can predict the density of doubly charged ions accurately. Do you use for that prediction empirical propellant utilization data?

P. J. WILBUR: In that model, you input to the model the plasma properties, the electron temperatures and densities that exist in the discharge chamber. You also input to it the propellant flow rate. It calculates the loss rate for ions and the loss rate for neutrals, assuming free molecular flow for the neutrals and bohm velocity losses associated with the ions. It then solves using experimental cross-section for the most part, for the densities of resonance, metastable, singly-ionized and doubly-innized species that are present in the discharge chamber. We have measured the double-ion densities coming out in the beam using a mass spectrometer and we have measured the plasma properties in the thruster simultaneously, and we have put the plasma properties into the computer program and it calculates within the 10% the double-ion density that we measured coming out of the beam. So the verification has been on double ions.

M. KRISHNAN: Have you observed any change in the ionization efficiency in the discharge region when going from the divergent to the cusped magnetic field configuration?

P. J. WILBUR: No, the cost of producing ions is not influenced significantly by the change in magnetic field configuration so far as we have learned.

AN EFFICIENT PROCEDURE FOR COMPUTING PARTIAL IONIZATION OF A GAS IN NUMERICAL FLUID DYNAMICS +

S. Garribba and L.Quartapelle *

CESNEF, Nucl.Engng.Dept., Politecnico di Milano
Milano, Italy 20133

Abstract

A numerical procedure is described that for the first time allows efficient solution for the three nonlinear and implicit equations of state relating the equilibrium properties of a partially (and singly) ionized neutral gas. Energy, pressure and Saha equations are encountered when solving the conservation laws of fluid dynamics.

In the computation, the values for the intensive variables, that is pressure, temperature and ionization coefficient, are iteratively obtained with a given accuracy starting from assigned values for energy and volume per unit mass. Iterative computation is performed only when the value for the ionization coefficient lies within the lower and the upper bounds fixed by the required number of significant digits; otherwise the two explicit equations of state for nonionized or for fully ionized gases are employed.

This procedure has been applied to the study of partial ionization produced in one-dimensional propagation of strong shock waves in hydrogen gas. The peaked shape of the density ratio vs. shock strength is clearly shown. The same procedure would also be easily applicable to steady or unsteady multidimensional flows where nonuniform ionization plays a substantial role.

I. Introduction

Problems occur in gas dynamics where partial ionization of a monatomic gas has a relevant influence on the flow characteristics. Cases are offered by the domain of strong shock waves propagation both in presence and without magnetic field [1]. Or by the stellar atmospheres with the influence of partial ionization on the pulsation phenomena[2]. The theoretical and numerical study of this class of problems requires the solution of the coupled system of constitutive equations and fluid dynamic conservation equations. Notable difficulties are encountered when dealing with equilibrium partial ionization as described by Saha equation. Indeed the nonlinear and implicit dependence of temperature and partial ionization on conserved quantities prevents any direct solution.

An efficient procedure is therefore presented for solving the three equations of state of a partially ionized gas as required by the commonly used finite difference schemes of numerical fluid dynamics. The range of applicability covers any singly ionizable monatomic gas in situations of thermodynamic equilibrium when radiation energy contributions can be neglected.

II. The equations of state of a partially ionized gas

First, the general form of the equations of state for a partially ionizable perfect gas must be established. When radiation effects are omitted and thermodynamic equilibrium is taken for granted, it is [3]

$$E=\frac{3}{2}N(1+\alpha)kT+N\alpha kT_i+N(1-\alpha)w_o+N\alpha w_1, \qquad (1)$$

$$P=N(1+\alpha)kT/V, \qquad (2)$$

$$\frac{\alpha^2}{1-\alpha}=2\frac{u_1}{u_o}\frac{V}{N}\left(\frac{2\pi m_e kT}{h^2}\right)^{3/2}\exp\left(-\frac{T_i}{T}\right). \qquad (3)$$

Here N is the number of atoms per unit mass; P,T,α, E and V are the thermodynamic variables, that is pressure, temperature, ionization coefficient, energy and volume per unit mass, respectively. T_i is the ionization temperature, u is the electronic partition function, w is the electronic excitation energy. Subscript o stays for the neutral atom while subscript 1 distinguishes the ion. Explicit forms for u and w

+ This research was supported by EURATOM under contract 109-73 PIPGI

* Also EURATOM JNRC, Ispra, Italy 21020

are given by Zel'dovich and Raizer [3].

The method for computation which is developed applies within the domain of first ionization of any atomic gas. For sake of definiteness, however, our treatment focuses to the sole case of atomic hydrogen. Now for a generic gas we will assume that the excited states of atoms and ions have a negligible influence on the thermodynamic equilibrium. Therefore $u_o=2$, $u_1=1$ and $w_o=w_1=0$. Particularly, for hydrogen gas it is always $u_1=1$ and $w_1=0$, and the preceding assumption amounts only to disregard the electronic excitation spectrum of the neutral atom.

Then, by the use of dimensionless variables equations (1-3) become

$$e = \frac{3}{2}(1+a)t+a \,, \qquad (4)$$

$$p = (1+a)\, t/v \,, \qquad (5)$$

$$\frac{a^2}{1-a} = vt^{3/2}\exp(-1/t), \qquad (6)$$

where definitions hold as follows $a \equiv \alpha$, $e \equiv E/E_o$, $v \equiv V/V_o$, $p \equiv P/P_o$, $t \equiv T/T_i$ and $E_o=kT_iN$, $V_o=N(u_o/2u_1)(h^2/2\pi m_e kT_i)^{3/2}$, $P_o=E_o/V_o$.

Dealing with hydrogen gas numerical values for the intrinsic constants are $T_i=1.56 \cdot 10^5$ °K, $kN = 8.317 \cdot 10^7$ erg/°Kg and $2u_1/u_o=1$. So that $E_o=1.30 \cdot 10^{13}$ erg/g, $V_o=4.03$ cm^3/g and $P_o= 3.22 \cdot 10^{12}$ dyne/cm^2.

Equations (4-6) express the relations that the five thermodynamic variables a, e, v, p and t obey at equilibrium. In numerical computations of fluid dynamics the finite difference schemes[4] produce at any mesh point and at any time step the values of energy and volume per unit mass. These schemes then require for the next time step the knowledge of pressure and, possibly, temperature and ionization coefficient. In other words, it is necessary to solve the three equations (4-6) with respect to the three unknowns p, t and a starting from assigned values of e and v. A demand which results into a highly nonlinear and implicit problem.

III. The method of solution

An effective numerical procedure for the solution of this problem should meet two main requirements. First, the computation of the complicated set (4-6) must be avoided, as far as the gas is in a nonionized or fully ionized state. For under these circumstances the condition a=0 or a=1 holds and use can be made of the simple and explicit relations that result from (4) and (5). Second, the solution must produce numerical values of prescribed and, desirably, variable accuracy. In this respect, we proceeded according with a line which seems, so to say, to kill the two birds with one stone.

Let us indeed assume that we need results with n significant digits. This means that the gas can be considered as nonionized when $a < 10^{-n} = a_{inf}$, whereas it can be regarded as fully ionized when $a > 1-10^{-n}=a_{sup}$. Now suppose that the range $v_{min}<v<v_{max}$ is known in advance. We can determine from equations (4-6) for all v two functions $e_{inf}(v)$ and $e_{sup}(v)$, which hold for the two cases $a = a_{inf}$ and $a = a_{sup}$, respectively. The construction of $e_{inf}(v)$ and $e_{sup}(v)$ has to be made only at the beginning of computations. It is performed by evaluating the coefficients of a suitable power expansion. Obviously, different values of n lead to different functions $e_{inf}(v)$ and $e_{sup}(v)$.

After this preliminary construction, given a pair (e, v), the computation proceeds as follows. The values $e_{inf}(v)$ and $e_{sup}(v)$ are computed and compared with e. If $e \leqslant e_{inf}(v)$ (or $e \geqslant e_{sup}(v)$), the simple equations of state for the nonionized (or for the fully ionized) perfect gas allow to determine the pressure p and the temperature t, directly. On the contrary, if $e_{inf} < e < e_{sup}$, the two unknowns p and a are eliminated from (4-6) to obtain a single equation in t,

$$f(t) = a(t) - (1-a(t))\, vt^{3/2}\exp(-1/t) = 0, \qquad (7)$$

where $a(t)=(2/3\ e-t)/(2/3+t)$. Then, given the pair (e,v) the equation is solved for t and the root is utilized to compute a and p through (4) and (5).

To solve (7) we have resorted to search algorithms, for the efficient iteration function methods lack the initial approximation which may guarantee convergence. Instead, it is always possible to generate a temperature interval $[t_l, t_h]$ such that $f(t_l)f(t_h) < 0$ and the root $t \in [t_l, t_h]$. In other words, it is possible to construct an interval $[t_l, t_h]$ suitable for starting any search algorithm.

Since for a fixed v, a is an ever-increasing function of t, the extremes can be set at $t_l = (e-1)/3$ and $t_h=2/3e$; these two values correspond with the two cases of complete ionization and null ionization, respectively. The lower extreme t_l, however, may become negative and cause computational difficulties. Therefore, for all practical purposes reference has been made to the value $t_l = \max\{(e-1)/3,\ 0.01\}$. Finally, it is worthy to say that, after

the evaluation of the various possible search algorithms, we found that binary search behaves well when the requirement is for one or two significant digits. In all other cases, appreciably higher efficiencies can be obtained by adopting the false position method.

IV. A test case on gas dynamic ionizing shock wave

As a test case for the numerical procedure we have considered the problem of partial ionization produced by a plane shock wave[5]. The one-dimensional flow has been simulated by solving the equations of gas dynamics in a finite difference form[6]. The inclusion of the artificial viscosity term allows smoothing of shock discontinuities.

Values of the thermodynamic quantities have been computed in the downstream region for various upstream conditions and compared with the exact values. These values have been obtained by using Hugoniot relation for the partially ionized gas. Let us refer by subscripts u and d to the upstream and downstream regions, respectively. Figure 1 and 2 display downstream ionization coefficient a_d as a function of upstream Mach number $M_u = U_u/W_u$. Here U is gas velocity and $W=(\partial p/\partial \rho)_S = c_p/c_v(\partial p/\partial \rho)_T$ stays for sound velocity.

Equations (4 - 6) allow to obtain explicit expressions for dependences of c_p, c_v and $(\partial p/\partial \rho)_T$ upon t and a . Figures 1 and 2 show six different profiles pertaining to specific volumes $v_u = 10^1, 10^2, 10^3, 10^4, 10^5, 10^6$. Higher values for v_u correspond with increasingly higher values for a_d. Similarly, Figures 3 and 4 give the dependence of the density ratio $K=v_u/v_d$ for the same families of upstream conditions. We note in passing that in Figure 3 curves merge towards the left end where ionization is practically absent. This fact is due to the well known scaling of the type $K = f(t_d, t_u)$ valid for a perfect gas without ionization. The values obtained in numerical gas dynamics simulation are represented in the figures by means of dots. The agreement among theoretical (computed) values and simulated values is excellent.

For the computation of exact values of a_d and K, the Hugoniot relation,

$$e_d - e_u = \frac{1}{2}(p_d + p_u)(v_u - v_d) \qquad (8)$$

has been applied to the gas defined by (4-6), to arrive at the form

$$t_d(1+a_d)K^2 - 2\left[2t_d(1+a_d) + a_d - 2t_u(1+a_u) - a_u\right]K - t_u(1+a_u) = 0. \qquad (9)$$

Given this, the density ratio K must be obtained by iteration. Indeed, assigned the upstream values (t_u, a_u), equations (9) and (6) express how K depends on one of the two variables t_d or a_d. Let us fix, for instance, t_d and start from a temptative value for K. Then relations (6) provide a value for a_d which may be introduced in (9) to give a closer approximation for K. Computation is repeated until satisfactorily convergent results are obtained.

V. Conclusion

The numerical procedure has been applied with considerable success to the propagation of a gas dynamic ionizing shock wave. Its domain of applicability, however, extends to any steady or unsteady multidimensional flow where nonuniform ionization has a role. Particularly, the procedure is tailored for situations where the exact amount of partial ionization has a sensible effect on other physical properties. Examples are given by the dynamics of optically thin radiative gases with radiation losses $O(\alpha^2)$ and by magnetogasdynamics when electrical conductivity depends on a variable electron density.

References

1. C.K. Chu, and R.A. Gross, Shock Waves in Plasma Physics; in Advances in Plasma Physics, Vol. 2, A. Simon and W.B. Thompson, eds.; Interscience Publishers, New York, N.Y. (1969).
2. R.F. Christy, Astrophys.J., 144,108 (1966).
3. Ya. B. Zel'dovich, and Yu.P. Raizer, Physics of Shock waves and High-Temperature Hydrodynamic Phenomena, Vol. 1, transl.; Academic Press, New York, N.Y. (1966).
4. P.J. Roache, Computational Fluid Dynamics; Hermosa Publishers, Albuquerque, N.M. (1972).
5. R.T. Taussig, Phys. Fluids, 8,166 (1965); Phys. Fluids, 9, 421 (1966).
6. R.D. Richtmyer, and K.W.Morton, Difference Methods for Initial Values Problems, 2nd ed.; Interscience Publishers, New York, N.Y. (1967).

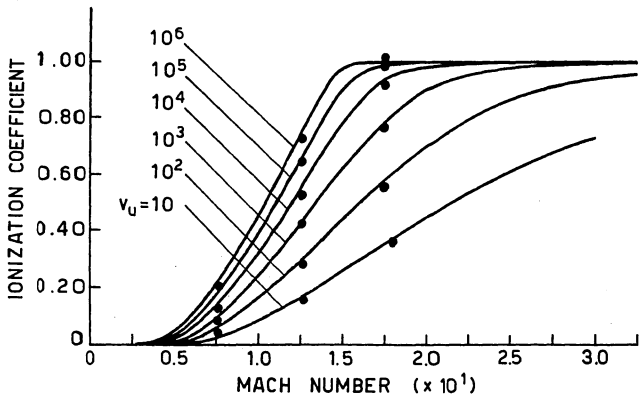

Figure 1. Dependence of ionization coefficient a_d on Mach number M_u for t_u=0.01

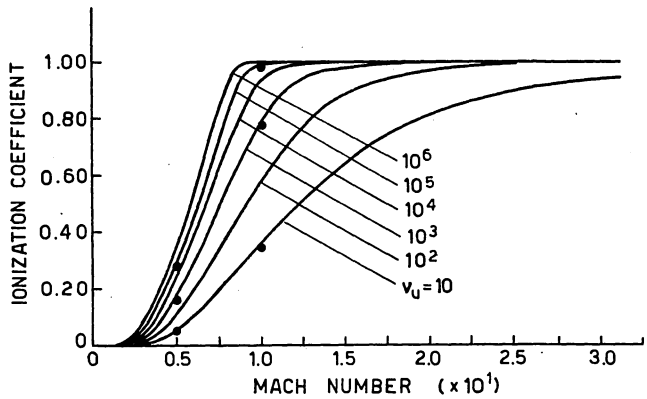

Figure 2. Dependence of ionization coefficient a_d on Mach number M_u for t_u = 0.03.

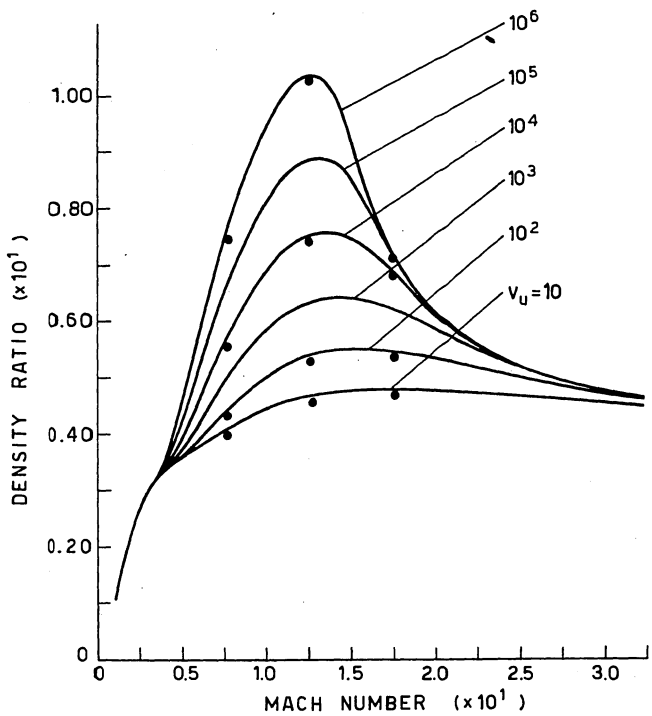

Figure 3. Dependence of density ratio K on Mach number M_u for t_u=0.01.

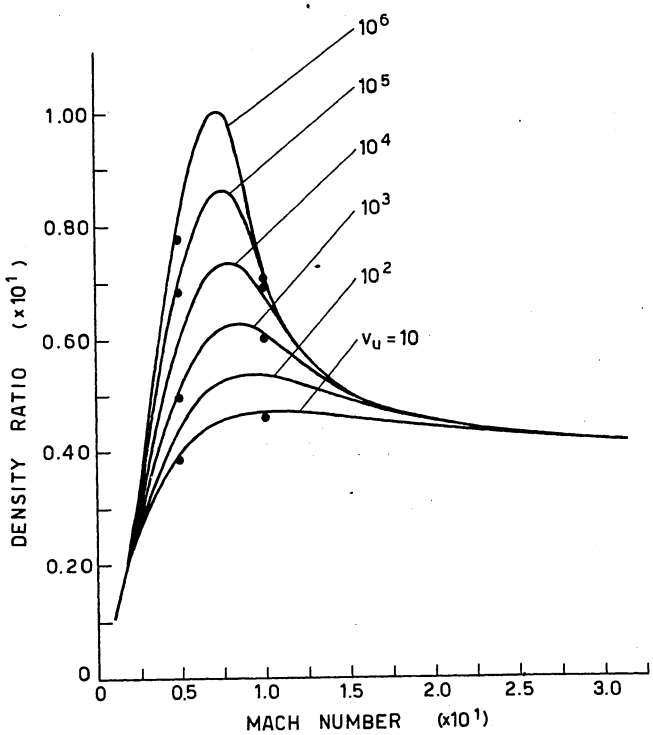

Figure 4. Dependence of density ratio K on Mach number M_u for t_u=0.03.

ANALYSIS OF NUCLEAR INDUCED PLASMAS†

Jerry E. Deese* and H. A. Hassan**
Mechanical and Aerospace Engineering Department
North Carolina State University
Raleigh, North Carolina 27607

Abstract

A kinetic model is developed for a plasma generated by fission fragments and the results are employed to study He plasma generated in a tube coated with fissionable material. Because both the heavy particles and electrons play important roles in creating the plasma, their effects are considered simultaneously. The calculations are carried out for a range of neutron fluxes and pressures. In general, the predictions of the theory are in good agreement with available intensity measurements. Moreover, the theory predicts the experimentally measured inversions. However, the calculated gain coefficients are such that lasing is not expected to take place in a helium plasma generated by fission fragments.

Introduction

Increased interest in gas core reactors[1] and the recent demonstration of direct nuclear pumping[2-4] focused attention on plasmas generated by the high energy fission fragments. Such systems are rather complex and the plasma generated in them is, in general, not in thermal equilibrium. Therefore, before one can predict their performance characteristics, one needs to develop a detailed and self-consistent kinetic model capable of predicting the behavior of the plasmas generated in these devices.

Several authors have analyzed the space-dependent volumetric production of ions by fission fragments passing through a background gas. Both Leffert, et al.[5] and Nguyen and Grossman[6] derived expressions for the spatial distribution of fission fragment production. In both of these analyses an energy independent empirical value W is assumed for the amount of energy required to produce an ion pair. The former utilized both linear and square energy-loss models for the heavy particles, while Nguyen and Grossman used the Bohr stopping equation for fission fragments. Rather than rely on am empirical constant Miley and Thiess[7,8] derived an expression for the ionization and excitation rates which takesinto account the effect of the energy distribution of the incident particles. Such a calculation requires estimation of the energy dependent cross section for excitation and ionization by heavy charged particles. A Bethe-Born type representation was employed for the case of helium excitation by alpha particles and fission fragments[7,8], and later Guyot, et al.[9] employed Gryzinski cross sections[10] for helium ionization by alpha particles and lithium ions.

The calculation of the electron energy distribution function in electric discharges and in the absence of a high energy volumetric source is a standard procedure. However, there are only a few analyses of distributions resulting from a flux of high energy particles where there is a high energy volumetric electron source. Calculations using a Monte Carlo method were carried out by Wang and Miley[11]. Later, Lo[12] and Lo and Miley[13] used a simplified version of the Boltzmann equation to determine the electron energy distribution in a helium plasma produced by a mono-energetic electron source. More recently, Hassan and Deese[14] presented a more elaborate Boltzmann equation formulation which took into consideration the primary electron spectrum.

In general, theoretical studies of excited state densities have assumed the electron distribution function to be a Maxwellian at some characteristic temperature. Russell[15] used such an assumption in calculating excited state densities in argon. Leffert, et al.[5] and Rees, et al.[16] also studied noble gas plasmas assuming the electron distribution function to be Maxwellian. More recently Maceda and Miley[17] calculated the number densities of the helium excited states using the non-Maxwellian distributions of Lo and Miley[13]; their results indicate a number of possible inversions.

In addition to the above analyses, there exists a number of experimental investigations dealing with nuclear pumped lasers and laser enhancement. Work carried out before 1972 is summarized in Ref. 18 while a summary of the nuclear laser effort at the University of Illinois along with an exhaustive list of references on virtually every aspect of radiation produced noble gas plasmas is included in the work of Thiess[19]. Of particular interest here are experiments studying individual atomic transitions at various pressures and additive concentration under fission fragment excitation. The earliest study of fission fragment excited spectra is that of Morse, et al.[20] who examined the effects of fission fragment radiation on He, A_r, N_2, and air. Guyot[21] measured the production of helium metastables by $B^{10}(n,\alpha)$ fission fragments, while Walters[22] measured the relative intensities of the various transitions in both helium and argon.

As a result of the numerous research efforts outlined above, actual nuclear pumped lasing has just recently been reported by several authors. McArthur and Tollefsrud reported lasing action in carbon monoxide as a result of nuclear excitation only. Helmick, et al.[3] demonstrated direct nuclear pumping in He-Xe gas mixtures. A third case of direct nuclear pumped lasing is that of DeYoung[4] in a neon-nitrogen mixture. Obviously the nuclear pumped gas laser research effort is still in its early stages with the validity of the concept having been demonstrated only recently. Historically experimental research work has demonstrated the feasibility of a particular laser concept, with subsequent theoretical development directed towards understanding the actual processes involved and optimization of operating conditions.

The object of this investigation is the development of a theoretical model for a plasma generated by high energy fission fragments.

† Supported, in part, by NASA Grant NSG 1058.
* Research Assistant.
**Professor.

The kinetic model treats particles in different quantum states as different species and uses the multifluid conservation equations of mass, momentum and energy to describe the resulting system. It takes into consideration the following kinetic processes: ionization, excitation and deexcitation, radiative recombination, spontaneous emission, associative ionization and dissociative and collisional recombination. Because both the heavy particles and electrons play important roles in creating the plasma, their effects are considered simultaneously. The rates of reactions involving electrons were calculated using electron distribution functions obtained from a solution of a Boltzmann equation appropriate for plasmas generated by fission fragments[14].

The above model is employed to study a helium plasma generated by fission fragments. Helium was chosen because of the availability of experimentally measured cross sections and rates and because of the availability of in-reactor measurements[22]. In general, the results show good agreement with experiment. Moreover, they indicate a number of possible laser transitions; all of them, however, are in the IR region.

Analytical Formulation

The systems to be modeled here are those appropriate for nuclear pumped lasers. Typically, they consist of tubes coated with fissionable material and filled with gas at some given pressure and temperature. The tube is placed in the high neutron flux region of a reactor. Under neutron bombardment fission fragments emerge from the coating and enter the gas. The ensuing energy transfer results in ionization and excitation of the background gas. A schematic of the slab geometry employed in this analysis is shown in Fig. 1.

Treating particles in different excited states as different species one can utilize the multifluid conservation equations to describe the plasma generated by the fission fragments. For the conditions under consideration, the steady state approximation is appropriate. In this approximation, the effects of gradients are assumed negligible. Thus, the conservation of species equations,

$$\frac{\partial n_s}{\partial t} + \nabla \cdot (n_s \vec{U}_s) = I_s + R_s \qquad (1)$$

reduces, as a result of this approximation, to

$$I_s + R_s = 0 \quad . \qquad (2)$$

In the above equations, s is a charged particle or any quantum state of the background gas and, for species s, n_s is the number density, $\vec{U}_s$ is the velocity and I_s and R_s are the production rates per unit volume resulting from nuclear and kinetic sources, respectively.

For very low Mach numbers the momentum equation reduces to

$$p \simeq \text{const.} \qquad (3)$$

where p is the pressure, while the energy equation takes the form

$$P_i = Q \qquad (4)$$

where P_i is the power input and Q is the conduction and radiation losses. For optically thin highly conducting gas, Eq. (4) reduces to

$$T \simeq T_i \qquad (5)$$

where T_i is the initial gas temperature.

The properties of the electrons are determined from an electron Boltzmann equation. The equation employed is that developed in Ref. 14. For the high pressures of interest the plasmas generated by the fission fragments are slightly ionized. Therefore, using the Lorentz gas approximation, the resulting Boltzmann equation for a quasi-steady plasma can be written as[14]

$$-\frac{v}{3}\frac{\partial}{\partial x_i}\left(-\frac{v}{\nu}\frac{\partial f_o}{\partial x_i}+\frac{eE_i}{m\nu}\frac{\partial f_o}{\partial v}\right)+\frac{eE_i}{3mv^2}\frac{\partial}{\partial v}\left[v^2\left(-\frac{v}{\nu}\frac{\partial f_o}{\partial x_i}\right.\right.$$

$$\left.\left.+\frac{eE_i}{m\nu}\frac{\partial f_o}{\partial v}\right)\right]+\frac{m}{M}\frac{1}{v^2}\frac{\partial}{\partial v}\left[\nu v^2\left(f_o+\frac{kT}{m}\frac{\partial f_o}{\partial v}\right)\right]$$

$$+\frac{N}{v}\sum\left[v'^2\,Q_s(v')f_o' - v^2\,Q_s(v)f_o\right]$$

$$+\left(\partial f_o/\partial t\right)_c = 0 \ , \qquad (6)$$

where

$$\frac{1}{2}mv'^2 = \frac{1}{2}mv^2 + \frac{1}{2}mv_s^2 \ , \qquad (7)$$

v is the velocity, e is the electric charge, m is the electronic mass, M is the mass of the heavy particles, N is the gas number density, ν is the collision frequency, $1/2\ mv_s^2$ is the excitation energy, Q_s is the excitation cross section and $(\partial f_o/\partial t)_c$ is the source term resulting from primary and secondary ionization and recombination. An explicit expression for $(\partial f_o/\partial t)_c$ together with the method of solution of Eq. (6) are given in Ref. 14.

The quantities I_s and R_s must be determined before the above system of equations can be solved for the various species present. To determine I_s and R_s, one needs to specify the important kinetic processes in the system. The major reactions included here, which are appropriate for noble gases, are

1. Fission fragment excitation
$$ff + X \rightarrow X_j + ff$$
2. Fission fragment ionization
$$ff + X \rightarrow X^+ + e + ff$$
3. Spontaneous emission
$$X_i \rightarrow X_j + h$$
4. Ionization and recombination
$$X_i + e \rightleftarrows X^+ + e + e$$
5. Electron excitation and de-excitation
$$X_i + e \rightleftarrows X_j + e$$
6. Radiative recombination
$$X^+ + e \rightarrow X + h$$
7. Excitation transfer
$$X_j + X \rightleftarrows X_k + X$$
8. Dissociative recombination
$$X_2^+ + e \rightleftarrows X_i + X$$
9. Collisional recombination
$$X^+ + X + X \rightarrow X_2^+ + X$$

10. Associative ionization

$$X + X_i \rightarrow X_2^+ + e$$

11. Electron stabilized recombination

$$X_2^+ + e + e \rightarrow X_i + X + e$$

12. Neutral stabilized recombination

$$X_2^+ + e + M \rightarrow X_i + X + M$$

13. Metastable ionization

$$X^* + X^* \rightarrow X^+ + X + e$$

14. Charge Transfer

$$X^+ + M \rightarrow M^+ + X$$

15. Penning ionization

$$X^* + M \rightarrow M^+ + X + e \qquad (8)$$

where M represents a substance other than the background gas or an impurity.

The term I_s is a result of reactions of type 1 and 2 while R_s is obtained from reactions of type 3-15. In general, for a reaction of the type

$$a_i A_i + a_j A_j \rightarrow a_s A_s + a_t A_t \qquad (9)$$

the contribution to the production rate of species s is

$$a_s k n_i^{a_i} n_j^{a_j} \qquad (10)$$

where a_ℓ (ℓ = i, j, s, t) denotes a stochiometric coefficient. The quantity k is the forward rate coefficient and is given by

$$k = \int f_i f_j g_{ij} \sigma_{ij} d\vec{V}_i d\vec{V}_j \qquad (11)$$

where, for species i, f_i is the energy distribution function, $\vec{V}_i$ is the velocity, $g_{ij} = |\vec{V}_i - \vec{V}_j|$ and σ_{ij} is the collision cross section. If i represents the stationary background gas and j a fission fragment or an electron, then Eq. (11) reduces to

$$k = \int f_j \sigma V_j d\vec{V}_j \; . \qquad (12)$$

The rate coefficients for reactions involving the background gas (or gases) are usually obtained from experiment. On the other hand reactions involving the fission fragments and electrons can, in principle, be calculated according to Eq. (12) from collision cross sections determined from experiment or theory and appropriate distribution functions. In this work the electron distribution function is calculated from Eq. (6). Unfortunately, the situation with regards to fission fragments is not well understood; this is because the fission fragments are characterized by initial energies ranging from 50 to 115 Mev, initial charges from 16e to 24e and masses from 70 to 160 atomic mass units. In addition no data is available on cross sections for ionization and excitation by fission fragments. Because of these uncertainties, the contribution of the fission fragments to excitation and ionization was estimated using two different approximate methods. In the first, the procedure outlined in Ref. 6 was used to estimate the average energy deposited in the gas per unit volume per unit time, E_f. The average number of ions produced per unit volume per unit time is given by dividing E_f by W, the energy expended per ion pair produced. Similarly, the total number of excited states produced is determined by dividing E_f by W_{ex}, the energy expended per excited state produced. Rees, et al.[16] determined that the total excited particle production rate from fission fragment is .53 times the ion production rate, thus

$$W_{ex} = W/.53 \; . \qquad (13)$$

This procedure determines only the total number of excited states produced by fission fragments and some model for the distribution of these states must be adopted. Because of the absence of a generally accepted procedure for the distribution of excited states a number of models have been employed here and these are discussed under Results and Discussions.

The other approach uses the procedure of Thiess and Miley[8] which is based on a heavy particle distribution function derived from a semiempirical slowing law together with ionization and excitation cross sections based on the Born or Gryzinski approximations. To utilize this procedure one needs to assume that the fission fragments fall into two groups: a light group with an average mass number of 96 and an average charge of 20e and a heavy group with an average mass number of 140 and an average charge of 22e.

Results and Discussion

The above model is applied to a study of He plasma generated by fission fragments and the results are compared with the measurements of Walters[22] who employed a tube of radius 1.85 cm coated with U_3O_8. To conform to the conditions of the experiment, the calculations allow for the presence of a nitrogen impurity in the system. For a given pressure, temperature, neutron flux and tube dimensions, the above model is capable of predicting the number densities of the helium excited states, the atomic and molecular ions and the electrons. From this, one can calculate the relative intensities and gain coefficients. For the calculations presented here, the gas temperature is assumed constant at 300°K, while the pressure ranged from 100-760 Torr, the neutron flux from 3.8 x 10^{11} - 10^{16} neutrons/cm^2.sec. and the nitrogen concentration from .001 to 50 parts per million.

All helium excited states with a principal quantum number of 5 or less are included in the calculations. The rates or cross sections for the reactions of types (3) through (15) indicated in Eq. (8) were obtained from Refs. 23-54 while Einstein coefficients for spontaneous emission were taken from Refs. 55 and 56. Because the experimental data is incomplete the products or the rates of some reactions had to be estimated and these are discussed next.

At the high pressures of interest here the recombination process in noble gases is complicated by the formation of molecular ions. For pressures greater than 5 Torr the reaction

$$He^+ + 2\ He \rightarrow He_2^+ + He \qquad (14)$$

quickly converts atomic ions into molecular ions[23]. The molecular ion recombination is governed by three reactions[24,25]

$$e + He_2^+ \rightarrow He + He^*$$

$$e + e + He_2^+ \rightarrow He + He^* + e$$

$$e + He + He_2^+ \rightarrow 2\ He + He^* \qquad (15)$$

where He^* denotes an excited state. The distribution of excited states produced by these reactions is not well known. However, recent studies[25-27] indicate that at least 70% of the excited states produced are atomic metastables in the pressure range of interest here. Although potential energy curves indicate other states such as the 2^3P states are produced in molecular ion recombination[57], it is assumed that He^* in the reactions indicated in Eq. (15) are atomic metastables.

Rates for associative ionization are available for atomic states of principal quantum number 3 and triplet states of principal quantum number 4, Refs. 26, 28-30. Cross sections for the excitation transfer reactions are available for n = 2 and n = 3 but only for the triplet states when n = 4, Ref. 26. Because these processes are important in the determination of the final distribution of excited states some estimate of the unavailable rates is required. It is assumed here that the associative ionization rates for n = 5 states are the same as the corresponding n = 4 states while the associative ionization cross sections for the n^1F states are assumed equal to those for the n^1D states. Moreover, three calculations were carried out in which the cross sections for associative ionization and excitation transfer reactions of the triplet n = 4 states were assumed to be one-third of, equal to, and three times the corresponding singlet reaction cross sections. Comparison of calculated and measured excited states showed that better agreement with experiment is obtained when $Q(4^1X) \leq Q(4^3X)$. Therefore, unless indicated otherwise, all calculations reported here employ this assumption.

As indicated earlier, when a 'W' value is used to estimate the total number of excited states further assumptions are needed to indicate which states are excited. From a study of the spectra of noble gases generated by the impact of alpha particles, Bennett[58] suggested that most of the excited states in He are n^1P states with the majority of them in the 2^1P state. His conclusion was based on the fact that calculated excitation cross sections, based on the Born approximation, are highest for the n^1P states. This assumption is contrasted with that of Guyot[21] where he assumed that most of the excited atoms resulting from the impact of alpha particles are in the 2^1S state and these are converted to the 2^3S states by electron impact. Calculations using both of the above models were carried out; for these calculations a value of W_{ex} = 85 ev was employed.

Comparison of the results with the experiments of Walters[22] requires that the effect of a nitrogen contaminant be taken into consideration. The gas used in the experiment contained a nitrogen contaminant of approximately 50 parts per million. The effect of the pressure on the number densities of the electrons and the two metastable states is given in Fig. 2 while Fig. 3 shows the effect of pressure on several of the higher states with and without a 50 parts per million nitrogen contaminant. For these figures, the neutron flux is 3.8×10^{11} neutrons/cm^2.sec. Considering pure helium first, it is seen that the electron number density decreases as the pressure increases. This is because the dominant helium recombination process is the neutral stabilized recombination of the molecular ion and this process becomes more efficient as the pressure increases. The dominant processes governing the excited states number densities are electron excitation from the ground state and the metastable state 2^3S, excitation transfer, associative ionization and spontaneous emission. As the pressure increases, the decrease in the electron density coupled with the increased effectiveness of the associative ionization and excitation transfer results in the decrease of the excited states shown in Fig. 3. Only the 2^3S and 2^1P states show an increase as the pressure increases; the rapid recombination resulting from the last reaction in Eq. (15) accounts for the 2^3S behavior.

As is seen from Figs. 2 and 3, the effect of nitrogen on the various species is quite significant. Both the helium molecular ion and the metastables are quickly converted to nitrogen ions whose dominant recombination process is dissociative recombination. This not only lowers the concentrations of the He ions and metastables but changes the electron number density variation with pressure as well. When nitrogen is present the dominant recombination process is the two-body dissociative recombination. This process does not become more efficient as pressure increases and as a result the electron number density increases with an increase in pressure. Thus, the net effect of nitrogen is two-fold: it lowers the number density of electrons and metastables making electron excitation from metastable states less important and, it changes the number density dependence on pressure. As a result of this, one would expect a significant effect on the higher excited states as well. Because the electron number density increases with pressure the electron excitation rates increase with pressure. Thus, as is seen in Fig. 3, the marked decrease in excited state population with pressure in the case of pure helium is not as pronounced when nitrogen is present. The figure also shows that the magnitudes of the number densities decrease with pressure.

The results indicated in Fig. 3 do not exhibit the peak around 200 Torr shown in Figs. 4-9 of Ref. 17. Both Walters[22] and Thiess[19] suggest that the associative ionization process may be a three-body process of the form

$$He^* + 2\ He \rightarrow He_2^+ + He \qquad (16)$$

rather than the two-body process

$$He^* + He \rightarrow He_2^+ \qquad (17)$$

assumed here. If this process is indeed three-body in nature its effectiveness will increase with pressure.

A study of the variation of the number densities with neutron flux for the case of a pure helium gas at 100 Torr has also been carried out. The behavior of the electrons and metastables is given in Fig. 4 and that of some higher states is shown in Fig. 5. The number densities of the higher states increase linearly with the flux at lower neutron flux levels. As the electron number density increases, the electron stabilized three-body recombination becomes important. Thus, population

densities highly dependent on electron excitation rates do not increase as rapidly at higher flux levels.

Because the nitrogen contaminant has a significant effect on the number densities, a determination of the concentration range where its effect becomes insignificant is of interest. Figure 6 shows a plot of the electron and metastable number densities vs. nitrogen concentration at 100 Torr and a neutron flux of 3.8×10^{11} neutrons/cm^2.sec. As is seen from the figure, the effect of nitrogen is negligible below a concentration of 10^{-8}.

All of the above results assume the 2^1P state to be the only excited state produced by fission fragments. Calculations using the procedure of Ref. 8, the TM model, have also been carried out. Boltzmann plots showing $\log \lambda I/g_i A = \log[hcn_i/4\pi g_i]$, where λ is the wave length, I is the intensity, A is Einstein's transition probability, g_i is the degeneracy, h is Planck's constant and c is the speed of light, vs. ε_u, the energy of the upper level, for pressures of 100 and 760 Torr are given in Figs. 7 and 8 for the 2^1P model and in Figs. 9 and 10 for the TM model. Error bars in these graphs indicate the spread in Walters' experimental data. Using the TM model, the triplet states are considerably underpopulated relative to the singlet states. Because Walters found the triplet states to be of the same order of magnitude for states with n = 3, it appears that the 2^1P model is more appropriate.

As is seen from Fig. 7, the 2^1P model gives good agreement with experiment at 100 Torr; the only discrepancy being the n^3D states which are overpopulated compared with the experimental measurements. At 760 Torr the agreement of the 2^1P model with experiment is not as good as at 100 Torr. All triplet states except the 3^3S are predicted to have a population greater than experimentally measured values. This could be due to an improper pressure dependence for associative ionization as discussed earlier. In general, singlet states have much higher emission coefficients and as a result, cascade losses play a larger role in the singlet system. The triplet system on the other hand is predominantly governed by associative ionization and excitation transfer processes and these have a greater dependence on pressure. Thus, it is expected that triplet states number densities will decrease more rapidly with pressure. Calculations have also been carried out assuming fission fragments produce only 2^1S states. However, for this case the 2^1S number density is higher than the 2^3S number density and this is not in agreement with available experiments[21].

When studying pure helium, two population inversions have been found throughout the entire range of pressures, neutron fluxes and fission fragment excitation models examined on the 3^1P - 3^1D (95.76μ) and 4^1P - 4^1D (216μ) lines[22,59]. In addition, for pressures less than 200 Torr and neutron fluxes less than 10^{14} neutrons/cm^2.sec. the TM model predicts an inversion of the 3^1S - 2^1P line (7281 Å). The expression for the gain coefficient is given in the Appendix. The gain coefficients together with other inversions, operating conditions and fission fragment models employed are summarized in Table 1. The addition of the nitrogen did not change the above results. However, the gain coefficients are slightly decreased because of greater depopulation of excited levels.

Figures 7-10 show only states of principal quantum number four or less; these states were the only states considered in the determination of the inversions present. Excitation transfer cross sections are not available for the n = 5 states and as a result these states are overpopulated. The importance of these reactions can be seen by performing calculations where these reactions are neglected for all states. The Boltzmann plot for such a case is shown in Fig. 11. Comparing Figs. 7 and 11, it is clear that excitation transfer plays an important role in determining the relative population of excited states and consequently, the presence of

Table 1 Gain Coefficients

Transition	Wavelength	Excitation Model	Pressure Torr	Neutron Flux	n_{N_2}/n_T	Gain Coefficient
3^1P - 3^1D	95.76 μ	2^1P	100	3.8×10^{11}	0.0	0.28×10^{-9}
3^1P - 3^1D	95.76 μ	2^1P	760	3.8×10^{11}	0.0	0.76×10^{-11}
3^1P - 3^1D	95.76 μ	2^1P	100	1.0×10^{16}	0.0	0.14×10^{-5}
3^1P - 3^1D	95.76 μ	2^1P	760	3.8×10^{11}	5×10^{-5}	0.42×10^{-11}
3^1P - 3^1D	95.76 μ	TM	760	3.8×10^{11}	0.0	0.15×10^{-9}
4^1P - 4^1D	216 μ	2^1P	100	3.8×10^{11}	0.0	0.12×10^{-9}
4^1P - 4^1D	216 μ	2^1P	760	3.8×10^{11}	0.0	0.24×10^{-11}
4^1P - 4^1D	216 μ	2^1P	100	1.0×10^{16}	0.0	0.16×10^{-6}
4^1P - 4^1D	216 μ	2^1P	760	3.8×10^{11}	5×10^{-5}	0.14×10^{-11}
4^1P - 4^1D	216 μ	TM	760	3.8×10^{11}	0.0	0.11×10^{-10}
4^3D - 4^3P	216 μ	2^1P	100	1.0×10^{16}	0.0	0.20×10^{-5}
3^1S - 2^1P	7281 Å	TM	100	3.8×10^{11}	0.0	0.24×10^{-8}

inversion. Similar conclusions hold when one assumes

$$Q(4^1X) = 3\ Q(4^3X)\ , \qquad (18)$$

as is seen from comparing Figs. 6 and 11.

Concluding Remarks

Considering the incompleteness of available cross sections, the predictions of the model are in good agreement with available relative intensity measurements and measured inversions. However, more complete rate data is needed for the accurate predictions of other possible inversions involving the higher states. The calculated gain coefficients are so small that, because of cavity losses, lasing is not expected to occur in helium. Thus, helium is not a good candidate for a nuclear pumped laser.

Appendix: Gain Coefficient

The possible lasing transitions in atomic helium involve electronic state transitions. The gain coefficient for transition from upper level m to lower level n is

$$\gamma(\nu) = \frac{c^3\, g_m}{8\pi\, \nu^2} A_{mn} \left[\frac{N_m}{g_m} - \frac{N_n}{g_n}\right] G(\nu) \qquad (A1)$$

where $G(\nu)$ is the shape factor, N_m and N_n the number densities of states m and n, g_m and g_n are their degeneracies, A_{mn} is the Einstein coefficient of spontaneous emission from level m to level n, and ν is the frequency of the transition.

The shape factor is affected by two processes, Doppler and pressure broadening. In general, for pressures greater than 30 Torr, pressure broadening is dominant. Thus, Doppler broadening is neglected in this analysis. For pressure broadening the shape factor $G(\nu)$ is given by

$$G(\nu) = \frac{2}{\pi \Sigma_t \nu_{st}} \qquad (A2)$$

where

$$\nu_{st} = \frac{2}{3}\left[2k\left(\frac{T_s}{m_s} + \frac{T_t}{m_t}\right)\right]^{1/2} Z_{st}\, n_t \qquad (A3)$$

In Eq. (A3), s represents the lasing gas and t represents other gases present in the system. When summing on t in Eq. (A2), t can be equal to s.

The quantities Z_{st} can be calculated from the Lennard-Jones potential parameters of the colliding molecules[60-62]

$$Z_{st} = d_{st}^2\, \Omega^{(2,2)}(T^*_{st}) \qquad (A4)$$

$$d_{st} = \sqrt{d_s\, d_t} \qquad (A5)$$

$$T^*_{st} = T/\varepsilon^*_{st} \qquad (A6)$$

$$\varepsilon^*_{st} = \frac{2\sqrt{\varepsilon^*_s\, \varepsilon^*_t}\ \sqrt{I^*_s\, I^*_t}}{(I^*_s + I^*_t)} \ . \qquad (A7)$$

The quantity $\Omega^{(2,2)}(T)$ is obtained from the empirical curve fit[63]

$$\Omega^{(2,2)}(T) = \frac{1.16145}{T^{0.14874}} + 0.52487 \exp[-0.7732\ T] + 2.16178 \exp[-2.43787\ T] - 6.435 \times 10^{-4}\ T^{0.14874} \sin\left(\frac{18.0323}{T^{0.7683}} - 7.27371\right) . \qquad (A8)$$

The required parameters for helium are[60,64]

$$d_s = 2.576 \times 10^{-8}\ \text{cm}$$

$$\varepsilon^*_s = 10.22\ ^\circ\text{K}$$

$$I^*_s = 24.586\ \text{ev} .$$

References

1. Schneider, R. T., Thom, K. and Helmick, H. H., "Lasers from Fission", XXVIth International Astronautical Congress, Lisbon, 1975.

2. McArthur, D. A. and Tollefsrud, P. B., "Observation of Laser Action in CO Gas Excited Only by Fission Fragments", Applied Physics Letters, Vol. 26, Feb. 1975, pp. 187-190.

3. Helmick, H. H., Fuller, J. L. and Schneider, R. T., "Direct Nuclear Pumping of a Helium-Xenon Laser", Applied Physics Letters, Vol. 26, March 1975, pp. 327-328.

4. DeYoung, R. J., "A Direct Nuclear Pumped Neon-Nitrogen Laser", Ph.D. Dissertation, University of Illinois, 1975.

5. Leffert, C. B., Rees, D. B. and Jamerson, F. E., "Noble Gas Plasmas Produced by Fission Fragments", Journal of Applied Physics, Vol. 37, Jan. 1966, pp. 133-142.

6. Nguyen, D. H. and Grossman, L. M., "Ionization by Fission Fragments Escaping from a Source Medium", Nuclear Science and Engineering, Vol. 30, Nov. 1967, pp. 233-241.

7. Miley, G. H. and Thiess, P. E., "A Unified Approach to Two-Region Ionization-Excitation Density Calculations", Nuclear Applications, Vol. 6, May 1969, pp. 434-451.

8. Thiess, P. E. and Miley, G. H., "Calculations of Ionization-Excitation Source Rates in Gaseous Media Irradiated by Fission Fragments and Alpha Particles", NASA SP-236, 1971, pp. 369-396.

9. Guyot, J. C., Miley, G. H. and Verdeyen, J. T., "Application of a Two Region Heavy Charged Particle Model to Noble-Gas Plasmas Induced by Nuclear Radiations", Nuclear Science and Engineering, Vol. 48, Aug. 1972, pp. 372-386.

10. Gryzinski, M., "Classical Theory of Atomic Collisions. I. Theory of Inelastic Collisions", Physical Review, Vol. 138, April 1965, pp. A336-A358.

11. Wang, B. S. and Miley, G. H., "Monte Carlo Simulation of Radiation-Induced Plasma", Nuclear Science and Engineering, Vol. 52, Sept. 1973, pp. 130-141.

12. Lo, R. H., "Energy Distributions of Electrons in Radiation Induced-Helium Plasmas", Ph.D. Dissertation, University of Illinois, 1972.

13. Lo, R. H. and Miley, G. H., "Electron Energy Distribution in a Helium Plasma Generated by Nuclear Radiation", IEEE Transactions on Plasma Science, Vol. PS-2, Dec. 1974, pp. 198-205.

14. Hassan, H. A. and Deese, Jerry E., "The Electron Boltzmann Equation in a Plasma Generated by Fission Products", to appear as a low-numbered NASA CR, 1976.

15. Russell, G. R., "Feasibility of a Nuclear Laser Excited by Fission Fragments Produced in a Pulsed Nuclear Reactor", NASA SP-236, 1971, pp. 53-62.

16. Rees, D. B., Leffert, C. B. and Rose, D. J., "Electron Density in Mixed Gas Plasmas Generated by Fission Fragments", Journal of Applied Physics, Vol. 40, March 1969, pp. 1884-1896.

17. Thom, K. and Schneider, R. T., "Nuclear Pumped Gas Lasers", AIAA Journal, Vol. 10, April 1972, pp. 400-406.

18. Maceda, E. L. and Miley, G. H., "Non-Maxwellian Electron Excitation in Helium", Bulletin of the American Physical Society, Vol. 20, Feb. 1975, p. 255.

19. Thiess, P. E., "Optical Emission and Kinetics of High Pressure Radiation-Produced Noble Gas Plasmas", Ph.D. Dissertation, University of Illinois, 1975.

20. Morse, F., Harteick, P. and Dondes, S, "Excited Species of Gases Produced in the Nuclear Reactor", Radiation Research, Vol. 29, Nov. 1966, pp. 317-328.

21. Guyot, J. C., "Measurement of Atomic Metastable Densities in Noble Gas Plasmas Created by Nuclear Irradiation", Ph.D. Dissertation, University of Illinois, 1971.

22. Walters, R. A., "Excitation and Ionization of Gases by Fission Fragments", Ph.D. Dissertation, University of Florida, 1973.

23. Beaty, E. C. and Patterson, P. L., "Mobilities and Reaction Rates of Ions in Helium", Physical Review, Vol. 137, Jan. 1965, pp. A346-A357.

24. Berlande, J., Cheret, M., Deloche, R., Gonfalone, A., and Manus, C., "Pressure and Electron Density Dependence of the Electron-Ion Recombination Coefficient in He", Physical Review A, Vol. 1, March 1970, pp. 887-896.

25. Deloche, R., Monchicourt, P., Cheret, M. and Lambert, F., "High-Pressure Helium Afterglow at Room Temperature", Physical Review A, Vol. 13, March 1976, pp. 1140-1176.

26. Cohen, J. S., "Multistate Curve-Crossing Model for Scattering: Associative Ionization and Excitation Transfer in Helium", Physical Review A, Vol. 13, Jan. 1976, pp. 99-114.

27. Johnson, A. W. and Gerardo, J. B., "Ionizing Collisions of Two Metastable Helium Atoms (2^3S)", Physical Review A, Vol. 7, March 1973, pp. 925A-928A.

28. Teter, M. P., Niles, F. E. and Robertson, W. W., "Hornbeck-Molnar Cross Sections for the n = 3 States of Helium", The Journal of Chemical Physics, Vol. 44, April 1 66.

29. Wellenstein, H. F. and Robertson, W. W., "Collisional Relaxation Processes for the n = 3 States of Helium. II. Associative Ionization", The Journal of Chemical Physics, Vol. 56, Feb. 1972, pp. 1077-1082.

30. Wellenstein, H. F. and Robertson, W. W., "Collisional Relaxation Processes for the n = 3 States of Helium. III. Total Loss Rates for Normal Atom Collision", The Journal of Chemical Physics, Vol. 56, Feb. 1972, pp. 1411-1412.

31. Rapp, D. and Englander-Golden, P., "Total Cross Sections for Ionization and Attachment in Gases by Electron Impact", The Journal of Chemical Physics, Vol. 43, Sept. 1965, pp. 1464-1479.

32. Dugan, J. L. G., Richards, H. L. and Muschlitz, E. G., "Excitation of the Metastable States of Helium by Electron Impact", The Journal of Chemical Physics, Vol. 46, Jan. 1967, pp. 346-351.

33. Holt, H. F. and Krotkov, R., "Excitation of n = 2 States in Helium by Electron Bombardment", Physical Review, Vol. 144, April 1966, pp. 82-93.

34. Cermak, V., "Individual Efficiency Curves for the Excitation of 2^3S and 2^1S States of Helium by Electron Impact", Journal of Chemical Physics, Vol. 44, May 1966, pp. 3774-3780.

35. Ferendeci, A. M., "Electron Excitation Cross Section of the He 2^1S State from Diffraction Losses in a He - Ne Gas Laser", Physical Review A, Vol. 11, May 1975, pp. 1576-1582.

36. St. John, R. M., Miller, F. L. and Lin, C. C., "Absolute Excitation Cross-Sections of Helium", Physical Review, Vol. 134, May 1964, pp. A888-A897.

37. Showalter, J. G. and Kay, R. B., "Absolute Measurement of Total Electron-Impact Cross Sections to Singlet and Triplet Levels in Helium", Physical Review A, Vol. 11, June 1975, pp. 1899-1910.

38. Jobe, J. D. and St. John, R. M., "Absolute Measurements of the 2^1P and 2^3P Electron Excitation Cross-Sections of Helium Atoms", Physical Review A, Vol. 164, Dec. 1967, pp. 117-121.

39. Kieffer, L. J., "Low-Energy Electron-Collision Cross-Section Data. Part II: Electron-Excitation Cross Sections", Atomic Data, Vol. 1, Nov. 1969, pp. 121-187.

40. Moiseiwitsch, B. L. and Smith, S. J., "Electron Impact Excitation of Atoms", Reviews of Modern Physics, Vol. 40, April 1968, pp. 124-353.

41. Phelps, A. V., "Absorption Studies of Helium Metastable Atoms and Molecules", Physical Review, Vol. 99, August 1955, pp. 1307-1313.

42. Benson, R. S. and Kulander, J. L., "Electron Impact Excitation Rates for Helium", Solar Physics, Vol. 27, Dec. 1972, pp. 305-318.

43. Wellenstein, H. F. and Robertson, W. W., "Collisional Relaxation Processes for the n = 3 States of Helium. I. Excitation Transfer by Normal Atoms and by Electrons", The Journal of Chemical Physics, Vol. 56, Feb. 1972, pp. 1072-1076.

44. Baker, D. J., Bedo, D. E. and Tomboulian, D. H., "Continuous Photoelastic Absorption Cross Section of Helium", Physical Review, Vol. 124, Dec. 1971, pp. 1471-1476.

45. Lowry, J. F., Tomboulian, D. H. and Ederer, D. L., "Photoionization Cross Section of Helium in the 100- to 250- Å Region", Physical Review A, Vol. 137, Feb. 1965, pp. 1054A-1057A.

46. St. John, R. M. and Nee, T. W., "Collisional Transfer of Excitation Energy in Helium", Journal of the Optical Society of America, Vol. 55, April 1965, pp. 426-432.

47. Jobe, J. D. and St. John, R. M., "Excitation of the 4F States of Helium", Journal of the Optical Society of America, Vol. 57, Dec. 1967, pp. 1449-1451.

48. Allison, D. C., Browne, J. C. and Dalgarno, A., "Collision Induced Deactivation of Metastable Helium", Proceedings of the Physics Society, Vol. 89, Sept. 1966, pp. 41-44.

49. Collins, C. B., Johnson, B. W. and Shaw, M. J., "Study of Excitation Transfer in a Flowing Helium Afterglow Pumped with a Tuneable Dye Laser. I. Measurement of the Rate Coefficient for Selected Quenching Reactions Involving $He(5^3P)$", Journal of Chemical Physics, Vol. 57, Dec. 1972, pp. 5310-5316.

50. Hurt, W. B., "Cross Section for the Reaction $He(2^3S) + He(2^3S)$", Journal of Chemical Physics, Vol. 45, Oct. 1966, pp. 2713-2714.

51. Biondi, M. A., "Charged-Particle Recombination Processes", Defense Nuclear Agency Reaction Rate Handbook, Bartner, M. H. and Baurer, T., eds., Second ed., 1972, Chapter 16.

52. Warneck, P., "Studies of Ion-Neutral Reactions by a Photoionization Mass-Spectrometer Technique. IV. Reactions of He^+ with N_2 and O_2", Journal of Chemical Physics, Vol. 47, Nov. 1967, pp. 4279-4281.

53. Schmeltekopf, A. L. and Fehsenfeld, F. C., "De-excitation Rate Constants for Helium Metastable Atoms with Several Atoms and Molecules", Journal of Chemical Physics, Vol. 53, Oct. 1970, pp. 3173-3177.

54. Mark. T. D. and Oskam, H. J., "Ion Production and Loss Processes in Helium-Nitrogen Mixtures", Physical Review A, Vol. 4, Oct. 1971, pp. 1445-1452.

55. Gabriel, H. A. and Heddle, D. W. O., "Excitation Processes in Helium", Proceedings of the Royal Society of London, Vol. 258, Nov. 1960, pp. 124-145.

56. Wiese, W. L., Smith, M. W. and Glennon, B. M., "Atomic Transition Probabilities. I. Hydrogen through Neon", NSRDS-NBS 4, National Bureau of Standards, Washington, D. C., 1966.

57. Cohen, J. L., "Diabatic-States Representation for $He^*(n \geq 3)$ + He Collisions", Physical Review A, Vol. 13, Jan. 1976, pp. 86-98.

58. Bennett, W. R., "Optical Spectra Excited in High Pressure Noble Gases by Alpha Impact", Annals of Physics, Vol. 18, June 1962, pp. 367-420.

59. Schneider, R. T., "On the Feasibility of Nuclear Pumping of Gas Lasers", Laser Interactions and Related Plasma Phenomenom, Vol. 3, H. J. Schwartz and H. Hora, eds., Plenum Publishing Co., New York, 1974, pp. 85-107.

60. Hirschfelder, J. O., Curtis, C. F. and Bird, R. B., Molecular Theory of Gases and Liquids. Second ed., John Wiley and Sons, New York, 1964, pp. 1110-1111.

61. Good, R. J. and Hope, C. J., "New Combining Rule for Intermolecular Distance in Intermolecular Potential Functions", The Journal of Chemical Physics, Vol. 53, July 1970, pp. 540-543.

62. Good, R. J. and Hope, C. J., "Test of Combining Rules for Intermolecular Distances. Potential Function Constants from Second Virial Coefficients", The Journal of Chemical Physics, Vol. 55, July 1971, pp. 111-116.

63. Neufeld, P. D., Janzen, A. R. and Aziz, R. A., "Empirical Equations to Calculate 16 of the Transport Collision Integrals $\Omega^{(1,S)*}$ for the Lennard-Jones (12-6) Potential", The Journal of Chemical Physics, Vol. 57, Aug. 1972, pp. 1100-1102.

64. Kieffer, L. J., "A Compilation of Electron Collision Cross Section Data for Modeling Gas Discharge Lasers", JILA Information Center Report 13, Sept. 1973, Information Center, Joint Institute for Laboratory Astrophysics, University of Colorado, Boulder, Colorado.

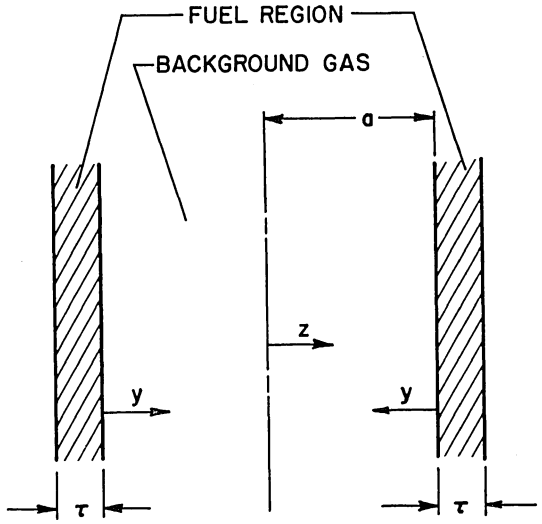

Fig. 1 Slab approximation of cylindrical geometry.

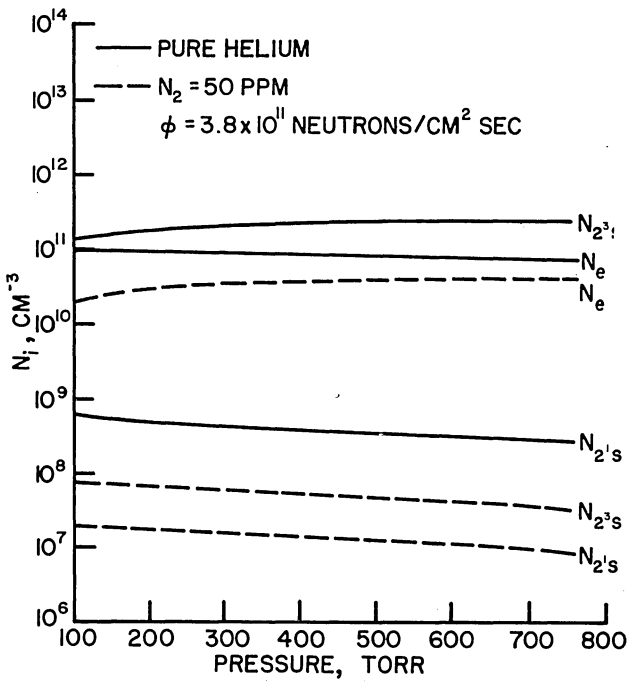

Fig. 2 Influence of pressure on electron and metastable number densities

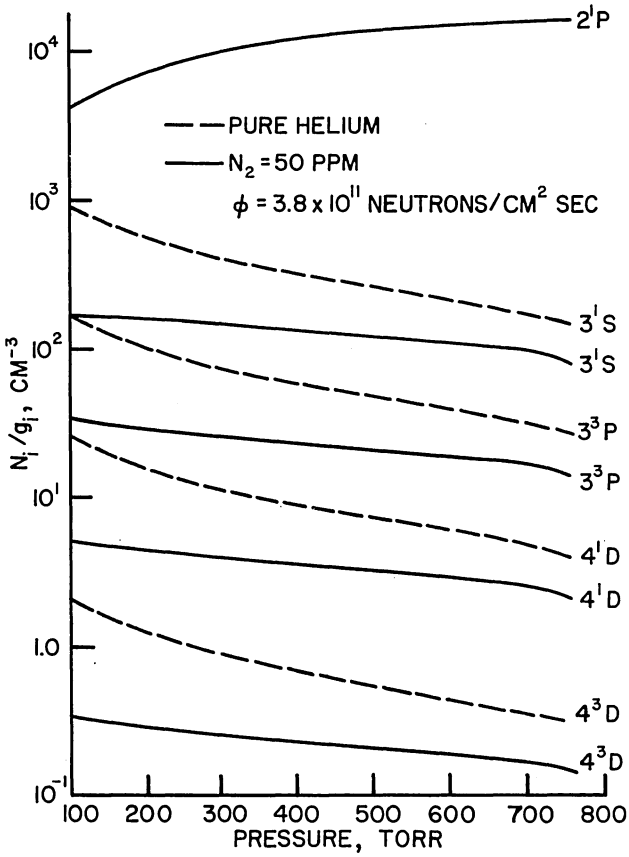

Fig. 3 Influence of pressure on selected excited state number densities.

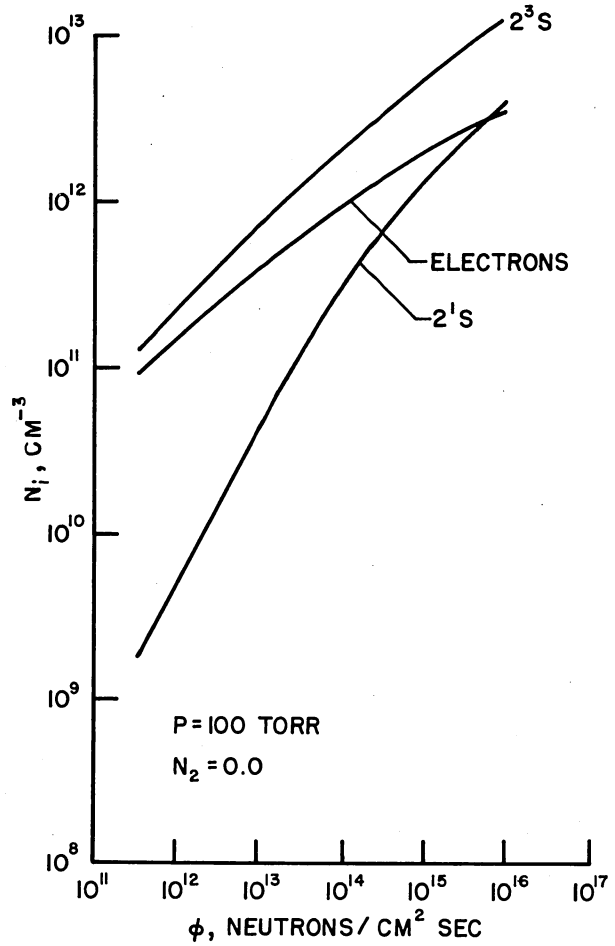

Fig. 4 Effect of neutron flux on electron and metastable number densities.

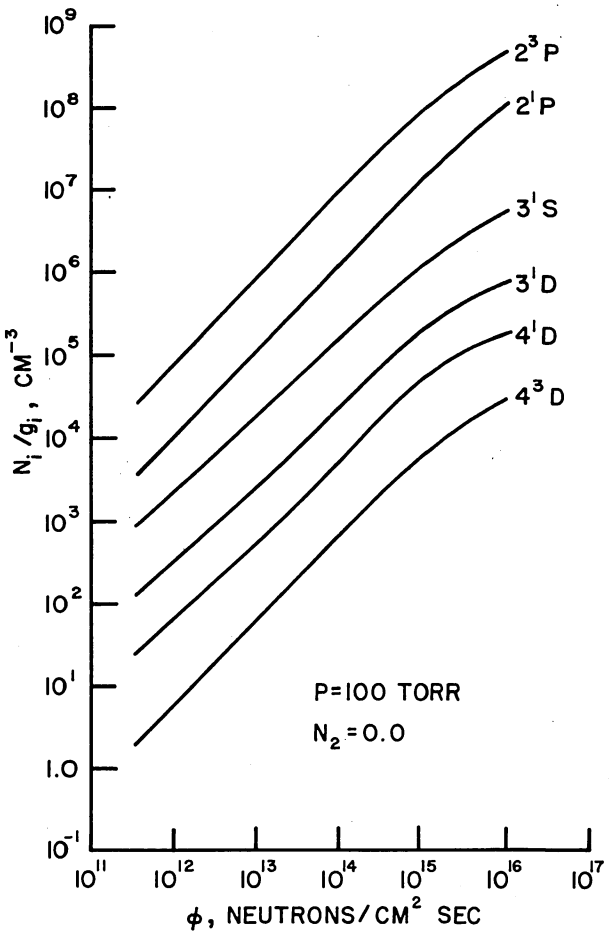

Fig. 5 Effect of neutron flux on the number densities of some excited states.

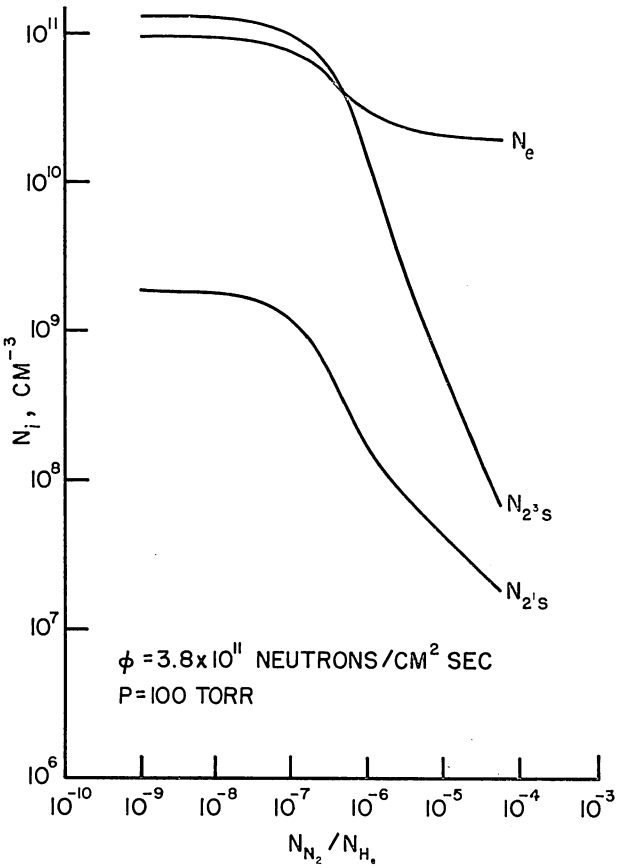

Fig. 6 Effect of a nitrogen contaminant on electrons and metastables.

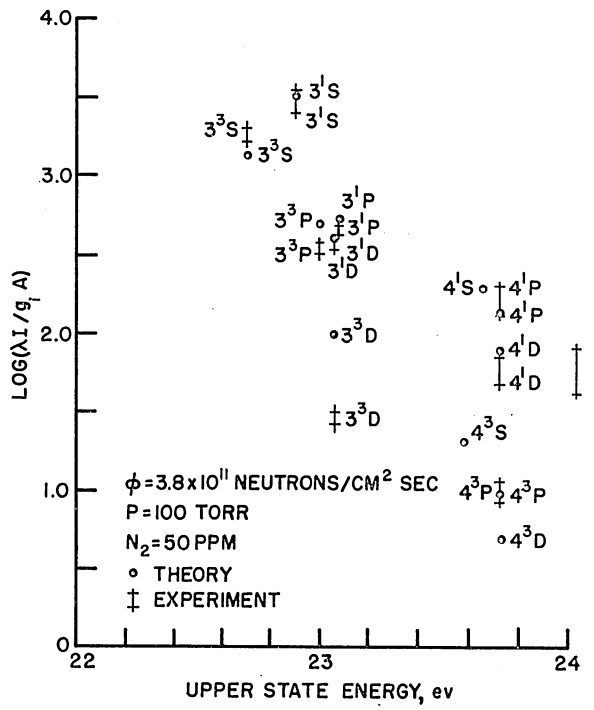

Fig. 7 Helium excited states at 100 Torr, 2^1P model.

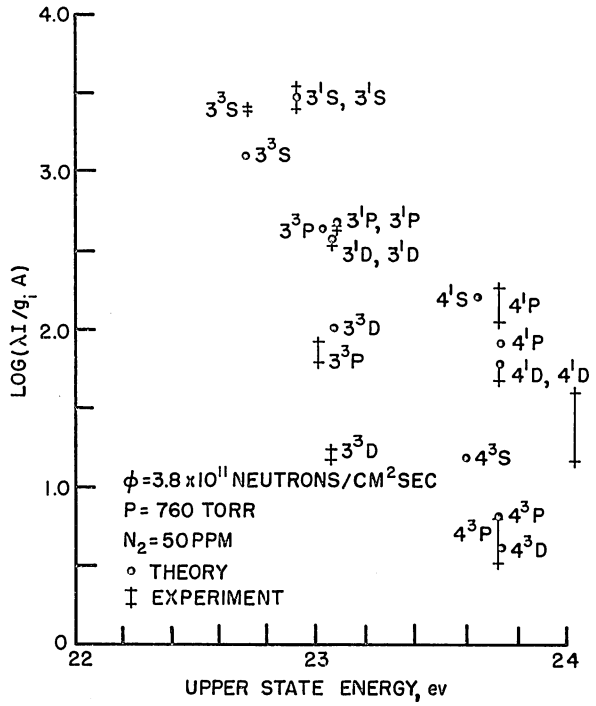

Fig. 8 Helium excited states at 760 Torr, 2^1P model.

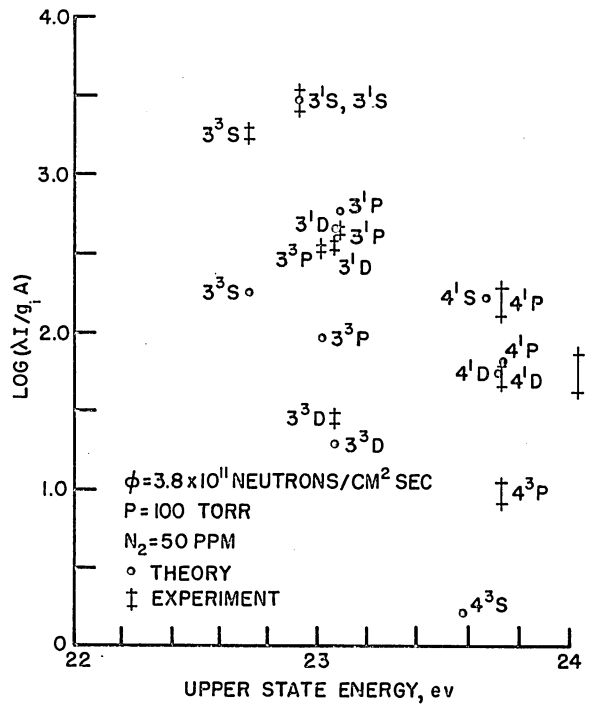

Fig. 9 Helium excited states at 100 Torr, TM model.

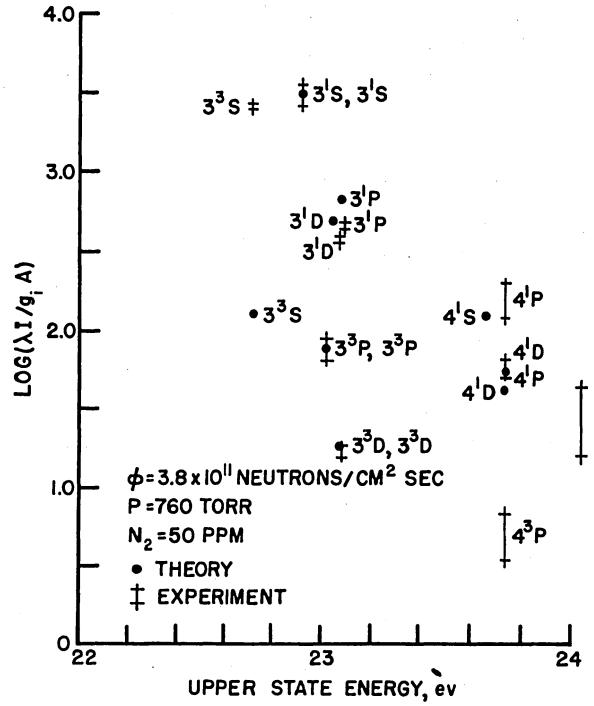

Fig. 10 Helium excited states at 760 Torr, TM model.

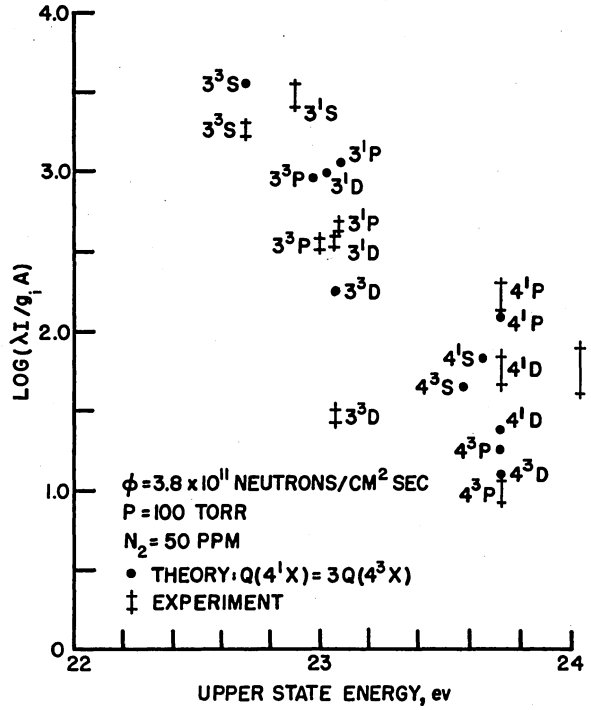

Fig. 12 Effect of associative ionization and excitation transfer rates for n = 4 on excited states.

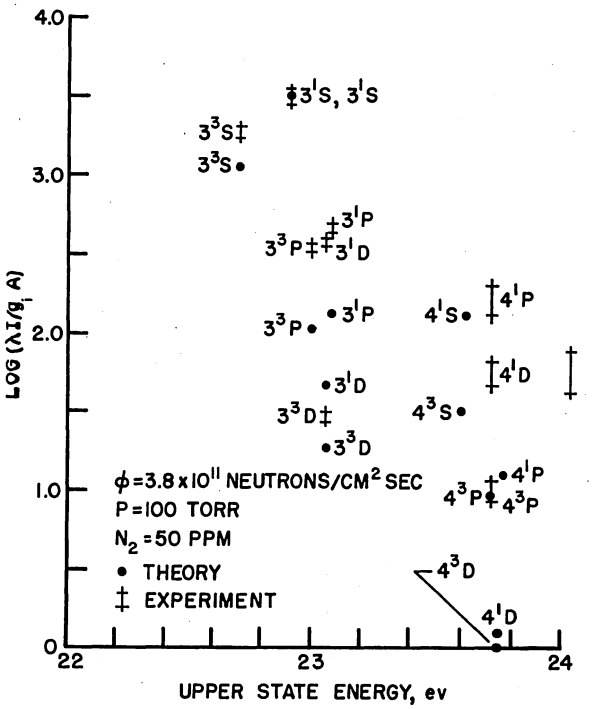

Fig. 11 Effect of excitation transfer reactions on excited states.

ENERGY DISTRIBUTIONS AND RADIATION TRANSPORT IN URANIUM PLASMAS*

G. Miley, C. Bathke†, E. Maceda and C. Choi
Nuclear Engineering Program
University of Illinois
Urbana, Illinois 61801

Abstract

Electron energy distribution functions have been calculated in a U^{235}-plasma at 1 atmosphere for various plasma temperatures (5000 to 8000°K) and neutron fluxes (2×10^{12} to 2×10^{16} neutrons/(cm^2-sec)). Two sources of energetic electrons are included; namely fission-fragment and electron-impact ionization, resulting in a high-energy tail superimposed on the thermalized electron distribution. Consequential derivations from equilibrium collision rates are of interest relative to direct pumping of lasers and radiation emission. Results suggest that non-equilibrium excitation can best be achieved with an additive gas such as helium or in lower temperature plasmas requiring UF_6.

An approximate analytic model, based on continuous electron slowing, has been used for survey calculations. Where more accuracy is required, a Monte Carlo technique is used which combines an analytic representation of Coulombic collisions with a random-walk treatment of inelastic collisions. The calculated electron distributions have been incorporated into another code that evaluates both the excited atomic state densities within the plasma and the radiative flux emitted from the plasma. Only preliminary results are available from the latter code at this time, however.

Introduction

Knowledge of distribution functions is essential to understanding radiation-induced plasmas and their applications. Prior to the present uranium plasma calculations, workers at Illinois considered various noble gases, both as potential nuclear-pumped laser candidates and to gain experience with analytic techniques with simpler cases. G. Miley[1,2] developed techniques to calculate the energy distribution of the primary ions. Subsequently, P. Thiess and G. Miley[3] reported early calculations for helium at the 2nd Uranium Conference; R. Lo and G. Miley[4] first reported the calculation of a full distribution of electron energy in a helium plasma created by nuclear radiation in 1974; and B. Wang and G. Miley[5] developed a Monte Carlo simulation model to evaluate the distribution function more precisely for cases both with and without an applied electric field. While consuming more computer time, the Monte Carlo method is viewed as a benchmark for testing analytic techniques which must, of necessity, contain many approximations.

Evaluation of the electron energy distribution and the resulting excited state densities in uranium-UF_6 plasmas are necessary to accurately determine the radiation emitted from a gaseous-core uranium reactor such as is currently under experimental study at Los Alamos Scientific Laboratory.[6] A gaseous-core uranium reactor is a potentially important source of radiation for the various applications such as chemical processing, isotope separation, and direct pumping of gas lasers.[7]

While early experiments will use UF_6, our calculations to date have concentrated on uranium plasmas for two reasons: First, an opportunity to develop the appropriate cross-sections and calculational techniques is afforded while working with a simpler, one-component case, and secondly, the uranium plasma is of ultimate interest for high-grade power reactors.

Plasma temperatures ranging from 5000°K to 8000°K at a pressure of 1 atm (the boiling point of uranium is 4407°K at 1 atm) with neutron fluxes from 2×10^{12} to 2×10^{16} neutrons/(cm^2-sec) are considered. The uranium plasma under study is unique in that it is a fissioning plasma. The neutron flux within the plasma causes fission-fragments to be formed. They in turn produce a non-Maxwellian electron flux which excites the atoms in the gas, creating radiation emission. Two important questions result: Are there any inverted energy levels that could lead to lasing? Does the line structure that is superimposed on the emission continuum cause any unique features relative to other uses?

The study has two distinct aspects: First, the effect of fission-fragments on the electron energy-distribution function in the plasma is evaluated.[8] Parametric studies of the neutron-flux (a measure of the fission-fragment density) and the temperature dependence of the distribution function are included as part of this work. Second, the excited-state densities within the plasma are studied.[9] Possible inversions are sought and the radiative transport of photons, i.e. the plasma emission spectrum, is considered.

In determining the rate of occurrence of fission reactions, the uranium is assumed to consist entirely of the U^{235} isotope. Furthermore, the neutrons are assumed to be in thermal equilibrium with the plasma so that the fission cross-section can be averaged over the neutron flux distribution using an effective neutron temperature. Some allowance for spectrum hardening is made in the more strongly absorbing cases.

Theoretical Models

In subsequent sections we concentrate on the electron energy distribution created by fission

*This work is supported by the U.S. NASA Grant NSG-1063.

†Present Address: Plasma Physics Laboratory, Princeton University, Princeton, NJ 08540

fragments. Over the density range of interest, electron-impact excitation-ionization dominates over the contribution by direct fission-fragment collisions. Consequently, it is important to have the correct energy-spectrum for primary electrons produced by fission-fragment impact, and this is calculated by techniques developed by Guyot and Miley.[10]

For the plasma parameters mentioned above, the densities of the various plasma constituents can be predicted by the Saha equations, and the densities are illustrated in this Fig. 1. A first order approximation of the perturbation to these densities caused by the production of fission-fragment generated electrons is only of the order of 1/10% for cases of interest here. Therefore, a further correction for radiation effects is generally negligible.

Despite their small number, the high energy electrons in the tail of the distribution make a significant contribution to excitation reactions, hence, this tail is calculated explicitly. An approximate, but useful, analytic formulation for the distribution function is obtained with the assumption of continuous slowing down of electrons. In an infinite, isotropic medium and in the absence of external forces or fields, the steady-state solution for the distribution function at high energies (i.e. for energies where recombination is negligible) is found to be[11,12]

$$f(E) = \frac{\int_E^\infty S(E')\, dE'}{\left.\frac{dE}{dt}\right|_E}, \qquad E > E_T. \tag{1}$$

The denominator, $\left.\frac{dE}{dt}\right|_E$, of Eq. (1) gives the energy loss rate of an electron at energy E due to Coulombic collisions and inelastic collisions (ionization and excitation of neutral and singlely ionized uranium). It is composed of a sum of energy loss rates for each type of collision, i.e.,

$$\frac{dE}{dt} = \left.\frac{dE}{dt}\right|_{\substack{\text{Coulombic}\\ \text{collisions}}} + \left.\frac{dE}{dt}\right|_{\substack{\text{ionization}\\ \text{collisions}}} + \left.\frac{dE}{dt}\right|_{\substack{\text{excitation}\\ \text{collisions}}} \tag{2}$$

Numerous treatments for $\left.\frac{dE}{dt}\right|_{\substack{\text{Coulombic}\\ \text{collisions}}}$ exist in the literature, such as the Fokker-Planck model.[13] However, the electron density in the uranium plasma is unique in that it does not satisfy the conditions necessary for Debye shielding, e.g. in a typical case less than one electron is contained per Debye sphere. Consequently, the more general energy loss rate of T. Kihara and O. Aono[14] is used, which incorporates collective interactions.

In the case of ionization and excitation, the energy loss rate may be obtained by

$$\left.\frac{dE}{dt}\right|_E = \langle E\rangle_{loss} \cdot \Sigma \cdot v \tag{3}$$

where v is the speed of a test electron relative to thermal electrons and Σ is the macroscopic inelastic cross section. The average energy loss per collision, $\langle E\rangle_{loss}$ is defined as

$$\langle E\rangle_{loss} \equiv \frac{\int_o^\infty \frac{d\sigma(E,E')}{dE'} \cdot E'\, dE'}{\int_o^\infty \frac{d\sigma(E,E')}{dE'}\, dE'} = \frac{\int_o^\infty \frac{d\sigma(E,E')}{dE'} \cdot E' dE'}{\sigma(E)} \tag{4}$$

where E is the energy of a test particle and E' is the energy lost by the test particle as a result of a collision. The microscopic cross section, $\sigma(E)$ and the energy transfer differential cross section, $\frac{d\sigma(E,E')}{dE'}$ are calculated from a Gryzinski model[15] using the data of Parks, et al.[16] for uranium atomic states.

While there are many uncertainties in these cross section estimates, this approach is the only one feasible in view of the scarcity of experimental data or detailed calculations. While absolute magnitudes for the resulting distributions will reflect this uncertainty, hopefully relative comparisons among the various calculations will be more accurate.

In the numerator of Eq. (1), the quantity S(E') is the electron production rate from all sources per unit spatial volume per unit energy. The electron sources are of two types, categorized according to their origin; namely, nascent electrons and secondary electrons. The former electrons are the result of fission-fragment-induced ionization of uranium while the latter are the result of electron-induced ionization of uranium. Since the secondary electron source is dependent upon the nascent electron source and the manner in which they thermalize, an expression for the total source, S(E) cannot be known a priori. Consequently, S(E) and the distribution function f(E) must be calculated in an iterative manner.

Computational Techniques

The starting point in the iterative scheme is the calculation of the nascent electron source S_o which requires a knowledge of the fission-fragment energy distribution. A simple estimate of this distribution can be obtained using the equivalence of Eq. (1). The source of fission-fragments is so narrow in energy that it can be considered as a delta function; but two distinct fission-fragments result from a single fission event at average energies of 67 MeV and 98 MeV and masses of 140 amu and 96 amu, respectively. Then, the fission-fragment distribution is

$$f_{FF}(E) = \frac{S'}{\left.\frac{dE}{dt}\right|_E}, \tag{5}$$

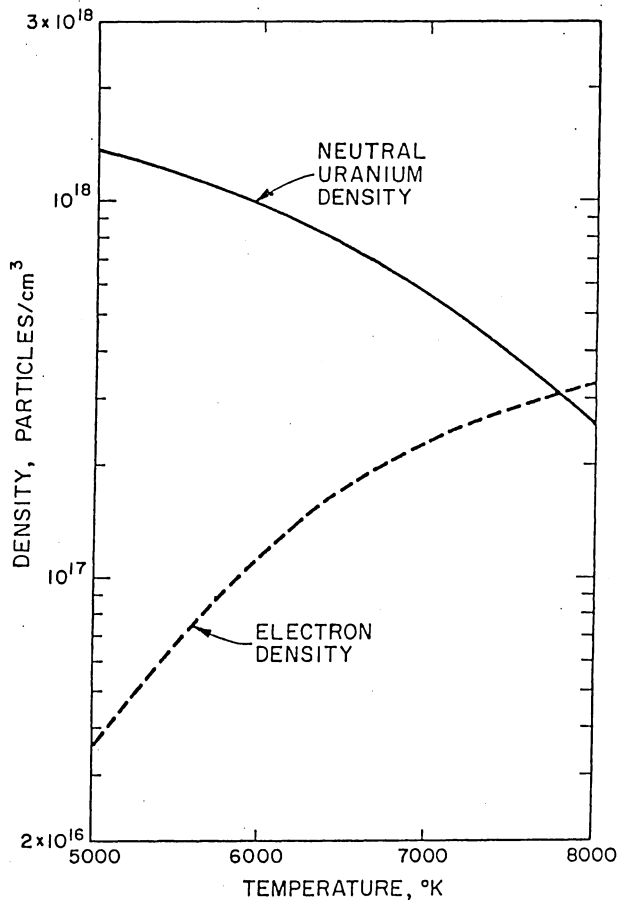

Fig. 1. The density of the uranium plasma constituents plotted versus temperature assuming a pressure of one atmosphere.

where S' represents the number of fission events/(cm^3-sec) and $\frac{dE}{dt}\Big|_E$ is the energy loss rate of a fission-fragment at energy E. The quantity S' is determined by the choice of the neutron flux and the temperature which indirectly yields the uranium density and an averaged fission cross section characterized by the plasma temperature.[17]

The fission-fragments experience electron capture over their entire track such that $q \sim q_o\, v/v_o$ where q_o and v_o represent the initial charge (~16e) and velocity, respectively. Consequently, the energy loss $\frac{dE}{dx}$ is a minimum at the beginning of their track. A semi-empirical formula[18] for the energy loss of a fission-fragment at energy E is given by

$$\frac{dE}{dx} = \frac{2E_o}{\lambda(E_o)} \left(\frac{E_o}{E}\right)^{-1/2} \qquad (6)$$

where E_o is the birth energy of the fission fragment and λ is its range (the latter is obtained from Eq. 3.50 of Ref. 18). Then, the fission-fragment distribution is

$$f_{FF}(E) = \frac{\lambda(E_o)\ S'}{2E} \left(\frac{M}{2E_o}\right)^{1/2} \qquad (7)$$

where M is the mass of the fission-fragment and the relationship $dE/dt = v\ dE/dx = \sqrt{2E/M} \cdot dE/dx$ has been utilized. The nascent electron source term S_o appearing in Fig. 2 is then obtained by averaging the fission-fragment distribution over a Gryzinski energy-transfer cross-section for ionization events, generalized for heavy, multicharged ions.[15,10]

The nascent electrons S_o relax into a primary electron distribution $f_o(E)$ according to Eq. (1). During the thermalization process, the primary electrons further ionize the background uranium generating a source of secondary electrons $S_1(E)$ (as with S_o, S_1 is obtained by averaging the primary electron distribution over a Gryzinski energy-transfer cross-section for ionization). This first generation of secondary electrons distribute themselves in energy as prescribed by Eq. (1), i.e. insertion of $S_1(E)$ in the equation yields $f_1(E)$, producing a second generation of secondary electrons $S_2(E)$. This process is continued until the sum of $S_i(E)$'s converges to S(E) and likewise the sum of the $f_i(E)$'s converges to f(E) (see Fig. 2). Convergence is readily ob-

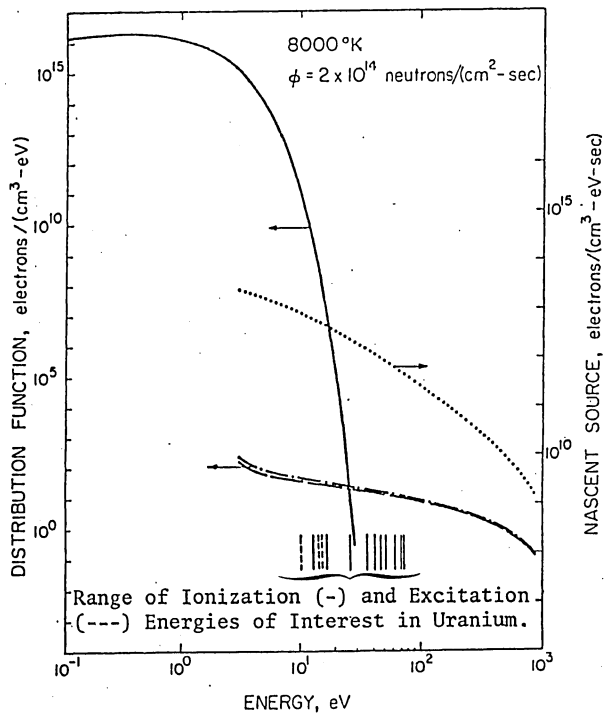

Fig. 2. The nascent source (....) versus energy as well as the distribution function plotted versus energy. The distribution consists of a Maxwellian (-) and the converged solution of the high-energy tail (-•-). The initial term in the series representation of f(E) is also plotted (--).

tainable within a few iterations, in agreement with earlier observations of a similar process by Fano and Spencer.[19]

Crucial to the evaluation of the electron energy distribution function is the accurate representation of the inelastic cross sections. Since they have not been measured experimentally, they were computed from a hydrogen model of Gryzinski,[15] modified for uranium by utilization of the atomic state data of Parks.[16]

As seen from Fig. 3, the uranium corss sections exhibit an abrupt rise at the threshold energy. The appearance of discontinuities in the slopes of the cross sections are indicative of one electronic state's participation in an event being overshadowed by another state; e.g. the discontinuity in the slope of the U^+ ionization cross section at 18 eV represents the appearance of an inner-electron ionization process which, at high energies, overshadows the ionization of the outer-most electron. At very large energies, the fine structure of the energy levels gives way to an 1/E energy dependence.

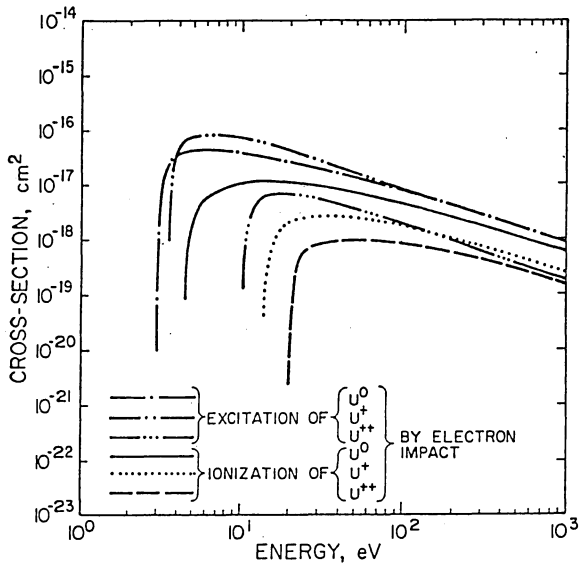

Fig. 3. The ionization and excitation cross sections for U, U^+, and U^{++} versus energy.

The excitation cross sections are found to be larger in magnitude than the corresponding ionization cross sections. An analogous trend is observed for cesium (see L. J. Kieffer's work[20]) which is quite similar in electronic structure. These trends can be attributed to the fact that such cross sections are in general inversely proportional to the energy transferred. Then, the smaller energy transfer afforded by excitation collisions results in the increased probability of their occurrence over ionization collisions.

Results, Distribution Calculations

Upon accumulation of the necessary cross sections, energy loss rates, source terms, and species' densities, the distribution function may then be evaluated as previously described. Results of such calculations were illustrated earlier in Fig. 2. It is observed that the distribution function is essentially composed of two parts: a thermalized bulk electron population plus a high-energy tail. While the present technique assumes that, based on earlier arguments, the lower energy distribution ($\lesssim$ 15 eV) follows a Maxwellian shape, two points should be stressed: First, the relative amplitude and temperature of this distribution have been determined in a self-consistent manner relative to the tail electrons (recall the balances previously cited). Second, for present purposes the main region of interest is the high-energy tail which can cause non-Maxwellian excitation and ionization. The bulk of the low energy electrons are energetically unable to cause excitations. Their only role is as a slowing-down agent for high energy electrons, and, to a first approximation, this is not too sensitive to the details of the low energy distribution.

At lower energies, near the region where the tail of the distribution and the Maxwellian join, the assumption of continuous slowing down is poor since the energy loss per collision can be comparable to the total electron energy. Since this region is important for subsequent excitation calculations, a more precise Monte Carlo model was employed for select cases.[8,21] This method employs a governing Boltzmann equation which relaxes the assumption of continuous slowing for inelastic collisions. The solution employs an analytic simulation of Coulombic collisions while ionization and excitation events are simulated in a traditional Monte Carlo, i.e. random walk, fashion. The secondary electron avalanche is included explicitly. A comparison of the Monte Carlo and analytic results is shown in Fig. 4 for a neutron flux of 2×10^{12} neutrons/(cm^2-sec).

The Monte Carlo results consistently fall below the analytic model, and this is attributed to the error introduced by the continuous slowing approximation in the latter. Fortunately, the error is not so great, however, as to completely invalidate the analytic model which it is thought can still provide insight into trends.

Parametric studies indicate that the amplitude of the high-energy tail is roughly linearly proportional to the neutron-flux level and inversely proportional to the temperature (see Figs. 5, 6 and 7). In both cases, the trends observed essentially follow the electron source term S(E) of Eq. (1). Increasing the neutron flux increases the nascent electron source term while decreasing the temperature results in an increase in the uranium density [$(n \sim (kT/p)^{-1}$] which in turn increases the nascent electron source term.

The absolute magnitude of the high-energy tail is also dependent upon the fraction of the energy loss rate of Eq. (1) contributed by Coulombic drag relative to inelastic collisions. As noted earlier, in cases where Coulombic collisions are important, the unified slowing model has been employed to account for collective behavior. The relative importance of this is illustrated in Fig. 8 for a case where Coulombic collisions are the dominant energy loss mechanism. It appears that the correction for collective effects is of order

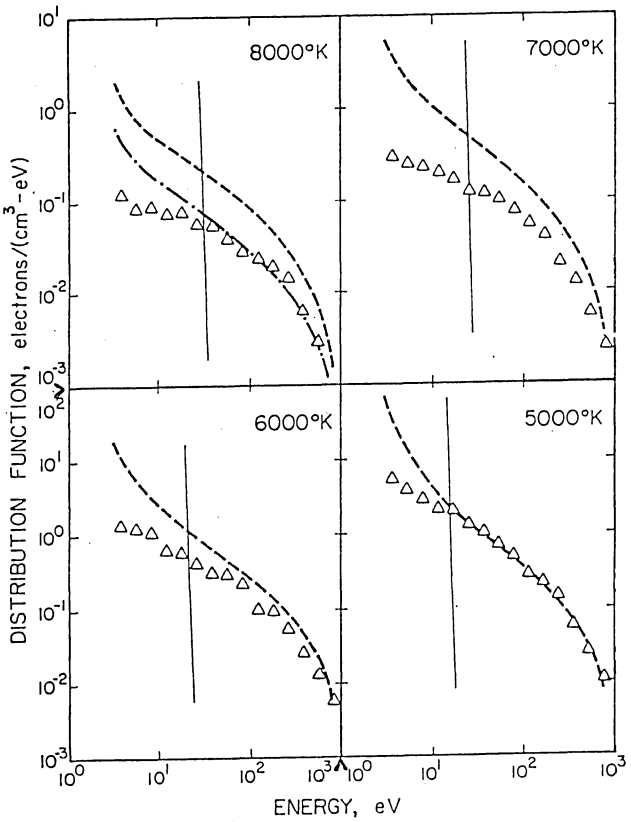

Fig. 4. A comparison of Monte Carlo results (Δ's) and analytic solution (dahsed line) for various temperatures at a neutron flux of $2x10^{12}$ neutrons/(cm^2-sec). A Maxwellian distribution = solid line. A vertically displaced analytic solution is also presented (-•-).

of 20%. This is not too serious, then, when it is considered that many of the cross-sections involved contain much larger uncertainties. Still, the unified model has been retained in the calculation since it is not difficult to do so and since this avoids unnecessary inaccuracies.

The tail of the electron distribution is much lower in magnitude relative to the thermalized Maxwellian in uranium than was the case found earlier in noble gases such as He.[4,5] This occurs because of the large contribution from thermal ionization at the elevated temperatures involved. Consequently, the contribution to excitation from tail electrons is not so important in the uranium cases. Still, since, as shown in Fig. 5, the energy levels of interest fall in the region of the tail, the latter electrons cannot be ignored. For example, for the plasma conditions of 8000°K and 2 x 10^{16} neutrons/(cm^2-sec), the calculated distribution causes 6 x 10^{14} more excitation events/(cm^3-sec) than would a Maxwellian distribution.

Since the non-Maxwellian region is of interest for pumping laser lines, these results suggest that pure uranium may not be as interesting for

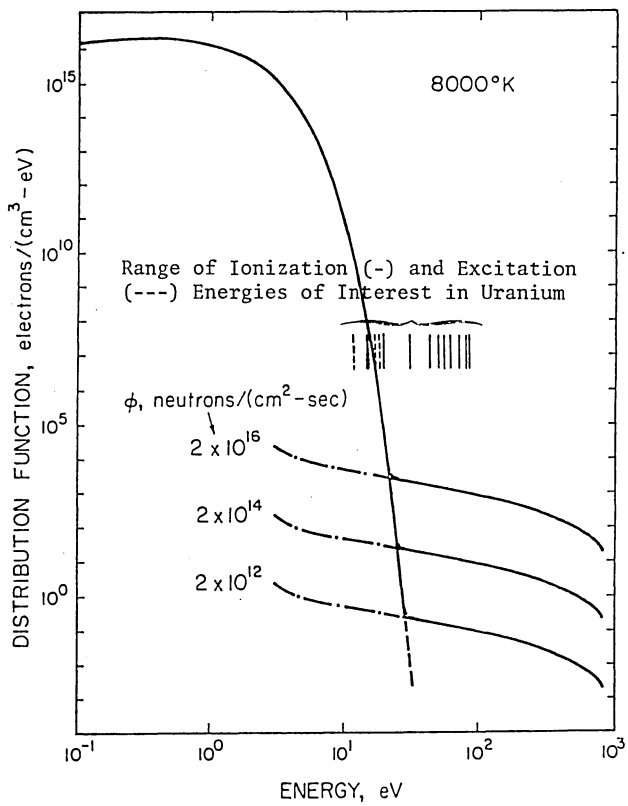

Fig. 5. The effect of varying the neutron flux upon the distribution function for a constant temperature of 8000°K.

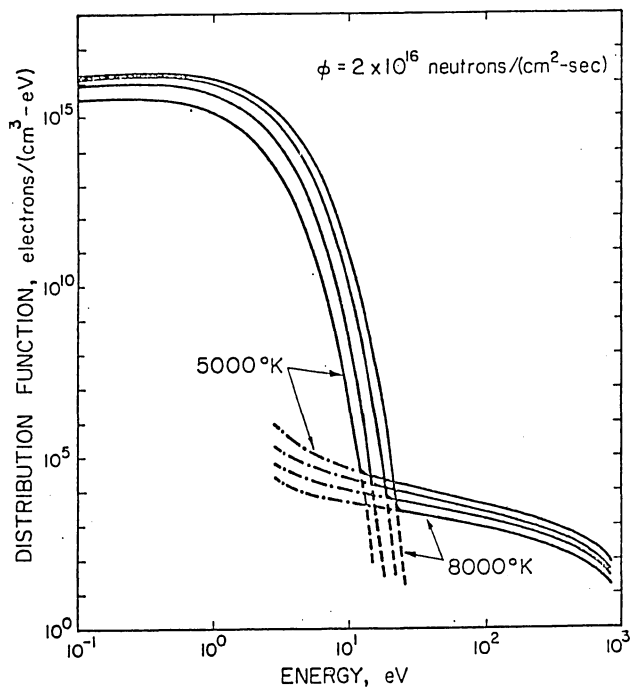

Fig. 6. The distribution function versus energy at a constant neutron flux of 2 x 10^{16} neutrons/cm^2-sec for temperatures of 8000° K, 7000°K, 6000°K, and 5000°K.

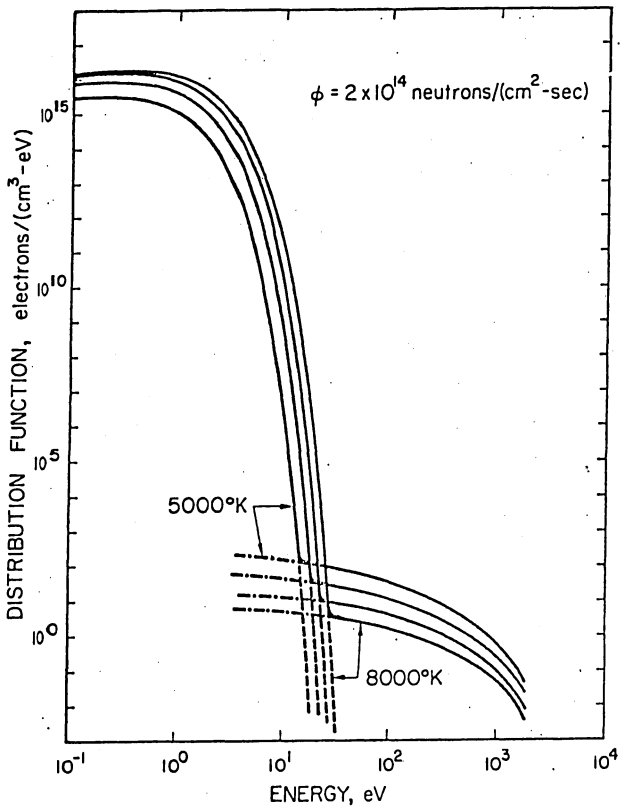

Fig. 7. The distribution function for a lower flux (2×10^{14} n/cm^2-sec versus 2×10^{16} n/cm^2-sec in Fig. 6).

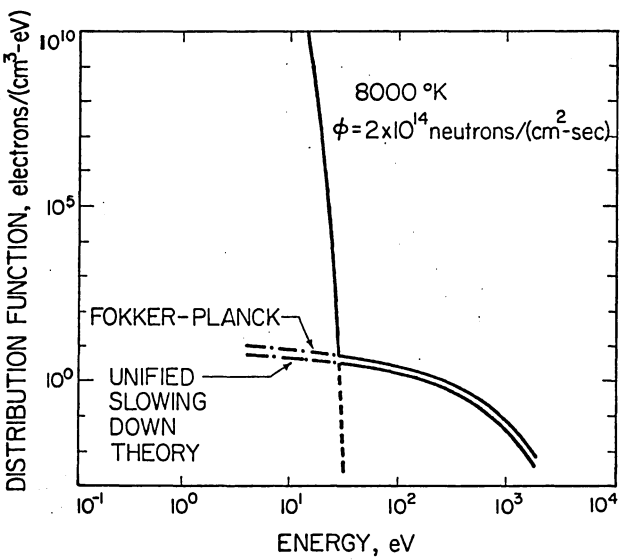

Fig. 8. Comparison of the effect of using different Coulombic slowing treatments.

this purpose as hoped. [This argument assumes collisional excitation; a recombination laser might be very attractive.] There are two ways to improve the situation, however. First, the thermalized electron population will lie at lower energies in low-temperature UF_6 plasmas, and this should lead to a dominance of tail-excitations. Second, as suggested by recent calculations,[22] mixtures such as He-U, Ar-U, etc. should be considered. Then, tail electrons can be used to excite the added gases which are selected to have energy levels that fall in the higher energy region (e.g. ~30 eV for He).

Excited State Densities and Radiation Transport

Techniques and data necessary to evaluate radiation transport in an uranium plasma have been developed over the past year. This work is still in process, but a brief description of the work to date will be presented.

To determine the excited state densities we consider the processes illustrated in Fig. 9. The electron distribution discussed above generates the excited state densities within the plasma. Radiation emitted from the excited states is amplified or absorbed within the plasma, possibly altering the excited state densities. Consequently, the radiation and state densities are coupled within the plasma.

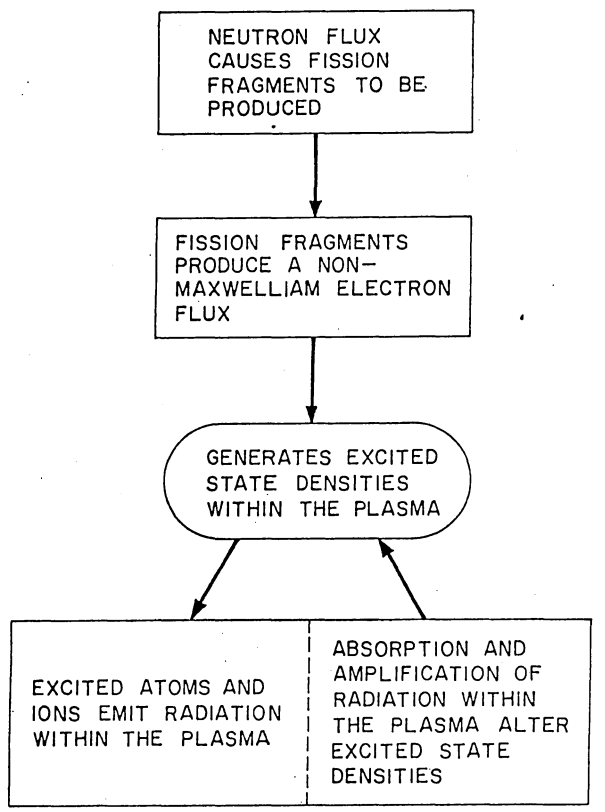

Fig. 9. Schematic representation of physical processes within a uranium plasma.

Before such calculations are possible, a model of uranium energy structure is necessary.[23] The state energy levels and inverse lifetimes were obtained using data from NBS[24] and LASL.[25,26] Using the intensity data in these reports, energy levels and inverse lifetimes were computed and normalized to the lifetime data of Klose.[27]

An example of the energy levels and the relative inverse lifetimes derived in this fashion is given in Table I. These results are obtained on the basis of a j-j coupling scheme which was selected to be consistent with the original analysis of measured radiation intensities. It is to be noted, for example, that a spontaneous emission of radiation from an initial state, 14644 cm^{-1}, to the final state, 0 cm^{-1}, is at least twice more probable than a transition to a higher final state, 620 cm^{-1}, about four times more than to the final state 6249 cm^{-1}, etc. Further discussion of these results is given in Ref. 23.

The time dependent rate equation for excited state q is

$$\frac{dN_q}{dt} = -\sum_{p<q} A_{qp} N_q + \sum_{p>q} A_{pq} N_p + \sum_{p\neq q} (B_{pq} g(\nu) \rho(\nu) N_p - B_{qp} g(\nu) \rho(\nu) N_q) - D_q \nabla^2 N_q + \sum_{p\neq q} N_p \int \phi(E) \sigma_{pq}(E) dE - N_q \sum_{p\neq q} \int \phi(E) \sigma_{qp}(E) dE - N_q \int \phi(E) \sigma_i(E) dE + \int N_{th}(E_{th}) N_i(E_i) \alpha(E_i, E_{th}) \cdot F_q(E_i, E_{th}) dE_i dE_{th} \quad (8)$$

In our model we assume a steady-state solution, hence the time derivative is set equal to zero. Since the system is large [e.g. about 1-m long with a 1-m diameter based on an experimental plasma design at Los Alamos[6]], we assume an infinite medium system where diffusion losses are negligible. With these two assumptions, Eq. (8) reduces to a matrix equation of the form

$$B_{pq} N_q = C_p. \quad (9)$$

As a test of the validity of this model, initial calculations were done for helium.[9] Some results from this study are reproduced in Table II. There, experimental values[28] for fission-fragment irradiation of He are compared with the theoretical computations for a single step (Case I) and double step (Case II) excitation. ("Double step" refers to excitation collisions originating from metastable states whereas "single step" processes start from the ground state.) Discrepancies arise due to the significant contribution of Maxwellian distribution, expecially for the more realistic conditions of Case II. However, it is important to notice that there are inversions predicted for the 3^1P-3^1D and 4^1P-4^1D states. These results are described in more detail in Ref. 9. Comparisons with other data and calculations, to the extent possible, showed good agreement, lending confidence to the model.

Radiation from the uranium plasma will consist of a continuum black-body type radiation with a discrete line structure superimposed. The continuum will be calculated using conventional techniques while perturbations due to line structure

Table I. Relative inverse lifetimes for some states of UI based on Ref. 24, Ref. 25 and Ref. 26. Energies are in cm^{-1}. * indicates data is from Ref. 24.

		FINAL STATE												
		0	620	3801	4276	4453	5762	5991	6249	7006	7104	7326	8119	10686
Initial State	15721	.001455*	.00127*		.000755	.00266	.00213		.00316		.00348	.00103		
	15638	.00143*	.004*	.00203*			.00159		.00255	.00239		.00356	.00319	
	15632	.00457*		.00101*					.00296	.00137		.00237	.00370	.00152
	14644	.00642*	.00281*						.00157			.00166	.00047	
	13463	.00178*	.00094*		.00047	.00168	.00096	.00014						

Table II. Fission-Fragment Excitation of He.

	SHIPMAN	CASE I	CASE II
$\frac{n_{3'P}}{n_{3'D}}$	1.7	1.189	0.693
$\frac{g_{3'D} n_{3'P}}{g_{3'P} n_{3'D}}$	2.83	1.982	1.155
$\frac{n_{4'P}}{n_{4'D}}$	1.8	0.855	0.65
$\frac{g_{4'D} n_{4'P}}{g_{4'P} n_{4'D}}$	3.00	1.425	1.083

will be obtained from the excited-state density calculation described above. A code to do this has been devised that divides the plasma into discrete regions to account for temperature and density variations. An iteration technique is employed to account for the radiation and state-density coupling, but this connection should only be important for a few strong lines.

Conclusion

Cross sections, lifetime data, etc. and methods have been developed for the calculation of the electron energy distribution in a fissioning uranium plasma. This is the first time such results are available. The thermalized component tends to dominate in high-temperature, pure uranium. It is suggested, however, that high-energy electrons in the tail of the distribution may be very effective in producing non-equilibrium excitation in mixtures where the additive gas has a relatively high threshold energy for excitation. The noble gases are examples of potentially attractive additives.

These methods of analysis are now being applied to lower temperature UF_6 which is of prime interest for near-term experimental endeavors. In addition, radiation emission spectra from the uranium plasma are under study.

References

1. G. H. Miley, "Fission-Fragment Transport Effects as Related to Fission-Electric Cell Efficiencies," *Nucl. Sci. Eng.*, *24*, 322 (1966).

2. G. H. Miley, *Direct Conversion of Nuclear Radiation Energy*, Am. Nucl. Soc., Hinsdale, IL (1970).

3. P. Thiess and G. Miley, "Spectroscopic and Probe Measurements of Excited State and Electron Densities in Radiation Induced Plasmas," *2nd Symposium on Uranium Plasmas: Research and Application*, p. 90 (1971).

4. R. Lo and G. Miley, "Electron Energy Distribution in a Helium Plasma Created by Nuclear Radiations," *IEEE Trans. on Plasma Sci., PS-2*, 198 (1974).

5. B. Wang and G. Miley, "Monte Carlo Simulation of Radiation-Induced Plasmas," *Nucl. Sci. Engr., 52*, 130 (1973).

6. H. H. Helmick, et al., "Preliminary Study of Plasma Nuclear Reactor Feasibility," *LA-5679* (1974); K. Thom, "High Grade Power from Fissioning Gases," NASA Report (1976).

7. K. Thom, "Gaseous Fuel Reactor Research," *3rd IEEE Int. Conf. on Plasma Sci.*, Austin, TX (1976).

8. C. G. Bathke and G. H. Miley, "Electron Distribution Functions in Uranium Plasmas," *Trans. Am. Nucl. Soc., 19*, 64 (1974).

9. E. L. Maceda and G. H. Miley, "Non-Maxwellian Electron Excitation in Helium," *Proc. 27th Annual Gaseous Electronics Conf.*, Houston, TX, p. 118 (1974).

10. J. C. Guyot, G. H. Miley and J. T. Verdeyen, "Application of a Two-Region Heavy Charged Particle Model to Noble-Gas Plasmas Induced by Nuclear Radiations," *Nucl. Sci. Engr., 48*, 373 (1972).

11. L. V. Spencer and U. Fano, "Energy Spectrum Resulting from Electron Slowing Down," *Phys. Rev., 93*, 1172 (1954).

12. G. Safonov, R. Witte, S. Altschuler and W. Simmons, "An Experiment for Pursuit of the Fission Laser," unpublished internal report, TRW Corporation, El Segundo, CA, July 1971.

13. D. V. Sivukhin, "Coulomb Collisions in a Fully Ionized Plasma," *Reviews of Plasma Physics*, Vol. 4, Consultants Bureau, New York (1966).

14. T. Kihara and O. Aono, "Unified Theory of Relaxations in Plasmas, I. Basic Theorem," *J. Phys. Soc. Japan, 18*, No. 6 (1963).

15. A. Burgess and I. C. Percival, "Classical Theory of Atomic Scattering," *Adv. Atom. Molec. Phys., 4*, p. 109-141 (1968).

16. D. E. Parks, et al., "Optical Constants of Uranium Plasmas," *NASA CR-72348*, N.T.I.S., Springfield, VA (1968).

17. R. W. Bussard and R. D. DeLauer, *Nuclear Rocket Propulsion*, McGraw-Hill Book Co., Inc., New York, p. 160 (1958).

18. See, for example, p. 108 of Ref. 2.

19. U. Fano and L. V. Spencer, "Quasi-Scaling of Electron Degradation Spectra," *Int. J. Rad. Phys. and Chem., 7*, 63 (1975).

20. L. J. Kieffer, "A Compilation of Electron Collision Cross-Section Data for Modeling Gas Discharge Lasers," *JILA Information Center Report*

#13, Univ. of Colorado, Boulder, CO, Sept. 1973.

21. C. Bathke, "Calculations of the Electron Energy Distribution Function in a Uranium Plasma by Analytic and Monte Carlo Techniques," Ph.D. thesis, Nuclear Engineering Program, Univ. of Illinois, Urbana, IL (1976).

22. M. Makowski, C. Choi and G. Miley, "Electron Energy Distribution in Radiation-Induced U-He Plasmas," *3rd IEEE Int. Conf. on Plasma Sci.*, Austin, TX (1976).

23. E. L. Maceda, C. G. Bathke and G. H. Miley, "Uranium Excited-State Parameters," *Trans. Am. Nucl. Soc.*, *22*, 153 (1975).

24. W. F. Meggers, C. H. Corliss and B. F. Scribner, *Tables of Spectral Line Intensities*, NBS Monograph 32, pt. 1, Washington (1961).

25. D. W. Steinhaus, L. J. Radzienski, R. D. Cowan, et al., "Present Status of the Analysis of the First and Second Spectra of Uranium (UI and UII) as Derived from Measurements of Optical Spectra," *LA-4501* (1971).

26. D. W. Steinhaus, M. V. Phillips, J. B. Moody, et al., "The Emission Spectrum of Uranium Between 19,080 cm^{-1} and 30,261 cm^{-1}," *LA-4944* (1972).

27. T. Z. Klose, "Mean Life of the 27887 cm^{-i} Level in UI," *Phys. Rev. A*, *II*, 1940 (1975).

28. G. R. Shipman, R. A. Walters, and R. T. Schneider, "Population Inversions in Fission Fragment Excited Helium," *Trans. Am. Nucl. Soc.*, *17*, 3 (1973).

RECENT MEASUREMENTS CONCERNING URANIUM HEXAFLUORIDE-ELECTRON COLLISION PROCESSES†

S. Trajmar, A. Chutjian, S. Srivastava,
and W. Williams
Jet Propulsion Laboratory,
California Institute of Technology
Pasadena, California 91103

and

D. C. Cartwright
Los Alamos Scientific Laboratory
Los Alamos, New Mexico 87544

Abstract

Scattering of electrons by UF_6 molecule was studied at impact energies ranging from 5 to 100 eV and momentum transfer, elastic and inelastic scattering cross sections were determined. The measurements also yielded spectroscopic information which made possible to extend the optical absorption cross sections from 2000Å to 435Å. It was found that UF_6 is a very strong absorber in the vacuum UV region. No transitions were found to lie below the onset of the optically detected 3.0 eV feature.

I. Introduction

Considerable need has developed recently for spectroscopic information and electron collision cross section data for UF_6 in connection with the UF_6 gas core reactor, isotope separation schemes and nuclear pumped lasers. Theoretical methods are not expected to yield reliable predictions for such a complex molecule and electron impact measurements have not been reported in the literature.

We summarize here the results of our investigations concerning electron scattering from UF_6. Some of these results have been published or submitted for publication very recently[1-3] and some of them are reported for the first time.

The photoabsorption spectrum of UF_6 has been studied by many workers. Recently, DePoorter and Rofer-DePoorter[4] obtained detailed absorption spectrum and absolute absorption cross sections in the 2000 to 4200Å region. Rabideau[5] also made absolute photoabsorption cross section measurements in the 1950 to 2500Å spectral region. An investigation of the absorption spectrum of UF_6 at low temperatures, in both solid and vapor phase, was carried out by Lewis *et al*[6] between 2000 and 4300Å. No such studies are available for wavelengths less than 2000Å.

The techniques of electron impact spectroscopy can be utilized (at high impact energies and low scattering angles) to give optical absorption cross sections.[7-9] On this basis Huebner *et al*[10] have reported apparent oscillator strength distributions for a number of molecules. Generally their data agree well with optically measured values even for incident electron energies as low as 100 eV. The same technique is utilized in the present investigation to extend the photoabsorbtion cross sections from 2000Å to 435Å.

At low incident energies and high scattering angles the electron impact energy-loss spectra are dominated by optically-forbidden transitions and yield information which is not available by the means of conventional optical spectroscopy.[11] This method was utilized here to search for optically-forbidden states.

The electron scattering intensities in both energy regions have been normalized to yield differential and integral cross sections and some of these results are reported here. Evaluation of the laboratory measurements are still in progress and will be reported later.

II. Apparatus and Method

Details of the experimental procedures have been published elsewhere.[1-3,12,13] Briefly, the apparatus consists of an electron gun which produces a collimated, energy-selected beam of electrons of impact energy E_o. The electron beam crosses the target UF_6 beam at 90°. This target beam is generated by flowing the UF_6 through a capillary array. Electrons scattered through a solid angle $d\Omega$ ($\sim 10^{-3}$ sr) at an angle θ with respect to the incident electron beam are detected and energy analyzed. An energy-loss spectrum is obtained by using pulse counting and multichannel scaling techniques. The energy resolution was about 80 meV (FWHM). The incident energy scale was calibrated against the He 19.35 eV resonance and the true zero scattering angle was determined from the symmetry of the scattering intensity around the nominal zero scattering angle. The critical features in the present experiments were that a. the gun, electron optics, and detector were differentially pumped relative to the scattering chamber, and b. the target UF_6 beam was condensed on a liquid nitrogen cold trap placed immediately above the scattering region. Even with these precautions, the electron optics became poisoned by the UF_6 after two weeks of operation.

†Supported in part by the National Aeronautics and Space Administration under Contract No. NAS7-100 to the Jet Propulsion Laboratory and in part by ERDA Order No. LS-76-5.

III. Elastic Scattering

The elastic scattering intensity (which includes rotational and vibrational contributions within the instrumental resolution) was measured as a function of scattering angle at fixed impact energies ranging from 5 to 75 eV. Under identical conditions the same procedure was applied to He and the ratio of the UF_6 scattering intensity to He scattering intensity was determined. From these intensity ratios absolute elastic scattering cross sections for UF_6 were obtained by a procedure utilizing He elastic scattering cross sections as secondary standards. The details of the procedure are described in Ref. 1. The differential and integral elastic cross sections as well as the momentum transfer cross sections are summarized in Table I.

IV. Photoabsorption Spectrum and Cross Sections

The electron impact energy-loss spectrum obtained at 100 eV impact energy and 5° scattering angle should be very closely the same as the optical absorption spectrum. This spectrum (Fig. 1) was utilized to get the generalized oscillator strength distribution or the relative optical absorption cross sections in the 4000 to 435Å region. The relative values were normalized to the absolute scale with the help of the cross sections of DePoorter and Rofer-DePoorter at 2255Å (5.5 eV). For detailed discussion see Ref. 2. The results are given in Table II and shown in Figs. 2 and 3. There is an excellent agreement between the optical and the electron impact results in the overlapping region except at around 3-4.5 eV energy losses where the cross

TABLE I. UF_6 Differential Elastic Cross Sections $\sigma(\theta)$, $(10^{-20} m^2/sr)$. The percentages contributed by the extrapolations of $\sigma(\theta)$ between 0° and 20° and between 135° and 180° to the elastic integral and momentum transfer cross sections are shown in parentheses. The data reported here for the 5 eV electron impact energy have been obtained by extrapolating $\sigma(\theta)$ values at other energies.

E_0 (eV) / θ(deg)	5	10	15	20	30	40	50	60	75
20	1.60	3.75	7.00	12.50	5.80	8.20	9.40	6.00	3.20
25	1.30	2.90	5.60	8.00	4.00	3.10	3.50	2.10	2.50
30	1.20	2.50	4.30	4.50	2.75	1.50	2.15	1.95	1.95
35	1.10	2.15	3.30	2.60	1.80	1.45	1.95	1.80	1.40
40	0.88	1.75	2.25	1.60	1.45	1.45	1.95	1.45	1.05
45	0.70	1.35	1.60	1.15	1.35	1.30	1.40	0.98	0.74
50	0.52	1.00	1.15	1.09	1.25	1.15	1.00	0.64	0.54
55	0.34	0.68	0.90	1.15	1.10	0.86	0.68	0.46	0.42
60	0.25	0.50	0.84	1.25	0.90	0.68	0.52	0.41	0.35
65	0.16	0.40	0.98	1.35	0.74	0.66	0.53	0.50	0.29
70	0.16	0.37	1.25	1.35	0.60	0.65	0.53	0.38	0.25
75	0.16	0.38	1.45	1.35	0.48	0.54	0.46	0.28	0.23
80	0.20	0.40	1.40	1.28	0.42	0.45	0.38	0.21	0.22
85	0.18	0.43	1.38	1.10	0.36	0.36	0.27	0.17	0.23
90	0.18	0.44	1.25	0.95	0.34	0.31	0.19	0.16	0.23
95	0.18	0.44	1.15	0.86	0.39	0.30	0.20	0.17	0.24
100	0.18	0.43	0.95	0.62	0.47	0.30	0.21	0.18	0.28
105	0.15	0.41	0.90	0.58	0.50	0.32	0.23	0.22	0.33
110	0.13	0.40	0.82	0.57	0.52	0.35	0.31	0.32	0.41
115	0.11	0.40	0.78	0.60	0.56	0.40	0.50	0.53	0.51
120	0.12	0.41	0.82	0.66	0.64	0.58	0.74	0.80	0.60
125	0.11	0.41	1.00	0.78	0.80	0.82	1.10	1.10	0.74
130	0.11	0.43	1.30	0.90	1.00	1.10	1.40	1.35	0.86
135	0.12	0.45	1.85	1.15	1.35	1.40	1.70	1.55	0.94
INTEGRAL $(10^{-20} m^2)$	4.3 (23%)	9.6 (25%)	25 (39%)	27 (43%)	17 (43%)	19 (55%)	22 (59%)	18 (60%)	9.5 (38%)
Mom. Transfer $(10^{-20} m^2)$	2.4 (27%)	5.9 (32%)	24 (55%)	19 (46%)	13 (54%)	13 (58%)	13 (55%)	13 (57%)	8.0 (47%)

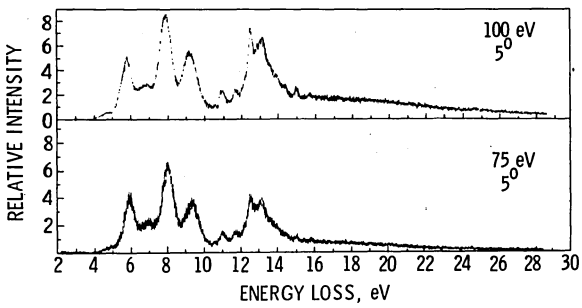

Fig. 1 Energy-loss spectra of UF_6 at 5° scattering angle for 75 eV and 100 eV electron impact energies.

sections are small and the electron impact curve could have some non-optical contributions.

A quantity of interest for some applications is the integral cross section σ_I^{opt} for a particular band between energy losses E_1 and E_2. This can be obtained by:

$$\sigma_I^{opt} = \int_{E_1}^{E_2} (d\sigma_n/dE)dE \ . \qquad (1)$$

We have calculated the integrated photoabsorption cross section using Eq. (1) with E_1 = 2.5 eV and E_2 = E where E is the energy of any portion of the spectrum. The results are shown in Fig. 4 and in Table III. From these data the integrated cross section for any arbitrary energy loss interval can be easily obtained.

From Fig. 3 we find that the spectrum of UF_6 at wavelength less than 2000Å exhibits considerable structure and the spectral features comprising this structure have stronger photoabsorption cross section than those observed above 2000Å.

TABLE II

Photoabsorption cross section per electron volt, $d\sigma/dE$, for selected values of the electron energy loss E. The wavelength λ equivalent to each energy loss E is also shown. The $d\sigma/dE$ values are the smoothed values obtained from Fig. 3.

E(eV)	λ(nm)	$d\sigma/dE$ (10^{-17} cm^2 eV^{-1})	E(eV)	λ(nm)	$d\sigma/dE$ (10^{-17} cm^2 eV^{-1})
4.0	310.0	0.014	16.5	75.2	3.06
4.5	275.5	0.086	17.0	72.9	3.26
5.0	248.0	0.15	17.5	70.8	3.34
5.5	225.5	1.15	18.0	68.9	3.34
6.0	206.6	1.27	18.5	67.0	3.64
6.5	190.8	0.99	19.0	65.3	3.76
7.0	177.1	1.15	19.5	63.6	3.76
7.5	165.3	2.49	20.0	62.0	3.83
8.0	155.0	4.03	20.5	60.5	3.76
8.5	145.9	1.65	21.0	59.0	3.64
9.0	137.8	3.11	21.5	57.7	3.64
9.5	130.5	2.72	22.0	56.4	3.45
10.0	124.0	0.92	22.5	55.1	3.26
10.5	118.1	0.88	23.0	53.9	3.37
11.0	112.7	1.76	23.5	52.8	3.14
11.5	107.8	1.57	24.0	51.7	3.07
12.0	103.3	2.30	24.5	50.6	3.45
12.5	99.2	7.66	25.0	49.6	3.45
13.0	95.4	7.17	25.5	48.6	3.26
13.5	91.9	5.29	26.0	47.7	3.26
14.0	88.6	4.22	26.5	46.8	2.88
14.5	85.5	2.99	27.0	45.9	2.88
15.0	82.7	3.41	27.5	45.1	2.88
15.5	80.0	2.87	28.0	44.3	2.79
16.0	77.5	2.99	28.5	43.5	2.68

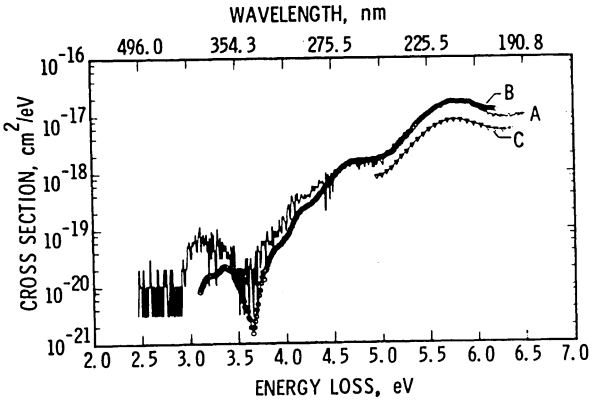

Fig. 2 A comparison of the present results (Curve A) with the photoabsorption spectra of DePoorter and Rofer-DePoorter have been normalized to the data of DePoorter and Rofer-DePoorter at 5.5 eV. The corresponding wavelengths (λ) in nanometers are indicated on top of the figure.

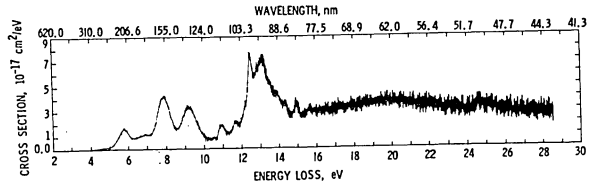

Fig. 3 Photoabsorption cross section of UF_6 derived from the electron impact energy loss data of Fig. 1 and normalized as indicated in Fig. 2.

TABLE III

Integral photoabsorption cross section, σ_I between energy losses 2.5 eV and E The wavelength λ equivalent to each energy loss E is also shown.

E(eV)	λ(nm)	$\sigma_I(cm^2)$	E(ev)	λ(nm)	$\sigma_T(cm^2)$
4.0	310.0	5.66×10^{-20}	16.5	75.2	3.01×10^{-16}
4.5	275.5	2.83×10^{-19}	17.0	72.9	3.14×10^{-16}
5.0	248.0	9.48×10^{-19}	17.5	70.8	3.27×10^{-16}
5.5	225.5	3.43×10^{-18}	18.0	68.9	3.42×10^{-16}
6.0	206.6	1.06×10^{-17}	18.5	67.0	3.56×10^{-16}
6.5	190.8	1.55×10^{-17}	19.0	65.3	3.74×10^{-16}
7.0	177.1	2.10×10^{-17}	19.5	63.6	3.89×10^{-16}
7.5	165.3	2.82×10^{-17}	20.0	62.0	4.05×10^{-16}
8.0	155.0	4.65×10^{-17}	20.5	60.5	4.22×10^{-16}
8.5	145.9	5.99×10^{-17}	21.0	59.0	4.39×10^{-16}
9.0	137.8	7.06×10^{-17}	21.5	57.7	4.55×10^{-16}
9.5	130.5	8.63×10^{-17}	22.0	56.4	4.71×10^{-16}
10.0	124.0	9.49×10^{-17}	22.5	55.1	4.87×10^{-16}
10.5	118.1	9.89×10^{-17}	23.0	53.9	5.00×10^{-16}
11.0	112.7	1.06×10^{-16}	23.5	52.8	5.15×10^{-16}
11.5	107.8	1.12×10^{-16}	24.0	51.7	5.27×10^{-16}
12.0	103.3	1.22×10^{-16}	24.5	50.6	5.40×10^{-16}
12.5	99.2	1.44×10^{-16}	25.0	49.6	5.54×10^{-16}
13.0	95.4	1.73×10^{-16}	25.5	48.6	5.67×10^{-16}
13.5	91.9	2.07×10^{-16}	26.0	47.7	5.79×10^{-16}
14.0	88.6	2.26×10^{-16}	26.5	46.8	5.93×10^{-16}
14.5	85.5	2.43×10^{-16}	27.0	45.9	6.05×10^{-16}
15.0	82.7	2.59×10^{-16}	27.5	45.1	6.17×10^{-16}
15.5	80.0	2.74×10^{-16}	28.0	44.3	6.29×10^{-16}
16.0	77.5	2.86×10^{-16}	28.5	43.5	6.39×10^{-16}

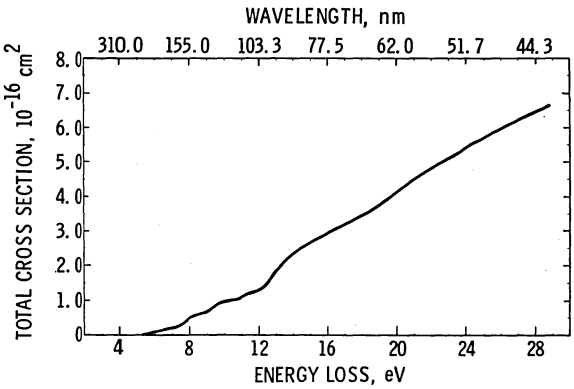

Fig. 4 Integral absorption cross sections between energy losses 2.5 and E eV as obtained from Eq. (1).

V. Electron Scattering at Low and Intermediate Impact Energies

In Fig. 5 are shown energy-loss (ΔE) spectra at an incident electron energy (E_0) of 20 eV, and at scattering angles (θ) between 20° and 135°. The elastic scattering peak (ΔE = 0 eV) is shown for each spectrum. Also shown above the top spectrum is the optical absorption spectrum of gaseous UF_6.[6,7] The locations of all peaks, in eV, are also indicated.

No transitions are found to lie below the onset of the first-detected feature at 3.0 eV. This is also confirmed in spectra (not shown) taken at E_0 = 10 eV, even closer to threshold. The feature in the 3.0-3.6 eV region must correspond to the lowest triplet and singlet charge-transfer excitations from a $t_{1u}\sigma$ orbital centered on the fluorine atoms to the a_{2u} uranium 5f orbital.[6] In general, the variation with θ of peak intensities in an energy-loss spectrum is known to give important information about the spin multiplicity of electronic transitions involved. For example, spin- and dipole-allowed transitions are strongly forward peaked in θ, while spin-forbidden transitions involving shorter-range exchange forces tend to be nearly isotropic.[11] The fact that there is no substantial change in Fig. 5 of the lowest-energy feature with θ is very likely due to the strong spin-orbit mixing in these states,[14] and/or to contributions from overlapping singlet and triplet vibronic excitations (including hot bands).[6] One also sees in Fig. 1 that the ratio in the optical spectrum of the (optically-allowed) 5.8 eV to the 3.3 eV (lowest-energy) feature is $\sim 10^3$, while in the 20° spectrum it is ~ 50. This fact points up the overall optically-forbidden character of the 3.3 eV feature.

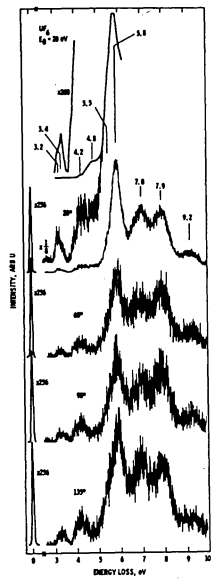

Fig. 5 Energy-loss spectra of UF_6 at 20 eV and at the indicated angles. The elastic peak is shown at ΔE = 0. The optical absorption spectrum of DePoorter and Rofer-DePoorter is shown for comparison. The peak energies in eV for both the optical and the electron impact spectra are indicated.

Other differences between the optical and electron scattering spectra exist in the intensities of features in the 3.6-5.0 eV region relative to the 5.8 eV excitation. First, the 4.2 eV excitation is greatly enhanced relative to the 5.8 eV feature in the electron-scattering spectra, and is clearly separated from the optically-allowed transition for $\theta > 20°$. This fact indicates that the 4.2 eV excitation is optically forbidden. Second, the fairly strong optical absorption at 4.8 eV is observed to "fill in" at θ = 20° but is practically absent at higher angles. This is indicative of a weak dipole-allowed transition. This feature has indeed been interpreted as a vibrationically-allowed transition.[6] We also note that the features observed above ΔE = 6.2 eV have not previously been reported.

An estimate of the absolute differential cross sections for the inelastic excitations can be obtained by measuring inelastic-to-elastic intensity ratios directly from the spectra (using the appropriate scale-change factor) and multiplying these ratios by the normalized absolute elastic DCS listed in Table I.

The interpretation of the UF_6 spectra or the determination of optical and electron impact cross sections in terms of individual transitions is quite difficult. Work is in progress along

this line. An example of the unfolding of the 10 eV, 60° spectrum is shown in Fig. 6. At the

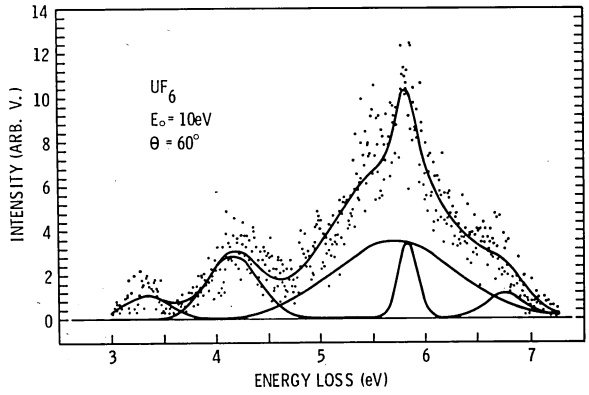

Fig. 6 Decomposition of UF_6 energy-loss spectrum.

present time, the results can be given only as electron impact excitation cross sections per unit energy-loss range at various energy losses or as the value of the cross section associated with a broad spectral feature without specifying the exact nature of the underlying transition(s). An example of this latter procedure is given in Fig. 7 and Table IV. The differential and integral cross sections for the broad features peaking at 3.3, 4.2 and 5.6 eV energy losses at 10 eV electron impact energy are given. These results have been obtained by determining the scattering intensity ratios at the specified peaks with respect to elastic scattering, correcting this ratio for the difference in the width of the inelastic and elastic features, then utilizing the absolute elastic cross sections of Ref. 1. Due to the uncertainties associated with the shape of the inelastic features, with the interpolations and extrapolations of the experimental measurements (which were carried out only at 20, 60, 90 and 135° scattering angles) and with the normalization procedures, these cross sections are considered to be accurate to within about a factor of two.

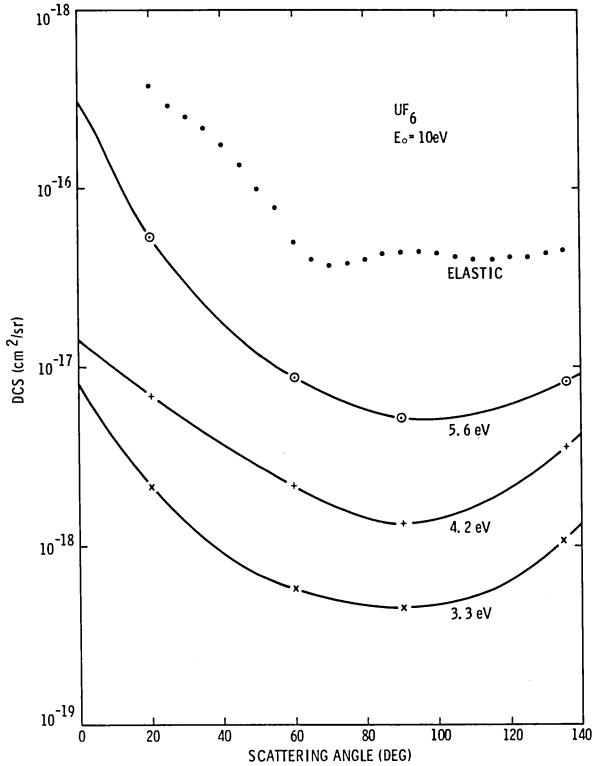

Fig. 7 Differential cross sections at 10 eV impact energy for elastic scattering and excitation of the features at 3.3, 4.2 and 5.6 eV energy-losses.

Table IV. Differential and integral electron impact excitation cross sections for the broad features located at 3.3, 4.2 and 5.6 eV energy losses. (10^{-19} cm^2/sr units)

	Cross Section		
θ(deg)	3.3 eV	4.2 eV	5.6 eV
0	80	140	3,000
10	41	100	1,250
20	21	70	510
30	13	51	280
40	9.2	38	170
50	7.0	28	120
60	5.8	21	88
70	5.0	16	70
80	4.5	14	58
90	4.4	13	51
100	4.6	14	50
110	5.3	17	53
120	6.5	21	60
130	8.7	29	71
140	14	40	81
Q	119.2	367.8	1,895

References

1. S. K. Srivastava, S. Trajmar, A. Chutjian and W. Williams, J. Chem. Phys. 64, 2767 (1976).

2. S. K. Srivastava, D. C. Cartwright, S. Trajmar, A. Chutjian and W. Williams, J. Chem. Phys. to appear (1976).

3. A. Chutjian, S. K. Srivastava, S. Trajmar, W. Williams and D. C. Cartwright, J. Chem. Phys. to appear (1976).

4. G. L. DePoorter and C. K. Rofer-DePoorter, Spectroscopy Letters 8, 521 (1975).

5. S. W. Rabideau (private communication).

6. W. B. Lewis, L. B. Asprey, L. H. Jones, R. S. McDowell, S. W. Rabideau, A. H. Zellmann and R. T. Paine, J. Chem. Phys. to appear (1976).

7. H. A. Bethe, Ann. Phys. 5, 325 (1930).

8. E. N. Lassettre and S. A. Francis. J. Chem. Phys. 40, 1208 (1964)

9. C. E. Kuyatt and J. A. Simpson in Atomic Collision Processes, M. R. C. McDowell, Ed. (North-Holland Publ. Co., Amsterdam, 1964), p. 141.

10. R. H. Huebner, R. J. Celotta, S. R. Mielczarek and C. E. Kuyatt, J. Chem. Phys. 59, 5334 (1973) and 63, 241 (1975).

11. S. Trajmar, J. K. Rice and A. Kuppermann, Advances in Chemical Physics, Vol. 18, Interscience Publishers (1970).

12. S. K. Srivastava, A. Chutjian and S. Trajmar, J. Chem. Phys. 63, 2659 (1975).

13. A. Chutjian, J. Chem. Phys. 61, 4279 (1974)

14. W. B. Lewis (private communication) estimates that the two states in the 3.3 eV feature are approximately equal mixtures of singlet and triplet character.

MEASUREMENT TECHNIQUES FOR ANALYSIS OF FISSION FRAGMENT EXCITED GASES

R. T. Schneider, E. E. Carroll, J. F. Davis, R. N. Davie, T. C. Maguire, and R. G. Shipman
University of Florida

Abstract

In pursuit of nuclear pumped lasers, experimental efforts have been directed towards the measurement of population inversions in gases and determination of the fission fragment interaction processes involved. Spectroscopic analysis of fission fragment excited He, Ar, Xe, N_2, Ne, Ar-N_2, and Ne-N_2 have been conducted. Boltzmann plot analysis of He, Ar and Xe have indicated a nonequilibrium, recombining plasma, and population inversions have been found in these gases. The observed radiating species in helium have been adequately described by a simple kinetic model. A more extensive model for argon, nitrogen and Ar-N_2 mixtures was developed which adequately describes the energy flow in the system and compares favorably with experimental measurements. The kinetic processes involved in these systems are discussed. These models have indicated a need for the measurement of the kinetic processes in fission fragment excited gases. A Cf^{252} source was used with a photon counting system to measure the life-times and collisional rate coefficients for gases excited by fission fragments. Experimental measurements of the energy deposition properties of fission fragments emanating from uranium oxide coatings were also performed. To develop efficient nuclear pumped lasers, the energy density requirements are high. These problems are discussed and a fissioning uranium plasma energy source is indicated. Spectral emission from Ar-N_2-UF_6 mixtures have shown that the addition of UF_6 has adverse affects on the emitting species. Further research is clearly indicated to understand the properties of fission fragment excited UF_6 and other gases which is necessary for the development of high-powered, efficient, nuclear pumped laser systems.

I. Introduction

The measurement techniques described in the following are intended for generation of design information for the eventual construction of an efficient nuclear pumped laser.

The desired information, therefore, deals with the detection of population inversions existing in a fission fragment excited gas — for the sake of achieving laser action — and with the explanation of the excitation mechanism itself — for the sake of obtaining a laser which has an efficiency large enough to be of practical interest.

The usual method of generating fission fragment excited gases for research purposes is to line a test cell with a uranium oxide coating. The test cell is then filled with the gas of interest and exposed to a neutron flux, usually in a nuclear reactor.

The usual method of exciting a nuclear pumped laser is depicted in Figure 1. The

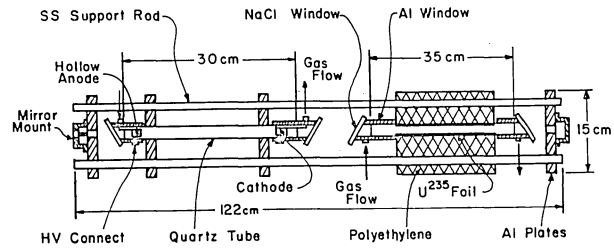

Figure 1. Section Drawing of Laser Assembly

device contains two stages, an electrically excited stage and the nuclear stage. Both stages are within the same cavity. The electrical stage serves for alignment purposes only and is not energized during neutron irradiation. The nuclear stage is surrounded by a polyethelene moderator, if a fast burst reactor is used as a neutron source.

The approach for a practical nuclear pumped laser is twofold, namely surface or volume excitation.

Surface excitation would surmise the use of a large surface area of solid fissile material in form of thin coatings, while the concept of volume excitation would employ a fissioning gas.

Both approaches show advantages and disadvantages. Since the main advantage of nuclear pumping seems to be the potentially very high input power density, volume excitation seems to have an advantage for large devices just on account of geometry. In principal, at best 50% of all fission fragments generated will ever enter the laser gas in the case of surface excitation, a limitation which does not hold for volume excitation. However, the particularities of the structure of the UF_6 molecule may prevent the buildup of laser action in an added laser gas. For this reason, further research in both fields, surface and volume excitation, is necessary.

II. Fission Fragment Excitation

One of the purposes of the research described in this chapter is to investigate

processes involved in the fission fragment excitation of gases. In addition, the research is aimed at the detection of population inversions created by fission fragments.

Fission fragment interaction with gases can be distinguished from other charged particles due to their higher mass (~97 for the light fragments and ~138 for heavy fragments) and their higher initial charge (20e and 22e, respectively). The fragments are born with average energies of 95 and 67 MeV. It should be noted that due to fission fragment's higher initial charge, many of the primary ions produced upon interaction with a gas will have charges exceeding unity. These doubly, triply or even higher ionized particles will quickly react with surrounding uncharged particles, forming ions of lower charge. Therefore, the distribution of ions, excited ions and excited neutrals produced by fission fragments is conceiveably different that one generated by other forms of ionizing radiation which displays less energetic interactions.

To study fission fragment excitation, the spectroscopic analysis of the radiation produced in a gas of interest by the interaction of charged particles was undertaken. Generally the experimental apparatus consists of a cylindrical test chamber lined with a $U^{235}O_2$ or $U_3^{235}O_8$ coating. This test chamber was pumped down to 10^{-8} torr before being filled with the test gas. The fission fragment excitation of the test gas is achieved by inserting the test chamber into the University of Florida Training Reactor. Upon irradiation with neutrons, the uranium oxide coating emits a fission fragment flux into the test gas.

If the gas being excited by any means is in local thermodynamic equilibrium and optically thin, the observed radiation intensity can be described by:

$$I = n_o \frac{g}{u} e^{-E/kT} \frac{hc}{\lambda} A. \qquad (1)$$

This relation can be rearranged as:

$$\ln \left(\frac{I\lambda}{gA}\right) = \ln c - \frac{I}{kT} E, \qquad (2)$$

where $c = \frac{n_o hc}{U} \times$ constant.

n_o: partial pressure of radiating species
g: statistical weight
U: partition function
E: excitation energy
T: temperature
A: transition probability
h: Planck's constant
k: Boltzmann's constant
c: velocity of light
λ: wavelength

For a Maxwell-Bolzmann distribution of excited states, a plot of $\ln(\frac{I\lambda}{gA})$ vs. excitation energy should result in a straight line, having the slope of $-\frac{1}{kT}$. Any deviation from straightness indicates over or under population.

A typical example is shown in Figure 2

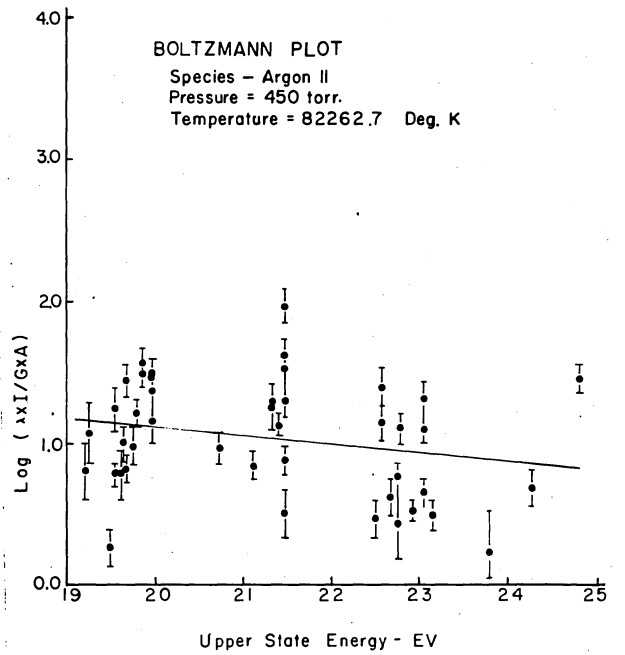

Figure 2. Nuclear Energy Produced Non-Equilibrum of Excited Ions.

for states of ArII, excited by fission fragments.[2] Since the gas was close to room temperature, it is obvious that the slope of the line does not describe a physically realized temperature. The observed states are nowhere near a Maxwell-Boltzmann distribution within the energy interval observed.

A measurement of the relative populations (~ to the factor $\frac{i\lambda}{gA}$) depends on the accuracy of the intensity measurement and on the accuracy of the knowledge of the transition probability. While the first is no particular problem, the latter certainly is. As a rule, only a few gases (e.g., H and He) are available for which most transition probabilities are known with satisfactory accuracy. Based on this method, the population inversion compiled in Table I have been detected.[3,4]

Measurements of the intensity of spectrum lines as a function of pressure give additional information on the excitation mechanism.[3] The points in Figure 3 indicate the measured intensity vs. pressure for several He lines excited by fission fragment. The population and depopulation

TABLE I. Experimentally Observed Population Inversions

GAS	UPPER LEVEL	LOWER LEVEL	TRANSITION	INVERSION RATIO
HeI	$4\ ^1P$	$4\ ^1D$	216μ	3.5 (max)
HeI	$3\ ^1P$	$3\ ^1D$	95μ	1.5 (max)
XeII	$(3p)\ 18_{1/2}$	$(3p)6p^4P^\circ_{3/2}$	4369Å	5.35
XeII	$(3p)6d^4P_{3/2}$	$(3p)6p^4P^\circ_{3/2}$	4180Å	8.61
XeII	$(3p)7s^4P_{1/2}$	$(3p)6p^4P^\circ_{3/2}$	4296Å	21.00

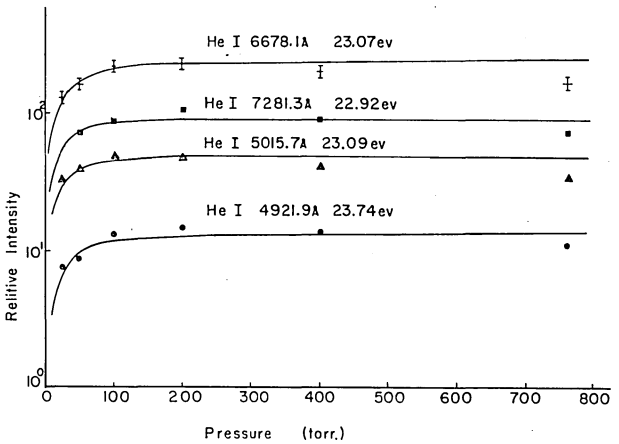

Figure 3. Pressure Dependence of Fission Fragment Excited Helium Lines

reactions of the two levels between which the transition under observation occurs, have to be described by a rate equation approach. The solid lines in Figure 3 were obtained with the following very simple model. The mechanisms accounted for are:

1) direct formation of an excited state by the reactions

$$ff + He \rightarrow He^*(n,\ell) + ff \quad (3)$$

$$e^- + He \rightarrow He^*(n,\ell) + e^- \quad (4)$$

2) excitation transfer between levels

$$He^*(n,\ell) + He \rightarrow He + He^*(n,\ell') \quad (5)$$

and by means of trapped resonance radiation.

3) radiative decay by spontaneous emission

4) depopulation by collision losses as in the reaction

$$He^* + 2He \rightarrow He_2^+ + e^- + He \quad (6)$$

and various other reactions with impurities.

The rate equation for this model is:

$$\frac{dn_i}{dt} = f_i p + a_{ji}N_j P - a_{ij}N_i P - N_i A_i - c_i N_i P \quad (7)$$

$$\frac{dn_j}{dt} = f_j p + a_{ij}N_i P - a_{ji}N_j P - N_j A_j - c_j N_j P \quad (8)$$

where f is the formation rate; a_{ij}, a_{ji}, the transfer rates i→j and j→i, respectively; c, deexcitation by collision; and A, transition probability. The rates f, a, and c are per unit pressure.

In this simple model, the energy storage capability of the metastable states of the noble gases was neglected. The specific energy available in these excited states of the rare gases has led to the production of many well-known laser systems (e.g., He-Ne, He-Xe, Ar-N_2). The collisions between metastable argon atoms and nitrogen cause excitation of the $N_2(C^3\Pi_u)$ state which gives rise to the second positive group emissions.

Experiments were undertaken whereby various quantities of N_2 were added to argon and the spectral output of the argon and nitrogen were monitored.[5] Figure 4

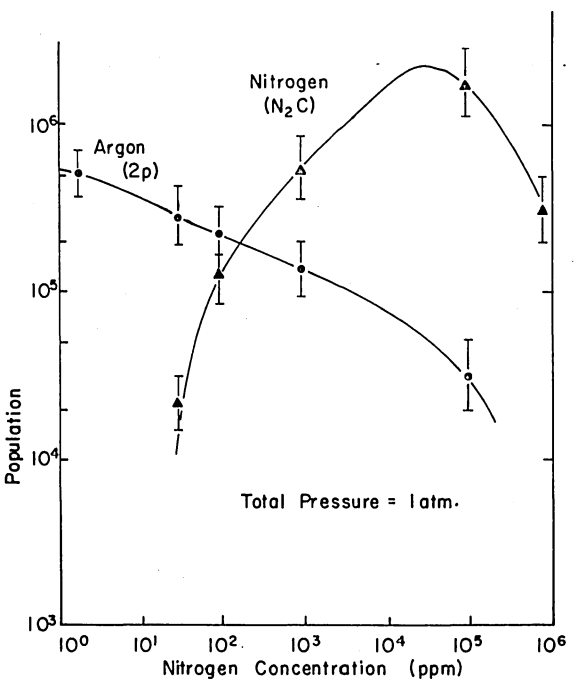

Figure 4. Measured Populations of Ar 2p Level and N_2C State vs N_2 Concentration for Fission Fragment Excitation.

indicates the populations of the $\tilde{2}_p$ levels of argon (Paschen notation) and the $N_2(C^3\Pi_u)$ state (designated N_2C) versus nitrogen concentration for a total pressure of one atmosphere. The N_2 second positive group is a prominent emission in all of the spectra containing N_2. The red ArI lines originating from the 2p levels of argon are all strongly quenched by the nitrogen, whereas the ArII lines (e.g., 4545A) are not radically affected. This suggests that the ArII excitation may be direct while, for the ArI lines, it may not.

To evaluate this data, a more sophisticated rate equation model than that used for helium was developed. For this study, the excited levels of argon were divided into six groups as indicated in Table 2. Each group was treated as a single excited level and assigned a transition probability that was an average over the gA values of the levels of that group. As indicated earlier, the energy deposition by fission fragments in a gas is primarily in the production of delta rays, and it is the delta rays and their secondary electrons that are primarily responsible for the excitation of the gas.

A resonably complete set of discrete ionization cross sections for argon excitation by electrons is given by Peterson and Allen.[6] They used combinations of data and theoretical extrapolations of the generalized oscillator strengths. Their calculations result in the final population for each excited state as a function of incident electron energy. These populations are a result of the degradation of the primary electrons and all generations of secondary electrons and is presented as an efficiency where:

$$\varepsilon = W_i \, N/E, \tag{9}$$

where, W_i = threshold of the level i;
N = number of excitations;
E = energy of the incident electron.

The efficiency versus incident electron energy is relatively constant for incident energies above approximately 80 eV. In Table 2 are the results of Peterson and Allen that correspond to our six groups of the atom and for the ion for incident electron energies of 100 eV.

From Platzman,[7] the average energy loss per ion pair, W, can be related to the equation:

$$W = \bar{E}_i + \sum_g E_{ex}(g)\left(\frac{N_{ex}(g)}{N_1}\right) + \bar{\varepsilon}_{se}, \tag{10}$$

where, $\bar{E}_i$ = the energy necessary to produce an ion;

TABLE 2. PROPERTIES OF THE SIX GROUPS OF ARGON

GROUP	LEVEL REPRESENTED (PASCHEN NOTATION)	AVERAGE ENERGY (EV)	AVERAGE gA ($\times 10^{-8}$)	ε	# EXCITED/100EV ABSORBED
AR(1)	1s	11.68	-	.08	.685
AR(2)	2P	13.21	1.3	0.04	.303
AR(3)	2s,3s',3d	14.1	0.5	0.04	.284
AR(4)	3P	14.59	0.055	0.005	.034
AR(5)	4d	14.77	0.1	0.008	.054
AR(6)	HIGHER LEVELS	15.2	0.021	0.019	.125
AR*	$2P^5\,{}^2P_{3/2}$	15.7	--	0.56	3.44
AR* (ADJUSTED)		15.7	--	0.594	3.79

E_{ex} = the energy for the excited atom in state g;

$\bar{\varepsilon}_{se}$ = the energy of the subexcitation electrons;

N_{ex}/N_i = the ratio of number of excited atoms to the number of ions.

For the noble gases, the quantity $\bar{E}_i$ exceeds the ionization energy I because of the energy used in producing excited ions and multiply charged ions. The ratio of $\bar{E}_i/I$ for the noble gases is approximately 1.06. This results in the adjusted value in Table 2 for the ε of Ar^+. Using Eq.(10) and the values in in Table 2, approximately 60% of the deposited energy is used in the formation of ions, 20% in the formation of excited states and 20% of the energy is left in subexcitation electrons. Thus, since a large portion of the deposited energy is used in the formation of ions, the resultant spectrum will, at least in part, be determined by recombination processes.

For pressures above a few torr, recombination in argon will proceed predominately through the molecular ion Ar_2^+ and not the ion Ar^+. This is due to the rapidity with which the ion is converted into the molecular ion by the process:

$$Ar^+ + Ar + Ar \rightarrow Ar_2^+ + Ar. \qquad (11)$$

The recombination of the molecular ion has a large rate coefficient and proceeds by the process of dissociative recombination.

$$Ar_2^+(\nu) + e \rightleftarrows (Ar_2^*)_{unstable} \rightarrow Ar^* + Ar + K.E. \quad (12)$$

where, ν indicates different levels of excitation of the Ar_2^+. The spectrum emitted in argon afterglows has indicated that the kind and number of excited species produced by dissociative recombination is dependent upon the initial energy of the Ar_2^+.[8] Figure 5 shows a single stable potential curve of the molecular ion and single repulsive branch of the unstable excited molecule.[9] Higher vibrations levels of the molecular ion will have smaller recombination coefficients and dissociate upon recombination into higher excited states of the atom.

To develop the model for the Ar-N_2 system, the interaction of fission fragments with a gas was divided into three categories. First is the excitation of the primary gas, Ar, by the incident fragment and secondary electrons. For the present analysis the argon ion, Ar^+, and six groups of excited levels of the atom, Ar(1)-Ar(6) was considered as discussed above. The second category to be considered was effects taking place in the argon after the primary excitation has been produced. An excited level of the atom may be further populated by cascading of higher laying populations into this level, by collisional excitation caused by electrons and atoms, and by dissociative recombination into this level. Deexcitation takes place via

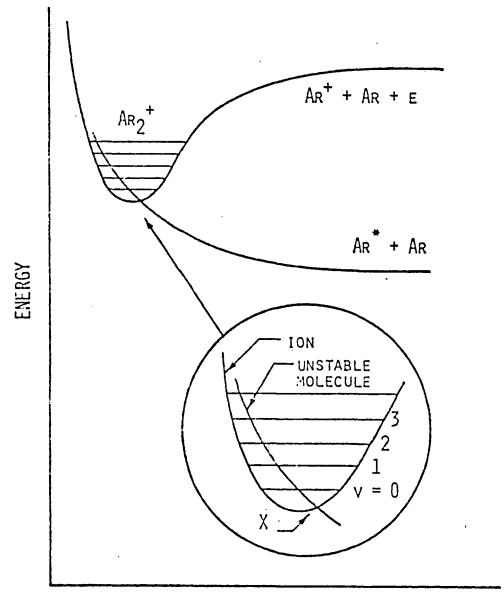

FIGURE 5: BISSOCIATIVE RECOMBINATION PROCESS IN ARGON

collisions with electrons or atoms, spontaneous emission and collisional processes leading to formation of molecules (dimers).

To account for recombination effects, the molecular ion was divided into two groups, Ar_2^+' and Ar_2^+". The Ar_2' comprises the lowest excited levels of the molecular ion which dissociate upon recombination into Ar(1), Ar(2) and Ar(3). The Ar_2^+" will comprise all higher states of the molecular ion and will be assumed to dissociate upon recombination into Ar(2), Ar(3), Ar(4), Ar(5), and Ar(6) and will also have collisional losses to form Ar_2^+' upon collisions with argon or impurity gases.

Two levels of the molecular argon were considered. First, the 3p levels of argon, Ar(4), will rapidly undergo 3-body collisions to produce a molecule Ar_2", the upper level of the 2250Å continuum observed in the experimental studies.[10] Secondly, the argon metastable, Ar(1), will also be converted by 3-body collisions to form an argon eximer, Ar_2'. Transitions from these dimers to the repulsive ground state will give rise to the 1250Å continuum.

The third category of interactions is due to the additional events caused by the addition of a second gas, in this case nitrogen. The addition of nitrogen will provide a path for collisional transfer of excitation from the argon to the nitrogen. The nitrogen will have two additional effects on the kinetics. First, it will

change the electron energy distribution, and secondly, it will collisionally relax the vibrational levels of the molecular ion. Both these latter two effects will undoubtedly change the excited species produced upon dissociative recombination.

Clearly to describe the system requires the knowledge of a large number of reactions. Considered in the present model were 89 reactions for 20 species. The flow chart in Figure 6 summarizes the reactions considered in the Ar-N_2 system.

measured populations of the argon 2p level and the N_2C state from Figure 4. The model solutions are within a factor of ten of the measured populations (within experimental error) and adequately predict the relative change in magnitude of the measured populations versus nitrogen concentration.

An experiment by DeYoung[11] was recently successful in lasing an argon 3d-2p transition by using the $^3He(n,p)T$ reaction to excite a ^3He-Ar gas mixture. Lasing was

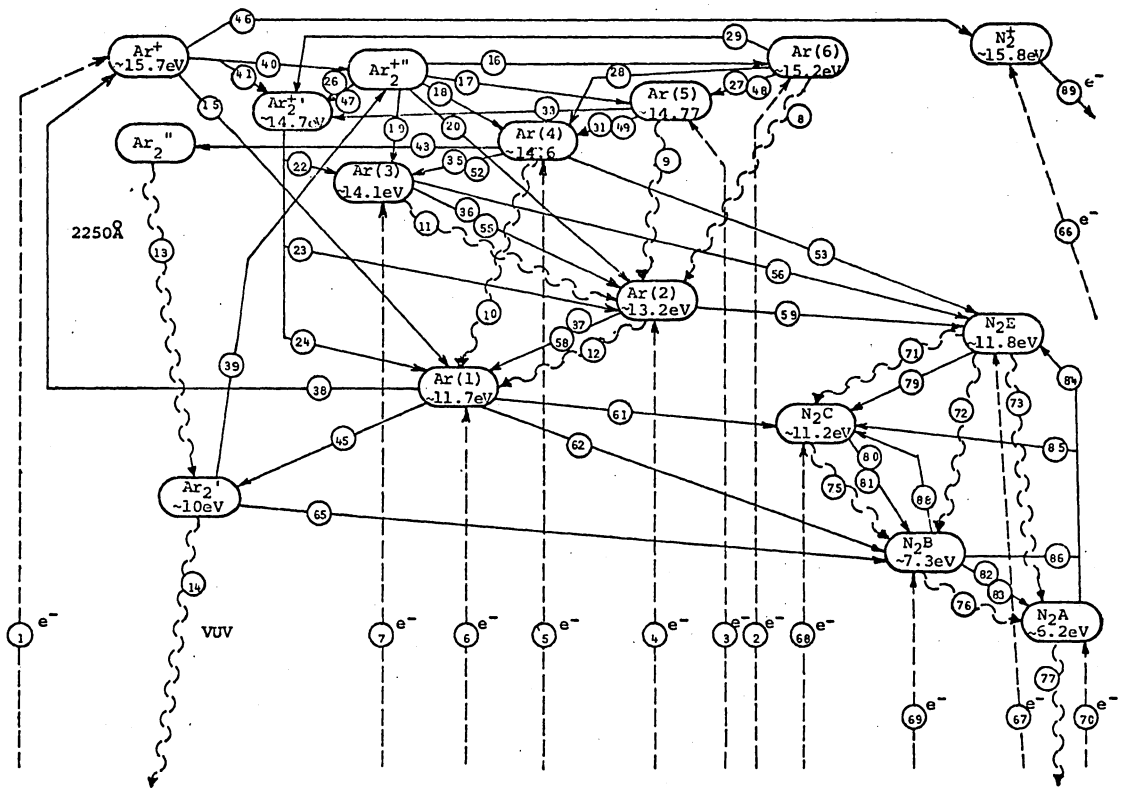

FIGURE 6. KINETIC MODEL FOR ARGON-NITROGEN MIXTURES EXCITED BY FISSION FRAGMENTS

The population of the species present can be found by solving a system of nonlinear simultaneous equations. Initially, each species equations was formed as a differential equation in time using all the source and sink reactions for that species. Then the differential equation is set to zero for the steady state case. The equations were solved using a Newton-Raphson iterative procedure for nonlinear simultaneous equations.

Computer solutions of the excited state population densities were obtained for a number of cases upon varying the nitrogen concentration, pressure, and energy deposition form. Figure 7 indicates the computer solution for the population of the species of interest versus nitrogen concentration at one atmosphere total pressure using an energy deposition rate germane to the experimental results. The heavy dark lines in Figure 7 indicate the

achieved at 1.79 microns in atomic argon at a total pressure ranging from 200 to 700 torr with 10% argon. The model predicts this population inversion. Figure 8 indicates the populations predicted by the model for various argon species based on 2 ppm nitrogen. Note that the Ar(3) group population (3d levels) exceeds the population of the Ar(2) group (2p levels). The energy deposition rate used assumes a uranium coated tube of 1.0 cm radius and a fission density of 4×10^{12} fissions/cm^3-sec in the coating.

Thus, it has been shown that the model describes the experimental results of fission fragment excitation of Ar-N_2 system with a reasonable accuracy. In addition, the model has indicated its usefulness by predicting a physically realizable nuclear pumped laser.

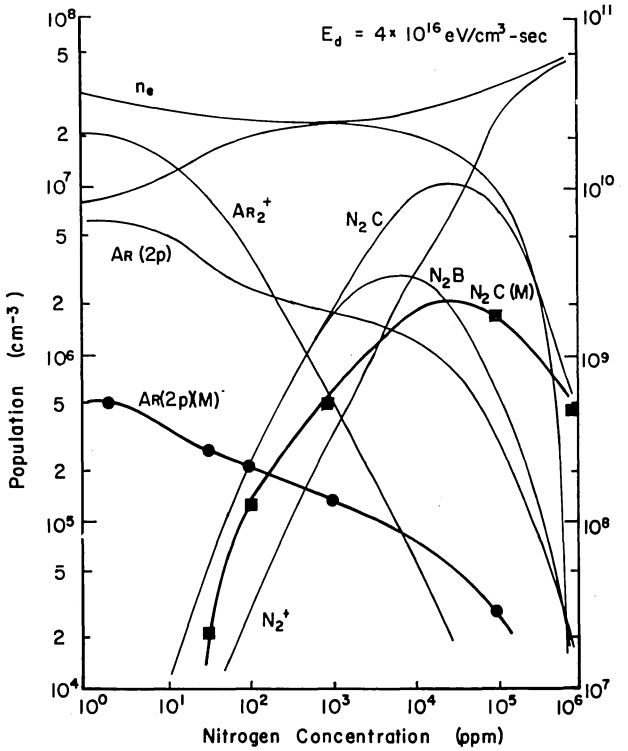

Figure 7. Population of Excited Ar and N_2 Species vs. N_2 Concentration For 750 torr Total Pressure

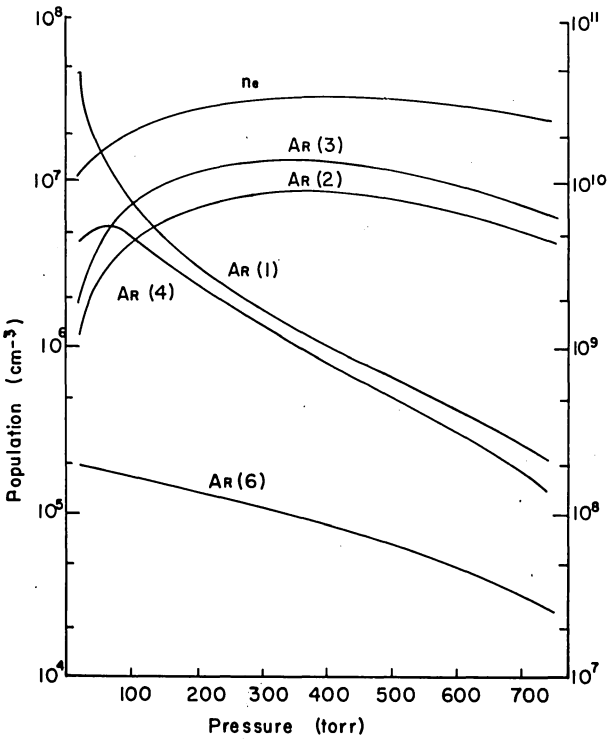

Figure 8. Population of Argon Excited Species vs. Pressure for 2ppm N_2.

III. Lifetime Measurements

One shortcoming of the methods described so far is the questionable accuracy in the knowledge of transition probabilities (or radiative life-times of the states) and collisional life-times. This problem can be alleviated somewhat if radiative life-times of the states are measured at the same experiment, where the relative line intensities are measured.

This can be done using a very moderate fission fragment flux. In the experiments described in the following,[12] a Cf^{252} source, located inside a small vacuum chamber, employing sapphire windows, was used. Cf^{252} undergoes spontaneous fission, and the source used emitted about 6×10^3 fission fragments per second. Figure 9 shows the experimental setup.

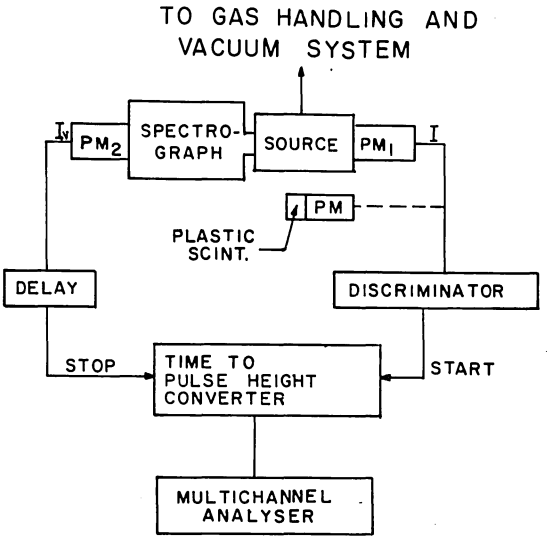

FIGURE 9. SYSTEM FOR LIFETIME MEASUREMENT

The birth of a fission fragment is signaled by a burst of γ-emission, which is detected by the plastic scintillator and attached photomultiplier. The resulting pulse starts the time to pulse height converter. The fission fragment traverses the vacuum chamber in a time small compared to the radiative lifetime of the atomic or molecular state under observation. Therefore, when the transition from the excited state to a lower state is finally made, a light pulse is emitted and observed by photomultiplier number 2 (PM_2).

The time to pulse height converter assigns this pulse a certain height, depending on the time passed after the start pulse. The multichannel analyzer will then store this pulse according to its height in the appropriate channel. The resulting distribution of observed pulses is an exponential decay as a function of channel numbers. The decay constant gives the collisional lifetime of the state.

An example is given in Figure 10 which

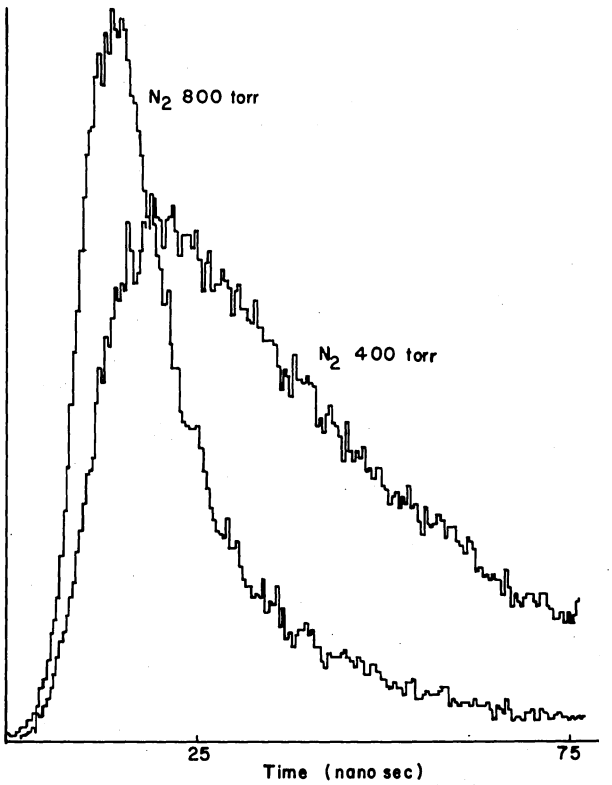

Figure 10. Decay Curves for Nitrogen $C^3\Pi_u$ State

shows the decay curves for 800 torr N_2 and 100 torr N_2. The time resolution of the system is 2.5 nsec. The radiative lifetime (or transition probability) can be obtained by measuring the collisional lifetime as a function of pressure and extrapolating back to zero pressure. Figure 11 shows this for the upper level of the 3371 N_2 line. The measured radiation lifetime is 45 nsec, which compares favorably with the literature values as indicated on the figure.

In order to apply this technique for measurement of population inversions, the Ar/N_2 system was chosen as a test case. The $C^3\Pi_u \rightarrow B^3\Pi_g$ transition has been lased using an electron beam by other research groups.[13,14] A computer model predicting the populations of the two levels involved was published in reference 14. The so predicted populations are reproduced in Figure 12.

From this figure, the lifetime of $N_2(B)$ is 131 nsec and of $N_2(C)$ is 18 nsec. The result of the measurement of these lifetimes using our system is shown in Figure 13. Our result is 300 nsec (as compared to 131 nsec) and 40 nsec (as compared to 18 nsec). However, our gas pressure was 1 atm as compared to 3 atm. A correction for the pressure difference would bring the two sets of data to a better agreement.

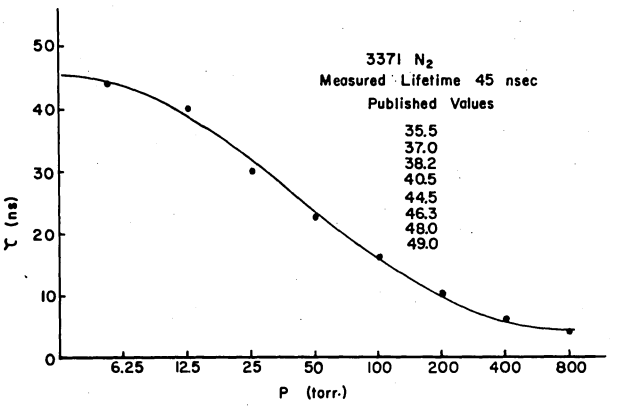

Figure 11. Measurement of The Radiative Lifetimes

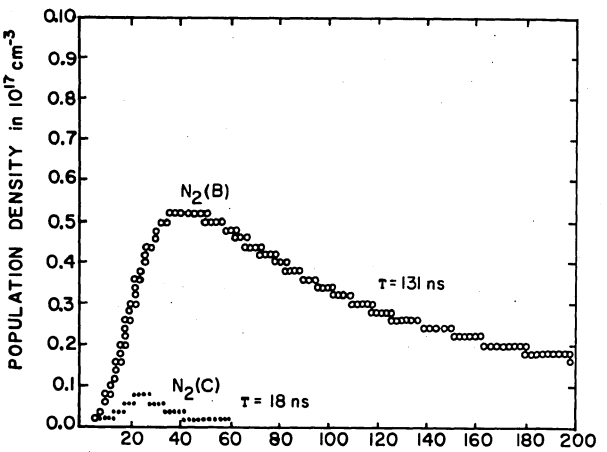

Figure 12. Population Densities of $N_2(B)$ and $N_2(C)$ vs. Time Due To Excitation of 3 Atm. Ar + 5% N_2 By A 2.5^2kA, 20 ns^2 Beam. (After Ref 14)

The advantage of the method described above is that it allows for search of population inversions caused by fission fragment excitation, without having to use a reactor, and the resulting complexity of the measurement procedures. The question which has to be addressed next is the extrapolation of the results obtained with these low fission fragment fluxes to higher fluxes which are typical for nuclear pumped lasers. The one test case described above seems to support the scaleability towards higher fluxes. However, further research is needed.

IV. Measurement of Fission Fluxes Emanating from Coatings

As indicated above, it is of interest to know: (a) How much energy is deposited in the laser gas, (b) Optimum coating thicknesses to maximize energy deposition and minimize cooling requirements, (c) The angular distribution of fission fragments emitted from coatings of different thicknesses, (d) The possibility of increasing energy deposition by increasing the surface area of the coating through surface corrugation.

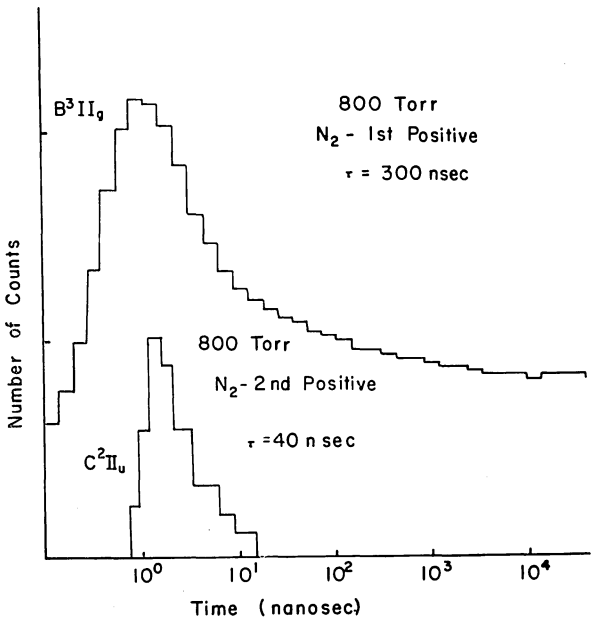

Figure 13. Lifetimes of Excited Nitrogen Levels In 95% Ar and 5% N_2 Mixture At 800 Torr.

Initial measurements use the chamber shown in Figure 14. An aluminum chamber

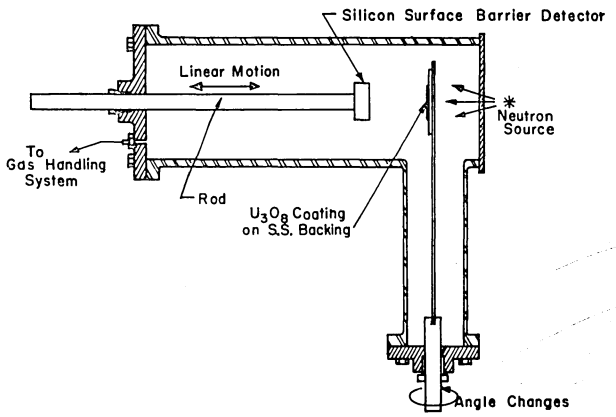

Figure 14. Fission Fragment Range and Energy Detector (FFRED)

was constructed which could be evacuated or filled with gases at various pressures. The fission fragment source was a U-235 U_3O_8 coating about 0.5cm x 2cm long made by the lacquer painting and firing technique. The coating can be rotated for angular distribution measurements. A silicon surface barrier detector about 2 cm in diameter detected the emitted alpha particles and fission fragments. The detector could be placed at various distances from the source to vary the geometrical efficiency or angular resolution. The entire assembly was placed in a polyethylene moderator with a 10 Ci Pu-Be neutron source to provide the neutron flux.

Coatings of various thicknesses of 93% enriched U-235 were made and the thickness assayed by alpha counting in a 2π-gas flow counter and by observation of the 185 keV gamma rays from the U-235 decay chain using a large Ge(Li) detector. (Most of the alpha particles actually were produced by U-234 decays.)

Pulses from the surface barrier detector were analyzed in a multichannel analyzer and typical spectra for two different thicknesses are shown in Figure 15.

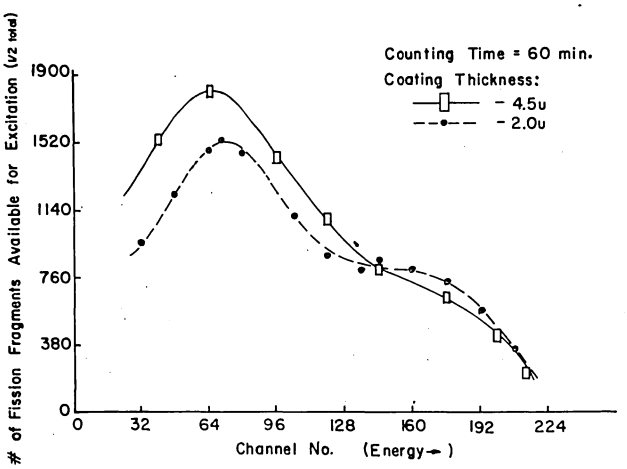

Figure 15. Typical Spectra of Fission Fragments From Two Different Source Thicknesses

The 4.5 micron coating produced more fission fragments, but mainly at lower energies where they are far less efficient at depositing their energy in gases.

Figure 16 shows the total number of

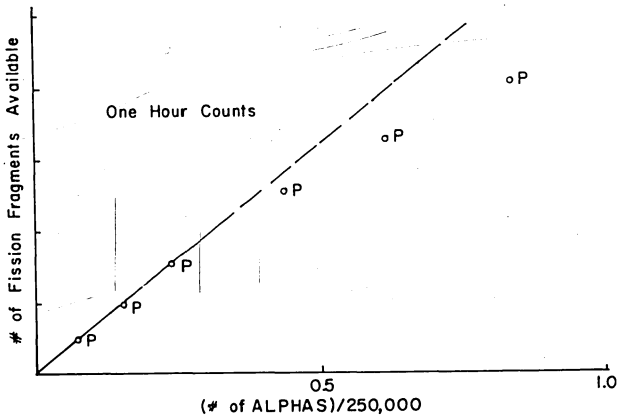

Figure 16. Fission Fragments Observed vs. Coating Thickness

observed fission fragments versus the number of alpha particles counted. The experimental points deviate from a straight line for the larger count rates where the coatings are thick enough to allow the alphas to penetrate. Some thick coatings were made on corrugated surfaces (grooves milled in the stainless steel backing plates) and the results fell on top of the other data indicating no improvement in the fission fragment fluxes for those geometries and coating thicknesses.

Angular distribution measurements on the fragments are continuing and measurement of the absolute energies deposited in different gases at different pressures are being made.

V. A Spectroscopic Study of a Fissioning Gas

One advantage of nuclear pumping over conventional laser excitation methods is the potential to obtain higher energy densities in a nuclear pumped laser. The achievement of high energy deposition into the lasing gas is thus of key interest.

The alternative approach is to employ a volume source of fission fragments. Sources made of solid fissionable materials, as described in the previous chapter, are limited by the fact that source thicknesses cannot exceed the range of fission fragments in the material. As pointed out, increased energy deposition can be obtained only by increasing the source surface area (i.e., many sources) or the neutron flux. Because UF_6 is the only known uranium bearing gas at physical conditions of interest, it is the prime candidate to serve as a fission fragment source in a nuclear pumped laser. Information is thus required on the suitability of UF_6 as a laser gas itself and the compatibility of laser gas mixtures with UF_6. Therefore, a spectroscopic investigation of light emitted by fission fragment excited UF_6 and UF_6-Ar-N_2 mixtures was conducted.[15]

The fission fragment flux supplied by the fissioning UF_6 was augmented by a flux emitted from a 3 micron thick, 93% enriched UO_2 planar source mounted along the inside wall of the gas cell. ArI, ArII, N_2 and N_2^+ emissions from the gas were spectroscopically monitored over the 2200-8000Å range as a function of UF_6 concentration in a 10:1 Ar-N_2 gas mixture at a total gas pressure of 760 torr.

The results indicated in Figure 17 show that all optical radiation from the fission fragment excitation of the N_2^+ and N_2 molecule is severly quenched by the addition of UF_6 to the gas mixture. The radiation coming from ArI is actually enhanced by small concentrations of UF_6 and not as severly quenched by higher concentrations of UF_6. Radiations coming from ArII is relatively unaffected by low concentrations of UF_6 and is moderately quenched at higher concentrations of UF_6. Pure UF_6 was found to emit no radiation due to fission fragment excitation over the spectral region investigated. The results of this study suggest that significant additional work will be required before a satisfactory fissioning laser gas mixture is identified. There is no indication however, that such a mixture cannot exist.

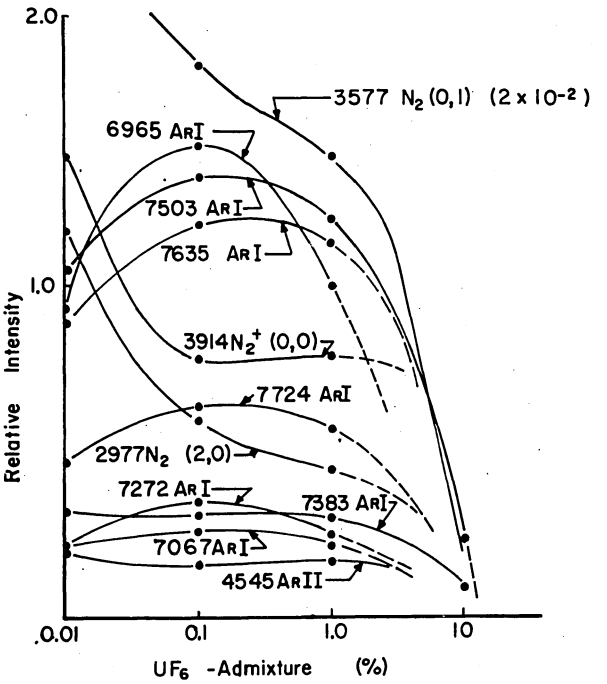

Figure 17. Relative Intensity of ArI, Ar II, N_2, and N_2^+ As A Function of UF_6 Admixture. Wavelength In Å

Acknowledgments

The work was supported by the National Aeronautics and Space Administration.

References

1. Helmick, H.H., Fuller, J.L, and Schneider, R.T., "Direct Pumping of a Helium Xenon Laser", Appl. Phys. Lett., 26,6,327, March 1975.

2. Schneider, R.T., "On the Feasibility of Nuclear Pumping of Gas Lasers", Laser Interaction and Related Plasma Phenomena, Vol. 3, pp. 85-107, edited by H.J. Schwarz and H. Hora, Plenum Publishing Corp., New York, (1974).

3. Shipman, G.R., Walters, R.A., and Schneider, R.T., "Population Inversions in Fission Fragment Excited Helium", Trans. Am. Nucl. Soc., 17,3 (1973).

4. Davie, R.N., Davis, J.F., and Schneider R.T., "Population Inversions Observed in Fission Fragment Excited Xenon", ANS Annual Meeting, 13-18, June 1976.

5. Davis, J.F., Dissertation, Univ. of Florida, Gainesville, Florida, to be published (1976).

6. Peterson, L.R., and Allen, J.E., "Electron Impact Cross Sections for Argon", Journal of Chem. Phy., 5b, No. 12, 6068 (1972).

7. Platzman, R.L., "Total Ionization in Gases by High-Energy Particles: An Appraisal of Our Understanding", Journal of App. Rad. and Isotopes, 10, 116-127 (1961).

8. Loeb, L.B., Basic Processes of Gaseous Electronics, Chapter 6, University of California Press (1961).

9. Biondi, M.A. and Holstein, T., Physics Rev., 82, 963 (1951).

10. Birot A, Brunet, H., Galy, J., Millet, P., Teyssier, J.L., "Continuous Emissions of Argon and Krypton in the Near Ultraviolet", Jour. of Chem. Phys., 63, No. 4, 1469 (1975).

11. DeYoung, R.J., Jaluska, N.W., Williams, M.D. and Hohi, F., "Direct Nuclear Pumped Lasers Using the Volumetric Helium-Three Reaction", The Princeton University Conference, Meeting No. 133, June 10-12, 1976.

12. Shipman, G.R. Ph.D. Dissertation, University of Florida, Gainesville, Florida, to be published (1976).

13. Hill, R.M., Gutcheck, R.A., Huestis, D.L, Mukherjee and Lorents, D.C., "Studies of E-Beam Pumped Molecular Lasers", Stanford Research Institute, (1974); also, Searles, S.K. and Hart, G.A, Appl. Phys. Letters, 25, 79 (1974).

14. Ault, E.R., Bradford, R.S. and Bhaumik, M.L., "UV Gas Laser Investigations, Semiannual Technical Report", Northrop Corporation, May 1975.

15. Davie, R.N., Albrecht, G., Carroll, E.E. and Schneider, R.T., "Optical Radiation of Fission Fragment Excited UF_6 and Ar-N_2 Mixtures", ANS Annual Meeting, 13-18, Toronto, June 1976.

DISCUSSION

D. C. LORENTS: I would like to comment about your quenching studies of UF_6. There are two possibilities. One is that it is just pure optical absorption by the UF_6; the other is that it is quenching of some excited state in the energy flow chain. Did you look at the relative intensities of the 1-0 vs the 0-0, in order to isolate that? Right in that region, there is a sharp dip in the absorption cross-section of UF_6.

J. F. DAVIS: We considered absorption because the sails we were using were three feet long and the active volume was only about 11 inches of that, so we feel that a large percentage of quenching was by absorption.

D. C. LORENTS: As far as I can see, the model you have is exactly the same model we use in the electron-beam excitation, but you said that there were some differences.

J. F. DAVIS: I have tried to take into account excitation of the upper state by higher excited states of argon collisionally exciting the nitrogen. By doing that, I could find agreement with the observed intensity of argon versus nitrogen concentration and also more adequately describe the population of the nitrogen. I was also then able to describe the relative trends of the argon continuum at 2250 Å. Even though a small percentage of the energy was flowing through these upper excited states of argon, it was the purpose of the study to try to describe those states too. Most of the energy is traveling very quickly through the metastable states, at a pressure of one atmosphere.

G. H. MILEY: Do you account for a change in electron energy distribution in the calculation?

J. F. DAVIS: No, I didn't take into account any change of the Boltzmann electron energy distribution with additional nitrogen.

G. H. MILEY: So this mixture will last with electron beams interacting with any gas or gas mixture.

J. F. DAVIS: When a fission fragment interacts with a gas, it is like a small e-beam; and we have a lot of small low-energy e-beams corresponding to each fission fragment. So I feel e-beam excitation and fission-fragment excitation are similar in that respect.

G. H. MILEY: How many groups of e-beams do you need to duplicate fission fragment excition?

J. F. DAVIS: With fission-fragment excitation, you have localized electron ionization, leading to polymer recombination effects, but if you proceed to a high enough fission fragment flux, such localized effects will begin to average out. We feel that we have accomplished this in the present case.

M. KRISHNAN: In your model of dissociative recombination, you say that molecular ions from different vibrationally excited levels result in dissociated atoms in different electronic configurations. Since electronic excitations involved energies of $\sim$ 1 e.v. and vibrational excitations involve much lower energies $\sim$ 0.1 e.v., it appears that the bulk of the energy for electronic excitation upon recombination arises from the dissociation energy of the molecule. If this is so, vibrational excitations should not play a major role in this recombination model.

THE PUMPING MECHANISM FOR THE NEON-NITROGEN NUCLEAR EXCITED LASER

G.W. Cooper, J.T. Verdeyen, W.E. Wells, G.H. Miley
Nuclear Engineering Program
and
Gaseous Electronics Laboratory
University of Illinois at Urbana-Champaign
Urbana, Illinois 61801

Abstract

The neon-nitrogen laser has generated considerable interest having been pumped directly by nuclear radiation. Lasing was observed on two transitions of atomic N, the $3p^2\ P^0_{\frac{3}{2}} \rightarrow 3s^2\ P_{\frac{3}{2}}$ (8629.24 Å) and the $3p^2\ D^0_{\frac{5}{2}} \rightarrow 3s^2\ P_{\frac{3}{2}}$ (9392.79 Å). The Ne-N_2 system also lases in an afterglow of an electrical discharge, which has similar characteristics to a nuclear radiation generated plasma. In order to determine the physical processes for pumping this laser, a detailed study of the afterglow system has been performed. The pumping mechanism has been found to be collisional-radiative electron-ion recombination. Microwave quenching of both the laser and spontaneous afterglow light have shown conclusively that a recombination process directly produces a nitrogen atom in either the upper laser level or, more likely, in a higher lying energy level which rapidly de-excites to the upper laser level. Studies of the temperature dependence of the recombination coefficient indicates a collisional-radiative process allowing the recombining ion to be tentatively identified as N^+. Since this process is highly compatible with the reactor produced plasma, it is not unreasonable to assume that this recombination process is also the pumping mechanism in the nuclear excited case.

I. Introduction

The electrically-excited neon-nitrogen laser was discovered in 1964[1] and several subsequent papers[2-4] have appeared. Lasing occurs on several transitions of atomic nitrogen during the afterglow of an electrical discharge and will hereafter be referred to as the afterglow neon-nitrogen laser. Last year interest was greatly revived in the neon-nitrogen laser when DeYoung et al,[5] succeeded in pumping this laser directly with nuclear radiation. They observed lasing on two transitions of atomic nitrogen: $3p^2\ D^0_{5/2} \rightarrow 3s^2\ P_{3/2}$ (9392.79 Å) and $3p^2\ P^0_{3/2} \rightarrow 3s^2\ P_{3/2}$ (8629.24 Å).

The results of a detailed investigation of the afterglow neon-nitrogen laser's pumping mechanism are presented here. The research was undertaken in order to provide a better understanding of the nuclear pumped laser which is necessary to fully evaluate the laser's ultimate applicability and to help identify possible analogous systems for nuclear pumping. The afterglow system was chosen for study because of the difficulty of doing diagnostics in the reactor environment. Since the characteristics of both the afterglow and nuclear-radiation-generated plasmas are dominated by their low electron temperatures,[6] it is quite probable that the pumping mechanism in both systems would be the same.

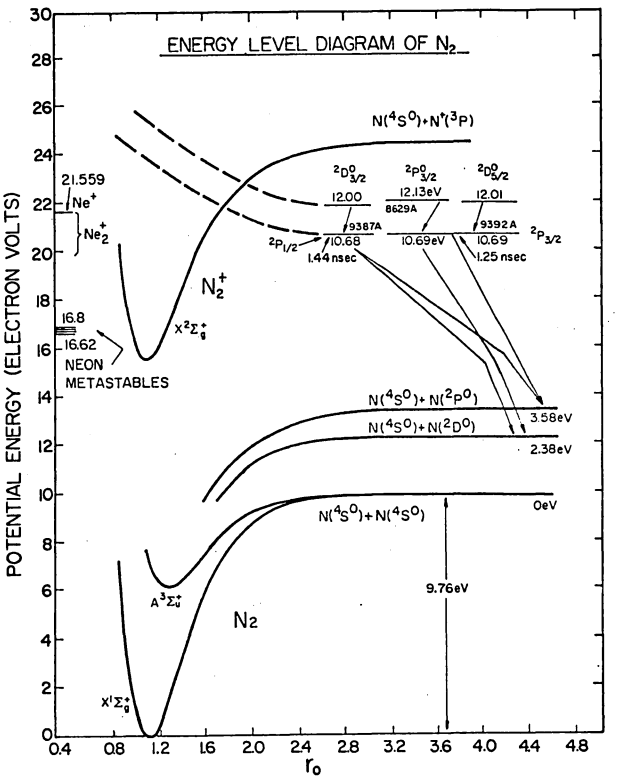

Fig. 1. Partial potential energy diagram of the N_2 molecule also showing some levels of N_2^+, atomic nitrogen and excited neon species.

The problem of the pumping mechanism is best described by considering the potential energy diagram of N_2 shown in Fig. 1. Also shown in this figure are the lasing levels of atomic nitrogen. As can be seen, it requires a minimum of 21.76 eV of energy to simultaneously dissociate N_2 and excite atomic nitrogen to the upper laser level. Since in neon-nitrogen lasers the neon density is typically 10^3 to 10^5 times greater than the nitrogen's, most of the input energy will go into the neon. Thus, the energy to pump the laser must come primarily from collisions of nitrogen with excited neon species. However, even Ne^+ has insufficient energy to excite the laser in one step. Therefore, the pumping process requires a minimum of two steps.

The fact that the neon-nitrogen laser operates in the afterglow strongly suggested that recombination was playing an integral role in the pumping mechanism since it is a major process in afterglows. Since two recombination processes, dissociative and collisional-radiative are rapid

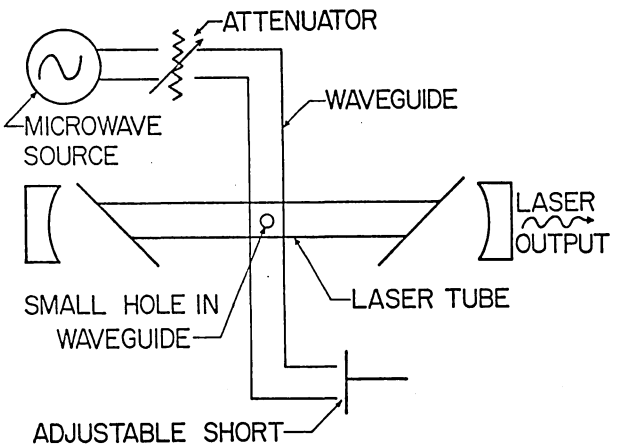

Fig. 2. Schematic of the microwave quenching experiments.

enough to be of importance and are both inversely proportional to electron temperature, the technique of microwave quenching[7] was employed. In this technique the electrons are selectively heated by a microwave pulse, and, as a result, the afterglow light which is primarily produced by recombining electron-ion pairs is "quenched." A diagram of the experimental set-up is shown in Fig. 2. The effects of electron heating on both the laser light and the spontaneous sidelight were monitored.

The microwave quenching experiments, to be described in part A. of the next section, have shown that the neon-nitrogen laser is pumped directly by a recombination event. Further microwave quenching experiments described in part B of the next section, have shown that the process is most likely collisional-radiative recombination and that N^+ is the recombining ion.

II. Results and Discussion

A. Microwave Quenching Experiments

The effects of microwave heating of the electrons on both the laser signal and the spontaneous emission of atomic nitrogen and neon have been investigated. The laser was found to be pumped directly by recombination. This conclusion is based on the following data.

Figure 3 shows the effect of microwave heating on the laser itself. The top trace shows the lasering in the afterglow in the absence of microwaves. The second trace shows the laser output as it was perturbed by the microwave pulse shown in the bottom trace. The laser intensity has obviously been quenched, indicating the inhibition of some process by microwave heating. Obviously, the electrons are not "cooled" by the microwaves, hence direct excitation from a lower state can be ruled out; it must be pumped from above. Thus, recombination must be playing an integral role in the pumping process.

Now consider Fig. 4 where the effect of microwave heating on the spontaneous sidelight of an atomic nitrogen laser transition (9393 Å) is compared to that of a neon line (8654 Å). Note that the time responses of the neon and nitrogen afterglow light to the microwave pulse are virtually

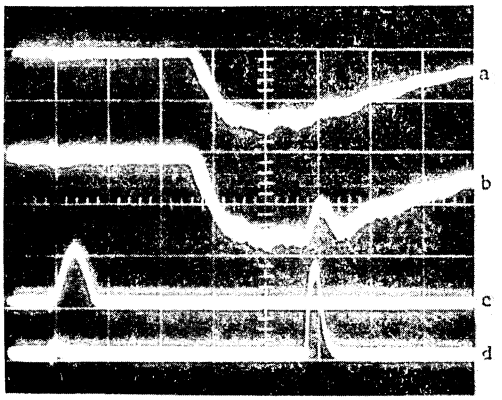

Fig. 3. Effect of microwave heating of the electrons on the laser output (9393 Å); (a) laser output in absence of microwaves, (b) laser output perturbed by microwaves, (c) current, (d) microwave pulse.

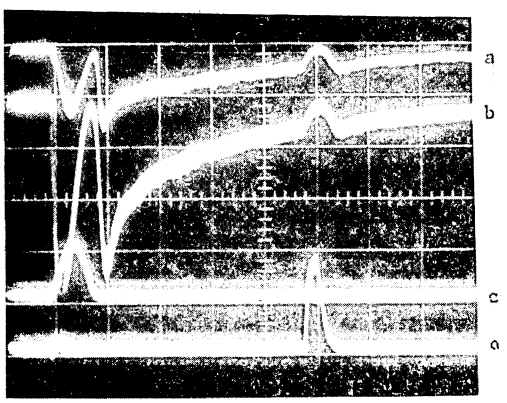

Fig. 4. Effect of microwave heating of electrons on both nitrogen's and neon's spontaneous sidelight; (a) nitrogen (9393 Å) (b) neon (8654 Å), (c) current, (d) microwave pulse.

identical. This implies that the role of recombination cannot be an indirect process, but must be directly pumping the laser. To elaborate, Atkinson and Sanders[4] proposed an indirect pumping scheme:

$$Ne_2^+ + e \rightarrow Ne\ (M) + Ne \qquad (1)$$

$$Ne\ (M) + N_2^* \rightarrow Ne + N + N_{UL}^*. \qquad (2)$$

Here a neon metastable, Ne (M), collides with a nitrogen molecule, N_2^*, that is sufficiently excited to allow the molecule to be simultaneously dissociated and leave a nitrogen atom, N_{UL}^*, in the upper lasing level. Recombination enters the pumping process as a major production mechanism of neon metastables. This or similar pumping schemes can account for quenching of the laser pulse by microwave heating since the neon metastables will cease to be produced. However, it cannot account for the near identical time responses of the neon

and nitrogen afterglow light. While it is true that electron heating inhibits production of neon metastables, it leaves those already produced unaffected. Therefore, since the process in Eq. (2) takes time, the response of the nitrogen afterglow light to the microwaves would be expected to be much slower than neon's response. Since it was not, the upper laser level must be being populated directly by a recombination event. That is, a process of the form

$$XN^+ + e \Rightarrow N^*_{UL} + \ldots \quad (3)$$

Here XN^+ represents the ion which upon recombining yields atomic nitrogen either directly in the upper lasing level or in a more highly excited state that rapidly de-excites to the upper lasing level. This recombination can be either dissociative or collisional-radiative. There were several candidates for the recombining ion: N_4^{+*}, NeN^+, N_3^{+*} and N^+. Note that N_2^{+*} and N_3^{+*2} must be highly excited, metastable-like states in order to dissociate to the upper laser level upon recombining. Although such states are possible, they have not been observed and have a low probability of existence. Similarly NeN^+, while energetically possible, has not as yet been observed. The experiments which allowed the ion to be identified as N^+ are described in the next section.

B. Sensitivity of the Recombination to Electron Temperature

Of the possible recombining ions, N_2^{+*}, NeN^+ and N_3^{+*} all must recombine dissociatively to yield atomic nitrogen while N^+ recombination must be collisional-radiative. The theoretical collisional-radiative recombination rate[8] varies $\sim T^{-9/2}$ while dissociative recombination[9] varies[e] $\sim T_e^{-1/2}$. Thus, N^+ could be either inferred or eliminated as the recombining ion by measurement of the electron temperature dependence of the nitrogen recombination. Measurement of the electron temperature dependence, using microwave quenching techniques,[10] indicated that the recombination was collisional-radiative, suggesting that the recombining ion was N^+. Thus Eq. (3) could be written more explicitly as:

$$N^+ + 2e \Rightarrow N^{**} + e \quad (4)$$

$$N^{**} \Rightarrow N^*_{UL} + h\nu \quad (5)$$

Here the double-barred arrows imply net rather than direct processes and N^{**} represents any energy level above the upper lasing level, N^*_{UL}.

In studying this recombination process, the absolute temperature was not determined. Instead, microwave quenching of the neon-nitrogen mixture was used to compare the temperature dependences of the neon and nitrogen recombination coefficients. Since the temperature dependence of neon recombination is well known,[11,12] such a comparison could provide information about the recombination process in nitrogen.

In Fig. 5, the ratio of quenched to unquenched light was plotted as a function of the attenuation of microwave power for both neon and nitrogen. The ratio of quenched to unquenched light provides a measure of the temperature-dependent recombination coefficient. Although the absolute electron temperature corresponding to each microwave attenuation was not known, the electron temperature was common to both neon and nitrogen recombination events.

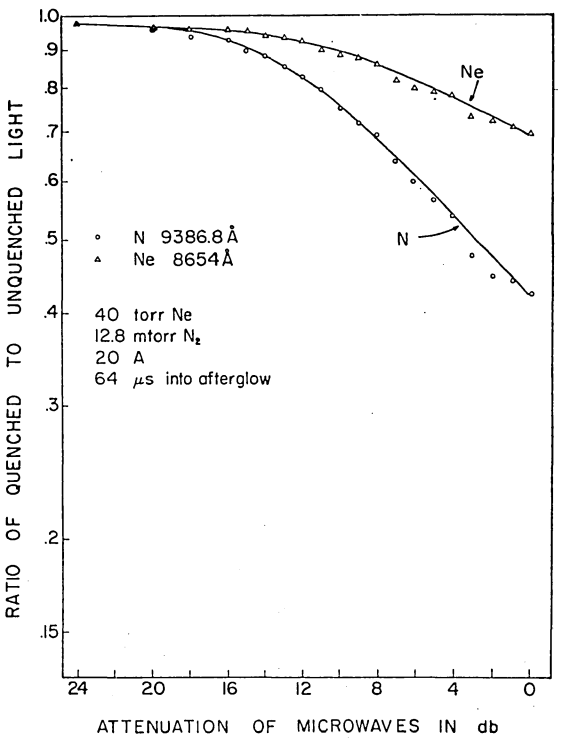

Fig. 5. Comparison of the electron temperature dependence of the recombination coefficients of neon and nitrogen at 40 torr total neon pressure.

The data shown in Fig. 5 were obtained at a total neon pressure of 40 torr, a pressure at which the dominant recombination process in neon is dissociative.[13,14,15] Consideration of the data in Fig. 5 shows that the nitrogen spontaneous light was much more sensitive to the electron temperature than that of neon. This difference implied that the recombination process producing excited atomic nitrogen was different from the dissociative process known to be dominant for neon under these conditions. Thus, these results seemed to rule out a dissociative recombination process for nitrogen, indicating that the mechanism must be collisional-radiative. Given the probable availability of N^+ as the recombining ion, the suggestion of a collisional-radiative mechanism for nitrogen recombination seemed a reasonable one.

The sensitivity of neon and nitrogen recombination to electron temperature was also measured at total neon pressures of 20 torr and 6 torr. The results are shown in Figs. 6 and 7, respectively, which can be compared with the 40 torr data in Fig. 5. The figures show that a total neon pressure of 20 torr, the difference between the temperature dependence curves for neon and nitrogen is not as great as the difference at 40 torr. At a total neon pressure of 6 torr, the curves for neon and nitrogen are nearly identical.

This change in the temperature dependence for neon, indicates a change in the recombination mechanism with decreasing pressure. This is as expected since the dissociative recombination process, which dominates for neon at 40 torr, is limited by the formation rate of Ne_2^+, which, in turn varies[15] as p^2. Thus at low pressures the formation rate of Ne_2^+ is too slow, and the

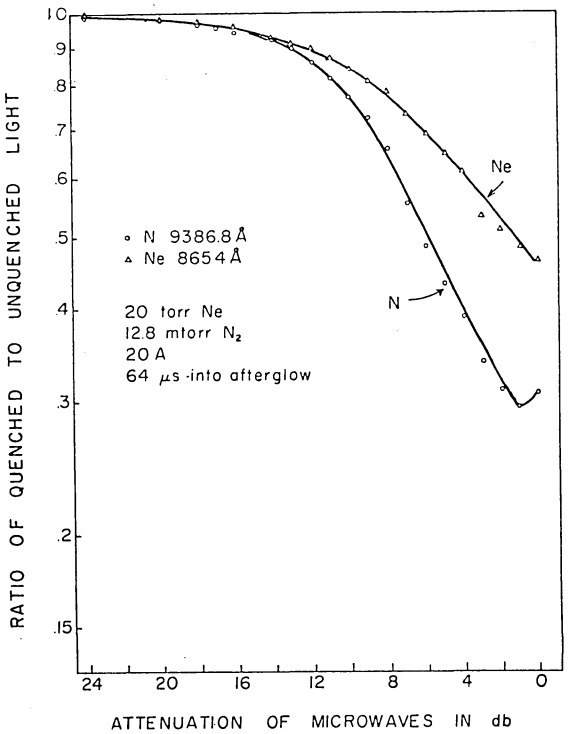

Fig. 6. Comparison of the electron temperature dependence of the recombination coefficients of neon and nitrogen at 20 torr total neon pressure.

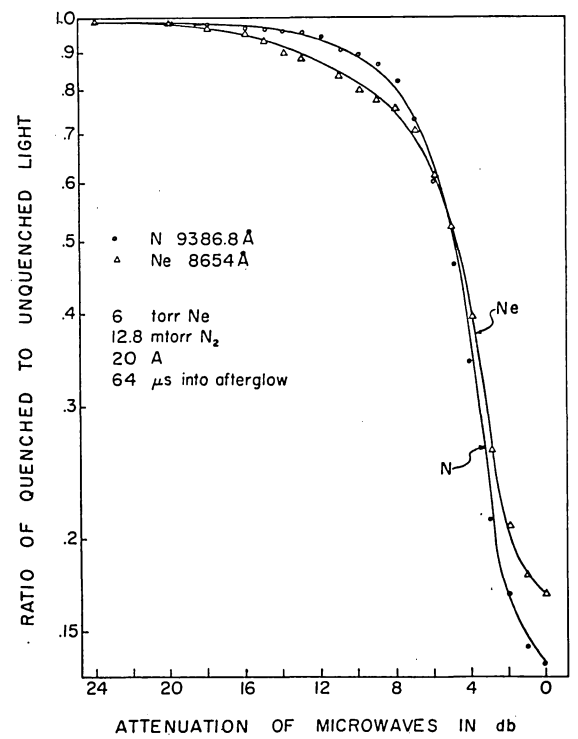

Fig. 7. Comparison of the electron temperature dependence of the recombination coefficients of neon and nitrogen at 6 torr total neon pressure.

collisional-radiative mechanism dominates for both neon and nitrogen.

C. Additional Considerations

The proposed pumping mechanism can be further considered in terms of its ability to account for the lasing observed. A first consideration is whether the collisional-radiative mechanism would be fast enough to produce the observed laser power. A recombination coefficient was estimated using the peak laser power (1 mW), and the electron density (10^{13} cm^{-3}) inferred from earlier microwave data. The estimated value of 5×10^{-9} cm^3 sec^{-1} seemed reasonable in the light of the theoretical values for collisional-radiative recombination coefficients given by Bates et al.[16] Thus the estimated recombination coefficient for the neon-nitrogen laser seemed compatible with a collisional-radiative mechanism.

An additional consideration is whether sufficient N^+ can be produced to support a collisional-radiative laser mechanism. Figure 8 shows a number of possible pathways for production of N^+. Since most of the cross-sections involved are unknown, an exact calculation of the rate of N^+ formation is not possible. Estimates of N^+ production by the more likely pathways do not rule out the formation of sufficient N^+ to support lasing, although the kinetics are made somewhat unfavorable by the

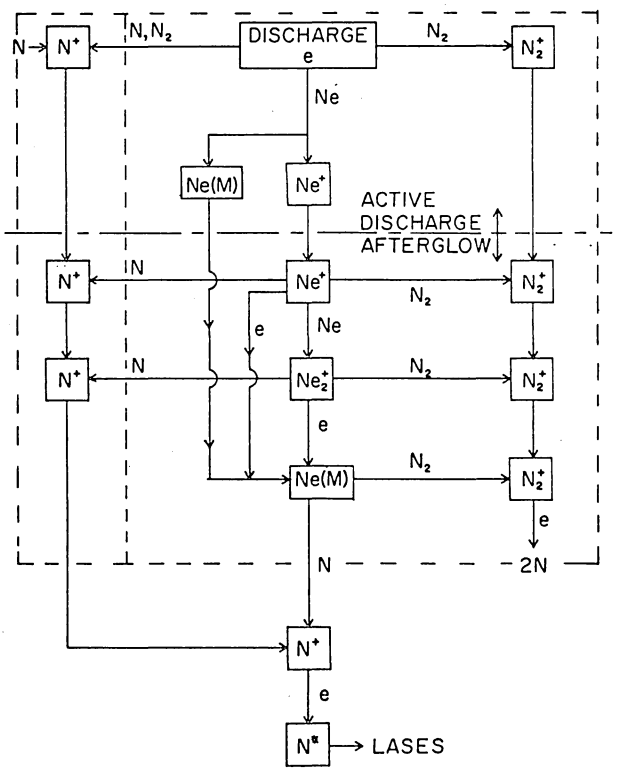

FLOW CHART FOR PRODUCTION OF N^+

Fig. 8. Flow chart showing possible pathways for production of N^+.

requirement for two collisions with excited neon. In this regard, the kinetics of formation of any other proposed recombining ion would suffer from even more serious problems due to the same requirement for two collisions with excited neon. However, given that sufficient nitrogen atoms are present from the active discharge (and prior ones), the Penning reaction of neon metastable with nitrogen atoms is estimated to be quite adequate to produce the required N^+ ions.

The helium-nitrogen and argon-nitrogen systems were also briefly investigated. The helium-nitrogen system has previously been reported to have lased[1-4] on the same transitions as does the neon-nitrogen laser. Microwave quenching experiments on the helium-nitrogen laser showed that this system was also being pumped directly by a recombination event. The argon-nitrogen system, however, could not be made to lase. These results tend to eliminate NeN^+ as the possible recombining ion since the existence of the analogous ion, HeN^+ is extremely improbable and the known ion[17] ArN^+ does not yield a laser. Also if the Penning reaction is a major production mechanism of N^+ as suggested above, the helium metastable could undergo the same reaction but the argon metastable has insufficient energy to ionize ground state atomic nitrogen. Thus the helium-nitrogen and argon-nitrogen results are compatible with the pumping mechanism being collisional-radiative recombination of N^+.

III. Summary

Microwave quenching experiments have shown that the neon-nitrogen afterglow laser is pumped directly by a recombination event. Measurements of the electron temperature dependence of the recombination coefficient have implied that this process is collisional-radiative recombination. This allows the recombining ion to be identified as N^+. The process of collisional-radiative recombination is highly compatible with the nuclear-radiation-generated plasma which has high electron densities at low temperatures. Therefore, it is not unreasonable to infer that the pumping mechanism for the nuclear-pumped neon-nitrogen laser is the same as for the afterglow laser. It should be pointed out, however, that the steps leading to the formation of N^+ could be quite different in the two lasers. Indeed, initial indications are that these steps are different and research is being pursued in this area.

References

[1] M. Shimazu and Y. Suzaki, Japan J. Appl. Phys., 3, 561, (1964).

[2] G. M. Janney, IEEE J. Quant. Electr., QE-3, 133, (1967).

[3] L. N. Tunitskii and E. M. Cherksav, Sov. Phys. - Technical Physics, 13, 1696, (1969).

[4] J. P. Atkinson and J. H. Sanders, J. Phys. B (Proc. Phys. Soc.), 1, 1171, (1968).

[5] R. J. DeYoung, W. E. Wells, G. H. Miley and J. T. Verdeyen, Appl. Phys. Lett. 28, 519, (1976).

[6] A. K. Bhattacharya, J. T. Verdeyen, F. T. Adler, and L. Goldstein, J. Appl. Phys., 38, 527, (1967).

[7] L. Goldstein, J. M. Anderson and G. L. Clark, Phys. Rev., 90, 486, (1953).

[8] E. Hinnov and J. G. Hirshberg, Phys. Rev., 125, 795, (1962).

[9] D. R. Bates and A. Dalgarno, in Atomic and Molecular Processes, ed. by D. R. Bates, (Academic Press, Inc., New York, 1962).

[10] C. L. Chen, C. C. Leiby and L. Goldstein, Phys. Rev., 121, 1391, (1961).

[11] L. Frommhold, M. A. Biondi, and F. J. Mehr, Phys. Rev., 165, 44, (1968).

[12] J. Philbrick, F. J. Mehr, and M. A. Biondi, Phys. Rev., 181, 271, (1969).

[13] T. R. Connor and M. A. Biondi, Phys. Rev., 140, A778, (1960).

[14] L. Frommhold and M. A. Biondi, Phys. Rev., 184, 244, (1969).

[15] A. P. Vituls and H. J. Oskum, Phys. Rev. A., 5, 2618 (1972).

[16] D. R. Bates, A. E. Kingston, and R. W. P. McWhirter, Proc. R. Soc., A267, 297, (1962).

[17] M. S. B. Munson, F. H. Field, and J. L. Franklin, J. Chem. Phys., 37, 1790 (1962).

DIRECT NUCLEAR PUMPED LASERS USING THE VOLUMETRIC ^3He REACTION*

R. J. De Young
Vanderbilt University, Nashville, TN

N. W. Jalufka, F. Hohl, and M. D. Williams
NASA, Langley Research Center, Hampton, VA

Abstract

Lasers pumped by energetic charged particles created directly by nuclear reactions have come into existence through the use of either Boron-10 or Uranium-235 coatings. A new class of nuclear-pumped lasers using the ^3He reaction has been developed at the Langley Research Center. Since helium is a major constituent of many gas lasers of interest, it is convenient to replace the usual ^4He with the ^3He isotope. In a thermal neutron flux, the $^3He(n,p)^3H$ reaction deposits energy nearly uniformly throughout the laser volume. The charged particles created (proton of 0.57 MeV and ^3H of 0.19 MeV) ionize and excite the gas media. By this method direct nuclear pumping of a ^3He-Ar (10% Ar) laser has been achieved. Results of reactor experiments are presented which show the scaling of laser output at 1.79μ (Ar I) with neutron flux and total ^3He-Ar pressure. Other laser systems presently under study at the Langley Research Center include the ^3He-Ne-O_2 (8446 Å OI) system. Spectra of nuclear pumped ^3He-Ne-O_2 taken at the Aberdeen Army Pulse Radiation Facility will be presented. The above systems are considered to be "proof of principle" systems and future more practical nuclear-pumped lasers, using excimer species, will be discussed.

I. Introduction

Attempts at pumping gas lasers by charged particles created from nuclear reactions have been made for many years.[1,2] Figure 1 shows the major nuclear reactions used to pump the laser medium. Recently, however, rapid progress has been accomplished in direct nuclear excitation with the development of nuclear-pumped lasers using either uranium-235[3,4,5] or boron-10[5] coatings on the internal walls of the laser cell. Coatings are basically inefficient for nuclear pumping since fissions occur primarily inside the coating and most of the charged-particle energy (80%) is lost in the coating. Since all the energetic charged-particles are created in the wall coating and then travel inward toward the laser cell centerline, homogeneous volume pumping cannot be realized. This effect results in such problems as the "gas-focusing effect" at higher pressures.

A much more efficient means of laser pumping incorporates the $^3He(n,p)^3H$ reaction. The ^3He reaction is initiated by a thermal neutron which is absorbed by the ^3He nucleus. The nucleus then disintegrates, producing a proton of 0.57 MeV and a triton of 0.19 MeV. Both these charged particles ionize and excite the gas medium homogeneously. Thus, homogeneous pumping can be achieved even at high pressures assuming no degradation of the neutron flux. Since He is a major constituent of many gas-laser systems, it is convenient (although expensive) to replace ^4He with the ^3He isotope. The ^3He reaction has previously been investigated with encouraging results but no proof of lasing.[6,7] We describe here the achieving, for the first time, of a nuclear-pumped laser using the volumetric ^3He reaction. This is the second most fundamental advancement in nuclear-pumped laser research; the first advancement was the demonstration of nuclear lasing by use of wall coatings. These advancements are expected to lead to an eventual self-critical nuclear-pumped laser system using UF_6.

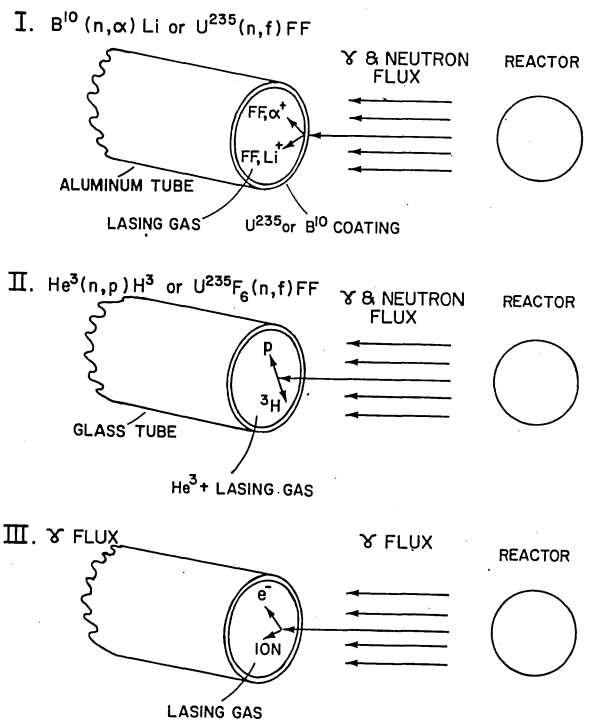

Figure 1. Nuclear reactions for direct nuclear excitation of lasers.

* This research has been carried out under partial support from NASA Grant NSG-1232.

II. Direct Nuclear-Pumped Volumetric ^{3}He-Ar Laser

Argon has many laser transitions which operate with high gain in the infrared region of the spectrum. Thus, it is a good candidate for volumetric nuclear pumping. In a recent experiment at the Army Pulse Radiation Facility, a mixture of ^{3}He-Ar was found to lase when exposed to the neutrons from a fast burst reactor.

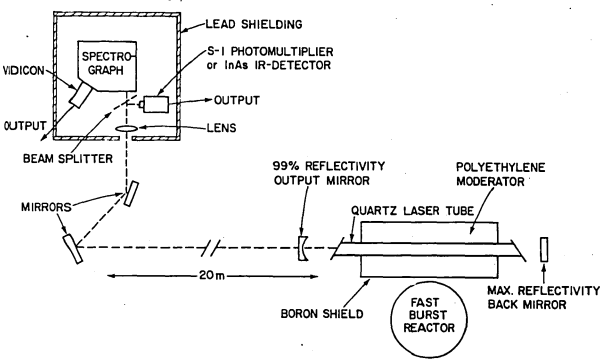

Figure 2. Experimental setup for nuclear-pumped laser experiments at the Army Pulse Radiation Facility.

The reactor experiment setup is shown in Fig. 2. The laser cell was constructed from quartz tubing, 81 cm long and 2 cm diameter, with each end cut at the Brewster angle. A dielectric-coated flat back mirror (99.5% reflective at 1.7μ) and a 2-meter radius of curvature output mirror (1% transmission at 1.7μ) were used to form the optical cavity. A 61 cm long by 15.5 cm diameter polyethylene moderator was placed around the laser cell to thermalize the fast neutrons generated by the Army Pulse Radiation Facility fast-burst reactor at the Aberdeen Proving Ground. A vacuum and gas-handling system was attached to the laser cell. The cell was baked-out prior to filling with research grade ^{3}He-Ar and base pressures on the order of 10^{-6} Torr were achieved. Electrodes were also attached to the laser cell which allowed electrically pulsed lasing at 1.79μ at low pressures (50 Torr). Using the electrically pulsed discharge the cavity mirrors and detection system were aligned. The detection system consisted of a variable filter wheel and an InAs (at 300°K) detector placed in a shielded cavity about 20 meters from the reactor. No radiation, gamma, or neutron noise was observed from the shielded InAs detector during any neutron pulse. The detector was calibrated for power output by using a c.w. 3.39μ He-Ne laser.

Figure 3 is a photograph of the laser output signal (upper trace) and the moderated neutron pulse (lower trace). Note the sharp laser threshold during the rise of the neutron pulse which is typical of nuclear-pumped lasers. The shape of the laser signal shows that energy is being deposited in the gas as long as a neutron flux is available and terminates only when the neutron flux ends. The laser produces an essentially steady-state output since the atomic and molecular processes

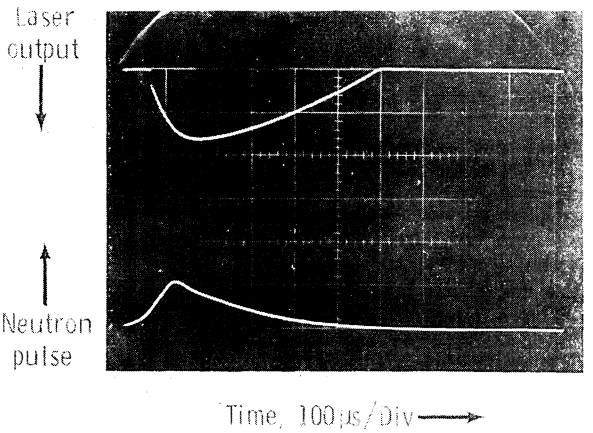

Figure 3. The upper trace shows the total laser output. The sharp threshold at ∿2.5 × 10^{16} n/cm^2-sec indicates lasing action. Total pressure is 200 Torr ^{3}He-Ar, 10% Ar. The average moderated neutron flux across the length of the laser cell is 8.4 × 10^{16} n/cm^2-sec. The moderated neutron pulse shape is shown in the lower trace.

operate on a much shorter time scale than the laser pulse shown in the photograph. The duration of the lasing pulse is simply dependent on the duration of the neutron flux available.

When the back cavity mirror was blocked, no lasing signal was observed. Also, when ^{4}He was substituted for ^{3}He during a neutron pulse, no detectable output was observed. Thus, the ^{3}He reaction did indeed pump the laser medium producing the first volumetric nuclear-pumped laser.

Figure 4 shows the scaling of the laser output at 1.79μ with the average moderator neutron flux over the length of the polyethylene moderator. A definite lasing threshold was noted at 1.4 × 10^{16} n/cm^2-sec. Note that with most high-gain c.w.

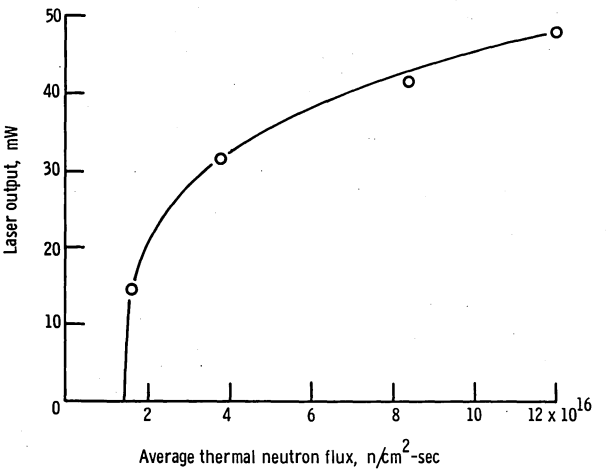

Figure 4. Laser output power (mW) at 1.79μ is shown vs. average moderated neutron flux along the length of the quartz laser cell. The total pressure was held constant at 400 Torr ^{3}He-Ar, 10% Ar. The laser threshold for low yield neutron pulses was 1.4 × 10^{16} n/cm^2-sec.

noble gas lasers, saturation effects appear soon after threshold is reached. Nevertheless, the output power of the nuclear-pumped laser continues to increase with neutron flux over the range investigated. The highest power output at 1.79μ was 50 mW with approximately 10^5W deposited in the gas volume.

Figure 5 shows the scaling of laser output power at 1.79μ with total pressure. Here the Ar concentration was held constant at 10%. Lasing took place from 200 to 700 Torr ^{3}He-Ar. Further studies are needed to determine the minimum and maximum pressures for laser operation. Also, the gas mixture of 10% Ar in ^{3}He used in the experiments may not be optimum for nuclear pumping. It is important to note that lasing took place at 700 Torr ^{3}He-Ar. This is the highest pressure reactor-driven nuclear-pumped laser to date, and demonstrates that a homogeneous discharge can be produced at high pressure with volumetric excitation.

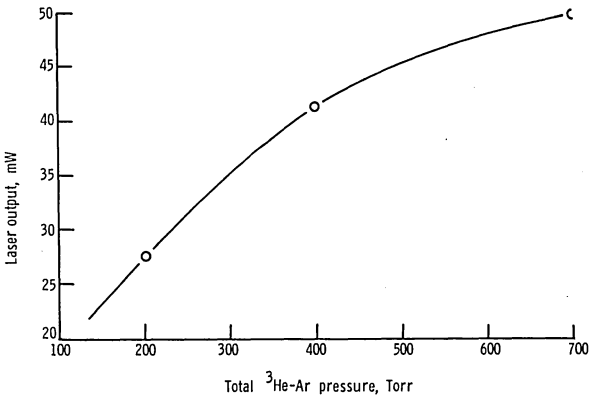

Figure 5. Laser output power (mW) at 1.79μ is shown vs. total ^{3}He-Ar pressure with the Ar concentration held constant at 10%. The average moderated neutron flux was held constant at 7.6×10^{16} n/cm^2-sec.

III. Electrically Pulsed He-Ar Laser

Using a fast-burst reactor to pump a laser medium is a slow process at best. On the average, only five reactor pulses per day can be achieved. Thus, it is desirable to use other means to study and optimize the laser parameters before nuclear pumping is attempted. With the He-Ar laser it has been found that a high-pressure (100 Torr) electrically-pulsed laser could be used to optimize the laser parameters.

Electrical lasing occurs, in the laboratory, at three wavelengths: 1.79μ, 2.31μ, and 1.27μ. Only the 1.79μ transition lases at high pressures (> 50 Torr He-Ar) and in the afterglow of the pulsed discharge. Thus, the 1.79μ transition was thought to be the best candidate for nuclear pumping for two reasons: First, high-pressure electrical lasing was achieved which indicated that pressure broadening of the transition did not adversely affect lasing behavior; and, second, electrical lasing took place in the afterglow of the discharge which indicated that processes such as collisional radiative recombination were important and lasing did not depend on a very sharp rise-time excitation pulse. The 1.27μ transition was found to be selfterminating; lasing stopped inside the voltage pulse and the transition was ruled out for nuclear pumping. Further research is needed at the reactor to definitely show that nuclear-pumped lasing is not occurring at 1.27μ and 2.313μ.

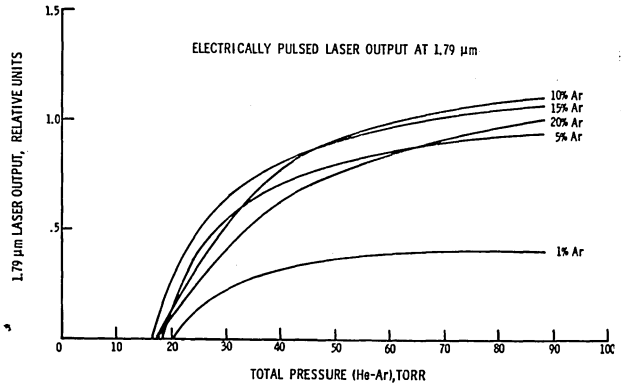

Figure 6. Electrically pulsed laser output at 1.79μ vs. total pressure of He-Ar in Torr for varying concentrations of Ar. Electrical pumping (E/P) was held constant.

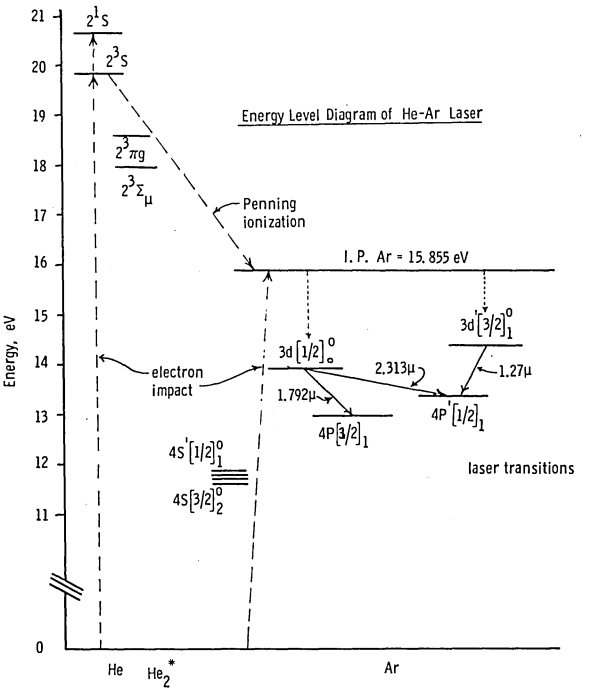

Figure 7. Energy level diagram of the He-Ar laser system showing the He atomic metastable species (far left), He_2 molecular species and the argon laser transitions of interest.

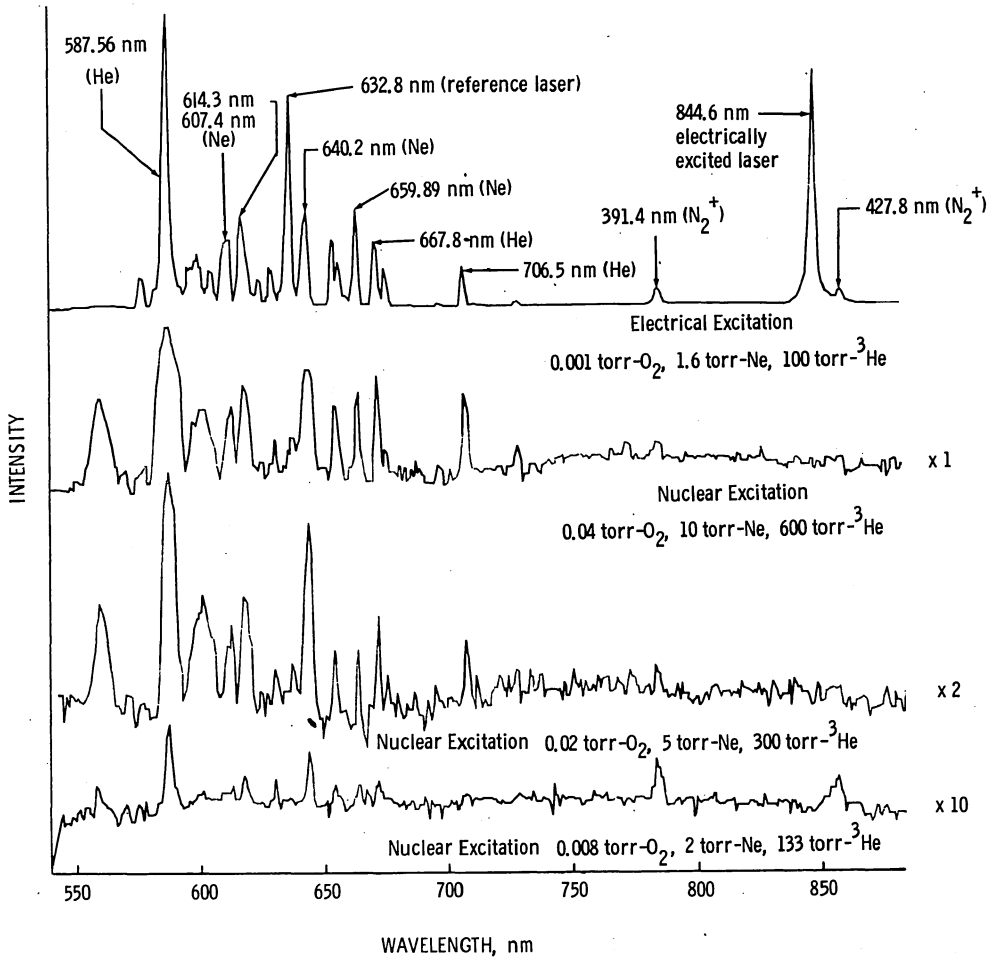

Figure 8. Comparison of nuclear and electrically excited ^{3}He-Ne-O_2 spectra. The nuclear spectra at 600 Torr is 10 times as intense as the spectra at 133 Torr. The average thermal neutron flux was held constant at 5×10^{15} n/cm^2-sec.

Figure 6 displays the results of a concentration study of lasing at 1.79μ versus total pressure of He-Ar. From the figure it appears that 10% Ar is very near the optimum concentration of Ar in He and, thus, this was the concentration used in the reactor experiments described earlier. Again, further research is needed to confirm that the electrically pulsed afterglow optimum concentration of 10% is the same optimum concentration under reactor excitation. It is hoped that electrically pulsed afterglow studies will help predict other more powerful and efficient nuclear-pumped lasers.

IV. Laser Excitation Mechanisms

Figure 7 is an energy level diagram of the He-Ar laser system. Note that there is no direct matching of energy levels between the helium and argon atoms. In the electrically pulsed laser experiments, lasing at 1.79μ was found in the afterglow, thus, direct electron input excitation of the upper laser level should be ruled out. The only other process that can adequately account for laser pumping is collisional radiative recombination of electrons with argon ions. The argon ions can be produced either by Penning ionization (by He 2^3 S metastable) or by direct electron impact ionization of argon. Collisional radiation recombination then occurs, eventually populating the upper laser level, the 3d [1/2]° state.[8] (The excess energy of recombination can be carried by either an electron, neutral atom, or molecule.) The 1.79μ transition probably has a higher gain than the 2.313μ transition and thus effectively quenches lasing on 2.313μ at higher pressures.

The addition of chlorine to the He-Ar laser was found to produce a substantial improvement in laser output[9,10] (factors of 2 to 6). This has been attributed to the depopulation of the argon 4S levels by resonant transfer to chlorine. Thus, back excitation from the 4S to the $4P[3/2]_1$ lower laser level is reduced and output power at 1.79μ increases. This same process will be attempted in the nuclear-pumped laser experiments.

V. ^3He-Ne-O_2 Spectra by Nuclear Excitation

The spectra shown in Fig. 8 is a comparison of He-Ne-O_2 spectra taken under nuclear and electrical pumping. The top trace is the He-Ne-O_2 spectra with lasing occurring at 8446 Å in OI under electrically pulsed excitation. The lower three traces show ^{3}He-Ne-O_2 spectra taken with nuclear excitation using the same laser cavity and cell used for the electrical excitation spectra. Note that nuclear excited lasing at 8446 Å is conspicuously missing from the nuclear induced spectra. Lasing has not been achieved in ^{3}He-Ne-O_2 for total pressures from 30 to 600 Torr and average thermal neutron fluxes from 8×10^{15} to 5×10^{16} n/cm^2-sec. Although lasing did not occur, the spectra of the nuclear and electrically pulsed discharges are very similar. The broadening of the nuclear spectra at high pressures is most probably due to the high-intensity light spilling over into adjacent channels of the optical multichannel analyzer used for recording the spectra.

These results indicate that the electrically pulsed discharge at high pressures (>50 Torr) may have the same dominant process as the nuclear-induced discharge. This should help immensely in predicting and optimizing future nuclear-pumped lasers.

VI. Summary

Listed in Table 1 is a summary of all nuclear-pumped lasers as of May 1976. The last four nuclear lasers have been pumped with reactors and are the most important for practical applications. Very rapid progress is now being made in this new field. The two major means of energy deposition, coating and volumetric sources, have been demonstrated, with the goal of a self-critical nuclear laser still being agressively sought. After examination of Table 1, it is encouraging to note that operating pressures are rapidly increasing. This is important if high-power nuclear lasers are to become a reality. In the future more attention must be paid to higher pressure excimer laser systems. Such systems are ideally suited for nuclear pumping since they operate at high pressures and have high saturation intensities. The lasing wavelengths are approaching the visible region of the spectrum which is of major interest in laser fusion and isotope separation. The duration of the laser output is also increasing and has reached essentially steady-state operation. This is of major importance since one of the major advantages of the nuclear-pumped laser is that it has the potential of being the only practical steady-state high-power laser system. Laser power outputs and efficiencies have been quite small (except for the CO laser) but this has been due to the high-gain

NUCLEAR PUMPED LASERS (May 1976)	WAVELENGTH	PRESSURE (TORR)	THERMAL FLUX THRESHOLD (n/cm^2-sec)	ENERGY DEPOSITED (J/ℓ) TIME PERIOD	LENGTH OF LASER OUTPUT	PEAK POWER DEPOSITED (W/ℓ)	PEAK LASER OUTPUT (WATTS) (J/ℓ)
γ-Pumped HF laser Los Alamos		1.3		≈ 923 12 nsec	12 nsec	8×10^{10}	5×10^8 92.3
γ-Pumped Xe Amplified spontaneous emission Livermore	~ 1700 Å	5,200 7,800 10,500 13,000 15,700		5×10^3 to 15×10^3 17nsec	31-10 nsec A.S.E.	2.7×10^{11} to 9×10^{11}	
Fission Fragment CO Laser Sandia Labs	5.1-5.6 μm	100	~5×10^{16}	200 150 μsec	50 μsec	1.3×10^6	2 - 6 0.2
Fission Fragment He-Xe Laser Los Alamos	3.0-4.2 μm	200	3×10^{15}	50 150 μsec	235 μsec	3.3×10^5	> .01 2.8×10^{-5}
$B^{10}(n,\alpha)\ Li^7$ Ne-N_2 Laser Univ. of Illinois	8629 Å and 9393 Å	75-400	1×10^{15}	313 to 1000 10 msec	6 msec	3×10^4 to 1×10^5	1.5×10^{-3} 2.4×10^{-5}
$He^3(n,p)H^3$ He-Ar Laser NASA-Langley	1.79 μ	200-700	1.4×10^{16}	24 to 270 150 μs	550 μsec	1.6×10^5 to 1.8×10^6	0.05

Table 1. A table of all published nuclear-pumped laser results as of May 1976. The γ-pumped results were obtained from underground nuclear explosions; the other lasers are reactor-driven.

laser systems studied thus far. Future research must move in the direction of low gain, high-saturation-intensity laser systems. In this regard, the excimer system appears very encouraging.

The assistance of the staff of the Aberdeen Army Pulse Radiation Facility and of Mr. J. Fryer is gratefully acknowledged.

References

1. Schneider, R. T.; and Thom, K.: Nuclear Tech. 27, 34 (1975).

2. Thom, K.; and Schneider, R. T.: AIAA J. 10, 400 (1972).

3. McArthur, D. A.; and Tollefsrud, P. B.: Appl. Phys. Lett. 26, 187 (1975).

4. Helmick, H. H.; Fuller, J.; and Schneider, R. T.: Appl. Phys. Lett. 20, 327 (1975).

5. De Young, R. J.; Wells, W. E.; Miley, G. H.; and Verdeyen, J. T.: Appl. Phys. Lett. 28, 519 (1976).

6. De Young, R. J.; Wells, W. E.; and Miley, G. H.: Appl. Phys. Lett. 28, 194 (1976).

7. Andriakhin, J. M., et al.: ZHETF, Pis. Red. 12, 83 (1970).

8. Pressley, R. J., ed.: Handbook of Lasers, (The Chemical Rubber Co., Cleveland, Ohio, 1971) Chap. 6, p. 210.

9. Dauger, A. B.; and Stafsudd, O. M.: Appl. Optics 10, 2690 (1971).

10. Dauger, A. B.; and Stafsudd, O. M.: IEEE Jour. of Quantum Electronics, QE-6, 572 (1970).

DISCUSSION

ANON: Did you test lasing by detuning the cavity?

R. J. De YOUNG: No, we didn't detune because of the experimental difficulty involved. However, we did, under conditions ideal for lasing, replace the ^{3}He with ^{4}He in the cavity. We observed no lasing, thus concluding that it is quite definitely the ^{3}He reaction that is pumping the laser and not any stray gammas or fast neutrons.

RECENT NUCLEAR PUMPED LASER RESULTS†

G. H. Miley, W. E. Wells, M. A. Akerman and J. H. Anderson
Nuclear Engineering Program
University of Illinois
Urbana, Illinois 61801

Abstract

Recent direct nuclear pumped laser research at the University of Illinois has concentrated on experiments with three gas mixtures (Ne-N_2, He-Ne-O_2, and He-Hg). One mixture has been made to lase and gain has been achieved with the other two. All three of these mixtures are discussed with particular attention paid to He-Hg. Of interest for DNP work is the 6150-Å ion transition in Hg^+. The upper state of this transition is formed directly by charge transfer and by Penning ionization.

Introduction

Research on radiation-induced plasmas has been pursued at the University of Illinois since 1963.[1-5] In the last decade, work has concentrated on plasmas suitable for nuclear lasers.[6-13] Previous reviews of this effort were presented in Refs. 14-18. Other experiments have dealt with nuclear enhancement of electrically pumped gas lasers.[19-23] Also, more recently the possible use of nuclear pumping for laser fusion applications has been proposed.[24-26]

Recent Direct Nuclear Pumped (DNP) laser research at the University of Illinois has centered on three gas mixtures. The first is neon-nitrogen which has been made to lase in the U. of I. TRIGA reactor.[27] The second is helium-neon-oxygen, for which gain has been measured.[28] The most recent work has concentrated on helium-mercury, in which gain also has been achieved. Work on the first two mixtures will be briefly reviewed while He-Hg results will be described in detail.

The Ne-N_2 DNP Laser

The neon-nitrogen laser is important for several reasons. It has the shortest wavelength and lowest neutron flux threshold of any DNP laser demonstrated to date. Also the pumping mechanism appears to lead the way to an important class of recombination driven DNP lasers.

The electrical pumping mechanism of the neon-nitrogen laser has been shown to be recombination. Recent studies by G. Cooper, et al.[29] indicate that collisional-radiative recombination of N^+ into the upper laser level is the most probable pumping mechanism. The basic question unanswered, however, is how N^+ is so efficiently formed in the radiation induced plasma. As can be seen from the energy-level diagram of Fig. 1, this would require

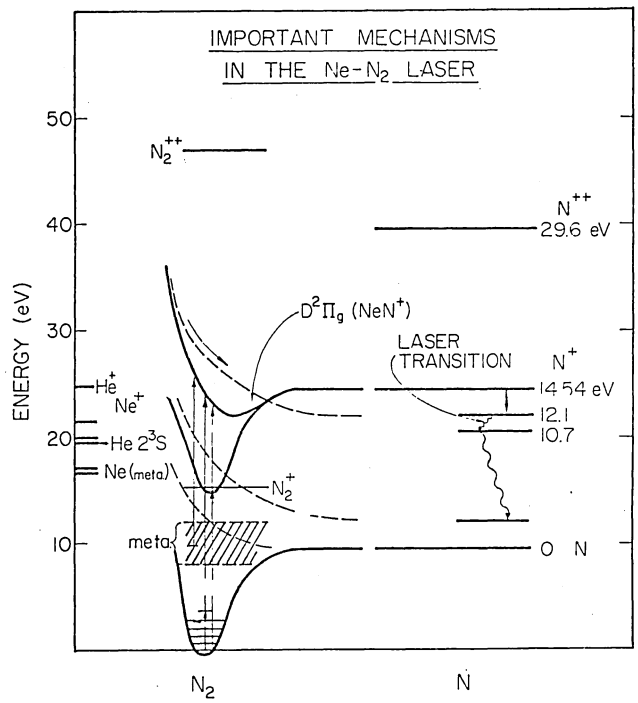

Fig. 1. Energy level diagram of the Ne-N_2 DNPL.

a two-step process if direct neon-nitrogen collisions are involved because the energy levels of Ne^+ and lower excited states are too low for one-step excitation. Further, there is strong evidence that absorption of nitrogen on the laser tube wall plays a role in the process. This has been demonstrated by the dependence on the previous history of nitrogen in the laser cell. We are currently pursuing research to understand this very complicated process.

Since the bulk of electrons in a DNP plasma are low energy, recombination can be more efficient than in electric field sustained plasmas where the electron temperature is high.[18]

In present experiments the laser is placed next to the reactor core and external optics are aligned to focus laser light on the slits of two monochromators and an S-1 photomultiplier. This is pictured in Fig. 2. A fan, driven by a high speed electric motor, alternately unblocks and blocks the back mirror so that gain and/or lasing can be positively identified.

†This work was supported by the Physical Science Division of ERDA.

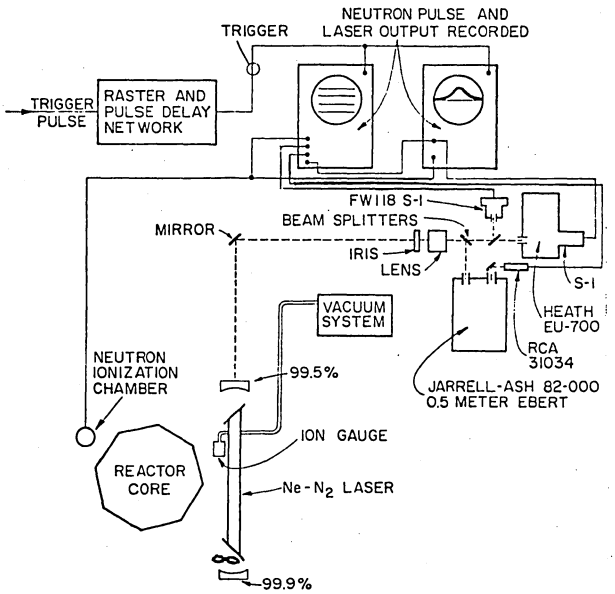

Fig. 2. Reactor experimental setup.

While lasing has been achieved with uranium coated tubes in other experiments,[30-32] a 0.4 mg/cm^2 coating of B^{10} is normally used on the inside surface of an aluminum tube which forms the laser discharge region. Excitation is then provided by the reaction:

$$_0n^1 + {}_5B^{10} \rightarrow {}_2He^4 + {}_3Li^7 + 2.3 \text{ MeV}$$

Figure 3 shows a typical Ne-N_2 laser output with the neutron flux profile superimposed. The top trace shows the 8629-Å laser line which tends to cut off near the peak of the neutron pulse.

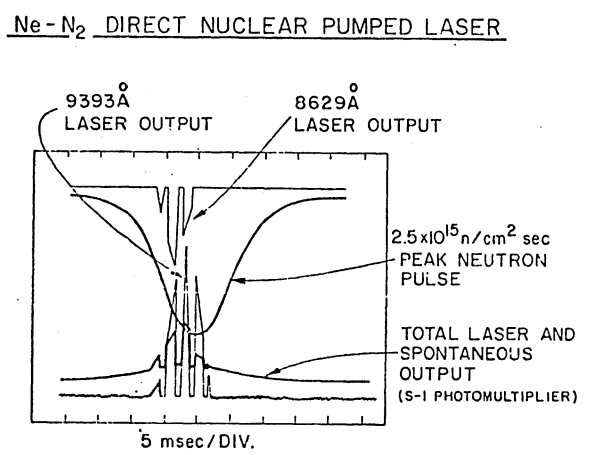

Fig. 3. Oscilloscope trace of Ne-N_2 DNPL. Shows laser output vs. time.

The 9393-Å transition shown on the trace lases about two milliseconds past the peak. This difference in timing is attributed to competition for excitation between the upper states.

Particular attention should be paid to the chopping of the signal which is the result of a fan inside the cavity (see Fig. 2). This provides an easy, but conclusive, proof of lasing even though the laser is behind 11 feet of concrete shielding. The same technique provides a sensitive method to measure gain and this will be discussed later with regard to optimizing He-Ne-O_2 and He-Hg mixtures. In addition to these details of the Ne-N_2 laser, a peculiarity with respect to the time history that may hold the key to the N^+ production mechanism in the reactor should be mentioned. When a small amount of N_2 is added to the normal mixture, lasing almost stops during the next pulse. Subsequent pulses where no N_2 is added yield much larger laser signals. The cycle is repeated when another small amount of nitrogen is added. This behavior, diagramed in Fig. 4, is interpreted as resulting from nitrogen being absorbed on the wall such that emission during the reactor pulse in some way contributes to N^+ production and subsequent lasing by recombination as discussed earlier.

He-Ne-O_2 Optical Gain

Early work with a Ne-O_2 laser utilizing B^{10} as the source of excitation showed promise.[33] However, results were erratic and it was difficult to control the small O_2 concentration required due to absorption on the tube wall. The discovery that the addition of large amounts of helium made high pressure electrical lasing possible was a breakthrough.[34] It also made possible the use of the $He^3(n,P)T$ reaction to produce excitation in the reactor, effectively controlled the oxygen absorption and provided effective pumping by col-

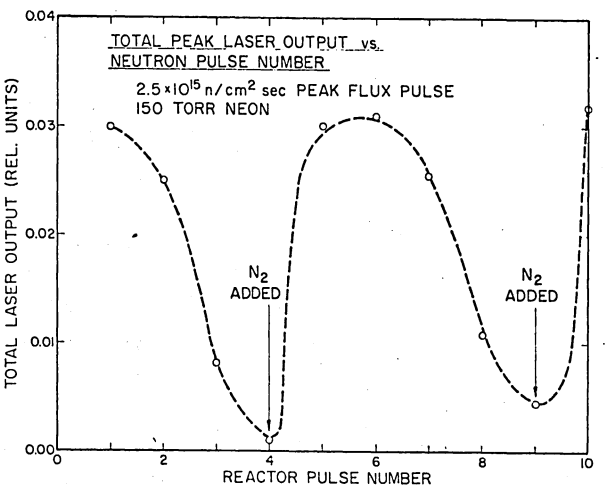

Fig. 4. Variation of total output vs. number of reactor pulse in a series of 10 pulses.

lision transfer. While actual lasing was not achieved, extensive chopper experiments (using the fan as previously described to alternately unblock and block the cavity) conclusively demonstrated gain on the 8446-Å line (the same line used in the electrical He-Ne-O_2 laser). This is illustrated in Fig. 5 where the chopped output from 8446 Å is shown along with two other lines, 7775 Å and 8780 Å. With helium pressures of 700 torr and a 0.2% O_2 concentration, gain was observed. The unblocked to blocked ratios of the two other lines, though within the high reflectivity bandwidth of the cavity mirrors, are roughly two, i.e. near the value expected for spontaneous emission. Since neither line is expected to invert, this demonstrates that the technique is working when compared to the 8446 Å output where ratios approaching 5 are observed. Such measurements indicate a gain of ~0.9% has been achieved with a mixture of 0.2% O_2 and 0.52% Ne at pressures up to 1 atm. Optimal mixtures are discussed in some detail in Ref. 28, and it is thought that higher neutron fluxes and rise time could lead to sufficient gain to make an attractive laser. If successful this could replace Ne-N_2 as the shortest wavelength to date.

He-Hg Optical Gain

This mixture differs from the first two mixtures in that energy transfers directly from helium ions and metastables to the upper laser level via thermal-energy charge-exchange and Penning ionization of metastable states, respectively. (see Fig. 6) This pumping mechanism is compatible with radiation-induced plasmas. The potential use of ^{3}He to achieve a volume source of excitation at high pressures is an important feature of He-Hg. Finally, when it lases, it will provide an output in the visible range.

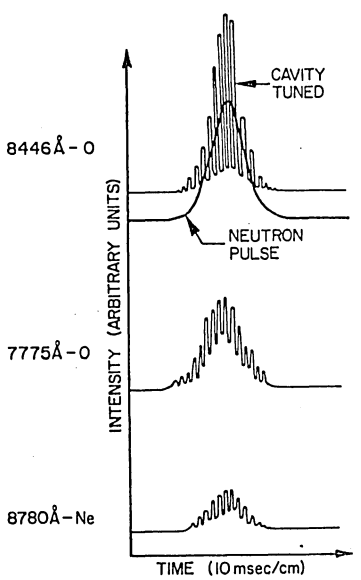

Fig. 5. Unblocked-blocked ratios vs. time. Shows comparison between 8446 Å oxygen transition exhibiting gain, and two others that do not.

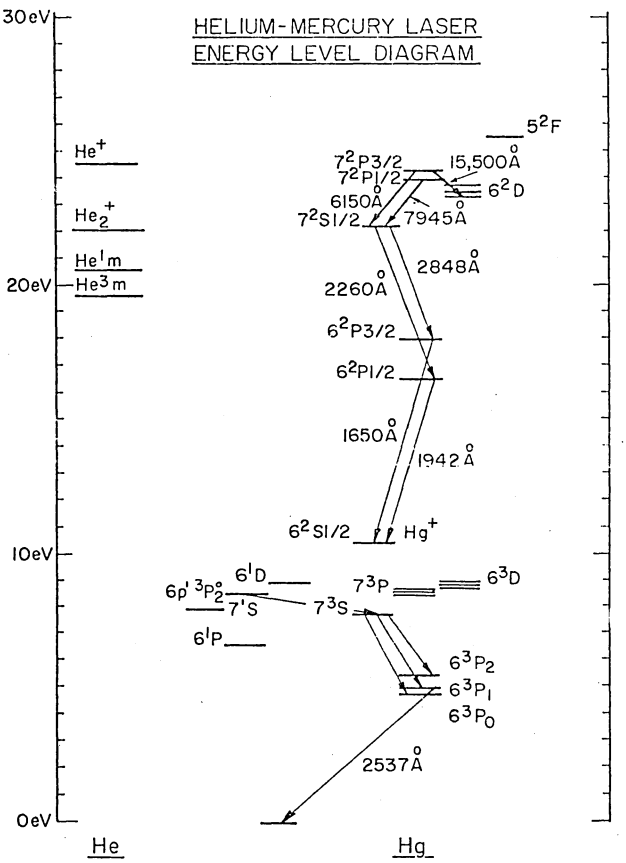

Fig. 6. Energy level diagram for the helium-mercury system. The 6150 Å-transition from the $7^2P_{3/2}$ level is shown.

The 6150-Å transition was first mentioned as a possible Direct Nuclear Pumped Laser by Andriakhin[35] who reported a large light output in the visible region of the spectrum when a He-Hg laser was operated in a pulsed reactor. At the University of Illinois a hollow cathode laser design[36] was adapted to operate next to the reactor core. The hollow cathode was a 60-cm length of aluminum cylinder 2.5 cm in diameter with an internal coating of B^{10}. It serves a dual purpose of being a hollow cathode for the electrical laser and providing the nuclear reactions for the DNP laser. The electrodes were contained in a pyrex tube that was wrapped with three sections of heater tapes. By heating the tube, the density of mercury within can be controlled. Three chromel-alumel thermocouples are used to monitor temperatures along the laser. Mercury is contained in two reservoirs which are maintained at a temperature slightly lower than that of the main tube.

Again, a chopping fan in the laser cavity provides unblocked to blocked measurements (see Fig. 7). The laser is mounted on an aluminum carriage and placed next to the core of the reactor.

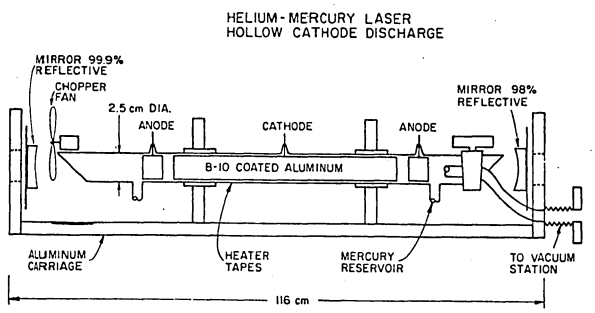

Fig. 7. He-Hg laser and carriage used in these experiments.

The placement of the laser is similar to the Ne-N_2 experimental arrangement shown in Fig. 2. The laser is evacuated with a forepump, and then filled to the desired helium pressure. When the reactor is pulsed, signals such as those shown in Fig. 8 are observed. The top trace shows the modulated 6150-Å signal produced by the chopper fan. The middle trace displays the neutron pulse while the bottom trace shows the modulated signal with the monochromator set at 6560 Å. The light thus collected could be from the 6560-Å He-II transition, or the 6563-Å H-I transition due to a gas impurity. As with the Ne-N_2 experiments shown earlier, this transition should not be inverted. It lies within the high reflectivity range of the cavity, hence, serves as a reference to demonstrate that no extraneous effects are occurring. As expected, the unblocked-blocked ratio for it is ~2, whereas the 6150-Å ratio is ~5 providing a clear demonstration of gain.

Unblocked to blocked ratio data from Fig. 8 are shown as a function of neutron flux in Fig. 9. The 6560 Å ratios remain at ~2 within the accuracy of the measurement. The 6150-Å ratios increase from ~2 at 4 x 10^{14} n/cm^2-sec to 4.8 at 3 x 10^{15} n/cm^2-sec, suggesting a threshold for gain <10^{14} n/cm^2-sec. In later experiments, the mirror alignment and mercury pressure were optimized and even higher ratios, approaching 8 were obtained. This is also shown in Fig. 9.

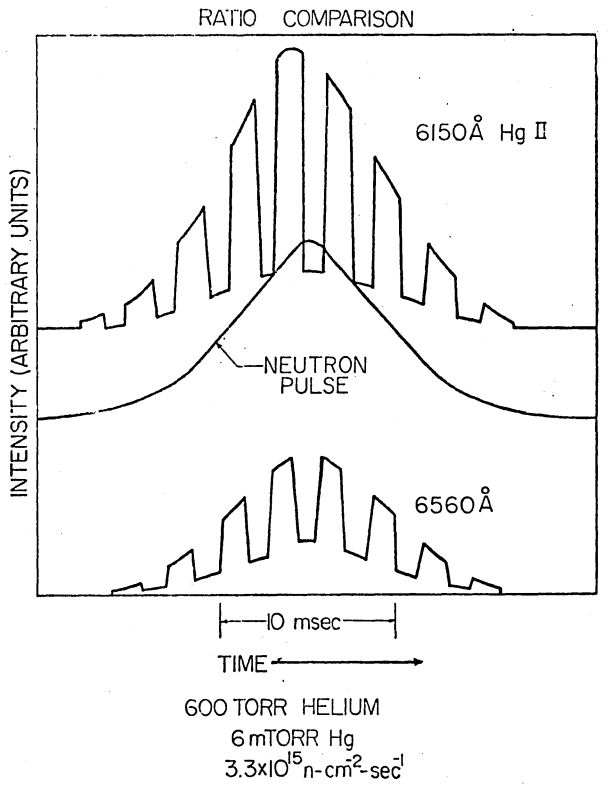

Fig. 8. Ratio comparison showing 6150-Å Hg-II transition with gain, and another transition for which gain is not expected. The helium and mercury pressures were 600 Torr and 6 mTorr respectively.

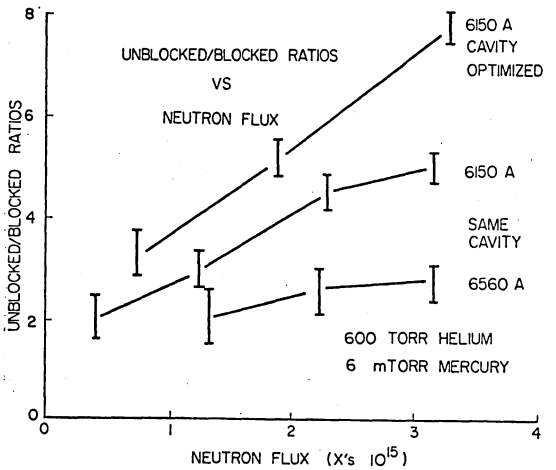

Fig. 9. Bottom two curves: Variation of unblocked-blocked ratios vs. neutron flux for Fig. 8. Top curve: The 6150-Å ratios vs. neutron flux for more optimal conditions.

The gain can be predicted from our unblocked to blocked ratios using the approximate ray-tracing theory of Ref. 28. In the present case, gains up to 1.5%/m are estimated. Losses for the present cavity are ≳5%, but if these losses can be reduced somewhat, the gain may be sufficient for lasing. If not, use of a higher neutron flux, such as can be obtained with a fast burst reactor, may be required.

Another important variable is the gas pressure. Preliminary attempts to optimize this are shown in Fig. 10 in which the unblocked to blocked

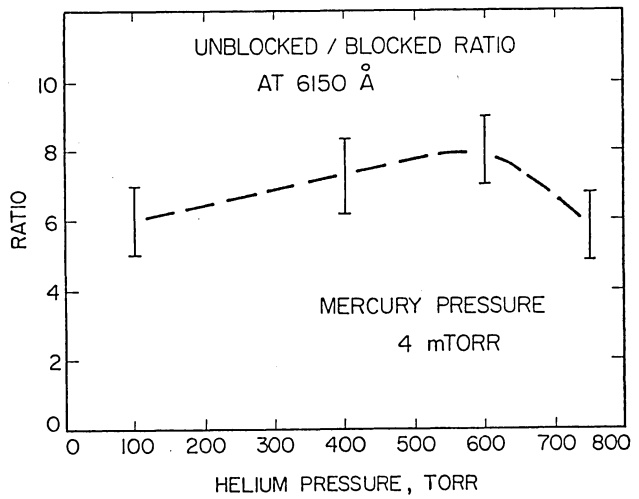

Fig. 10. Ratios vs. helium pressure, showing a maximum value around 600 Torr.

ratio is shown as a function of helium pressure for a fixed mercury pressure (~4 mTorr). A broad peak is observed near 600 Torr helium pressure. A similar curve with mercury pressure as the variable shows ~4 mTorr to be the optimum mercury pressure.

He-Hg Spectra

A camera compatible with the GCA McPherson EU-700 monochromator was constructed to photograph the spectra generated in reactor tests of DNP lasers. Figure 11 shows a side view cutaway of the reactor thruport, in which the laser plasma tube is placed, while the monochromator and camera are at the exit. Poloroid 57 film was used to photograph the spectra, though the camera is compatible with any 4"x5" sheet film.

Figure 12 is a photograph of the helium-mercury spectra between 5450 Å and 6400 Å.[37] The left strip shows the spectra created during a

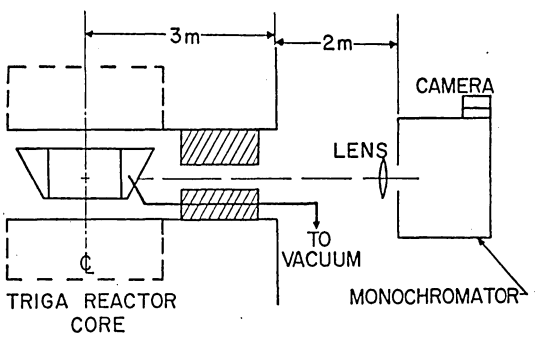

Fig. 11. Reactor arrangement for making photographic spectra measurements (not to scale).

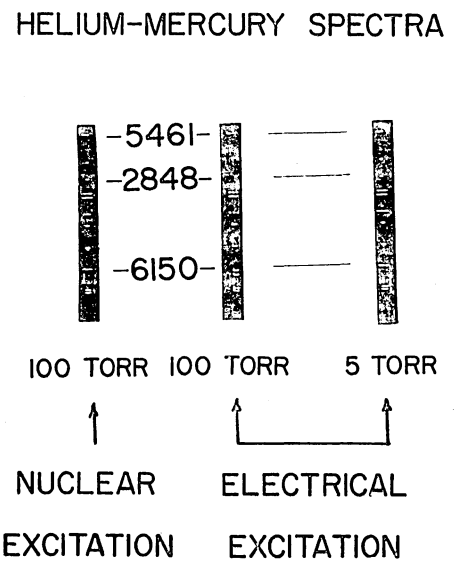

Fig. 12. Spectra for three different conditions: On the left the 6150-Å line is present at 100 Torr with nuclear excitation, while two electrical excitation spectra are shown at right for comparison.

neutron pulse at 100 Torr helium pressure. The right strip shows the same wavelength range at 5 and 100 Torr, but with electrical excitation only.

It is observed that the 6150-Å line is present in the 5-Torr electrical case but disappears at 100-Torr. In the nuclear case it remains clearly visible at 100-Torr, emphasizing that there is a difference in pumping mechanisms whereby high pressure operation with nuclear pumping may be uniquely possible. The excitation mechanisms are not well understood yet, however, so the details of the mechanisms involved must await further study.

There are other differences between the two spectra that do not show up in this reproduction of the spectra. Two Ångström resolution has been achieved with the camera-monochromator combination and an integrated neutron flux of 6.6×10^{14} n/cm^2.

Conclusion

Several schemes for producing DNP lasers have been described along with the experimental work that has been accomplished to date. A nuclear pumped laser operating on two wavelengths in the near IR and two other systems that have nuclear-induced population inversions have been discussed. One of these, the He-Hg system, potentially offers a visible laser. In addition, a simple means of identifying gain using a modulated cavity has been described. Finally, a means of photographing spectra and some results with He-Hg have been described.

DNP laser research at the University of Illinois has centered not only on a search for

high pressure, high power nuclear lasers, but also on a search for the unique mechanisms that will allow suitable systems for future applications to be predicted.

Figure 13 lists a summary of nuclear lasers produced as of May 1976,[27,30-32,35,38] that utilize research reactors and have been described in archival literature. Referring to the Illinois results, the Ne-N_2 laser exhibits the lowest thermal neutron flux threshold, shortest wavelengths, and longest duration of any of the DNP lasers. Further, it appears to employ a recombination pumping scheme, that could be the precursor of other more efficient and powerful lasers. The He-Ne-O_2 and the He-Hg systems are both promising in that gain has been observed experimentally. They represent a search for suitable lasers that utilize ^{3}He as a volume source, i.e., they can operate at high pressure, and also have wavelengths in or near the visible.

NUCLEAR PUMPED LASERS MAY 1976	PUMPING REACTION	WAVELENGTH	THERMAL FLUX THRESHOLD (n/cm^2-sec)	LENGTH OF LASER OUTPUT	PEAK LASER POWER
^{3}He-Hg MOSCOW STATE	^{3}He(n,p)T	LASING IMPLIED BUT UNVERIFIED		1 msec	?
CO SANDIA LABS	^{235}U(n,F)FF	5.1-5.6μ	~5×10^{16}	50μsec	2-6 W
He-Xe LOS ALAMOS UNIV. OF FLORIDA	^{235}U(n,F)FF	3.5μ	3×10^{15}	150μsec	>.01 W
Ne-N_2 UNIV. OF ILLINOIS	^{235}U(n,F)FF and ^{10}B(n,α)^{7}Li	8629Å and 9393Å	1×10^{15}	6 msec	1.5mW
^{3}He-Ar NASA LANGLEY	^{3}He(n,p)T	1.79μ	1.4×10^{16}	365μsec	50 mW

Fig. 13. Summary of DNPL experiments performed with research nuclear reactors.

References

1. G. H. Miley and P. Thiess (eds.), "Proceedings of the Illinois 1963 Summer Institute on Direct Conversion," Vol. I, II, and III. Sponsored by AEC-ASEE; published, N.E. Program, University of Illinois (1964).

2. G. H. Miley, "Fission-Fragment Energy Spectra Effects in Fission-Electric Cell Efficiency Calculations," *Trans. Am. Nucl. Society, 7,* No. 2 (1964).

3. A. K. Bhattacharya, L. Goldstein, F. T. Adler, J. T. Verdeyen and E. P. Bialecks, "Microwave Measurement of Dynamic Reactor Response," *Appl. Phys. Letters, 5,* 242 (1964).

4. G. H. Miley, "Fission-Fragment Effects as Related to Fission-Electric-Cell Efficiencies," *Nuc. Sci. and Eng., 24,* 322-331 (1966).

5. G. H. Miley, *Direct Conversion of Nuclear Radiation Energy,* American Nuclear Society, Hinsdale, IL, pp. 7-12 (1970).

6. J. C. Guyot, G. H. Miley and J. T. Verdeyen, "Metastable Densities in Noble-Gas Plasmas Created by Nuclear Radiations," *J. of Appl. Phys., 42,* 5379 (1971).

7. J. C. Guyot, G. H. Miley and J. T. Verdeyen, "Application of a Two-Region Heavy Charged Particle Model to Noble-Gas Plasmas Induced by Nuclear Radiations," *Nuc. Sci. and Eng., 48,* 373-386 (1972).

8. P. E. Thiess and G. H. Miley, "Optical Emission from Noble-Gas Plasmas Created by Alpha Particles," *Trans. ANS, 16,* 134 (1971).

9. P. E. Thiess and G. H. Miley, "Optical Spectra of High-Pressure Helium Irradiated by Alpha Particles," *Trans. ANS, 15,* 706 (1972).

10. P. E. Thiess and G. H. Miley, "New Near-Infrared and Ultraviolet Gas-Proportional Scintillation Counters," *IEEE Trans. Nuc. Sci., NS-21,* p. 125 (1974).

11. P. E. Thiess and G. H. Miley, "Optical Spectra Produced in Neon and Argon Mixtures by Ionizing Radiation," *Trans. Am. Nucl. Soc., 19,* 64 (1974).

12. P. E. Thiess and G. H. Miley, "Optical Spectra of High-Pressure Helium Mixtures Irradiated by Alpha Particles," *Trans. Am. Nucl. Soc., 16,* 56 (1971).

13. J. C. Guyot, G. H. Miley and J. T. Verdeyen, "Calculated and Measured Atomic Metastable Densities in Noble-Gas Plasmas Induced by Nuclear Radiations," *Trans. Am. Nucl. Soc., 16,* 135 (1971).

14. J. C. Guyot, G. H. Miley, J. T. Verdeyen and T. Ganley, "On Gas Laser Pumping Via Nuclear Radiations," *Trans. of the Symp. of Research on Uranium Plasmas and their Technological Application, NASA SP-236* (1970).

15. G. H. Miley, "Nuclear Radiation Effects on Gas Lasers," in *Laser Interactions,* (Schwarz and Hora, eds.), Plenum Press, pp. 43-57 (1972).

16. G. H. Miley, J. T. Verdeyen, T. Ganley, J. Guyot and P. Thiess, "Pumping and Enhancement of Gas Lasers via Ion Beams," *11th Symp. on Electron, Ion and Laser Beam Technology* (R.F.M. Thomley, ed.), San Francisco Press, Inc. (1971).

17. G. H. Miley, J. T. Verdeyen and W. E. Wells, "Direct Nuclear Pumped Lasers," *Proc. 28th Gaseous Electronics Conf., BB-1,* Univ. of MO at Rolla (1975).

18. G. H. Miley and W. E. Wells, "Direct Nuclear Pumped (DNP) Laser," *IXth Int. Conf. on Quantum Electronics, Amsterdam, The Netherlands, B-5* (1976).

19. T. Ganley, J. T. Verdeyen and G. H. Miley, "Enhancement of CO_2 Laser Power and Efficiency by Neutron Irradiation," *Appl. Phys. Letters, 18,* no. 12, p. 568 (June 1971).

20. R. J. DeYoung, W. E. Wells and G. H. Miley, "Enhanced Output from He-Ne Laser by Nuclear Preionization," *1974 Int. Electron Devices Meeting,* Washington, DC (Dec. 1974).

21. R. J. DeYoung, E. Seckinger, W. E. Wells and G. H. Miley, "Studies of Nuclear Radiation Enhancement and Pumping of Noble Gas Lasers," Paper 2A10, *1974 Int. IEEE Conf. on Plasma Science, Univ. of TN, Knoxville, TN* (1974).

22. R. J. DeYoung, M. A. Akerman, W. E. Wells and G. H. Miley, "Studies of Radiation-Induced Laser Plasmas," *1975 Int. Conf. on Plasma, 3D2, Univ. of MI, Ann Arbor, MI, 75CH0987-8-NPS* (1975).

23. M. A. Akerman, M. Konya, W. E. Wells and G. H. Miley, "Nuclear Radiation Enhancement of a Helium-Mercury Laser," *Trans. Am. Nucl. Soc., 22,* 133 (1975).

24. G. H. Miley, *Fusion Energy Conversion,* Published by the American Nuclear Society (1976).

25. G. H. Miley, "Direct Pumping of Lasers by Fusion Reactors," *Trans. Am. Nucl. Soc., 15,* 633 (1972).

26. W. E. Wells, "Laser-Pellet Fusion by Energy Feedback to a Direct Nuclear Pumped Auxiliary Laser," *Proc. 1975 IEEE Conf. Plasma Science, 3D4, Univ. of MI, Ann Arbor, MI* (1975).

27. R. DeYoung, W. E. Wells, G. H. Miley and J. T. Verdeyen, "Direct Nuclear Pumping of an Ne-N_2 Laser," *Appl. Phys. Letts., 28,* 519 (May 1976).

28. R. J. DeYoung, W. E. Wells and G. H. Miley, "Optical Gain in a Neutron-Induced ^{3}He-Ne-O_2 Plasma," *Appl. Phys. Letts., 23,* 194 (Feb. 1976).

29. G. Cooper, J. T. Verdeyen, W. Wells and G. H. Miley, "The Pumping Mechanism for the Neon Nitrogen Nuclear Excited Laser," *The Third Conf. on Partially Ionized Plasmas, Princeton University* (1976).

30. D. A. McArthur and P. B. Tollefsrud, "Observation of Laser Action in CO Gas Excited Only by Fission Fragments," *Appl. Phys. Letters, 26,* 181 (1974).

31. H. H. Helmick, J. L. Fuller and R. T. Schneider, "Direct Nuclear Pumping of a Helium-Xenon Laser," *Appl. Phys. Letters, 26,* 327 (1975).

32. J. W. Eerkins, Technology Review Program for Research and Technology Division, Air Force Systems Command (Jan. 1967) (unpublished).

33. E. L. Seckinger, "Study of the Neon-Oxygen Laser under Heavy Particle Bombardment," M.S. thesis, Univ. of Illinois (1974) (unpublished).

34. R. J. DeYoung, W. E. Wells and G. H. Miley, "Lasing in a Ternary Mixture of He-Ne-O_2 at Pressures up to 200 Torr," *J. of Appl. Phys., 47,* No. 2 (April 1976).

35. V. H. Andriakhin, V. V. Vasil'nov, S. S. Krasil'nikov, V. D. Pis'mennyi and V. E. Khvostinov, "Radiation of Hg-He^3 Gas Mixture Bombarded by a Neutron Stream," *JETP Letters, 12,* 2, p. 58 (July 1970).

36. H. Wieder, R. A. Meyers, C. L. Fisher, C. G. Powell and J. Colombo, "Fabrication of Wide Bore Hollow Cathode Hg^+ Lasers," *R.S.I., 38,* No. 10, p. 1538 (Oct. 1967).

37. M. A. Akerman, W. E. Wells and G. H. Miley, "Charge Exchange Phenomena in a Nuclear Radiation Produced He-Hg Plasma," *1976 IEEE Int. Conf. on Plasma Science, 3C10, Univ. of TX at Austin, 76CH1083-5-NPS* (1976).

38. N. W. Jalufka, R. J. DeYoung, F. Hohl and M. D. Williams, "A Nuclear Pumped ^{3}He-Ar Laser Excited by the ^{3}He(n,p)^{3}H Reaction," To be published, *Appl. Phys. Letters,* Aug., 1976.

NUCLEAR FISSION FRAGMENT EXCITATION OF ELECTRONIC TRANSITION LASER MEDIA

D. C. Lorents, M. V. McCusker, and C. K. Rhodes
Molecular Physics Center
Stanford Research Institute, Menlo Park, California 94025

Abstract

The properties of high energy electronic transition lasers excited by fission fragments are examined. Specific characteristics of the media including density, excitation rates, wavelength, kinetics, fissile material, scale size, and medium uniformity are assessed. The use of epithermal neutrons, homogeneously mixed fissile material, and special high cross section nuclear isotopes to optimize coupling of the energy to the medium are shown to be important considerations maximizing the scale size, energy deposition, and medium uniformity. A performance limit point of ~ 1000 j/liter in ~ 100 μsec pulses is established for a large class of systems operating in the near ultraviolet and visible spectral regions. It is demonstrated that e-beam excitation can be used to simulate nuclear pumping conditions to facilitate the search for candidate media. Experimental data for the kinetics of a XeF^* laser operating in $Ar/Xe/F_2/UF_6$ mixtures are given. These reactor-pumped systems are suitable for scaling to volumes on the order of $(\text{meters})^3$.

I. Introduction

Pulsed neutron generators are a compact source of enormous energy in the form of fast fission fragments. The Sandia SPR III reactor,[1] whose operating parameters are summarized in Table I, represents a modern configuration which dissipates several megajoules of energy in a single pulse. Efforts have been underway for several years to realize methods for producing coherent radiant energy with a nuclear energy source.[2] The first successful efforts to obtain laser oscillation in fission-fragment-pumped media were recently reported in several laboratories.[3] In this paper, we will discuss the considerations necessary to efficiently convert fission fragment energy to coherent radiation. Several critical aspects of this coupling will be examined, particularly specific medium characteristics such as density, wavelength, kinetics, fissile material, scale size, energy deposition, and uniformity. We will show that efficient coupling of a pulsed reactor with an appropriate gain medium will result in megajoule outputs of coherent energy at ultraviolet and visible wavelengths.

Table I

Operating characteristics of SPR III

Neutron Flux (cavity)	$\sim 10^{19}$ n-sec^{-1} cm^{-2}
Prompt Neutron Pulse Width	~ 50 μsec
Average Neutron Energy	~ 200 keV
Cavity Volume	~ 15 liter

II. Reactor-Medium Coupling

A. Energy Deposition, Medium Density and Composition

Optical fission-fragment-excited laser systems require efficient coupling of the fission fragment energy to the laser medium. The basic fission process involving uranium is

$$n + U^{235} \xrightarrow{\sigma_f} Z_1 + Z_2 + \bar{\nu}n \qquad (1)$$

which released ~ 165 MeV of kinetic energy in the two highly ionized fragments. These fission fragments transfer their energy to a host medium by several processes, including charge exchange, collisional stripping, direct ionization, and Auger processes, all of which lead to ionization and excitation of the host material. As the considerations of Leffert, Rees, and Jamerson[4] indicate, the energy per ion pair produced by fission fragments in rare gases, W_{ff}, is close to the corresponding value, W_e, for electrons. This is reasonable physically because the ionization and excitation in both cases is produced largely by secondary electrons at energies much lower than that of the primary particle. To a good first approximation, then, ~ 50% of the energy deposited in dense rare gases by fission fragments will produce electronic excitation, just as in the case of electrons.[5] Therefore, we can apply the knowledge gained recently from energy transfer studies of e-beam-excited rare gases and rare gas mixtures to the potential fission-fragment-pumped media.

In general, we desire a medium whose properties are such that it minimizes the kinetic losses through efficient coupling to the upper laser level while simultaneously utilizing physical mechanisms that are basically insensitive to the kinetic temperature. The main limitations on the optical gain include gas heating, optical absorption by all species present, and medium inhomogeniety. The limitation due to gas heating arises from the fact

that many laser molecules dissociate at elevated temperatures. This effect establishes an upper limit on the energy deposited in the gas (and therefore on energy output), and we can estimate that upper limit as follows. The deposited energy, E_d, is related to the optical efficiency η, the medium density ρ, and the maximum permissible temperature rise of the medium ΔT_g, by the specific heat equation

$$E_d \leq \frac{3\rho k \Delta T_g}{2(1-\eta)} \quad . \tag{2}$$

For example, if we restrict ΔT_g to $\leq 1000^{o}K$ and assume $\eta = 0.10$ and a host material consisting of argon at a density $\rho_{Ar} \simeq 10^{21}$ cm^{-3} ($\sim$ 50 amagats), these conditions permit an energy deposition E_d of 2×10^4 joules/liter and provide (at the stated efficiency) $\sim 2 \times 10^3$ J/liter of laser energy.

At the high gas density indicated, the fission fragment range will be low ($R_{ff} < 1$ mm).[4] This imposes the condition that the fissile material be homogeneously incorporated into the laser medium if we are to achieve uniform deposition over dimensions $R \gg R_{ff}$. Homogeneously mixed fissile material also insures efficient deposition of the fission fragment energy in contrast to configurations involving foils of fissile material located at the boundary of the medium, for which only $\sim$ 20% of the energy is deposited in the gas. On the other hand, it requires the existence of a fissile material (such as UF_6) that is volatile at moderate temperatures.

The density of fissile material required to generate a given energy deposition can be calculated from the relation

$$E_d = j_n \langle \sigma_f \rangle \rho_f \tau \epsilon_f \quad , \tag{3}$$

where j_n is the neutron flux, $\langle \sigma_f \rangle$ is the fission cross section averaged over the neutron energy spectrum, τ is the neutron pulse duration, and ϵ_f is the energy released per fission. The cavity neutron flux typical of current pulsed reactors (SPR III) is approximately 10^{19} n/cm^2-sec in an $\sim$ 50 μsec pulse as indicated in Table I. In order to maximize the fission cross section of the fissile material, the neutrons must be moderated to low energies. We assume that this moderation process can reduce half the neutrons to $E_n \leq 0.4$ eV within a pulse length of $\sim 10^{-4}$ sec[6] (passage of the neutrons through 2.5 cm of polyethylene will produce this partial moderation). Fission cross sections [7,8] for U^{234} and Am^{242m} as a function of neutron energy are presented in Figure 1; these curves show the importance of moderating the neutron energies.

For these conditions, fission-generated energy deposition is shown in Figure 2 as a function of U^{235} and Am^{242m}. These estimates were made assuming a flat energy distribution for neutrons over the range $0 < E_n \leq 0.4$ eV. We see that $\sim$ 100 torr of U^{235} leads to a deposition of 6 kj/ℓ, while the

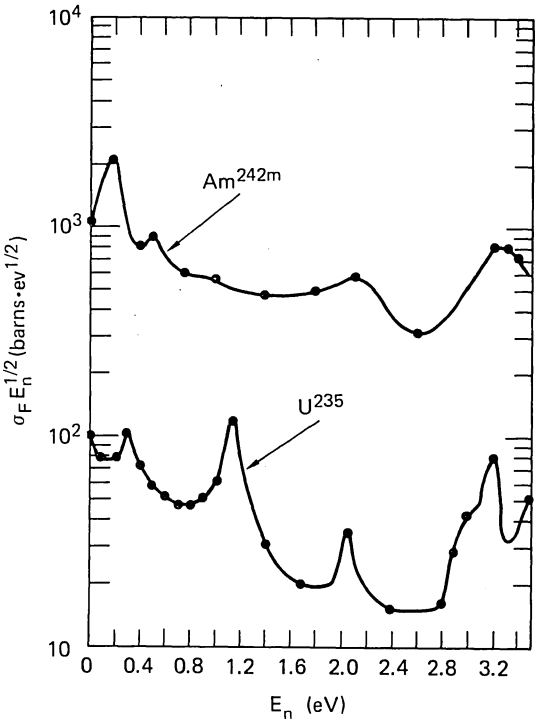

Fig. 1 Fission cross sections σ_f as a function of neutron kinetic energy E_n for U^{235} and Am^{242m}.

same energy density can be achieved with approximately one tenth the fissile material density for Am^{242m} because of its larger fission cross section at these neutron energies. Reducing the neutron energies to thermal values would in turn reduce the amount of U^{235} required for a given energy deposition, but it would also increase the pulse length and reduce the power density. On the other hand, americium has a high fission cross section for neutron energies as high as 1 eV. Other transplutonic materials such as Cm^{245} which has a fission cross section [9,10] and other properties intermediate[11] between those of U^{235} and Am^{242m} will be discussed in section E. These densities of fissile material are low enough that they may not interfere with the basic kinetics of the excitation process; we address this point later.

The ability to deposit the maximum permissible energy density in a laser gas mixture can be achieved with e-beams as well as with this proposed fission-fragment-pumping technique. A major advantage of the latter technique is that the pumped volume is limited only by the range of low energy neutrons, which is on the order of meters, whereas e-beam systems are limited by the range of high energy electrons, which is on the order of centimeters. Furthermore, the weight and volume of a reactor pump is expected to be substantially smaller than that of an e-beam pump of comparable energy.

We conclude on the basis of the above considerations that the laser medium for a high energy fission-fragment-pumped laser will consist of a

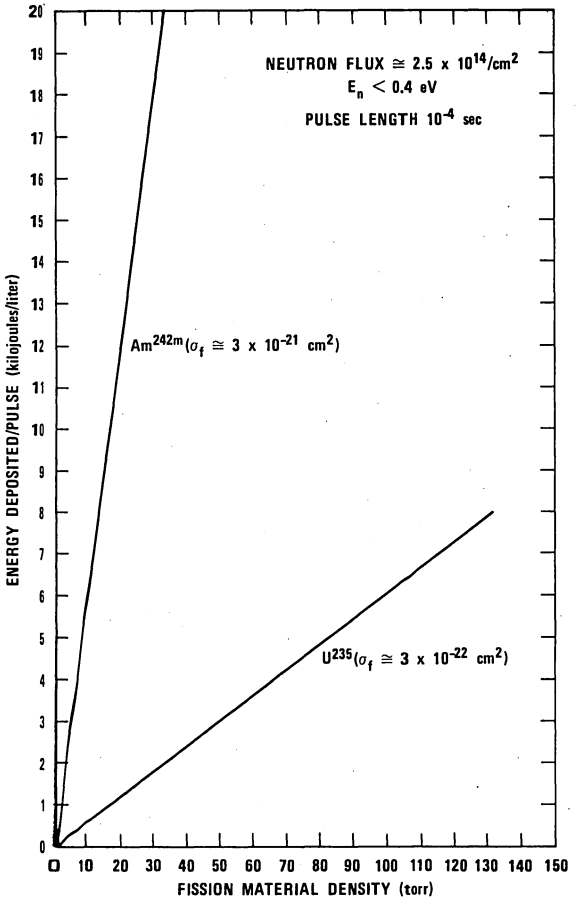

Figure 2 Deposited energy E_d as a function of fissile material density ρ_f for U^{235} and Am^{242m} assuming the performance characteristics of the SPR III pulsed reactor as noted in the text. The vapor pressure of UF_6 (111.9 torr) at 25°c is indicated.

large volume, high density gas (e.g., argon) containing a homogeneous mixture of ~ 10 to 100 torr of a volatile fissile material. The actual laser molecule could be any of several candidates already demonstrated with e-beam-excitation, e.g., Ar-N_2, Ar-I_2, XeO, ArF, KrF, or XeF. It is essential that the laser kinetics allow essentially cw operation in order to utilize all the excitation from the relatively long pulse of neutrons, but this is apparently the case in the systems suggested.

B. Scale Dimensions and Medium Uniformity

The maximum volume that can be pumped by neutron-induced fussion is set by the range of neutrons in the medium, which is set in turn by the scattering and absorption lengths for the neutrons. The scattering length will be governed by the primary constituent, say Ar, which has a total scattering cross section for thermal neutrons of ~ 10^{-24} cm^2 (Ar^{40}). For Ar densities of $10^{21}/cm^3$, this corresponds to a scattering length of ~ 10 meters. The absorption will be due to the volatile fissile specie; total neutron capture cross sections are 1.5 to 2 times the fission cross sections shown in Figure 1. The absorption length will in fact be controlled by the energy deposition by the relation

$$\ell_{abs} = \frac{<\sigma_f>}{<\sigma_T>} \frac{j_n \tau \epsilon_f}{E_d} \quad ; \qquad (4)$$

for the conditions described above, this is on the order of 3 meters. Thus, the maximum dimensions of the pumped volume will be governed by absorption of neutrons. It is this ability to uniformly pump such large volumes that provides the major scaling advantage of this proposed technique.

The range of the neutrons is sufficiently large that the transit time of moderated neutrons through the gas can exceed the neutron pulse length. In fact, for 0.2 eV neutrons ($v_n \sim 6 \times 10^5$ cm/sec), the distance travelled during a 100 μsec pulse is ~ 60 cm. For very large volumes, the neutron pulse will be essentially a travelling excitation wave. This should not be a problem if appropriate output coupling of the laser energy can be achieved.

It is important that the neutron velocity be large compared to acoustic velocities, v_s, so that pulse-generated disturbances do not disturb the optical homogeneity of the flow.[12] Since $v_s \leq 5 \times 10^4$ cm/sec, this is always true. However, acoustic disturbances could arise near the boundaries at the end of a long pulse, since $R_{disturbance} \sim v_s \cdot \tau \sim 5$ cm for $\tau = 10^{-4}$ sec. Use of fissile materials with large fission cross sections for epithermal neutrons allows minimal pulse lengths, which also minimizes the effects of acoustic disturbances.

C. Kinetic Properties

Fission-fragment excitation of dense atomic gases occurs, as noted earlier, by the same basic mechanisms as excitation by energetic electrons. This enables direct utilization of the considerable kinetic knowledge acquired in studies of electron-beam-excited material.[13] In particular, electron beams excite the rare gases and produce metastable atoms and excimers with an energy efficiency[5] of ~ 50%. In addition, several e-beam-pumped laser media have been demonstrated in the visible to near uv range that utilize energy transfer from excited rare gas donor species to either atomic or molecular acceptors.[14] Among these are Ar/N_2, Ar/I_2, XeO, rare-gas-halides and He_2^+/N_2.

It follows that these previously demonstrated media will function properly under excitation by fission fragments provided that (a) at the densities required the fissile additives do not interfere appreciably with the kinetic processes, (b) the neutron transport, apart from fission, is not adversely affected, (c) any additional optical losses arising from the fissible additive are sufficiently

small, and (d) the laser medium can operate quasi-cw. Points (a) and (c) will establish an upper limit on the fissile additive, and thereby the achievable energy deposition as shown in Fig. 2. Point (b) is not a limiting factor for the materials, densities, and scale dimensions under consideration. Issue (c) is examined in section D below.

It is important to note that the kinetic studies that will be required to evaluate candidates for fission-fragment excitation can be validly performed on media excited with electron beams over most of the desired parameter space. The comparison between e-beam and neutron-induced fission excitation is illustrated in Figure 3. In principle, electron beam machines can be used to simulate nuclear excitation and demonstrate lasing characteristics within the entire space below the limitation established by the foil, which includes all but the highest energy operating points in Fig. 3. Reactors such as SPR III can be used to evaluate the operational behavior at the limits of the high energy performance of media whose kinetic and optical characteristics had been obtained by simpler methods.

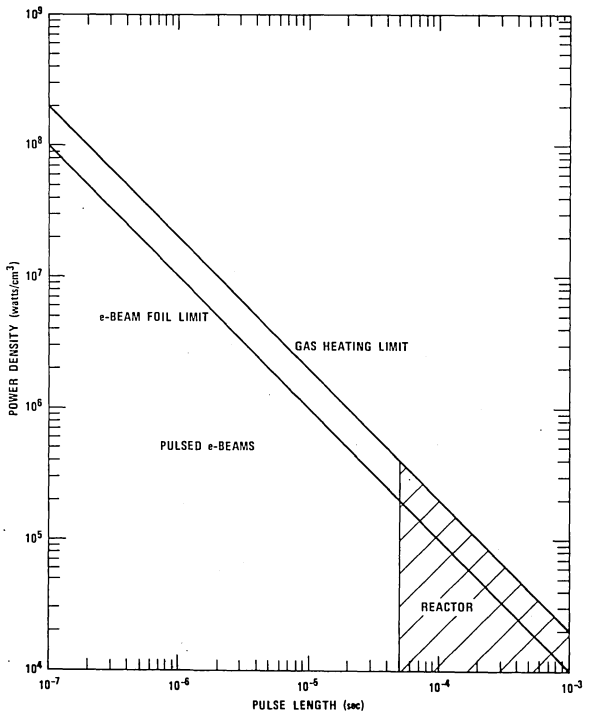

Figure 3 Excitation rate (P/V) in watts/cm^3 as a function of excitation time τ for high pressure rare gas materials by conventional pulsed electron beam devices and fission fragment concepts coupled to a pulsed reactor. The electron beam foil limitation is indicated.

From the kinetic viewpoint, we desire a minimum required fissile additive density ρ_f. This favors the use of high fission cross section materials and high neutron fluence reactor concepts [c.f. Eq. 3]. Although many volatile compounds involving fissile material are known, UF_6, because of its high vapor pressure[15] at room temperature and its low radioactivity, is an obvious initial candidate.

To test the feasibility of these suggestions, we have made e-beam excitation studies of the fluorescence of XeF^* from mixtures of $Ar/Xe/F_2$ to which depleted UF_6 was added. Measurements of the fluorescence spectrum, fluorescence intensity, and fluorescence decay time of $XeF^* \sim 3511$ Å were made on the gas mixtures excited with a Febetron 706 and the results are shown in Table II. We note first that the XeF^* is not formed in material containing only UF_6. In light of the quenching data noted below, we conclude that the reaction

$$Xe^* + UF_6 \xrightarrow{k} XeF^* + UF_5 \qquad (5)$$

is relatively slow, with a rate $k \lesssim 10^{-11}$ cm^3/sec.

Table II

XeF^* fluorescence measurements in $Ar/Xe/F_2/UF_6$ mixtures

(pressures in torr)

Ar	Xe	F_2	UF_6	XeF Spectra Observed
1500	10	4	0	normal
1500	10	4	4	normal
1500	10	0	4	none
1500	10	0	100	none
				Emission Intensity
760	40	4	0	1
760	40	4	4	1
760	40	4	10	0.6
760	40	4	50	0.36

Xenon fluoride emissions are easily seen with 4 torr of F_2 and no UF_6; when 4 torr of UF_6 is added to this mixture no change is observed in the spectrum intensity, or decay rate of the XeF^*. For mixtures containing 50 torr of UF_6 and only 4 torr of F_2, the XeF^* is approximately one-third as intense as with no UF_6, indicating that Xe^* quenching by UF_6 is of the order of 0.1 that of F_2. These results indicate that UF_6 is quite inert to reaction with electronic excited states, and may be added in quantities at least equal to the laser additive. These observations have extremely important and positive implications for fission fragment pumping using UF_6.

D. Medium Optical Characteristics

Optical losses due to the fissile additive may prevent laser action, even when no kinetic inter-

ference is present. For illustration, we show in Figure 4 the optical absorption cross section of UF_6 as a function of wavelength in the range 200-400 nm according to the recent data of DePoorter and Rofer-DePoorter.[16] Naturally, the best region for oscillation in a medium containing UF_6 is at wavelengths from 400 nm to the infrared where the absorptions are known to be very small. Nevertheless, it may be possible to operate successfully in the region near the deep absorption minimum at ~ 340 nm, which very closely matches the I_2^* and XeF^* transitions. Indeed, it may be that the blue band of XeF^* ~ 4200Å is a better candidate since UF_6 absorption in that region is extremely low. Again, the use of lower densities of high fission-cross section material would undoubtedly mitigate this problem.

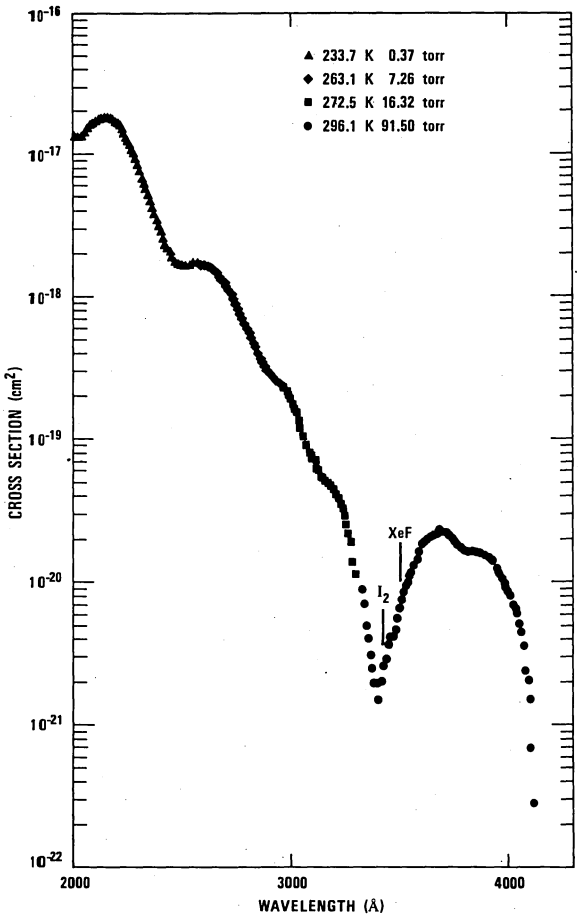

Figure 4 Optical absorption cross section of UF_6 in the range 200-400 nm according to the data of DePoorter and Rofer-DePoorter. The positions of the XeF^* (351 nm) and I_2^* (342 nm) laser transitions are also indicated.

E. Special Nuclear Materials

The previous discussion has shown that nuclear materials with high fission cross sections, particularly in the epithermal region, reduce many of the limitations which arise in the consideration of excitation of laser media by fission fragments. Several transplutonic materials represent an improvement over U^{235} by up to roughly a factor of ten. An example of this comparison is illustrated in Figure 2, which compares the performance of U^{235} with Am^{242m}. Other materials such as Cm^{245} and Cf^{249} also have very attractive properties. The main parameters of interest are the nuclear lifetimes, the resonance integrals for fission (I_{nf}) and neutron capture ($I_{n\gamma}$), the availability, and the existence of a suitably volatile compound as a carrier.

Table III contains the lifetimes and resonance integrals for several nuclear materials.[9,10] We observe that Cm^{245} has a lifetime roughly one third that of Pu^{239}, decays solely by α emission and has a large ratio of fission to capture resonance integrals.[11] Although some reasonably volatile metal-organic compounds[17] of the transplutonics such as Am and Cm are known to exist,[18] insufficient data are currently available for a complete evaluation.

Table III

Properties of transplutonic materials

Isotope	$\tau_{\frac{1}{2}}$ (yr)	$I_{nf}^{\dagger}$ (b)	$I_{n\gamma}^{\dagger}$ (b)
U^{235}	7×10^8	275	144
Pu^{239}	2.4×10^4	301	200
Am^{242m}	152	1570	(200)
Cm^{245}	8.5×10^3	750	101
Cf^{249}	350	1610*	625

*Dominated by a resonance at $E_n = 0.7$ eV with an area of 8000 eV-barns.

† $I_i \equiv \int_{0.5}^{\infty} \frac{\sigma_i(E)}{E} dE$

III. Conclusions

Estimates of the performance limits of fission fragment excited laser systems radiating in the near ultraviolet and visible regions indicate that extremely high energy outputs appear feasible using pulsed reactor neutron generators. Transverse scale dimensions of greater than one meter appear practical. Scale size and medium density considerations show that high density gas phase media containing homogeneously integrated fissile material are superior to foil configurations. The use of fissile materials with large fission cross sections, particularly in the epithermal range, increase the medium scale size and relax kinetic and optical constraints. Simulation of the conditions produced by fission fragment excitation can be achieved over most of the relevant parameter space by studies of

candidate media with excited electron beams. Systems of this nature may have application as photolytic drivers for the high peak power systems required for laser fusion.

IV. Acknowledgements

The expert technical assistance of H. Nakano is acknowledged. In addition, we thank Richard K. Pearson for his generous loan of UF_6 material. We acknowledge several very informative conversations on transplutonic materials with J. Browne, including his unpublished data on fission cross sections. We also thank E. K. Hulet for information regarding transplutonic compounds. Special thanks for discussions related to the preparation of the manuscript go to D. J. Eckstrom. Finally, we acknowledge informative discussions on transplutonic materials with R. Reitz and L. Wood.

References

1. L. L. Bonzon, J. A. Reuscher, T. R. Schmidt, Sandia Pulsed Reactor III (SPR III): Predicted Performance Characteristics, SLA-73-0812, November 1973.

2. K. Thom and R. T. Schneider, J. AIAA 10, 400 (1972).

3. D. A. McArthur and P. B. Tollesfrud, Appl. Phys. Lett. 26, 187 (1974), H. H. Helmick, J. L. Fuller, and R. T. Schneider, Appl. Phys. Lett. 26, 327 (1975), R. J. DeYoung, W. E. Wells, J. T. Verdeyen, and G. H. Miley, IEEE/OSA Conf. on Laser Engineering and Appl., Washington D.C., May 1975.

4. C. B. Leffert, D. B. Rees, and F. E. Jamerson, J. Appl. Phys. 37, 133 (1966).

5. D. C. Lorents, Physica 82C, 19 (1976).

6. D. McArthur, private communication.

7. J. R. Stehn, et al., Neutron Cross Sections Vol III, Z=88-98, BNL 325, 2nd ed., February 1965.

8. C. D. Bowman, G. F. Auchampaugh, S. C. Fultz, P. W. Hoff, Phys. Rev. 166, 1219 (1968).

9. J. C. Browne, private communication.

10. R. W. Benjamin, Survey of Experimentally Determined Neutron Cross Sections of the Actinides, Savannah River Laboratory Report DP-1324 (1973).

11. S. Raman in Nuclear Cross Sections and Technology, Vol 1, edited by R. A. Schrack and C. D. Bowman (U.S. Dept. of Commerce, Washington, D.C. 1975).

12. Walter N. Podney, Harold P. Smith, Jr., and A. K. Oppenheim, Phys. Fluids 9, 2357 (1966).

13. R. M. Hill, D. L. Huestis, and C. K. Rhodes in Laser Induced Fusion and X-Ray Laser Studies, edited by S. Jacobs, M. Sargent III, and C. Cantrell (Addison-Wesley, Reading, Mass., 1976); C. K. Rhodes, IEEE J. Quantum Electron, QE-10, 153 (1974).

14. S. K. Searles and G. A. Hart, Appl. Phys. Lett. 25, 79 (1974); M. McCusker et al., Appl. Phys. Lett. 27, 363 (1975); J. J. Ewing and C. A. Brau, Appl. Phys. Lett. 27, 557 (1975); H. T. Powell, J. R. Murray, C. K. Rhodes, Appl. Phys. Lett. 25, 730 (1974); J. J. Ewing and C. A. Brau, Appl. Phys. Lett. 27, 350 (1975); E. R. Ault, R. S. Bradford, M. L. Bhaumik, Appl. Phys. Lett. 27, 413 (1975); C. B. Collins and A. J. Cunningham, Appl. Phys. Lett. 27, 137 (1975).

15. D. Brown, Halides of the Lanthanides and Actinides (Wiley-Interscience, New York, 1968).

16. G. L. DePoorter and C. K. Rofer-DePoorter, LA-UR-75-792, Los Alamos Scientific Laboratory, Los Alamos, New Mexico (1975).

17. E. K. Hulet, private communication.

18. T. J. Marks, J. Organometal. Chem. 95, 301 (1975); E. Cernia and A. Mazzei, Inorganica. Chimica Acta 10, 329 (1974); R. G. Hayes and J. L. Thomas, Organometal. Chem. Rev. A7, 1 (1971).

DISCUSSION

R. V. HESS: Did you pump with noble gas-alkali mixtures?

D. C. LORENTS: No, we have not looked at noble gas-alkali systems in our laboratory. We have looked at Zenon-Mercury. That system seems to be rather complicated, and I would not recommend it.

DEVELOPMENT OF A HIGHER POWER FISSION-FRAGMENT-EXCITED CO LASER*

D. A. McArthur
Sandia Laboratories
Albuquerque, New Mexico 87115

Abstract

Since our initial observation of lasing at $\lambda \sim 5\mu$ in cooled, reactor-excited CO, we have continued to develop this laser in a small experimental program. The early gain measurements and laser feasibility experiments did not use parameters typical of efficient electrical CO lasers, but did show that the CO laser is promising as a potentially efficient reactor-excited laser. In our recent experiments, we have observed that moderate dilution of the CO with Ar lowers the reactor excitation threshold for lasing. We have also developed very smooth and rugged fission coatings on ceramic substrates, to minimize fouling of laser mirrors. Finally, a new laser apparatus has been constructed which more closely resembles large electrically-excited CO lasers. In initial experiments this new laser has produced a laser energy $\sim$ 15 mJ (or $\sim$ 100 W peak power), which represents a factor of 50 increase in laser energy and a moderate increase in efficiency. Measurements of the energy emerging from the foils indicate that excitation of the gas is still below optimum values. Laser action at room temperature has also been observed. Modifications to the new apparatus are being made to permit systematic variation of parameters, which should lead to further efficiency improvements.

I. Introduction

When the Sandia nuclear pumping program began in late 1972, there was no clearly demonstrated case of laser action using only a laboratory nuclear reactor. Because of the relatively high excitation rates available from our SPR-II reactor, we decided to survey a number of possible laser media that had been studied by earlier workers, in an effort to observe at least one clear-cut case of lasing. No evidence of lasing was seen in CO_2, DF, HF, He-Ne, and Ar^+, although intense light emission was often seen. However, the emission either decreased when laser mirrors were added, or was independent of laser mirror orientation.

Because of the relatively low power input rate available with nuclear pumping, it appeared that the $\sim 5\mu$ wavelength laser operating on the vibrational bands of CO might be very suitable for reactor pumping. This laser is a very efficient, electrically-excited laser, operating between vibrational levels which have very long lifetimes even at high pressures. Finally, selective excitation is not required to obtain an inversion, since a strongly non-equilibrium population distribution spontaneously develops in CO if the gas is highly excited vibrationally yet remains translationally cold. Thus the most important uncertainties were how much gas heating would be caused by fission fragment excitation, and what fraction of the fission fragment energy would go into vibrational excitation of the CO.

Early in 1974 optical gain was observed in pure CO gas cooled initially to 77 K. After making initial studies of the gain as a function of wavelength and excitation rate, a laser apparatus was constructed, and clear evidence of lasing was obtained. This evidence consisted of a $>10^3$-fold increase in the signal seen by a distant detector, only when highly-reflecting mirrors were placed in the apparatus and were properly aligned. A small laser energy was also measured, from which an estimated laser efficiency $\sim$ 0.1% was obtained. These results, the first clear demonstration of lasing in a medium excited only by fission fragments, were described in an internal report in July, 1974,[1] and published in the literature after a patent application was filed.[2]

II. Potential Efficiency of Reactor-Excited CO

The initial series of gain measurements in pure CO showed a factor of ten smaller gain amplitude, compared to that observed in electrically-excited CO lasers.[3] Otherwise, the gain behavior was similar to pulsed electrically-excited CO lasers in overall time dependence and in its dependence on the vibrational band and the rotational quantum number within each band. Fig. 1 shows measured peak gain in pure CO for a reactor temperature rise ΔT_R of 320°C, with

*This work supported by U. S. Energy Research and Development Administration

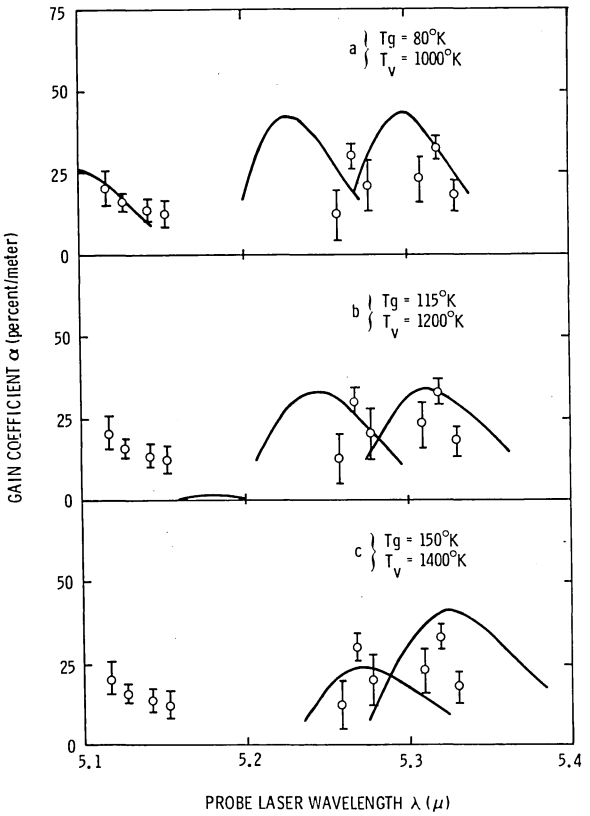

Fig. 1 Measured Peak Gain in CO and Calculated Wavelength Dependence of Gain.

calculated gain curves for various gas temperature assumptions. A threshold energy deposition was also required to observe gain: Fig. 2 shows that the gain on the $\lambda = 5.27$ μ line goes to zero well before the gas energy deposition (which is proportional to ΔT_R) approaches zero. The smaller gain magnitude could well be caused by the low excitation per CO molecule associated with the undiluted CO gas used. Intensity modulation of the probe laser beam and a pressure rise in the gain cell upon excitation both indicated the presence of some gas heating by the fission fragments. The widths of the gain pulses increased slightly for the higher -v bands, which may also indicate gas heating.

Fitting the gain measurements with an approximate steady-state vibrational distribution, assuming a transient gas temperature ranging between 80 K and 150 K, implies that 25 to 70 percent of the deposited fission fragment energy is appearing as vibrational excitation of pure CO.[4] Demonstrated physical mechanisms which might contribute significantly to such high vibrational excitation efficiencies are direct vibrational excitation by low-energy secondary electrons, and

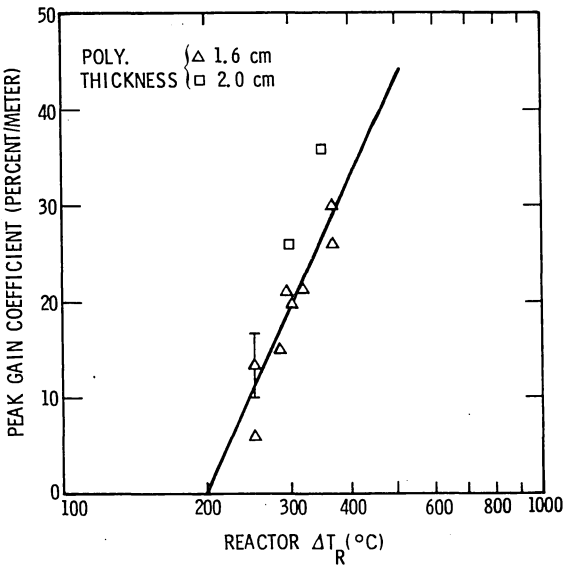

Fig. 2 Dependence of Gain on Energy Deposited in Pure CO.

conversion of electronic excitation of CO molecules into vibrational excitation. Other possible mechanisms are direct vibrational excitation by recoil ions, and vibrational excitation resulting from recombination of complex ions such as $(CO)_2^+$.[4]

The Sandia program has continued to concentrate on the development of the CO reactor-excited laser, because our initial measured efficiency with CO is still much higher than those of the reactor-excited He/Xe or Ne/N_2 lasers,[5] and because of the high vibrational pumping implied by our initial gain measurements. Preliminary systems and reactor design studies also showed that very large lasers ($E_{laser} \gtrsim 1$ MJ) could be built if a high-efficiency laser medium could be found.[6] These large lasers would use arrays of thin foils to excite the laser medium, and could potentially achieve overall efficiencies ∿ 10% with an efficient laser medium, in spite of the inherent foil losses. Since electrically-excited CO lasers have achieved efficiencies > 60%, and since the CO wavelength has potential applications to laser pellet fusion, the laser-heated-solenoid fusion concept, and weaponry, further development of the reactor-excited CO laser was undertaken.

III. Experimental Development Steps

A. Lasing in CO Diluted with Ar

One of the first development steps was the demonstration that CO/Ar mixtures could be made to lase with direct nuclear pumping, and the qualitative demonstration

that CO/Ar laser mixtures have a lower threshold than pure CO.[6] Ar or N_2 are often used as diluents in electrical CO lasers, because they allow a fixed amount of excitation energy to be concentrated in the vibrational modes of fewer CO molecules. This concentration greatly increases the gain and efficiency of the laser. The lower threshold observed with nuclear-pumped 50/50 CO/Ar mixtures indicates that this process is also occurring to some extent in nuclear pumping.

B. Foil Coating Developments

In our nuclear-pumped laser research we have chosen to excite the gas with a thin fission foil coating, on a substrate with high thermal conductivity and specific heat (alumina). Compared to homogeneous excitation with He^3 or UF_6, excitation with a foil allows much greater flexibility in choice of laser gas mixture and laser wavelength. We have also used uranium oxide coatings rather than metallic uranium foils, because the thin oxide coatings are chemically stable at high excitation densities even in the presence of reactive laser gases, and because the substrate acts as a heat sink which reduces the danger of destroying or warping the exciter foil at high excitation densities. The reliability of the laser apparatus and the amount of excitation of the laser gas are determined by the foil coating quality. Therefore, we have put considerable effort recently into new foil construction methods and into methods for measuring the energy output of the foil, which are described in this section.

In our previous experiments the energy emerging from the fission foil coatings (and therefore the excitation energy of the gas) was calculated, by using a three-dimensional neutron transport code to calculate the fission density in the foil coating,[7] and then assuming a perfect, 93%-enriched $^{235}U_3O_8$ or $^{235}UO_2$ coating to calculate the fraction of the fission fragment energy emerging from the coating.[8] The neutron transport calculations were checked by measuring the thermal neutron fluence at the alumina cylinders for a known geometry.[1] No independent check was made of the parameters which determine the foil energy output and efficiency (foil thickness, chemical composition, and isotopic enrichment). However, there were qualitative indications (size of laser pulse energy, size of pressure rise in the excited gas) that the early foils were emitting the expected amount of energy. A severe disadvantage of these early foils was that at high excitation densities they released flakes of coating material, which fouled the laser mirrors and prevented laser action unless the mirrors were cleaned or replaced after each reactor burst.

To improve the bonding of the foil coatings to the substrate, and to improve their mechanical quality and uniformity, an improved foil coating process was developed,[9] which has resulted in very smooth, durable U_3O_8 foils on Al_2O_3 and BeO substrates. These foils cannot be scratched off the substrates, and the foil surface replicates the initial smoothness of the ceramic substrates, so that high optical reflectivity is obtained for high angles of incidence. Thus we no longer have any problems with foil flaking or damage by the neutron irradiation rates routinely used.

However, it appears that these new foils are generating significantly less energy than expected from the measured neutron fluence which irradiates them. For example, lower laser energies and lower pressure rises in the excited gas than expected have been observed in experiments using these recently-constructed foils. Therefore, measurements have been made of both the total energy created in the foil (which is related to the foil coating enrichment, the total mass of uranium, and the neutron fluence which irradiates the foil) and the fission fragment energy emerging from the foils (which is related to the foil structure and enrichment). We believe that these calorimetric measurements are the first of this type for nuclear-pumped lasers, and an improved laser efficiency measurement should result from data of this kind.

Figure 3 shows a special calorimeter (the Fission Fragment Calorimeter), designed to measure directly the energy emerging from the fission foil coating.[10] The calorimeter element consists of a 1.9 cm diameter cylinder of 3.6×10^{-3} cm thick aluminum, suspended by four 1.3×10^{-2} cm diameter tantalum support wires. The element is surrounded by a thick aluminum collimator and support structure which restricts the length of exposed element to about 2.2 cm. The calorimeter assembly fits into the 2.7 cm diameter alumina fission foil with a small clearance. The element temperature rise is measured by a thermopile consisting of four chromel-constantan thermocouples cemented to the upper end of the element, with their reference junctions heat-sinked to the calorimeter support structure.

To measure the total energy produced in the foil coating, the alumina cylinder is used as a calorimeter, its temperature rise being measured with a ribbon-type copper-constantan thermocouple bonded to the outside surface of the cylinder at its axial center. The reference junctions in this case were protected from direct

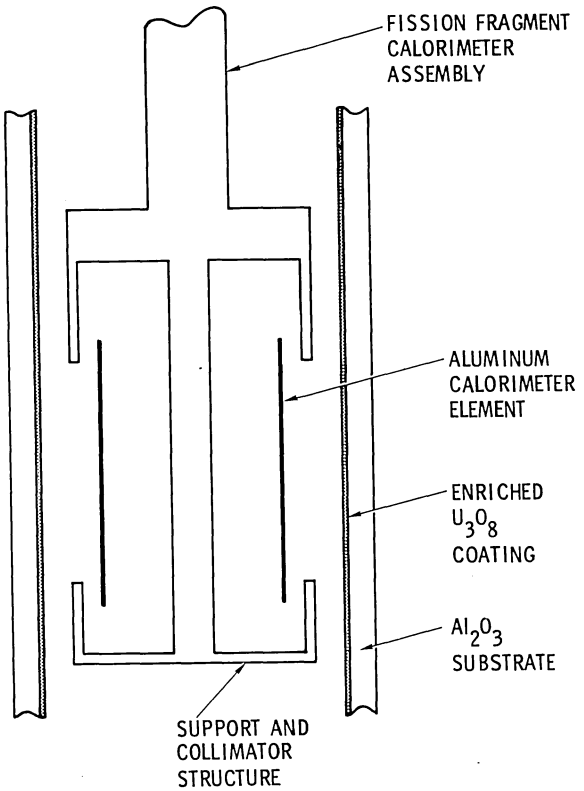

Fig. 3 Diagram of Fission Fragment Calorimeter.

irradiation by fission fragments, but not heat-sinked to any structure. The entire alumina cylinder was isolated from the stainless steel walls of the vacuum chamber by small felt pads and a thin plastic support.

Figure 4A shows a typical alumina temperature rise signal, which has a small negative background component (which is probably caused by differential radiation heating of the reference junctions and the measuring junction). The fission foil temperature signal is delayed by thermal conduction through the wall of the alumina cylinder, and reaches nearly its final value in ≃ 0.3 sec for an evacuated laser chamber. The alumina temperature rise measures the average fission energy/cm^2 retained by the entire cylinder.

Figure 4B shows a typical Fission Fragment Calorimeter signal, which in an evacuated laser chamber measures the energy per cm^2 emerging from the fission coating over an axial region ∿ 2.2 cm long (after an ∿ 30% correction is made for the geometrical collection efficiency of the calorimeter element). The background signal of the Fission Fragment Calorimeter

MEASUREMENT OF FISSION FOIL EFFICIENCY

A. Foil Substrate Temperature Rise

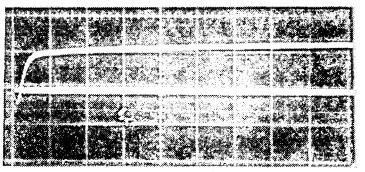

B. Fission Fragment Calorimeter

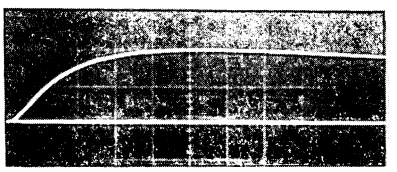

Fig. 4 Typical Alumina Temperature Rise and Fission Fragment Calorimeter Signals.

was measured to be ≲ 5% at the peak of the calorimeter signal, by covering the sensitive area of the calorimeter at the collimator surface with thin sheets of aluminum or plastic.

The axial variation of the fission fragment flux was also measured in two ways (Figure 5): (1) The fission fragments emerging from the coating were collected on a strip of thin aluminum, and the axial variation of the fragment β activity was measured;[11] and (2) the density of fission fragment tracks in a Lexan target was measured as a function of axial position.[12]

The fission fragment activity data of Figure 5 were used to calculate the fission energy created per unit area of the

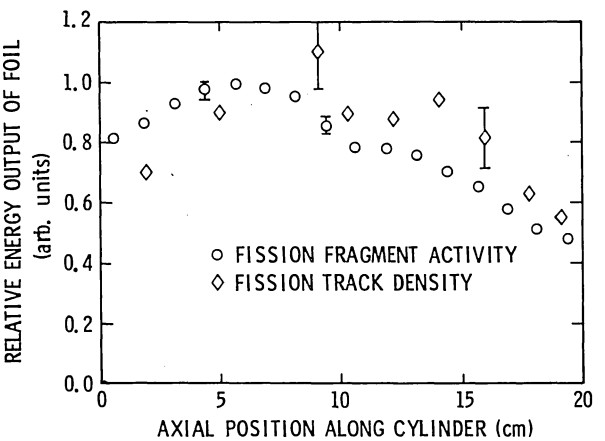

Fig. 5 Measured Axial Variation of Energy Output of Fission Foils.

foil at the same axial position as the Fission Fragment Calorimeter. The ratio of these signals yielded a measured foil efficiency of 12 ± 2%, which is in good agreement with the calculated efficiency (12%) of a perfect U_3O_8 coating having the measured thickness of 5μ.[9] However, the magnitudes of both energy signals are lower (by a factor of ∿ 3.5) than would be expected from the measured thermal neutron fluence and the assumption of 93% enrichment. The simplest resolution of this discrepancy would be to assume that the foils are actually about 30% enriched. Samples of the coating solution have been sent for enrichment analysis, but the results are not yet available.

One of the recently-constructed alumina cylinders was also sectioned, polished, and observed under an optical microscope (Figure 6). Identification of the size of the foil coating is not very precise, because of surface distortions produced by the polishing process, and because some slight discoloration extends into the alumina substrate. A very thin black region of thickness ∿ 3-5μ appears in the sections, but it may be a crack instead of a coating. Because these optical observations are not very precise, samples are now being prepared for electron microprobe analysis, to make a quantitative measurement of the uranium distribution.

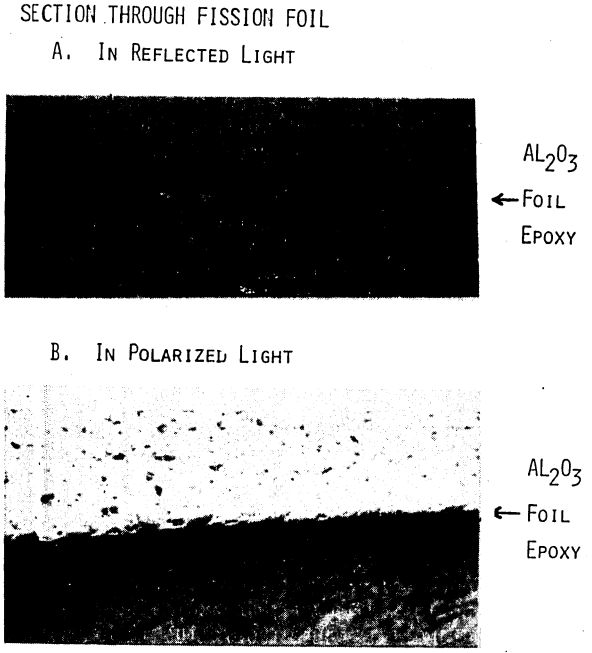

Fig. 6 Optical Observation of Foil Coating Region

If laser gas is added to the chamber, a different time dependence is obtained for the alumina substrate temperature rise. For an evacuated chamber with the fission fragment calorimeter removed, most of the emitted fragment energy will be deposited in the opposite surface of a long alumina cylinder, and the temperature rise will be characteristic of all the fission energy created in the foil. However, with a high-pressure gas fill, all the emitted fission fragment energy would be deposited in the gas, and could contribute to heating of the alumina only by thermal transport back to the foil surface through the gas. The calculated time constants for thermal conduction to the foil surface range from ∿ 0.15 sec at 100 Torr CO to ∿ 0.6 sec at 400 Torr CO, for example.[13] The presence of the gas also increases the heat conduction between the alumina cylinder and the walls of the laser chamber, but calculations of this heat loss show that it is not a function of pressure in the range from 100 to 400 Torr,[13] and is very slow compared to the time behavior of the alumina temperature. Figure 7 shows the alumina temperature rise for 104 Torr and 400 Torr of a 50/50 CO/Ar mixture, and the temperature difference between the two cases. It appears that the higher-pressure gas is absorbing from 10-15% of the energy from the foil (as expected from the foil efficiency measurement), and is returning almost all of it to the foil over about a 5 sec time period, which is much longer than the calculated thermal relaxation time of heated CO or Ar gas.[13] These data then raise the possibility that much of the energy deposited in the gas is being stored (perhaps as vibrational energy), converted slowly to thermal energy, and then conducted back to the relatively cool foil. Further experiments with gases which quench vibrational excitation, and efforts to reduce the background signal, are planned to test this hypothesis.

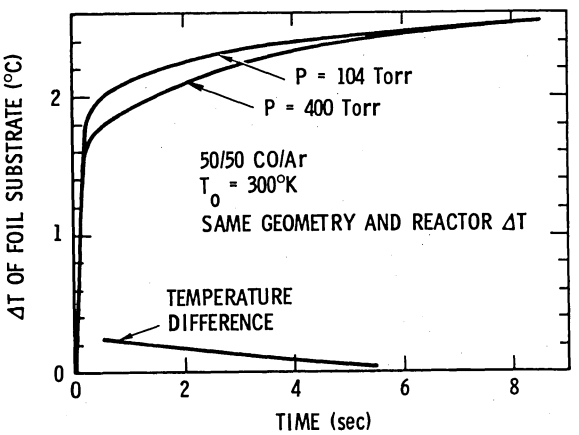

Fig. 7 Effect of Gas Pressure on Foil Substrate Temperature Rise.

C. Folded-Path Laser

To obtain a valid laser efficiency measurement, the laser must have a high total gain and be operating well above threshold. The SPR-II reactor produces a high neutron flux only over a limited region of space, so to obtain a high total gain it is necessary to fold the excited optical path back and forth in this small region. The segments of the optical path should also be approximately horizontal so that gas decomposition products do not tend to collect on the folding mirrors or the Brewster windows. Finally, the mirror mounts should be designed so that optical alignment can be performed after the laser excitation chamber is in thermal equilibrium at 77 K. An apparatus with these features, the Sandia Folded-Path Laser, is shown in Fig. 8. Excitation is provided by an array of cylindrical fission foils surrounding the folded optical path. This apparatus scales up the total gain by about a factor of 12 (neglecting losses in the folding mirrors and differences in the average excitation over the larger volume).

Preliminary data have been taken with this apparatus at relatively low excitation levels, because of neutron absorption in the complex apparatus and the low energy output of the new foils. Weak laser pulses have been observed as late as 0.6 to 1.2 msec after the neutron excitation pulse, which indicates that energy can be stored in the laser medium. To obtain reliable lasing it was necessary to align the laser mirrors after the apparatus had approximately reached thermal equilibrium. The measured laser energy has been increased by a factor of $\sim$ 50 to 15 mJ (corresponding to $\sim$ 100 watts power), without optimizing any parameters such as gas mixture or output mirror coupling. Taking into account the measured lower energy output of the fission foils, the (non-optimized) laser efficiency is $\gtrsim$ 1% at 77°K.

Experimental problems in the apparatus have made systematic parameter variations difficult: vacuum leaks develop when the temperature is cycled, beam distortion results from cooling the Brewster windows, and the thermal equilibration time of the massive apparatus is > 5 hours. Modifications are presently being made to correct some of these problems. We expect further improvements in efficiency and energy output as a result of optimizing laser parameters.

IV. Observation of Lasing at Room Temperature

Many experimental problems can be avoided, and useful parameter studies made, if laser action could be obtained at room temperature with this new, longer laser. Therefore searches for lasing were made in CO/N_2 and CO/Ar mixtures at a gas temperature $\sim$ 300 K. Laser action was not observed in 50/50 or 25/75 CO/N_2 mixtures, bur several laser pulses were observed in 50/50 CO/Ar (the only mixture tried). Figure 9 shows a typical laser

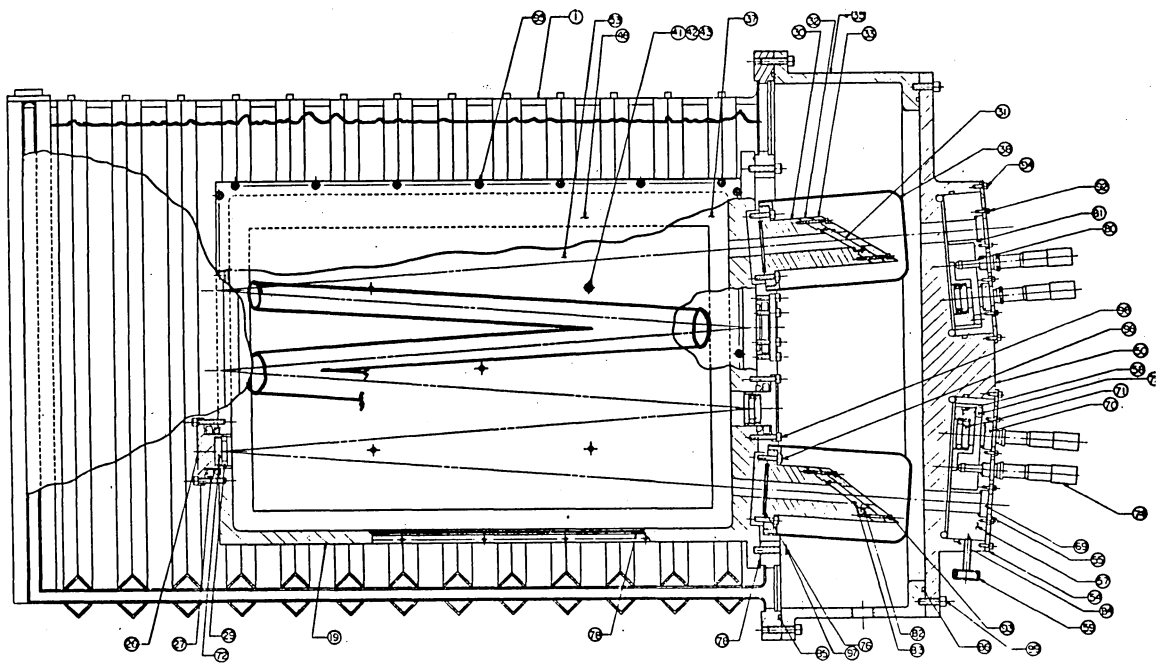

Fig. 8 Drawing of Sandia Folded Path Laser, Showing Gas Excitation Cylinders and Level of Liquid Nitrogen Coolant.

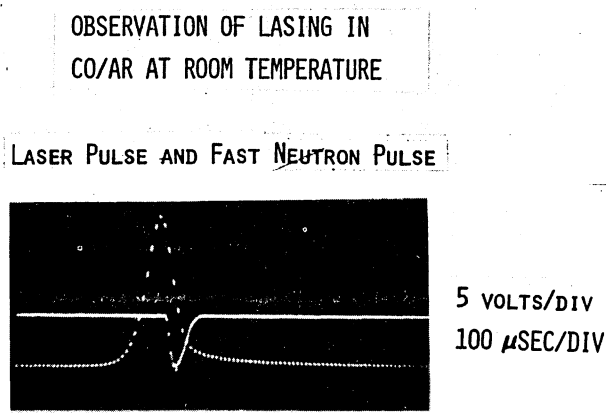

Fig. 9 Observation of Laser Action in CO/Ar at Room Temperature.

pulse (solid curve), ∿ 50 μsec wide and beginning slightly after the peak of the fast neutron pulse from the reactor (dashed curve). Data were taken for two different thicknesses of polyethylene moderator, and with and without Brewster's Angle Windows (B.A.W.) in the laser cavity. Figure 10 shows that increasing the neutron moderation and removing the B.A.W. reduce the laser threshold by ≃ 30%. The laser energy was not measurable with a laser calorimeter, but was obtained by integrating the Ge:Au detector signal traces.

Using reasonable values for the losses in the laser cavity mirrors, B.A.W., and the pathfolding mirrors, the gain coefficient at T = 300 K is $\alpha \gtrsim .04$ percent/cm, or about a factor of 10 lower than measured previously at 77 K.

The observation of lasing at 300 K is also indirect evidence that an appreciable fraction of the fission fragment energy is converted to vibrational excitation of the CO gas. The gain measurements at T ∿ 77 K discussed in Ref. 4 and Section II imply high vibrational excitation efficiency, if vibration-vibration (V-V) relaxation is sufficiently fast at these low temperatures. However, it has been proposed instead that the observed gain might result from a small amount of direct excitation to levels with v ∿ 12, followed by very slow V-V relaxation out of these levels.[14] Since the V-V rates vary rapidly with gas temperature, these rates are as much as 500 times faster at T = 300 K than at T ∿ 100 K. If slow V-V relaxation were responsible for most of the gain observed, it would be expected that the gain would drop by a factor 100 in going from a gas temperature of 100 K to 300 K. Since lasing is observed at 300 K, the gain appears to decrease by only about a factor of 10 over this

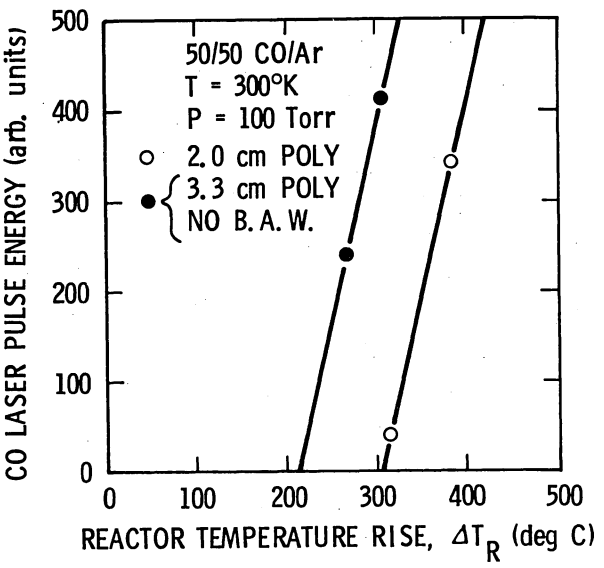

Fig. 10 Dependence of Laser Energy on Reactor Energy Deposition.

temperature range, which implies that slow V-V relaxation is not the dominant cause of the gain observed at T ∿ 100 K.

V. Conclusions

The physics of the CO excitation processes will determine whether a very efficient (∿ 50%) CO reactor-excited laser can be made, and also determine exactly how the laser must be constructed. The most important physics uncertainties are: (1) What fraction of the input energy goes directly into gas heating, and by what paths? (2) What fraction goes rapidly into vibrational excitation, and by what paths? and (3) How does the excitation change with changes in the gas mixture?

Several experimental approaches are now being pursued at Sandia to answer these questions. In the limited gain data available at present there are no strong indications of an unusual vibrational distribution. However, if more accurate gain measurements over a wider wavelength range were made for various gas mixtures, a much better picture of the excitation process might emerge. Laser energy and spectrum measurements might yield insight into the excitation processes, if the focusing effects caused by non-uniform gas excitation do not disrupt the lasing process too much. An accurate method for measuring the gas temperature as a function of time during the excitation pulse is also being developed.

As an example of how the answers to these questions may affect the laser

construction, if the gain drops primarily because of gas heating, it may be possible to re-cool the gas in an expansion and extract the available vibrational energy as CO laser light.

References

1. D. A. McArthur and P. B. Tollefsrud, Sandia Laboratories Report SAND-74-0106, (July 1974) (unpublished).

2. D. A. McArthur and P. B. Tollefsrud, Appl. Phys. Lett. 26, 187 (15 Feb. 1975).

3. D. A. McArthur and P. B. Tollefsrud, Trans. Am. Nucl. Soc., 19, 356 (1974).

4. D. A. McArthur and P. B. Tollefsrud, IEEE J. Quantum Electr., QE-12, 244 (April 1976).

5. H. H. Helmick, J. L. Fuller and R. T. Schneider, Appl. Phys. Lett., 26, 327 (15 March 1975); R. J. DeYoung, W. E. Wells, J. T. Verdeyen, and G. H. Miley, IEEE J. Quantum Electr., QE-11, No. 9, p. 97D (1975).

6. D. A. McArthur, T. R. Schmidt, P. B. Tollefsrud and J. S. Philbin, Trans. Amer. Nucl. Soc., 21, 21 (1975).

7. J. Kimlinger and E. F. Plechaty, Lawrence Radiation Laboratory, Livermore, CA, Rep. UCRL-50532, (Oct. 1968).

8. E. E. Lewis and R. Pfeffer, Nucl. Sci. and Eng., Vol. 27, pp 581-585 (1967).

9. T. M. Kerley and D. J. Sasmor, Sandia Laboratories, unpublished work.

10. Designed by G. H. Miller, G. J. Lockwood, and L. E. Ruggles, Sandia Laboratories, Albuquerque, N.M. 87115.

11. B. L. O'Neal, Sandia Laboratories, Albuquerque, N.M. 87115.

12. R. I. Ewing, Sandia Laboratories, Albuquerque, N.M. 87115.

13. E. U. Condon and H. Odishaw, Eds., Handbook of Physics, McGraw-Hill, 1958, New York, Part 5, Chapter 4.

14. C. P. Holmes, Air Force Weapons Laboratory, Kirtland AFB, N.M., private communication.

REVIEW OF COAXIAL FLOW GAS CORE NUCLEAR ROCKET FLUID MECHANICS*

By

Herbert Weinstein
Illinois Institute of Technology
Chicago, IL 60616

Abstract

In a prematurely aborted attempt to demonstrate the feasibility of using a gas core nuclear reactor as a rocket engine, NASA initiated a number of studies on the relevant fluid mechanics problems. These studies were carried out at NASA laboratories, universities and industrial research laboratories. Because of the relatively sudden termination of most of this work, a unified overview was never presented which demonstrated the accomplishments of the program and pointed out the areas where additional work was required for a full understanding of the cavity flow. This review attempts to fulfill a part of this need in two important areas.

Introduction

The concept of a gas core nuclear reactor appears to have first been discussed in the open literature about 20 years ago. The context in which it was discussed was as a rocket engine. The obvious advantages of the proposed engine was that the propellant could be heated to very high temperatures, resulting in high specific impulse and that high propellant flow rates could be achieved resulting in high thrust levels. No other advanced concept proposed at that time promised this highly desirable combination of the requirements of manned, interplanetary travel.

The coaxial flow gas core reactor concept as first proposed, was deceptively simple.[1] A low velocity inner stream of fissioning fuel gas was surrounded by a very fast-moving propellant stream. The hot inner gas transferred energy to the outer stream by thermal radiation, which was absorbed by the propellant because it was seeded with absorbing particles. In theory, at least, enough fuel could be fed into the cavity to maintain a critical mass. However, there were some economic limitations on the rate of fuel loss. The fluid mechanics studies which were undertaken to determine the rate at which fuel had to be fed into the reactor cavity to make up for the loss are the subject of this review.

The early fluid mechanics studies were begun before extensive nuclear studies had been made. In the earliest studies, it had not been apparent that the fuel had to be present in a large fraction of the cavity diameter and that the cavity length-to-diameter ratio had to be of the order of one. These conditions were necessary in order to keep the critical mass requirements within reason. From these early studies and the simultaneous nuclear studies, the idea of a reactor cavity with samll L/D and large fuel volume fraction emerged.

The fluid mechanics studies were redesigned to take into account the new picture of the cavity geometry. As further work progressed, it was seen that the flow was actually a turbulent, entrance region flow, almost totally dependent on the inlet configuration and conditions. The flow was transitional and unique, and the usual assumptions of similarity and self-preservation were not valid for analytical studies, making necessary a large experimental program. Furthermore, in the actual reactor cavity, extremely large temperature and density variations would exist and a fundamental understanding of the cavity flow was seriously lacking.

A program was set up by NASA to develop the basic understanding for the coaxial flow GCR fluid mechanics so that concept feasibility could eventually be determined. The program involved several laboratories after the initial concept formulation at Lewis Research Center. These were Lewis, United Aircraft Research Laboratories, Princeton University and the Illinois Institute of Technology. Later, Aerojet Nuclear Company and the TAFA Division of the Humphreys Corporation were included. The experiments and analyses were carried out at the installation most suited for the type of work involved.

In January 1973, policy and budgetary factors forced the termination of much of NASA's space nuclear program. Almost all of the fluid mechanics research in the coaxial flow GCR program ended abruptly. A unified overview was never presented which demonstrates the accomplishments of the program and points out areas where additional work is required for a full understanding of the cavity flow. This review is an attempt to fulfill a part of this need.

The space limitations on this paper make it impossible to discuss all of the work done within the program. The two areas where discussion and comparison of work is most useful are in the a) the factors which influence containment in cold flow studies; and b) the effects of heat generation on containment. The work in these areas have not received any critical review in the past. Therefore, this paper will be limited to discussion of these two areas. The papers discussed are limited to those from which the author feels a significant point can be made. Some important work has been neglected because of the space limit. The review is structured in such a way as to compare and contrast the related work of the program, rather than to preserve the chronological order of the work. Unfortunately, in such a structuring it often happens that a single work is discussed in several parts without ever giving the whole. However, it is felt that the significant results of the program will be made more clearly visible with this approach and apologies are tendered to the authors whose works have been so treated.

* Work performed under NASA Grant NSG7039

Factors Influencing Cold Flow Containment

In order to discuss the factors which influence containment of inner stream fluid in a confined coaxial flow, it is necessary to describe the various sub-regions of flow that exist along with their dominant characteristics. Figure 1 is a schematic of confined coaxial flow with the sub-regions labeled. Starting at the upstream center is the inner stream potential core. This region is dominated by inertial forces and pressure rather than shear forces. The shear forces do, however, control its size and for some cases the inner potential core may not exist. Surrounding the potential core is an annular mixing region which separates the inner and outer stream potential flows. It is a transitional shear layer with a rapidly growing turbulence level (for the typical turbulent case). It is dominated by the velocity difference between potential flows and the shapes of the inner and outer stream velocity profiles at the tip of the separating duct. The inner and outer stream turbulence levels and scales also have a moderate effect on the mixing region. The outer fluid potential flow is also dominated by inertial forces and pressure as well as by continuity effects due to the growing boundary layer on the confining duct. The annular mixing region thickens downstream to the point where it merges with itself and the inner stream potential core ends. At this point it can be said that the momentum defect of the trailing edge wake disappears. The flow downstream of this point is made up of at most, three regions. They are the jetlike or wakelike (depending on velocity ratio) "free" shear flow region, the outerstream potential flow and the duct boundary layer. For enough downstream, the "free" shear flow region and boundary layer will merge and eventually fully-developed pipe flow will be approached in the duct.

The regions of interest in this paper are those upstream of the merger of the duct wall boundary layer and the "free" shear flow as contained by the dashed line in Figure 1. The main parameter for determining the nature of the flow is the velocity ratio of the streams. The Reynolds number has a second order effect and only on certain regions of the flow. The variation of velocity ratios can be broken up into three ranges for purposes of discussion.

When the velocity ratio is close to one, the predominant feature of the flow is the annular mixing region separating the potential flows. This mixing region is the wake from the trailing edge of the separating duct. Its spreading rate is affected by the velocity profiles in both streams at the trailing edge of the separating duct. the velocity difference across the region and by the turbulence levels in both streams. The effects of the initial turbulence becomes more pronounced as the scales become of the order of the mixing region thickness or greater, and, possibly, as the fluctuating velocity magnitude becomes of the order of the velocity difference or greater.

These effects are brought out in photographs of bromine-air coaxial flow experiments performed at Lewis Research Center.[2,3,4] The experiments were performed for a range of velocity ratios and inner and outer stream Reynolds numbers. At each set of values of the parameters, runs were made with honeycomb inserts in: a) neither duct; b) the inner stream duct; c) the outer stream duct; d) both ducts. For the outer-stream-to-inner-stream velocity ratios of about 0.2 to 2, the mixing region appeared laminar for inner jet Re of 2400 or less. With a honeycomb section inserted in the inner stream duct only, the laminar appearance remained for almost all inner jet Re achieved, up to about 4000. There are two resulting effects of this homeycomb which can affect the mixing region transition. First, the velocity profile will be very flat and the total momentum defect will be decreased substantially. When the inner stream has the higher initial velocity, this decrease in momentum defect may be the most stabilizing feature of the honeycomb. There will also be a decrease in the scale of turbulence due to the honeycomb since the scale will be bounded by the width of the honeycomb passages rather than the duct diameter. The authors imply that this is probably the primary stabilizing effect. When the honeycomb was also added to the outer stream inlet, the stabilizing effect was diminished but did not disappear. When the honeycomb was present in the outer stream only, the mixing region was turbulent over a wider range of parameters than with no honeycomb at all. Of the conclusions to be reached from all this data, the most clearly visible is that the outer stream velocity profile has a great effect on the mixing region for velocity ratios close to one. The thicker it is, the more stable the region is. This fact is borne out by the buffer region studies which are discussed subsequently. The outer stream turbulence appears to have a lesser effect on transition. Another conclusion from the above is that inner stream turbulence has some effect and decreasing its scale is stabilizing. However the changes in turbulence scale have not been separated from changes of the inner stream boundary layer thickness and the annular wake momentum defect in these studies. It also appears that decreasing the momentum defect while only narrowing the wake a small amount is stabilizing. When both honeycombs were present and the wake was very narrow the result was destabilizing even though the momentum defect was smallest as were the turbulent scales. The stability of the annular mixing region is probably governed by the level of vorticity in the region more than any other factor. The turbulence in both the inner and outer potential flows is decaying and instabilities in the mixing region are growing. The local vorticity will affect the rate at which the instabilities grow.

The annular mixing region becomes of decreasing importance as the velocity ratio deviates from one. As the velocity ratio becomes very small compared to one, the flow becomes that of a primary jet entraining a surrounding, secondary stream. Recirculation zones can be set up if the secondary stream can not meet the entrainment requirements of the primary jet. This recirculation zone is in the form of a ring pressed against the outer duct wall a few diameters downstream of the initial face.[5] This range of velocity ratios is not the one of interest here, and will not be discussed further.

The range of velocity ratios of interest for the coaxial flow GCR contains all those above a value of about 2 or 3. The most pertinent feature of this range is the solid cylindrical wake of the inner duct rather than the wake of its thin wall.

The wake is partially filled by the inner stream fluid and for lower values of the velocity ratio the wake effect is partially mitigated. This can be thought of in terms of there being enough inner stream fluid to satisfy the entrainment requirements of the outer stream flow. However, as the velocity ratio becomes large enough, there is not enough inner stream fluid to satisfy the entrainment requirements of the outer stream and something similar to separation takes place with the development of radial pressure gradients and recirculating eddies behind the blunt cylinder end.[6] Figure 2 shows the development of the recirculation eddie as velocity ratio is increased. As the inner stream is entrained or accelerated along its outer edge, the streamlines move outward as they come closer together. Streamlines close to the centerline must diverge as a result of the deceleration of the fluid in order to satisfy the continuity condition. Thus, a region of positive pressure is generated on the centerline. If the pressure rise exceeds the dynamic head at the centerline, reversal of the flow takes place with the formation of a recirculation eddy. In this case, it is said that the inner stream cannot meet the entrainment requirements of the outer stream. If, however, the momentum of the inner stream is high enough, the accelerated outer region will reach the centerline before a complete reversal can take place. Here, the entrainment requirements are met.

The velocity is not the only factor in determining if recirculation will take place in a given coaxial flow. As has been mentioned before, the outerstream velocity profile is also very important. Its effect has been illustrated in terms of the flow induced upstream along the centerline by a cylindrical vortex sheet downstream of, and at the radius of, the inner duct.[6] This vortex sheet represents the boundary layers of the inner and outer streams. The thinner the dominant outerstream boundary layer is, the more "concentrated" its vorticity and the greater the strength of the vortex sheet. When the induced velocity, which increases with vortex sheet strength, reaches the magnitude of the inner stream velocity, recirculation is incipient.

The containment of inner stream fluid can now be discussed in terms of the regimes and types of flow possible. It is obvious that recirculation will strongly enhance mixing and result in poor containment because the inner stream will be mixed internally with recirculated fluid and rapidly accelerated by and mixed with outer stream fluid, usually in a highly turbulent process. If recirculation is prevented from occurring, then the mixing takes place in the annular mixing region followed by the cylindrical wake. The containment will be affected by the magnitude of the velocity gradients and the level of the turbulence. Suppressing the turbulence and maintaining small gradients will increase containment and these two conditions can usually be accomplished simultaneously.

It was recognized rather early in the program that large velocity gradients in the initial plane (narrow outer stream boundary layer on the trailing edge) would greatly affect mixing and an analytical investigation was performed which demonstrated this. The investigation was on the effects of a momentum buffer region on the mixing and containment.[7] It was found that there were optimum values of buffer region velocity ratio and thickness. The initial profiles of all three streams were taken as plug without singularities at the ends of the separating ducts. The total outer stream flow remained constant while the amount in the buffer region was varied. This latter condition caused the outer stream to inner stream velocity ratio to increase as the buffer region was made thicker. However, the general conclusion that decreasing the velocity gradients or vorticity increased containment was demonstrated for the restricted range of conditions studied in this work.

In an experimental investigation[8] done at IIT in order to study the effects of free stream turbulence on the mixing, velocity and concentration profiles were measured for initial velocity profiles which were different from those in a previous investigation.[9] These profiles did not differ markedly but it still can be seen from the results that when the initial, outer stream boundary layers in the second investigation were thicker, higher containment was the result. In this investigation, a screen was placed in the outer stream upstream of the initial face. This resulted in lower turbulence intensities in the outer stream, and a change in outer stream initial velocity profile due to tripping of the boundary layer on the outside of the inner duct. Results with the screen were compared to similar results taken with a boundary layer trip device which gave an outer stream profile similar to that with the screen but with higher turbulence intensities. Little difference in mixing and containment was seen due to the differing turbulence intensities. However, the velocity ratio was quite high in most of the cases of this investigation and the solid cylindrical wake effect was the dominant one. For the cases where velocity ratios were high, the existence of a recirculation eddy was shown by moving a thread of cotton along the centerline and observing it being pulled upstream near the exit of the inner duct.

A series of experiments performed at UARL[10,11,12] was conducted to determine how containment could be improved by tailoring initial velocity profiles and turbulence levels. In a coaxial flow experiment, Scott industrial foam was placed across the entire duct at the inlet plane. It was shown that recirculation was suppressed up to very high velocity ratios. The effect of the foam is clearly seen in Figure 3. In frames a and b, no foam was present and the inner stream, visualized with iodine, shows large scale turbulence on the edge and rapid mixing. In frames c and d with foam present, it is seen that the inner stream has a smooth edge and maintains its integrity to a much higher velocity ratio. In a parallel investigation at IIT, shadowgraphs of a similar experiment were obtained and are shown in Figure 4.[13] Scott foam was placed at the initial face of the same apparatus used in reference as shown in the first frame. Pictures were taken at several velocity ratios with and without a cone that produced, in a crude way, a buffer region between inner and outer streams. The inner stream was freon 12 and the outer stream was air. It can be seen here also, that the inner stream maintains its integrity and shows smaller turbulence scales with the foam present and that the cone provides for a wider inner stream and a smaller scale of turbulence. What is most important in these two figures is that the inner stream decreases in width going through the foam.

The radial pressure gradient which is set up by the entrainment of inner stream fluid and results in a high pressure region at the upstream end of the recirculation eddy when foam is not present causes instead a radial inflow inside the foam. The initial profile at the downstream end of the foam is much smoother and monotonically increasing from the centerline to the beginning of the outer duct boundary layer. Because this new initial profile has no minimum surrounded by inflection points, the shear layer generated turbulence, is of much smaller scale and lower intensity. The effect of the foam on the free stream turbulence is probably of no importance at all. The major effect of the foam then is on the initial velocity profile and the elimination of the radial pressure gradient. The work at UARL also included detailed measurements on a coaxial flow with a buffer layer and the Scott foam and it was shown that containment could be increased dramatically over a two-stream system without foam.

The investigation that initiated work on the spherical geometry with coaxial flow was carried out at Lewis Research Center.[14] It was noted that because of pressure vessel design and wall cooling requirements, a spherical cavity shape would be more likely than a cylindrical one. The investigation was to determine if the spherical shape could be used advantageously for increasing containment. In the proposed design, propellant would be introduced all along the cavity wall to satisfy the wall cooling requirements and also to induce the inner stream to occupy a greater fraction of the cavity volume. The flow experiment was carried out in a two-dimensional cavity with flat top and bottom and curved walls. The inner stream was smokey air introduced through a "shower-head" nozzle. Outer stream air entered all along the porous curved side walls. Pictures taken through the flat top were used to obtain concentration measurements and for flow visualization. The propellant entered the cavity with a radially inward directed velocity which was adjusted to be fairly uniform over the whole length of curved wall. The results were very encouraging. The flow appeared to be steady with a large volume of dense, smokey air in the middle of the cavity. Containment was calculated, based on the measured density of smokey air at the showerhead exit to be very large at a flow rate ratio of 25. These results were understood to be of a very preliminary nature because it was a two-dimensional mockup of a three-dimensional flow and the Reynolds number of 1100 was quite low. However, they indicated that further work was warranted.

A series of experiments were then performed at UARL to determine containment levels in a spherical cavity.[15,16] In an exploratory study, various types of fuel or inner stream injection configurations were studied separately and then the best design was used in an exploration for the optimal outer stream injection configuration. The spherical configuration for the "best" case containment studies is shown in Figure 5. The inner stream is injected through a porous sphere. The outer stream is injected at the top and bottom of the cavity with a tangential velocity component but the central section gives essentially, only an axial component of velocity to the propellant. The reasons for this design being the "best" for spherical geometry is that it comes closest to the cylindrical case in design. Containment measured in the spherical geometries at UARL was always lower than that measured in cylindrical designs. The basic problem of the spherical design is in the radial pressure gradients which exist with curving streamlines. The tangential component of the outer stream at the top of the cavity sets up a radial pressure gradient with a pressure minimum at the centerline near the fuel injection point. This pressure gradient apparently works against the entrainment of inner stream fluid by the outer stream. However, at the downstream end of the cavity, the inward curving streamlines must begin to curve back out so that the fluid can exit the chamber through the nozzle. This reverse curvature causes a high pressure area at the centerline near the cavity exhaust. This high and low pressure system is very favorable for the formation of large recirculation eddies. These large eddies are visible in many of the flow visualization studies with spherical geometries. Furthermore, the pressure field set up around the fuel injection location is very complex because of the pressure gradients and may tend to influence the inner stream fluid velocity profile at the injector surfaces while the entrainment necessary to "pull" the inner stream out to large radius against the pressure gradient probably also results in increased mixing of streams.

The conclusion that can be drawn from these containment studies at this time is that containment in cold flow studies is greatest when the radial pressure gradients are minimized and the initial velocity profiles are smooth, monotonic and have small velocity gradients. This combination of virtues has best been accomplished in the cylindrical coaxial flow experiments conducted at UARL.

Effects of Heat Generation on Containment

Most of the studies done on the containment of fissionable material or fuel in the cavity considered only the cold flow of gases. The effects of the very large heat generation rate in the fuel gas were neglected because of the difficulties encountered in treating them both analytically and experimentally. The few studies that have been performed on "hot flows" do not readily yield values for containment but rather indicate how the heat release will affect the containment as it is determined from cold flow studies.

The experimental work done on hot flows include a series of investigations by Grey and coworkers at Princeton University on a flowing argon plasma and cold coaxial stream of several different gases.[17,18,19] Cold flow data was also taken for comparison. Their work also included an analysis of coaxial flow mixing. Both laminar and turbulent flows were investigated. The earlier work centered on the laminar case, but results showed that a laminar flow could not be maintained in their apparatus. In the turbulent flow studies, maps of concentration, velocity and temperature were obtained with a cooled probe technique. The flow in this system was dominated by a wake effect which the investigators attempted to quantify, and high inlet turbulence level. Schlieren pictures of the flow field showed that the coaxial field fluid which issued from a section of tubes maintained its individual jet stratification for at least one inner jet diameter downstream, inhibiting mixing to

some extent. However, the wake effect was, in general, so strong that mixing occurred very rapidly. The important conclusions that were drawn from this work are that the effects of core temperature on the concentration profiles are not large and that containment of argon within a cylinder defined by the argon inlet duct diameter is essentially complete. Furthermore, the spreading rate of the argon appears to be less with the hot flow cases than in similar cold flow cases. These conclusions are stated here because they are in disagreement with published results from a later series of arcjet studies.

This later series of hot flow studies was done at the TAFA division of the Humphries Corp.[20,21,22,23] TAFA's objective was to develop an induction heated plasma simulation of a gas core reactor. Data consisting of concentration, temperature and stagnation pressure measurements[20] were taken in a coaxial flow of argon plasma and air or hydrogen. The plasma was induced by a radio-frequency field after the arc was started up with a D.C. discharge. The air/argon mass flow ratios used were 0.6, 5.55 and 19.7 and the hydrogen/argon mass flow ratio was limited to one value of 1.67. Both hot flow and cold flow runs were performed and it was concluded from a comparison that "the plasma eliminates all turbulent recirculation present in the cold flow and appears to behave as if it had a definite skim or boundary similar to a gas/liquid interface." Some of the hot and cold flow concentration data is reproduced in Figures[6-8]. Figure 6 shows concentration measurements for cold laminar, axial flow of argon and air. Both streams have equal volumetric flow rates of 100 SCFH. The parabolic lines of constant mole fraction are cited as evidence of purely laminar flow. However, the data apparently invalidate the concentration measuring scheme employed. The mean mixed mole fraction of air for this case is 0.50. Yet at two diameters downstream, the parabolic flow averaged mole fraction of air is at least 0.70. Furthermore, at this axial station the velocity profile is probably closer to plug than parabolic, and a plug profile averaging would give a mean, mixed mole fraction of air of about 0.8. This indicates that concentration measurements are accurate to, at best, about $\pm$ 50%. Other data is presented for cold and hot flows successively for different mass flow rate ratios. In these cases there is a tangential or swirl component of the velocity of the argon to stabilize the arc.

The discrepancy between the measured concentrations and the mean mixed mole fraction exists for the cold flow case of each of the mass flow ratios investigated. The equal velocity case, $W_{air}/W_{argon} = 0.67$, is shown in Figures 7 and 8 for the cold flow and hot flow, respectively. In the cold flow case, at 2" downstream the air mole fraction is shown as 0.5 at the centerline. The region off the centerline must have considerably higher mole fractions of air yet the mean mixed mole fraction of air is 0.451 according to a mass balance. Another peculiar feature of the TAFA results is visible in Figure 8 for the hot flow. At the initial plane of the mixing region the argon concentration ranges as high of 0.50 in the entering air stream. This peculiarity exists in most of the remaining data for both hot and cold flow.

One possible explanation for the disagreement can be based on the measuring device employed. A sample of fluid was removed from the flow field with an aspirating probe. If the probe sucked in fluid at a rate higher than the local flow rate in the field, it would perturb the flow field considerably and result in the measurement of a concentration averaged over a volume quite large compared to the probe tip.

Another observation that can be made from these data is that the inner stream spreads rapidly radially outward past the radius of the argon duct. This is in direct disagreement with essentially all other cold coaxial flow experiments with the outer stream to inner stream velocity ratio substantially greater than one.[9,16] The Princeton hot flow studies which also had a swirl component to stabilize the arc, show a decrease in spreading rate from the cold flow to hot flow experiments as do the TAFA experiments, but the Princeton measurements also conclude that the argon does not spread beyond the inner duct radius. Stagnation pressure traverses for both hot and cold flow cases were also made at TAFA. The probe used was the sampling probe. However, no attempt to orient the probe in the streamline direction was made so that pressures reported may not be true stagnation pressures. These apparent inconsistencies and disagreement with previous work make it premature to base conclusions of high containment on the TAFA work.

A second conclusion drawn from the TAFA work is that the plasma has a "hard skin." This is based on high speed photographs showing 250 micron tungsten particles "bouncing" off the plasma fireball". It is not clear that this conclusion has been confirmed by reference to observations made by other investigators working with arcs which are not in RF fields. An alternate possible explanation of the bouncing relates to the Leidenfrost phenomenon which explains why a drop of water will bounce off a hot frying pan. The tungsten particle would begin to vaporize as it entered the very hot plasma region. The high rate of vapor generation would then drive the particle back out of the arc.

It is also true that electrostatic fields exist in the plasma due to the RF field. Calculations of the electrostatic force required to balance the gravitational force on the particle indicate a charge equivalent to 10^3 to 10^4 electrons on the surface of the tungsten is required. It is possible that a charge of this magnitude could be accumulated by the tungsten as it passes through the outside fringe of the plasma since tungsten would tend to "poison" the arc. These alternative explanations for the bouncing particles are also not conclusive. However, the existence of a "hard plasma skin" should be left open to question until it is confirmed in a plasma without an RF field.

In a later report covering tests which were carried out by TAFA on a curved permeable wall induction torch, the plasma was maintained by vaporizing solid material which ionized.[22] After startup, the plasma was fed by the vaporized solid with no through-put of ionizing gas. The solid to coolant gas mass flow ratio was between 1/1500 to 1/5000. Because of the very different processes taking place, the relationship to containment requirements in a cavity reactor are not clearly established.

In this report, experiments were also carried out with a flowing argon plasma and with a coolant gas flow all of which entered the flow field radially through a porous wall. In these tests, as in the previous ones, the hot flow conditions were said to prevent all recirculation due to wake effects. This could be explained as being due rather to the rapid expansion of the argon stream which in turn is due to its rapid temperature rise. In fact, a gas experiencing a temperature change from 300°K to 9000°K would expand in volume by a factor of 30. Since the confining walls prevent radial expansion of the argon, the axial velocity of the argon increases by a factor on the order of 30. In all the tests performed at TAFA, except one, the initial (cold) velocity ratio was about 34 or less, and the exceptional case was about 45. If these ratios are divided by 30, it is seen that actual velocity ratios in the plasma region are order one or less, so that the strong wake effect which causes recirculation is just not present in the hot flow cases. This axial expansion of the inner stream is also apparent in the Princeton work where velocity traverses are presented. However, the incomplete data sets make it difficult to demonstrate it quantitatively. Figure 9 shows a case with initial velocity ratio of about 1 where initial velocities are based on initial plane average conditions. However, the centerline temperature at the initial plane of the mixing region is 6000°R, and the centerline velocity is almost 3 times the coolant gas velocity. The centerline temperature decays to 3000°R in two diameters and the centerline velocity falls to about half of the initial value, indicating expansion and contraction take place almost entirely in the axial direction, for these experiments where the outer fluid was not confined.

An analytical study of the effects of heat generation on an entrance region coaxial flow was performed at IIT.[24] In this study, the equation set was formulated to represent the gross behavior of the flow field and to avoid the complexity of a more detailed analysis. The field was modeled as a laminar, confined coaxial flow for which the boundary layer assumptions are valid. Only radial radiative transport of energy was considered and the two fluids were assumed to be immiscible. The results for one typical case are shown in Figure 10. Here z is axial distance made dimensionless on outer duct radius times Reynold's number, and α is the location of the interface between the two immiscible streams. Subscript α is the value of the inner stream property at the interface. The centerline velocity changes from 1/10 the outer stream value at the initial plane, to 1.4 times the initial value of that of the outer stream. The centerline temperature increases very rapidly and then actually falls off slightly as the thermal radiation becomes dominant. It is also seen that the interface location falls rapidly from 0.7 to about 0.3 as the centerline velocity increases by a factor of 14 and centerline temperature increases by a factor of only 3. If the velocity increase was due only to thermal expansion axially along the centerline, the velocity change there would be only by about a factor of 3. However, there is expansion of all the inner stream due to heat generation and the energy radiated to the outer stream causes expansion of the outer stream also, and all this fluid expands radially inward to some extent, because of the confining wall. This effect, coupled with the buildup of the wall boundary layer accounts for the additional increase in centerline velocity. This type of behavior is indicated in the TAFA results for their hot flow cases (Figure 8). In all their cases, the lines of high constant mole fraction of argon stretch out to a considerable extent in a narrow region along the centerline. This is consistent with the idea of a radially shrinking, axially expanding core of argon.

It is difficult to draw conclusions from the relatively small amount of work done on how the internal heat generation affects containment. In the discussion of the previous section, it was seen that cylindrical coaxial flow gave the best cold-flow containment found to date. However, the cylindrical boundary causes large axial acceleration when internal heat generation is present. It is possible then, that a spherical cavity outer boundary may be desirable for containment with heat generation. The key to success would be to use the induced radial pressure gradients to force the thermal expansion to take place radially instead of axially while mixing and entrainment are minimized by inducing axial streamlines downstream of the expansion.

It would appear at this time that the most important work still to be done to evaluate the coaxial flow GCR concept feasibility is in this area of coupling the heat generation to the fluid mechanics. Both experimental and analytical studies are necessary to determine optimal cavity shape and inlet flow details. The untimely termination of the major part of the GCR program ended several efforts in this area before they obtained the definitive results necessary to make a realistic evaluation of concept feasibility.

References

1. Weinstein, H. and Ragsdale, R. G., "A Coaxial Flow Reactor - A Gaseous Nuclear Rocket Concept," American Rocket Society, Preprint 1518-60, 1960.
2. Ragsdale, R. G. and Edwards, O. J., "Data Comparisons and Photographic Observations of Coaxial Mixing of Dissimilar Gases at Nearly Equal Stream Velocities," NASA TN D-3131, 1965.
3. Taylor, M. F. and Masser, C. C., "Photographic Study of a Bromine Jet in a Coaxial Airstream," NASA TN D-4660, 1968.
4. Masser, C. C., "A Photographic Study of a Bromine Jet in a Coaxial Airstream with Honeycomb at the Injection Plane," NASA TM-X-1900, October, 1969.
5. Barchilon, M., and Curtet, R., "Some Details of the Structure of an Axisymmetric Confined Jet with Backflow," J. of Basic Eng., 86, P777 (1964).
6. Rozenman, T., and Weinstein, H. "Recirculation Patterns in the Initial Region of Coaxial Jets" NASA CR-1595, May 1970.
7. Ragsdale, R. G., "Effects of a Momentum Buffer Region on the Coaxial Flow of Dissimilar Gases" NASA TN D-3138.
8. Kulik, R. A., Leithem, J. J. and Weinstein, H., "Effect of Free Stream Turbulence on Coaxial Mixing," NASA CR-1336, May, 1969.

9. Zawacki, T. S., and Weinstein, H. "Experimental Investigation of Turbulence in the Mixing Region Between Coaxial Streams," NASA CR-959.

10. Johnson, B. V. and Clark, J. W., "Experimental Study of Multi-Component Coaxial-Flow Jets in Short Chambers," NASA CR-1190, April, 1968.

11. Johnson, B. V., "Exploratory Experimental Study of the Effects of Inlet Conditions on the Flow and Containment Characteristics of Coaxial Flows," United Aircraft Corp. NASA CR-107051, 1969.

12. Bennett, J. C., and Johnson, B. V., "Experimental Study of One-and Two-Component Low-Turbulence Confined Coaxial Flows," NASA CR-1851, June 1971.

13. Kulik, R. A., and Weinstein, H. Private Communication, 1971.

14. Lanzo, C. D., "A Flow Experiment in a Curved-Porous-Wall Gas-Core Reactor Geometry," NASA TM-X-1852, August, 1969.

15. Johnson, B. V., "Exploratory Study of the Effects of Injection Configurations and Inlet Flow Conditions on the Characteristics of Flow in Spherical Chambers," NASA CR-1965, January, 1972.

16. Johnson, B. V., "Experimental and Analytical Study of One and Two Component Flows in Spherical Chambers," NASA CR-2282, August 1973.

17. Grey, J., William, P. M., and Fradkin, D. B., "Mixing and Heat Transfer of an Argon Arcjet with a Coaxial Flow of Cold Helium," NASA CR-54438, October 1964.

18. Grey, J., Sherman, M. P., Williams, P. M., "Laminar Arcjet Mixing and Heat Transfer: Theory and Experiments," AIAA J., 4, p.986, (1966).

19. Williams, P.M. and Grey, J., "Simulation of Gaseous Core Nuclear Rocket Mixing Characteristics Using Cold and Arc Heated Flows," NASA CR-690.

20. Dundas, P. H., "Induction Plasma Heating: Measurement of Gas Concentrations, Temperatures, and Stagnation Heads in a Binary Plasma System,", NASA CR-1527, February, 1970.

21. Vogel, C. E., "Experimental Plasma Studies Simulating a Gas-Core Nuclear Rocket," AIAA Paper No. 70-691, June, 1970.

22. Vogel, C. E., "Curved Permeable Wall Induction Torch Tests," NASA CR-1764, March, 1971.

23. Poole, J. W. and Vogel, C. E., "Induction Simulation of Gas Core Nuclear Engine," NASA CR-2155, February, 1973.

24. Bobba, G. K. M., "Laminar Confined Coaxial Flow with Heat Generation," Ph.D. Thesis, Illinois Institute of Technology, December 1974.

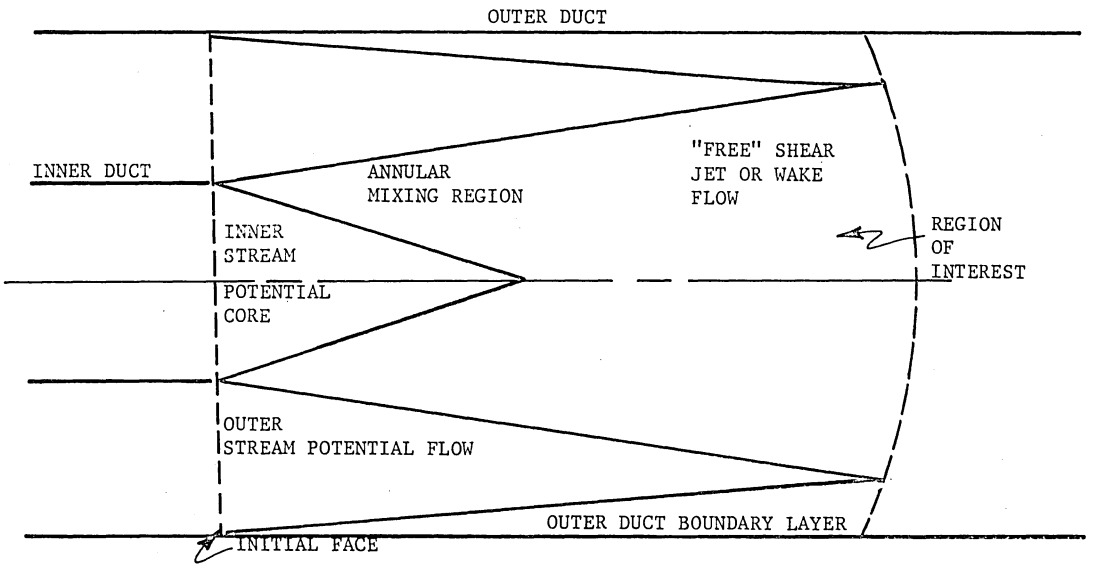

FIGURE 1. Schematic of Flow Regimes in Ducted Coaxial Flow

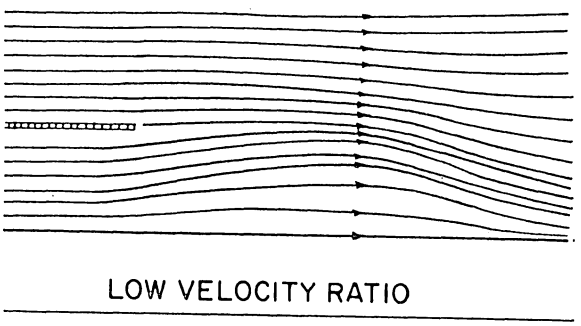

LOW VELOCITY RATIO

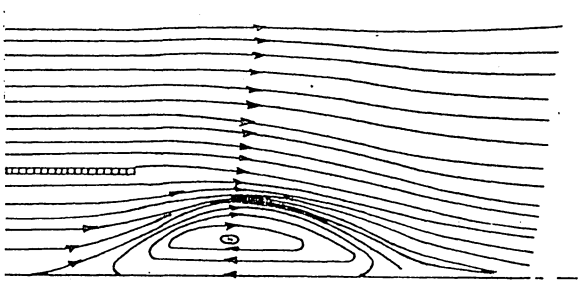

HIGH VELOCITY RATIO

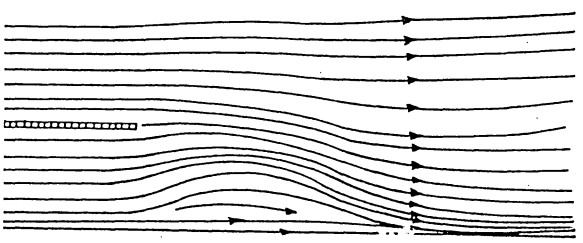

INTERMEDIATE VELOCITY RATIO

Figure 2. Effect of Velocity Ratio on the Streamlines in the Initial Region of the Coaxial Jet[6]

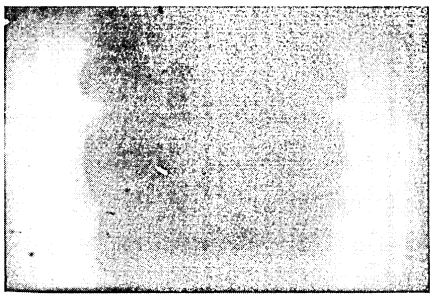

a) - Coaxial flow at a mass flow ratio of 30; no foam material.

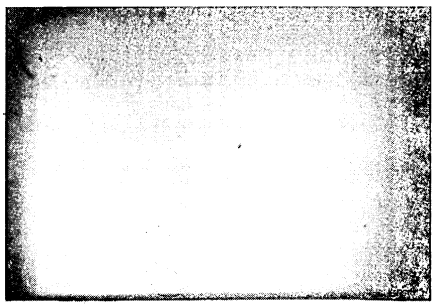

b) - Coaxial flow at a mass flow ratio of 50; no foam material.

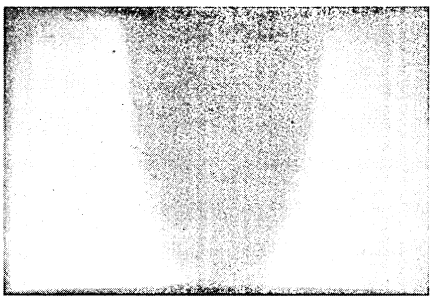

c) - Coaxial flow at a mass flow ratio of 30; with foam material present.

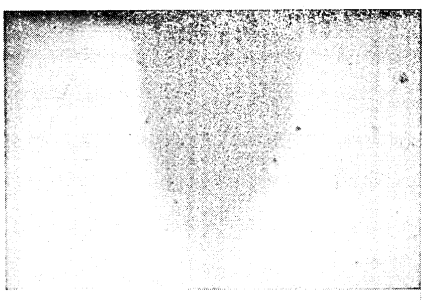

d) - Coaxial flow at a mass flow ratio of 130; with foam material present.

Figure 3. Coaxial Flow With and Without Foam Covered inlet[10]

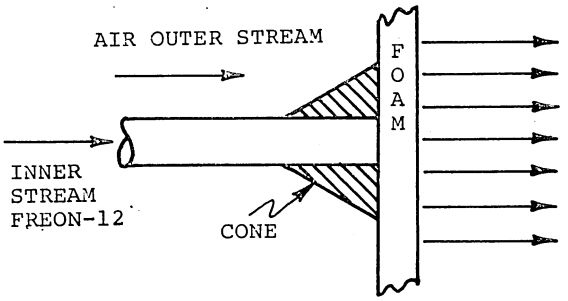

a) Schematic of Configuration

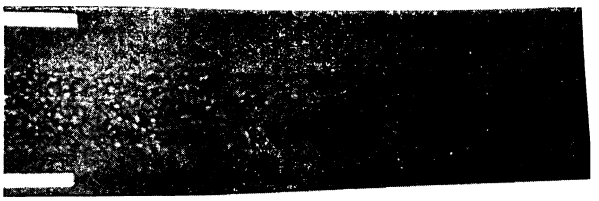

b) Foam Without Cone, ν_o/ν_i = 25.

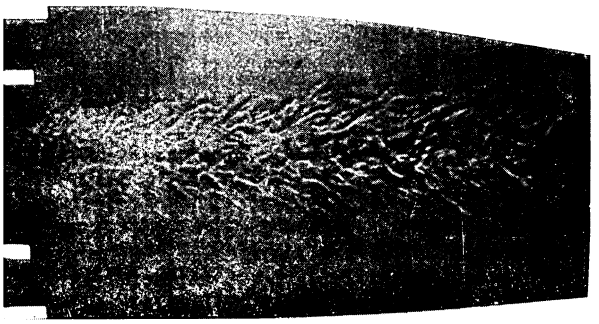

c) Foam With Cone, ν_o/ν_i = 25.

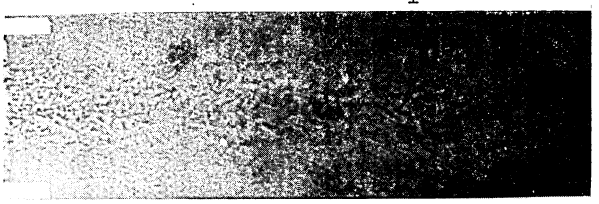

d) Foam Without Cone, ν_o/ν_i = 75.

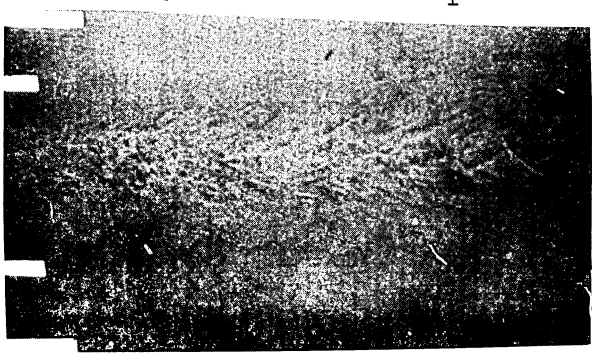

e) Foam With Cone, ν_o/ν_i = 75.

Figure 4. Shadow graphs of a Freon 12 Air Coaxial Jet System Downstream of a Foam Covered Inlet.[13]

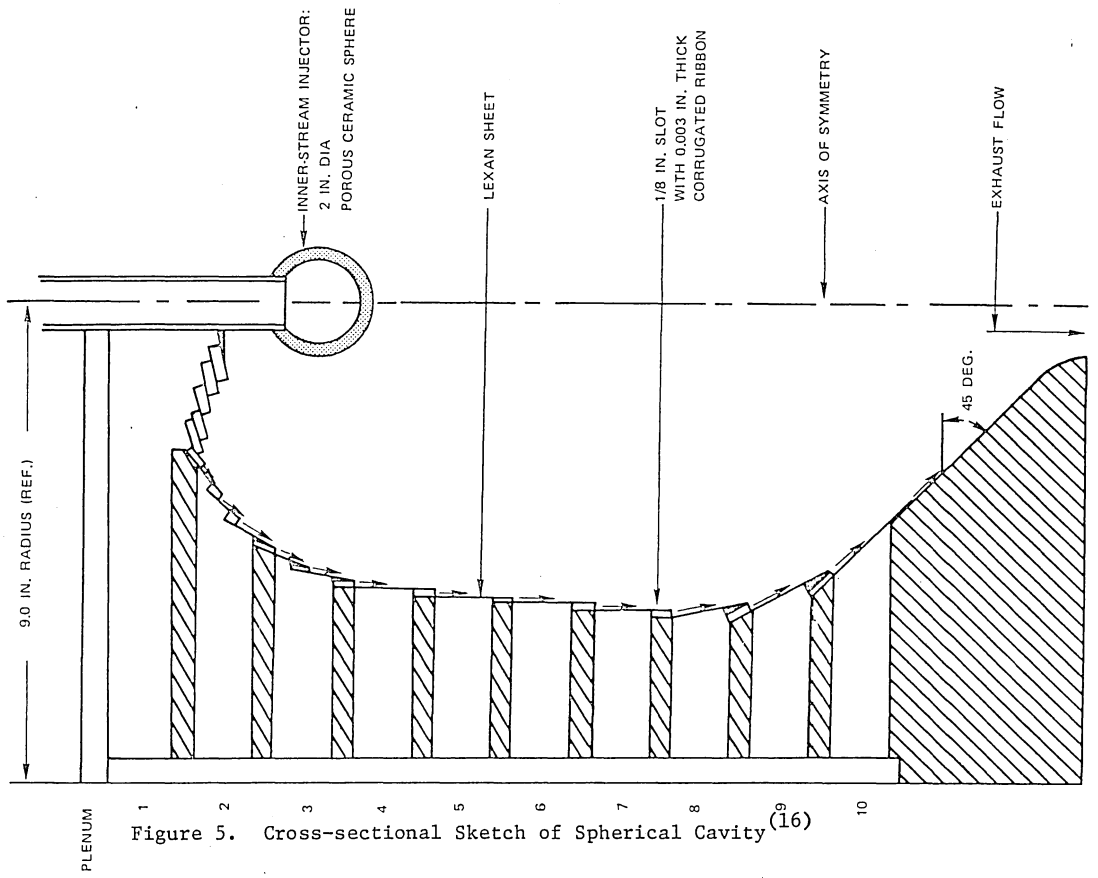

Figure 5. Cross-sectional Sketch of Spherical Cavity(16)

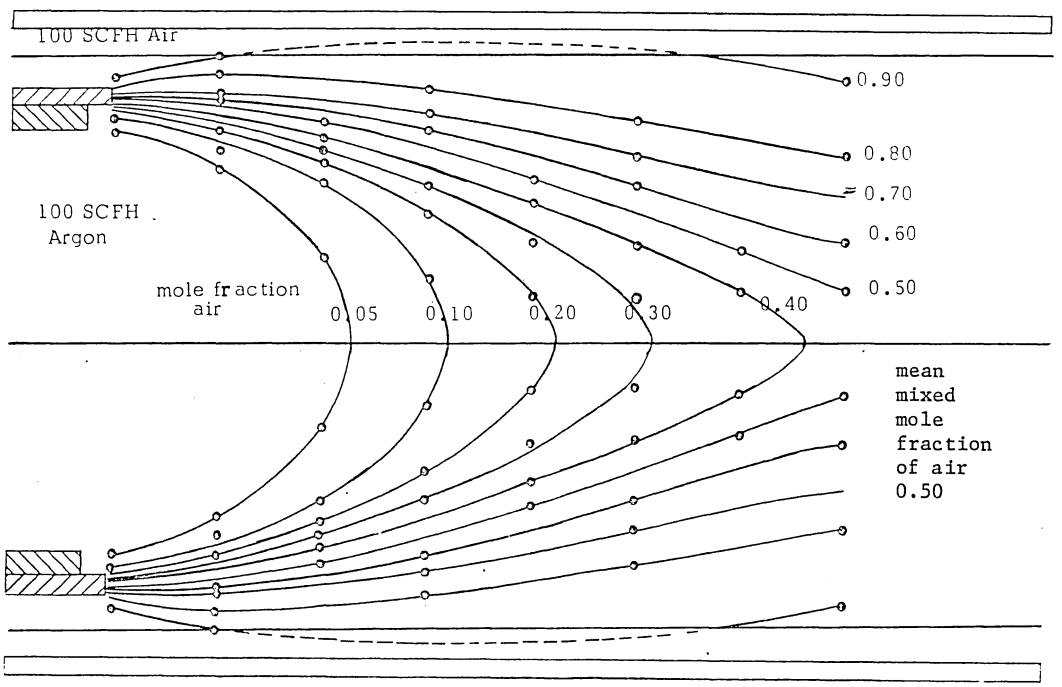

Figure 6. LAMINAR MIXING PATTERN FOR ISOTHERMAL CONDITIONS (20)

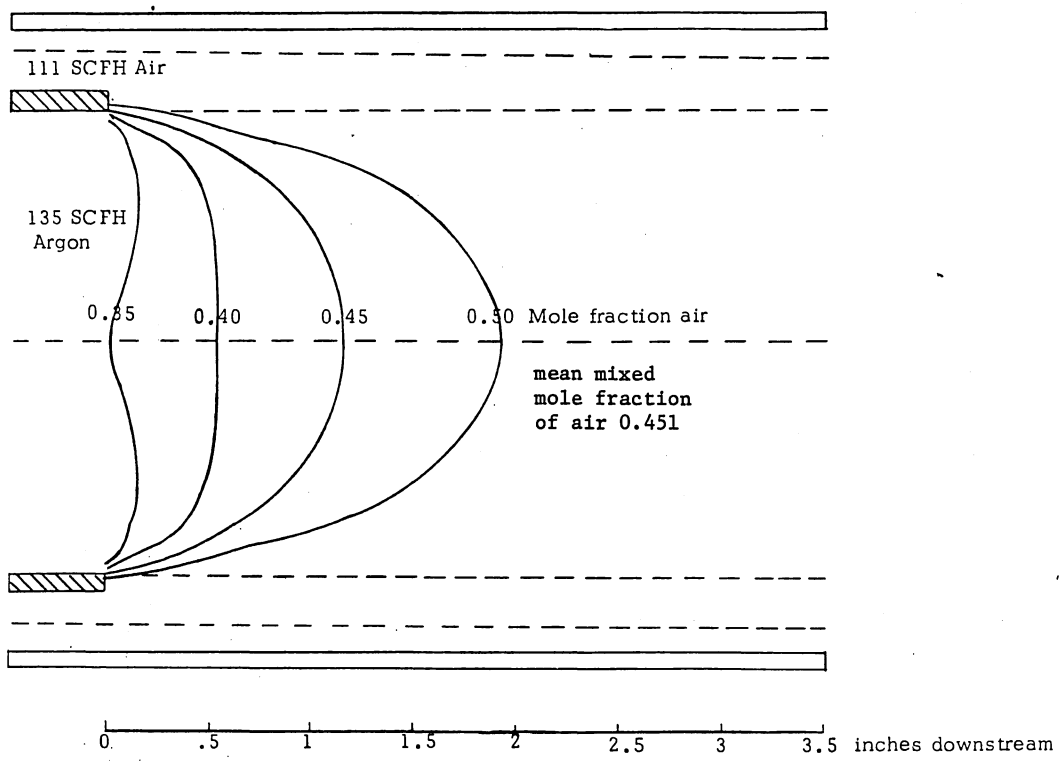

Figure 7. MIXING MAP WITHOUT PLASMA
AIR/ARGON MASS RATIO=0.67[20]

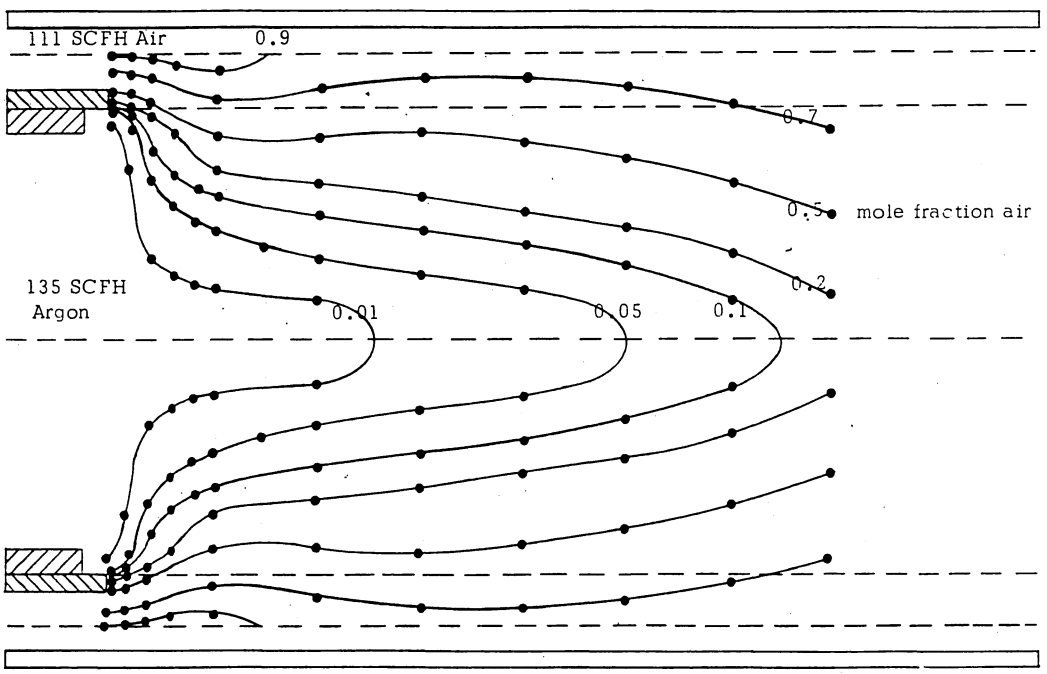

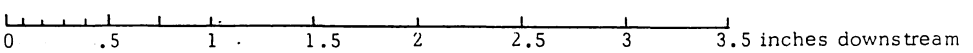

Figure 8. MIXING MAP WITH PLASMA
AIR/ARGON MASS RATIO=0.67[20]

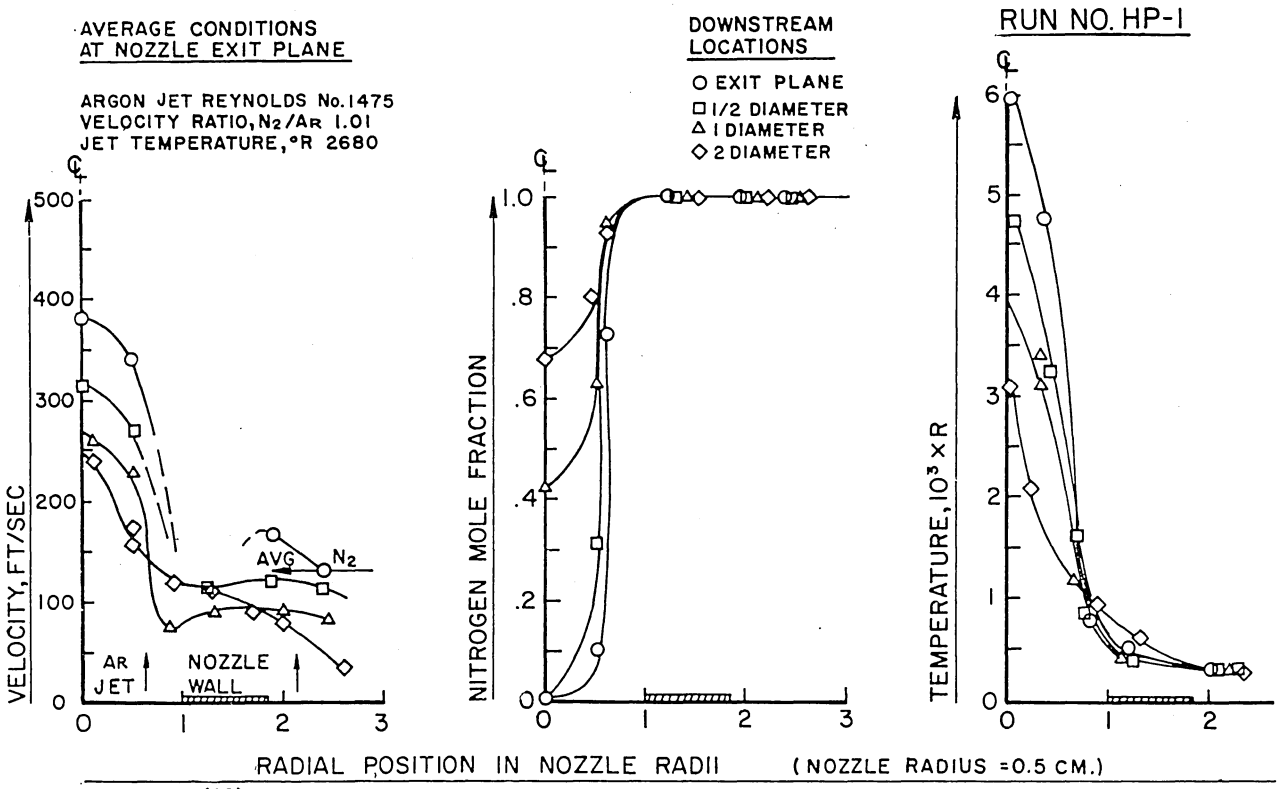

Figure 9.[19]

HALF-PROFILES OF ARGON ARCJET JET MIXING WITH COAXIAL NITROGEN FLOW

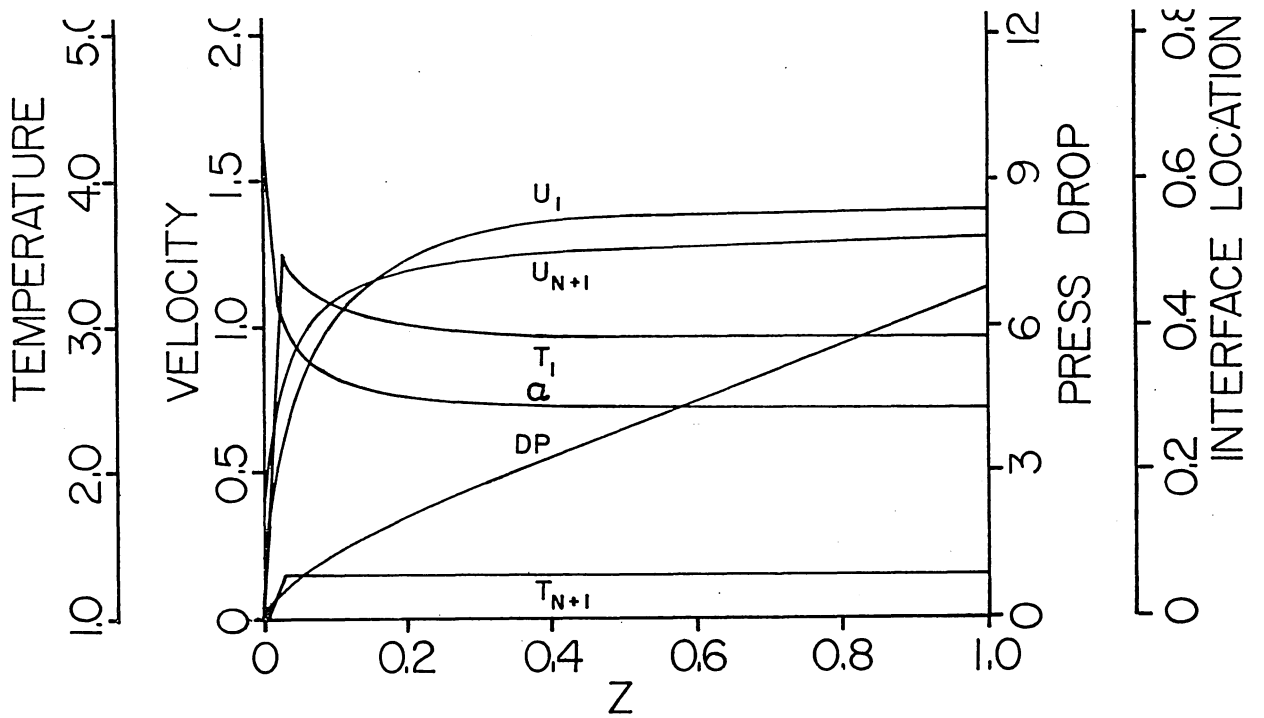

Figure 10. Axial Development of Central and Interfacial Axial Velocities and Temperatures, Pressure Drop and Location of Interface - Constant Generation per Unit Volume Case[24]

DISCUSSION

J. L. MASON: Isn't the analytical modelling of this kind of flow extremely difficult because of the need of fitting flow that requires different models together with complex boundary conditions in between?

H. WEINSTEIN: The analytical modelling is very difficult. I tried to bring that out when I said that this was an entrance region flow and you get none of the benefits of similarity or self-preservation. You can't characterize the turbulence. The turbulences in the mixing regions are different. We have free-shear generated turbulence in the annular mixing region; we have boundary layer turbulence decaying in that region. We have free-stream turbulence which has only minor interaction with the flow. We have turbulence which is building in the outer stream boundary layer. Nobody really knows how to treat the interaction of the different kinds of growing turbulence.

J. L. MASON: You mentioned that there was a capability of maintaining laminar flow under one scheme of interest.

H. WEINSTEIN: It is not laminar flow. I tried to say that the integrity of the stream is preserved. I didn't want to say laminar flow. These are unstable flow situations. We can delay transition but we can't prevent it. These are transitional flows, and we are going to get turbulent transition. We would like to delay transition somewhat, because the L/D ratio is very small, and if we can delay transition a little it would be helpful.

PROPERTIES OF RADIO-FREQUENCY HEATED ARGON CONFINED URANIUM PLASMAS*

Ward C. Roman
Fluid Dynamics Laboratory
United Technologies Research Center
East Hartford, Connecticut

Abstract

An experimental investigation was performed to aid in determining the characteristics of uranium plasma core reactors. Pure uranium hexafluoride (UF_6) was injected into an argon-confined, steady-state, rf-heated plasma within a fused-silica peripheral wall test chamber. Exploratory tests conducted using an 80 kW rf facility and different test chamber flow configurations permitted selection of the configuration demonstrating the best confinement characteristics and minimum uranium compound wall coating. The test chamber selected was 10-cm-long and 5.7-cm-inside diameter; operating pressures were up to 12 atm. A UF_6 handling and feeder system to provide a controlled and steady flow of heated UF_6 at temperatures up to 500 K and mass flow rates up to 0.21 g/s was employed. Follow-on tests were conducted using the UTRC 1.2 MW rf induction heater facility at rf power levels up to 85 kW and test times up to 41.5 minutes. To permit estimating the total uranium atom number density radial profile and confined uranium mass in the rf uranium plasma, combined plasma emission and dye laser absorption measurement techniques were employed. A cw single-frequency tunable dye laser and optical scanning system were adapted to operation at the $\lambda = 591.54$ nm uranium (UI-neutral atom) line (laser line half-width $\approx 10^{-4}$ nm). The results indicated the total uranium atom number density reached a maximum of approximately 10^{16} atoms/cm^3 at the centerline of the plasma (T_e = 9800 K). To permit a detailed post-test analysis of the milligram quantities of residue deposited on the different components of the test chamber, profilometer, IR spectrophotometer, scanning electron microprobe, x-ray diffractometer, electron microscope, and Ion Scattering Spectrometer instruments were employed. Uranyl fluoride (UO_2F_2) was the principal compound found on the test chamber peripheral wall. The overall test results demonstrated applicable flow schemes and associated diagnostic techniques have been developed for the fluid-mechanical confinement and characterization of uranium within an rf plasma discharge when pure UF_6 is injected for long test times into an argon-confined, high-temperature, high-pressure, rf-heated plasma.

Introduction

Fissioning uranium plasma core reactors (PCR) based on the utilization of fissile nuclear fuel in the gaseous state could be used as a prime energy source for many space and terrestrial applications. In addition to aerospace propulsion applications, several new space power and/or terrestrial options are being considered; these include:

(1) Direct pumping of lasers by fission fragment energy deposition in UF_6 and lasing gas mixtures.

(2) Optical pumping of lasers by thermal and/or nonequilibrium electromagnetic radiation from fissioning UF_6 gas and/or fissioning uranium plasmas.

(3) Photochemical or thermochemical processes such as dissociation of hydrogenous materials to produce hydrogen.

(4) MHD power conversion systems for generating electricity.

(5) Advanced closed-cycle gas turbine driven electrical generators.

Reference 1 discusses the overall status of plasma core reactor technology, the various energy conversion concepts, conceptual designs of various configurations, and a summary of all current research directed toward demonstrating the feasibility of fissioning uranium PCR's.

A principal technology required to establish the feasibility of fissioning uranium plasma core reactors is the fluid mechanical confinement of the hot fissioning uranium plasma with sufficient containment to both sustain nuclear criticality and minimize deposition of uranium or uranium compounds on the confinement chamber peripheral walls. Figure 1 is a sketch of one unit cell configuration of a plasma core reactor. The reactor would consist of one or more such cells imbedded in beryllium oxide and/or heavy-water moderator and surrounded by a pressure vessel. In the central plasma fuel zone, gaseous uranium (injected in the form of UF_6 or other uranium compound) is confined by argon buffer gas injected tangentially at the periphery of the cell. In applications in which it is desired to couple thermal radiation from the fissioning uranium plasma to a separate working fluid, the thermal radiation is transmitted through the argon buffer gas layer and subsequently through internally-cooled transparent walls to a working fluid channel such as shown in Fig. 1. The channels would contain particles, graphite fins, or opaque gases to absorb the radiation. The mixture of nuclear fuel and argon buffer gas is withdrawn from one or both endwalls at the axial centerline. For other applications in which it is desired to extract power in the form of nonequilibrium, fission-fragment-induced short wavelength radiation emissions, the transparent wall would be removed and a medium such as lasing gas mixtures would be mixed with either the fissioning uranium

*Research sponsored by NASA Langley Research Center, Contract NAS1-13291, Mod. 2.

fuel or buffer gas. The reason for this distinction is that most transparent wall materials have intrinsic radiation absorption characteristics at the short wavelengths expected to be emitted from the plasma in the form of fission-fragment-induced nonequilibrium electromagnetic radiation.

A long-range program plan for establishing the feasibility of fissioning gaseous UF_6 and uranium plasma reactors has been formulated by NASA. Reference 2 summarizes the plan which comprises the performance of a series of experiments with reflector-moderator cavity reactors. A review of the past work is contained in Ref. 3. Los Alamos Scientific Laboratory (LASL) is currently performing these cavity reactor experiments.

Integrated into this plan is the development of equipment and techniques to demonstrate operation of an argon/UF_6 injection, separation, and recirculation system to efficiently separate UF_6 from argon in a form adaptable to subsequent recycling in the rf-heated uranium plasma experiment. Also included will be continued experiments to demonstrate techniques for minimizing the deposition of uranium compounds in the exhaust duct systems.

The uranium plasma experiments described herein comprise part of the development of the long lead time technologies required to proceed with the uranium plasma core reactor experiments.

Other previously reported experiments[4] have been conducted on the confinement of argon rf plasmas. These tests were directed primarily toward development of a high-intensity, high-power-density plasma energy source (equivalent black-body radiating temperatures ≤ 6000 K). Some of these initial exploratory tests included direct injection of very dilute mixtures of UF_6 (typically, 1% UF_6 in an argon carrier-gas) into the argon rf plasma. Coating of the fused-silica peripheral wall occurred but short-time sustained plasma operation was demonstrated.

The study described herein presents some recent results of the uranium plasma confinement tests with pure UF_6 injection and the associated diagnostics and measurement techniques as applicable to plasma core reactors.

Description of Principal Equipment

The experiments reported herein were conducted using the UTRC 1.2 MW rf induction heater system operating at approximately 5.4 MHz. The rf output was supplied by two power amplifier tubes (440 kW output each) which drive a resonant tank circuit; the output of the two power amplifiers was resonated by a push-pull resonator. The entire resonator section consisted of two arrays of ten vacuum capacitors located within a 1.7-m-dia cylindrical aluminum test tank. The rf power was deposited into the plasma by a pair of single-turn 9-cm-dia water-cooled work coils. The front of the test tank was a removable dome containing five 10-cm-dia windows for observation and/or diagnostic equipment access.

In support of the rf plasma experiments, a UF_6 handling and feeder system to provide a controlled and steady flow of heated UF_6 at temperatures up to 500 K was employed. Figure 2 is a schematic diagram of the UF_6 handling and feeder system. The system was designed to provide UF_6 mass flow rates up to about 5 g/s and subsequent possible injection of UF_6 into test chambers operating at pressures up to approximately 20 atm.

The principal components of the system were the UF_6 boiler, the boiler heat supply system, and the UF_6 condenser (exhaust) system. The boiler was a 2ℓ Monel cylinder rated at 200 atm working pressure. Monel was selected because of its resistance to chemical attack by hot, pressurized UF_6. A heat exchanger to provide internal heating was located in the bottom of the boiler. The thermocouple walls, heat exchangers, and UF_6 flow lines were all fabricated from 6.4-mm-OD Monel tubing. As shown in Fig. 2, electrical resistance heater tape was wrapped around the majority of components. In the tests reported herein, use of the electrical heater assembly surrounding the UF_6 boiler was sufficient to provide the required flow rates; in future tests employing higher UF_6 flow rates for longer periods, electrically-heated gaseous N_2 will be supplied to the UF_6 boiler heat exchanger. Based on the results of exploratory UF_6 handling and flow metering tests, the need for elimination of as much contamination as possible from the UF_6 supply and flow handling system became apparent.

A Matheson UF_6 calibrated linear mass flow meter (Monel transducer) was located in the UF_6 transfer line to provide on-line determination of the UF_6 mass flow rate prior to entering the UF_6 injector within the test chamber. The exhaust from the test chamber, comprised of argon, UF_6, and other volatile uranium compounds, was collected in the UF_6 condenser system located downstream of the test chamber. A neutralizing trap ($NaOH+H_2O$) was located downstream of the condenser system to remove any residual uranium or uranium compounds which passed through the flow trap shown in Fig. 2.

Figure 3 is a sketch showing a cross section of the basic test chamber configuration employed in the 1.2 MW rf induction heater tests with pure UF_6 injection. For simplicity, only half the symmetric chamber is shown. This test chamber configuration was selected based on the results of exploratory rf plasma tests using the UTRC 80 kW rf induction heater facility[5]. These exploratory tests were conducted at an rf frequency of 13.56 MHz and with the test chamber at atmospheric pressure and discharge power levels on the order of 10 kW. Four different test chamber flow configurations were tested to permit selection of the configuration demonstrating the best uranium vapor confinement characteristics and minimum wall

coating. The test chamber configuration shown in Fig. 3 incorporated several features including the ability to change: the axial location of the on-axis UF_6 injector, the injection area of the argon vortex injectors, and the ability to vary the distribution of exhaust gas flow and cooling water to the different components. The left endwall (not shown in Fig. 3) had provision for removing the exhaust gas through an axial bypass annulus located on the periphery of the endwall. Figure 4 contains a photograph showing details of this test chamber configuration with a uranium rf plasma present as viewed through the center view port of the test tank. The argon vortex was driven from the right endwall by a set of eight equally-spaced stainless-steel vortex injectors located tangent to the periphery of the endwall. In addition to the axial bypass provision in the left endwall, both endwalls had the option for removing varying amounts of the exhaust gas through the on-axis thru-flow ducts. As shown in Fig. 3, the UF_6 injector, located on-axis and concentrically within the right endwall, was fabricated from a 50-cm-long three concentric copper tube assembly and in the majority of tests was located with the injector tip extending 2 cm into the test chamber. High pressure water (20 atm) heated to approximately 350 K via a steam heat exchanger flowed at 0.14 ℓ/s between the concentric tubes of the UF_6 injector. This provided cooling relative to the hot plasma environment while still maintaining a high enough temperature in the injector to permit flowing the pressurized gaseous UF_6 without solidification in the UF_6 transfer line/injector. A vacuum start technique was used in all tests; the rf plasma was ignited at approximately 10 mm Hg using breakdown of the argon gas at a resonator voltage of about 4 kV.

The total power deposited into the uranium rf plasma was obtained from an overall test chamber energy balance by summing the power lost by radiation, power deposited into the annular coolant of the peripheral wall, power deposited into the endwall assemblies, power convected out the exhaust ducts, as well as, power deposited into the heat exchanger and UF_6 injector assembly.

The power radiated from the uranium rf plasma was measured using a specially constructed radiometer and chopper wheel assembly. The total power radiated from the plasma and in selected wavelength bands was calculated assuming isotropic radiation including allowance for blockage due to the rf work coils. Still pictures (using neutral density filters) taken through the various view ports were used for estimating the discharge diameter and shape.

Figure 5 is a schematic diagram of the optical diagnostic system used for the absorption and emission measurements in the rf plasma tests with pure UF_6 injection. A uranium lamp (hollow cathode type) was used as the reference standard. A confocal Fabry-Perot spectrum analyzer with a free spectral range of 8 GHz ($\approx 10^{-2}$ nm) was used to define and calibrate the tuned wavelength spectrum. A power meter (together with a beam splitter) was used to permit continuous monitoring of the dye laser output power at the particular wavelength line selected. A phase-sensitive-detector and lock-in amplifier and a dual set of chopper/signal generator assemblies (capable of multiple frequency operation) were used in the system, as shown in Fig. 5. A pair of fixed front surface mirrors were used to direct the approximately 1.5-mm-dia laser beam into the aluminum test tank (parallel to the major axis of the discharge). A beam expander (1.5-cm-dia aperture) and collimator was located inside the test tank. Another fixed front surface mirror was located in the test tank approximately 6 cm behind the axial midplane of the fused-silica tube test chamber at an angle of 45 deg to the discharge major axis. The centerline of the expanded and collimated laser beam traversed the concentric set of fused-silica tubes which form the test chamber, 0.75-cm-off-axis, as shown in Fig. 3. The laser beam exited from the aluminum test tank through an aperture and the central view port. A 10-cm-dia aerial lens (f/1.8, focal length = 34.3 cm) was located inside the test tank to aid in focussing the laser beam onto the slit of the monochromator and to correct for the beam divergence through the test chamber. The final optical tracking system used for making the chordal scans of the plasma emission and absorption, as shown in Fig. 5, evolved after several preliminary designs, ray tracing analyses, and bench test experiments. The optical system design had to account for a certain amount of refraction through the test chamber geometry employed. The effect of the concentric fused-silica tubes was twofold. The refractive effects of concentric, right circular cylinders filled alternately with gas, quartz, water, quartz, and air were calculated and are easily predictable. The second effect (surface imperfections), however, was not smoothly varying and cannot be compensated for in the lens and optical system design. This effect had to be calibrated out for each test (i.e., once the rotational orientation of the two concentric fused-silica tubes was selected, they were maintained in that orientation until completion of that particular test). The remainder of the optical diagnostic system included a fixed front surface mirror, a 10-cm-dia, 20-cm-focal length lens, a rotating front surface mirror, and a 0.25 (f/3.5 optics) or 0.5 m (f/8.6 optics) monochromator system. The output signal from the photomultiplier (S-20 response) was connected to a signal processor and displayed on a strip-chart recorder. A specially constructed rf shielded signal generator and controller system was used for operating the mirror motor drive. The mirror drive assembly had an independent frequency, amplitude, and off-set control. The system was set-up to image a source of cross-sectional radius 1.5 cm without vignetting within the monochromator system. Since the source and slit exist in conjugate planes at a magnification ratio of 1.57, the 25 μm square slit

arrangement used in the monochromator represented a scanning aperture 39 μm square at the plane of the plasma discharge centerline (both emission and absorption). For emission measurements, the dye laser beam was blocked and the chopper assembly (85 Hz) located adjacent to the central view port of the test tank was used. For absorption measurements, the chopper assembly adjacent to the dye laser head was used (650 Hz). Calibration checks were included to verify that the dye laser output beam (λ = 591.54 nm) power remained essentially constant for relatively long time periods. Fine tuning was accomplished during the actual UF_6 rf plasma tests by tuning the central frequency control of the dye laser system to maximum absorption. The λ = 591.54 nm uranium line was selected because it is a relatively strong uranium I (neutral atom) line and appears well-defined in the spectral emission scans. The lower state for this line is the uranium I ground state. The half-width of the laser line at this wavelength was approximately $\Delta\lambda = 10^{-4}$ nm.

The signal generator and controller for the scanning mirror was set up to provide a different scanning rate (approximate factor of 2X) between the plasma discharge centerline to the 1.5 cm off-axis location and the return scan from the off-axis location back to the discharge centerline. Typically 10 s was required for a scan. The optical tracking system was checked out first with only an argon rf plasma present. This permitted a verification of tracking reproducibility and isolation of the instrumentation from extraneous vibration and/or rf interference effects.

To permit a detailed analysis of the samples of residue collected from the various components of the test chamber after rf plasma tests with pure UF_6 injection, the following UTRC instrumentation was employed. Of these, several have unique features.

1. Profilometer -- permitted quantitative determination of the magnitude of surface coating/etching/erosion that may take place on the surface of the fused-silica tube.

2. IR Spectrophotometer -- permitted compound identification using IR spectrophotometric absorption measurements (2.5-40 μm wavelength range) of reference material, standard compounds and small samples of residue removed from test chamber components.

3. Scanning Electron Microprobe -- permitted determination of the elements present in the residue samples and also scanning electron micrographs. Showed topographical and compositional variations and permitted x-ray mapping of the individual elements present.

4. X-ray Diffractometer -- permitted identification of compounds present in the residue samples by subjecting them to copper Kα radiation and comparing the resulting x-ray diffraction patterns with reference standards.

5. Electron Microscope using selected area diffraction (SAD) -- permitted identification of compounds present in the residue samples by subjecting them to electron bombardment. Also provided indication of relative crystallinity of the material.

6. Ion Scattering Spectrometer (ISS)/Secondary (or sputtered) Ion Mass Spectrometer (SIMS) -- permitted identification of the various elements and compounds present in the residue samples. The unique features of this instrument that distinguish it from the other instruments described above are (1) it is sensitive to just the outer monolayer of the surface; (2) its sensitivity is as high as one part of a monolayer per million; (3) it gives positive identification of the compounds; and, (4) it can detect hydrogen and distinguish isotopes of uranium.

Discussion of Test Results

TABLE I is an example of the typical operating conditions obtained in the emission and absorption measurement tests conducted in the 1.2 MW rf plasma tests with pure UF_6 injection using the test configuration shown in Fig. 3. For this particular case, the mass flow rate of the injected UF_6 was 3.2×10^{-2} g/s. In other tests, chamber pressures up to 12 atm and rf plasma power levels up to 85 kW were employed.

To establish the range of dye laser uranium line absorption (I/I_o) levels through the plasma, several preliminary tests were conducted for various mass flow rates of UF_6. The dye laser line was set at the peak of the λ = 591.54 nm line (Uranium I-neutral atom) and the 1.5-mm-dia beam (typically 50 mW) traversed the plasma discharge on the centerline axis at the axial midplane location (see Fig. 3). UF_6 mass flow rates employed ranged from 1.3×10^{-2} g/s to 8.2×10^{-2} g/s. For reference, at the UF_6 mass flow rate of 8.2×10^{-2} g/s approximately 98% of the incident intensity of the 591.54 nm dye laser line was absorbed in a single pass through the uranium rf plasma. After operating for approximately 1.5 minutes at this flow rate, the UF_6 injector valve was rapidly shut off. The signal did not immediately return to the initial value because of outgassing of residual hot UF_6 in the transfer lines and injector assembly. Trace amounts of UF_6 were still observed entering the plasma after approximately 10 minutes. After waiting for all the residual UF_6 to outgas, the signal approached the initial value, indicating a very small amount of wall coating had occurred. Post-test inspection of the inner fused-silica tube verified this condition.

The introduction of pure UF_6 directly into the plasma resulted in a significant increase in the total radiation emitted from the plasma (220

to 1300 nm range) as measured with the radiometer system; a significant amount of this radiation increase occurred in the visible and near-UV wavelength bands.

Figure 6 shows an example of the radial variation in the uranium rf plasma temperature and transmission as determined from the single wavelength ($\lambda = 591.54$ nm) chordal scan measurements, at the axial midplane, of the emission and absorption using the instrumentation shown in Fig. 5. The chordal scan measurements of the emission and absorption by the uranium plasma served as input data to a computer program used to calculate the emission and absorption coefficients. Previously developed analytical techniques for absorption/emission coefficient determination for optically-thick plasmas were adapted to the UTRC data acquisition system[6,7]. Prior measurements conducted with similar geometries indicated vortex-confined rf plasma discharges of this type to be rotationally symmetric. Rotational symmetry of the plasma facilitates reduction of the measured chordal emission and absorption data to corresponding radial data by means of the Abel inversion procedure. Under conditions of local thermodynamic equilibrium (LTE) and for plasma transmission between approximately 0.2 and 0.8 (i.e., $0.2 \leq I/I_o \leq 0.8$), analytical techniques have been developed for determining the radial spectral absorption and emission coefficients. Since the absorption and emission coefficients are related via Kirchhoff's law, the radial temperature profile can be determined without knowledge of particle densities or transition probabilities. This is particularly important for uranium where much data are still unknown. The sketch in the lower portion of Fig. 6 is a simplified cross section of the test chamber and indicates the location used for the chordal scan measurements. Also shown for reference in Fig. 6 is a temperature profile determined from an argon-only rf plasma test under similar test conditions, but with no injection of UF_6. In addition to the centerline maximum temperature peak of about 9800 K, a distinct off-axis temperature peak of about 8700 K is also evident for the uranium plasma case. The introduction of pure UF_6 into the rf plasma resulted in a suppressed temperature profile at the off-axis position between a radial distance of approximately 0.2-0.8 cm. The off-axis peaks can be attributed primarily to the mechanism of depositing rf power into an annular region.

To complement these measurements and verify the validity of the results, separate Uranium I ($\lambda = 591.54$ nm) absorption line width measurements were made using the dye laser system shown in Fig. 5. This information was used to calculate an absorption coefficient from which comparisons were made between the neutral (UI) uranium number density radial distribution as determined from emission calculations and from absorption calculations; reasonable agreement was obtained.

To aid in the determination of the total uranium atom number density distribution within the rf plasma discharge, UF_6 and/or UF_6/Ar equilibrium calculations were made for the current range of test parameters utilizing a computer code based on the procedure described in Ref. 8 (partial pressures from 10^{-4} to 1 atm and temperatures from 300 to 10,000 K). The following species were included: UF_6, UF_5, UF_4, UF_3, F, F^-, F_2, U, U^+, U^{++}, U^{+++}, and e^-. Figure 7 is an example of these calculations for the equilibrium composition of UF_6 at a partial pressure of 10^{-3} atm. For all practical purposes, at pressures of approximately 1 atm, complete thermal decomposition of UF_6 has occurred at temperatures of about 5000 K. Figure 7 illustrates the mole fraction of the various constituents as a function of temperature. Note the very steep slope of the mole fractions of the various fluoride compounds of uranium in the 2000 K regime and that at approximately 7000 K, the concentration of singly-ionized uranium (UII) increases; separate measurements of the rf plasma characteristics indicate that the rf plasma with argon vortex buffer gas injection only has average temperatures in excess of 7000 K for the type of operating conditions reported herein. In all the calculations, local thermodynamic equilibrium was assumed and lowering of the ionization potential was not included. Similar calculations of the variation of the total number density of uranium atoms and ions as a function of UF_6 injection partial pressures with equilibrium temperature as the variable parameter have also been completed for UF_6/Ar mixtures at various total pressures.

It was anticipated that operating the rf plasma with pure UF_6 injection at relatively high power and pressure levels may have resulted in significant pressure broadening to the width of the uranium, $\lambda = 591.54$ nm, emission and absorption line. To better estimate the absorption line half-width, several measurements were made at different pressures corresponding to approximately the same test conditions. Calculations of the doppler width for the uranium $\lambda = 591.54$ nm line (no pressure broadening) at 1000 K yields a half-width of approximately 0.75 GHz. The doppler line width varies as the square root of temperature. Therefore, at a temperature of approximately 10,000 K, the doppler width would be approximately 2.34 GHz. This compared favorably with the 2.5 GHz experimentally measured using the dye laser system and spectrum analyzer. At a chamber pressure of 2 atm, the measurements indicated a line width (at one-half maximum intensity) of approximately 3.5 GHz. For reference, 8 GHz corresponds to 10^{-2} nm.

Additional calculations were completed using these data, the partition functions for Uranium I and II as a function of temperature[9], the radial distributions of temperature and transmission shown in Fig. 6, and the variation of uranium neutral atom number density with UF_6 partial pressure to calculate the neutral uranium atom number density as a function of radius.

Figure 8 shows the results obtained for the radial variation of total uranium atom (UI+UII+UIII) number density as a function of radial distance from the centerline of the rf plasma with pure UF_6 injection corresponding to the test conditions given in TABLE I and Fig. 6. The numbers in parentheses are corresponding estimated values of the total uranium species partial pressure in atm. In this particular case, the total uranium atom number density reached a maximum of approximately 10^{16} atoms/cm^3 at the centerline of the plasma. Based on this plot, an estimate was made of the total confined uranium masssbased on these measurements of the neutral uranium species; this value was calculated to be 0.03 mg of uranium. The calculations also indicated that a relatively large fraction of the total confined uranium atoms existed at the outer portion of the plasma discharge.

These results were compared to the uranium total number density obtained from independent x-ray absorption measurements.[10] At comparable test conditions to those shown in TABLE I and assuming a 23-cm-diagonal path length and a 9.5-cm-diagonal path length, the corresponding uranium total number densities were 2.8×10^{16} and 6.4×10^{16} atoms/cm^3, respectively. The agreement is reasonable when one considers that the x-ray measurements included contributions due to all species (including cold UF_6 etc. in the boundary). Other x-ray measurements at higher UF_6 injection mass flow rates (up to 9.3×10^{-2} g/s) resulted in uranium densities up to approximately 4×10^{17} atoms/cm^3.

The photograph shown in Fig. 9 illustrates the degree of wall coating incurred on various fused-silica tube peripheral walls after tests with pure UF_6 injection. Part of the tests included incorporation of different modifications to both the test chamber and flow control scheme to further improve the confinement characteristics of the uranium plasma while at the same time aid in minimizing the wall coating by uranium compounds. These fused-silica tubes were subsequently analyzed during post-test inspections. The degree of coating extended from a relatively heavy to a fairly light coating as can be seen in the photograph in Fig. 9. The majority of the coating occurred in the central region of the fused-silica tubes. Some residue was also observed at both end regions adjacent to the O-ring seal location. A representative example of the IR spectrophotometric absorption measurements taken of some of the residue collected from the inside surface of the fused-silica tube after the plasma tests with pure UF_6 injection is shown in Fig. 10. In all cases a thin wafer KBr matrix was used with the Perkin-Elmer IR spectrophotometer to obtain the IR absorbance trace as a function of wavelength. In the majority of the tests the IR spectrophotometric measurements indicated a combination of uranyl fluoride and uranium oxide present on the inside surface of the fused-silica tube; traces of SiO_2, silicon grease and water vapor were also noted.

A follow-on series of long run time uranium rf plasma tests indicated that the addition of silicone grease to the O-rings and use of as-received UF_6 (i.e., no NaF filter) resulted in a significant contribution to the residue coating on the fused-silica tubes. Part way into the test series it became obvious that the use of silicon O-rings, and unfiltered argon from the laboratory bottle farm, also resulted in an increase in the residue deposited on the fused-silica tubes as a function of test time. To aid in reducing this residue, the O-rings were coated with Kel-F oil. This particular lubricant, arrived at after trying other materials such as hydrocarbons, fluorosilicone, and halocarbons, provided the seal necessary between the fused-silica tube and the endwall while eliminating the silica gel present in the silicone grease which apparently reacted on the surface and caused additional deposits. With the O-ring lubricant change, filtering the as-received UF_6 through a NaF trap to remove the hydrogen fluoride contamination, and filtering the argon through a zeolite trap resulted in a reduction in the residue wall coating by approximately a factor of 2. In a test employing all these modifications, the uranium rf plasma was operated continuously for 41.5 minutes at a UF_6 flow rate of 2.2×10^{-2} g/s; 30.4 mg of total residue was deposited on the peripheral wall. Approximately 10 mg of this was attributed to the lubricant initially applied to the O-ring seal which remained on the fused-silica tube.

In other tests, aimed at determining the range of mass flow rates of injected UF_6 possible, greater than an order of magnitude increase in flow rates were achieved (21×10^{-2} g/s) while still maintaining the rf plasma in a confined-steady-state mode.

Results of measurements using the profilometer indicated the maximum residue wall coating on the ID of the fused-silica tube to be approximately 1 μm in thickness; detailed analysis of the surface indicated a combination of residue deposition and surface etching had occurred. The electron photomicrographs and x-ray mappings of the sample residue indicated the predominance of uranium and silicon as compared to fluorine and oxygen. The results from the x-ray and electron diffraction analyses indicated traces of several oxides of uranium. This was also verified by the IR spectrophotometry absorption measurements shown in Fig. 10. Another check on the predominance of UO_2F_2 was obtained from measurements using the secondary ion mass spectrometer (SIMS). Based on the Atomic Mass Units (AMU) between 225 to 300, the presence of various uranium oxide compounds was verified.

Additional analyses were also conducted of the residue coating on the endwall surfaces, UF_6 injector, and exhaust ducts. In general, the following trends were observed. UF_4, UO_2, and UO_2F_2 were identified as residue constituents on the endwall surfaces. The same constituents were identified as

being present on the UF_6 injector; in addition, αUO_3 was also detected. The electron microprobe x-ray maps also showed the distinct presence of Cu in quantities comparable to the U. The exhaust ducts contained traces of UO_2F_2, U_3O_8, and UF_4. The electron photomicrographs of the various samples of residue removed from the different components each possessed a different crystalline structure. Recall that UO_2F_2, UO_2, SiO_2 (and a trace of γUO_3) were identified as residue constituents on the fused-silica tube peripheral wall.

The analysis techniques developed and applied during this portion of the research program will be applicable to future experiments which include development of techniques for reconstituting the gaseous compounds in the plasma exhaust mixture, minimizing the wall coating, and conditioning the exhaust gas such that it is in a form suitable for reinjection into the plasma (recycled-closed-loop operation).

Summary and Conclusions

An experimental investigation was conducted using an argon vortex confined uranium rf plasma discharge to aid in developing the technology necessary for designing a self-critical fissioning uranium plasma core reactor. Pure UF_6 was injected, using a specially developed UF_6 transfer and injection system, into a 5.7-cm-ID by 10-cm-long test chamber containing the plasma and comprised of a water-cooled fused-silica tube peripheral wall and copper endwalls. Complementary diagnostic instrumentation and measurement techniques were developed which permitted characterizing the uranium plasma and traces of the uranium compound residue deposited on the test chamber walls. Included was an optical scanning method for uranium plasma emission and absorption measurements using a cw single-frequency tunable dye laser system. These measurements provided input to a computer program (optically thick case) which calculated the spectral emission and absorption coefficients and the corresponding radial temperature profile using Kirchhoff's law. The measurements indicated, at chamber pressures of about 2 atm, rf discharge power levels of about 60 kW, and injected UF_6 mass flow rates of approximately 3×10^{-2} g/s, that uranium plasma temperatures of 9800 K occurred at the plasma centerline location with a distinct off-axis peak ($\approx$ 8700 K) occurring at an $r/R = 0.6$. Edge of plasma temperatures were approximately 6000 K. From these data and additional experimental measurements of the uranium neutral atom (UI) absorption line width ($\approx$ 3.5 GHz at λ = 591.54 nm), the radial variation of total uranium atom (UI+UII+UIII) number density within the rf plasma was determined. (Approximately 10^{16} atoms/cm^3 at the axial midplane centerline of the rf plasma discharge.) These atom number densities were found to be comparable by two independent measurement techniques (x-ray absorption measurements and U plasma emission/absorption measurements).

Modifications made to the test chamber configuration and flow control scheme and evaluated by the various analysis techniques resulted in a reduction in the residue material deposited on the components of the test chamber. At UF_6 mass flow rates of 2.2×10^{-2} g/s, test times up to 41.5 minutes were achieved with less than about 20 mg of actual uranium compound residue wall coating. In separate tests to maximize the UF_6 mass injection flow rate, up to an order of magnitude increase was achieved (2.1×10^{-1} g/s) while still maintaining the plasma in a confined mode of operation. Six different complementary analysis techniques were employed and uranium compound reference standards developed at UTRC to permit post-test characterization and identification of the residue coatings deposited on the peripheral wall of the test chamber. The "mist-like" residue found on the inside diameter of the fused-silica tube during post-test analysis was identified as primarily uranyl fluoride (UO_2F_2).

The overall test results have demonstrated that applicable flow schemes and associated diagnostic techniques have been developed for the fluid-mechanical confinement and characterization of uranium vapor within a plasma discharge when pure UF_6 is injected steady-state for long test times into an argon-confined, high-temperature, high-pressure, rf-heated plasma.

References

1. Latham, T. S., et al.: Applications of Plasma Core Reactors to Terrestrial Energy Systems. AIAA Paper 74-1074, AIAA/SAE 10th Propulsion Conference, San Diego, CA., October 21-23, 1974.

2. Rodgers, R. J., et al.: Preliminary Design and Analyses of Planned Flowing Uranium Hexafluoride Cavity Reactor Experiments. United Technologies Research Center Report R76-912137-1, March 1976.

3. Helmick, H. H., et al.: Preliminary Study of Plasma Nuclear Reactor Feasibility. Los Alamos Scientific Laboratory Report LA-5679, August 1974.

4. Roman, W. C. and J. F. Jaminet: Development of RF Plasma Simulations of In-Reactor Tests of Small Models of the Nuclear Light Bulb Fuel Region. United Aircraft Research Laboratories Report L-910900-12, September 1972.

5. Roman, W. C.: Plasma Core Reactor Simulations Using RF Uranium Seeded Argon Dischrages. AIAA 8th Fluid and Plasma Dynamics Conference, Paper No. 75-861, Hartford, CT., June 1975.

6. Freeman, M. P. and S. Katz: Determination of the Radial Distribution of Brightness in a Cylindrical Luminous Medium With Self-Absorption. J. Opt. Soc. Amer., 50, 826, 1960.

7. Elder, D. W., et al.: Determination of the Radial Profile of Absorption and Emission Coefficients and Temperatures in Cylindrically Symmetric Sources with Self Absorpition. Appl. Opt., Vol. 4, No. 5, May 1965.

8. Gordon, S. and B. J. McBride: Computer Program for Calculations of Complex Chemical Equilibrium Compositions, Rocket Performance, Incident and Reflected Shocks, and Chapman-Jouquet Detonations. NASA SP-273, 1971.

9. Krascella, N. L.: Theoretical Investigation of the Composition and Line Emission Characteristics of Argon-Tungsten and Argon-Uranium Plasmas. United Aircraft Research Laboratories Report G-910092-10, Spetember 1968.

10. Roman, W. C.: Laboratory-Scale Uranium Plasma Confinement Experiments. United Technologies Research Center Report R76-912205-1 (to be published).

List of Symbols

AMU	Atomic mass unit, dimensionless
f	RF operating frequency, MHz
I_o	Incident or source intensity, arbitrary units
I/I_o	Transmission, dimensionless
$\log_{10}(I/I_o)$	Absorbance, dimensionless
ℓ	Liters
$\dot{m}_{AR}$	Argon mass flow rate, g/s
$\dot{m}_{UF_6}$	UF_6 mass flow rate, g/s
N_{UI}	Number density of neutral uranium atoms, atoms-cm^{-3}
N_{UII}	Number density of singly-ionized uranium atoms, atoms-cm^{-3}
N_{UIII}	Number density of doubly-ionized uranium atoms, atoms-cm^{-3}
N_{UT}	Total number density of uranium atoms, atoms-cm^{-3}
P	Pressure, atm, mm Hg, or torr
P_c	Chamber pressure, atm
Q_T	Total rf dishcarge power, kW
R	Radius of plasma, cm
r	Radial distance, cm
T	Temperature, deg K
λ	Wavelength, nm or microns
χ_i	Mole fraction of species i, dimensionless
$\Delta\lambda$	Wavelength band, nm
α,γ	Designation of different crystalline forms of uranium compounds

Table I

Summary of Operating Conditions for Chordal Scan Measurements of Test V Conducted in 1.2 MW RF Induction Heater With Rf Plasma and Pure UF_6 Injection

See Fig. 3 for Sketch of Test Chamber Configuration
See Fig. 5 for Schematic of Diagnostic System Used for Chordal Scan Measurements.

Argon Injection Mass Flow Rate	2.58 g/s
Argon Injection Velocity	21.6 m/s
Percent Axial Bypass Flow	48
UF_6 Injection Mass Flow Rate	3.2×10^{-2} g/s
UF_6 Injection Velocity	0.7 m/s
Mass Ratio	0.012
Chamber Pressure	1.95 atm
RF Discharge Power	58 kW
RF Operating Frequency	5.4210 MHz
Power Radiated (220-1300 nm)	19.5 kW
Fraction of Total Discharge Power Radiated	0.34
Discharge Diameter at Axial Midplane	2.8 cm
Test Time	2 min
Residue Deposition	8.1 mg

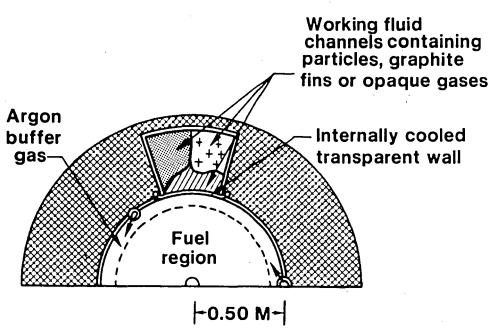

Fig. 1 Details of Plasma Core Reactor Unit Cell.

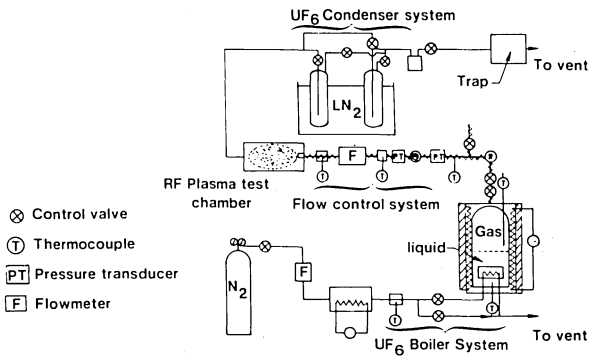

Fig. 2 Schematic Diagram of UF_6 Transfer System.

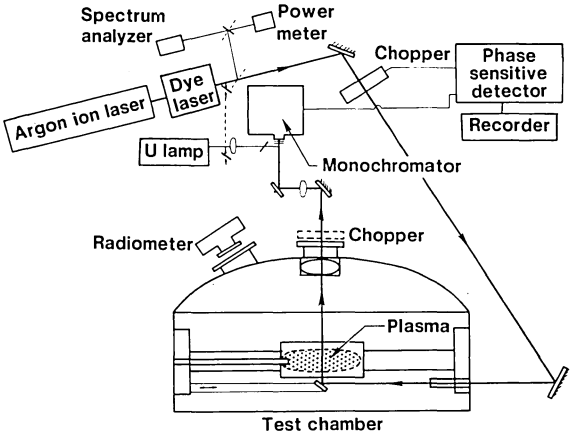

Fig. 5 Schematic of Optical Diagnostic System Used for Absorption and Emission Measurements in RF Plasma Tests With Pure UF_6 Injection.

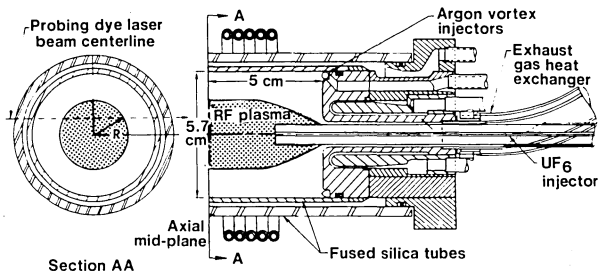

Fig. 3 Sketch of Test Chamber Configuration Used in Tests in 1.2 MW RF Induction Heater With Pure UF_6 Injection.

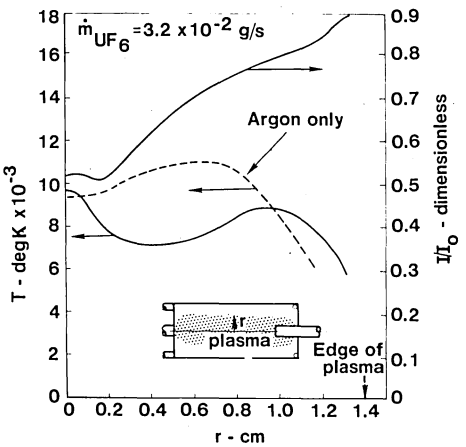

Fig. 6 Example of Results of Radial Variation in Temperature and Transmission Obtained With Pure UF_6 Injection Into RF Argon Plasma.

P=2.4 atm Q_T=52 kw f=5.4778 MHz d=2.9 cm

$\dot{m}_{Ar}$=2.2 G/S $\dot{m}_{UF_6}$=0.09 G/S

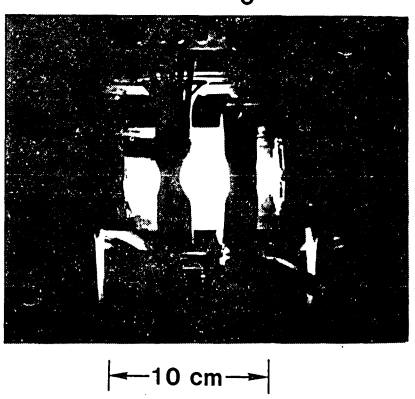

Fig. 4 Photograph of RF Argon Plasma in 1.2 MW RF Induction Heater Test Chamber With Pure UF_6 Injection.

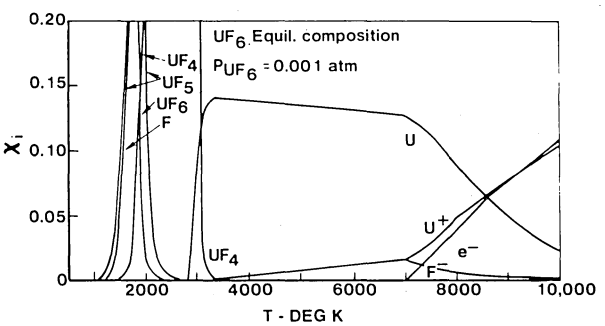

Fig. 7 Equilibrium Composition of UF_6 at a Partial Pressure of 0.001 atm.

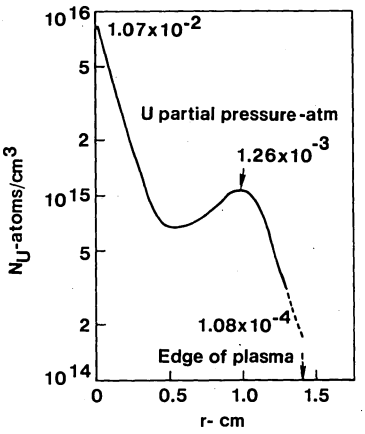

Fig. 8 Radial Variation of Total Uranium Atom (UI,UII,UIII) Number Density for UF_6 RF Plasma Test Case V.

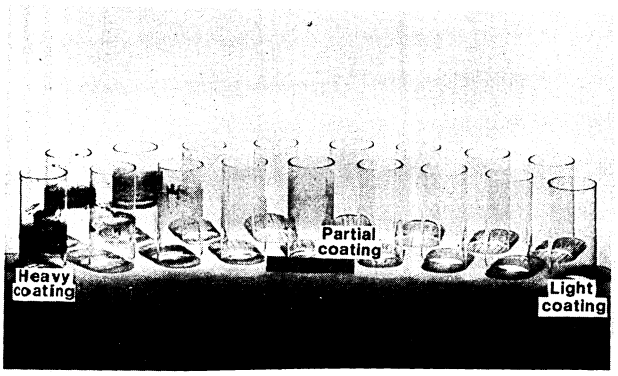

Fig. 9 Photograph of Fused-Silica Tubes Used in RF Plasma Tests With Pure UF_6 Injection and Incorporating Modifications to Test Chamber/Flow Scheme.

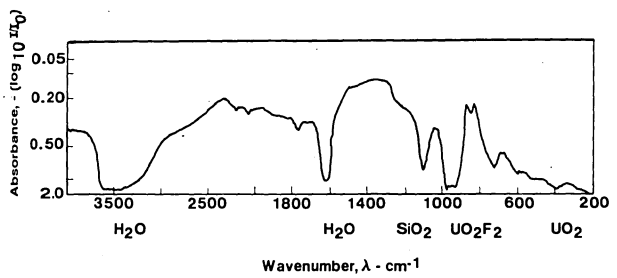

Fig. 10 Example of IR Spectrophotometry Absorption Measurements Obtained From Post-Test Analysis of Residue Wall Coating.

DISCUSSION

D. H. DOUGLAS-HAMILTON: What kind of radiation intensities do you expect to propagate through your quartz window?

W. C. ROMAN: About 27 kilowatts per square centimeter.

T. S. LATHAM: Another point we are discovering with UF_6 is that it is a very strong UV absorber which means that the radiating spectrum is very much like a black body at the edge of the fuel cloud, and we have less UV content with uranium hexaflouride as a nuclear fuel than we used to calculate for pure uranium. So the UV loading on the fused silica walls with UF_6 fuel should be substantially reduced over what it was with pure fuel.

THE EMISSION CHARACTERISTICS OF URANIUM HEXAFLUORIDE+ AT HIGH TEMPERATURES

N. L. Krascella
United Technologies Research Center
East Hartford, Ct.

Abstract

An experimental study was conducted to ascertain the spectral characteristics of uranium hexafluoride (UF_6) and possible UF_6 thermal decomposition products as a function of temperature and pressure.

Relative emission measurements were made for UF_6/Argon mixtures heated in a plasma torch over a range of temperatures from 800 to about 3600 K over a wavelength range from 80 to 600 nm. Total pressures were varied from 1 to approximately 1.7 atm. Similarly absorption measurements were carried out in the visible region from 420 to 580 nm over a temperature range from about 1000 to 1800 K. Total pressure for these measurements was 1.0 atm.

The emission results exhibited relatively no emission at wavelengths below 250 nm over the range of temperatures investigated. At temperatures in excess of 1800 K an additional emission band centered at 310 nm appears and becomes more well defined at higher temperatures. Essentially no pressure effect was observed with respect to emission at pressures up to 1.7 atm.

"Effective" spectral absorption cross-sections were determined at five temperatures between 1000 and 1800 K and in the wavelength region between 420 and 580 nm. The cross-sections ranged in value from about 9×10^{-20} to 2×10^{-19} cm^2.

I. Introduction

Extensive experimental and theoretical research has been conducted with respect to various aspects of fissioning gaseous plasmas over the past two decades. These studies have been generally directed toward high performance nuclear space propulsion systems[1]. In addition to space applications, the Plasma Core Reactor (PCR) concept has been recognized as a possible candidate energy source for various terrestrial applications[2]. The very high operating temperatures generated by fissioning plasmas tend to enhance efficiencies of various thermodynamic cycles compared to conventional power generating systems or nuclear reactors with solid fuel elements. Furthermore, the high operating temperatures associated with gaseous fissioning reactors provide a source of very intense electromagnetic radiation with a number of possible applications involving direct coupling of energy by radiative processes.

Although most of the applications of the PCR require extensive basic research and technological development, the potential benefits from the use of these devices warrant continued investigation of the concept. Possible PCR space and/or terrestrial applications are:

(1) High-thrust, high-specific-impulse space propulsion systems.

(2) Advanced high-temperature, closed-cycle gas turbine electrical power generation.

(3) MHD conversion systems for electrical power generation.

(4) Photochemical and/or thermochemical processing.

(5) Direct pumping of lasers by deposition of fission fragment energy in UF_6 or other gas mixtures.

(6) Optical pumping of lasers by thermal and/or nonequilibrium radiation emitted by a gaseous fissioning UF_6 or uranium plasma.

A typical unit cavity of a PCR device is illustrated in Figure 1. In the PCR concept a high-temperature, high-pressure plasma is sustained via the fission process in a uranium gas injected as UF_6 or other uranium compound. Containment of the plasma is accomplished fluid-mechanically by means of an argon-driven vortex which also serves to thermally isolate the hot fissioning gases from the surrounding wall.

For applications which employ thermal radiation emitted from the plasma, an internally-cooled transparent wall can be employed to isolate the nuclear fuel, fission fragments, and argon in a closed-circuit flow loop and permit transfer of the radiant energy from the plasma to an external working fluid. For applications which employ fission fragment induced short wavelength nonequilibrium radiation emitted from the plasma,

+Research sponsored by NASA Langley Research Center, Contract NAS1-13291 Mod. 2.

the working fluid such as lasing gases can be either mixed with fissioning gas or injected into the peripheral buffer gas region such that there is no blockage of radiation due to the intrinsic absorption characteristics of transparent material wavelengths.

Three fundamental areas of research are required to demonstrate the feasibility of the PCR concept: (1) nuclear criticality; (2) fluid mechanical confinement; and, (3) transfer of energy by radiation processes. Various aspects of these areas of technology are currently being investigated at United Technologies Research Center (UTRC). In addition, cavity reactor experiments which employ gaseous UF_6 are currently being performed at Los Alamos Scientific Laboratory (LASL) as part of the planned NASA program to determine the feasibility of plasma core reactors.

The present report summarizes recent results of emission and absorption measurements in hot UF_6/argon mixtures at various wavelengths, temperatures and pressures. These data are required to provide basic absorption data for radiation transport calculations and relative emission data for subsequent comparison of theoretical calculations with experimental results.

II. Test Equipment

The equipment used in the experimental evaluation of the spectral properties of UF_6 and possible UF_6 decomposition products consisted of three major components. These were the plasma torch-optical plenum assembly, the monochromator, and the UF_6 transfer system. A schematic of the overall system is shown in Figure 2; details of these components as well as other auxiliary equipment are discussed in the following sections.

Plasma Torch-Plenum Assembly

A plasma torch facility, designed and developed by UTRC, was used to provide hot UF_6/argon mixtures for all experimental determinations. A cross-sectional schematic of the plasma torch illustrating the major torch components is depicted in Figure 3. The principal components of the torch are a pin-type cathode, a hollow conically-shaped anode, an argon injector, a UF_6 injector and two external magnets. The cathode is a hemispherical-tipped 2 percent thoriated tungsten rod 0.1 cm in diameter and was provided with means for independent water cooling. The cathode extended partially into the water-cooled conically-shaped copper anode as shown in Figure 3. Argon was injected tangentially through eight equally spaced 0.016-cm-diameter holes located at the base of the cathode assembly. The aerodynamic swirl imparted by the argon injection system was augmented magnetically by means of two external magnets located concentrically about the anode as shown in Figure 3.

A Rapid Electric, Model SRV/MAN, 200 kw dc power supply was used to provide power to the discharge. The external magnets were supplied by Hypertherm, Model H-444 dc power supplies rated at 16.2 kw (90 v, 180 A) with a 60 percent duty cycle. The large magnet was connected to two paralleled units to provide higher current (360 A) and thus, a greater magnetic field. The smaller magnet was supplied by one unit.

A UF_6 injector was located immediately adjacent to and downstream of the anode. Preheated UF_6 was injected into the argon stream heated by the torch via two 0.016-cm-diameter holes. The aerodynamically mixed high temperature gas stream was then introduced into the cylindrical stainless-steel plenum (see Figures 2 and 3). The plenum was equipped with six optical ports (3 oppositely positioned pairs) which enabled viewing the high temperature gas stream spectroscopically in absorption or emission. The optical path through the mixed gas stream was 10.2 cm in length. The hot exhaust gases were subsequently cooled in a heat exchanger consisting of multiple copper coils prior to being neutralized in a sodium bicarbonate trap system (See Figure 2).

A high pressure (40 atm) water pump was used to provide cooling water for critical torch components. Separate water flow loops were used to cool the cathode, anode, external magnets and the UF_6 injector. Water cooling was not provided for the optical plenum. Each cooling water flow loop contained a flow meter to monitor water volumetric flow and a thermocouple to monitor exit water temperature. Inlet water temperature was also monitored by means of a thermocouple. Thus, power dissipation in various components could be calculated. Similarly a flow meter was installed in the argon line to the torch to provide means for quantitatively measuring argon mass flow in the system. Three thermocouples were attached to the plenum to monitor wall temperatures in the vicinity of the optical ports as shown in Figure 3. A fixed thermocouple was inserted into the hot gas flow downstream of the plenum and immediately prior to the heat exchanger. In addition, a scanning thermocouple system (tungsten - 5 percent rhenium vs tungsten - 26 percent rhenium thermocouple) was installed such that temperature scans could be made in the UF_6/argon mixture parallel to the optical path.

The plenum was equipped with both a transducer and a gauge for monitoring total pressure in the system. All thermocouples associated with monitoring water, component and exit-gas temperature were copper-constantan. Temperatures were monitored by means of an eight channel Sanborn recorder.

Monochromator

A McPherson Model 235, half-meter scanning monochromator of the Seya-Namioka type was used for all spectral measurements. Entrance and exit slit

systems contained three slit widths; 100, 200, and 400 μm. A 1200 G/mm and a 300 G/mm gratings were available for use. The 1200 G/mm grating was blazed at 150 nm and covered the range from 50 to about 300 nm. The 300 G/mm grating was blazed at 550 nm and covered a wavelength range from 50 nm to about 1200 nm. Scanning speeds could be varied in twelve steps from 0.025 nm/min to 100 nm/min for the 1200 G/mm grating and from 0.1 nm/min to 400 nm/min for the 300 G/mm grating.

The radiation detector system consisted of a McPherson Model 650 detector assembly and a Model 790 detector electronic system. The detector contains a sodium salicylate coated window and an EMI Model 9635B "dialkali" coated photomultiplier. The sodium salicylate-photomultiplier system is sensitive from 50 to about 600 nm. The 600 nm upper wavelength limit is dictated by the photodetector cut-off. The detector output was monitored on one channel of a Hewlet-Packard dual channel recorder.

A 2.5 cm diameter transition section approximately 30 cm in length was used to provide an enclosed optical path between the plenum and the monochromator. The end of the transition piece in contract with the inner wall of the plenum was fitted with a 0.6 x 1.9 cm slit to minimize flow of UF_6 into the external optical path. The transition section was equipped with a window mount to permit use of a lithium fluoride window when scanning at wavelengths above approximately 120 nm. In addition, an argon purge system was installed in the transition section to provide a slight back-pressure of gas with respect to the plenum in order to prevent flow of UF_6 from the plenum into the monochromator or onto the windows. In addition, the monochromator housing and the window assembly used in conjunction with the tungsten-halogen source lamp for absorption measurements were provided with argon purging to prevent possible contamination by UF_6 vapors.

UF_6 Transfer System

The transfer system consisted of a two ℓ Monel supply canister rated at 200 atm with appropriate shut-off and metering valves as indicated in Figure 2. Two chromel-alumel thermocouples were installed in the canister to monitor the temperature of the UF_6 liquid and gas phases. A Matheson linear mass flow meter was used to determine UF_6 mass flow rates during various experiments. The mass flow meter output was continuously monitored on the second channel of the Hewlet-Packard dual channel recorder during all tests involving UF_6 flow. The canister, valves, mass flow meter and all lines in the UF_6 transfer system were electrically heated by means of Variac controlled heater tapes. Chromel-alumel thermocouples were placed in various components to monitor temperatures at strategic locations in the UF_6 flow loop.

III. Experimental Procedures

A series of preliminary experiments were conducted to determine the operating parameters of the plasma torch system and to establish cooling water flow requirements for the facility. This series of tests was conducted with argon flow only; no UF_6 was used nor were spectral scans made. During these tests water flow and temperatures were monitored as well as temperatures for various system components. Similarly, gas exit temperatures were measured. In addition, these tests indicated that run time decreased markedly (about 3 minutes) at operating conditions which yielded temperatures above approximately 2000 K. The limiting factor was primarily attributable to thermal overloading of the external magnet power supplies.

It should be noted that the flow rate of argon determines the gas-mixture temperature in the plenum to a very large degree. Thus, variation of the argon flow to obtain various UF_6-to-argon mass ratios was precluded. Changes in UF_6-to-argon mass flow were accomplished by varying the quantity of UF_6 injected into the gas stream.

Subsequently, spectral studies with flowing UF_6 were undertaken. Normal procedure involved initiating the discharge on argon injected at a low flow rate to facilitate start-up. The argon flow and discharge current were then increased to predetermined values and the system allowed to equilibrate. Spectral scans were then conducted to determine the emission from argon without UF_6 flow. Prior to starting, the UF_6 transfer system was preheated to a temperature of approximately 430 K. UF_6 was not injected until the injector temperature was greater than 350 K to prevent condensation of UF_6 in the injector ports with resultant clogging of the UF_6 injector system. After the UF_6 injector reached operating temperature, UF_6 flow was initiated and monitored by means of the linear mass flow meter until constant flow was obtained. Constant UF_6 flow usually was achieved between 30 to 60 seconds after flow was initiated. Spectral scans in either emission or absorption were commenced after equilibration of UF_6 mass flow.

Temperature scans were taken immediately after the spectral scans were completed. The temperature and spectral scans were not conducted simultaneously because of objectionable photodetector noise levels generated by the scanning thermocouple drive-motor.

Spectral data were recorded at a rate of 400 nm/min when using the 300 G/mm grating and at 100 nm/min when using the 1200 G/mm grating. The high scan rates were required because of realtively short plasma torch operating times at high temperatures and to minimize exposure of the equipment to hot corrosive UF_6. Monochromator slit

width was constant at 100 μm for all emission and absorption measurements.

Initial spectral results were of poor quality because of high noise levels due to mechanical vibrations. Subsequently, the monochromator table was equipped with "isopads" and additional mounting support provided for the plasma torch-plenum assembly. In addition, a metallic bellows was installed in the transition section between the plenum port and the monochromator entrance slit to minimize vibrational coupling between the two systems. With these changes the vibration was reduced to negligible levels.

A tungsten-halogen lamp (quartz envelope) was used as the radiation source for the absorption measurements. Absorption measurements were conducted as follows. First, a spectral scan was made at a given argon mass flow rate and gas temperature to determine the emission due to hot argon. In all cases investigated no argon emission could be observed except under very high amplifier gain as compared to the lamp or UF_6 emission. Consequently, the incident radiation, I_o, was measured by irradiating the hot argon with the lamp at the specified operating conditions. Next, a UF_6 flow was established and the combined radiation, $I_{UF_6} + I_t$, (from the lamp and UF6 emission) was measured. This determination gives the total radiation emitted by the hot UF_6 and the quantity of lamp radiation which is transmitted through the plasma. Finally, the emission due to UF_6, i.e., I_{UF_6}, was determined with the lamp extinguished. Thus the relative intensity transmitted through the absorbing plasma was determined and is given by:

$$\frac{(I_{UF_6} + I_t) - I_{UF_6}}{I_o} = \frac{I_t}{I_o} \qquad (1)$$

Shut-down procedure involved termination of UF_6 flow followed by careful purging of UF_6 transfer lines and the UF_6 injector system with argon preheated to a temperature of approximately 500 K. Failure to adequately purge the system with hot argon invariably resulted in condensation of UF_6 upon cooling and complete clogging of the small ports in the UF_6 injector.

Wavelength calibration of the two gratings was periodically effected using a mercury discharge lamp placed at the entrance slit to the monochromator.

IV. Results and Discussion

Relative Spectral Emission

A series of twenty-six separate emission scans were made for wavelengths in the region between 120 to 600 nm. The 300 G/mm grating was used for these studies along with the lithium fluoride window. The window was utilized to eliminate the possible contamination of the monochromator components by UF_6. Experimental parameters including temperature, UF_6 and argon mass flow rates, the calculated partial pressure of UF_6 and the UF_6-to-argon mass flow ratio are summarized in Table I for these twenty-six runs. The pressure in the optical plenum was maintained at 1.0 atm for all twenty-six cases described in Table I.

It should be noted that the maximum range for a sheathed tungsten thermocouple is approximately 3000 K. Therefore, the value of 3560 K (scan number 26) represents the result of three temperature estimates. These are: (1) an extrapolation of the thermocouple calibration curve to higher temperatures, (2) heat balance for the system which defines an average gas temperature and (3) a correlation between observed temperature profiles (obtained with the scanning thermocouple) and an average gas temperature as determined by the thermocouple in the partially cooled gas stream well downstream of the optical path.

Three representative gas-mixture (UF_6/argon) temperature profiles are shown in Figure 4 as a function of relative position along the optical path in the plenum immediately adjacent to the UF_6 injector. The profiles are relatively flat usually exhibiting a maximum temperature variation of less than approximately 100 K. Since a relatively large thermocouple was used (0.32 cm-dia) the steep temperature gradient adjacent to the walls of the optical plenum are not evident in Figure 4. Wall temperatures measured at the outer surface of the plenum ranged from 800 to about 1500 K and depended essentially upon the argon flow rate and the run duration. There was no direct correlation between wall temperatures and gas temperature since spectral scans were initiated as soon as possible to reduce run time and exposure to UF_6. In essence, equilibrium between the gas-mixture and wall temperature was not necessarily established prior to spectral scanning. The effect of this thermal nonequilibrium of the walls on spectral scans was negligible as noted on repetitive spectral scans at nearly identical gas temperatures but different wall temperatures.

Results of typical emission scans are illustrated in Figure 5 as a function of wavelength for several temperatures between approximately 1000 K and 3600 K. The relative intensities shown in Figure 5 have been corrected for various variable experimental parameters such as photodetector response and different scale factors. The emission due to argon was always found to be negligible compared to UF_6 (at least 1 order of magnitude less), thus no correction for argon emission was required. In addition, the measured relative emission intensities have been normalized by dividing the corrected intensities by the corresponding calculated partial pressure of UF_6. Therefore these results illustrate the emitted intensities per unit pressure (mm Hg) of UF_6 injected into the system.

The long wavelength limit (580 nm) was dictated by the photodetector response which rapidly approached zero between 580 and 600 nm. In all cases experimentally investigated, the emitted intensity reached negligible levels between 250 and 300 nm. No significant emission was observed at wavelengths less than about 250 nm at all temperatures although wavelength scans were made down to the lithium fluoride cut-off at approximately 120 nm.

All spectral traces shown in Figure 5 exhibit similar characteristics particularly in the visible region between 380 and 580 nm. The first appearance of a new emission band at a wavelength of about 310 nm is noted at about 1800 K and becomes more pronounced with increasing temperature. In addition there is an enhancement in emission at wavelengths less than about 380 nm with an increase in temperature.

The spectral emission results of Figure 5 were integrated between 300 and 580 nm to determine the variation in relative total emission as a function of temperature. These calculated total emission results are depicted in Figure 6 as a function of temperature and are normalized with respect to the integrated results at 3560 K. No data below 300 nm or above 580 nm were used because of the very weak signal observed. The total intensity between 300 and 580 nm increases rapidly up to a temperature of about 1700 K and then much less strongly at higher temperatures as shown in Figure 6. The emission increases approximately by nine orders of magnitude between 800 and 3600 K. A summary of these results as well as integrated intensities at lower temperatures is shown in Table II. Equivalent integrated blackbody data over the same temperature range and in the same wavelength range are also illustrated by the dashed line in Figure 6.

Fractional integrated intensities per 40 nm wavelength intervals were calculated from the results of Figure 6. These calculated results are shown in Figure 7 as a function of the wavelength at the center of each 40 nm interval for four representative temperatures between 1400 and 3600 K. The results in Figure 7 illustrate the enhanced emission at wavelengths below 400 and 450 nm as the temperature is increased and the corresponding decrease in emission with increasing temperature at longer wavelengths. Additional calculated fractional intensities not shown in Figure 7 are tabulated in Table III for all temperatures investigated.

The calculated equilibrium composition of a UF_6/argon mixture is shown in Figure 8 as a function of temperature at a total pressure of one atmosphere and for a partial pressure of UF_6 equal to 0.5 mm Hg. Comparison of the spectral emission results of Figure 5 with the composition data of Figure 8 indicate that the appearance of the new band (peak $\lambda \sim 310$ nm) occurs at about 1800 K and approximately coincides with the appearance of the UF_6 decomposition products, UF_4 and UF_5 as well as fluorine atoms, F. Assignment of the band to a specific species is not possible on the basis of these data. Further assessment of the spectral results with specific components from the thermal decomposition of UF_6 are precluded because of the complexity of the composition scheme at higher temperatures.

It is known from black-body relationships that only about 0.21 percent of the total emitted radiation occurs at wavelengths less than 300 nm for a black-body at a temperature of 3500 K. Therefore relatively little emission of radiation was anticipated for UF_6 and/or its decomposition products at the same temperature or at lower temperatures. Although the previously described experimental results indicated no radiation below 250 nm at any temperature, a series of three emission scans were made to confirm these results and to examine the spectral region below the lithium fluoride wavelength cut-off at approximately 120 nm. These scans were accomplished in a windowless mode using the 1200 G/mm grating at temperatures of 1050, 1400 and 2280 K. Additional experimental parameters are enumerated in Table IV. No radiation (line, band or continuum) was observed in confirmation of the previous results. Therefore, additional scans in the windowless mode were discontinued.

A final series of six emission studies were conducted at total plenum pressures up to 1.7 atm to examine the effect of pressure on the emission from hot UF_6 and its thermal decomposition products. The various experimental parameters for these cases are summarized in Table V. The result of these tests did not indicate an appreciable pressure effect as shown by a comparison of the relative spectral emissions at a temperature of about 2400 K for a total pressure of 1.0 and 1.7 atm (see Figure 9). Similar results were obtained at other temperatures and pressures. The two curves depicted in Figure 9

are also indicative of the reproducibility of the previous emission results at similar temperatures observed in the scans at a total pressure of 1.0 atm.

Spectral Absorption

Finally, a series of five experiments were performed to ascertain the absorption characteristics of UF_6 in the visible region and at elevated temperatures. A typical set of transmission results at a temperature of 1270 K are shown in Figure 10 as a function of wavelength between 420 and 580 nm. The figure illustrates the source intensity (tungsten-halogen lamp) I_o, the combined intensity from the emitting UF_6 plus the transmitted source intensity ($I_{UF_6} + I_t$) as well as the emission from the hot UF_6, I_{UF_6}.

The relative spectral transmission derived from the results of Figure 10 and similar results for other temperatures are shown in Figure 11. These data were used to determine an "effective" spectral cross-section over the wavelength of interest as follows:

$$\frac{I_t}{I_o} = \exp - (\sigma NL) \qquad (2)$$

where I_t/I_o is the transmission (Figure 11), N, the number density, L the path length and σ the cross-section. The quantity σ is an "effective" cross-section since the UF_6 may be partially decomposed, particularly at higher temperatures. Furthermore, the individual spectral details associated with each absorbing species cannot be ascertained. Therefore, the particle density factor serves to define an "effective" cross-section per unit UF_6 pressure. Calculated "effective" cross-section results are graphically depicted in Figure 12 as a function of wavelength at the temperatures studied.

The magnitude of the "effective" cross-section varies from about 2×10^{-19} cm^2 at short wavelengths to a minimum of approximately 9×10^{-20} cm^2 at the long wavelengths. Tabulated values of the cross-section at 10 nm intervals are summarized in Table VII for the five temperatures investigated.

IV. Conclusions

The broad-band relative spectral emission characteristics of UF_6 and its thermal decomposition products have been experimentally examined over a range of wavelengths (80 to 600 nm), pressures (1.0 to 1.73 atm) and temperatures (800 to 3600 K). The "effective" absorption cross-sections of UF_6 and its thermal decomposition products have been determined over the wavelength range from 420 to 580 nm and at five temperatures between approximately 1000 and 1800 K.

The following conclusions are inferred from these experimental investigations:

1. The total integrated intensity between 300 and 580 nm increases with temperature between 800 and 3600 K. The increase in intensity between 800 and 3600 K is about nine orders of magnitude.

2. There is no significant emission of radiation at wavelengths between 80 and approximately 250 nm for the temperature regime investigated.

3. The appearance of a new emission band centered at approximately 310 nm is associated with the appearance of substantial quantities of UF_6 thermal dissociation products at temperatures in excess of 1800 K.

4. The emission of radiation from UF_6 or its dissociation products does not exhibit a measurable pressure dependence at total pressures up to 1.7 atm.

5. The "effective" absorption cross-sections at wavelengths between 420 and 580 nm vary from 9×10^{-20} to about 2×10^{-19} cm^2.

References

1. Thom, K., R. T. Schneider, and F. C. Schwenk: Physics and Potentials of Fissioning Plasmas for Space Power and Propulsion. Paper No. 74-087. Int'l. Astronautical Federation (IAF) XXVth Cong., Amsterdam, 30 Sept. 5 Octo. 1974.

2. Latham, T. S., F. R. Biancardi, and R. J. Rodgers: Applications of Plasma Core Reactors to Terrestrial Energy Systems. AIAA Paper 74-1074, AIAA/SAE 10th Propulsion Conference, San Diego, Calif., October 21-23, 1974.

3. Roback, R.: Thermodynamic Properties of Coolant Fluids and Particle Seeds for Gaseous Nuclear Rockets. UARL Report C-910092-3, Prepared under NASA Contract NASw-847, September, 1964.

Symbols

G/mm	Number of lines or grooves/mm of grating surface
I	Relative intensity for absorption measurements, see Fig. 12 - dimensionless
I_o	Relative source lamp intensity or incident intensity - dimensionless
I_t	Relative transmitted intensity - dimensionless
$I_\lambda(T)$	Relative spectral emission at temperature T - dimensionless
$I_t(T)$	Relative total or integrated emission at temperature T, dimensionless
$I_{\Delta\lambda}(T)$	Relative integrated spectral emission per wavelength interval, - dimensionless
L	Path length - cm
$\dot{m}$	Mass flow rate - g/sec

N Number density, cm^{-3}
P Pressure, atm or mm Hg
r Relative position - dimensionless
T Absolute temperature - K
λ Wavelength - nm or μ
σ Effective cross-section - cm^2 per molecule of UF_6

TABLE I

SUMMARY OF EXPERIMENTAL CONDITIONS FOR EMISSION STUDIES

(Lithium Fluoride Window, 120 < λ < 600 nm)

P_{total} = 1.0 atm

No.	Temp. K	$\dot{m}_{UF_6}$ g/s	$\dot{m}_{Ar}$ g/s	P_{UF_6} mm Hg	$\dot{m}_{UF_6}/\dot{m}_{Ar}$
1	810	0.062	0.79	6.8	7.9×10^{-2}
2	1070	0.056	1.46	3.2	3.8×10^{-2}
3	1030	0.016	1.21	1.1	1.3×10^{-2}
4	1260	0.010	1.08	0.80	9.3×10^{-3}
5	1320	0.046	2.49	1.6	1.8×10^{-2}
6	1330	0.048	1.93	2.2	2.6×10^{-2}
7	1330	0.035	2.49	1.2	1.4×10^{-2}
8	1330	0.050	2.49	1.7	2.0×10^{-2}
9	1340	0.012	1.46	0.71	8.2×10^{-3}
10	1360	0.002	1.08	0.16	1.9×10^{-3}
11	1400	0.065	2.49	2.3	2.6×10^{-3}
12	1400	0.065	3.16	1.8	2.1×10^{-2}
13	1400	0.042	1.47	2.5	2.9×10^{-2}
14	1510	0.014	2.49	0.48	5.6×10^{-3}
15	1510	0.011	1.10	0.86	1.0×10^{-2}
16	1530	0.020	2.49	0.70	8.0×10^{-3}
17	1680	0.12	1.48	6.9	8.1×10^{-2}
18	1730	0.11	3.49	2.7	3.2×10^{-2}
19	1810	0.012	1.46	0.71	8.2×10^{-3}
20	1860	0.043	3.49	1.1	1.2×10^{-2}
21	2060	0.0086	4.71	0.16	1.8×10^{-3}
22	2300	0.0084	5.08	0.14	1.7×10^{-3}
23	2430	0.0056	5.08	0.10	1.1×10^{-3}
24	2740	0.016	5.46	0.25	2.9×10^{-3}
25	2770	0.026	4.91	0.53	5.3×10^{-3}
26	3560*	0.013	5.46	0.21	2.4×10^{-3}

*Estimated value - see text for discussion

TABLE II

SUMMARY OF TOTAL INTENSITIES INTEGRATED BETWEEN 300 AND 580 NM

Temp. K	No.*	$I_t(T)$
810	1	1.63×10^{-4}
1050	2,3	4.12×10^{-1}
1260	4	1.38×10^{1}
1340	5 thru 10	1.55×10^{3}
1400	11, 12, 13	3.78×10^{3}
1520	14, 15, 16	6.45×10^{3}
1710	17, 18	2.78×10^{4}
1840	19, 20	4.43×10^{4}
2060	23	7.46×10^{4}
2300	22	1.11×10^{5}
2430	23	1.62×10^{5}
2760	24, 25	2.43×10^{5}
3560	26	7.21×10^{5}

*Denotes runs which were averaged.

TABLE III

SUMMARY OF FRACTIONAL INTENSITIES AT VARIOUS TEMPERATURES

Wavelength Interval nm	Fractional Intensities 3560°K	2740°K	2430°K	2300°K	2060°K	1810°K	1700°K	1500°K	1400°K	1330°K	1260°K	1050°K	810°K
300-340	4.72	3.51	4.76	3.68	3.47	2.12	1.53	1.67	1.17	0.44	.490	.094	.012
340-380	8.64	7.15	8.52	7.28	8.56	6.83	5.12	4.56	4.00	2.09	1.73	.790	.223
380-420	15.5	15.7	14.3	15.2	14.8	11.9	9.19	12.9	9.26	8.27	10.41	6.88	7.46
420-460	20.3	21.8	21.5	22.2	22.9	20.4	20.5	22.7	21.0	23.2	22.4	23.4	32.1
460-500	19.3	19.9	20.1	20.5	19.2	22.3	23.1	22.2	24.4	24.4	23.5	25.5	31.3
500-540	17.1	17.9	17.2	17.7	17.0	20.2	21.7	19.9	21.4	22.8	22.1	23.0	22.8
540-580	14.5	14.8	13.6	13.4	14.2	16.9	18.8	16.2	18.2	19.7	19.5	20.3	7.09

TABLE IV

SUMMARY OF EXPERIMENTAL
CONDITIONS FOR EMISSION STUDIES

(Windowless Mode, $80 < \lambda < 300$ nm)

$P_{total} = 1.0$ atm

No.	Temp. K	$\dot{m}_{UF_6}$ g/s	$\dot{m}_{Ar}$ g/s	P_{UF_6} mm Hg	$\dot{m}_{UF_6}/\dot{m}_{Ar}$
27	1050	.043	1.46	2.53	2.5×10^{-2}
28	1400	.044	2.49	1.52	1.8×10^{-2}
29	2280	.046	5.10	0.78	9.02×10^{-3}

TABLE V

SUMMARY OF EXPERIMENTAL
CONDITION FOR EMISSION STUDIES AT HIGH PRESSURES

(Lithium Fluoride Window, $120 < \lambda < 600$ nm)

No.	Temp. K	$\dot{m}_{UF_6}$ g/s	$\dot{m}_{Ar}$ g/s	P_{UF_6} mm Hg	$\dot{m}_{UF_6}/\dot{m}_{Ar}$	P_{total} atm
30	1050	.056	1.46	3.29	3.8×10^{-2}	1.22
31	1350	.044	1.93	1.96	2.3×10^{-2}	1.37
32	1880	.012	3.49	2.96	3.4×10^{-3}	1.63
33	2030	.043	4.71	0.79	9.1×10^{-3}	1.62
34	2410	.009	5.08	0.15	1.8×10^{-3}	1.73

TABLE VI

SUMMARY OF EXPERIMENTAL CONDITIONS
FOR ABSORPTION STUDIES

(Lithium Fluoride Window, 420 nm $< \lambda <$ 580 nm)

$P_{total} = 1.0$ atm

No.	Temp. K	$\dot{m}_{UF_6}$ g/s	$\dot{m}_{Ar}$ g/s	P_{UF_6} mm Hg	$\dot{m}_{UF_6}/\dot{m}_{Ar}$
A	980	0.091	.79	9.8	.12
B	1050	.095	.79	10.0	.12
C	1270	.107	1.46	6.3	.073
D	1440	.102	1.46	6.0	.070
E	1770	.099	1.46	5.8	.068

TABLE VII

SUMMARY OF "EFFECTIVE" CROSS-SECTIONS
AT VARIOUS TEMPERATURES

Wavelength nm	Cross-Section, cm^2 T = 980 K	1050 K	1270 K	1440 K	1770 K
420	5.75-19	6.03-19	8.54-19	6.02-19	4.82-19
430	5.21	5.46	7.52	4.99	4.53
440	4.71	4.94	6.64	4.06	4.21
450	4.24	4.45	5.82	3.31	3.92
460	3.85	4.03	5.09	2.63	3.64
470	3.51	3.68	4.43	2.17	3.29
480	3.18	3.33	3.84	1.84	3.05
490	2.91	3.05	3.34	1.57	2.74
500	2.71	2.84	2.92	1.36	2.50
510	2.55	2.67	2.59	1.18	2.30
520	2.44	2.56	2.38	1.10	2.10
530	2.40	2.52	2.26	1.02	1.97
540	2.44	2.56	2.28	9.69-20	1.83
550	2.53	2.66	2.40	8.91	1.90
560	2.71	2.84	2.66	8.91	1.93
570	2.98	3.13	3.07	8.91	2.10
580	3.38	3.54	3.69	8.91	2.30

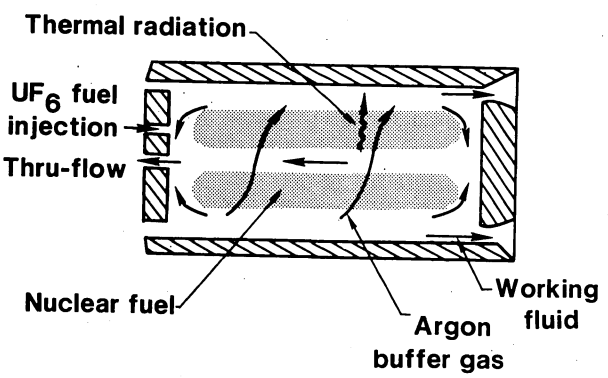

Fig. 1 Schematic of a unit cavity of a plasma core reactor.

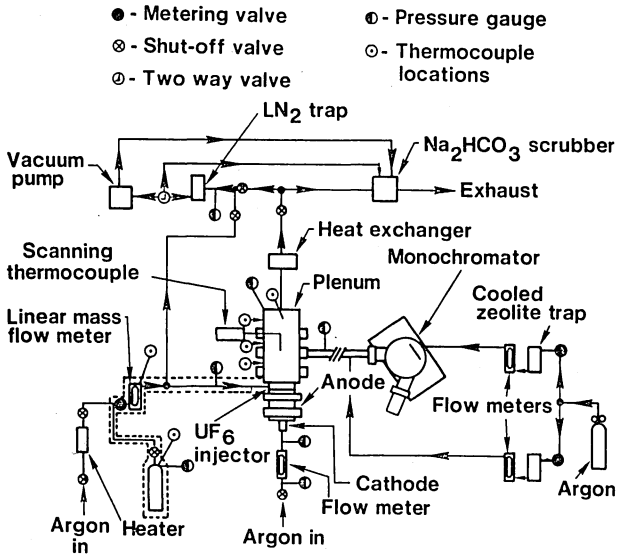

Fig. 2 Schematic of UF_6 plasma torch system.

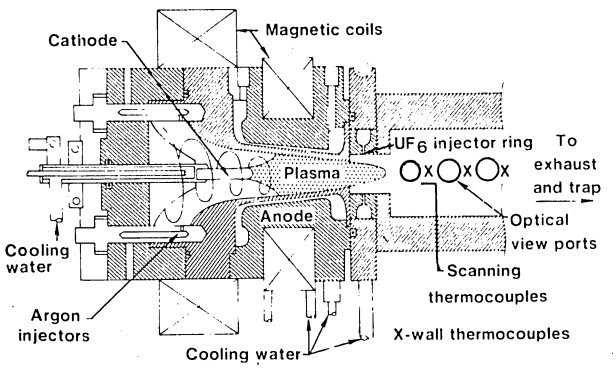

Fig. 3 Schematic of plasma torch assembly.

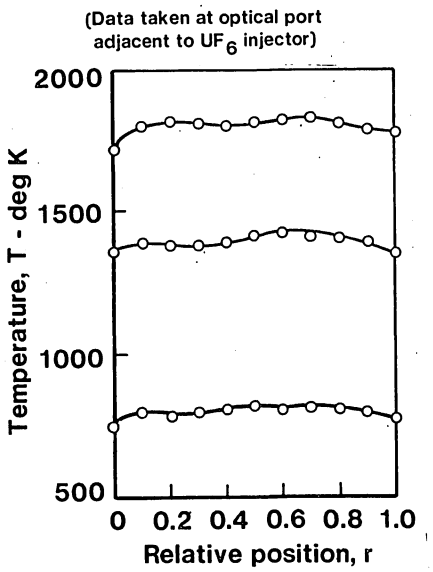

Fig. 4 Typical temperature profiles along the optical path in the plenum.

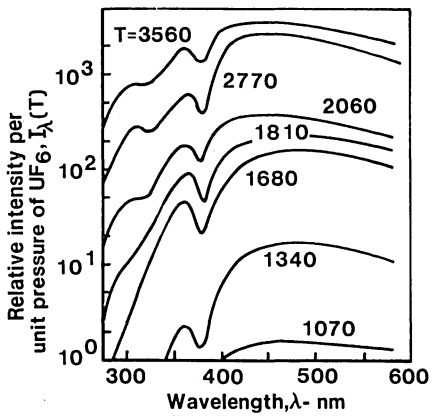

Fig. 5 Comparison of the relative spectral intensity of UF_6 at various temperatures between 1000 and 3600 deg. K.

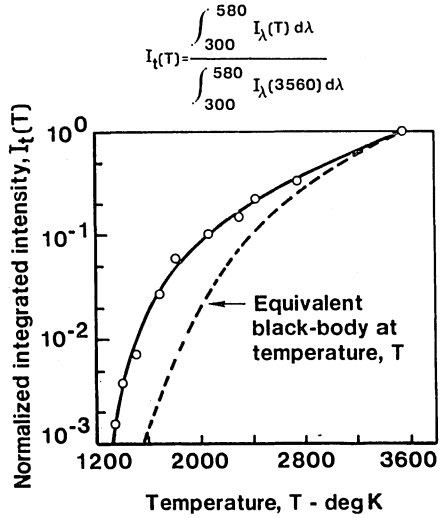

Fig. 6 Normalized integrated intensity from 300 to 580 nm as a function of temperature.

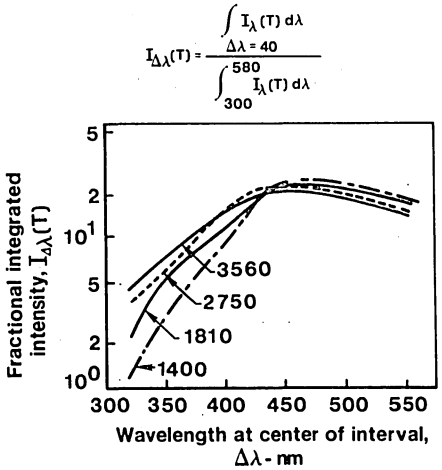

Fig. 7 Fractional integrated intensity per 40 nm wavelength intervals.

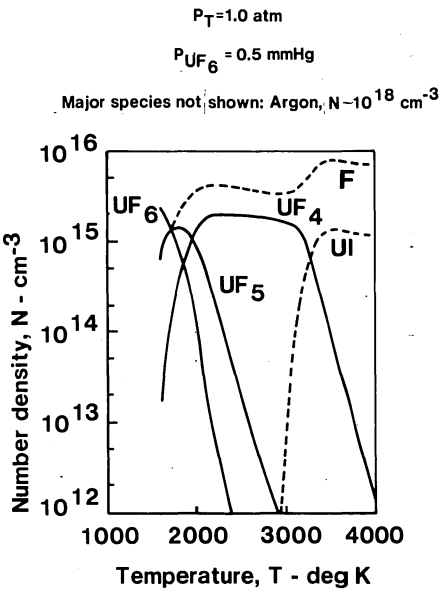

Fig. 8 Composition of UF_6/argon mixture as a function of temperature.

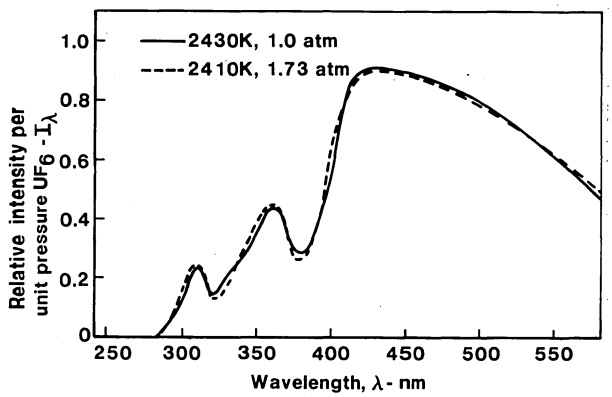

Fig. 9 Comparison of relative spectral emission at total pressures of 1.0 and 1.73 atm.

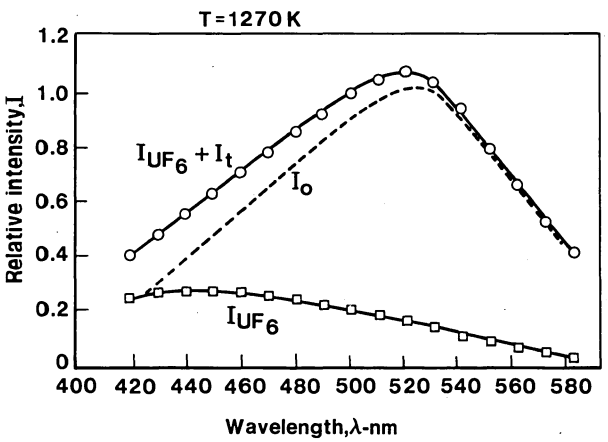

Fig. 10 Typical relative intensity results for absorption measurements.

Sym	No.	T	Mass flow g/sec		P_{UF_6}
		K	UF_6	Ar	mmHg
•	A	980	0.091	0.79	9.8
◇	B	1050	0.095	0.79	10.0
○	C	1270	0.107	1.46	6.3
□	D	1440	0.102	1.46	6.0
△	E	1770	0.099	1.46	5.8

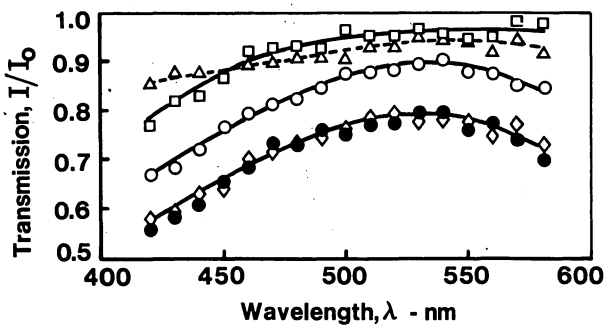

Fig. 11 Relative spectral transmission at various temperatures.

No.	T	Mass flow g/sec		P_{UF_6}
	K	UF_6	Ar	mmHg
A	980	0.091	0.79	9.8
B	1050	0.095	0.79	10.0
C	1270	0.107	1.46	6.3
D	1440	0.102	1.46	6.0
E	1770	0.099	1.46	5.8

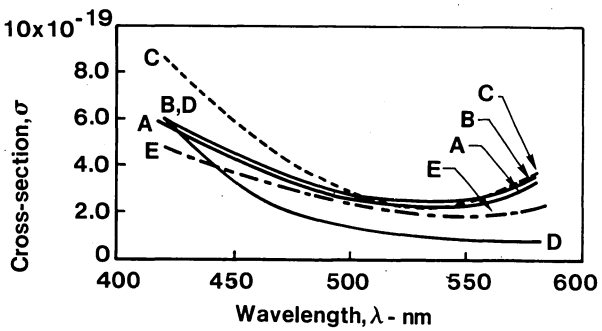

Fig. 12 "Effective" spectral cross-section at various temperatures.

URANIUM PLASMA EMISSION AT GAS-CORE REACTION CONDITIONS

M. D. Williams, N. W. Jalufka, and F. Hohl
National Aeronautics and Space Administration, Langley Research Center
Hampton, Va.

and

J. H. Lee
Vanderbilt University
Nashville, Tenn.

Abstract

The results of uranium plasma emission produced by two methods are reported. For the first method a ruby laser was focused on the surface of a pure U^{238} sample to create a plasma plume with a peak plasma density of about 10^{20} cm^{-3} and a temperature of about 38,600 K. The absolute intensity of the emitted radiation, covering the range from 300 to 7000 Å was measured. For the second method, the uranium plasma was produced in a 20 kilovolt, 25 kilojoule plasma-focus device. The 2.5 MeV neutrons from the D-D reaction in the plasma focus are moderated by polyethylene and induce fissions in the U^{235}. Spectra of both uranium plasmas were obtained over the range from 30 to 9000 Å. Because of the low fission yield the energy input due to fissions is very small compared to the total energy in the plasma.

I. Introduction

Electromagnetic radiation is expected to be the prime medium for obtaining high-grade power from plasma-core reactors. The same radiation will play an important role in the internal transfer of energy and steady-state operation of the reactors. Effective development of these reactors requires a knowledge of their spectral characteristics at expected operating conditions. Two experiments at the Langley Research Center produce uranium plasmas that approximate gas-core reactor conditions and have been used to record segments of the spectrum from the x-ray region to the near infrared region.

II. Plasma-Focus Experiment

The plasma-focus apparatus[1] is a coaxial plasma gun connected to a capacitor bank. Figure 1 is a cross-sectional view of the gun's coaxial cylindrical geometry. The center electrode is 5 cm in diameter and the inside diameter of the outer electrode is 10 cm. Inner and outer electrodes are connected to lower and upper collector plates, respectively, which are, in turn, connected to a capacitor bank through spark-gap switches. The capacitor bank stores 25 kJ of energy at 20 kV. When discharged, a current sheath forms over the surface of the insulator at the base of the center electrode. The J x B force drives the plasma up the annular region between the electrodes. Just past the end of the center electrode the plasma is forced toward the gun's axis by the strong self-induced magnetic field. The plasma reaches the focus condition just as the capacitor bank reaches a maximum current of one megampere in three microseconds. Deuterium (at ~5 Torr pressure before the discharge) is swept before the plasma sheath

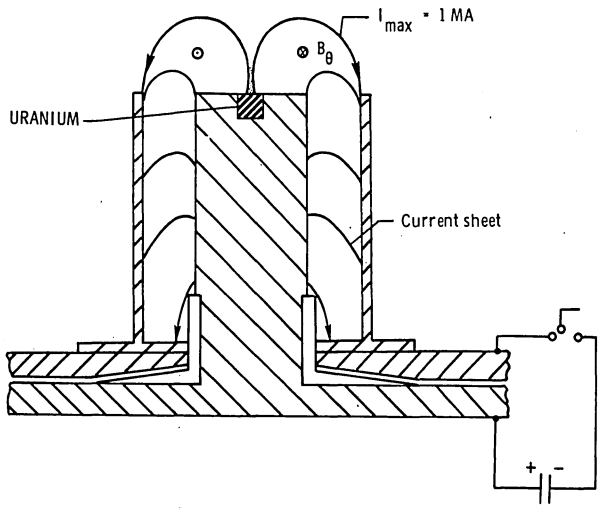

Figure 1. Plasma Focus Electrode Arrangement

to the focal position to form a very hot (50×10^6 K) dense ($>10^{19}/cm^3$) plasma which emits intense bursts of neutrons, gammas, x-rays, and practically the entire EM spectrum. Simultaneously, the end of the center electrode begins eroding at its centerline. A solid uranium sample placed at this position is partially evaporated by impingement of energetic electron and ion beams emitted from the plasma-focus region. The uranium plasma rises about 2 cm above the electrode surface in less than 2 microseconds. Neutrons ($\sim 10^9$) produced by the plasma focus are reflected back

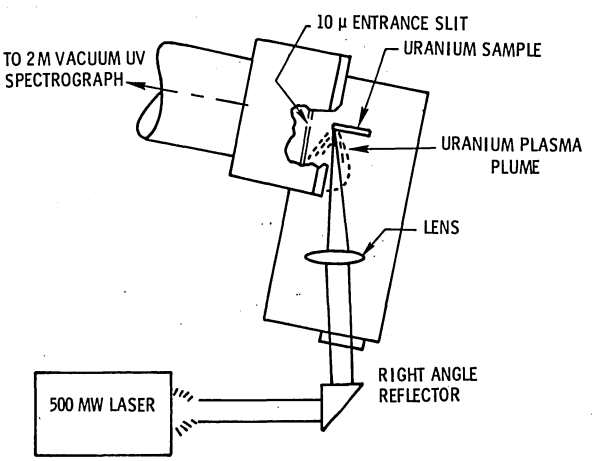

Figure 2. Experimental Arrangement for the Laser Produced Uranium Plasma Experiment

into the uranium plasma by a polyethylene moderator which surrounds the focus and is about 15 cm away. The temperature and pressure of the uranium plasma have been estimated at 1 to 5 eV and 160 to 800 atmospheres, respectively.

Thus, the plasma-focus experiment produces a uranium plasma which approximates expected gas-core reactor conditions, including some fission action of the uranium 235.

III. Laser Plasma Experiment

The laser plasma has been produced by focusing the radiation of a Q-spoiled ruby laser onto the flat surface of a solid U^{238} sample. Four to six joules of energy were contained in the laser pulse. The pulse duration at half-maximum was 20 nanoseconds. The uranium sample was contained in a vacuum chamber at the focal point of a quartz lens near the entrance slit of a spectrograph. Figure 2 shows the general experimental arrangement. Plasma created by the laser's rapid heating of the sample expanded perpendicular to the sample surface. Placement of the sample relative to the spectrograph entrance slit made possible the observation of different cross sections of the plume. Each cross section exhibited different plasma conditions. A cross section near the surface was found to approximate gas-core reactor conditions of temperature (~38,600 K) and pressure (~500 atm.).

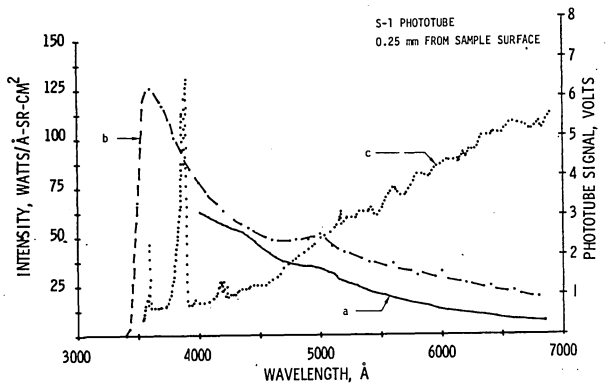

Figure 3. Spectra of Uranium Plasma and Carbon Arc
(a) Calibrated and time-resolved spectrum of uranium plasma 0.25 mm from sample surface;
(b) Phototube data scaled in volts;
(c) Unscaled carbon arc spectrum.

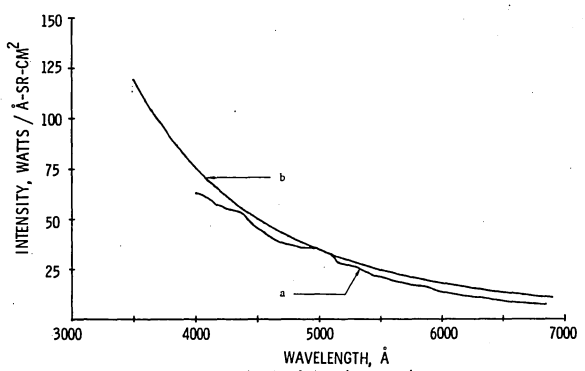

Figure 4. Comparison of Uranium Plasma and Blackbody Emission. (a) Calibrated uranium spectrum 0.5 mm from sample surface; (b) Spectrum of 38,600 K blackbody.

IV. Spectra

Visible spectra from 3500 Å to 7000 Å and ultraviolet spectra from 300 Å to 1600 Å have been observed in the laser plasma experiment.

The visible spectra[2] were recorded with a half-meter monochromator equipped with a 1200 line/mm grating blazed at 5000 Å. Photomultiplier tubes were used to observe 8 Å portions of the spectrum and the resulting electrical pulses were recorded on oscillograms. A carbon arc was used to calibrate the absolute intensity of the spectrum. The resulting data were computer processed and are shown in figure 3. Figure 4 is a comparison of these data with the curve for a 38,600 K blackbody.

The UV spectrum was recorded in a similar experiment.[3] A 2-meter vacuum spectrograph/monochromator was used with sodium salicylate-coated photomultiplier tubes to record the spectra at 25 Å intervals. The data are shown in figure 5. An absolute intensity calibration of this spectrum was not made due to the lack of a good UV standard. Instead, intensity estimates were calculated by using the best available data on the optical components involved. The corrected spectra shows a continuum peak at 750 Å. This corresponds to a blackbody temperature

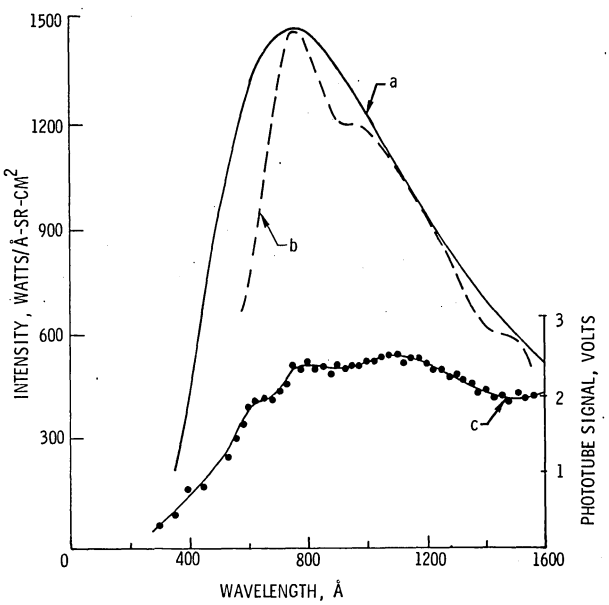

Figure 5. Time-Resolved Ultraviolet Spectrum of Uranium Plasma Generated Near the Edge of the Sample Surface. (a) Blackbody curve (38,600 K) normalized to the peak of the corrected spectrum; (b) Corrected spectrum; (c) Phototube data.

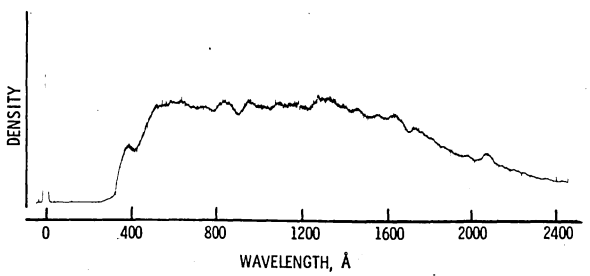

Figure 6. Density Trace of Spectrogram of Uranium Plasma

of 38,600 K. For the estimated particle density of 10^{20} cm^{-3}, the plasma pressure was about 500 atmospheres. A spectrogram (Fig. 6) was made to provide better wavelength resolution. It shows the magnitude of line emission and other structure in comparison to the continuum emission. The maximum instantaneous power of the observed plasma was of the order of 10^{11} W/m^2.

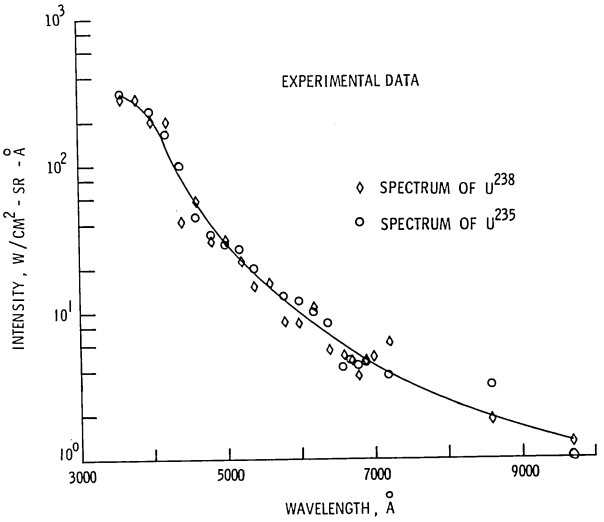

Figure 7. Absolute Intensity of Uranium Plasma Emission

Visible and ultraviolet spectra were also observed from the plasma-focus experiment. Visible measurements ranged from 3500 Å to 10,000 Å in the near IR. The experimental apparatus was similar to that used in the visible laser plasma measurements, including a carbon arc calibration source. Both U^{238} and U^{235} were used to generate the observed plasma in an effort to detect any spectral differences caused by fission action. Figure 7 shows the resultant measurements. Each data point is the average of many shots due to experimental nonreproducibilities. However, within experimental error, no differences could be detected between the spectra of U^{235} and U^{238}. Also, no nonthermal radiation peaks could be detected.

The search for a spectral difference between plasmas of the two isotopes was extended into the extreme ultraviolet spectrum. A one-meter Seya-Namioka spectrograph/monochromator viewed the spectrum from approximately 100 Å to about 600 Å. A 1-meter grazing incidence spectrograph covered the spectral segment from 30 Å - 400 Å. Both spectrographs were connected to the experiment through a special differentially-pumped vacuum system. First, the Seya-Namioka spectrograph was used. Its spectrogram (Fig. 8) revealed the possibility of a spectral difference between the two isotopes at wavelengths less than about 200 Å. So the Seya-Namioka spectrograph was replaced by the grazing incidence spectrograph to provide lower wavelength coverage with greater spectral resolution. The grazing incidence spectrogram (Fig. 9) revealed a radiation peak at about 93 Å which varied greatly in intensity from shot to shot. There appeared to be a larger peak for the U^{235} results. However, because of the large intensity variation from shot to shot, no definite difference in the spectrum from the two uranium isotopes could be established. The intensity variation of the peak at 93 Å could not be correlated with any experimental parameter such as neutron yield and is probably due to nonreproducibilities in the observed plasma. Both spectrographs used a platinum-coated grating ruled with 600 lines/mm at a 1° blaze angle. At an 85° angle of incidence the blaze wavelength of the grazing incidence spectrograph was about 93 Å. This contributed to the amplitude of the observed peak. No calculations or

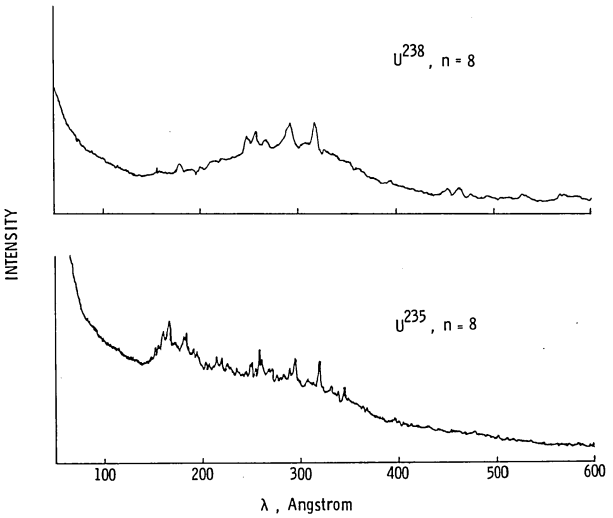

Figure 8. Comparison of Plasma Focus Produced U-238 and U-235 Plasma in the Region From 100 to 600 Angstroms

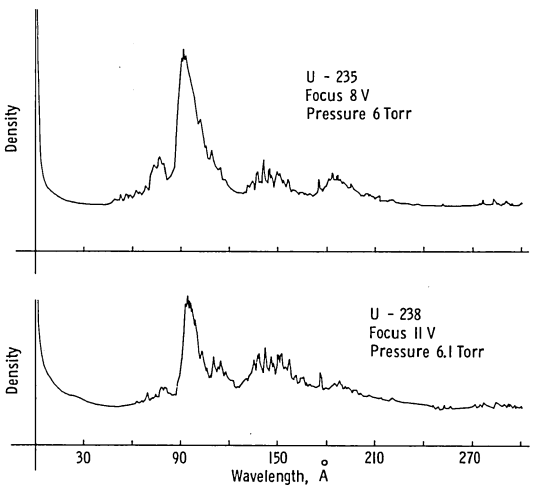

Figure 9. Comparison of Plasma from Produced U-235 and U-238 Plasma in the Region From 30 to 270 Angstroms

comparison to a UV source were made to establish absolute intensity values. Three factors are believed to be the major contributors to the apparent continuum of the spectrograms: (1) Light diffracted from the central image; (2) Light scattered by the ruled edges of the grating and a very light film on the grating surface; (3) the compacting of many line transitions at some wavelengths. Hence, the spectrogram is primarily due to line transitions of uranium and copper (eroded from

electrodes). The copper lines were verified by replacing the uranium sample at the end of the plasma-focus electrode by a copper sample. Figure 10 shows that indeed some of the lines observed in the uranium plasma were copper lines. It also shows that most of the radiation peak at 93 Å was real (not due to the blaze effect) and was caused by the uranium plasma.

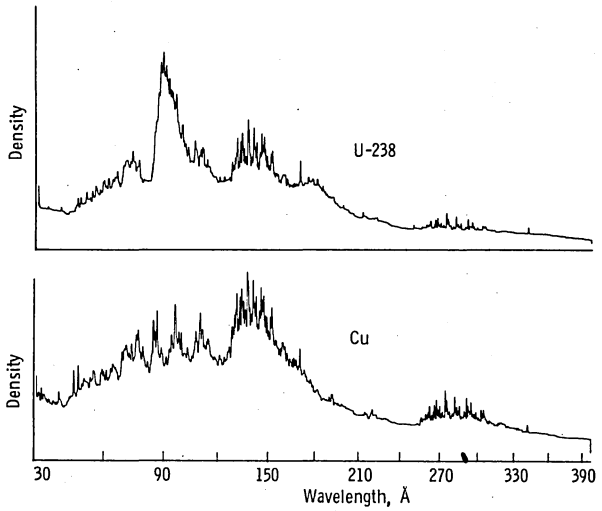

Figure 10. Comparison of Plasma Focus Produced Copper and Uranium Spectra

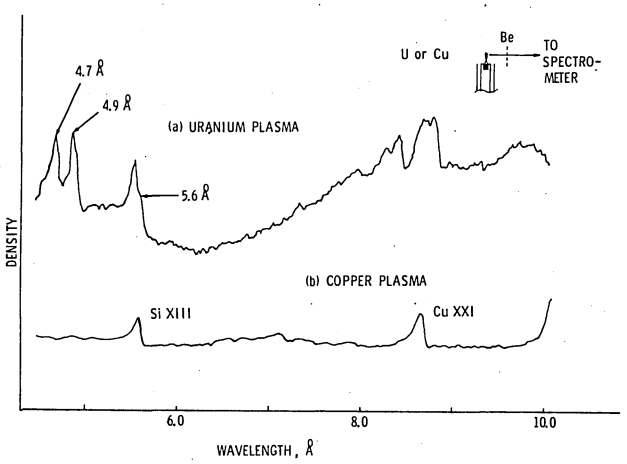

Figure 11. Comparison of Soft X-Ray Spectrum from Copper and Uranium Plasmas

A segment of the soft x-ray spectrum (3Å - 9Å) emitted by uranium and copper plasmas in the plasma focus are represented in figure 11. These spectra were obtained with a bent crystal spectrograph and recorded on x-ray film.[4] The uranium spectrum shows a significant increase in white x-ray emission which varies with the square of the atomic number. It also shows characteristic lines at 4.7, 4.9, 5.6, 8.7, and 8.8 Å. Especially strong lines below the 4 Å wavelength may be due to non-thermal electron beams (E_γ > 5 KeV) from the plasma focus. The expected large density of highly energetic electrons associated with fission fragments in a gas-core reactor could produce similar hard radiation with deleterious effects on the first reactor wall.

V. Conclusions

Spectral segments from the near infrared to the soft x-ray region have been recorded using two experiments which produce uranium plasmas that simulate expected gas-core reactor conditions. These spectra illustrate qualitatively and, in the visible region, quantitatively the radiation characteristics that may be expected from gas-core reactors operating at several hundred atmospheres pressure and several eV temperature. Line emission and other structure were insignificant compared to continuum radiation from the infrared region to several hundred angstroms. Intensities approached those of a blackbody of the same temperature. No large nonthermal radiation features could be found at the high plasma temperatures and pressures investigated. At wavelengths shorter than those where blackbody radiation is significant, line radiation was prevalent, especially at approximately 93 Å. X-ray spectra indicate that line emission will make an important contribution to the total x-ray energy. No radiation effects from fission action was detected. However, this was probably due to the low fission yield available in the experiment. Much higher fission yields may yet prove to be the cause of nonthermal features in the radiation spectrum.

References

1. Lee, J.H.; McFarland, D.R.; Hohl, F.; and Kim, K.H.: Production of Fissioning Uranium Plasma to Approximate Gas-Core Reactor Conditions. Nuclear Technology, vol. 22, June 1974.

2. Williams, M.D.; and Jalufka, N.W.: Visible Spectral Power Emitted from a Laser-Produced Uranium Plasma. NASA TM X-72626.

3. Williams, M.D.: Ultraviolet Spectrum Emitted from a Laser-Produced Uranium Plasma. Journal of Opt. Soc. Am. vol. 63, p. 383, March 1973.

4. Lee, J.H. et al.: Investigation of High Energy Radiation from a Plasma Focus. Final Report, NASA Grant NGR 43-002-031, August 1975.

To be published in the Proceedings of the
3rd Conference on Partially Ionized and Uranium
Plasmas, Princeton, New Jersey, June 10-12, 1976

BNL 21531

STUDIES ON COLOR-CENTER FORMATION IN GLASS UTILIZING MEASUREMENTS MADE DURING 1 to 3 MeV ELECTRON IRRADIATION*

K. J. Swyler and P. W. Levy
Brookhaven National Laboratory
Upton, New York 11973

Abstract

The coloring of NBS 710 glass has been studied using a new facility for making optical absorption measurements during and after electron irradiation. The induced absorption contains three Gaussian shaped bands. The color center growth curves contain two saturating exponential and one linear components. After irradiation the coloring decays and can be described by three decreasing exponentials. At room temperature both the coloring curve plateau and coloring rate increase with increasing dose rate. Coloring measurements made at a fixed dose rate but at increasing temperature indicate: 1) The coloring curve plateau decreases with increasing temperature and coloring is barely measurable near 400°C. 2) The plateau is reached more rapidly as the temperature increases. 3) The decay occurring after irradiation cannot be described by Arrhenius kinetics. At each temperature the coloring can be explained by simple kinetics. The temperature dependence of the decay can be explained if it is assumed that the thermal untrapping is controlled by a distribution of activation energies.

I. Introduction

The search for materials which will remain transparent to light while subjected to intense nuclear irradiation requires both engineering and basic radiation damage data quite different from that generally available from completed studies. As is well known, almost every normally transparent substance becomes colored by exposure to radiation. Some materials, e.g. photochromic glasses, become colored in the process of absorbing completely negligible amounts of energy. In contrast, substances like very pure fused silica or crystalline Al_2O_3 do not become colored in the visible until the radiation has imparted hundreds of joules. The coloring of these substances is clearly attributable to color-center formation. Unfortunately almost all of the available information on radiation induced color-center formation is not appropriate for evaluating materials which must remain transparent during energetic particle irradiation. In the past almost all studies on the coloring of glasses and crystals were made by irradiating the samples in an x-ray or gamma-ray source or in a reactor and then taking the samples to a spectrophotometer for measurement at a later time. Clearly, if the absorption changes appreciably between irradiation and measurement such measurements do not provide data that is applicable during irradiation. In particular, if the coloring contains a large decaying component, measurements made in this way will seriously underestimate the absorption during irradiation.

In addition to the uncertainties introduced by making measurements sometime after irradiation, very little data is available to evaluate effects dependent on two other important practical parameters, sample temperature and irradiation dose rate. It is well known that the F-center formation in the alkali-halides does not have a simple dependence on temperatures. Also, at a given temperature both the coloring rate and the maximum coloring increase with increasing dose rate. Roughly the same behavior is to be expected from fused silica and other glasses. However, there is very little data available to test this supposition.

To study the basic physics of radiation induced electronic and atomic displacement processes

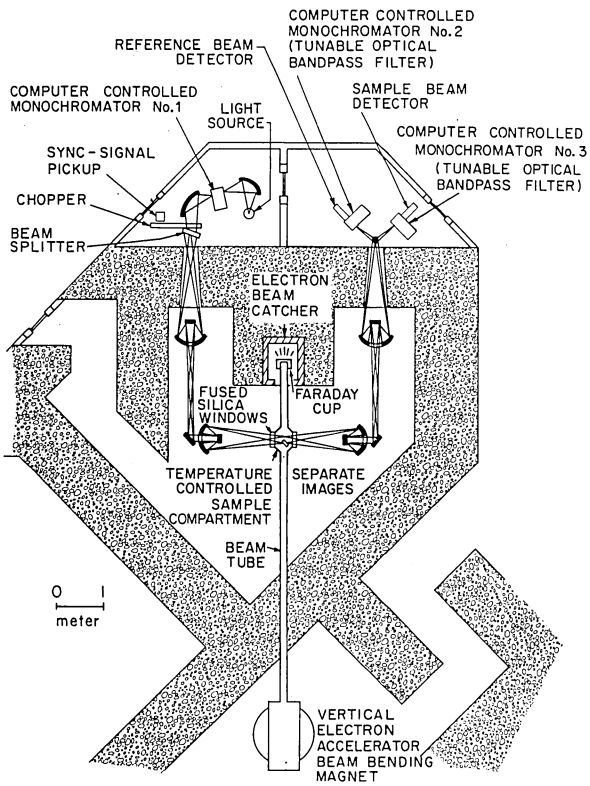

Figure 1. The experimental facility for measuring optical absorption and luminescence during and after 0.5 to 3.0 MeV electron irradiation.

*Research supported by the U.S. Energy Research and Development Administration.

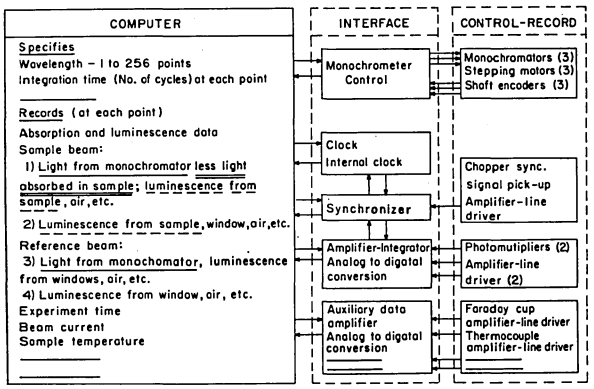

Figure 2. The control and data acquisition system for the double-beam spectrophotometer shown in Figure 1.

and to obtain engineering data on radiation effects in nonmetals two facilities have been constructed at Brookhaven National Laboratory to make optical measurements during irradiation. Inasmuch as measurements can be made during and after irradiation they are not subject to the inadequacies described above. One of these special facilities is used to study the optical properties of samples during ^{60}Co irradiation. It has provided data on the coloring of KCl[1] and NaCl[2] at room temperature, KCl at 85K,[3] the effect of strain applied during irradiation on KCl,[4] the coloring of barium alumnoborate glasses at room temperature,[5] and the coloring, radioluminescence and thermoluminescence of natural and synthetic quartz between 80 and 300K.[6] The barium alumnoborate glass study provided many results which will be described in a later section.

The other facility, which will be described briefly in the next section, is used to simultaneously measure the optical absorption and luminescence of substances during irradiation with electrons at any energy between 0.5 and 3 MeV. This equipment provides data on the absorption changes occurring after irradiation and, in addition, on any phosphorescence occurring after irradiation. Most importantly, the absorption and luminescence measurements are not restricted to a single wavelength. An entire 256 point absorption spectrum and a 256 point luminescence spectrum can be recorded every 40 seconds. At the moment, these measurements cover the range 200 to 400 nm or 400 to 800 nm. However, the range can be extended to 11 microns or more by installing suitable light sources and detectors.

A small number of radiation induced coloring studies utilizing measurements made during gamma-ray irradiation were cited above. Even fewer studies using measurements made during electron irradiation can be found in the literature. Included in these is a study of the electron bombardment induced coloring of fused silica,[7] particularly the absorption at 215 nm with the sample at various temperatures between 100 and 500 C. A survey of the radiation induced absorption and the radioluminescence of optical glasses, Al_2O_3, crystal quartz and fused silica produced by 2.5 MeV electron irradiation has been reported recently.[8] In addition, there are a number of studies on radiation effects in fibre optics that contain a large amount of information on the radiation induced coloring of glasses.[9-12] Lastly, there are previous reports on the radiation induced coloring of the NBS 710 glass described in this paper.[13-15] For convenience, information in the previous reports which is particularly pertinent for this discussion is included here. Consequently, the room temperature studies at different dose rates and the resolution of the growth and decay curves into components are described in reference 13. Additional studies describing the coloring and decay at a constant dose rate and at different temperatures will be described in this paper.

II. The Facility for Making Optical Measurements During Electron Irradiation

The equipment used to make optical measurements before, during and after electron irradiation is illustrated in Fig. 1. Electrons at any energy between 0.5 and 3.0 MeV are produced in a vertical electron accelerator. After emerging from the accelerator they are magnetically deflected 90 degrees into a horizontal tube that transmits the beam into the irradiation chamber. This tube is equipped with a variety of focusing coils, several Faraday cups, and a thin gold scatterer. The Faraday cups and scatterer can be inserted or removed from the beam at will. The thin gold scatterer insures that the sample is uniformly irradiated. The beam parameters can be adjusted with the sample in place but not exposed to radiation. When desired, the irradiation is initiated, or terminated, by a fast acting cup which can be moved in or out of the beam within 0.5 seconds. During irradiation the beam traversing the sample is monitored by a Faraday cup located downstream from the sample. The incident electron energy is always adjusted to insure that the particles pass through the sample. With the arrangement described above it is possible to obtain reproducible irradiations at known beam currents and avoid all of the difficulties associated with "turning-on" the accelerator.

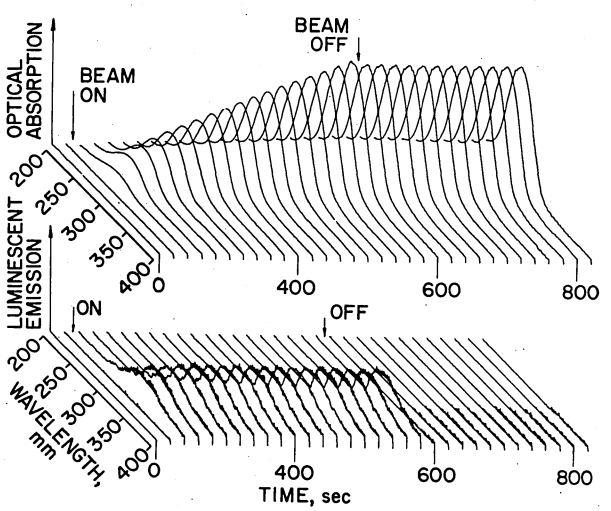

Figure 3. F-center growth and radioluminescence from single crystal LiF during irradiation. After irradiation this sample did not exhibit detectable phosphorescence and the radiation induced coloring changed very little.

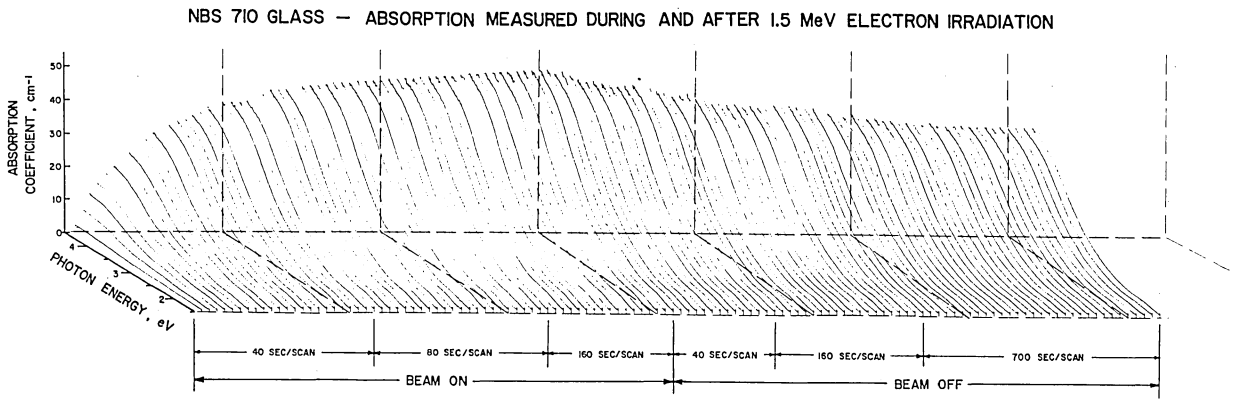

Figure 4. A "3-D" plot of the absorption induced in NBS 710 glass by 1.5-MeV electron irradiation and the decay of the absorption after the irradiation has been terminated. Spectra were recorded at 40 second or longer intervals. Every other spectrum has been omitted.

The simultaneous optical absorption and luminescence measurements are made with the computer controlled double-beam spectrophotometer shown in Fig. 1. Monochromator No. 1 provides a monochromatic beam for absorption measurements. The beam is chopped, split into sample and reference beams, and focused by the optical system into sample and reference images in the target chamber. Both beams are subjected to equal changes in window absorption and luminescence, air glow and any other perturbations occurring during and after irradiation.

After passing through the target area the beams are focused on monochromators Nos. 2 and 3. Monochromator No. 2 serves both as a tunable optical bandpass filter for absorption measurements and as an analyzing monochromater for luminescence spectrum measurements. When operating in the bandpass mode the monochromators prevent all luminescence from reaching the phototubes except that in specified wavelength regions. In the presence of luminescence from the sample this increases the signal to noise ratio for absorption measurements by orders of magnitude. Actually, for all measurements described in this paper, a bandpass monochromator, No. 2, was used only in the sample beam. The reference beam was focused directly on the photomultiplier. This arrangement is demonstrably quite adequate for the glass studies described below since they did not exhibit strong luminescence.

The monochromator is entirely computer controlled. As many as 256 preselected points may be measured during each scan. If all 256 points are recorded the scans may be repeated every 40 sec. or at longer intervals. Scans with fewer points require less time and at a single wavelength data points may be recorded at millisecond intervals. The computer specified wavelengths, time interval between scans, number of signal averaging cycles, etc. At each wavelength four measurements are made to determine the optical absorption and luminescence. They and other functions of the control and data acquisition system are outlined in Fig. 2. In the present configuration the sample to reference beam intensity ratio is determined before each irradiation measurement and often checked afterwards. Tests over long periods of time and day-to-day experience indicate that this ratio remains so stable there is not necessity to install devices to measure this ratio during measurements.

After each scan the absorption and luminescence data and other information such as sample current, beam current, etc., is transferred to magnetic tape. In turn, the recorded data is processed on a large computer. An absorption and luminescence spectrum is obtained for each scan. These spectra are fully corrected for absorption and luminescence in the target windows, air glow surrounding the irradiation chamber or attributable to exchange gas in the sample furnace, etc. It is particularly noteworthy that the luminescence spectra may be fully corrected for radiation induced self absorption in the sample. Thus one can determine unequivocally if a change in luminescence is real or is caused by self absorption.

A typical data set for a sample which exhibits strong radioluminescence is shown in Fig. 3. This plot shows both the radioluminescence and the F-center absorption exhibited by single crystal LiF during electron irradiation. Spectra are shown at 40 second intervals. After 450 seconds the electron beam was "turned-off" by interposing the rapid acting Faraday cup. During irradiation the luminescence rises rapidly to a constant value, remains at that level until the irradiation is terminated, and then drops abruptly to a negligible level. Concomitantly, the LiF F-center absorption increases monotonically and when the beam is interrupted the absorption drops negligibly or not at all. LiF is the only substance measured to date which, at room temperature, does not show large absorption changes when the irradiation is terminated.

The absorption spectra obtained from NBS 710 glass recorded during and after irradiation is shown in Fig. 4. This plot was made from separate measurements in the 200 to 400 and 400 to 800 nm regions and "joined" during computer processing. It shows both growth and coloring during irradiation and the decay occurring after the irradiation was terminated. This glass does not, for all practical purposes, exhibit luminescence during irradiation nor phosphorescence after irradiation. This data will be used to illustrate many of the radiation induced color center growth and decay kinetics illustrated in the next section.

III. The Kinetics of Radiation Induced Color Center Growth

To begin this discussion of color-center formation during irradiation and the growth or decay of centers after the irradiation, consider the process that applies to a single center, or, equivalently, a single absorption band. This may be assumed to be formed by trapping of an electron on an electron trap. However, with straightforward changes in charge (sign) the discussion applies equally well to centers formed by hole trapping. First, electron traps occur in crystals and glasses at points where the normal lattice is perturbed. This can occur at lattice sites containing substitutional impurities, at vacancies or divacancies, or where interstitial atoms occur between the atoms on normal lattice sites. These defects may, or may not, be in valence or charge states different from that associated with the normal lattice at the same point. For example, if a negative atom is missing from the lattice, to form a negative ion vacancy, the lattice will be lacking an electron, i.e. there will be a local charge unbalance. Next, if a radiation-induced ionization electron comes close enough to the negative-ion vacancy it will be trapped. In fact, an electron trapped on a negative-ion vacancy is the well-known F-center. Such centers have many of the properties of atoms and molecules and impart color to the host crystal by undergoing optional absorption transitions. Similarly, two side-by-side vacancies (a divacancy) may trap two electrons to become an M-center. Likewise a Ca^{++} ion on a normal Na^{+} lattice site has a high probability of being an electron trap since local charge neutrality may be established by trapping a charge of this sign. A very large number of different kinds of defects can be electron traps. Even neutral substitutional atoms such as a K^{+} ion on a Na^{+}, site may be traps. In certain crystals, at low temperatures, charges may be "self-trapped" on normal lattice sites. An example is the self-trapped hole which forms V_k centers in alkali halides. However, for this discussion it is necessary to consider only the more common defect and impurity related traps.

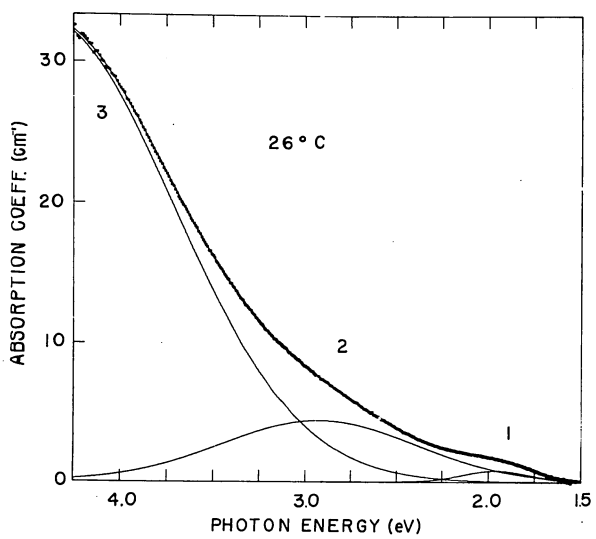

Figure 5. A typical radiation induced absorption spectrum for NBS 710 glass. The spectrum has been resolved into three Gaussian shaped bands.

Each type of trap undergoes a number of different radiation related processes. The important processes will be described below, in turn. Let N_o be the concentration of traps prior to any irradiation. Typical values of N_o are in the 10^{14} to $10^{18}/cm^3$ ranges. Consider first the processes that occur during irradiation. Let ϕ be the dose rate. It can be expressed in any unit but it is convenient to think of it in terms of ion pairs per unit time created by the incident radiation. Then if N(t) is the concentration of color centers which have already been formed by irradiation at time t, the concentration of uncolored centers or empty traps is (N_o-N). The probability that these empty traps are converted to centers at time t is proportional to the product of (N_o-N) and the ionization electron concentration ϕ or $f\phi(N_o-N)$ where $f\phi$ is simply the fraction of uncolored centers converted to centers per unit time.

Up to this point it has been assumed that the number of traps is fixed, a contention that is most appropriate for impurity related traps. However, in many cases defect related traps may be introduced during irradiation. In this case the concentration of traps, both filled and unfilled, could be a complicated function of irradiation time. In fact, the numerous different color center vs. dose, or growth, curves obtained for the barium alumnoborate glasses, described in reference 5, can all be "explained" by different trap vs. dose curves. Only the simples possible curve will be considered here. That is, it will be assumed that the trap concentration can be described by the equation $P = N_o + k\phi t$ where P is the total number of traps at time t. This is equivalent to assuming that the trap concentration initially has the value N_o and increases linearly with irradiation time or dose. In this situation the rate of color-center formation is given by $f\phi(N_o + k\phi T - N)$.

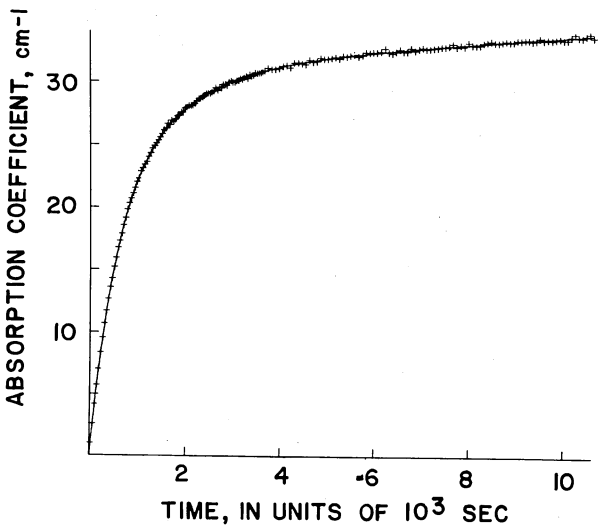

Figure 6. Growth curve of the absorption at 4.0 eV vs. irradiation time in NBS 710 glass. The dose rate was 2.2 Mrad/h. The solid line through the data points was computed from the equations in the text and contains two saturating exponential and one linear components.

In addition to color-center formation by charge trapping there are two important processes that reduce the rate of color-center formation during irradiation. The first of these is electron-hole recombination. The probability that a trapped electron will encounter a mobile ionization produced hole is proportional to the product of the trapped electron concentration, N, and the mobile or free hole concentration. The latter is proportional to the dose rate; more specifically it is $\phi\tau_h$, where τ_h is the hole lifetime. Thus, at any time t, when the trapped electron concentration is N, the probability of recombination is given by ϕrN. The quantity r includes τ_h and other factors such as the cross-section for recombination.

The other important process which tends to reduce the trapped electron concentration is thermal untrapping. This is well known and is usually called an Arrhenius-type process. The probability that a trapped charge can escape from the trap by thermal motion is proportional to $s \exp(-E/kT)$ where s is the "attempt-to-escape" frequency, E is the activation energy for untrapping, and k and T have the usual meaning. Thus if at time t there are N trapped charges the number escaping per unit time is just uN where $u = s \exp(-E/kT)$.

So far only thermal untrapping from the color centers thermselves has been described. The information available now indicates that more than one process may contribute to the observed decay of a given center. For example, part (one component of) of the decay can be attributed to untrapping from the center and other parts (components) to electron-hole recombination with holes thermally released by hole traps. Also, as discussed in detail below, it would appear that the color center decay processes may be more complicated than the simple Arrhenius process.

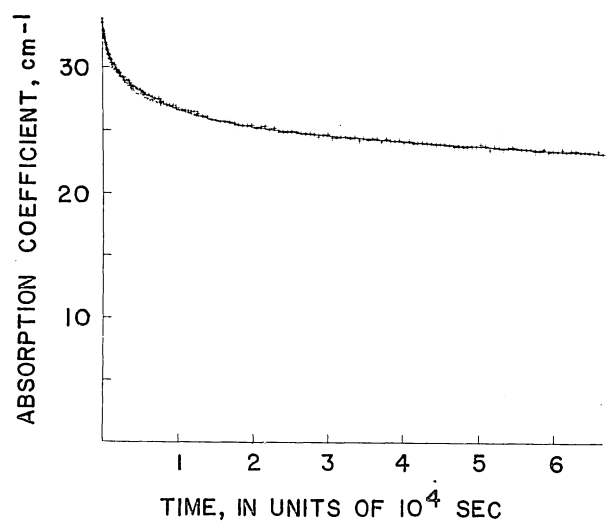

Figure 7. Decay of the absorption at 4.0 eV in the NBS 710 glass after irradiation. The solid line through the data points was computed from the equations in the text and contains three exponential components.

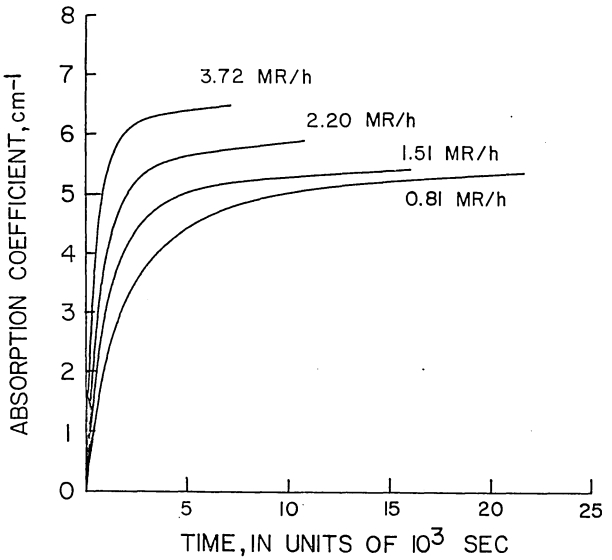

Figure 8. Growth of the radiation induced coloring at 2.6 eV in NBS 710 glass at different dose rates.

The simplest equation which might be expected to realistically describe the growth of color centers during and after irradiation can be obtained by combining the coloring, recombination and untrapping processes described above. Namely,

$$\frac{dN}{dt} = f\phi(N_o + k\phi - N) - r\phi N - uN \quad . \qquad (1)$$

If the sample is uncolored when the irradiation is started, i.e. if N=0 at t=0, the solution of this is

$$N = \frac{f\phi}{\phi(f+r)+u}\left[\left(N_o - \frac{k\phi}{\phi(f+r)+u}\right)\left(1-e^{-[(f+r)\phi+u]t}\right) + k\phi t\right]$$

This can be written

$$N = A_i(1-e^{-a_i t}) + \alpha_L t \qquad (2)$$

where

$$A_i = \frac{f}{f+r+u/\phi}\left[N_o - \frac{k}{f+r+u/\phi}\right] \qquad (3)$$

$$a_i = (f+r)\phi+u \qquad (4)$$

$$\alpha_L = \frac{fk\phi^2}{(f+r)\phi+u} \qquad (5)$$

This simple treatment predicts that the growth curve will, in general, contain a linear and saturating exponential component. Also, it predicts that the constants in the growth curve have explicit dependencies on the dose rate. For example equation (5) indicates that the exponential constant a_i is a linear function of the dose rate with a non-zero intercept if $u \neq 0$. This accurately describes the growth of F-centers in KCl at 85K[3] and the coloring of one preparation

of barium alumnoborate glass.[5] However, coloring curves obtained from a large fraction of the substances studied to date contain 2, 3, or occasionally 4, saturating components. There are a large number of different ways of extending the treatment given above to include more than one saturating exponential component. These range from simple ones, e.g. there could be two types of percursors for a given center; or complicated situations which cannot be described mathematically other than by coupled differential equations.[5,16,17] In any case, it appears that appreciable physical insight about the radiation induced coloring process can be obtained by analyzing data in terms of the (admittedly) simple treatment described above.

IV. The Decay of Color Centers After Irradiation

As mentioned above, there are very few substances that do not show color-center decay after being irradiated at room temperature. In fact, the only example in this category that we can cite is the F-center coloring of LiF. In terms of the model developed above the decay behavior should be particularly simple, namely, if D_0 color centers are present at the termination of irradiation the concentration D at a later time t is $D=D_0\exp(-ut)$. Obviously, a plot of ln D vs. t should be linear.

Most importantly, $u=s\exp(-E/kT)$ and a plot of ln u vs. 1/T is the well-known Arrhenius plot from which one obtains the activation energy E from the slope and a quantity proportional to s from the intercept. Decay data at different well-controlled temperatures is needed to determine an accurate value of E.

The currently available data, most of which is confined to room temperature, indicates that the radiation induced color centers do decay exponentially at room temperature. However, with few exceptions, the observed decay consists of two or more components. One class of explanations for multiple components is discussed in ref. 5. Here it is sufficient to point out that a center

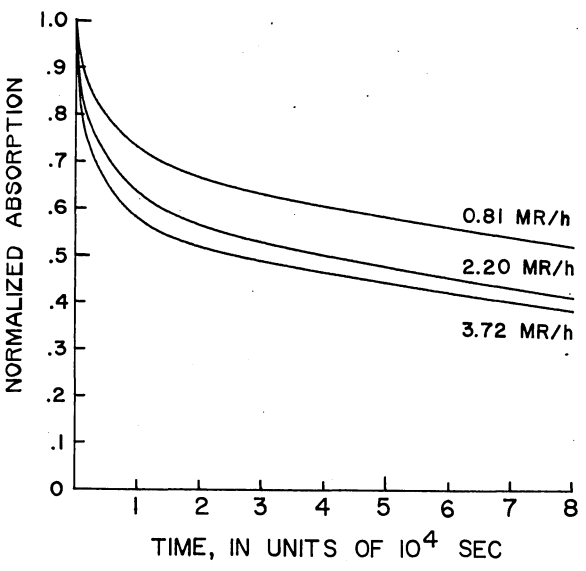

Figure 9. Decay of the absorption in NBS 710 glass after the samples were colored at different dose rates.

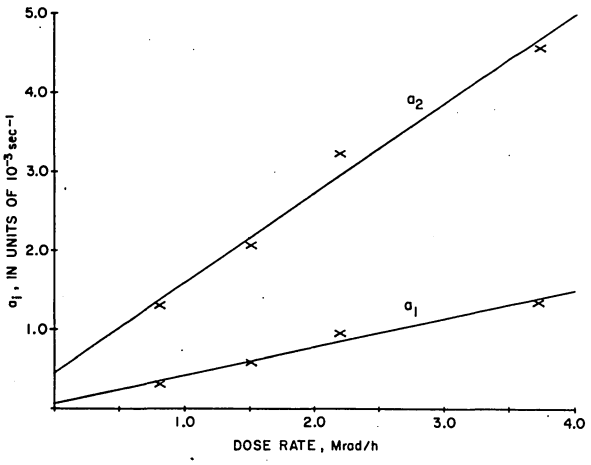

Figure 10. The exponential growth constant a_1, obtained from the data shown in Fig. 8. The growth kinetics described in the text predicts that this quantity will be a linear function of dose rate.

may decay by thermal untrapping of the trapped charge and by recombination with opposite sign trapped charges released by other traps. In this way any number of decay components may occur.

There is very little, if any, data available to determine if the temperature dependence predicted by this model is obeyed. One of the prime objectives of the study described in this paper is to determine if this model applies to radiation induced color centers in glass. As will be shown, it apparently does not.

V. Radiation Induced Color Center Formation in NBS 710 Glass

Many of the initial measurements on this glass, made with the equipment described above, are given in reference 15. A number of these will be described here, but only those that are necessary to provide reasonable understanding.

Experimental Details: All measurements described below were made on NBS 710 glass which consists of 70.5% SiO_2, 8.7% Na_2O, 7.7% K_2O, and 11.6% CaO. Samples were roughly 1 by 2 cm and 1 mm thick. The largest surfaces were polished and accurately parallel. The electron beam energy was 1.5 MeV which is more than sufficient to insure that the incident particles pass entirely through the sample. This is necessary to prevent charge buildup in the glass. The samples were irradiated in either the "room-temperature" irradiator or in a stainless steel furnace. The latter consists of a solid stainless block with two fused silica optical windows and two thin "havar" windows to transmit the electron beam into the furnace, through the sample and into a Faraday cup. Electrical heaters are contained in the block. The sample contains helium at a pressure sufficient to insure that the sample remains at the furnace temperature. Measurements indicate that the glass temperature is known to about one degree and a worst case calculation indicates that during irradiation the maximum uncertainty is 3, or at most 4, degrees. The furnace is electronically controlled and remains within 0.1C of the indicated temperature.

Optical measurements were made before, during and after irradiation. Usually, one measurement is made, at a given temperature and beam current, in the 200 to 400 nm range and another in the 400 to 800 nm range. During processing the data is "joined" to produce numerous absorption spectra such as is illustrated in Fig. 4.

The dose imparted to the sample, i.e. the dose rate, is computed from the measured beam current, the sample thickness, and published dE/dx tables. In the 1 to 3-MeV range dE/dx is almost independent of E which means that energy degradation in the gold scatterer, havar windows, etc. does not introduce uncertainties. At the moment the absolute dose rates given below may be in error by as much as 40 or 50 percent. However, the error in the relative dose rates is only a few percent.

Absorption Spectra: An absorption spectra recorded at room temperature is shown in Fig. 5. Also, this figure shows the resolution of the spectrum into Gaussian shaped absorption bands. Although it is not illustrated, all spectra recorded at higher temperatures can be resolved into the same set of bands. This is also true for spectra recorded after the irradiation is terminated.

Growth and Decay at Room Temperature and Different Dose Rates: Absorption spectra were recorded at room temperature and at dose rates ranging from 0.81 to 3.72 Mrad/h. In every case the decay was also studied. A typical growth curve is shown in Fig. 6. This and all other growth curves are accurately represented by the equation

$$\alpha(t) = \sum_{i=1}^{2} A_i(1-\exp(-a_i t)) + \alpha_L t \quad . \qquad (6)$$

The solid line through the data points (most easily seen in the 0 to 10^3 sec region) was computed from equation (6) after the constants had been determined with a computerized best fit procedure. More explicitly, the growth curves are very accurately described by equation (6).

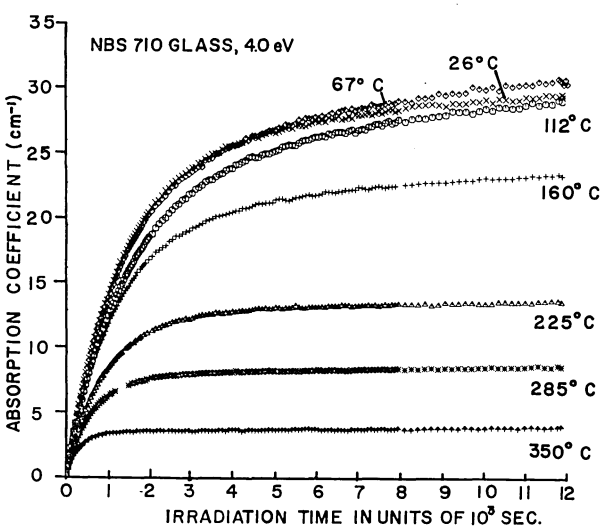

Figure 11. The growth of the absorption at 4.0 eV in NBS 710 glass at different temperatures and at a constant dose rate of approx. 1 Mrad/hour.

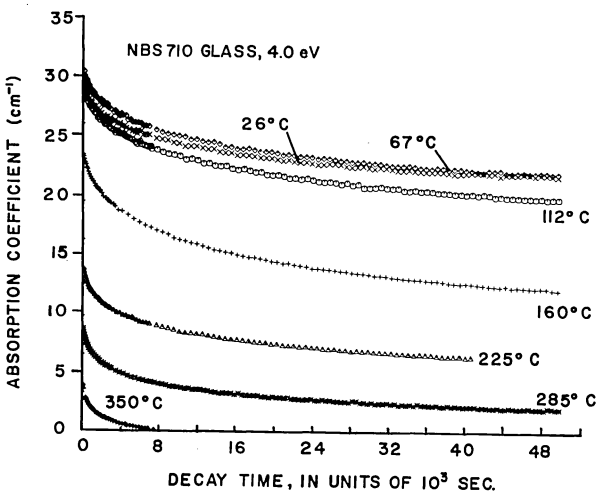

Figure 12. The decay, following irradiation, of the absorption at 4.0 eV for each of the growth curves shown in Fig. 11.

A typical decay curve, obtained after the data used for Fig. 6 had been recorded, is shown in Fig. 7. Although it is hard to discern, this figure contains a curve through the data points computed from the equation

$$\alpha(t) = \sum_{i=1}^{3} D_i \exp(-d_i t') \quad . \qquad (7)$$

where t' is the time after the irradiation is terminated and the constants were obtained by a best-fit procedure. In other words, the decay occurring after irradiation is very accurately represented by the sum of three exponential components.

Growth curves obtained at four different dose rates are shown in Fig. 8. Three of the corresponding decay curves are contained in Fig. 9. After these curves have been fitted to equations (6) or (7), data is available to evaluate some of the predictions obtained from the "simple kinetic treatment" described above. For example, equation (4) predicts that the exponential constants, the a_i, should be linear functions of the dose rate. That this is observed is shown by Fig. 10. From such results one concludes that the simple kinetic treatment adequately describes the coloring of NBS 710 glass at room temperature.

Growth and Decay at a Constant Dose Rate and at Different Temperature: The growth of the radiative induced coloring of the NBS 710 glass at different temperatures and at a fixed dose rate of approx. 1 Mrad/hour is shown in Fig. 11. It is apparent that there are two marked dependencies on temperature. First, as the temperature increases the steady-state or equilibrium level of the coloring decreases. However, in contrast, the rate of approach to the equilibrium level increases with increasing temperature. Also, in the temperature, dose rate and irradiation time regimes covered by this data there are not any indications that the coloring curves contain a maximum. In other words, the curves do not increase to a maximum and then decrease as the irradiation continues. A detailed analysis of the growth characteristics will be published elsewhere.

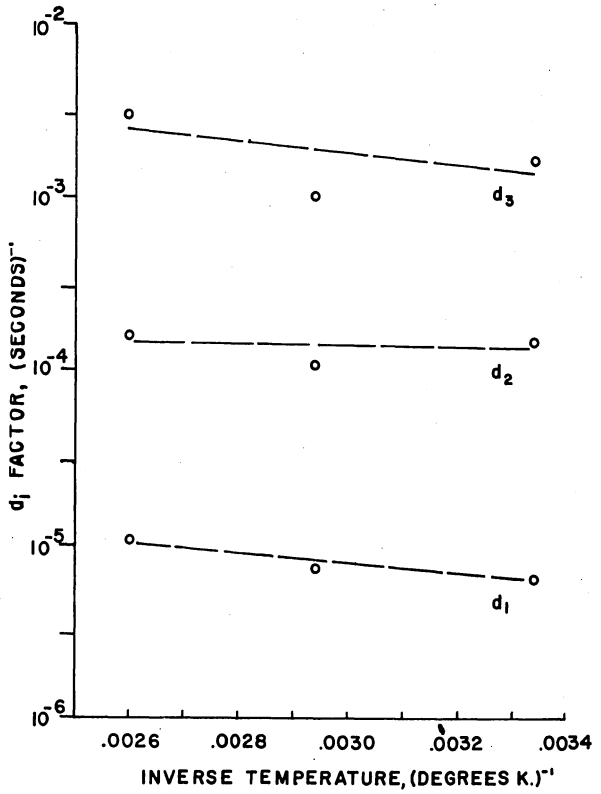

Figure 13. An Arrhenius plot computed from decay data, for the NBS 710 glass, such as is shown in Fig. 12. The activation energies obtained from this plot are much too small to attribute the temperature dependence shown in Fig. 12 to simple Arrhenius kinetics.

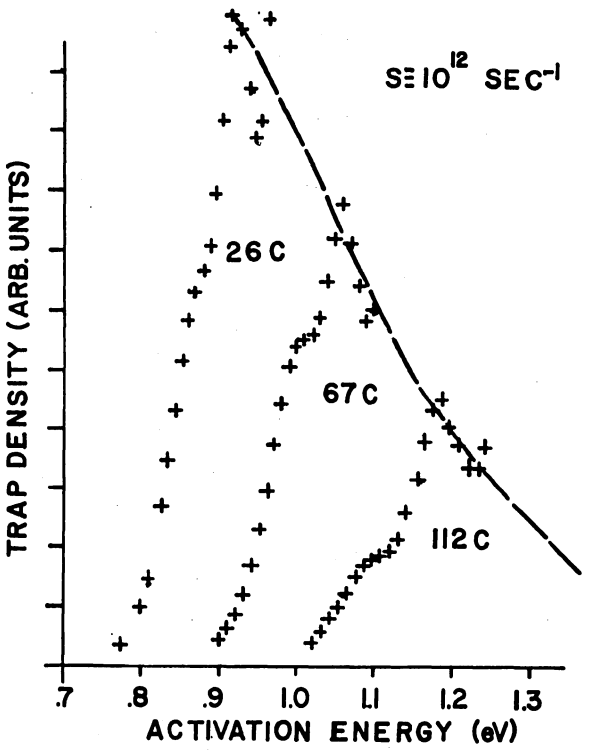

Figure 14. Part of a trap density vs. activation energy distribution curve obtained by applying the Primak-Holmes analysis to decay data such as is shown in Fig. 11. This plot supports the contention that the observed dependence of the decay data on temperature can be attributed to a distribution of thermal untrapping energies.

The decay of the coloring after irradiation, recorded with the samples maintained at the irradiation temperature, is shown in Fig. 12. Although not illustrated by plots, all of these curves can be accurately resolved into exponential decay components. This is in accord with the room temperature measurements and the kinetic theory described above. An Arrhenius plot constructed from the decay data is shown in Fig. 13. This plot is not in accord with the kinetic theory in two respects. First, the points are not linear and, second, when it is assumed that the data can be approximated by straight lines the activation energies obtained are appreciably too low to account for the observed decay at the different temperatures. Thus one must conclude that the decay is not attributable to a simple Arrhenius process. More specifically, one must conclude that the decay cannot be described by the $u = s \exp(-E/kT)$ equation.

Distribution of Activation Energies: There are a number of physical processes which could account for the color-center decay measurements made after irradiations at different temperature. These include tunneling, combinations of tunneling and Arrhenius processes, temperature assisted tunneling, recombination of so-called geminate pairs, and processes involving distributions of activation energies. This last mentioned situation arises when the thermal untrapping process is characterized by a distribution of activation energies, not by a single energy.[8,17]

In probability terms, the usual single valued activation energy is characterized by a delta-function distribution whereas the non-single-valued case is characterized by a probability distribution in E space. A good example is a Gaussian distribution specifying the density of traps with activation Energy E. In this case, traps characterized by the entire distribution of activation energies are filled when the sample is irradiated at low temperature. At an intermediate temperature the shallow or low activation energy traps are emptied as soon as they trap charges. Finally, if a sample is irradiated at a very high temperature all traps are unstable and no trapped charges are retained.

Because of the random nature of glass lattices it is likely that they will exhibit distributions of activation energies and other parameters. For example, a given defect in crystal quartz will have the same local surroundings wherever it occurs. In contrast, in fused silica the same defect will be subjected to local surroundings which vary from point to point. Thus the thermal untrapping energy, E, will be the same for each trap in crystal quartz. However, in glassy quartz the energy will be spread out in a distribution. The larger the local fluctuations the wider the distribution.

A method for determining distributions of thermal untrapping energies has been worked out by both Primak[18] and Holmes.[19] The details are too lengthy to reproduce here and can be obtained from the original references. However, the data shown in Fig. 12 is quite suitable for this purpose. Figure 14 shows the distribution obtained when the method is applied to the 26, 67, and 112C curves and it is assumed that $s = 10^{12}$. At such temperatures, the structure in the data to the left of the peak could represent the actual distribution, or it might be the result of approximations included in the analysis, or a combination of these. The curve to the right of the peak should be indicative of the distribution in the energy region that is unstable at the indicated temperature. The extension of each data set to higher activation energies requires decay data for impractically long times. In any case, the data is sufficient to indicate that the observed dependence on temperature, i.e. data in Figs. 11 and 12, can be explained by assuming that the activation energy for thermal untrapping is not single-valued but can be described as a distribution of trapping levels and a range of activation energies. Perhaps it need not be stated explicitly, but this conclusion does not rule out the possibility that this data represents still another process; it indicates that the observed dependencies are compatible with the assumption that the activation energies are described by a distribution.

VI. Summary

Using recently completed equipment for making optical absorption during electron irradiation, the radiation induced coloring of NBS 710 glass has been studied at room temperature at various dose rates, and at different temperatures using a fixed dose rate. At room temperature, the coloring curves recorded during irradiation and the decay of the coloring after irradiation are in accord with a simple kinetic theory based on three postulates: 1) the color-centers are formed by charge trapping on defects that exist in the sample before irradiation and increase linearly during irradiation, 2) the color-center concentrations are diminished during irradiation by electron hole-recombination and by thermal untrapping, and 3) the decay occurring after irradiation results from thermal decay. The measurements made at temperatures between room temperature and 400C indicate that the coloring during irradiation is in agreement with the simple kinetic theory but the decrease occurring after irradiation is not in accord with the postulated Arrhenius type thermal decay. These are a number of different physical processes that could account for this discrepancy. The data obtained to date indicates that the observed decay is consistent with the assumption that there is a distribution of activation energies for thermal untrapping from the observed color-centers, in contrast to the single-valued energy usually observed.

This data, as well as measurements made on alkali halides,[1-4] indicates that studies on irradiation induced coloring are best made by making measurements during irradiation. In fact, it would appear that this is the only reliable way to determine if materials to be used during irradiation will maintain the required characteristics.

References

1. P. W. Levy, P. L. Mattern and K. Lengweiler. Phys. Rev. Letters 24, 13 (1970).
2. P. L. Mattern, K. Lengweiler and P. W. Levy. Solid State Comm. 9, 935 (1971).
3. K. Lengweiler, P. L. Mattern and P. W. Levy. Phys. Rev. Letters 26, 1375 (1971).
4. P. W. Levy, P. L. Mattern, K. Lengweiler and M. Goldberg. Solid State Comm. 9, 1907 (1971).
5. P. W. Levy, P. L. Mattern, K. Lengweiler and A. M. Bishay. J. Am. Ceramic Soc. 57, 176 (1974).
6. P. L. Mattern, K. Lengweiler and P. W. Levy. Radiation Effects 26, 237 (1975).
7. G. E. Palma and R. M. Gagosz. J. Phys. Chem. Solids 33, 177 (1972).
8. M. J. Treadaway, B. C. Passenheim and B. D. Kitterer. IEEE Trans. on Nuclear Science NS-22, 2253 (1975).
9. G. H. Sigel, Jr., B. D. Evans, R. J. Gintner, E. J. Friebele, D. L. Griscom and J. Babiskin. Naval Research Laboratory Report 2934 (1974).
10. B. D. Evans and G. H. Sigel, Jr. IEEE Trans. on Nuclear Science NS-21, 113 (1974); NS-22 2462 (1975).
11. P. L. Mattern, L. M. Watkins, C. D. Skoog, J. R. Brandon and E. H. Barsis. IEEE Trans. on Nuclear Science NS-21, 81 (1974).
12. P. L. Mattern, L. M. Watkins, C. D. Skoog and E. H. Barsis. IEEE Trans on Nuclear Science NS-22, 2462 (1975).
13. K. J. Swyler, W. H. Hardy, II, and P. W. Levy. Bull. Am. Phys. Soc. 20, 431 (1975).
14. K. J. Swyler and P. W. Levy. Bull. Am. Phys. Soc. 21, 345 (1976).
15. K. J. Swyler, W. H. Hardy, II, and P. W. Levy. IEEE Trans. on Nuclear Science NS-22, 2256 (1975).
16. P. W. Levy. J. Am. Ceramic Soc. 43, 389 (1960).
17. J. H. Mackey, H. L. Smith and J. Nahum. J. Phys. Chem. Solids 27, 1773 (1966).
18. W. Primak. Phys. Rev. 100, 1677 (1955).
19. D. K. Holmes. Proc. of the 1960 Prague Symp. on Chem. Effects of Nuclear Transformations, IAEA, Vienna, 499 (1961).

DISCUSSION

J. BLUE: In your basic assumption that the optical effects are only due to trapped electrons, is it possible there that the conduction electron density gets high enough that there is an interaction between the light and electrons in the conduction band?

P. W. LEVY: At some level the effects that I have been talking about will perhaps be low, and then be comparable to such things as the conduction band, or rather the free-carrier absorption in these materials. Under the very high dose rates that are applicable to this discussion, there is a possibility that there is a free atom contribution to the absorption. The data to confirm that is not available. I have said everything in terms of electrons. You can apply this same idea for whole color centers and mixtures.

HEAT TRANSFER EVALUATION IN A PLASMA CORE REACTOR

Donald E. Smith, Timothy M. Smith and
Maria L. Stoenescu
Plasma Physics Laboratory, Princeton University
Princeton, New Jersey 08540

Abstract

Numerical evaluations of heat transfer in a fissioning uranium plasma core reactor cavity, operating with seeded hydrogen propellant, have been performed. A two-dimensional analysis is based on an assumed flow pattern and cavity wall heat exchange rate. Various iterative schemes were required by the nature of the radiative field and by the solid seed vaporization. Approximate formulations of the radiative heat flux are generally used, due to the complexity of the solution of a rigorously formulated problem. The present work analyzes the sensitivity of the results with respect to approximations of the radiative field, geometry, seed vaporization coefficients and flow pattern. The results present temperature, heat flux, density and optical depth distributions in the reactor cavity, acceptable simplifying assumptions, and iterative schemes. The present calculations, performed in cartesian and spherical coordinates, are applicable to any most general heat transfer problem.

Problem Definition

The complexity of rigorous calculations for a general heat transfer analysis in highly radiative media makes the use of approximate formulations particularly attractive. The most appropriate compromise between simplicity and accuracy has to be determined finally by the purpose of the evaluations.

The energy conservation for a unit volume of a one-component gas in steady state is given by Equation (1). The solution of this equation for the spatial distribution of the enthalpy requires additional information on the flow, the shear stress tensor and on conductive and radiative heat fluxes.

Both for the implications it has on the computational procedures and for the self-consistency of equation (1) it is important to know whether the heat fluxes are completely described by the parameter temperature.

Three cases are differentiated on Table 1 for the correlation between the radiative heat flux and the temperature: One, in which the radiative heat flux in a given point depends on the local temperature, valid, as seen further, for a gas in local thermodynamic equilibrium (LTE), grey and optically thick; the second, in which the radiative heat flux depends on the temperatures of all the regions in the gas, valid for LTE, and the third, in which the radiative heat flux cannot be described by the temperature, and data on bound electron and atomic velocity distribution functions is necessary.

Various expressions of the radiative heat flux are shown in relations (2) - (8). The general expression of the radiative heat flux is presented in relations (2) - (2b) and is illustrated in Figure 1. The radiative heat flux calculation requires the knowledge of all local emission absorption and scattering coefficients, and integration over directions, at each point in space, for every frequency interval. The spectral source function, including the scattering source is represented in relation (2c), and may depend on temperature for LTE or on atomic distribution functions for non-equilibrium (NE). The magnitude of the radiative intensity resulting from relation (2) may differ considerably from an equilibrium black body intensity at the local temperature. If the medium would have uniform temperature, including the boundaries, the calculated intensity would be equal to the source function of the nearest element, therefore equal to the black body intensity. For a nonuniform temperature medium, the radiative heat flux is different from zero and contains, in LTE, information on temperatures of various regions of the gas.

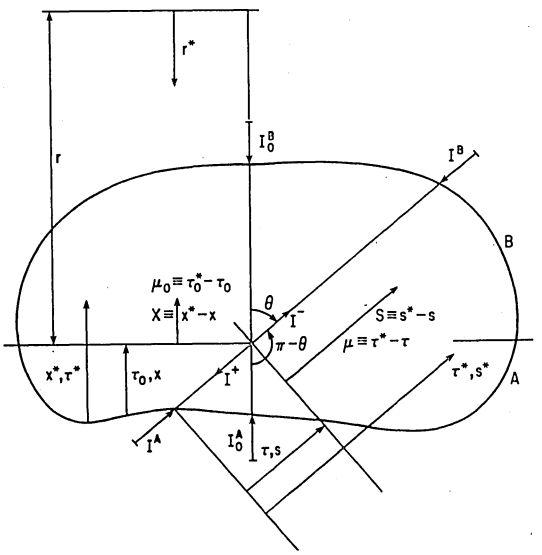

Fig. 1. Variables in radiative heat transfer equations.

Relation (3) is a contracted form of relation (2), valid for cases in which the source function, absorption coefficient, and boundary value of the spectral intensity have a planar symmetry (thus the surfaces A and B are parallel planes), and the scattering part of the source function is negligible. (An equivalent of relation (3) for a spherically symmetric spatial distribution is described in a future publication).

For LTE conditions, the source functions in relation (3) depend exclusively upon the local temperature, as expressed in relation (4), or in relation (5) which represents the analogue of relation (4) for the total radiative flux, if the

absorption coefficient is independent of frequency ("grey gas").

Further simplifications of relation (5) may be obtained for specific distributions of the properties of the medium. Relation (6) is valid for slowly varying T^4 with respect to the optical depth; relation (7) is a variant of relation (6) for large optical depth between the point at which the heat flux is calculated and one of the boundaries; and relation (8), known as the "diffusion approximation", represents a similar variant for large optical depth throughout the medium.

The conductive heat flux for quasi-equilibrium situations and in the absence of diffusion currents, is represented in relation (9) and is therefore a function of the local temperature and pressure.

It results that for a system in LTE, equation (1), completed with the appropriate relation from (2) - (8) for the radiative heat flux, and with relation (9) for conductive heat flux, and with assumptions concerning the flow pattern and shear stress tensor, constitutes an apparently self-consistent nonlinear, second order differential equation for the unknown temperature. (Complete self-consistency would exist for a flow pattern independent of temperature.) For a system in NE additional equations or experimental data are needed for the optical coefficients.

In the present study the shear-stress tensor is considered negligible, and variant (10) of the energy conservation equation is solved numerically in two dimensions, in polar and cartesian coordinates, for a nuclear gas core reactor cavity. Equation (11) represents the expansion of equation (10) in spherical coordinates. As the heat transfer in the present reactor concept is mostly radial, part of the results are given for a one-dimensional solution of equation (11), along the radius, for assumed non-radial transfer.

Computational Procedure

Three separate procedures have been developed to integrate equation (10) and therefore determine the energy distribution and transfer in a Gas Core Nuclear Reactor.

The first procedure is a radial one-dimensional solution of equation (11) completed with any of the expressions (6), (7) or (8) for the radiative heat flux and with (9) for the conductive heat flux. Assumptions are made for the distribution of the polar temperature gradient and, consistent with the mass continuity equation, for the distribution of mass flow rate. Equation (11) is integrated numerically propagating solutions for temperature and heat flux from the cavity wall to the cavity center, for guessed boundary values of the temperature and heat flux at the wall. Due to the nature of relations (7) and (8) which determine the heat fluxes at given radius as function of temperature and mass flow rate values at larger radii previously considered in the computation (the velocity profile is necessary to determine the stage in the seed vaporization process which contributes to the local opacity), the solution is completely determined by the boundary and does not require iterations on temperature profiles. The requirement of zero flux at the cavity center is set to determine iteratively either the pressure or the fuel radius. If relation (6) is used for the radiative heat flux instead of (7) or (8), the solution propagation from wall to center becomes iterative on the temperature profile itself which greatly complicates the procedure indicated on Table 2 but only slightly alters the solution. For this reason all results shown for the one-dimensional radial analysis are based on expression (7) for the radiative heat flux.

The second procedure is similar to the first, but here the radiative heat flux is calculated directly from relation (2) through a numerical integration of the radiative intensities. Iterations on entire temperature profiles are involved. The convergence has been tested on a trial case, however only results from the first iteration are presented here.

The third procedure is developed to model the two-dimensional behavior of the physical parameters in the propellant region. The method consists of an iterative search for a consistent two-dimensional temperature profile. The iteration proceeds by improving the values of certain functions and their derivatives with respect to the non-radial direction. The method employs a two-dimensional version of equation 7, 9 and 10, and has proven to be rapidly convergent.

Description of Results

Figures 2, 3, and 4 show cavity profiles for variations in propellant mass flow rate, cavity pressure, and seed vaporization rate, respectively. In each of these figures, the solid-line profile represents a result for a nominal case, characterized by the following parameters:

$T_\omega = 600°K$	Cavity wall temperature
$q_\omega = 1.72 \times 10^8$ erg/cm^2-s	Total heat flux incident on cavity wall
$p = 200$ atm	Cavity pressure
$R_c = 30$ cm	Cavity radius
$M_p = 0.25$	Propellant seed mass fraction
$F_p = 46$ g./s.	Propellant mass flow rate
$M_f = 0.68$	Uranium fuel pressure fraction
$R_{sv} = 1.0$	Normalized seed vaporization rate
$\Psi^{th}_n = 1.6 \times 10^{14}$ neutron/cm^2·s	Thermal neutron flux at the fuel edge

Values of these parameters for each figure (2) - (4) are nominal unless otherwise indicated. In each case treated, the fuel radius is adjusted so that boundary conditions are satisfied.

In Firure 5, the total heat flux for the nominal conditions is shown together with its radiative and conductive components.

Figure 6a shows, for the propellant region, the nominal radiative heat flux, which was calculated using relation (7), and also the radiative

heat flux found by a numerical integration of radiative intensities using relations (2) and (2b) and the nominal temperature and absorption coefficient profiles. Equilibrium values were taken for emission coefficients. Relation (7) predicts significantly larger values than those predicted by (2) and (2b) in the optically thin region of the propellant. Figure 6b makes the same comparison in the fuel region as does Figure 6a in the propellant region, except that, due to large values of absorption coefficient in the fuel, far greater accuracy was required for the numerical integration of intensities. The nominal radiative heat flux (relation (7)) has the smallest values in Figure 6b; successive degrees of accuracy in integration of intensities (relations (2), (2b)) produce successive profiles which approach the nominal profile from above.

Conclusions

The computational procedures developed have the capability of analyzing a general heat transfer problem in one or two spatial dimensions. They are able to take into consideration data on LTE or non-equilibrium optical coefficients, optical properties of the boundaries and data on vaporization kinetics of solid particle additives. The results provide information on energy transfer and distribution in a Plasma Core Fissioning Reactor for given boundary conditions and negligible shear-stress tensor, and constitute a partial analysis of a coupled heat-transfer $\longleftrightarrow$ fluid-dynamic study.

The heat transfer analysis is performed rigorously, though the presented results are based on local thermodynamic equilibrium emission coefficients. The diffusion approximation of the heat flux was proven inappropriate to describe the propellant region, particularly the transparent domain containing vaporized seed.

The conductive heat flux is treated assuming negligible diffusion of various componets at the uranium-plasma-propellant interface and negligible turbulent mixing, as if an ideal perfectly flexible and transparent wall would separate the two media. Both assumptions are clearly unrealistic. Though the radiative heat flux dominates the heat transfer, and is independent of the type of flow for similar mass distributions, the conductive and radiative heat fluxes have the same order of magnitude in regions of high temperature gradients, and errors in the conductive heat flux evaluation influence the overall results.

An effort continuation in the study of heat transfer and fluid dynamics of highly radiative gases is estimated necessary, before reliable predictions of advanced concepts performance could be made.

Acknowledgement

To Stanley Chow, who compiled information on physical properties of the propellant and fuel, and performed initial computations in propellant heat transfer.

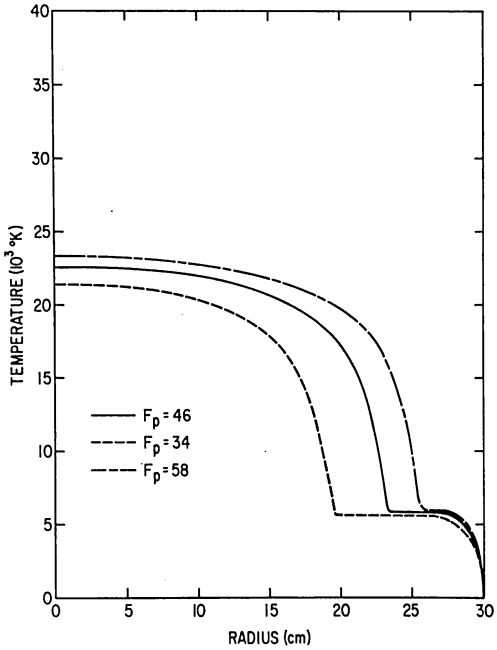

Fig. 2a. Variation of Temperature with Propellant Mass Flow Rate.

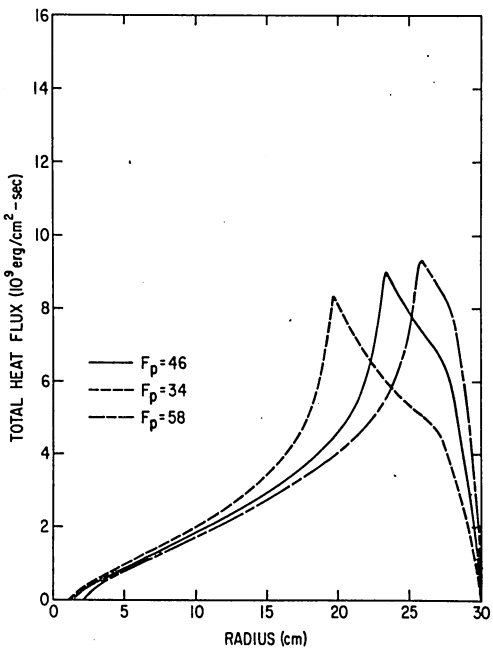

Fig. 2b. Variation of Total Heat Flux with Propellant Mass Flow Rate.

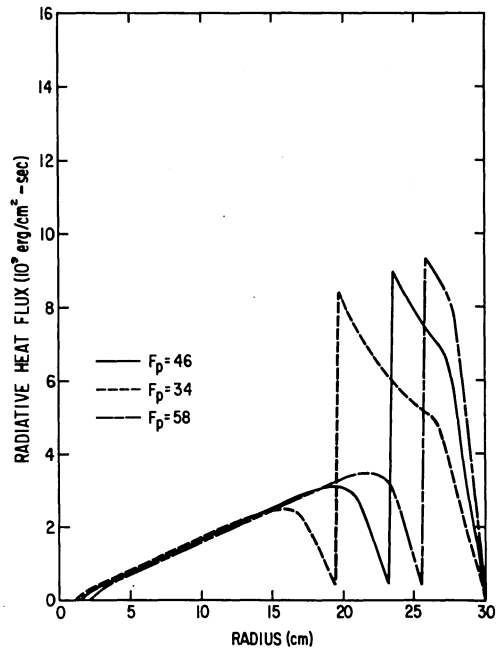

Fig. 2c. Variation of Radiative Heat Flux with Propellant Mass Flow Rate

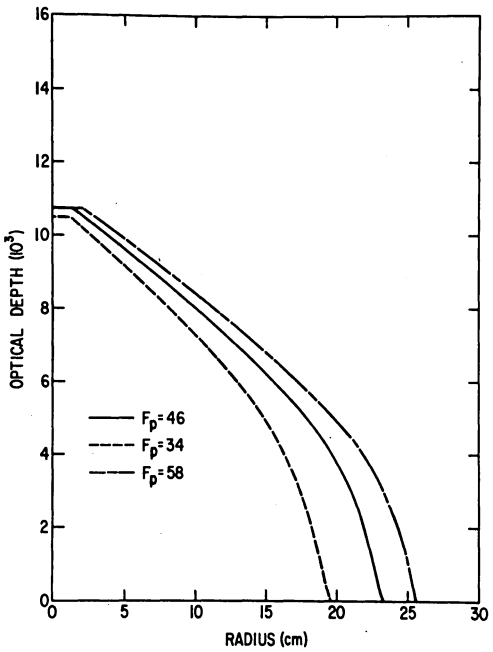

Fig. 2e. Variation of Optical Depth with Propellant Mass Flow Rate - Fuel Region.

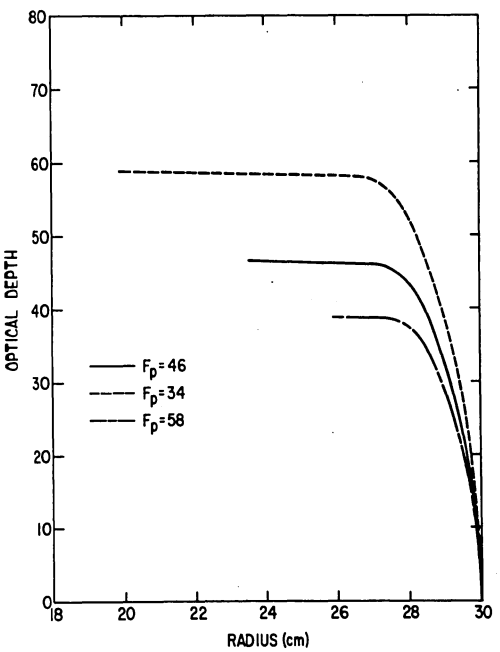

Fig. 2d. Variation of Optical Depth with Propellant Mass Flow Rate - Propellant Region.

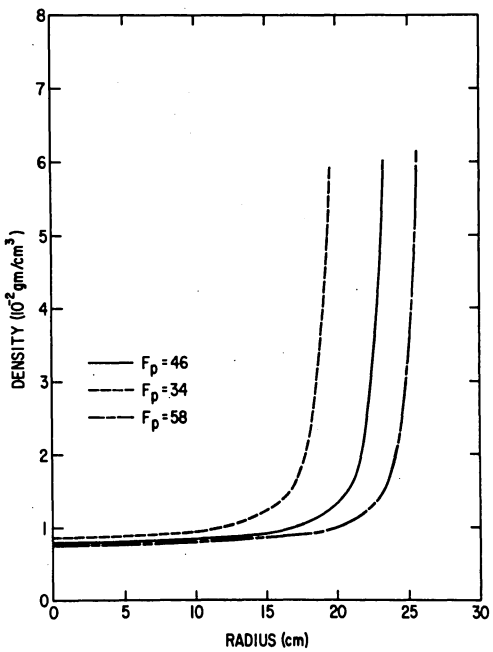

Fig. 2f. Variation of Uranium Fuel Density with Propellant Mass Flow Rate.

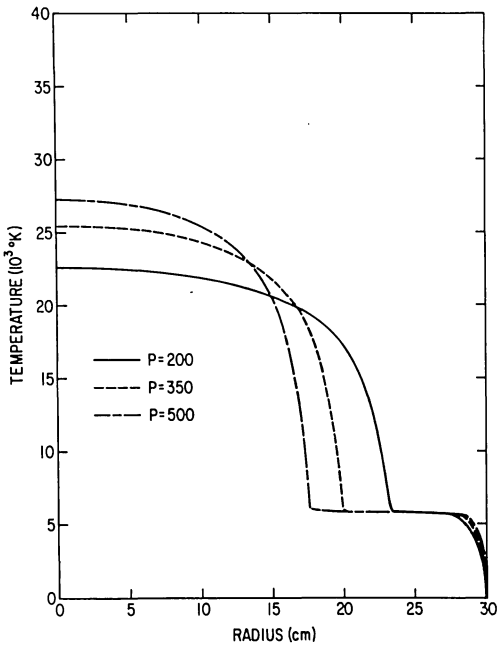

Fig. 3a. Variation of Temperature with Pressure

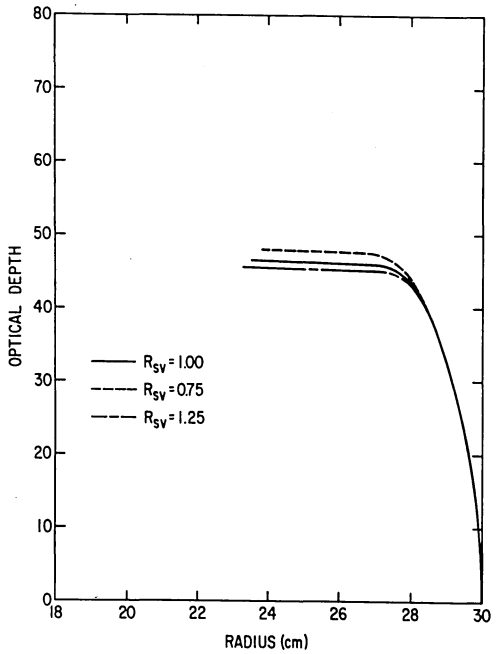

Fig. 4. Variation of Optical Depth with Normalized Seed Vaporization Rate - Propellant Region

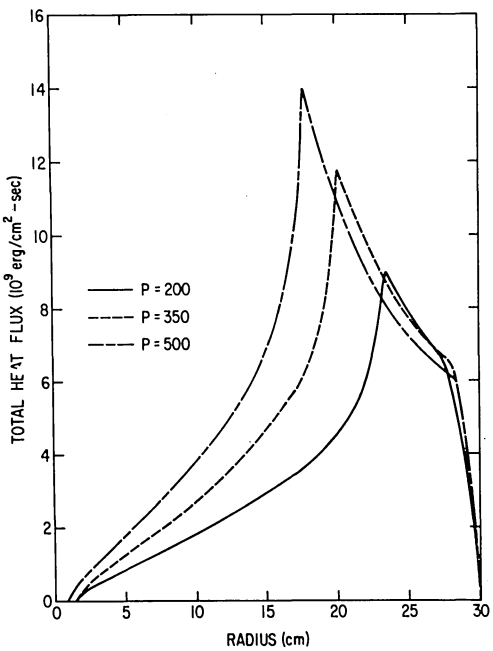

Fig. 3b. Variation of Total Heat Flux with Pressure

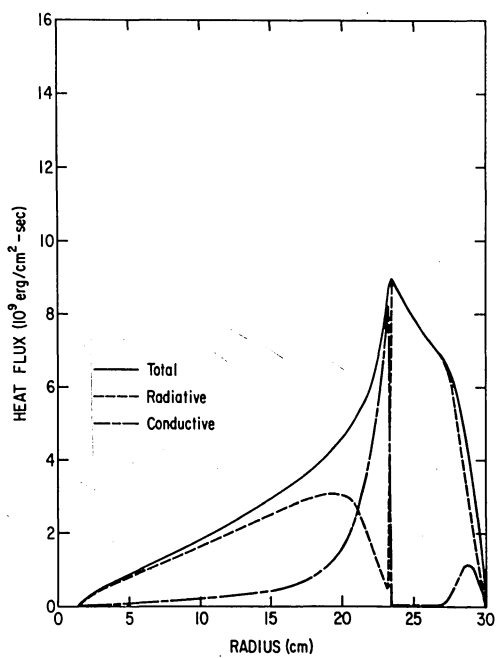

Fig. 5. Total Heat Flux and Components - Nominal Case

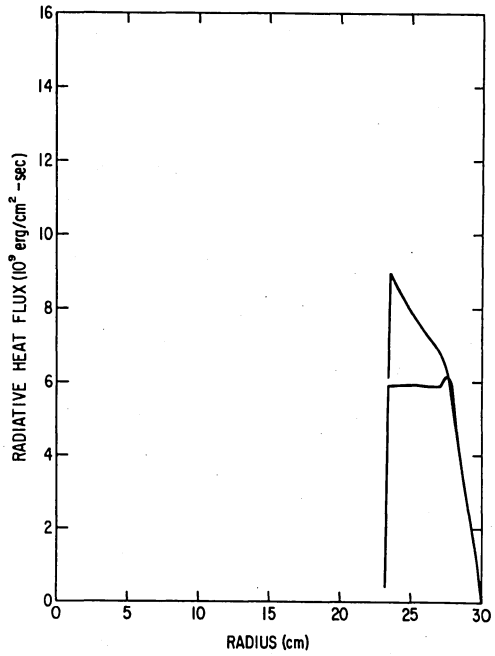

Fig. 6a. Comparison of two Physical Models of Radiative Heat Transfer - Propellant Region

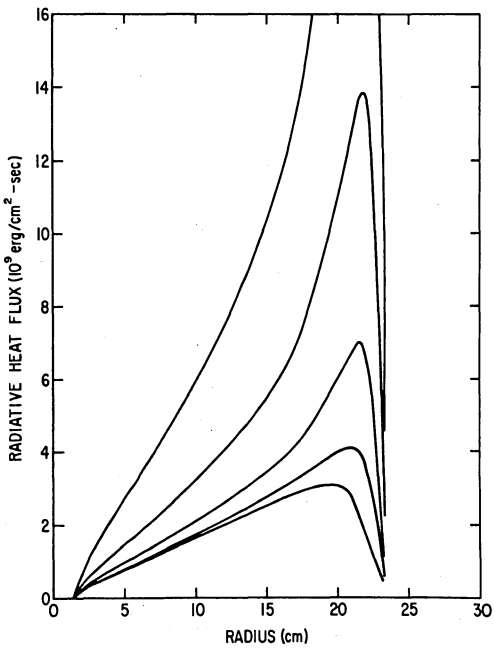

Fig. 6b. Sensitivity of Intensity Integration to step size - Fuel Region

Table 1.

Correlation between Radiative Heat Flux and Temperature

$\vec{q}_{rad}(\vec{r}) \longleftrightarrow T(\vec{r})$	
$\vec{q}_{rad}(\vec{r}) \equiv f\left[T(\vec{r}),p\right]$	LTE,grey,thick
$\vec{q}_{rad}(\vec{r}) \equiv f\left[T(\text{all } \vec{r}),p,\text{boundary radiation}\right]$	LTE
$\vec{q}_{rad}(\vec{r}) \equiv f\left[\begin{matrix}\text{bound electrons and atoms}\\ \text{energy distribution functions}\end{matrix}\right]$	NE

Table 2.

One-Dimensional Heat Transfer Flow Chart

Input System Parameters

Input lower and upper bounds for R_f

Do R_f bounds bracket solution? — no → print error message

yes

Guess new R_f using bisection method — STOP

Propagate values for temperature, total heat flux, radiative heat flux, conductive heat flux, and optical depth from cavity wall to cavity center.

Use the following relations for propagation

#10 energy balance
9 conductive heat flux

either #6, #7, #8 radiative heat flux

Is $Q_{tot}(r=o) = 0$? — yes → output solution

Redefine bounds for R_f — STOP

Note: Physical properties of plasma (ρ, a_R, etc.) are dependent on known local properties (T, P, etc.) of the plasma.

Total energy conservation equation, steady state:

$$\rho \vec{v} \cdot \text{grad} \frac{H}{\rho} + \text{div}(\vec{v} \cdot \hat{\tau}) + \text{div} \vec{q}_c + \text{div} \vec{q}_{rad} = \Sigma S - \frac{H}{\rho} S_m \quad . \tag{1}$$

$$\frac{H}{\rho} = e_{atomic} + \frac{v^2}{2} + \frac{p}{\rho} = \frac{v^2}{\rho} + \sum_s \frac{\rho s}{\rho} \left(\int_o^T c_p \, dT + h_s^o \right) \tag{1a}$$

H - total enthalpy per unit volume

e_{atomic} - internal atomic energy plus kinetic atomic energy

ρ - mass density

p - scalar pressure

$\vec{v}$ - average flow velocity

$\hat{\tau}$ - shear stress tensor

$\vec{q}_e$ - conductive heat flux

$\vec{q}_{rad}$ - radiative heat flux

ΣS - sum of energies from all sources

S_m - mass source

s - index ranging over component species of gas

Spectral radiative heat flux:

$$q_\nu = q_\nu^+ - q_\nu^-$$

$$= \int_o^{2\pi} \int_{\pi/2}^{\pi} I^+(\tau_\nu) \cos\theta \sin\theta \, d\theta \, d\rho - \int_o^{2\pi} \int_o^{\pi/2} I^-(\tau_\nu) \cos\theta \sin\theta \, d\theta \, d\rho \tag{2}$$

$$I_\nu^+(\tau_\nu) = I_\nu^B \, e^{-(\tau_\nu^B - \tau_\nu)} + \int_{\tau_\nu}^{\tau_\nu^B} S_\nu \, e^{-(\tau_\nu^* - \tau_\nu)} \, d\tau_\nu^* \tag{2a}$$

$$I_\nu^-(\tau_\nu) = I_\nu^A \, e^{-\tau_\nu} + \int_o^{\tau_\nu} S_\nu e^{-(\tau_\nu - \tau_\nu^*)} \, d\tau_\nu^* \tag{2b}$$

$$S_\nu = \frac{\varepsilon_\nu}{a_\nu} + \frac{\sigma}{4\pi} \int_{\omega'} I(\omega') \phi(\omega', \omega) \, d\omega' \tag{2c}$$

Spectral radiative heat flux for planar symmetry:

$$q_\nu = 2\pi \int_o^{\pi/2} \left[I_{\nu o}^B \, e^{-\frac{\tau_{\nu o}^B - \tau_{\nu o}}{\cos\theta}} + \frac{1}{\cos\theta} \int_{\tau_{\nu o}}^{\tau_{\nu o}^B} S_\nu(\tau_\nu^*) e^{-\frac{\tau_{\nu o}^* - \tau_{\nu o}}{\cos\theta}} \, d\tau_{\nu o}^* - I_{\nu o}^A \, e^{-\frac{\tau_{\nu o}}{\cos\theta}} - \frac{1}{\cos\theta} \int_o^{\tau_{\nu o}} S_\nu(\tau_\nu^*) \, e^{-\frac{\tau_{\nu o} - \tau_{\nu o}^*}{\cos\theta}} \, d\tau_{\nu o}^* \right] \times \cos\theta \sin\theta \, d\theta =$$

$$= 2\pi \left[I_{\nu o}^B \, E_3(\tau_{\nu o}^B - \tau_{\nu o}) + \int_{\tau_{\nu o}}^{\tau_{\nu o}^B} S_\nu(\tau_\nu^*) \, E_2(\tau_{\nu o}^* - \tau_{\nu o}) \, d\tau_{\nu o}^* - I_{\nu o}^A \, E_3(\tau_{\nu o}) - \int_o^{\tau_{\nu o}} S_\nu(\tau_\nu^*) \, E_2(\tau_{\nu o} - \tau_{\nu o}^*) \, d\tau_{\nu o}^* \right] \tag{3}$$

$$E_n(\xi) \equiv \int_o^1 \mu^{n-2} \exp\left(-\frac{\xi}{\mu}\right) d\mu \quad . \tag{3a}$$

Spectral radiative heat flux for planar symmetry and LTE:

$$q_\nu = 2\pi I_{\nu o}^B \, E_3(\tau_{\nu o}^B - \tau_{\nu o}) - 2\pi \, I_{\nu o}^A \, E_3(\tau_{\nu o}) + 2\pi \int_{\tau_{\nu o}}^{\tau_{\nu o}^B} \frac{8\pi h\nu^3}{c^3} \frac{1}{e^{h\nu/kT^*} - 1} \times E_2(\tau_{\nu o}^* - \tau_{\nu o}) \, d\tau_{\nu o}^* - 2\pi \int_o^{\tau_{\nu o}} \frac{8\pi h\nu^3}{c^3} \frac{1}{e^{h\nu/kT^*} - 1} \times E_2(\tau_{\nu o} - \tau_{\nu o}^*) \, d\tau_{\nu o}^* \tag{4}$$

Radiative heat flux for planar symmetry,

LTE, and 'grey' gas:

$$q_{rad} = 2\pi\, I_o^B\, E_3(\tau_o^B - \tau_o) - 2\pi\, I_o^A\, E_3(\tau_o)$$

$$+ 2\sigma \int_{\tau_o}^{\tau_o^B} T^{*4}\, E_2(\tau_o^* - \tau_o)\, d\tau_o^*$$

$$- 2\sigma \int_{o}^{\tau_o} T^{*4}\, E_2(\tau_o - \tau_o^*)\, d\tau_o^* \qquad (5)$$

Radiative heat flux for planar symmetry,

LTE, 'grey' gas, $\frac{\partial^2 T^4}{\partial \tau_o^2} \simeq 0$

$$q_{rad} = 2\pi\, I^B\, E_3(\tau_o^B - \tau_o) - 2\pi\, I^A\, E_3(\tau_o)$$

$$+ 2\sigma T^4 \left[E_3(\tau_o) - E_3(\tau_o^B - \tau_o) \right]$$

$$- 2\sigma \frac{dT^4}{d\tau_o} \left[(\tau_o^B - \tau_o)\, E_3(\tau_o^B - \tau_o) \right.$$

$$\left. + \tau_o\, E_3(\tau_o) + E_4(\tau_o^B - \tau_o) + E_4(\tau_o) - \frac{2}{3} \right] \qquad (6)$$

Radiative heat flux for planar symmetry,

LTE, 'grey' gas, $\frac{\partial^2 T^4}{\partial \tau_o^2} \simeq 0$, $\tau_o^B - \tau_o >> 1$:

$$q_{rad} = 2\sigma T^4\, E_3(\tau_o) - 2\pi\, I(A)\, E_3(\tau_o)$$

$$- 2\sigma \frac{dT^4}{d\tau_o} \left[\tau_o\, E_3(\tau_o) + E_4(\tau_o) - \frac{2}{3} \right]$$

$$\text{if } \tau_o^B - \tau_o >> 1 \qquad (7)$$

Radiative heat flux for LTE, 'grey' gas,

$\frac{\partial^2 T^4}{\partial \tau^2} \simeq 0$, $\tau^B - \tau >> 1$, $\tau >> 1$:

$$q_{rad} = -\frac{4\sigma}{3} \frac{dT^4}{d\tau_o} \quad \text{if} \quad \tau_o >> 1 \qquad (8)$$

Conductive heat flux

$$\vec{q}_c = -\, k_c\, \text{grad}\, T \qquad (9)$$

Energy conservation, scalar pressure, steady state

$$\rho\, \vec{v}\, c_p\, \text{grad}\, T + \text{div}(\vec{q}_c + \vec{q}_{rad}) = S \qquad (10)$$

Equation (10) in spherical coordinates

$$\rho\, v_r\, c_p \frac{\partial T}{\partial r} - \frac{1}{r^2} \frac{\partial}{\partial r} (r^2\, q_{c,r} + r^2\, q_{rad,r})$$

$$= S - \rho\, v_\theta\, c_p \frac{1}{r} \frac{\partial T}{\partial \theta}$$

$$- \frac{1}{r \sin\theta} \frac{\partial}{\partial \theta} (\sin\theta \cdot q_{c,\theta} + \sin\theta \cdot q_{rad,\theta}) \qquad (11)$$

RESEARCH ON PLASMA CORE REACTORS

G. A. Jarvis, D. M. Barton, H. H. Helmick, William Bernard, and R. H. White
University of California, Los Alamos Scientific Laboratory
Los Alamos, New Mexico 87545

Abstract

Experiments and theoretical studies are being conducted for NASA on critical assemblies with one-meter diameter by one-meter long low-density cores surrounded by a thick beryllium reflector. These assemblies make extensive use of existing nuclear propulsion reactor components, facilities, and instrumentation. Due to excessive porosity in the reflector, the initial critical mass was 19 kg U(93.2). Addition of a 17-cm-thick by 89-cm-diameter beryllium flux trap in the cavity reduced the critical mass to 7 kg when all the uranium was in the zone just outside the flux trap. A mockup aluminum UF_6 container was placed inside the flux trap and fueled with uranium-graphite elements. Fission distributions and reactivity worths of fuel and structural materials were measured. Finally, an 85,000 cm^3 aluminum canister in the central region was fueled with UF_6 gas and fission density distributions determined. These results will be used to guide the design of a prototype plasma core reactor which will test energy removal by optical radiation.

Introduction

T. S. Latham and collaborators[1] at the United Technologies Research Center (UTRC) have recently suggested several attractive applications of cavity reactor systems aimed at meeting future critical energy needs. Uranium fuel in gaseous or plasma form permits operation at much higher temperatures than possible with conventional solid fueled nuclear reactors. Higher working fluid temperatures in general imply higher thermodynamic cycle efficiencies, which lead to proposals for advanced closed-cycle gas turbine driven electrical generators and MHD power conversion systems for electricity production. Cycle efficiencies ranging from 50 to 65 percent are calculated for these systems.

Further, the possibility of energy extraction in the form of electromagnetic radiation allows consideration of many photochemical or thermochemical processes such as dissociation of hydrogeneous materials to produce hydrogen. Lasers may be energized either by direct fission fragment energy deposition in uranium hexafluoride (UF_6) and lasing gas mixtures or by optical pumping with thermal or non-equilibrium electromagnetic radiation flowing out of the reactor.

*This work was supported by the Research Division, Office of Aeronautics and Space Technology, National Aeronautics and Space Administration, NASA Contract No. W-13755.

The Los Alamos Scientific Laboratory (LASL) has a modest program to acquire experimental and theoretical information needed for the design of a prototype plasma core reactor which will test heat removal by optical radiation. Experiments are being conducted on a succession of critical assemblies with large low-density cores surrounded by a thick moderating reflector. Static assemblies, first with solid fuel, then with UF_6 in containers, will be followed by others with flowing UF_6.

Plasma Core Assembly (PCA) Design

In the first quarter of 1974, a joint working group formed by NASA from LASL and UTRC personnel produced an engineering feasibility design study revealing the possibility of constructing a large beryllium reflected cavity reactor from existing nuclear propulsion program materials and control components.[2]

Reactor Component Availability

Substantial quantities of beryllium reflector parts were stored at Los Alamos and the Nevada Reactor Development Station after the termination of the nuclear propulsion program. Beryllium reflector assemblies from 11 Rover/NERVA reactors, representing an original cost of approximately $5 million, were transferred to Los Alamos. Also, four additional beryllium reflector assemblies, including a set of 18 stepping motor driven control drum actuators, were available at Los Alamos.

LASL Facilities

The facilities of the LASL Critical Experiments Group include three remotely controlled critical assembly laboratories, called Kivas, equipped with a variety of critical assembly machines of varying complexity. A central control building houses control rooms, offices, and laboratory space. Parts of these facilities are available for the initial phases of the plasma core reactor project.

The cavity-type assemblies will be on the "Mars" critical assembly machine (Fig. 1) located in Kiva 1. This machine was built early in the Rover program and was used for neutronic and core optimization studies for the Kiwi, Phoebus, and Nuclear Furnace reactors. Early beryllium-reflected cavity reactor experiments were also performed on this machine.[3,4] Figure 1 shows the Mars machine with a Phoebus II reflector installed. The overall size is similar to that of the planned cavity assemblies. Some of the 18 control drum actuators are visible above the

reflector.

The principal features of the Mars machine are:

1. A framework that includes a base plate for supporting the reflector, an upper platform for mounting the existing control drums, and a personnel platform.

2. Provision for removing a fueled core from the reflector. The core is supported on the platen of a hydraulic cylinder, which is centered beneath the reflector and can be retracted as a safety device.

3. Provision for removing the core from beneath the machine. The lowered core assembly rests on a cart that may be rolled out on guide rails from beneath the reflector to provide easy access for alterations to the core.

Reflector Design

The critical assembly reflector design makes use of beryllium from most of the Rover reactor types. Figure 2 shows reflector parts from several of the Rover reactors assembled to form a cross section of the cylinderical reflector wall. Figure 3 identifies major Rover beryllium components by location. The end plugs of Nuclear Furnace, Pewee, and Honeycomb reflector pieces, shown in Fig. 2 and 3, consist of beryllium that averages 90% of normal density. Graphite fillers, 38-mm thick separate these from 190-mm-thick NRX and Kiwi B sectors of beryllium also at 90% normal density. A succeeding graphite annulus 44-mm thick is followed by a 203-mm-thick Phoebus II assembly which contains 18 control drums and is beryllium at 87.5% normal density.

All of the Rover beryllium reflector components have holes in them required for coolant flow, tie rod access, instrumentation lead channels, reflector density adjustment, and control drum containment. These lead to loss of neutrons by streaming and result in increased critical mass if left unfilled. Calculations indicate a reactivity loss of about 25¢ for each percent reduction in the density of the Be reflector.

Figure 4 shows the calculated penalty for substituting a 50-mm annular zone of graphite for beryllium as a function of the location of the graphite in the reflector. In the outer two-thirds of the reflector, high purity graphite is a good substitute for beryllium but is of little help in the inner region. The reflector encloses a 1.02-m-diam by 1.05-m-high cavity in which the various solid and gaseous uranium fuel cores will be studied.

Experimental Program

Core Number 1

A homogeneous uranium distribution in the cavity, simulated by use of uranium metal foils laid on a set of ten equally spaced aluminum discs, Fig. 5, had a critical mass of 19-kg U(93.2). The reactivity swing for the 18 control drums was 6.1$. Figure 6 gives the control drum calibration curve. Measured reactivity worths of core materials are uranium 73¢/kg, aluminum -3¢/kg, and graphite 2.5¢/kg.

Core Number 2

An early goal for the Plasma Core Assembly was to operate with a central zone of UF_6 gas surrounded by a zone of solid uranium fuel. To mock up this situation core number 2 consisted of uranium metal foil attached to a 0.94-m-diam thin-walled aluminum cylinder, Fig. 7, centered within the cavity. A critical mass similar to that for core 1 was indicated by subcritical comparison.

The critical mass of about 19 kg is more than a factor of two higher than calculated for uniformly distributed fuel in an idealized reflector, indicating undermoderation in the reflector and/or contaminants having high thermal neutron absorption cross sections in the beryllium and graphite. Neutron leakage through the large number of small straight coolant channels in the beryllium also tends to increase the critical mass value.

The beryllium specification limited the iron content to less than 0.18% by weight. One-dimensional criticality calculations showed that this amount of iron would increase the critical mass by about 9%. Two-dimensional criticality calculations indicated that two hundred parts per million boron containment in the graphite would account for the excess critical mass if boron alone were the cause. The large critical mass is believed to be due to a combination of the effects discussed above.

Core Number 3

The simplest solution to the neutron undermoderation problem was to add a zone of beryllium to the cavity. A suitable beryllium annulus 0.55-m i.d. by 0.89-m o.d. by 1.04-m high, Fig. 8, was formed from Pewee and Honeycomb parts. This structure had a mean density 85% that for normal beryllium and was surrounded by a 0.94-m-diam aluminum cylinder to support uranium metal foil. The initial critical mass with all uranium in the outer fuel zone was 6.84-kg U(93.2).

The reactivity worth of the control drums is influenced by the amount of uranium in the core. Since core number 3 with its added inner beryllium zone sharply reduced the critical uranium loading, the control drums were recalibrated, using positive period measurements. The reactivity swing for one control drum is 22.4 cents, giving 4.03$ for the 18 control drums. Figure 9 gives the calibration curve for the entire 18 control drums.

The control drum worth is now only two thirds that for the empty cavity configuration of cores one and two, but is considered adequate for the planned experiments.

Table I lists the reactivity worths of uranium, aluminum, and carbon for indicated positions in core number 3.

It should be noted that the uranium worth values of Table I imply an appreciably greater fission density in the central zone than in the outer fuel zone. The additional neutron moderation in the flux trap results in a central zone uranium reactivity worth six times that for uranium in the outer zone. As the fission density in a highly thermalized system varies as the square root of the reactivity, UF_6 in the central zone will benefit from a fission density enhancement of about 2.4 over that for uranium in the driver zone.

The effects of flux trapping by an additional beryllium zone within a cavity surrounded by an undermoderating reflector was examined using one-dimensional neutron transport calculations on an equivalent spherical mockup of the PCA cylindrical geometry. The calculated fission density in the central zone was 2.3 times that for the outer or driver fuel zone.

Core Number 4

Core number 4 uses the beryllium flux trap of core 3 and uranium-graphite Rover fuel elements in the outer driver zone, Fig. 10. The inner experimental zone is provided with a mockup of an aluminum UF_6 container to be used in later experiments. Low density uranium-graphite fuel elements are used in this region to simulate UF_6 loadings.

Table II gives the loading specifications for the uranium-graphite fuel elements.

Figure 11 shows the available fuel element holes in the driver and experimental zones. Figure 12 shows core No. 4 positioned to be raised into the PCA reflector.

Material Reactivity Evaluations

Reactivities for uranium and other materials were measured in the central experimental and driver zones. Results agreed with those found for core 3.

As seen in Table 1, uranium has a much higher reactivity worth in the inner zone than in the outer or driver zone, so that the critical mass will decrease as uranium is added to the central region of the core. Figure 13 shows the measured variation of critical mass with the fraction of fuel in the inner zone.

Fission Density Measurements

Fission density distributions were determined for two different core loadings

TABLE I

REACTIVITY WORTHS OF MATERIALS IN PCA CORE NO. 3.

Material	Material location	Worth in cents/kg
U (93.5%)	On axis	+ 3350
U (93.5%)	Near end of Al support	+ 554
Al	On axis	- 10.8
Al	At Al support	- 3.0
Honeycomb C	On axis	- 1.4
PCA Reflector C	On axis	- 3.2

TABLE II

Element Location	Uranium Density	Uranium/Element
Driver zone	400 mg U/cm^3	82.8 g
Experimental zone	100 mg U/cm^3	20.7 g

for the experimental and driver fuel zones by beta scanning U-loaded Al wires irradiated in the central holes of selected fuel elements. Figure 14 shows the fuel element configuration and wire locations. Figure 15 shows the core mid-plane radial fission distribution. The fission density rises slowly from the center outwards. The ratio of the central element to driver element fission density values is 2.40, in good agreement with the value of 2.4 noted in section III-c which was determined from uranium reactivity measurements. Figure 16 gives fission distributions for two central fuel zone axial positions.

Core Number 5

UF_6 gas was used as the fuel for this core in the inner zone using the UTRC double walled canister and gas handling system. A Be flux trap separated the gas from a driver fuel element zone composed of lightly loaded uranium - graphite fuel rods described in the previous section. Figure 17 is a photograph showing the canister mounted on a ram underneath the reflector ready for assembly. Two pie sections of the lower Be end plug have been removed to show the flex lines that connect the canister to the gas handling system in the foreground.

Figure 18 is a schematic of the gas handling system. $^{235}UF_6$ in the supply bottle is a solid at room temperature. This bottle is immersed in a hot water bath and heated for one hour at about boiling temperature (88°C). This converts the solid to a gas and by suitable valving, a known amount of the gas is trapped in the transfer bottle of the same manifold. Verification of the amount of gas in the transfer bottle is obtained by weighing the bottle and contents. The entire gas system and canister are next heated to about 66°C using heat tapes and hot flowing He gas. This requires about three hours. The UF_6 now remains in the gas phase for critical operations.

Recovery of the UF_6 is accomplished by pumping down the canister and gas system through a glass liquid nitrogen (LN) trap. Material recovery is evaluated by weighing the glass trap and contents. After completing the recovery cycle, we find very little residue in the canister, as affirmed by running the reactor at delayed critical. However, weighing showed that some UF_6 remained in the transfer system. We suspect that the majority of this material is in the corrugated flex lines linking the gas system to the canister. Table III shows the results obtained from out two transfer operations.

UF_6 Reactivity Evaluation

A lightly loaded Kiwi fuel element was placed in the region between the canister and the Be flux trap in order to re-evaluate the reactivity worth of uranium in the central region. A value of 2.95 cents/g U was obtained which translates to 1.99 cents/g UF_6. An initial operational limit of one dollar for the gas in the core restricts the UF_6 to a minimum of 50 grams.

Three fission density distributions were measured in the gas core along paths as indicated in Figure 19. U-loaded Al wires were placed on the central axis and on a parallel line displaced 10 cm radially from this axis. Another wire was on a diameter at the mid-plane of the core. The wires were irradiated for 10 minutes at a power level of about 70 watts and then scanned with a beta counter to obtain the data plotted in Figure 20. We found similar distributions for the two core loadings of 12 to 24 grams of UF_6. The radial traverse, not shown, is flat to within 0.1%, as expected for such a light uranium loading. An earlier experiment noted in section III-c, using 393 grams of uranium in a solid uranium-graphite fuel mock-up of the gas core, had a 3% rise in fission density from the center to the core edge, indicating a slight uranium self shielding effect. The axial fission density falls off about 8% from the mid-plane to the core end. This results from holes in the reflector end walls for plumbing and thinner beryllium in this region.

Concluding Remarks

A beryllium reflected critical

TABLE III

SUMMARY OF DELAYED CRITICAL RUNS ON PCA

	UF_6 Gas Transferred (g)	Reactivity Change (cents)	UF_6 Recovered (g)	UF_6 left in canister (g)	UF_6 left in lines (g)
Run 1	12.0	20	3.6	2.2	6.2
Run 2	24.6	50	14.9	2.5	7.2

assembly has been constructed which is suitable for performing tests on static and flowing UF_6 cores and ultimately on advanced models employing hydrodynamical containment of the UF_6 by a flowing buffer gas. Dividing the core into a driver zone containing a major fraction of the fuel in solid form separated by a neutron flux trap from a central experimental zone for gaseous fuel has several advantages:

1. The fission density in the gas fueled region is boosted by a factor of 2.4 over that in the driver zone.

2. An ideal gas core geometry with length about three times the diameter is available.

3. Initial evaluation of reactor safety problems for the flowing UF_6 fueled core critical.

References

1. Latham, T. S., F. R. Biancardi, and R. J. Rodgers: Applications of Plasma Core Reactors to Terrestrial Energy Systems. AIAA Paper No. 74-1074, AIAA/SAE 10th Propulsion Conference, San Diego, California, October 21,23, 1974.

2. Helmick, H. H., G. A. Jarvis, J. S. Kendall* and T. S. Latham*: Preliminary Study of Plasma Nuclear Reactor Feasibility. Los Alamos Scientific Laboratory report LA-5679, July 1974. *United Aircraft Research Laboratories.

3. Jarvis, G. A. and C. C. Byers: Critical Mass Measurements for Various Fuel Configurations in the LASL D_2O Reflected Cavity Reactor. AIAA Paper No. 65-555, AIAA Propulsion Joint Specialist Conference, June 1965.

4. Paxton, H. C., G. A. Jarvis, and C. C. Byers: Reflector-Moderated Critical Assemblies. Los Alamos Scientific Laboratory report LA-5963, July 1975.

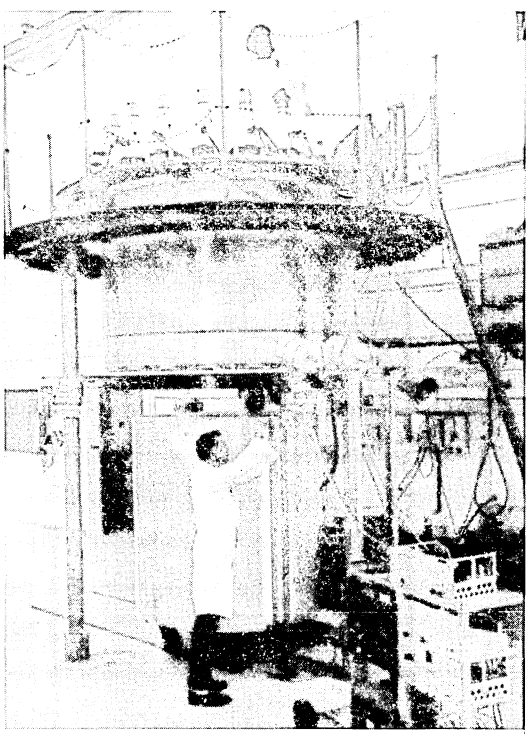

Fig. 1 Mars machine with Phoebus II Rover Assembly.

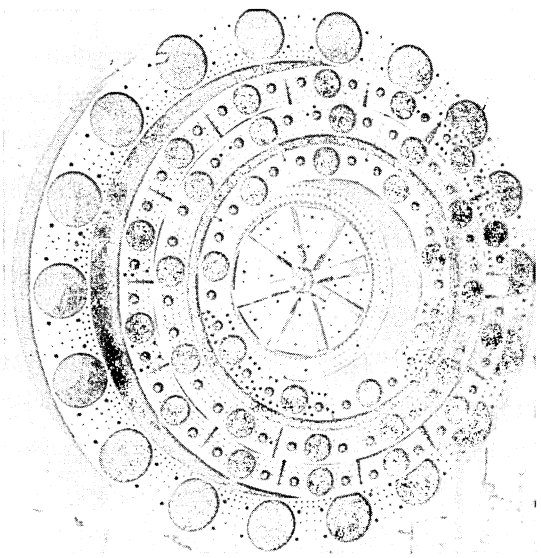

Fig. 2 Rover beryllium reflector components used in PCA.

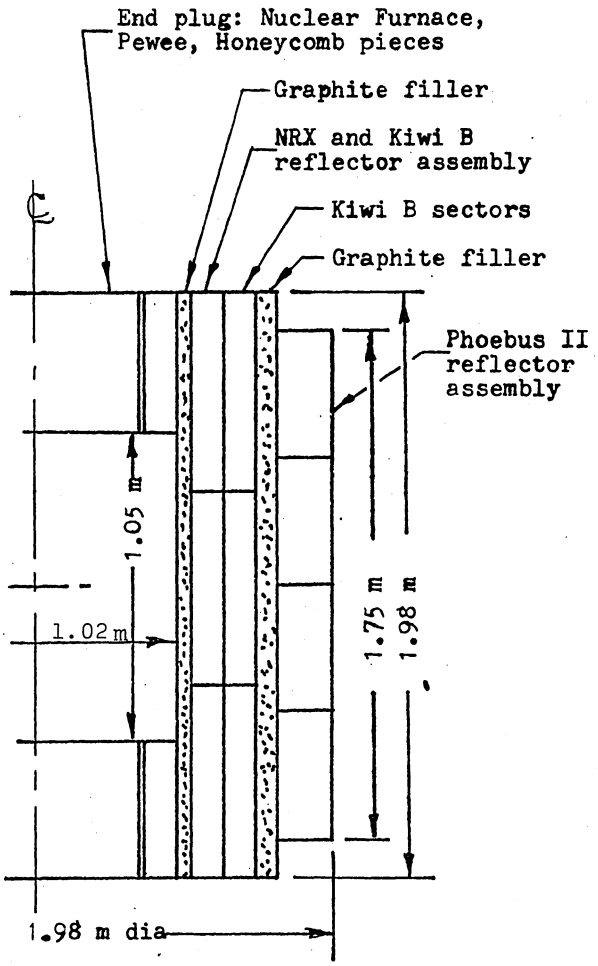

Fig. 3 Plasma core assembly reflector.

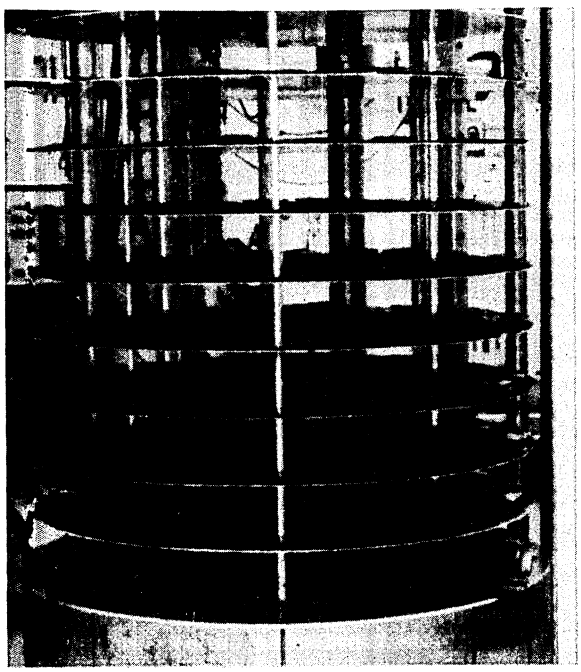

Fig. 5 Core No. 1

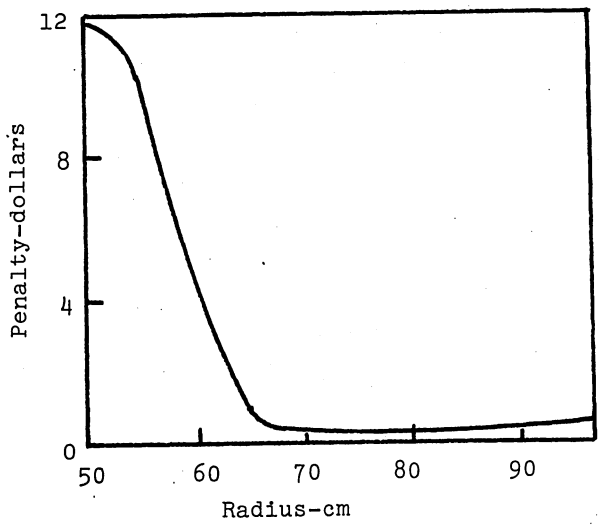

Fig.4 Reactivity loss associated with substitution of graphite for Be.

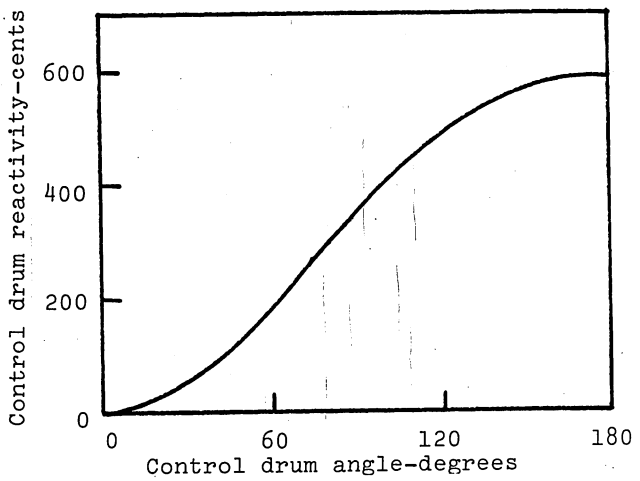

Fig. 6 Control drum calibration curve for core number one.

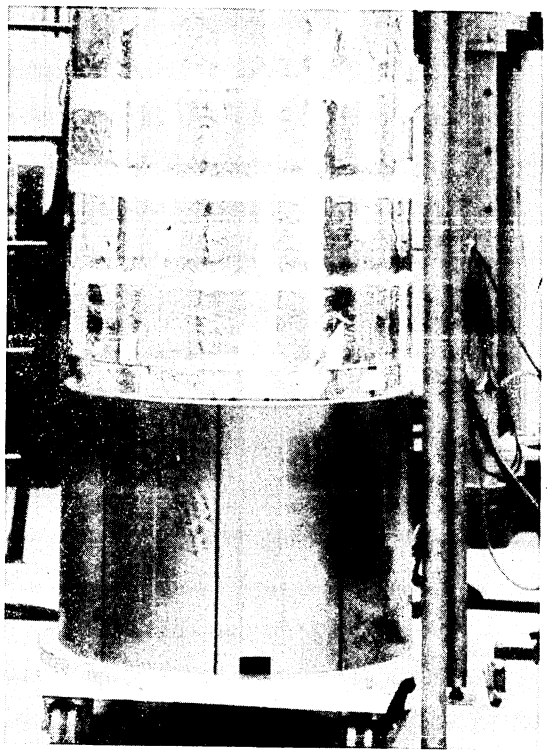

Fig. 7 Core No. 2

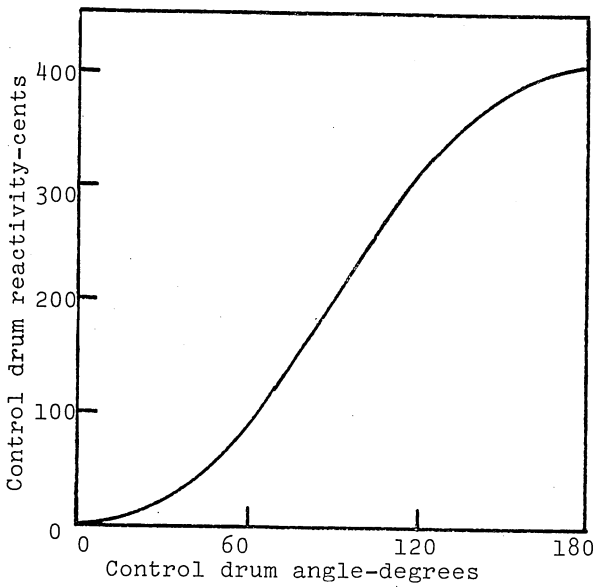

Fig. 9 Control drum calibration for core number three.

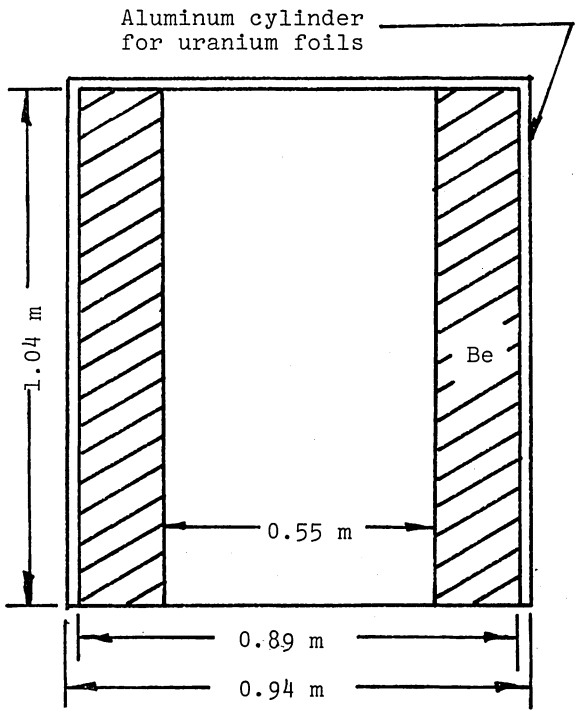

Fig. 8 Core 3

Fig. 10 Core number four with partial load of U-graphite driver fuel rods.

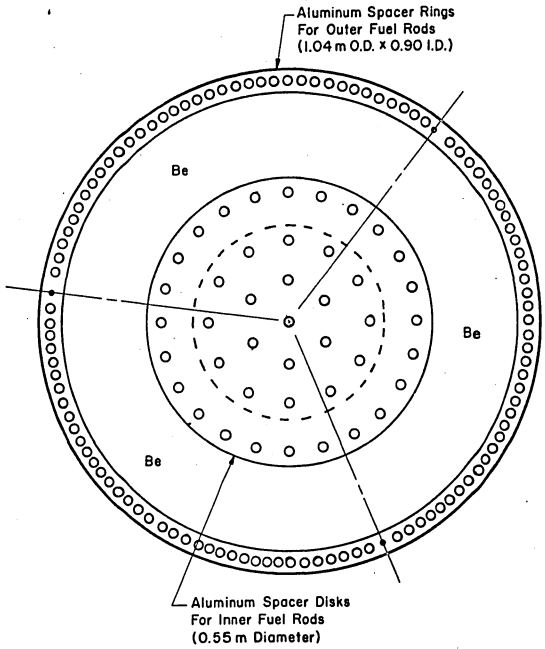

Fig. 11 Aluminum support structure for supporting U-graphite rods for core number four.

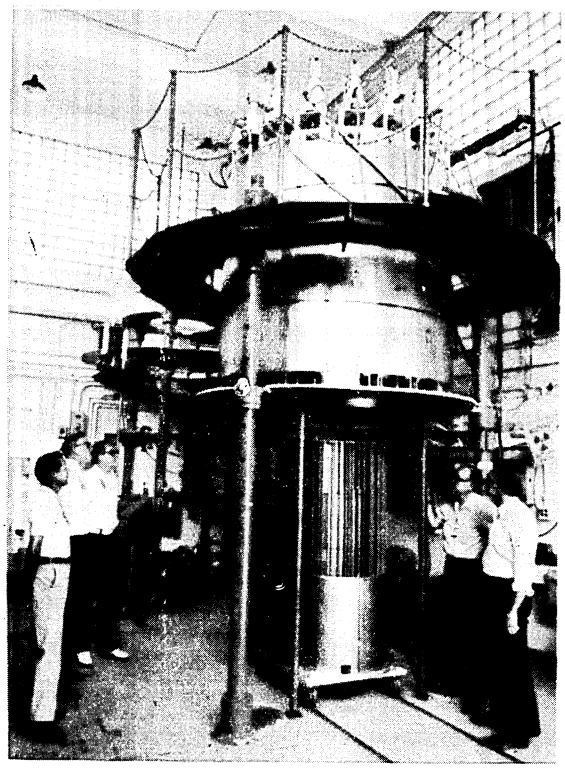

Fig. 12 Mars machine with core number four ready for assembly.

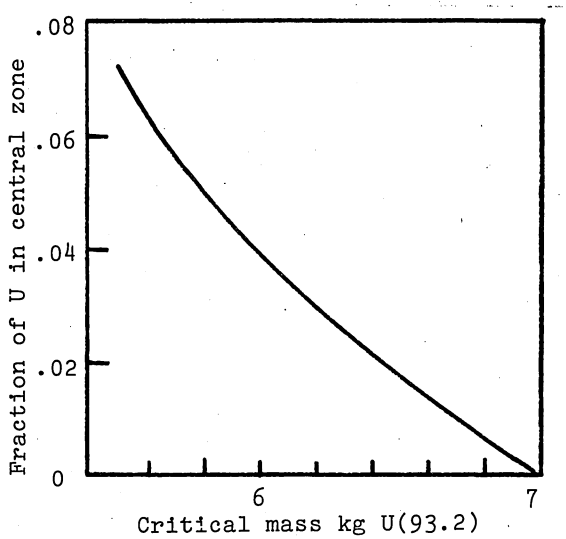

Fig. 13 Critical mass dependence on fraction of U in the center fuel zone.

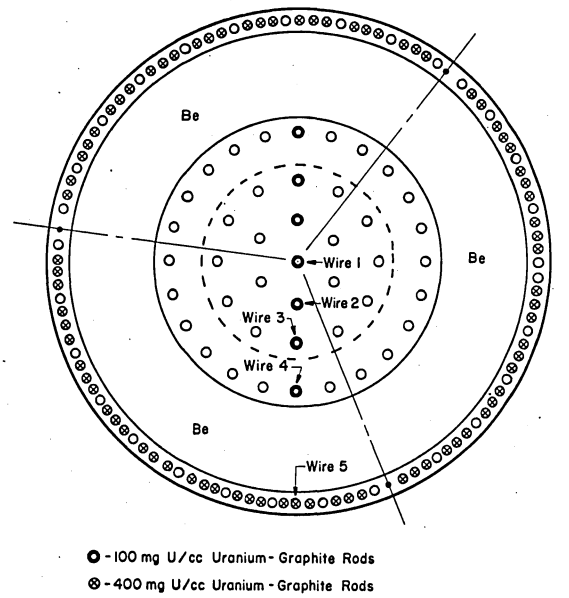

Fig. 14 Fuel element loading and wire positions for core No. 4

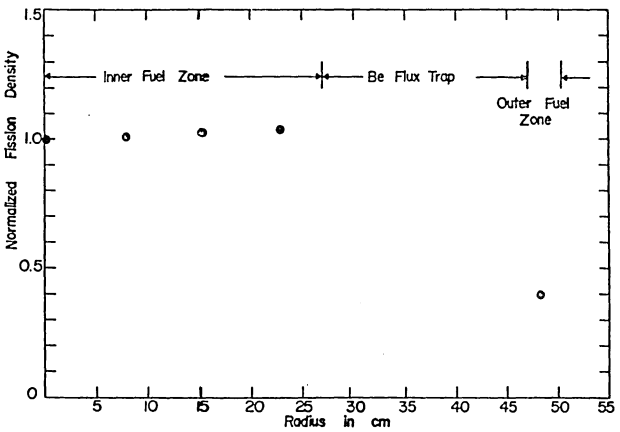

Fig. 15 Radial fission distribution, core No. 4

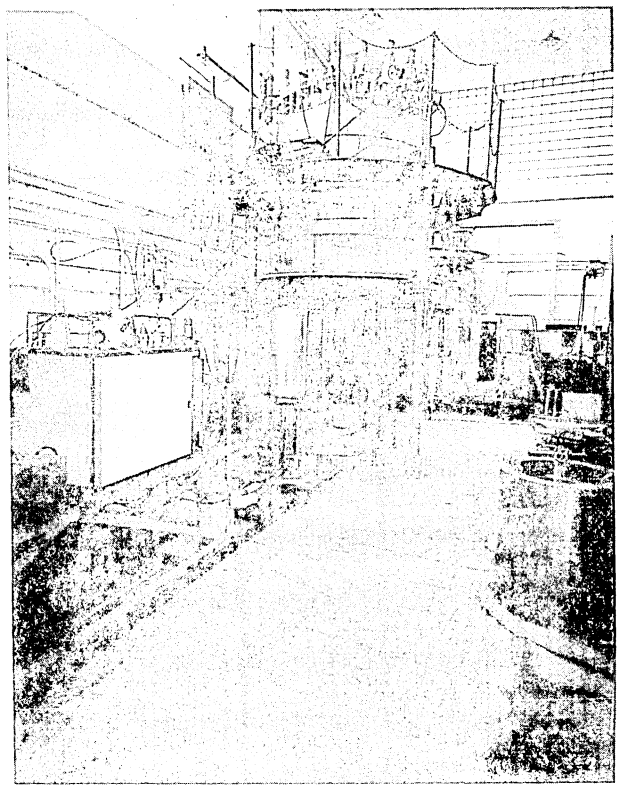

Fig. 17 Core number five with aluminum canister for UF_6 gas.

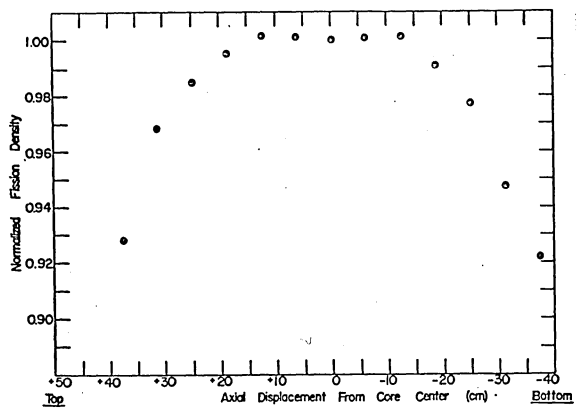

Fig. 16 Axial fission distribution, core No. 4

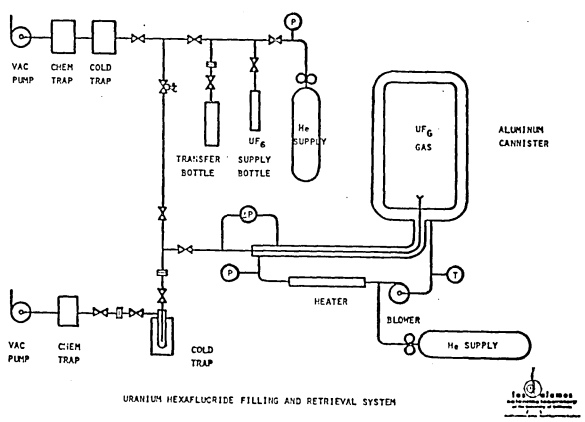

Fig. 18 Schematic of UF_6 gas handling system.

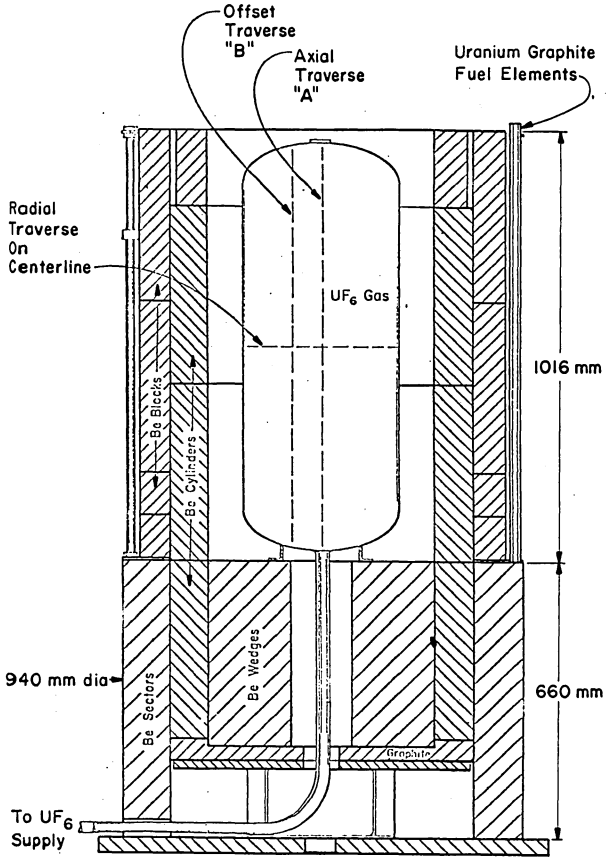

Fig. 19 Location of fission wires in core number five.

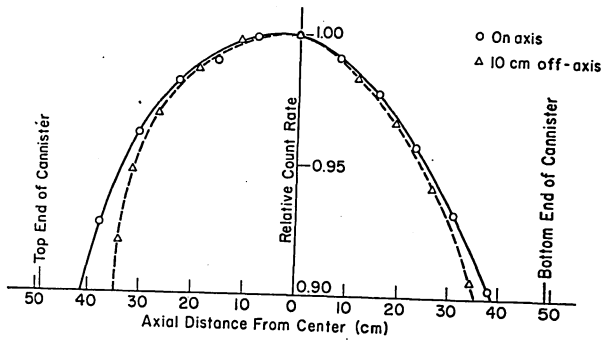

Fig. 20 Axial fission distributions, core No. 5

DISCUSSION

ANON: Why did you use argon as your buffer gas?

T. S. LATHAM: Argon is a higher density buffer gas, giving a higher density per mole. Thus at a given pressure, more UF_6 can be confined with argon rather than helium.

PARAMETRIC ANALYSES OF PLANNED FLOWING URANIUM HEXAFLUORIDE CRITICAL EXPERIMENTS*

R. J. Rodgers, Research Engineer
and
T. S. Latham, Chief Project Engineer
United Technologies Research Center
East Hartford, Connecticut

Abstract

Analytical investigations were conducted to determine preliminary design and operating characteristics of flowing uranium hexafluoride (UF_6) gaseous nuclear reactor experiments in which a hybrid core configuration comprised of UF_6 gas and a region of solid fuel will be employed. The investigations are part of a planned program involving National Aeronautics and Space Administration (NASA), Los Alamos Scientific Laboratory (LASL), United Technologies Research Center (UTRC), and other organizations to perform a series of experiments of increasing performance, culminating in an approximately 5 MW fissioning uranium plasma experiment.

The results indicate that confined flow tests of a gaseous UF_6-uranium fuel element hybrid core configuration appear feasible. A preliminary design is described for an argon buffer gas confined, UF_6 flow loop system for future use in flowing critical experiments. Flowing gaseous UF_6 would be confined within the cavity core canister by tangential injection of argon buffer gas to produce a radial inflow vortex flow pattern. Initial calculations to estimate the operating characteristics of the gaseous fissioning UF_6 in a confined flow test at a pressure of 4 atm, indicate temperature increases of approximately 100 and 1000 K in the UF_6 may be obtained for total test power levels of 100 kW and 1 MW for test times of 320 and 32 s, respectively.

Introduction

Extraction of power from the fission process with the nuclear fuel in gaseous form allows operation at much higher temperatures than those of conventional nuclear reactors with solid fuel elements. Higher operating temperatures in general lead to more efficient thermodynamic cycles and, in the case of fissioning uranium plasma core reactors, result in many possible applications employing direct coupling of power in the form of electromagnetic radiation.

A program plan for establishing the feasibility of fissioning UF_6 gas and uranium plasma reactors has been formulated by NASA and is described in Refs. 1 and 2. Briefly, the series of reactor tests consists of gaseous nuclear reactor experiments of increasing performance, culminating in an approximately 5 MW fissioning uranium plasma reactor experiment. Initial reactor experiments will consist of low-power, self-critical cavity reactor configurations employing undissociated, nonionized UF_6 fuel at near minimum temperatures required to maintain the fuel in gaseous form. Power level, operating temperature, and pressure will be systematically increased in subsequent experiments to approximately 1000 kW, 1800 K, and 20 atm, respectively. The final 5 MW reactor experiment will operate with a fissioning uranium plasma at conditions for which the injected UF_6 will be dissociated and ionized in the active reactor core.

Cavity reactor experiments have been conducted to measure critical masses in cavity reactors at both LASL and at the National Reactor Testing Station (NRTS) in Idaho Falls. Critical mass measurements have been made on both single cavity and multiple cavity configurations. In general, nucleonics calculations have corresponded to within a few percent of the experimental measurements. A review of these experiments is contained in Ref. 3. These studies provide the basis for selecting additional experiments to demonstrate the feasibility of the plasma core nuclear reactors.

Analytical investigations described herein were performed to formulate a preliminary design for an argon-buffer-gas-confined UF_6 flow system loop. This design will be used in future cavity reactor experiments in which hot flowing UF_6 is to be confined within a cavity core canister by tangentially injected argon buffer gas. Calculations of principal operating parameters for 100 kW and 1 MW cavity reactor experiments with buffer-gas-confined flowing UF_6 were made to define the control requirements for the gas flow systems and the reactor experiments.

Initial Reactor Series Tests

The initial series of planned low-power critical cavity reactor experiments has been conducted at LASL. These critical cavity reactor experiments consisted of sequential tests on the following core loading configurations: (1) distributed uranium foil core loadings in a right circular cylinder, 1-m-dia by 1-m-long cavity surrounded by a 50-cm-thick beryllium reflector-moderator, and (2) hybrid fuel loading configurations in which the central 54-cm-dia by 1-m-long portion of the core cavity volume contained an aluminum (Al) canister filled with a gaseous UF_6-Helium (He) mixture surrounded by a 17.2-cm-thick annular beryllium moderator region surrounded in turn by a region containing solid nuclear fuel elements. Results of the foil loading tests are described in Ref. 4.

*Research sponsored by Los Alamos Scientific Laboratory, Contract XP5-54474-1.

The tests were conducted to determine critical mass loadings, control drum calibrations, and overall control drum reactivity worth, reactivity worths of the structural Al, and the reactivity penalty due to holes required in later experiments for introducing increased amounts of gaseous UF_6 and for observing possible fission fragment induced electromagnetic radiation emission.

The second series of planned cavity reactor experiments will employ flowing gaseous UF_6-He mixtures. The experiments will employ a hybrid fuel loading geometry in which approximately 10 percent of the core cavity volume will contain a canister similar to that used in the initial critical experiments. In the planned experiments, gaseous UF_6 will be mixed with varying amounts of He and circulated within a closed flow loop through a canister located in the central region of the core. That portion of the total flowing UF_6 inventory contained in the core canister will be included in the total critical mass loading. The remaining portion of the flowing UF_6 inventory will be contained in the flow lines and associated hardware external to the cavity volume. UF_6 not in the canister is not neutronically part of the active core except for that UF_6 contained in the flow lines within the lower section of reflector-moderator. Initially, most of the fuel loading will be comprised of solid fuel in the form of distributed uranium foil or solid fuel elements fabricated for earlier Rover program[1] reactors. The flowing UF_6 tests will be conducted using the canister and gaseous circulation flow system described in Ref. 5. These tests will provide basic reactor physics and engineering data for design of subsequent reactor tests in which flowing UF_6 will be fluid-mechanically confined away from the canister peripheral walls by argon buffer gas.

Reflector Moderator Configurations

The basic beryllium reflector-moderator was assembled from available materials from the Rover program(1). The reflector-moderator configuration is shown in Fig. 1. The reflector surrounds a right circular cylindrical cavity approximately 54-cm-dia x 1-m-long. The reflector-moderator configuration contains an approximately 6.5-cm-wide annulus for locating solid fuel or distributed uranium foil between the inner Pewee beryllium and the outer beryllium reflectors. Criticality measurements(4) indicated that a uranium foil loading of 6.7 kg was required for criticality with uniformly distributed foil in both the gap between the inner Pewee beryllium and outer beryllium reflectors, and the central cavity. The reflector-moderator configuration shown in Fig. 1 is well-suited for flowing UF_6 critical experiments in which the core canister would be located within the approximately 54-cm-dia x 1-m-long cavity. The total outer beryllium reflector thickness is $\approx$ 50 cm.

The reflector-moderator is mounted on the Pajarito Critical Assembly Facility at LASL. This facility is described in detail in Ref. 6. The critical assembly facility has a framework which includes a base plate for supporting the reflector, an upper platform for mounting the control drums, and a personnel platform. In addition, provision is made for removing the fueled core from the reflector by lowering a platen on a hydraulic ram centered beneath the reflector. Further provision for removing the core from beneath the machine is also made. When lowered, the core assembly rests on a cart which may be rolled out on guide rails from beneath the reflector to provide easy access for maintenance and modification of the core assembly.

Analyses of Flowing UF_6 Experiments With Buffer Gas Confinement

As part of the cavity reactor experimental program continuing at LASL, the third phase of the planned series will involve performing reactor experiments in which flowing UF_6 will be fluid-mechanically confined in a central volume of a core cavity by A or He buffer gas injected tangentially from the cavity peripheral walls. The objective of the cavity reactor experiment program is directed toward demonstrating the feasibility of fissioning uranium plasma reactors. Toward this end, a final approximately 5 MW reactor experiment will operate with a self-critical fissioning uranium plasma confined by A buffer gas at conditions such that the injected UF_6 will be dissociated and ionized in the reactor core. In examining a near-term series of buffer gas confined UF_6 experiments, a hybrid reactor (driver zone plus a fissioning UF_6 gaseous core) configurations will be used to determine the operating characteristics as well as to obtain basic engineering data for plasma core reactors. The hybrid fuel and reflector-moderator configuration which is shown in Fig. 1 and which is assembled for flowing UF_6 and static UF_6 cavity reactor experiments, could also be employed in the initial buffer gas confined UF_6 experiments.

Core Canister Assembly and Gas Flow Systems

The results of a preliminary design of an A buffer gas confined UF_6 canister, UF_6 and A flow system, and a UF_6 separation and reprocessing system for use in these future cavity reactor experiments are indicated in sketches of the core canister assembly and schematic diagram of the flow systems shown in Figs. 2 and 3, respectively. The core canister assembly is made-up of two concentric 6061-0 Al canisters and has an approximately 34-cm-ID inner canister. The outer canister is 37-cm-dia and is used to provide a flow region for thermal control of the inner canister, as well as a safeguard against leakage of the fuel into the external environment. The overall length of the canister assembly is approximately 94 cm. The canister dimensions are such that it occupies a volume of approximately 0.08 m^3. A continuous flow of A buffer gas is injected tangentially from a single slot which extends along the entire length of the canister

peripheral wall. The tangential injection of A buffer gas creates a radial inflow vortex and, therefore, a radial pressure gradient within which the fuel is contained. Some of the injected A flows directly through the buffer gas region and prevents the fuel mixture from reaching the peripheral wall. This bypass flow is withdrawn through a perforated section of the peripheral wall which extends along the entire length of the inner canister and which is just upstream and adjacent to the A injection slot. The bypass flow is then removed from the canister assembly via an axial duct located behind the perforated section of the peripheral wall and between the inner and outer canister walls. The ratio of bypass flow to thru-flow is adjusted to give the best fuel containment. Some of the A buffer gas flows radially inward in the endwall boundary layer and is removed from the cavity via thru-flow ports located on the centerline in both endwalls.

Continuous fuel injection into the vortex flow will be accomplished from one endwall through discrete injectors usually located at a constant radius well away from the centerline, typically 75 to 80 percent of the canister radius. Some of the injected fuel is confined within the vortex central region. However, a portion of the fuel mixes rapidly with the A buffer gas flow in endwall boundary layers and exhausts with the A flow. The thru-flow exhaust stream typically consists of a high concentration of confined fuel and A buffer gas. The bypass flow consists of mostly A buffer gas with small concentrations of fuel. In addition to the canister, the buffer-gas-confined UF_6 flow systems shown in Fig. 3 consists of the fuel reprocessing system, a fuel recirculation system, and a buffer gas recirculation system.

The fuel reprocessing system is used to treat the effluent flow from the canister. Its primary purpose is to separate the UF_6 from the A buffer gas. This is accomplished by cold trapping in a continuously sequenced set of heat exchangers. After a prescribed desubliming time, each heat exchanger will be evacuated to remove the remaining noncondensible gases, then heated to drive the pure gaseous UF_6 to a condenser where it will be liquefied. The minimum UF_6 concentration in the outlet process gas stream is limited by its temperature and corresponds to the UF_6 vapor pressure at that temperature. The temperature of the outlet process gas stream is approximately 225 K for which the corresponding UF_6 vapor pressure is approximately 0.001 atm. The trace UF_6 remaining in the process gas stream will be removed from the gas stream in a NaF absorption-desorption bed. Desorption of the NaF bed can be effected subsequent to the reactor test or series of tests.

The fuel recirculation system which is composed of a pump, heater, and connecting heated flow lines, is used to process liquid UF_6 and to provide for re-injection of UF_6 into the core canister in gaseous form. The buffer gas recirculation system which is composed of an A pump, heater and connecting flow lines, is used to process the A buffer gas for re-injection into the core canister. The buffer gas has been stripped of trace UF_6 quantities by the NaF chemical trap. A more detailed description of the flow systems is given in Ref. 7.

UF_6 Contained Mass Calculations

Extensive experiments have been conducted to determine the containment characteristics of radial-inflow vortexes for application to the gas core nuclear rocket program[8-11]. The results of those experiments also have application in the plasma core reactor program [1,12], as well as the buffer gas confined flowing UF_6 cavity reactor experiments. In these investigations, a light gas, air or He, was used to drive the vortex and a heavy gas was injected separately to simulate gaseous nuclear fuel to be contained within the central region of the vortex test chamber. Fluid mechanics experiments have indicated that a radial inflow vortex is well-suited for applications which require the preferential containment of the heavy gas within the light gas created vortex flow. The radial-inflow flow pattern is characterized by an essentially laminar radial stagnation surface across which there is no inward radial buffer gas flow. The radial position of this surface is nominally defined to be the edge-of-fuel location; that is, the radial location outwardly beyond which the density of fuel is assumed to be essentially zero. The radial stagnation surface can be located as far from the centerline as 80 to 90 percent of the total vortex radius. In a fissioning UF_6 fuel region a negative temperature gradient through the buffer gas region to the peripheral wall, insures that a positive density gradient exists through the buffer gas region and this should reduce the diffusion of fuel radially outward through the buffer gas.

Calculations were performed to determine the mass of UF_6 which can be confined in the central region of an A vortex within a core canister with the same volume and dimensions as shown in Fig. 1. In this configuration, the UF_6 is contained within a vortex flow and away from the canister wall by A buffer gas injection tangentially from the peripheral wall of the canister. Based on containment experiments of isothermal two-component gas vortexes[8], a radial stagnation surface was selected for the calculations at a fuel region to cavity radius ratio of 0.75, where the cavity radius is 16.92 cm. The cylindrical length of the fuel region was taken to be approximately 91 cm. Both the A and fuel mixture (UF_6 and He) are to be injected initially into the cavity at a temperature of approximately 400 K.

Calculations of the amount of UF_6 which could be contained within the above described fuel region were performed with the following assumptions: (1) the density at all locations in the

fuel region is constant and equal to the density of A at the radial stagnation surface which is assumed to be at a temperature of 400 K; (2) the fuel region gaseous constituents (UF_6-He-A) are at a uniform temperature equal to or greater than the A buffer gas temperature of 400 K; (3) the ratio of total volume-averaged partial pressure of the fuel mixture, (UF_6+He) in the entire canister to the buffer gas pressure at the peripheral wall, P_F/P_{TOT}, is between 0.3 and 0.4. The results of calculations of the mass of UF_6 contained in the vortex for total cavity pressures of 1, 4, and 10 atm and for temperatures between 400 and 2000 K are shown in Fig. 4. The UF_6 contained mass is relatively insensitive to temperature and ranges from approximately 45 to 450 g as the total pressure within the canister is varied from 1 to 10 atm. These are the approximate ranges in the variables of pressure, temperature, and mass of UF_6 expected in the A buffer gas confined flowing UF_6 low-power cavity reactor experiments. The Al canister will be located in a cylindrical cavity approximately 54 cm in diameter and 100 cm in length. The UF_6 fuel containment canister, hybrid fuel and associated reflector-moderator configuration, as shown in Fig. 1, will be used in this series of reactor experiments.

Calculations of operating characteristics of this reactor configuration were performed, based on a maximum total number of fissions per tests of 1×10^{18}. This fission limitation has been used to conform to present operating procedures for critical tests at the LASL Pajarito site. The calculated critical mass of a similar configuration was 4.37 Kg of U (0.935 U-235) as reported in Ref. 12, was obtained using a spherical reactor model in a one-dimensional neutron transport theory computer code calculation. The calculation also assumed a relative fission power density (specified as W/g of U-235) for fuel in the canister to that in the surrounding solid fuel to be 2.3 as calculated and reported in Ref. 4. The UF_6 fission rate ratio is a function of the fission power density ratio, ϕ^{UF_6}/ϕ^{SOLID}, between UF_6 and solid fuel; the UF_6 mass, M_{UF_6}, contained in the canister; and critical mass, M_C, and is given by the expression

$$FR_{UF_6} = \frac{\frac{\phi^{UF_6}}{\phi^{SOLID}} \left[M_{UF_6} \left(\frac{MW_{U235}}{MW_{UF_6}} \right) (.935) \right]}{\left[M_C + \left(\frac{\phi^{UF_6}}{\phi^{SOLID}} - 1.0 \right) M_{UF_6} \left(\frac{MW_{U235}}{MW_{UF_6}} \right) (.935) \right]}$$

where the UF_6 is assumed to be 0.935 U-235. The variation of UF_6 fission rate ratio with contained mass of UF_6 is shown in Fig. 5. As the fission rate ratio varies from 0.01 to 0.20, the corresponding mass of UF_6 contained in the canister varies from approximately 30 to 685 g.

Operating Power Deposition Levels

The characteristicsvariation of total operating power with the associated maximum time at which the reactor experiment can be operated at that power level such that the total number of fission is equal to 1×10^{18} is shown in Fig. 6. The total power ranges from 32 MW to 8.89 kW as the time at these power levels varies from 10 to 3600 s, respectively.

A substantial portion of the total energy released is associated with the solid, static fuel region and, therefore, an important feature of the A buffer gas confined UF_6 flowing experiments is to determine the distribution of power which can be deposited in the UF_6 gaseous fuel contained in the canister. The variations of power deposited in the UF_6 is shown in Fig. 7 for total operating times between 1 and 360 s, The manner in which the power deposited in UF_6 varies for a given total operating time at power is shown as the fission rate ratio of UF_6 to total fission rate varies from 0.01 to 0.20. For example, at a fission rate ratio of 0.10, the power deposited in the UF_6 ranges from 3.2 MW to 8.89 kW for a maximum operating time at full power which varies from 1 to 360 s, respectively. As discussed previously, these ranges of power and time are determined by a value for total number of fissions per test equal to 1×10^{18}, aand the calculated ratio of fission power density of UF_6 to solid fuel of 2.3.

Based on the probable values of canister dimensions, buffer gas injection geometry, temperature, and vortex flow parameters, a nominal design value for total buffer gas weight flow of 200 g/s was estimated for the confined UF_6 flowing reactor experiment. Also, based on isothermal fluid mechanics flow experiments[8], an A bypass ratio of 0.96 has been chosen which should provide good fuel mixture containment in the central region of the vortex flow. This infers that 0.96 of the total injected A flow will be removed from the canister through a perforated section of canister wall via the axial duct located behind this section. The remaining A flow is removed from the canister with the fuel mixture via the on-axis thru-flow ducts. The average time the A resides in the canister between injection and removal is designated as the A residence time and is estimated as, $\tau_A = M_A/W_A$, where M_A is the mass of the A contained in the canister and W_A is the total A weight flow.

Calculations were performed in which the fuel residence time was equal to both one and five times the buffer gas residence time. Fuel weight flow can then be determined by the relationship between mass, residence time, and weight flow. As a result of the variation in fuel weight flow, energy will be removed by convection from the fuel mixture in the canister at different rates. This effect has been included in the results shown in Fig. 8, where the variation in power deposited in UF_6, for total pressures of 1, 4, and 10 atm and for fuel to

buffer gas residence time ratios, τ_F/τ_A, of 1 and 5, are shown as a function of time at power to reach a given bulk-average fuel mixture temperature. For example, when 60 kW is deposited in the UF_6, the reactor could operate at power for 30 and 34 s, respectively, for a total canister operating pressure of 4 atm and fuel-to-buffer gas residence time ratios of 1 and 5. The variation in the required time at power to reach a given gasbbulk-averaged temperature is shown in Fig. 9 for total pressures of 1, 4, and 10 atm,,fuel-to-buffer gas residence time ratios of 1 and 5 and P_F/P_{TOT} ratios of 0.3 and 0.4.

The parametric calculations described above were performed over the ranges of pressure, temperature, power, and gaseous residence time in t the canister, for vortex containment geometry and conditions which are expected to exist in the UF_6 confined experiments. A relationship exists between the temperature and containment characteristics of the gas in the buffer-gas-confined fuel region. The analytical constraint assumed for containment is to require that from the radial stagnation surface inward, the density at any location be equal to the density of the A buffer gas at the radial stagnation surface. With this constraint and for a given total canister gas pressure, there exists an upper limit on the amount of UF_6 (which has the highest molecular weight) that can be mixed with A and He at a given temperature. Thus, a further increase in the amount of UF_6 confined in the fuel region can occur if either the total canister gas pressure increases, or if energy is added to the fuel region gas such that the fuel region temperature increases while the total canister gas pressure and density in the fuel region remain fixed. In the latter instance, constant density is attained by replacing some light gas, He, by an equivalent amount of heavy gas, UF_6.

Summary of Results

Based on the analytical results presented in Figs. 4 through 9, it appears feasible to conduct initial argon buffer-gas confined flowing UF_6 tests using a canister geometry similar to that used in the static UF_6 tests[4] and planned flowing UF_6 tests. Specific operating characteristics for six different tests have been selected from the parametric data in Figs. 4 through 9 and are given in TABLE I. Operating characteristics are shown for power levels of 100 kW and 1 MW, and for total cavity pressures of 1 and 4 atm. This pressure range was chosen for the calculations of the buffer gas confined flowing UF_6 tests because of the upper limit of 4 atm pressure for the aluminum canisters designed for the static UF_6 tests and planned flowing UF_6 tests. Higher performance buffer gas confined flowing UF_6 tests are planned with canisters designed to operate at a pressure in the range of 10 atm. The results indicate that for a total pressure of 1 atm and total power of 100 kW, small UF_6 gas temperature increases of 5 and 27 K are expected in which the fuel residence time is 1 and 5 times the buffer gas residence time, respectively. A considerably higher total power would be required to bring about a 500 to 1000 K increase in UF_6 gas temperature. The small amountsof UF_6 contained, $\approx$ 40 g, and short residence time of the gases, at a pressure of 1 atm, do not appear to be conducive to generating a hot UF_6 gas. The results in TABLE I, for which the total canister pressure is 4 atm, are considerably more interesting. Temperature increases in the UF_6 gas of 100 to approximately 1000 K have been calculated for a total power level between 100 kW and 1 MW, respectively. An important effect to be cognizant of is illustrated by comparing the results for a pressure of 4 atm as the total power is increased. For equivalent gas residence times, the amount of UF_6 which can be contained increases as the gas temperature increases in order to satisfy the conditions of constant total pressure and a constant total density in the fuel region equal to the A buffer gas density at a temperature of 400 K. Therefore, for an initial UF_6 contained mass, as the total power is increased, the power deposited in the UF_6 increases proportionately with an accompanying increase in UF_6 gas temperature. This allows an increase in the contained UF_6 mass until a new steady-state level is reached.

References

1. Helmick, H. H., G. A. Jarvis, J. S. Kendall, and T. S. Latham: Preliminary Study of Plasma Nuclear Reactor Feasibility. Los Alamos Scientific Laboratory Report LA-5679, Prepared Under NASA Contract W-13721, August 1974.

2. Thom, K., R. T. Schneider, and F. C. Schwenk: Physics and Potentials of Fissioning Plasmas for Space Power and Propulsion. International Astronuatics Federation, XXVth Congress, Amsterdam, Holland, September 30 - October 5, 1974.

3. Latham, T. S., F. R. Biancardi, and R. J. Rodgers: Applications of Plasma Core Reactors to Terrestrial Energy Systems. AIAA Paper 74-1074, AIAA/SAE 10th Propulsion Conference, San Diego, CA., October 21-23, 1974.

4. Bernard, W., H. H. Helmick, G. J. Jarvis, E. A. Plassmann, and R. H. White: Research Program on Plasma Core Assembly. Los Alamos Scientific Laboratory Report LA-5971-MS, May 1975.

5. Jaminet, J. F. and J. S. Kendall: Initial Test Results of Circulation System for Planned Flowing Uranium Hexafluoride Cavity Reactor Experiments. United Technologies Research Center Report R76-912134-1, March 1976.

6. Orndoff, J. D. and H. C. Paxton: Operating Procedures for the Pajarito Site Critical Assembly Facility. Los Alamos Scientific

Laboratory Report LA-4037-SOP, Rev. 1973.

7. Rodgers, R. J., T. S. Latham, and J. F. Jaminet: Preliminary Design and Analyses of Planned Flowing Uranium Hexafluoride Cavity Reactor Experiments. United Technologies Research Center Report R76-912137-1, May 1976.

8. Jaminet, J. F. and A. E. Mensing: Experimental Investigation of Simulated-Fuel Containment in RF Heated and Unheated Two-Component Vortexes. United Aircraft Research Laboratories Report J-910900-2, Prepared Under Contract SNPC-70, September 1970.

9. Mensing, A. E. and J. F. Jaminet: Experimental Investigations of Heavy-Gas Containment in R-F Heated and Unheated Two-Component Vortexes. United Aircraft Research Laboratories Report H-910091-20, Prepared Under Contract NASw-847, September 1969.

10. Kendall, J. S.: Experimental Investigation of Heavy-Gas Containment in Constant-Temperature Radial-Inflow Vortexes. United Aircraft Research Laboratories Report F-910091-15, September 1967. Also issued as NASA CR-1029.

11. Mensing, A. E. and J. S. Kendall: Experimental Investigation of Containment of a Heavy Gas in a Jet-Driven Light-Gas Vortex. United Aircraft Research Laboratories Report D-910091-4, March 1965. Also issued as NASA CR-68926.

12. Rodgers, R. J., T. S. Latham, and N. L. Krascella: Analyses of Low-Power and Plasma Core Cavity Reactor Experiments. United Technologues Research Center Report R75-911908-1, Prepared Under Contract XP4-54459-1, May 1975.

List of Symbols

FR_{UF_6}	UF_6 fission rate/total fission rate, dimensionless
M_c	Critical mass, Kg of U
M_{UF_6}	Mass of confined UF_6, g
MW_{UF_6}	Molecular weight of UF_6, g/mole
MW_{U-235}	Molecular weight of U-235, g/mole
P_F/P_{TOT}	Ratio of volume-averaged fuel to peripheral wall pressure, dimensionless
P_{TOT}	Total pressure, atm
Q_{TOT}	Total power, W
Q_{UF_6}	Power deposited in contained UF_6, W or kW
T_{CL}	Gas temperature, deg K
T_{EOF}	Temperature at edge-of-fuel, deg K
$t_{Q_{TOT}}$	Time of full power, s
$t_{T_{CL}}$	Time at power to reach temperature, s

Greek Symbols

τ_A	Argon residence time in canister, s
τ_F	Fuel residence time in canister, s
$\frac{\phi^{UF_6}}{\phi^{SOLID}}$	Power density ratio, dimensionless

TABLE I

CALCULATED OPERATING CHARACTERISTICS FOR ARGON BUFFER-GAS CONFINED UF_6 CAVITY REACTOR EXPERIMENTS

Total Fissions = 1×10^{18}
Power Density in UF_6 = 2.3 Power Density in Solid Fuel

Total Pressure, atm	1	1	4	4	4	4
Total Power, kW	100	100	100	100	1000	1000
Power Deposited in UF_6, kW	1.3	1.3	4.8	5.2	56	65
Mass of UF_6 Confined, g	37	38	150	162	175	205
Temperature Increase in UF_6, K	5	27	20	100	240	1040
Test Time, s	320	320	320	320	32	32
Fuel Mixture Residence Time, s	0.3	1.5	1.2	6.0	1.2	6.0
Argon Residence Time, s	0.3	0.3	1.2	1.2	1.2	1.2

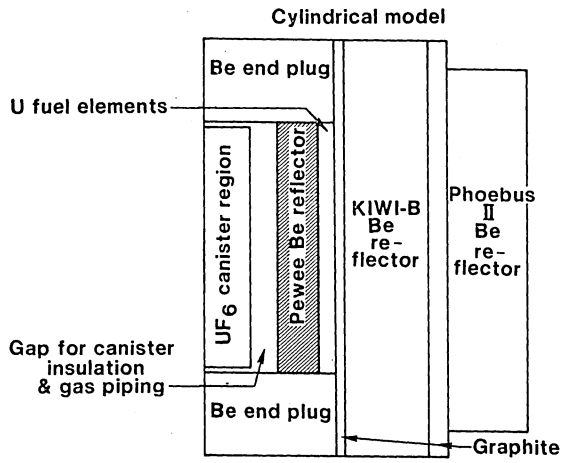

Fig. 1 Reflector-Moderator Configuration for Low-Power Critical Experiments.

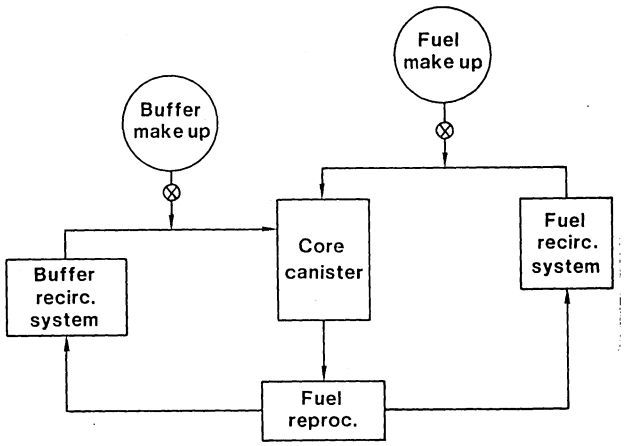

Fig. 3 Preliminary Schematic of Fuel Confinement Flow System.

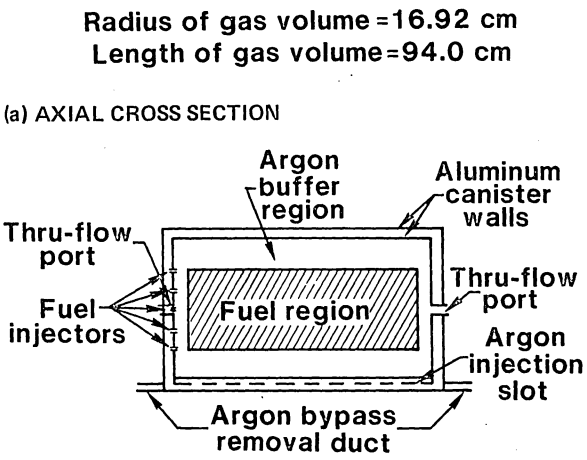

Fig. 2 Canister Injection and Exhaust Configuration for Buffer Gas Confined UF_6 Flowing Experiments.

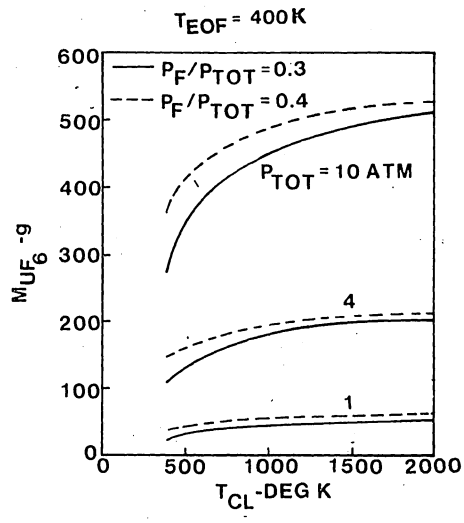

Fig. 4 Variation of UF_6 Contained Mass With Gas Temperature.

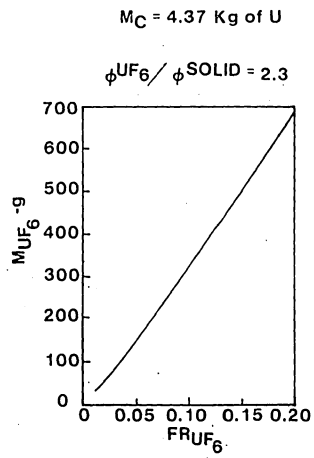

Fig. 5 Variation of UF_6 Contained Mass With Fission Rate Ratio.

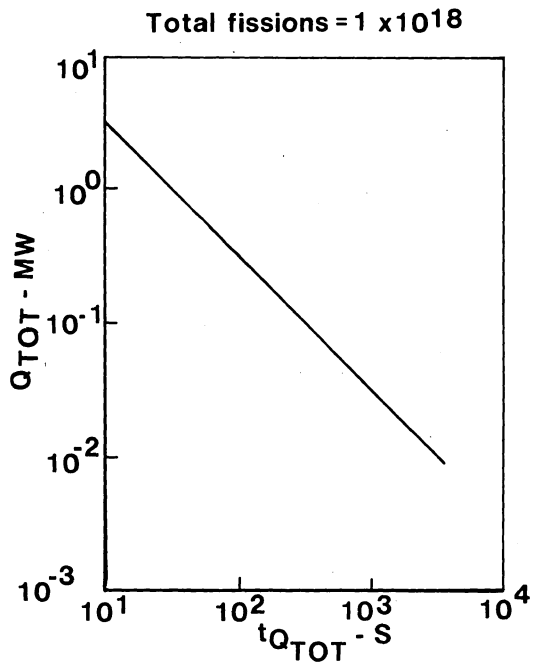

Fig. 6 Variation of Total Operating Power With Maximum Time of Operation Between 10 and 3600 Seconds.

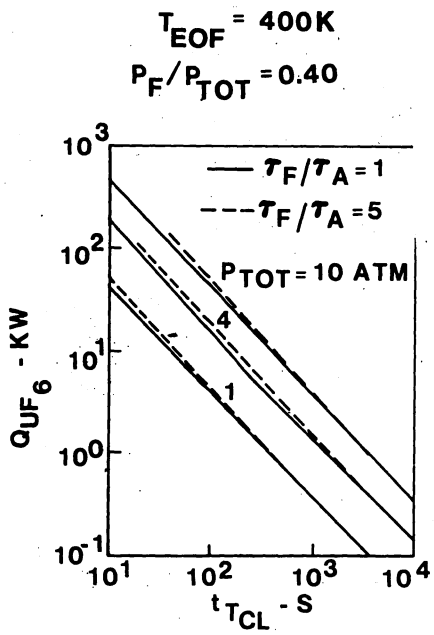

Fig. 8 Variation of Power Deposited in Contained UF_6 With Time at Power to Reach Temperature.

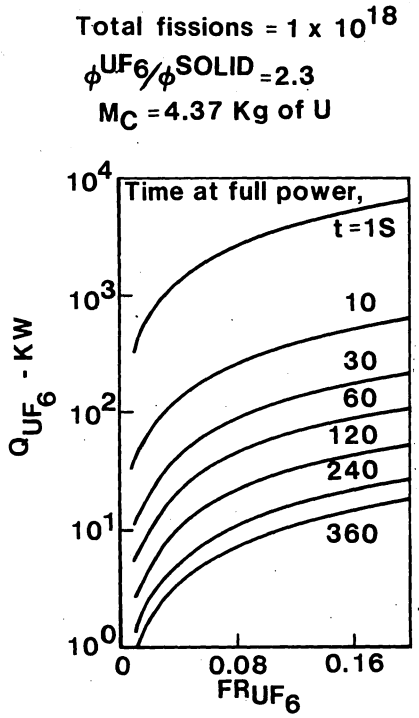

Fig. 7 Variation of Power Deposited in UF_6 With Fission Rate Ratio for Operating Time Between 1 and 360 Seconds.

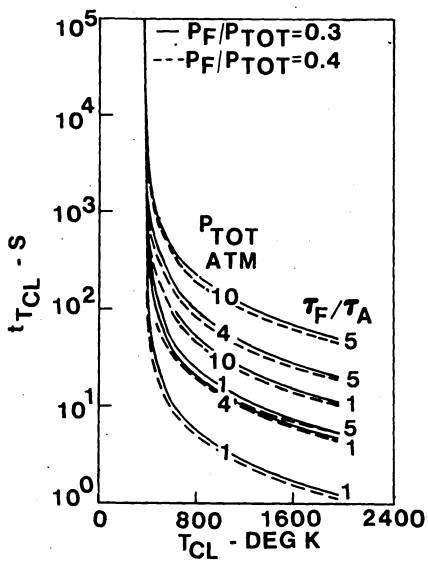

Fig. 9 Variation of Time at Power for Contained UF_6 to Reach Temperature.

DISCUSSION

J. BLUE: If the object of this experiment is to observe the uranium plasma with a fairly high fission density, another way to do this without having the complications of criticality would be to take the aluminum can and have it bombarded with 100 microamperes of 500 MEV protons. You could achieve the same kind of fission product power densities without the complications of criticality and it would allow you to do some instrumentation that you are not able to do in a reactor environment where you have to bring diagnostics into a high flux region or else you have to take your instruments so far away that the information obtained is diluted in value.

R. J. RODGERS: What is the deposition profile of the proton beam in the gas? Does it really simulate energy deposition in the gas?

J. BLUE: Energy deposition in the gas is the result of the protons causing fission, so when a uranium fission, there is very little difference whether it was fissioned by a neutron or a proton. It is true there is some difference in the energy distribution. The protons themselves also produce ionization of the gas. The ionization caused by the protons is very much like the ionization caused by gamma rays. So it would be unreasonable to expect that the protons would do anything that would be drastically different. The advantage with proton beams is that you can focus them onto the region and you can make the density higher because you make the volume smaller than the volume you are talking about here.

T. S. LATHAM: We have done years of small-volume simulation with our RF plasma experiments. One of the things we are striving to do now is to get up to cannister sizes and flow volumes that are more like full-scale devices.

H. H. HELMICK: The reason we are doing criticality experiments is that in looking at all the options at LASL, these are the cheapest experiments. To mount an experiment at LANF is a very long leadtime job that is pretty expensive because of the large number of people involved in that facility; we know that sooner or later we need to do the checkouts we are talking about now, and since it is easy to conduct this with merely a four-man team, it is a factor of 20 cheaper than equivalent experimental time at LANF.

CIRCULATION SYSTEM FOR FLOWING URANIUM HEXAFLUORIDE CAVITY REACTOR EXPERIMENTS*

J. F. Jaminet and J. S. Kendall
Power Systems Technology Section, Fluid Dynamics Laboratory
United Technologies Research Center
East Hartford, Connecticut

Abstract

Research related to determining the feasibility of producing continuous power from fissile fuel in the gaseous state is presented. In addition to high-thrust, high-specific-impulse space propulsion applications, development of gaseous nuclear reactors could open new options for meeting future energy needs. Accomplishment of the UF_6 critical cavity experiments, currently in progress, and planned confined flowing UF_6 initial experiments requires development of reliable techniques for handling heated UF_6 throughout extended ranges of temperature, pressure, and flow rate. The development of three laboratory-scale flow systems for handling gaseous UF_6 at temperatures up to 500 K, pressures up to approximately 40 atm, and continuous flow rates up to approximately 50 g/s is presented.

A UF_6 handling system fabricated for static critical tests currently being conducted at Los Alamos Scientific Laboratory (LASL) is described. The system was designed to supply UF_6 to a double-walled aluminum core canister assembly at temperatures between 300 K and 400 K and pressures up to 4 atm. A second UF_6 handling system designed to provide a circulating flow of up to 50 g/s of gaseous UF_6 in a closed-loop through a double-walled aluminum core canister with controlled temperature and pressure is described. This system will be used in planned cavity reactor experiments at LASL in which UF_6 will flow through an active cavity reactor core region. Data from flow tests using UF_6 and UF_6/He mixtures with this system at flow rates up to approximately 12 g/s and pressures up to 4 atm are presented. A third UF_6 handling system fabricated to provide a continuous flow of UF_6 at flow rates up to 5 g/s and at pressures up to 40 atm for use in rf-heated, uranium plasma confinement experiments is described.

Introduction

Research to investigate the possibility of producing continuous power from fissile fuel in the gaseous state is presently being conducted. In addition to high-thrust, high-specific-impulse space propulsion applications, development of gaseous fueled nuclear reactors could open new options for meeting future energy needs, such as: (1) magnetohydrodynamic electric generating power systems; (2) photochemical or thermochemical dissociation of water to produce hydrogen; and (3) direct nuclear pumping of lasers by fission fragment energy deposition in UF_6 and lasing gas mixtures.

Extraction of power from a fission process with nuclear fuel in gaseous form allows operation at much higher temperatures than conventional nuclear reactors, leading to more efficient thermodynamic cycles. The continuous peprocessing of gaseous nuclear fuel leads to a low steady-state fission product inventory in the reactor and limits the buildup of long half-life transuranium elements.

A series of experiments utilizing a beryllium reflector-moderator cavity critical assembly has been initiated at LASL to establish the feasibility of fissioning UF_6 gas reactors and/or uranium plasma reactors.[1] The cavity critical assembly, shown in the photograph in Fig. 1, has provision for raising or lowering a fueled core from the reflector and removing the core from beneath the reflector assembly. A core canister assembly containing gaseous UF_6 is positioned within the reflector cavity. Cavity configurations of systematically increasing complexity will be used to progress from simply distributed uranium foil experiments to the use of flowing, vortex-confined, gaseous UF_6 fuel. Future experiments are being planned in which an approximately 5 MW self-critical fissioning uranium plasma core reactor will be operated.

Accomplishment of the static UF_6 critical cavity experiments, currently in progress, and planned confined flowing UF_6 initial experiments requires the development of reliable techniques for handling heated UF_6 throughout extended ranges of temperature, pressure, and flow rate. This paper describes the development of three laboratory-scale flow systems for handling gaseous UF_6 at temperatures up to 500 K, pressures up to approximately 40 atm, and continuous flow rates up to approximately 50 g/s.

UF_6 Handling System for Static Critical Tests

A UF_6 handling system was fabricated for static critical tests currently being conducted at LASL[2]. The major components of the static handling system are the thermally controlled 4 ℓ capacity UF_6 supply system, the 85 ℓ internal volume double-walled aluminum core canister

*Research sponsored by Los Alamos Scientific Laboratory, Contracts XP4-54459-1 and XP5-54474-1.

and the N_2 flow system used for core canister thermal control. The aluminum core canister is similar to that used in the flowing UF_6 handling system and is described in detail in the following section.

The general arrangement of the static UF_6 handling system is shown in the photograph in Fig. 2. The system is mounted on a movable frame and is attached through stainless steel flexible hoses to the double-walled aluminum core canister assembly. This allows the core canister assembly to be raised and lowered into position within the cavity critical assembly. Materials in the handling system were limited to the use of Monel, stainless steel, and aluminum due to the extreme chemical reactivity of UF_6. Gaseous UF_6 is introduced into the canister by control of the UF_6 supply oven temperature. The UF_6 is removed from the cavity and returned to the supply cylinders by cryopumping and desublimation. Also shown in the photograph are connections to vacuum and cold-trap systems for purging and filling of the UF_6 handling system.

The UF_6 supply system is designed to supply UF_6 to the core canister at temperatures between 300 K and 400 K and pressures up to 4 atm. The system is shown schematically in Fig. 3. This system consists of four 1000 ml Monel cylinders connected through a manifold to the UF_6 supply line which is in turn directly connected to the aluminum core canister. The cylinders are located within a circulating flow oven whose temperature can be controlled within approximately ± 1 C. The oven provides the heat required to vaporize UF_6 within the supply cylinders and produce the desired test pressure. The supply system is double-valved to reduce the possibility of leakage of UF_6 into the oven environment. Each cylinder is equipped with a manual Monel diaphragm shutoff valve. In addition, the manifold connecting the four supply cylinders is equipped with a stainless steel remotely actuated bellows valve. A copper coil is soldered to the bottom of each cylinder through which liquid N_2 may be passed to cryopump the UF_6 out of the canister and into the cylinders.

Thermal control of the UF_6 supply in the core canister and flexible ducts connecting the core canister to the UF_6 supply is provided by flowing heated N_2 through the flexible ducts and core canister assembly. The N_2 flow system is also shown in the schematic in Fig. 2. The major components of the N_2 system are the bellows pump, N_2 heater, pressure control system, and N_2 flow meter. A bellows pump having a 2.4 ℓ/s capacity is utilized to provide a flow of circulating N_2 through the system. The pressure within the N_2 system is automatically adjusted, using a pressure control system, to a value greater than the core canister pressure. The N_2 is heated by a 2500 W resistance heater located downstream of the bellows pump in the flow system. Also included in the N_2 flow system are a flow meter, pressure gages, control valves, and associated equipment utilized in tests to determine the flow characteristics of the N_2 loop. Static pressure and vacuum leak tests were performed on the gas flow system upon completion of fabrication. The UF_6 system was determined to be helium leak tight over the range of pressures from approximately 5×10^{-9} atm to 10 atm.

A series of initial tests using this equipment was conducted to verify the operational characteristics of the system. Thermal response tests were conducted to determine the rate of heatup and cooldown of each system component. This information was necessary for documentation of the transient thermal characteristics of the system. The results of the thermal response tests indicated that no rapid rate-of-change temperature fluctuations are likely to occur in the system during the static critical tests.

UF_6 Handling System for Flowing Critical Tests

A UF_6 handling system was designed and fabricated to provide a circulating flow of up to 50 g/s of gaseous UF_6 or a UF_6-He mixture in a closed-loop with controlled temperature and pressure.[3] The major components of the flowing UF_6 system are similar to the static UF_6 handling system except for the addition of a UF_6 pump, flow loop, and flow and pressure instrumentation.

The UF_6 and N_2 circulation system including the core canister is completely enclosed within a Lucite safety enclosure to prevent any possibility of UF_6 leakage to the surrounding environment. A 30,000 ℓ/min airflow is continuously exhausted from the safety enclosure to a scrubber system. In the scrubber the airflow is continuously washed by a spray of water/sodium bicarbonate solution and then passed through an absolute HEPA filter prior to venting to the atmosphere. The HEPA filter removes > 99.999 percent of all particles greater than 0.3 μm dia.

The UF_6 circulation system shown in the photographs in Figs. 4 and 5 is mounted on a movable frame and is attached through flexible lines to the double-walled aluminum core canister assembly. The circulation system equipment is shown in the photographs in Figs. 4 and 5 prior to installation of heating tapes and insulation used during test operation. Gaseous UF_6 is introduced into the circulation system by increasing the UF_6 supply oven temperature, thereby creating a high UF_6 vapor pressure. The UF_6 is removed from the circulation system by desubliming the UF_6 from a UF_6-He mixture which is continuously pumped through one of the oven supply cylinders. The circulation system equipment is designed for operation at test pressure levels up to 4 atm and temperatures up to 400 K.

Details of the UF_6 circulation system are shown in the schematic in Fig. 6. The circulation system equipment is comprised of two gas flow

systems, the UF_6 supply and flow system and the N_2 flow system. The UF_6 supply system consists of two 1.0 liter volume UF_6 supply cylinders which are connected through appropriate valving and piping to the UF_6 flow, or circulation, system. One of the cylinders is a single-port Monel cylinder which provides a convenient location for additional UF_6 storage. The other cylinder, called the transfer cylinder, is a stainless steel cylinder designed to allow flow through the cylinder from the UF_6 circulation system. This design provides for removal of the UF_6 from a UF_6-He mixture in the circulation system by continuous desubliming of the UF_6 as the UF_6-He mixture flows through the cylinder. The cylinder has two close-coupled valves allowing the cylinder to be removed from the oven for filling and weighing. Weighing of the cylinder before and after a UF_6 transfer is the method utilized to determine the exact amount of UF_6 which is either transferred into or removed from the circulation system. The present accuracy of the weighing procedure is estimated to be ± 0.5 g. UF_6 is transferred into both cylinders by cryo-pumping and removed by heating to produce a high UF_6 vapor pressure. A copper coil is brazed to the bottom of each cylinder through which liquid N_2 is passed to cryo-pump or desublime the UF_6 into the cylinder. During the cryo-pumping or desubliming process the upper halves of the cylinders are heated to approximately 350 K using the supply system oven to prevent plugging of the cylinder inlet tubing with UF_6. A vacuum connection is provided in the cylinder flow loop to provide for removal of any air that is trapped in the lines when the transfer cylinder is reconnected into the loop.

The cylinders are located within an air circulating-flow oven whose temperature can be controlled within approximately ± 1 K. The oven provides the heat required to vaporize UF_6 within the cylinders and produce a desired UF_6 vapor pressure. The heated UF_6 from the supply cylinders is used to charge the complete circulation system including the double-walled core canister assembly.

The UF_6 flow system consists of a 2.4 ℓ/s bellows pump, a Monel venturi and differential pressure transducer assembly, and appropriate tubing, flexible hoses, and valving to allow circulation of UF_6 through the double-walled core canister assembly. The bellows pump was modified for operation at temperatures up to 450 K by thermally-isolating the motor from the pump body and replacing the crank bearings with special high-temperature versions. The pump is located in a sealed enclosure which is pressurized and heated by the N_2 flow system. This configuration greatly increases the efficiency of the pump at high system static pressures by eliminating the differential static pressure across the bellows.

All components and tubing are wrapped with heater tapes and covered with at least 1.3 cm thickness of Carborundum "Fiberfrax" insulation to maintain the UF_6 in a superheated state by reducing thermal losses. To prevent condensation on the solid surfaces within the circulation system, temperatures in the circulation system are maintained at least 25 K greater than the saturation temperatures corresponding to the system operating pressure. Thus, at a system pressure of 4 atm, the temperatures are maintained at values of approximately 400 K or higher.

Pressure measurements of the UF_6 circulation system were made using three special Monel 6.8 atm maximum full-scale absolute pressure transducers. A Monel venturi was used to measure the UF_6-He mixture flow rate in the UF_6 circulation system. A special wet/wet-type 0.34 atm maximum differential pressure transducer made of 316 stainless steel was used to measure the differential pressure across the venturi assembly.

Thermal control of the UF_6 in the core canister assembly and flexible ducts is provided by flowing heated N_2 through the annular regions in the core canister assembly and the coaxial flexible metal ducts (see Fig. 6). The heated N_2 flow system consists of two 14,000 rpm centrifugal blowers in series, a 750 W resistance heater, and a heater temperature controller. The two 140 slm maximum centrifugal blowers for circulating the heated N_2 were modified for operation at temperatures up to 450 K and pressures up to 5 atm by substituting viton gasket material and fabricating metal cases to replace the original plastic cases. The N_2 flow rate is maintained constant and is monitored by measurement of the pressure difference across the blowers. In initial tests of the N_2 flow system at a system pressure of 1 atm, tests with two different flowmeters resulted in an N_2 flow rate of approximately 225 slm with a total differential pressure across both centrifugal blowers of 0.22 atm. All subsequent tests were conducted without a flowmeter in the N_2 system to minimize thermal losses and with the N_2 system differential pressure across the blowers equal to approximately 0.22 atm.

The N_2 flow system is designed to be maintained at a pressure slightly higher than the UF_6 system pressure during UF_6 flow tests. This serves to eliminate any possibility of UF_6 leakage into the N_2 flow loop which would increase the difficulty of recovering the UF_6. Any UF_6 remaining in the UF_6 circulation system or that has escaped into the N_2 flow system can be removed by using the N_2 purge and vacuum system shown in Fig. 6. The vacuum system flow is first passed through a cold trap maintained at liquid N_2 saturation temperature, 78 K. The flow then passes through a NaF chemical trap before being exhausted from the vacuum pump to the scrubber system.

Core Canister Assembly

The core canister assembly shown in detail in Fig. 7 is made up of two concentric 6061-0 aluminum canisters. Alloy 6061 was selected as the primary canister material due to its low thermal neutron

cross section, strength properties, and weldability. The physical dimensions were chosen such that the approximate 85 ℓ volume of UF_6 contained within the inner canister will occupy approximately 40 percent of the volume enclosed by the reflector-moderator configuration. The core canister and flexible metal hose assembly is designed to be raised and lowered into and out of its operating position within the cavity critical assembly. The 34-cm-OD inner canister has provision for positioning fission wires at two locations and also has provision for installation of a 13-cm-dia fused-silica window at the top of the canister for transmission of possible fission fragment-inducedopptical radiation emission which may be produced during the cavity experiments. During the tests described herein, an aluminum plate with provision for pressure and temperature sensors was installed in lieu of the fused-silica window. The 37-cm-OD outer canister is designed to enclose an annular flow region for thermal control of the inner canister. During flow tests the inner canister contains flowing UF_6 at a preselected pressure and temperature. The heated UF_6 flows to and from the core canister via heated flexible ducts. Control of the UF_6 temperature in the core canister assembly and coaxial flexible ducts is provided by flowing heated nitrogen to the annulus in the core canister and coaxial flexible ducts. The canister design for the present flowing UF_6 cavity reactor experiments is similar to that fabricated for the static critical experiments. However, several changes have been made in the flowing UF_6 canister design. These include provision for the continuous flow of UF_6 into and out of the canister, the addition of larger diameter tubing for the inlet and outlet flow, and a larger diameter (13 cm) viewport at the top of the canister.

Final assembly leak tests were performed on the core canister assembly both during and upon completion of fabrication. The inner canister was evacuated to approximately 10^{-5} Torr and leak tested using a helium leak detector. After completion of assembly of the outer canister around the inner canister, the outer canister was also evacuated to approximately 10^{-5} Torr and leak tested using a helium leak detector. The helium leak detector was sensitive to a leak rate of approximately 3.5×10^{-7} std. cc/s. Static pressure tests up to 6 atm were also conducted on the complete core canister assembly. No leakage was noted in any part of the canister core assembly during any of these tests.

Results of UF_6 Circulation System Tests

Initial UF_6 circulation system tests consisted of vacuum leak tests in which the complete UF_6 system was sealed-off and the rate of pressure rise monitored. This test resulted in a pressure rate-of-rise of approximately 3.7 μm/hr from a base pressure of 10^{-5} Torr over a 72 hour time period. Initial UF_6 circulation system flow tests consisted of flow measurements with 1 atm pressure of He in the system. The three absolute pressure transducers were monitored and indicated pressure pulses of less than 1 percent of full-scale at the outlet of the bellows pump. However, considerable pulsation at a frequency of 28.2 Hz was noted in the output of the differential pressure transducer at the venturi. These pressure pulsations originated from the bellows pump.

The output of the 4 pressure transducers was measured using a Honeywell Visicorder. All 4 transducers were calibrated in-situ in preliminary tests using a Wallace and Tiernan 0-6.8 atm maximum full-scale pressure gage connected to the flow system. During initial operation of the flow system, the proper heater control settings to provide approximately uniform temperature around the flow system were determined. The flow system was operated at temperatures up to approximately 360 K and the UF_6 supply oven up to 450 K. Using the inlet and outlet temperatures at the core canister, it was calculated that the total thermal loss to the atmosphere from the core canister was approximately 18.1 W at a canister fuel operating temperature of 338 K.

The UF_6 circulation system was operated as follows. Beginning with the system initially filled with dry He at 1 atm, the N_2 flow system was filled to 1 atm and all heaters, as well as the UF_6 bellows pump and N_2 blowers, were turned on. The heater controllers were usually set higher than the normal operating setting initially and gradually reduced during the system heatup to shorten the heatup time. The complete flow loop reached normal operating temperatures in less than 1 hour.

The initial loading of UF_6 into the circulation system was accomplished as follows. The complete UF_6 circulation system, with dry He at 1 atm, and the N_2 flow system were brought up to the desired operating temperature. The bellows pump was shutoff and the heated He evacuated from the UF_6 circulation system. UF_6 from the supply oven at a temperature of approximately 425 K (greater than 10 atm vapor pressure) was then piped to the UF_6 circulation system. A transfer of 463 g of UF_6 to the circulation system was then accomplished. For the measured circulation system volume of 90.05 ℓ this quantity of UF_6 results in a vapor pressure of approximately 0.41 atm at a temperature of 340 K.

Following the introduction of the UF_6 into the circulation system, flow tests were conducted using first pure UF_6 and subsequently various UF_6-He mixture ratios. Additional He was then added to bring the circulation system to a preselected total pressure. He was used in the circulation system to tailor the UF_6-He mixture density to correspond to that of pure UF_6 at the higher temperature which will exist in the planned critical fissioning UF_6 cavity experiments. This provides data enabling better simulation of the core canister flow conditions expected in future tests.

The results of initial tests with He only, UF_6 only, and UF_6-He mixtures are shown in Fig. 8. wherein the fuel mass flow rate is plotted versus the total pressure in the circulation system and core canister. The three flow loop gas composi-

tions are delineated as indicated by the three types of symbols. The variation in mass flow rate at a given total pressure for the He and UF_6-He data was obtained by throttling the circulation system flow using valve No. 2 (see Fig. 6) during dynamic tests.

As would be expected, the mass flow rate increases with increasing gas density, or system total pressure and with increasing gas molecular weight. The maximum mass flow rate obtained was 12.5 g/s at 3.55 atm pressure. Future tests are planned in which much greater loadings of UF_6 in the circulation system at temperatures up to approximately 450 K will be conducted. It should then be possible to obtain the approximate 50 g/s design mass flow rate of the system.

Dynamic simulation pressure tests of the circulation system were conducted in which the inlet and outlet valves (Nos. 2 and 3 in Fig. 6) were throttled or shut off completely for short periods of time with the bellows pump operating. In all tests, the pressure changes were slow and easily controlled. This is to be expected since the core canister volume (85 ℓ) is large compared to the capacity of the bellows pump (2.4 ℓ/s).

A special UF_6 transfer test using the transfer and recovery system in the supply oven was conducted. Using a transfer bottle containing 789 g of UF_6 in the supply oven, 25 g of UF_6 was transferred to the evacuated and heated circulation system. Helium was then added to bring the circulation system up to 1 atm total static pressure. Recovery of the UF_6-He mixture was then accomplished as follows. Referring to Fig. 6, Valve 1, the air-operated valve, and the four hand valves in the transfer bottle loop in the supply oven were opened. Valve 2 in the circulation system was throttled almost completely closed allowing only a slight bypass flow in the main UF_6 circulation system. The supply oven and, therefore, the upper half of the transfer bottle was heated to approximately 350 K. Liquid N_2 was simultaneously passed through the transfer bottle cooling coils thus chilling the lower half of the bottle. After approximately one hour of operation, measurements indicated that 20 $\pm$0.5 g of the 25 $\pm$0.5 g of UF_6 originally transferred into the circulation system were recovered. This was accomplished using the original transfer bottle in the supply oven which therefore still contained 764 g of UF_6 at the start of the recovery operation. Evidence from this test indicates this transfer and recovery system will be suitable for use in flowing UF_6 critical experiments.

UF_6 Handling System for RF Plasma Confinement Tests

A high pressure UF_6 supply system for rf plasma confinement tests was fabricated to supply UF_6 to test chambers operating at pressures up to 20 atm and to provide UF_6 at mass flow rates up to 5 g/s. The principal components of the system are the UF_6 boiler, the boiler heat supply system, and the UF_6 condenser system. A schematic diagram of the flowing UF_6 system is shown in Fig. 9.

The UF_6 boiler was fabricated by electron beam welding two 200-atm-rated working pressure, 1 ℓ capacity, Monel gas sampling cylinders to form a single 2 ℓ capacity cylinder. A multiturn coil heat exchanger, fabricated from 6.4-mm-dia Monel tubing, was installed in the bottom of the UF_6 boiler. Thermocouple wells which protrude into the gaseous or liquid UF_6 are installed at the top and bottom of the boiler.

Two 1750 W semicylindrical electrical heaters, which surround the boiler, were used to bring the boiler to desired equilibrium temperature and pressure prior to flowing UF_6 from the boiler. During flow conditions, gaseous N_2 heated by electrical heaters may be supplied to the heat exchanger in the UF_6 boiler. The N_2 flow rate and electrical power may be varied to control the amount of heat supplied to the heat exchanger in the UF_6 and, thus, to control the rate of evaporation of UF_6 in the boiler. During periods when no UF_6 is flowing, the hot N_2 can be bypassed around the boiler.

During operation of the system, the gaseous UF_6 flows from the boiler, through a metering valve and a Matheson linear mass flow meter prior to entering the test chamber. The gaseous UF_6 is collected in the UF_6 condenser system located downstream of the simulated experiment chamber. The condenser consists of two 500 ml capacity 120 atm stainless steel cylinders immersed in a bath of liquid N_2. A 6.1 ℓ/s vacuum pump is used to evacuate the system before UF_6 flow tests are initiated. During tests the vacuum pump was isolated from the flow system by a welded bellows valve. After completion of a test the trapped UF_6 was heated and transferred to a NaOH trap for removal of UF_6 by chemical reaction as Na_2UO_4 or $Na_2U_2O_7$.

A number of initial tests were made of the high pressure UF_6 flow system. All UF_6 flow lines, valves, and the flow meter were heated by means of electric heating tape. Recorders were used to monitor thermocouples, pressure transducers, and flow meter output. At a UF_6 boiler temperature of 500 K and a pressure of approximately 40 atm a maximum UF_6 flow rate of 5.6 g/s was achieved.

The high pressure UF_6 handling system was used extensively in rf-plasma confinement tests to simulate flow and thermal conditions expected in initial uranium plasma core reactor experiments.[5] During these tests the system operated reliably and satisfactorily met the flow and pressure requirements of the plasma test program. The operating experience gained in the tests with all three UF_6 handling systems verified the importance of maintaining uniform system temperature, minimum water vapor content, and system cleanliness to insure system performance and reliability.

Future work on UF_6 handling systems involves the development of UF_6 flow systems for cavity critical experiments in which UF_6 is continuously injected and confined in an argon vortex flow in the core canister. Equipment for continuously separating the UF_6 from the argon and reprocessing the UF_6 for reuse is presently being designed.[5]

References

1. Helmick, H. H., G. A. Jarvis, J. S. Kendall, and T. S. Latham: Preliminary Study of Plasma Nuclear Reactor Feasibility. Los Alamos Scientific Laboratory Report LA-5679, August 1974.

2. Kendall, J. S. and R. C. Stoeffler: Development of Equipment for Handling Uranium Hexafluoride in Cavity Reactor and Plasma Experiments. United Technologies Research Center Report R75-911909-1, May 1975.

3. Jaminet, J. F. and J. S. Kendall: Initial Test Results of Circulation System for Planned Flowing Uranium Hexafluoride Cavity Reactor Experiments. United Technologies Research Center Report R76-912134-1, March 1976.

4. Roman, W. C.: Laboratory-Scale Uranium RF Plasma Confinement Experiments. United Technologies Research Center Report R76-912205, May 1976.

5. Rodgers, R. J., T. S. Latham, and J. F. Jaminet: Preliminary Design and Analyses of Planned Flowing Uranium Hexafluoride Cavity Reactor Experiments. United Technologies Research Center Report R76-912137-1, March 1976.

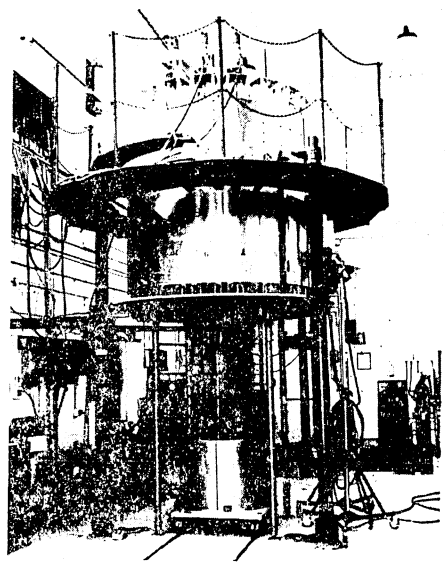

Fig. 1 LASL Critical Cavity Assembly.

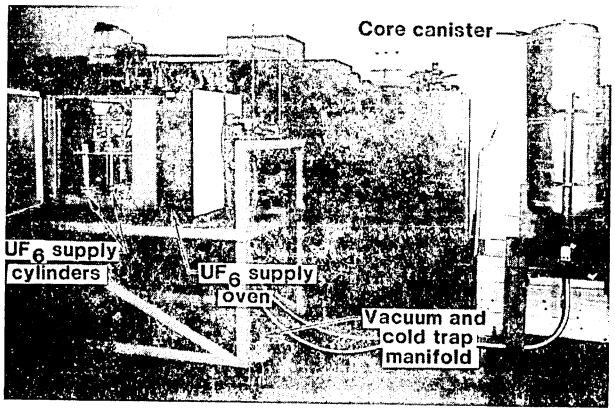

Fig. 2 Photograph of UF_6 Handling Equipment for Static Tests.

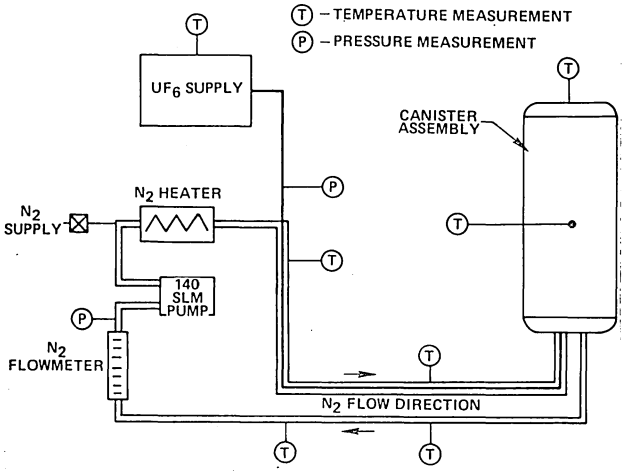

Fig. 3 Schematic of UF_6 Handling Equipment for Static Tests.

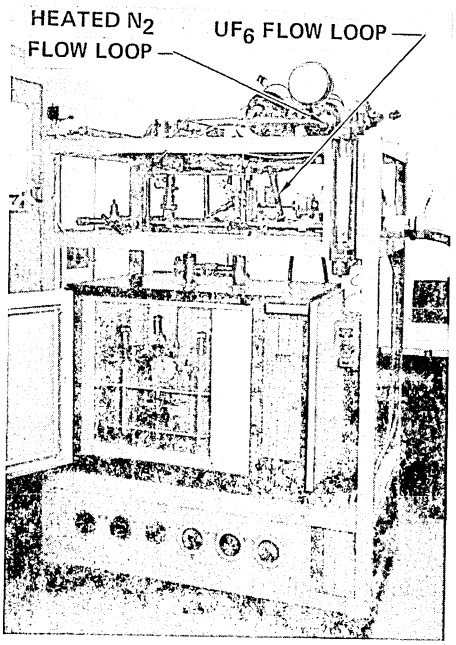

Fig. 4 Photograph of UF_6 and N_2 Flow Loops.

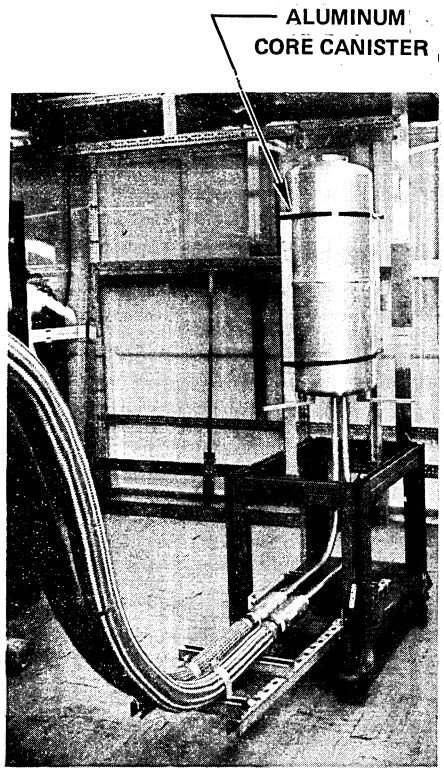

Fig. 5 Photograph of Core Canister for UF_6 Flow Tests.

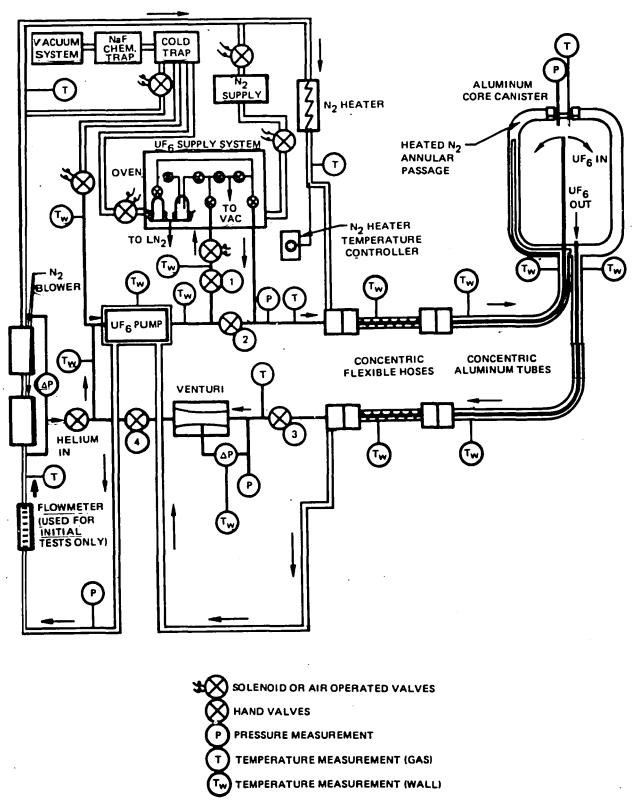

Fig. 6 Schematic of UF_6 Handling Equipment for Flow Tests.

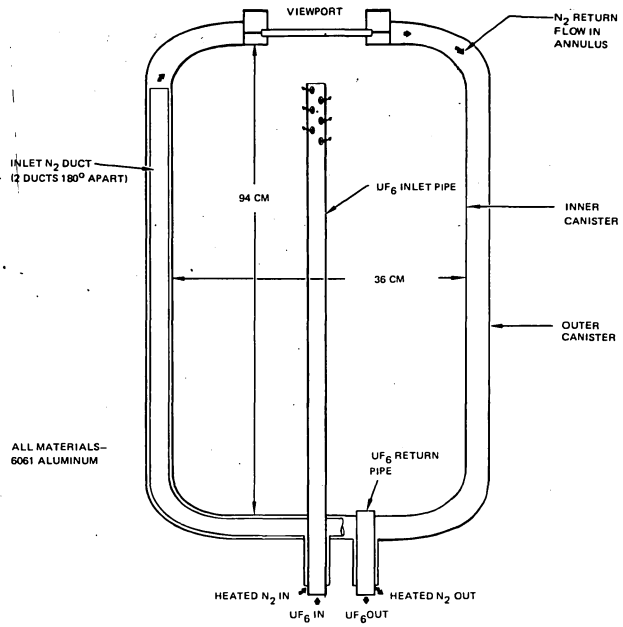

Fig. 7 Sketch of Core Canister Assembly.

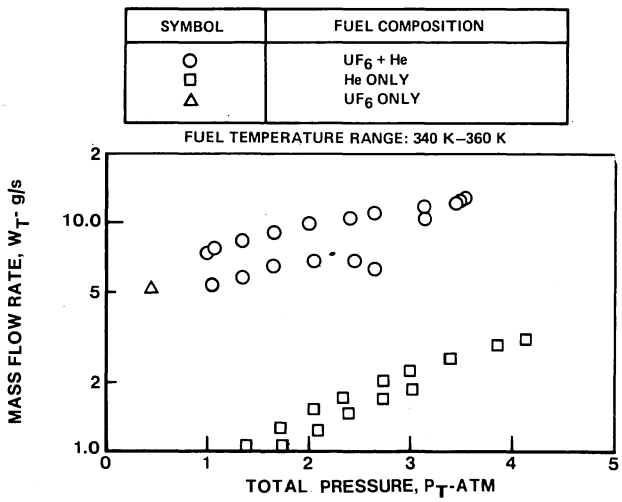

Fig. 8 Results of Initial UF_6 Flow Tests.

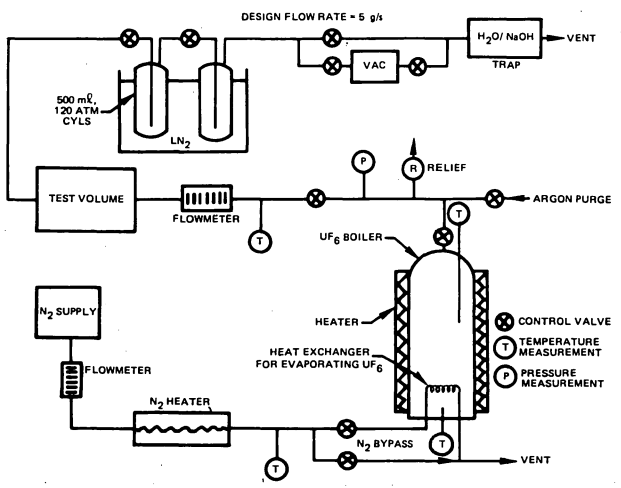

Fig. 9 Schematic of UF_6 Handling Equipment for RF Plasma Confinement Tests.

DISCUSSION

T. C. MAGUIRE: Do you have to worry about decomposition products interacting with the aluminum?

T. S. LATHAM: The answer to the question is "no." The UF_6 does not react with water vapor that may be trapped or other impurities. That is what causes the deposition on the materials.

Measurements of Uranium Mass Confined in High Density Plasmas*

R. C. Stoeffler
Power Systems Technology Section, Fluid Dynamics Laboratory
United Technologies Research Center
East Hartford, Connecticut

Abstract

An x-ray absorption method for measuring the amount of uranium confined in high-density, rf-heated uranium plasmas is described. Preliminary tests were conducted to calibrate the measurement system using argon, uranium hexafluoride (UF_6), and mixtures of argon and UF_6 at room temperature. A comparison of measured absorption of 8 keV x-rays with absorption calculated using Beer's Law indicated the method could be used to measure uranium densities from 3×10^{16} atoms/cm^3 to 3×10^{18} atoms/cm^3.

Tests were conducted to measure the density of uranium in an rf-heated argon plasma with UF_6 injection and with the power to maintain the discharge supplied by the United Technologies Research Center (UTRC) 1.2-MW rf induction heater facility. The uranium density was measured as the UF_6 flow rate through the test chamber was varied. A maximum uranium density of 3.85×10^{17} atoms/cm^3 was measured.

The system consisted of an x-ray generator, the test chamber for containing the test gases, and the x-ray detection components. Eight Kev x-rays emitted from the target of a CA 8-S/copper x-ray diffraction tube were collimated with a 0.025-mm-wide slit and reflected at the Bragg angle from a magnesium oxide crystal monochromator before passing through the test chamber. The test chamber consisted of a 57-mm-ID fused-silica tube with metal endwalls having 0.025-mm-thick beryllium windows. The x-rays were detected using a Norelco scintillation detector. A Tennelec TC 216 linear amplifier and single-channel analyzer was used to process the output signal from the scintillation detector and to provide an input signal into a Tennelec 545 counter-timer and a TC 590 ratemeter.

I. Introduction

Research to investigate the prospects for producing nuclear power from fissile fuel in the gaseous state has been conducted for several years. Most of this work was concentrated on the gaseous nuclear reactor technology required for high-performance space propulsion systems. However, in addition to high-thrust, high-specific-impulse space propulsion applications, gaseous fueled nuclear reactors offer several new options for meeting future energy needs.

Extraction of power from the fission process with nuclear fuel in gaseous form allows operation at much higher temperatures than conventional nuclear reactors. Higher operating temperature, in general, leads to more efficient thermodynamic cycles and, in the case of fissioning uranium plasma core reactors, results in applications using direct coupling of energy in the form of electromagnetic radiation. The continuous reprocessing of gaseous nuclear fuel leads to a low steady-state fission product inventory in the reactor and limits the buildup of long half-life transuranium elements.

Cavity reactor experiments and theoretical analyses performed over the past fifteen years have demonstrated that available analytical techniques for calculating cavity reactor nuclear characteristics are reasonably accurate[1]. These studies have provided a basis for selecting additional experiments to demonstrate the feasibility of plasma core nuclear reactors.

The x-ray absorption method described in this paper was developed to provide a method for measuring uranium density in two-component UF_6 confinement experiments which will be accomplished prior to the planned future cavity reactor experiments. The x-ray method can be used to measure uranium densities of 10^{16} atoms/cm^3 to 10^{19} atoms/cm^3 expected to be present in these experiments. Present optical methods are not well suited for measurement of uranium densities greater than approximately 10^{16} atoms/cm^3 in the experimental configuration used in the two-component tests.

II. System for X-Ray Absorption Measurements

The system used to make UF_6 and argon x-ray absorption measurements during calibration and rf-heated uranium plasma tests is shown schematically in Figure 1. The system consists of the x-ray generator, the test chamber for containing the test gases (argon, UF_6 and argon-UF_6 mixtures), and the x-ray detection components. The x-ray generator consists of a Diano Corporation CA 8-S/copper x-ray diffraction tube with an XRD-6 x-ray power supply and controller supplied by single phase 220 V/40 A service through a 7.5 kVA isolation transformer. The emitted x-rays from the target pass through a collimator with a vertically oriented 0.025-mm-wide slit and are reflected at the Bragg angle for 8 keV ($\lambda = 0.154$ nm) x-rays from a magnesium oxide crystal monochromator before passing through the test chamber. The test chamber consists of a

*Research sponsored by NASA Langley Research Center Under Contract NAS1-13291, Mod. 2.

57-mm-ID fused-silica tube with metal endwalls. The endwalls contain ports for supplying and exhausting test gases and x-ray viewing ports having windows which appear almost totally transparent to 8 keV x-rays. The distance between the windows is 22.4 cm. The x-rays were detected using a Norelco scintillation detector (photomultiplier tube with a thallium-activated sodium iodide crystal mounted in a lighttight enclosure at the window end) with a high voltage 0.9 kV regulated dc power supply. A Tennelec TC 216 linear amplifier and single-channel analyzer is used to process the output signal from the scintillation detector and to provide an input signal into a Tennelec TC 545 counter-timer and a TC 590 ratemeter. The ratemeter output signal was recorded using strip chart recorders. The scintillation detector output was also displayed using an oscilloscope. The ratemeter and oscilloscope signals were used as visual aids during alignment of the components of the x-ray measurement system.

III. Description of Chamber-Crystal-Slit System and Procedure Used in Calibration Tests

Details of the test chamber and the chamber-crystal-slit arrangement used during calibration tests are shown in Figure 2a and the photograph in Figure 3. The test chamber consists of a 57-mm-ID fused-silica tube and two copper endwalls. The x-ray beam from the x-ray collimator (having a 0.025-mm-wide vertically-oriented slit) was reflected at the Bragg angle for 8 keV x-rays parallel to the chamber axis through 6.35-mm-dia ports located in each endwall. The ports were sealed using 0.125-mm-thick mylar windows. X-rays transmitted through the detector viewing port are detected, through a 0.635-mm-wide slit (vertically oriented) using the scintillation detector. During these tests, the crystal was located approximately 3.8 cm from both the exit of the x-ray collimator and the source viewing port window and, the 0.634-mm-wide slit was located approximately 2.54 cm and 12.7 cm from the detector viewing port window and detector, respectively (as measured along the beam path).

Calibration tests were made, using this test chamber-crystal-slit system, with pure argon, pure UF_6, and argon-UF_6 mixtures at 300 K in the test chamber. During tests with pure argon or pure UF_6, x-ray absorption was determined by comparing the x-ray intensity, I_o, obtained with the chamber evacuated to the x-ray intensity, I, obtained with the chamber at known pressures of argon or UF_6. Absorption measurements were made for argon pressures from 5 mm Hg (1.7×10^{17} atoms/cm^3) to 700 mm Hg (2.4×10^{19} atoms/cm^3) and UF_6 pressures from 5 mm Hg (1.7×10^{17} atoms/cm^3) to 86 mm Hg (2.9×10^{18} atoms/cm^3). The following procedure was used in calibration tests with UF_6-argon mixtures. I_o was measured with the chamber evacuated. The chamber was filled with UF_6 to a known pressure (UF_6 pressure ranged from 5 mm Hg to 52.5 mm Hg). Argon was added to the chamber at partial pressuressin steps up to 700 mm Hg. At each step the intensity, I, was measured. The absorption by UF_6 was determined by comparing I for each UF_6 and argon partial pressure with the intensity, I_o, multiplied by I/I_o for the partial pressure of argon as calculated from Beer's law.

IV. Description of Chamber-Crystal-Slit System and Procedure Used in RF-Heated Plasma Tests

Details of the test chamber and chamber-crystal-slit arrangement used during the rf-heated plasma tests are shown in Figure 2b and the photograph in Figure 4. The rf-heated plasma test configuration differs slightly from that used during the calibration tests. The system is arranged so that the x-ray beam traverses the plasma core region diagonally (path length equal to 23.0 cm) passing through the chamber axis where the maximum uranium density is expected to occur. Accordingly, 6.35-mm-wide by 19-mm-long x-ray viewing ports are located in the brass endwalls, as shown in Figure 2b, to allow passage of the x-ray beam. During these tests 0.025-mm-thick beryllium windows were used to seal the viewing ports. X-rays transmitted through the detector viewing port are detected by the scintillation detector through a 0.635-mm-wide vertically oriented slit mounted on the face of the detector. The crystal was located approximately 12.7 cm and 4.4 cm from the exit of the x-ray collimator (with 0.025-mm-wide vertically oriented slit) and source viewing port window, respectively. The 0.635-mm-wide slit mounted on the face of the detector was located approximately 4.6 cm from the detector viewing port.

This test chamber-crystal-slit system was calibrated using pure argon and the procedure described previously. Argon absorption measurements were made for argon pressures from 50 mm Hg (1.7×10^{18} atoms/cm^3) to 1790 mm Hg (5.8×10^{20} atoms/cm^3).

The following procedure was used to determine uranium density from x-ray absorption measurements in an rf-heated argon plasma with UF_6 injection. The x-ray intensity, I_o, was measured with the test chamber evacuated. Argon was injected tangentially (through vortex injectors shown in Figure 2b) into the test chamber and exhausts to vacuum through an axial thru-flow exhaust and axial bypass exhaust ducts.[2] The chamber pressure was maintained at 10 mm Hg until the rf discharge was initiated and then increased to a pressure sufficient for operation with UF_6 injection, approximately 1275 mm Hg (power to maintain the discharge was supplied by the UTRC 1.2-MW rf induction heater facility). The variation of x-ray intensity, I_A, with amount of rf power supplied to the rf-heated argon plasma was measured (rf power was varied from 30 kW to 56 kW). UF_6 was injected axially into the test chamber and the variation of x-ray intensity, I, with UF_6 flow rate was measured (UF_6 flow rate was varied from 0.013 g/s to 0.134 g/s in a series of thirteen tests). UF_6 density was determined by computing

the ratio $I/I_A = (I/I_o)/(I_A/I_o)$ for comparable rf power levels) and using Beer's law, $I/I_o = e^{-\mu N_i L}$ where μ is the absorption cross section for uranium in cm^2/atom, ($\mu = 1.12 \times 10^{19}$ cm^2/atom for uranium and 8.0 keV x-rays), N_i is the number density in atom/cm^3, and L is the path length in cm.

V. Results From Calibration Tests With Pure Argon

Data obtained using the calibration system and the rf-heated plasma system and pure argon at 300 K are presented in Figure 5. The measured variation of fraction of x-rays transmitted, I/I_o, with variation in argon pressure, P_A, is compared with the theoretical variation calculated using Beer's law and the perfect gas law. Data obtained using the calibration system are given by the circular symbols and data obtained using the rf-heated plasma system are given by the triangular symbols. Agreement between experiment and theory is good for intensity ratios up to approximately 10^{-2} (argon pressures up to approximately 900 mm Hg). At pressures greater than 900 mm Hg the argon appears (except for one data point) less dense than that predicted using Beer's law. It is possible that the x-ray beam is not monochromatic and that at large values of absorption, I/I_o less than 10^{-2}, the intensity of high-energy components (possibly harmonics) in the beam becomes important relative to the intensity of the primary components (absorption decreases with increasing x-ray energy) making the measured argon density appear less than that given by theory. It would be possible to operate at argon pressures greater than 900 mm Hg and intensity ratios greater than 10^{-2} by using an x-ray tube having a target such as molybdenum which emits x-rays having energies (17.8 keV) greater than those emitted from a copper target x-ray tube. However, measurement of uranium densities near 10^{16} atoms/cm^3 would be more difficult (theoretical $I/I_o = 0.992$ for 17.8 keV x-rays compared with 0.974 for 8 keV x-rays).

VI. Results From Calibration Tests With Pure UF_6

Data obtained using the calibration system and pure UF_6 at 300 K are presented in Figure 6. The measured variation of the fraction of x-rays transmitted, I/I_6, with UF_6 pressure, P_{UF_6}, is compared with theory.

During these tests it was necessary to replenish the UF_6 supply system with UF_6. Data obtained before the UF_6 was replenished is in good agreement with theory. During initial tests conducted after the UF_6 was replenished, the system was contaminated (apparently with HF since the quartz test chamber and pressure gauge glass were etched) and apparent uranium and fluorine compounds were deposited in the system (white deposits on inside of quartz tube are evident in Figure 3). During subsequent calibration tests it appeared that the injected UF_6 reacted with the contaminants in the system resulting in a reduction of UF_6 density with time and, therefore, an increase in x-ray intensity with time. The data obtained during these tests have been corrected for the timewise drift in x-ray intensity. These data are also in good agreement with theory; however, the discrepancies between experiment and theory are greater than those which occurred before the system was contaminated. In general, the agreement between data and theory is good. However, for intensity ratios, I/I_o, greater than approximately 10^{-2} (UF_6 pressures greater than approximately 60 mm Hg) the UF_6 (as did argon) appears less dense than that predicted using Beer's law.

VII. Results From Calibration Tests With Mixtures of Argon and UF_6

Data obtained using the calibration system and mixtures of argon and UF_6 are presented in Figure 7. Data obtained before and after apparent contamination of the system (open and solid symbols, respectively) are presented for UF_6 partial pressures from 5 mm Hg up to 52.5 mm Hg and argon partial pressures from 0 to 700 mm Hg. In general, the data indicate fair agreement with theoretical intensity ratios. The data also indicate that the measured density of UF_6 decreases with increasing argon pressure and that this difference increases with increasing UF_6 pressure. This behavior would be expected, based on results obtained for pure argon and pure UF_6, when the partial pressures of argon and UF_6 are such that the total fraction of x-rays transmitted is less than about 10^{-2}. The dashed curve through the data in Figure 7 corresponds to a total fraction of x-rays transmitted equal to 10^{-2}. For data located to the right of the dashed curve the total fraction transmitted is less than 10^{-2} and to the left greater than 10^{-2}.

VIII. Results From Tests With RF-Heated Uranium Plasmas

X-ray absorption measurements were made in a series of thirteen tests to determine uranium density in rf-heated uranium plasmas. During these tests 3.2 g/s of argon were injected tangentially around the UF_6 which was injected axially at flow rates between 0.013 g/s and 0.134 g/s. The chamber pressure was controlled to be 1275 mm Hg and the rf-power in the plasma increased from 38 kW at a UF_6 flow rate of 0.013 g/s to 75 kW at a flow rate of 0.134 g/s. The flow was exhausted through the thru-flow and axial bypass exhausts.

In some tests the rf-power deposited in the plasma with UF_6 injection was greater than that which could be maintained with pure argon buffer injection. To determine uranium density by comparing x-ray intensities obtained with and without UF_6 injection, it was necessary to isolate effects of changes in rf-power level. The variation of intensity ratio, I_A/I_o, for pure argon, with

amount of rf-power deposited in the plasma was measured and is shown in Figure 8 (circular symbols). A straight line approximation is used to represent and extrapolate the data to rf-power levels which occurred during operation with UF_6 injection. The measured variation of intensity ratio, I/I_o, for argon-UF_6 mixtures with rf power is also shown in Figure 28 (square symbols with UF_6 flow rates in g/s given next to the symbols).

The fraction of x-rays transmitted through the UF_6, I/I_A, was determined using the measured fraction transmitted through the argon-UF_6 mixture, I/I_o, and the fraction transmitted through argon I_A/I_o obtained from the straight line approximation shown in Figure 8, at equivalent rf-power levels.

The intensity ratio I/I_o was used with Beer's law for uranium to calculate the uranium number density. The variation of uranium number density with UF_6 flow rate is shown in Figure 9. The variation is presented for assumed UF_6 path lengths of 23.0 cm and 9.5 cm (circular and square symbols, respectively; with rf-power levels noted next to the symbols). The data indicate that the uranium number density increases with increases in UF_6 flow rate and that the rate of increase decreases for UF_6 flow rates greater than approximately 0.08 g/s. Maximum uranium densities of 1.65×10^{17} atoms/cm^3 (path length = 23.0 cm) and 3.85×10^{17} atoms/cm (path length = 9.5 cm) were measured for a UF_6 flow rate equal to 0.093 g/s.

In some tests at UF_6 flow rates greater than approximately 0.093 g/s the measured x-ray intensity decreased with time (for fixed test conditions) indicating that UF_6 or uranium compounds were being deposited on the windows. Further evidence that UF_6 or uranium compounds had been deposited on the windows was obtained in subsequent tests with pure argon after the UF_6 injection was stopped. X-ray intensity ratios were significantly less than those attained with pure argon prior to UF_6 injection. The data presented in Figure 8 were obtained from tests in which the x-ray intensity obtained with UF_6 injection did not decrease with time and in which intensities obtained with pure argon subsequent to tests with UF_6 injection were approximately the same as intensities obtained prior to UF_6 injection.

The results presented here indicate that this x-ray absorption technique can be used to supplement the optical methods for determining the amount and distribution of uranium vapor confined in the uranium plasma for rf tests in which the atom density of confined uranium might be expected to exceed levels greater than approximately 10^{16} atoms/cm^3.

IX. References

1. Helmick, H. H., G. A. Järvis, J. S. Kendall, and T. S. Latham: Preliminary Study of Plasma Nuclear Reactor Feasibility. Los Alamos Scientific Laboratory Report LA-5679, August 1974.

2. Roman, W. C.: Laboratory-Scale Uranium RF Plasma Confinement Experiments. United Technologies Research Center Report R76-912205, May 1976.

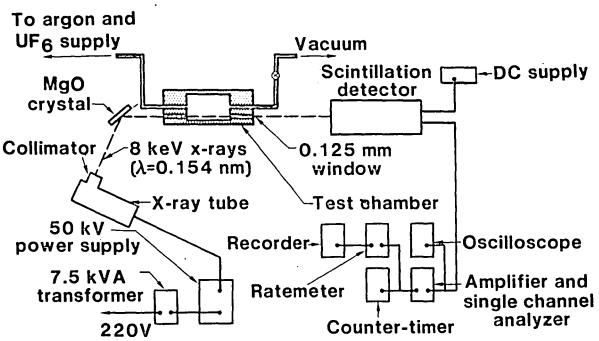

Fig. 1 System for UF_6 and Argon X-ray Absorption Measurements

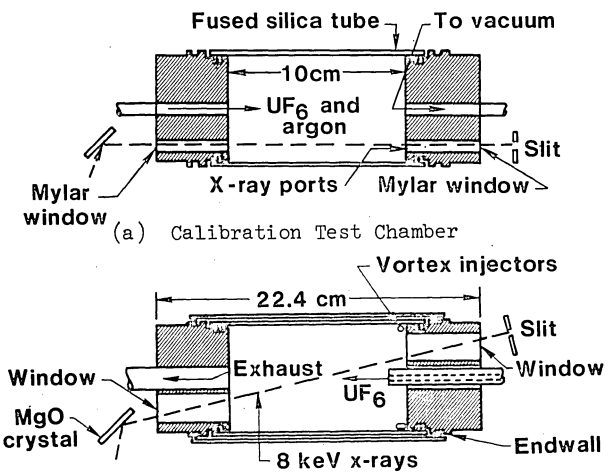

(a) Calibration Test Chamber

(b) RF-Heated Plasma Test Chamber

Fig. 2 Sketch of Test Chambers for UF_6 and Argon X-ray Absorption Measurements.

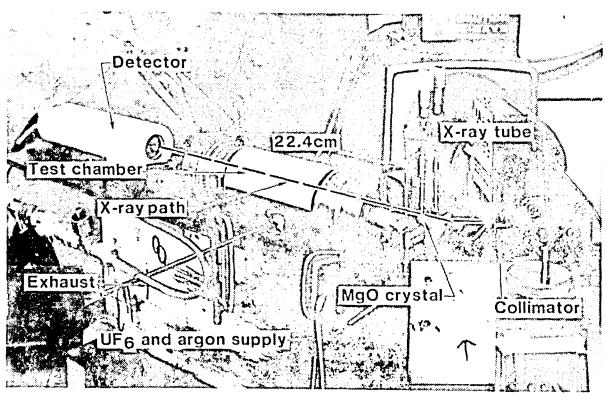

Fig. 3 Photograph of System for UF_6 and Argon Absorption Measurements in Calibration Tests.

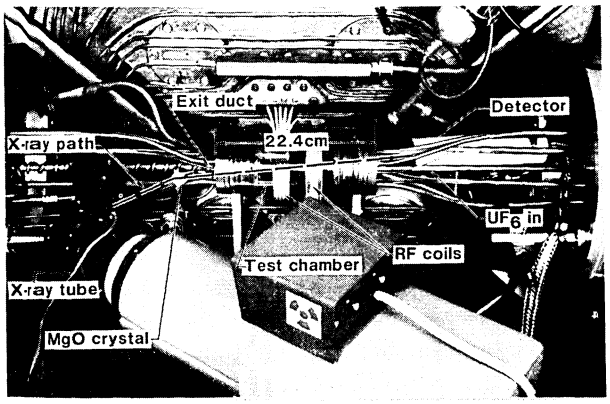

Fig. 4 Photograph of System for UF_6 X-ray Absorption Measurements in RF-Heated Plasma Tests.

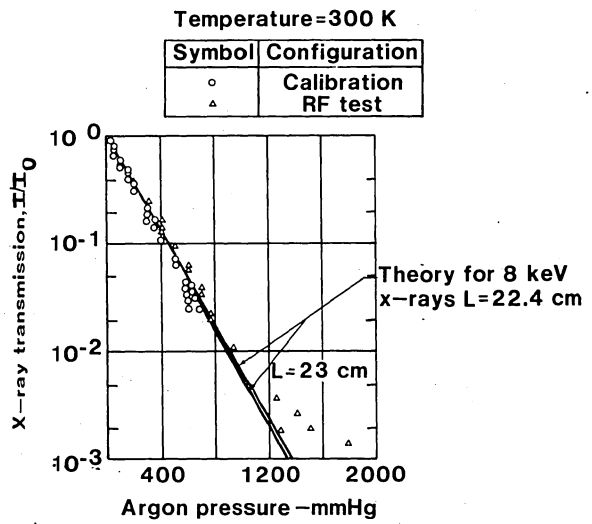

Fig. 5 Measured Variation of Transmission of 8 KeV X-rays With Argon Pressure.

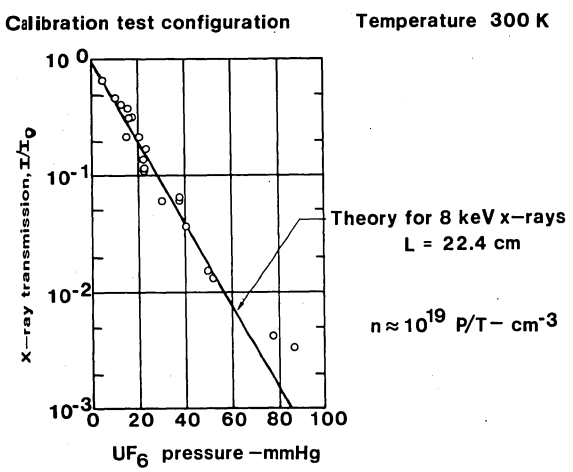

Fig. 6 Measured Variation of Transmission of 8 KeV X-Rays With UF_6 Pressure.

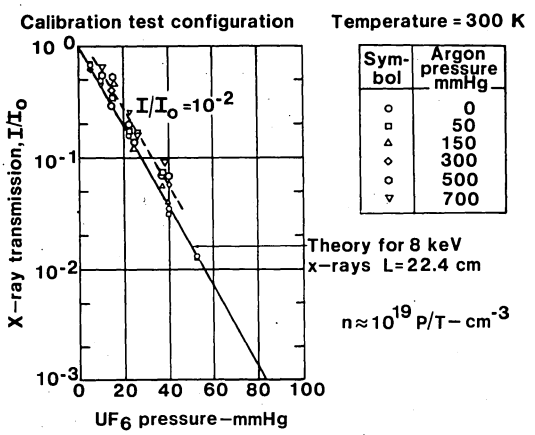

Fig. 7 Measured Variation of Transmission of 8 KeV X-Rays With UF_6 Pressure for Several Argon Pressures.

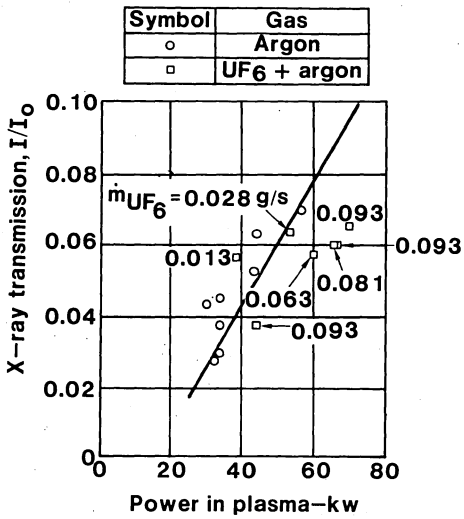

Fig. 8 Variation of Fraction of X-rays Transmitted for Argon and UF_6-Argon Mixtures With RF Power.

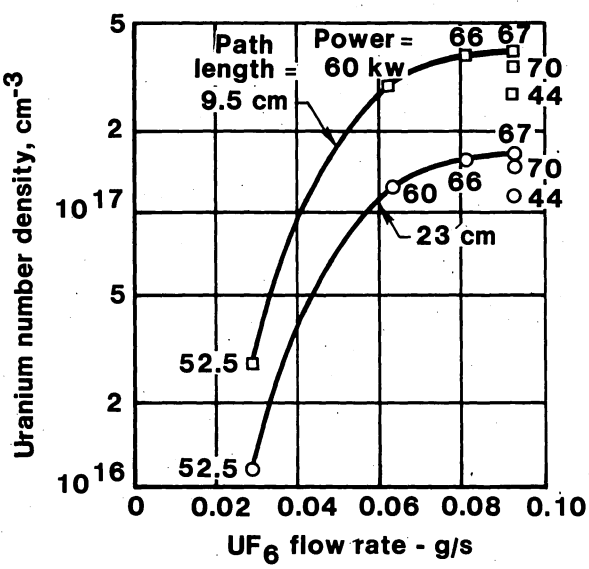

Fig. 9 Variation of Measured Uranium Density With UF_6 Flow Rate.

DISCUSSION

M. D. WILLIAMS: I noticed you use a magnesium oxide crystal for reflectors. What is the reflectance of that crystal? What is the signal-to-noise ratio?

R. C. STOEFFLER: Signal-to-noise ratio was at least 100 for the cases where we were measuring the maxium densities.

R. T. SCHNEIDER: Why did you choose the X-ray technique as compared to regular nuclear assay techniques?

T. S. LATHAM: We haven't looked at nuclear array techniques. We chose the soft X-ray because it had a significantly different cross-section from the argon, and our calculations indicated it would give us measurements in the range of uranium to argon.

MAGNETOPLASMADYNAMIC THRUSTER APPLICATIONS

E. V. Pawlik
Jet Propulsion Laboratory
Pasadena, California

Abstract

Advance study activities within NASA indicate that electric propulsion will be required to make certain types of potential missions feasible. The large power levels under consideration make magnetoplasmadynamic thrusters a good candidate for these applications since this type of electric thruster is best suited to operation at high power levels. This paper examines the status of the magnetoplasmadynamic thruster and compares it to the ion thruster which also is a candidate. The use of these two types of electric propulsion devices for orbit raising of a self-powered large satellite is examined from a cost standpoint. In addition the use of nuclear electric propulsion is described for use as both a near-earth space tug and for an interplanetary exploration vehicle. These preliminary examinations indicate that the magnetoplasmadynamic thruster is the lowest cost thruster and therefore merits serious consideration for these applications.

Introduction

Planning activities at NASA are presently concerned with using electric propulsion for various applications that range from multiwatt levels for satellite station keeping to multi-megawatt levels for orbit raising of a space power station. Propellant weight savings over long mission lifetimes can be obtained by using the high exhaust velocities that the electric propulsion devices are capable of achieving. These weight savings can make the use of electric propulsion economically attractive when compared to the use of chemical propulsion for these missions.

The growing need for high power levels for electric propulsion is indicated in the Outlook for Space Studies (Ref. 1) and Ref. 2. Commencing in the mid-1980's, large payloads such as communications networks and satellite power stations, are expected to be placed in geosynchronous earth orbit. The transportation of these large payloads from shuttle orbit (500 km or 270 nm altitude) to geosynchronous orbit (35,806 km or 19,323 nm altitude) will require high electrical power levels for propulsion. In addition, the exploration of the solar system will also require high power levels for high energy missions such as sample return from the outer planets. Power levels in the range of 400 to 1000 kW are currently being examined.

Presently two thruster types can be considered for these primary propulsion applications. These are the ion thruster and the magnetoplasmadynamic (MPD) thruster. The ion thruster is a highly developed device having received a high level of continuous funding for the last 15 years with several flight tests being conducted. The most advanced ion thruster suitable for primary propulsion has been developed at Hughes Research Laboratories (Ref. 3). This ion thruster produces a 30 cm diameter beam and uses mercury as the propellant. It requires about 3 kW input power to its power processor and operates at a specific impulse near 3000 sec. A near term possible application for this device is a high energy solar electric propulsion mission such as an out-of-ecliptic mission described in Ref. 4. Whereas a modular approach is visualized when using these devices, the present module size is much too small for many of the high power missions currently being studied. Drawbacks for this thruster include (1) low thrust density, - large thrust areas are required for large power levels resulting in large thruster modules and a large number of thrusters, (2) a high degree of complexity, - the operation of a thruster requires 14 power supplies and integrate logic built both into the power processor and into software for the digital computer required to monitor thruster operation, (3) high cost, - the ion thruster is labor-intensive, containing many areas that are extremely sensitive to changes in geometry and fabrication processes, (4) limited reliability, - life and flight tests of this type of thruster have been plagued with problems that accent the difficulty in obtaining high reliability.

An attractive alternative to the ion thruster is the MPD thruster. This thruster type has never advanced beyond initial laboratory tests and therefore a comparison between the two devices can only be made in terms of projections of the anticipated MPD thruster that could be developed against a mature ion thruster technology. Whereas a long history also exists for the MPD thruster, a continuous high support level has been lacking. Furthermore, a focused system activity such as a flight demonstration was never initiated. The advantages of the MPD thruster are the antithesis of the ion thruster drawbacks. These include (1) high thrust density, - thrust densities up to 10,000 times higher than those of the ion thruster can be obtained resulting in a small number of reasonable size thrusters for a given application, (2) simplicity, - thruster operation should require only a single power supply, (3) low cost, - simple construction and insensitivity to small dimensional changes should result in low cost flight units, and (4) high reliability, simple construction and minimum number of different power level requirements should result in a much more reliable thruster than the ion thruster.

Performance is an additional area of comparison between the two thrusters. The

This paper presents the results of one phase of research carried out at the Jet Propulsion Laboratory, California Institute of Technology, under Contract NAS 7-100, sponsored by the National Aeronautics and Space Administration.

performance of the ion thruster when used with mercury propellant is well known. Relatively high efficiency levels have been demonstrated. Earth orbiting applications, however, potentially require operation with argon as the propellant in order to minimize environment effects. Although ion thruster performance with gaseous propellants can be projected with a high degree of accuracy, limitations exist at low levels of specific impulse. The MPD thruster is known to demonstrate its best efficiency at high power levels of operation. It has also demonstrated relatively efficient operation in the low specific impulse region where the ion thruster cannot operate on low density gaseous propellants. Achievable performance levels of a developed MPD thruster over a range of specific impulse values can only be approximated by drawing from on-going research activities.

In this paper, areas where the MPD thruster could find application are identified. Clear advantages exist over chemical propulsion. Demonstrated advantages over the ion thruster will depend upon further development of the MPD thruster.

Thruster Description

Brief descriptions of the ion and MPD thrusters are included in this section. Table I presents projected performance data for each thruster type. Additional information for the ion thruster can be found in Ref. 5.

Ion Bombardment Thruster - This thruster is highly developed to operate with mercury as a propellant. Operation on other gases such as argon, nitrogen, and xenon have also been reported. The propellant is metered into an ionization chamber where it is ionized by electron bombardment. The ionized propellant is accelerated electrostatically by two closely spaced dished grids of very precise geometry. A retarding potential applied to the exterior grid prevents exhaust plasma electrons from returning to the thruster. The electrons stripped from the propellant are replenished by an ancillary electron source labeled a neutralizer. Maximum thrust levels are directly proportional to the accelerator grid area. Thruster complexity is increased over the simple concept described above due to multiple propellant source, electromagnetic field, heater, and keeper electrode requirements. These are required in order to achieve high performance and long lifetimes.

Table I. Electric Thruster Characteristics

A. 50-cm Ion Thrusters

Exhaust Velocity (km/s)	60	80	100
Efficiency	0.63	0.75	0.785
Power Input (kWe)	40.5	83	146.5
Thrust (N)	0.85	1.55	2.3
Mass (kg)	6.5	6.5	6.5
Temperature (°K)	900	950	950
Cost ($K)	15	15	15

B. 7.5 MWe MPD Thruster

Exhaust Velocity (km/s)	10	25	50
Efficiency	0.5	0.5	0.5
Power Input (kWe)	7500	7500	7500
Thrust (N)	750	300	150
Mass (kg)	700	700	700
Temperature (°K)	1700	1700	1700
Cost ($K)	100	100	100

MPD Thruster - This thruster usually consists simply of a central cylindrical cathode and a concentric axisymmetric anode. Anode cooling is normally required and a high voltage spike is required to initiate a discharge. Operation at high-current levels provides self-induced magnetic fields resulting in a lighter and more efficient thruster than when electromagnets are used. Two mechanisms contribute to the plasma acceleration. These are (1) an aerodynamic force due to heating and expansion of the propellant and (2) acting of j x B volume forces formed by the discharge current and the azimuthal self-magnetic field. A schematic of a typical thruster experimental test setup is shown in Fig. 1.

MPD Thruster Status

The MPD thruster was the subject of a large number of experimental investigations from about 1960 to 1968 when this work was severely curtailed due primarily to a lack of identifiable applications for high power level thrusters. The ion thruster appeared at that time to be a more viable candidate for any near term applications. In addition, considerable uncertainties had arisen regarding the performance obtainable with the MPD thruster. The most serious problem was entrainment of ambient low pressure gas into the thruster exhaust plume. An excellent review of this early phase of the work is described in Ref. 6.

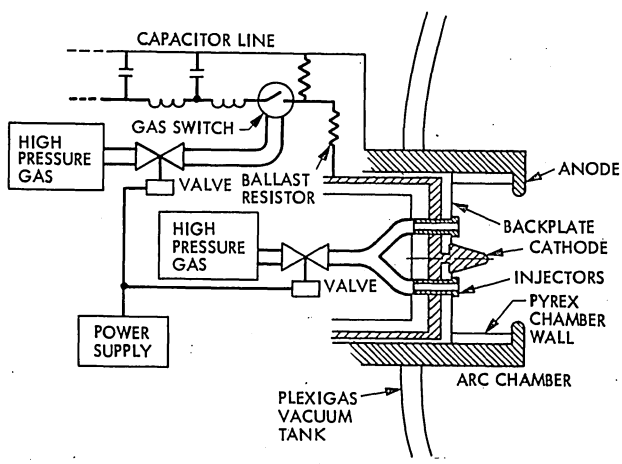

Fig. 1. Typical quasi-steady MPD research apparatus.

During the period described above, the thruster was initially conceived as an arc jet which imparted thermal energy to a propellant flow passing through an arc. Modifications were introduced early to utilize j x B forces as the governing thrust producing mechanism. Several thruster approaches were explored in mainly an empirical fashion toward increasingly higher levels of thrust efficiency and specific impulse levels. However, much of this early performance data is not considered reliable because of the entrainment problem and the possibility of interactions between the thruster electromagnetic fields and the vacuum tank walls. Most of these experimental thrusters were designed to operate at a power level between 20 to 100 kW. Lifetimes of 50 to 75 hours were achieved.

Efforts to minimize test environment interactions with the thruster resulted in a quasi-steady state technique being evolved (Ref. 7). This quasi-steady state concept requires the application of a current pulse of sufficient duration and magnitude to allow the arc current and mass flow to reach a steady state. Stable and diffuse current patterns can be established in several tens of microseconds in a coaxial configuration (Ref. 8). These techniques resulted in more realistic values of thruster performance being obtained. Maximum thruster efficiencies were found to range from 10 to 30% and specific impulse values of 3000 sec for the heavy propellants to 400 sec for the light propellants. Pulse techniques offer the additional attraction of being able to operate at the higher power levels during the pulse while operating from a low average power level. The efficiency of the MPD thruster, which has been found to increase with power level (Ref. 9), can therefore be maintained at a higher level. In addition, varying the duty cycle provides power throttling capabilities without any apparent sacrifices in overall efficiency allowing the thruster output to be matched to variations in a power supply during a mission.

Basic limitations previously appeared to exist, limiting thruster operation because of coupling between arc current and accelerated mass flow rate. As arc currents are increased for a given propellant flow rate, a point is reached above which various undesirable effects occur such as insulator and electrode ablation, mass recirculation, and terminal voltage fluctuations. The onset of these effects was taken as an upper limitation on arc current for a given flow rate. Recent results (Ref. 10) have shown that this limitation is associated with cathode phenomena. Modification of the cathode area allows these limitations to be breached. The higher values of arc current associate with larger cathode areas implies greater exhaust velocities based on the fundamental self-field thrust relation $T \alpha J^2$.

The projected performance of this MPD thruster is shown in Fig. 2. The existing performance and trend are indicated along with a performance projection obtained from Ref. 11. Ion thruster projected performance obtained from Ref. 12 is also included on the figure for comparison. All cost comparison made in this paper assume the use of a 7.5 MW thruster capable of operating either steady state or in a pulsed mode.

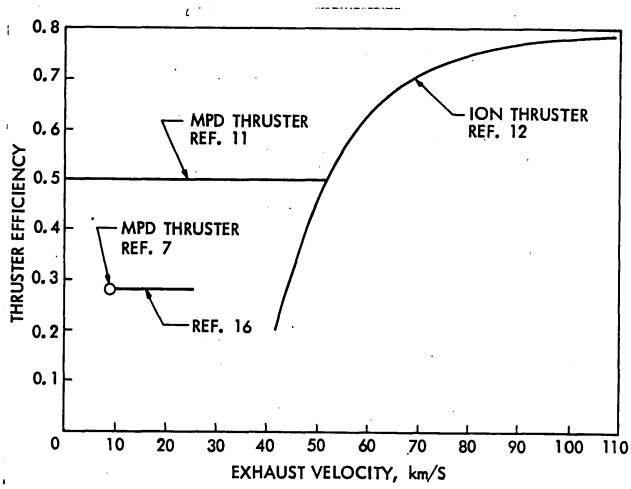

Fig. 2. Electric thruster efficiency with argon.

Space Power Platforms Applications

With the advent of an operational shuttle vast opportunities will open up for the use of space. Near earth applications will require increasing amounts of electric power for space base support, space industrialization and manufacture, and possibly generation of power as an electric utility. At the present time it is visualized that these platforms will begin on a moderate scale and that increasingly larger space power platforms will be required to generate this power, which will be transmitted to other satellites or to earth by laser or microwave transmission. Power levels under consideration range from 100's of kilowatts in the 1985 to 1995 time period to 100's of megawatts after 1995 and eventually growing to 1000's of megawatts. The orbit for these platforms would be in geosynchronous earth orbit (GEO) at nearly continuous sunlight and at a fixed position relative to earth.

Transportation of the building materials for this power platform from the shuttle low earth orbit (LEO) to GEO is a major consideration in the economic viability of this concept. Chemical and electrical propulsion are both being examined for this application. The ΔV required for impulsive transfer from LEO to GEO is 4300 m/sec. The electric propulsion option will require a higher energy spiral orbit and therefore will require 6200 m/sec with an additional 10% gravity gradient torques. Use of electric propulsion would permit the platform to be assembled in LEO and then draw upon its electrical power for vehicle transfer to the higher orbit. The low thrust levels of electric propulsion are consistent with this concept since the low thrust level thrusters could be distributed over the lightweight structure, thereby minimizing further structural requirements during orbit raising.

A cost analysis of the various transportation options is described in Ref. 13. The cost for the chemical delivery of payload to GEO is estimated at $330/kg. Costs using electric propulsion are

shown in Fig. 3 for a 4000 MW platform. The mass to power levels are consistent with flight times that range from 10 to 120 days from LEO to GEO (Fig. 4). The shorter flight times occur with lower exhaust velocities and with smaller mass to power ratios. In this analysis it is assumed that the full array power is used for propulsion during the orbit transfer. The cost advantage that is evident for the MPD thruster for this application accrue mainly due to the lower exhaust velocity, lower power processing mass, and the high thrust density advantage that the MPD thruster can provide. Thruster and power processor weights were used to arrive at comparative costs using the same cost/kg for each. The cost curves of Fig. 3 increase at lower exhaust velocities due to the increased propellant consumption. For the same power available the heavier mass will have a higher mass to power ratio requiring longer trip time and propellant resulting in increased costs.

Based on projected efficiencies and subject to the cost estimates used, the MPD thruster appears promising as a candidate for this type of application. Further work is required on the MPD thruster in order to obtain better performance and cost estimates.

Nuclear Electric Propulsion Applications

Future exploration of the solar system will require the use of nuclear electric propulsion to accomplish many of the planned high energy missions. Work is underway at JPL and ERDA on the design of a nuclear electric propulsion (NEP) spacecraft capable of accomplishing these missions (Ref. 14). The spacecraft will utilize a fast nuclear reactor power source, thermionic conversion of heat to electric power, and electric propulsion for electric power to thrust. High specific impulse thruster operation will be required for these missions (near 9000 sec). The large exhaust area that ion thrusters require creates problems in incorporating these thrusters into a spacecraft. Recently the operation of an MPD thruster operating from a thermionic converter matrix has been

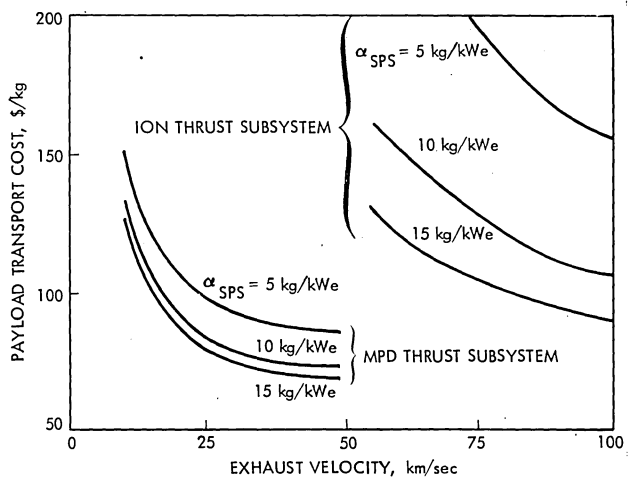

Fig. 3. LEO to GEO transportation costs - self-powered 4000 MWe SEP without solar degradation (Ref. 13)

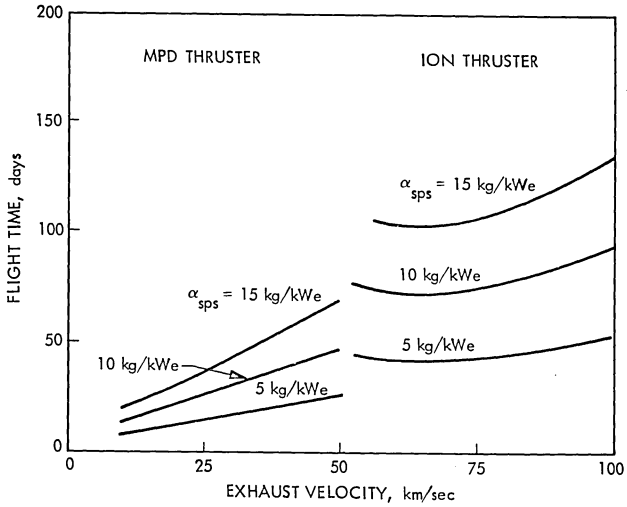

Fig. 4. LEO to GEO flight time - self-powered 4000 MWe SEP without solar degradation (Ref. 13)

examined (Ref. 15) for a 400 kW thrust power level. A system schematic is shown in Fig. 5. The system weights involved were found to be comparable with those of an ion thruster system. Power conversion efficiencies of 90% were calculated. The small MPD thruster size makes integration into the NEP spacecraft a much less complex task. Higher efficiencies, specific impulse levels, and lifetimes will, however, be required of the MPD thruster before it can effectively compete with the ion thruster for this application.

Another use of the NEP vehicle could be for transfer of cargo from LEO to GEO. A drawing of an NEP vehicle used as a cargo transfer vehicle is shown in Fig. 6. The cargo would be transferred in containerized pallets. The container would be brought up to LEO in a separate shuttle launch with the sequence of operations being as depicted in Fig. 7. A logistics depot would be required to maintain separation between the shuttle and the nuclear spacecraft. Cargo transfer vehicles of this type would be required to supply materials for manned GEO satellites, space manufacturing and also if a space station were to be assembled in GEO. The economics again determines the most optimum approach. The cost analysis from Ref. 13 is shown for this nuclear earth tug application in Fig. 8. The cost of this tug using the MPD thrusters is much lower than when using the ion thruster. This is because the orbit

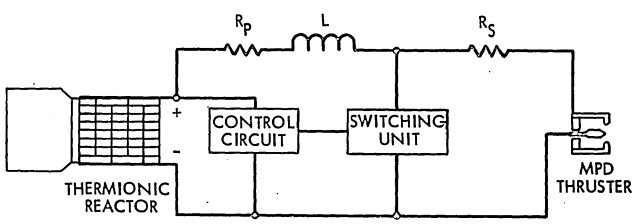

Fig. 5. Self inductive type of circuit for coupling a thermionic reactor and a MPD thruster.

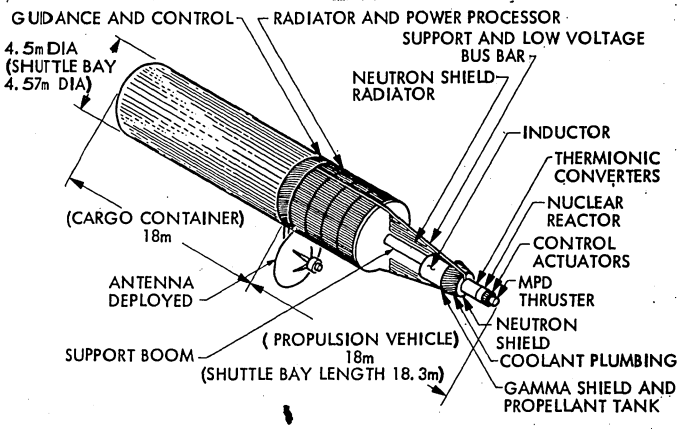

Fig. 6. Nuclear electric propulsion cargo transfer vehicle.

transfer time is less with the low specific impulse. In this case a clear optimum is indicated at an exhaust velocity of about 20 km/s, in the region where MPD thrusters have recently been operated (Ref. 16).

Summary

On the basis of cost comparisons and projected performance, space applications exist for the MPD thruster in both the orbit raising of a power platform and for a nuclear cargo tug. Performance improvements over those presently projected for this thruster would also make the MPD thruster a candidate for use on interplanetary exploration vehicles. An evaluation of the potential for such performance improvement is currently in progress.

In light of these potential uses and recent research that has indicated possible thruster improvements, it appears highly desirable to initiate an MPD thruster development program in the near future.

References

1. Outlook for Space Reference Volume, "A Forecast of Space Technology," prepared by a NASA Task Group, July 15, 1975.

2. Melbourne, W. G., et al, "On Performances Computations with Pieced Solutions of Planetocentric and Heliocentric Trajectories for Low Thrust Missions, JPL Sps No. 37-36, Vol. IV, 1965.

3. King, H. J., et al, "Low Voltage 30 cm Thruster," NASA CR-120919, Feb. 1972.

4. Yen, C. L., "Optimal Orbit Transfer for Out-of-Ecliptic Missions Using a Solar Electric Spacecraft", paper 75-420 AIAA 11th Electric Propulsion Conference, New Orleans, March 1975.

5. Kaufman, H. R., "Technology of Electron-Bombardment Ion Thrusters", Advances in Electronics and Electron Physics, Vol. 36, Academic Press, 1974.

6. Nerheim, N. M., and Kelly, A. J., "A Critical Review of the Magnetoplasmadynamic (MPD) Thruster for Space Applications," JPL Technical Report No. 32-1196, February 15, 1968.

7. Malliaris, A. C., et al, "Performance of Quasi-Steady MPD Thrusters at High Power," AIAA Journal, Vol. 10, No. 2, February 1972.

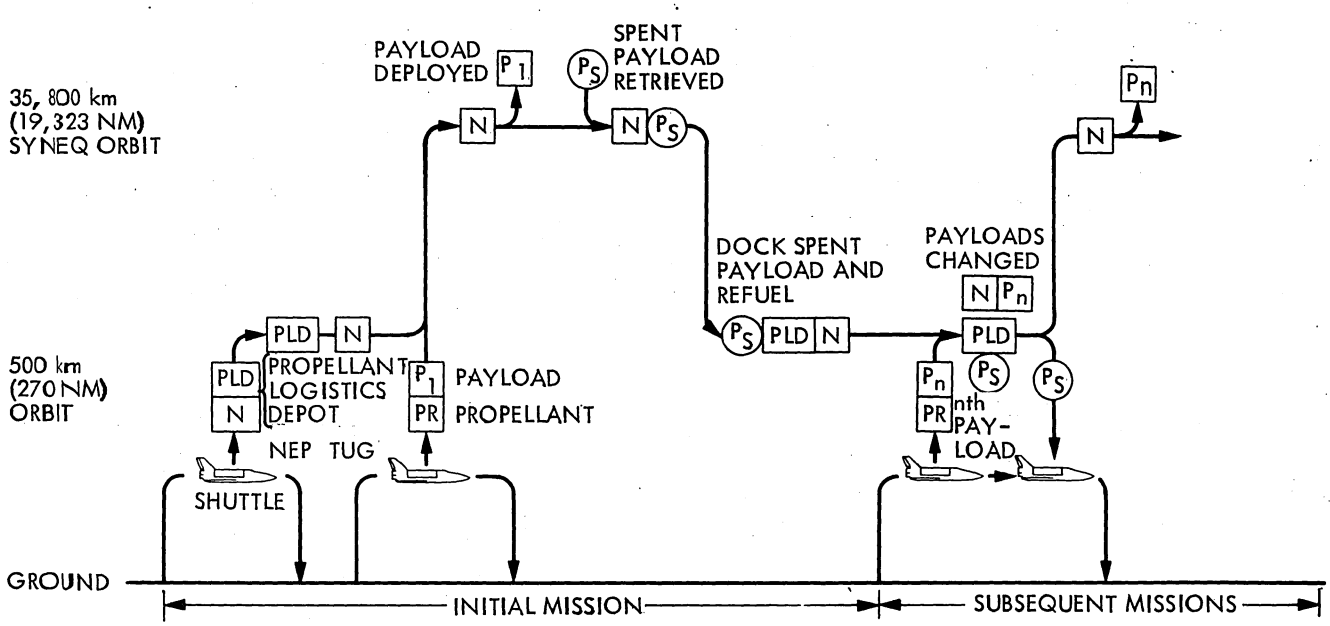

Fig. 7. Baseline NEP tug geosynchronous orbit mission profile.

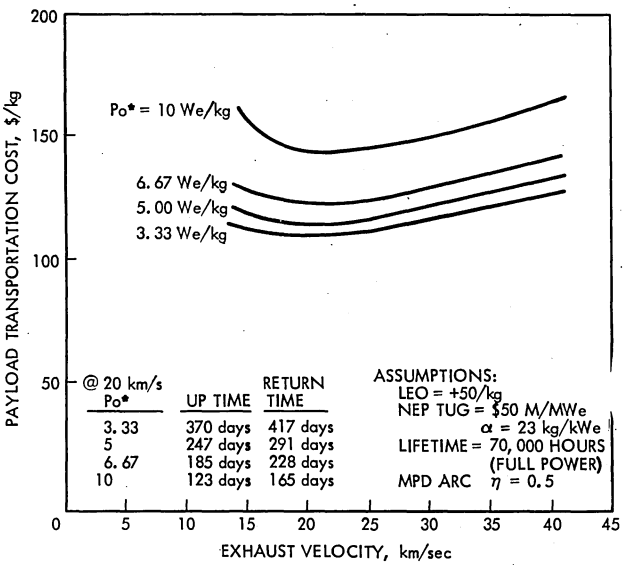

Fig. 8. Transportation costs to GEO for a reusable NEP tub.

8. Clark, K. E., "Quasi-Steady Plasma Accelerator," Report 859, Dept. of Aerospace and Mechanical Sciences, Princeton University, Princeton, N. J., May 1969.

9. Saber, A. J. and Jahn, R. G., "Anode Power Deposition in Quasi-Steady MPD Arcs," AIAA Paper 73-1091, AIAA 10th Electric Propulsion Conference, October 1973.

10. Boyle, M. J., Clark, K. E., and Jahn, R. G., "Flow Field Characteristics and Performance Limitations of Quasi-Steady Magnetoplasmadynamic Accelerators, AIAA Paper 75-414, AIAA 11th Electric Propulsion Conference, March 1975.

11. Clark, K., Private communication, Princeton, 1976.

12. Byers, D., Private Communication, NASA Lewis Research Center 1976.

13. Stearns, J., "Large-Payload Earth Orbit Transportation with Electric Propulsion," JPL TM to be published.

14. Estabrook, W. C., Phillips, W. M., and Hsieh, T., "System Design for a Nuclear Electric Spacecraft Utilizing out-of-core Thermionic Conversion," JPL TM to be published.

15. Britt, E. J., et al, "Inductively Coupled TI-MPD Spacecraft Electric Propulsion", 11th IECEC, Stateline Nevada, September, 1976.

16. Rudolph, L. K., Jahn, R. G., Clark, K. E. and VonJaskowsky, W. F., "Performance Characteristics of Quasi-Steady MPD Discharges," Proposed AIAA paper for 12th Electric Propulsion Conference, November 1976.

DISCUSSION

J. P. LAYTON: Have you identified the overall thruster system including its feeding, valving, tightening, etc.? Some delineation of the overall systen that other people could use when they are doing concepting for primary propulsion for this system would be very useful.

E. V. PAWLIK: Work hasn't proceeded that far as yet.

MINI-CAVITY PLASMA CORE REACTORS FOR DUAL-MODE SPACE NUCLEAR POWER/PROPULSION SYSTEMS*

Stanley Chow
Princeton University
Princeton, New Jersey

Abstract

A mini-cavity plasma core reactor is investigated for potential use in a dual-mode space power and propulsion system. In the propulsive mode, hydrogen propellant is injected radially inward through the reactor solid regions and into the cavity. The propellant is heated by both solid driver fuel elements surrounding the cavity and uranium plasma before it is exhausted out the nozzle. The propellant only removes a fraction of the driver power, the remainder is transferred by a coolant fluid to a power conversion system, which incorporates a radiator for heat rejection. In the power generation mode, the plasma and propellant flows are shut off, and the driver elements supply thermal power to the power conversion system, which generates electricity for primary electric propulsion purposes. Neutronic feasibility of dual mode operation and smaller reactor sizes than those previously investigated are shown to be possible. A heat transfer analysis of one such reactor shows that the dual-mode concept is applicable when power generation mode thermal power levels are within the same order of magnitude as direct thrust mode thermal power levels. However, adequate uranium plasma retention still needs to be demonstrated and mission analyses are required to identify the mission capabilities of this concept and compare them with alternative approaches.

1. Introduction

In 1971, Hyland of the NASA Lewis Research Center offered an alternative to the much larger coaxial plasma core reactor with his mini-cavity concept shown in Figure 1.[1] By surrounding the cavity with uranium carbide fuel elements, a neutronics analysis showed that a substantial reduction in size is possible from the all-plasma fuel configuration. Hyland has shown that the reactor is small enough to be carried in the space shuttle cargo bay and would be appropriately sized for automated space missions.

Work on the mini-cavity reactor concept was discontinued at the Lewis Research Center following the cancellation of the United States nuclear rocket program in 1973. The present NASA effort is devoted to the lower cost uranium hexafluoride program which will contribute enormously to the basic understanding of all plasma core concepts.

Should interest in the mini-cavity reactor be revived, an additional benefit of this reactor configuration should be considered. Hyland has only analyzed his reactor for propulsion purposes. By extracting thermal power from the solid fuel elements, long-term electric power is available via a power conversion system. The use of the reactor for both electric power generation and propulsion purposes is called dual mode operation.

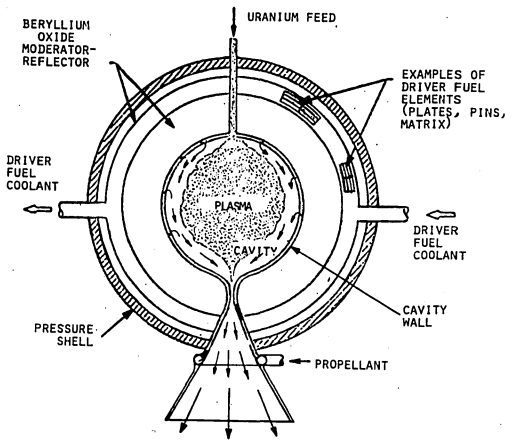

Figure 1 Mini-Cavity Plasma Core Engine

The idea of a dual-mode space nuclear reactor system originated with Beveridge [2] for the solid core NERVA (Nuclear Engine for Rocket Vehicle Applications) and later at Los Alamos Scientific Laboratory for the SNRE (Small Nuclear Rocket Engine).[3] In each case, an electric power conversion system was tacked on to the engine by utilizating its hydrogen-cooled structural elements (tie-tubes) as an energy source. Subsequent to thrust termination, the power system was designed to deliver long-term power: 10 kWe for the SNRE and 25 kWe for NERVA.

The power generated by these two systems was intended for use in payload operations, e.g., spacecraft communications, attitude control by small electric thrusters, etc. However, the real advantage of the dual-mode concept lies in its ability to generate sufficiently high electric power levels (0.1 MWe or greater) for use in primary electric propulsion. Thus, the high-thrust nuclear propulsion mode is employed for planetocentric operations, where high thrust-to-mass ratios are desired, and the low thrust electric propulsion mode is utilized for heliocentric operations, where high effective exhaust velocities are optimum.

It is desirable to see if the mini-cavity plasma core reactor is capable of dual mode operation in useful propulsion and electric power ranges. The

*This research was performed for a M.S.E. thesis and was supported by NASA grant NGR-31-001-328.

dual mode system is shown in Figure 2, including the engine and power conversion systems. Either a dynamic (Brayton or Rankine) or direct (thermionic) power conversion system may be used. The thermionic system may utilize either in-core or out-of-core diodes. In addition, heat pipes may be used to remove heat from the driver region instead of the usual coolant fluid.

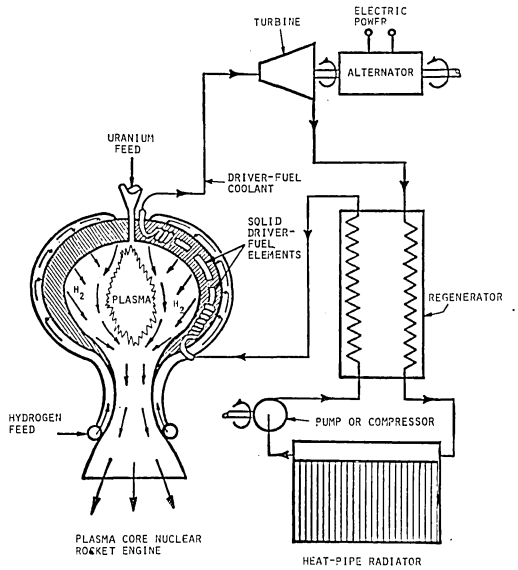

Figure 2 Nuclear Fission Plasma Core Dual-Mode System Concept

In the propulsive mode, hydrogen is injected radially inward through the pressure shell. The propellant absorbs a certain amount of driver power as it passes through the solid regions of the reactor. It then undergoes further heating from the fissioning plasma in the cavity region before being exhausted through a nozzle to produce thrust. Meanwhile, the excess driver thermal power which is not absorbed by the propellant is transported away by the coolant fluid to a radiator where it is dissipated into space.

In the power generation mode, the hydrogen and plasma flows are shut off and the remaining gases in the core are exhausted into space. The reactivity of the driver is increased to maintain reactor criticality and the driver power level is adjusted as dictated by electric power requirements. In this mode, the driver thermal power is removed solely by the coolant fluid or by heat pipes.

II. Analysis

A spherical model is adopted to describe the mini-cavity reactor and is shown in Figure 3. Only variations in the radial direction are considered. The use of a one-dimensional model may introduce sizable errors, but is appropriate for this preliminary investigation.

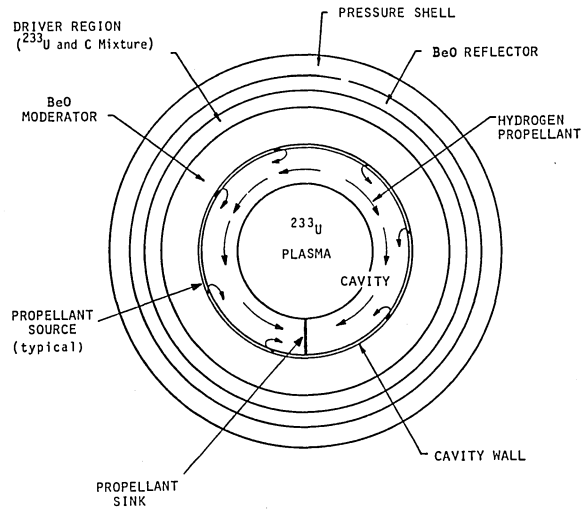

Figure 3 Spherical Reactor Analytical Model

The analysis is based on the use of the general energy equation:

$$\rho\bar{v} \cdot \nabla h + \nabla \cdot \overline{q_c} + \nabla \cdot \overline{q_r} = S \qquad (1)$$

where ρ is the fluid density, $\bar{v}$ is the fluid velocity, h is the fluid enthalpy, $\overline{q_c}$ is the conductive heat flux vector, $\overline{q_r}$ is the radiative heat flux vector, and S is the internal energy generation per unit volume.

The source term S is the energy generated in the plasma core or solid driver region by nuclear fission. In order to evaluate this term, the neutron flux through the reactor is calculated. Again, because of the first-order nature of this analysis, the simplest one-group diffusion method is used.

The neutron flux has the general solutions

$$\phi = \frac{E_1 \cos(Br)}{r} + \frac{E_2 \sin(Br)}{r} \qquad (2)$$

for the fueled regions and

$$\phi = \frac{E_3 e^{\frac{r}{L}}}{r} + \frac{E_4 e^{-\frac{r}{L}}}{r} \qquad (3)$$

for the remaining regions. E_i are constants composed of region radii and material properties, B is the buckling, L is the diffusion length, and r is the radial position.

The pressure shell is essentially transparent to thermal neutrons and therefore the neutron flux ϕ_6 vanishes for this region. Equations

(2) and (3) are applied to the five remaining regions along with ten boundary conditions which require the flux to remain finite at the center, the flux to vanish at the extrapolated boundary, and the neutron fluxes and current densities $(\frac{d\phi}{dr})$ to be continuous across the interfaces. The neutron fluxes are then expressed in terms of a constant and the driver buckling B_4.

Specifying the driver power will determine the constant. The driver buckling must have a value such that the reactor is critical. This is accomplished by changing the driver reactivity until the condition is met.

The total reactor power Q is the sum of the plasma core power Q_c and the driver power Q_d, or

$$Q = Q_c + Q_d = 4\pi\varepsilon\left[\int_0^{r_1} \Sigma^f \phi_1 r^2 dr + \int_{r_3}^{r_4} \Sigma^f \phi_4 r^2 dr\right] \quad (4)$$

where ε is the average energy released per fission event, Σ^f is the macroscopic fission cross section, ϕ_1 and ϕ_4 are the neutron fluxes through the plasma and driver regions respectively, r_1 is the radius of the plasma, and r_3 and r_4 are the inner and outer radii of the driver region respectively.

Since equation (4) is temperature dependent through the plasma macroscopic fission cross section, it must be solved an iterative method. An initial temperature distribution is assumed throughout the entire reactor and then the neutron flux is calculated in each region for a critical reactor. The neutron flux distribution is then utilized to calculate a new temperature distribution by using the heat transfer analysis described in the following paragraphs. The new distribution is compared with the old and the entire process is repeated until the error between successive distributions is reduced to a specified value.

The heat transfer analysis is applied to the uranium plasma, propellant, and solid regions. Starting with the stationary, spherically symmetric plasma, equation (1) becomes:

$$\frac{1}{r^2}\frac{d}{dr}[r^2(q_r + q_c)] = S \quad (5)$$

If q_c is assumed to be small compared to q_r, equation (5) can be readily integrated:

$$q_r = \frac{1}{r^2}\int_0^r r^{*2} S\, dr^* \quad (6)$$

The source term S can be written as:

$$S = \varepsilon \Sigma^f \phi_1 \quad (7)$$

where ϕ_1 is the plasma neutron flux obtained from the neutronic analysis.

Since the plasma is optically thick, the radiative heat flux can be written as:

$$q_r = -\frac{16\sigma}{3a_R} T^3 \frac{dT}{dr} \quad (8)$$

where σ is the Stefan-Boltzmann constant, a_R is the Rosseland mean absorption coefficient, and T is the temperature.

Since the heat flux vanishes at the center and the plasma edge temperature is found from the propellant heat transfer analysis, equations (6) to (8) are used to determine the plasma temperature distribution.

The radial component of the energy equation (1) for the propellant region is given by:

$$\rho V_r \frac{dh}{dr} + \frac{d}{dr}(q_r + q_c) + \frac{2(q_r + q_c)}{r} = 0 \quad (9)$$

where V_r is the radial velocity component.

Calculation of the true radial velocity distribution would require the solution of the two dimensional Navier-Stokes equations. This is not appropriate for this preliminary analysis, and therefore a very simple model is used to describe the radial velocity. It is assumed that the velocity decreases linearly from the cavity wall to a value of zero at the propellant/plasma interface.

The conductive heat flux is simply

$$q_c = -K_c \frac{dT}{dr} \quad (10)$$

where K_c is the thermal conductivity.

The radiative heat flux is written as

$$q_r = 2\sigma T_2^4 E_3(\tau) - 2\sigma T^4 E_3(\tau) + 2\sigma \frac{dT^4}{d\tau}\left[\tau E_3(\tau) + E_4(\tau) - \frac{2}{3}\right] \quad (11)$$

where $E_n \equiv \int_0^1 u^{n-2} e^{-\frac{t}{u}} du$ = exponential integral

$\tau \equiv \int_0^r a_p\, dr^*$ = optical depth

a_p = absorption coefficient of the seeded gas

and T_2 = cavity wall temperature.

By specifying T_2 and the inlet propellant velocity at the wall, equations (9) to (11) are solved for the propellant temperature distribution in the core.

It is assumed that all heat transfer in the solid regions is by conduction, and that all power generated in the driver region is extracted by the inflowing propellant or by the working fluid of the power conversion system. Since solid-gas heat transfer coefficients are unknown, the temperature distributions in the solid regions and in the propellant in these regions are assumed to be identical. Therefore, the Poisson equation is solved for the driver region and the Laplace equation for the remaining solid regions (reflector, moderator, and pressure shell).

The solutions are

$$T = a + \frac{b}{r} - \frac{q_d r^2}{6K_c} \qquad (12)$$

for the driver region and

$$T = C + \frac{d}{r} \qquad (13)$$

for the remaining regions. a, b, c, and d are constants evaluated from the boundary conditions which require temperatures and heat fluxes to be continuous across interfaces and temperatures to be specified at the cavity wall and at the outer wall of the pressure shell.

q_d is an effective power density which is evaluated in the following manner. Q_d, the driver power, is distributed between the propellant and the power conversion system working fluid. The parameter K is defined as the fraction of the driver power delivered to the power conversion system. Therefore, (1-K) Q_d is absorbed by the propellant in the driver region, and the total propellant power Q_p is given by:

$$Q_p = Q_c + (1-K)\ Q_d. \qquad (14)$$

q_d is then equal to $(1-K)Q_d/[4/3\pi(r_4^3-r_3^3)]$. K is determined from the fuel element operating temperature.

The analysis used above describes the propulsive mode and provides a method to determine reactor power allocations. Therefore, for given reactor conditions, the driver power can be varied to obtain a range of core, total propellant, and heat rejection powers.

In this mode, the thermal power KQ_d extracted by the power conversion system working fluid is rejected into space by the radiator (except possibly for a small amount needed for housekeeping purposes). Therefore, the power conversion system is essentially idle in the propulsive mode.

In the power generation mode, the fuel and propellant flows are shut off and all the thermal power produced in the driver region is delivered to the power conversion system. The first step in analyzing the power mode is to investigate reactor criticality. This is accomplished with the neutronics analysis developed above, with plasma and propellant densities taken small enough to simulate an evacuated cavity. If a reactor is critical in the power mode, it will also be critical in the propulsive mode, as the plasma contributes only a small positive reactivity.

A heat transfer analysis was not performed for the reactor operating in the power mode; however, conclusions drawn from the propulsive mode anlaysis may be extrapolated to determine the general characteristics of the dual-mode system. As in the propulsive mode, the thermal power is assumed to be delivered to the power conversion system via heat pipes or a working fluid.

If the driver fuel elements were operated at the same power level for both modes, the total energy delivered to the power conversion system would be greater during the power mode, since there is no propellant flow to draw off a fraction of the driver power. However, the driver power can and should be operated at a lower power level in the power mode, since lifetime requirements (e.g., several years) dictate lower material temperatures than in the relatively short-term propulsive mode. Thus the maximum driver power in the power mode should be KQ_d, the same as is absorbed by the working fluid in the propulsive mode. Then the temperature constraints imposed in the propulsive mode will not be violated in the power mode. Power levels may be further decreased from KQ_d as necessary for lifetime needs.

The electric power Q_e generated by the system is then

$$Q_e = \eta_{pcs}\ Q_d' = \eta_{pcs}\ KQ_d \qquad (15)$$

where η_{pcs} is the efficiency of the power conversion system and Q_d' is the driver power in the power mode.

The engine mass can only be estimated in this preliminary study. It is the sum of the reactor, turbupump, nozzle, control, and structural masses. The total system mass is the sum of the engine and power conversion systen (including radiator) masses. All except the reactor mass are calculated by simple power-dependent scaling.

It should be noted that the radiator mass is also dependent on radiator sink temperature as well as the amount of heat to be rejected. It is difficult to say whether the radiator mass is greater in the power or propulsive mode without a cycle analysis. The more massive radiator should be used for both modes.

III. Discussion of Results

The accuracy of the model used here is checked against the more sophisticated model used by Hyland. For a 500-atmosphere reactor with a driver power of 19.7 megawatts, a core power of 4.95 megawatts is calculated as compared to Hyland's value of 4.55 megawatts. It is therefore concluded that this model is accurate enough for a preliminary survey.

However, this configuration rejects a sizable amount of thermal power: 17.7 megawatts. It is clearly desirable to operate at lower driver power levels. In addition, Hyland fixed his reactor dimensions to fit in the shuttle bay. Smaller size reactors should be investigated.

The first step is to estimate the minimum size reactor which could be critical either with or without the core. Accurate definition of the true minimum size reactor, which would require a detailed parametric study incorporating variable reactor region dimensions and compositions, is not considered appropriate for this study.

Hyland's reactor is again used as the reference reactor and various parameters are perturbed. Three temperatures must be fixed in the solid regions for the analysis to proceed: the maximum solid fuel driver temperature (set at 2000 K), the reactor inlet temperature (set at 293 K), and the cavity wall temperature (1523 K).

A constant α is defined as the dimensionless new reactor radius ($\alpha = 1$ corresponds to Hyland's reactor dimensions). The region sizes of the new reactor are obtained by multiplying the corresponding dimensions of the reference reactor by α. Therefore, the dimensions of the regions are always in the same proportion as Hyland's reactor for each reactor examined.

It is assumed that there is no plasma present in the cavity and K is arbitrarily selected as 0.5. With K and the temperature constraints selected, α is a function only of Q_d. Therefore an α is generated for each Q_d selected.

However, α must also satisfy the criticality requirement. For the fuel loading of 20 kg of ^{233}U in the driver region, the reactor becomes subcritical below $\alpha = 0.708$. Table 1 shows the dimensions and mass of this minimum size reactor as compared with that of Hyland, indicating a considerably smaller mass than Hyland's, which in turn was itself considerably lower than that of the all-plasma fuel concepts. This suggests that the dual-mode plasma-core engine could provide excellent payload performance.

The calculations are then repeated with plasma in the cavity to determine the core power. Although the driver fuel provides almost all the reactor's reactivity, the plasma contributed a small positive reactivity which can be controlled, by increasing neutron absorption with control devices in the driver region, to prevent the reactor from becoming supercritical.

Table 1 Minimum Size Reactor Dimensions and Mass

	Hyland's	Minimum
Radius of Plasma, m	0.213	0.1508
Radius of Cavity, m	0.3048	0.2158
Thickness of Inner Moderator, m	0.1524	0.1079
Thickness of Driver Region, m	0.0508	0.0360
Thickness of Outer Moderator, m	0.0508	0.0359
Pressure Shell Thickness, m	0.0512	0.0363
Overall Reactor Radius, m	0.61	0.432
Reactor Mass, kg	3388	1215

Note

1. Fraction K of power delivered to power generation system is 0.5.
2. Dimensions of minimum-sized reactor are 70.8% of Hyland's reactor.
3. Maximum driver fuel element temperature 2000 K, shell temperature 293 K, and cavity wall temperature 1523 K.

For this minimum size reactor with K = 0.5, the driver power was 2.89 megawatts and the core power 0.206 megawatts - too low for propulsive mode operation. Therefore, it is of interest to examine other driver powers for the minimum size reactor.

In order to satisfy the temperature constraints, (1-K) Q_d is kept constant as Q_d is varied. The results are presented in Figure 4, which shows K plotted against the core/driver ratio Q_c/Q_d for various total powers (sum of the driver and core powers), Q. This map is then used to calculate the overall system performance.

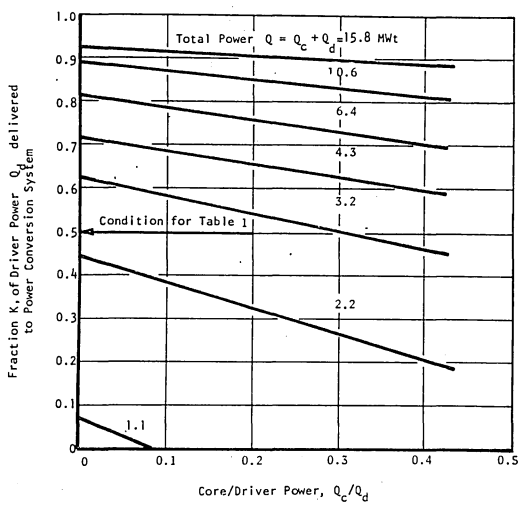

Figure 4 Power Level and Distribution Map for Minimum-Size Plasma Core Reactor

Table 2 shows the breakdown in power allocations and masses for two values of Q_c/Q_d. The total propellant power is given by equation (14) and the electric power by equation (15), with the power conversion system efficiency taken to be 0.25. The engine mass includes reactor, turbopump, nozzle, control, and structure masses. The total system mass is obtained by summing the engine mass and power conversion system mass.

Table 2 Breakdown of Total System Mass for Minimum Reactor Mass

(For Two Values of Core/Driver Power Ratio)

Total Power, (Q) MWt	Core/ Driver Power, (Q_c/Q_d)	Propellant Power, (Q_p) MWt	Electric Power, (Q_e) MWe	Engine Mass, kg	Power Conversion Mass, kg	Total System Mass, kg
2.2	0.1	1.44	0.190	1 284	760	2 044
	0.4	1.88	0.081	1 290	320	1 610
3.2	0.1	1.51	0.422	1 310	1 690	3 000
	0.4	2.13	0.266	1 316	1 060	2 376
4.3	0.1	1.62	0.669	1 339	2 680	4 019
	0.4	2.47	0.456	1 348	1 830	3 178
6.4	0.1	1.84	1.14	1 393	4 560	5 953
	0.4	3.20	0.800	1 408	3 200	4 608
10.6	0.1	2.22	2.10	1 502	8 380	9 882
	0.4	4.45	1.54	1 525	6 150	7 675
15.8	0.1	2.66	3.28	1 637	13 100	14 737
	0.4	5.81	2.50	1 668	9 990	11 658

These results are used to plot Figure 5, which shows the variation of total system mass versus propellant thermal power and electric power for various values of Q_c/Q_d .

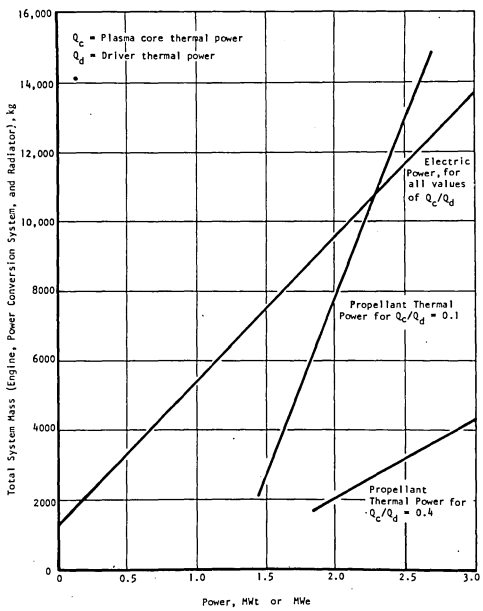

Figure 5 Total System Mass vs Electric and Propellant Thermal Powers

Note that there are two curves for the propellant thermal power, since this quantity is dependent on Q_c/Q_d . However, the electric power curve is quite insensitive to Q_c/Q_d so that only one curve is needed to represent all Q_c/Q_d values.

From Figure 5, it can be concluded that for the minimum-sized reactor, dual mode operation is limited to high electric power requirements (greater than 1 MWe). This limitation is imposed by the fact that if interesting levels of propulsive power are to be utilized, the reactor must be operated at high total power. Therefore, a large amount of driver power must be delivered to the power conversion system.

For example, if a dual mode system is required to produce 2.0 MWt of propellant power at Q_c/Q_d = 0.1, Figure 5 can be used to find the electric power and the system mass. In this case, the system mass is 8000 kg and the electric power produced in the power mode is 1.6 MWe.

It is observed from Table 2 that the power conversion system mass dominates the total system mass at the higher powers. It is beneficial to the performance if the power conversion system mass can be reduced, suggesting the use of advanced heat pipe, Brayton cycle, and thermionic conversion technology.

A full map of possible reactor sizes and power levels is not explored in the present study; clearly this needs to be done before the scale, configuration, or performance specifications for reactor models can be selected.

IV. Conclusions

The mini-cavity plasma core reactor was found to be capable of dual-mode operation. A reference reactor was found to have excess reactivity, and as a result the reactor size was substantially reduced (about 30%). The resulting reactor was smaller than any other plasma core concept previously investigated. It was critical with or without plasma present in the cavity and therefore was neutronically feasible for dual mode operation.

The fraction of driver power removed to the power conversion system K was plotted against the ratio of core to driver power Q_c/Q_d for several total reactor powers. From this map propellant thermal powers, electric powers, engine mass, power conversion system mass, and total system mass were calculated and used to generate a performance map of total system mass versus electric or propellant thermal power for various Q_c/Q_d .

It was observed that this reactor possesses characteristics for dual-mode applications which require the driver thermal power level during the power mode to be of the same order of magnitude as the nozzle exhaust power level during the propulsive mode. For example, one dual mode system produces 2.0 MWt of propellant thermal power in the propulsive mode, 1.6 MWe of electric power in the power mode (utilizing a 25% efficient power conversion system), and has a total system mass of 8000 kg. Such an electric power output can be used by magnetoplasmadynamic arcjets for primary electric propulsion.

The analysis is preliminary in nature. The neutronics calculations should be redone using a multigroup method (diffusion or transport code). Better representation of the heat transfer and fluid dynamics processes occurring in the cavity is needed. A two-dimensional heat transfer analysis of the driver region is necessary, particularly in the power mode. Systems analyses are needed for the power conversion system

(including radiator) and various subsystems such as the nozzle and turbopump. Finally, a broad range of reactor sizes and powers should be examined.

Aside from this analysis, two critical questions must be answered. The first is the feasibility of uranium plasma retention, which should be answered by planned reactor experiments. The second concerns the usefulness of the dual mode concept. Mission analyses are required to determine what missions are appropriate for this concept and how it compares with alternative methods such as a chemical-nuclear electric rocket combination.

References

1. Hyland, R.E., "Mini Gas-Core Propulsion Concept," NASA TM X-67958, October 1971.

2. Beveridge, J.H., "Feasibility of Using the NERVA Rocket Engine for Electrical Power Generation," AIAA Paper No. 71-639, June 1971.

3. Booth, L.A., and Altseimer, J.H., "The Nuclear Rocket Energy Center Concept," Los Alamos Scientific Laboratory Report LA-DC-72-1262, 1972.

4. Chow, S., Grey, J., and Layton, J.P., "Preliminary Analysis of Mini-Cavity Plasma Core Fission Reactors for Dual-Mode Space Nuclear Power and Propulsion Systems," Princeton AMS Report No. 1230, October 1975.

DISCUSSION

F. C. SCHWENK: What kind of thrust levels were you getting?

S. CHOW: 400 Newtons.

F. C. SCHWENK: So when you were using the propulsive mode with the plasma, it was still a fairly low thrust machine.

J. GREY: If you look way back in the early 1960's, one felt that the ideal rocket would be one that gave high thrust to mass ratios in the neighborhood of a planet and very high specific impulse when not near a planet. So we therefore said we have been looking at this dual mode thing for a long time in the solid core configuration, and the solid core system constraints are such that you get at least an order or two of magnitude ratio between the direct thrust and the amount of power available for electric, because you are taking most of the heat out on direct thrust. This gas core system uniquely offers an opportunity to have all those power levels where the electric power is very high (the same order of magnitude) as direct thrust. It turned out there were some missions that looked very nice with this, but we haven't yet compared them with missions which might be done the same way with, say, a chemical rocket plus a nuclear reactor, and that is a comparison that must be made.

PLASMA CORE REACTOR APPLICATIONS*

T. S. Latham, Chief Project Engineer
and
R. J. Rodgers, Research Engineer
United Technologies Research Center
East Hartford, Connecticut

Abstract

Analytical and experimental investigations are being conducted to demonstrate the feasibility of fissioning uranium plasma core reactors and to characterize space and terrestrial applications for such reactors. Uranium hexafluoride (UF_6) fuel is injected into core cavities and confined away from the surface by argon buffer gas injected tangentially from the peripheral walls. Power, in the form of thermal radiation emitted from the high-temperature nuclear fuel, is transmitted through fused-silica transparent walls to working fluids which flow in axial channels embedded in segments of the cavity walls.

Radiant heat transfer calculations were performed for a six-cavity reactor configuration; each cavity is approximately 1 m in diameter by 4.35 m in length. Axial working fluid channels are located along a fraction of each cavity peripheral wall. The remainder of the cavity wall is constructed of highly reflective aluminum which focuses radiant energy onto the working fluid channels. Results of calculations for outward-directed radiant energy fluxes corresponding to radiating temperatures of 2000 to 5000 K indicate total operating pressures from 80 to 650 atm, centerline temperatures from 6900 to 30,000 K, and total radiated powers from 25 to 2500 MW, respectively.

Applications are described for this type of reactor such as (1) high-thrust, high-specific-impulse space propulsion, (2) highly efficient systems for generation of electricity, and (3) hydrogen or synthetic fuel production systems using the intense radiant energy fluxes.

Introduction

Since 1955, various researchers have considered the prospects for utilizing nuclear energy with fissile fuel in the gaseous state. Most of this work was concentrated on the gaseous nuclear reactor technology required for high-performance space propulsion systems. The current research program on gaseous nuclear reactors includes continued consideration of high-thrust, high-specific-impulse space propulsion applications and, in addition, plasma core reactor (PCR) applications for meeting terrestrial energy needs.

Extraction of energy from the fission process with the nuclear fuel in gaseous form allows operation at much higher temperatures than those of conventional nuclear reactors with solid fuel elements. Higher operating temperatures, in general, lead to more efficient thermodynamic cycles and, in the case of fissioning uranium plasma core reactors, result in many possible applications employing direct transfer of energy in the form of electromagnetic radiation. The applications for PCR's require significant research and technology development, but the benefits in potential increases of domestic energy resources and utilization, reductions in environmental impact, and the development of new highly-efficient techniques for extracting energy from the fission process with nuclear fuel in the gaseous or plasma state justify an investment to establish the feasibility of fissioning uranium PCR's as a prime energy source.

Possible applications for plasma core reactors are:

(1) High-thrust, high-specific-impulse space propulsion.

(2) Advanced closed-cycle gas turbine driven electrical generators.

(3) MHD power conversion systems for generating electricity.

(4) Photochemical or thermochemical processes such as dissociation of hydrogenous materials to produce hydrogen.

(5) Thorium--Uranium-233 thermal breeder reactor with gas turbine driven electrical generators.

(6) Direct nuclear pumping of lasers by fission fragment energy deposition in lasing gas mixtures.

(7) Optical pumping of lasers by thermal and non-equilibrium electromagnetic radiation from fissioning UF_6 gas and/or fissioning uranium plasmas.

Cavity reactor experiments have been conducted to measure critical masses in cavity reactors to obtain data for comparison with theoretical

*Research sponsored by NASA Langley Research Center, Contract NAS1-13291, Mod. 2.

calculations at both Los Alamos Scientific Laboratory (LASL) and the National Reactor Testing Station (NRTS) in Idaho Falls. Critical mass measurements have been made on both single cavity and multiple cavity configurations. In general, nucleonics calculations have corresponded to within a few percent of the experimental measurements. A review of these experiments is contained in Ref. 1. These studies provide the basis for selecting additional experiments to demonstrate the feasibility of the plasma core nuclear reactors.

A program plan for establishing the feasibility of fissioning UF_6 gas and uranium plasma reactors has been formulated by NASA and is described in Refs. 2 and 3. Briefly, the series of reactor tests consists of gaseous nuclear reactor experiments of increasing performance, culminating in an approximately 5 MW fissioning uranium plasma reactor experiment. Each reactor experiment in the series will yield basic physical data on gaseous fissioning uranium and basic engineering data required for design of the next experiment. Initial reactor experiments will consist of low-power, self-critical cavity reactor configurations employing undissociated, nonionized UF_6 fuel at near minimum temperatures required to maintain the fuel in gaseous form. Power level, operating temperatures, and pressures will be systematically increased in subsequent experiments to approximately 100 kW, 1800 K, and 20 atm, respectively. The final 5 MW reactor experiment will operate with a fissioning uranium plasma at conditions for which the injected UF_6 will be dissociated and ionized in the active reactor core. A review of the initial UF_6 reactor experiments in the planned series conducted at LASL is given in the Proceedings of this conference and in Ref. 4. Discussions of experimentally realized nuclear pumped lasers are also given in the Proceedings of this conference (Session III) and in Ref. 5.

The analytical investigations reported herein were performed to examine potentially attractive applications for gaseous nuclear reactors fueled by UF_6 and its decomposition products at operating temperatures of 2000 to 6000 K and pressures of approximately 100 to 650 atm. Emphasis was placed on predictions of performance of this class of gaseous nuclear reactors (1) as the primary energy source for high-thrust, high-specific-impulse space propulsion applications, (2) as the energy source for highly efficient systems for generation of electricity, (3) as the source of high intensity photon flux for heating seeded working fluid gases for applications such as hydrogen production and MHD power extraction, and (4) in a Thorium--Uranium-233 nuclear breeding fuel cycle. Configurations to permit the coupling of the intense radiant energy fluxes to working fluids are presented. Energy conversion systems using the gaseous nuclear reactor as the prime energy source were analyzed to determine system performance and thermodynamic efficiencies. Conceptual designs are presented which indicate the overall features of the application systems and the method of integration of the principal components with the gaseous nuclear reactor energy source.

Plasma Core Reactor Configurations

In the plasma core reactor (PCR) concept a high-temperature, high-pressure plasma is sustained via the fission process in a uranium gas injected as UF_6 or other uranium compounds. Containment of the plasma is accomplished fluid-mechanically by means of an argon-driven vortex which also serves to thermally isolate the hot fissioning gases from the surrounding wall. For applications which employ thermal radiation emitted from the plasma, an internally-cooled transparent wall can be employed to isolate the nuclear fuel, fission fragments, and argon in a closed-cycle flow loop and permit transfer of the radiant energy from the plasma to an external working fluid. For applications which employ fission-fragment-induced, short wavelength, nonequilibrium radiation emitted from the plasma, the working fluid such as lasing gases can be either mixed with fissioning gas or injected into the peripheral buffer gas region such that there is no blockage of radiation due to the intrinsic absorption characteristics of transparent materials at short wavelengths. The PCR configurations discussed below are for applications based on use of intense thermal radiation transmitted through transparent walls to working fluids; closed-loop circulation of gaseous nuclear fuel and buffer gas is an intrinsic feature of the configurations.

Geometry of Unit Cells and Reactor

Concepts for coupling radiant energy from a fissioning plasma to working fluids are shown in Fig. 1. The unit cell shown at the top of Fig. 1 is from the nuclear light bulb space propulsion concept described in Ref. 6. Energy is transferred by thermal radiation from gaseous uranium fuel through an internally-cooled transparent wall to seeded hydrogen propellant. The fuel is kept away from the transparent wall by a vortex flow field created by the tangential injection of buffer gas near the inside surface of the transparent wall. The buffer gas and the entrained gaseous nuclear fuel pass out through ports located on the centerline of the endwall of the cavity.

An alternate unit cell configuration is shown at the lower left of Fig. 1. The fuel and buffer gas zone is surrounded by a reflective aluminum liner with axial working fluid channels along portions of the periphery of the fuel cell surface. The reflective liner would be made of aluminum, for example, which has a reflectivity of approximately 0.9 for the spectral distribution of thermal radiation emitted from the nuclear fuel. The liner materials which are highly reflective to thermal radiation reduce heating of the cavity surfaces and concentrate the thermal radiation onto the

working fluid channels. The working fluid could be heated by being passed over graphite fins which are not surrounded by fused-silica tubes. Or, the graphite fins could be replaced by micron-sized particles or opaque gases to absorb the thermal radiation from the fissioning plasma.

A working fluid assembly which consists of a series of uncooled U-tube-shaped fused-silica coolant passages is shown in the lower right of Fig. 1. The tubes have walls sufficiently thick to withstand compressive pressure loads should it be desirable to operate the working fluid at a pressure significantly lower than that in the fissioning uranium plasma region. Interstitial zones surrounding the U-tubes are filled with inert gas (argon or helium) at the same pressure as the plasma region. Working fluid such as helium passes through the fused-silica tubes and is heated by convection from high temperature graphite fins inside the fused-silica tubes which absorb thermal radiation emitted from the plasma. The upper limit on working fluid outlet temperature imposed by a limit on the fused silica operating temperature would be approximately 1200 K.

A sketch of a conceptual design of a plasma core reactor for use in generating electricity is shown in Fig. 2. The reactor consists of six unit cells which are imbedded in a beryllium oxide reflector-moderator and surrounded by a pressure vessel. Each of the six unit cells is a separate cylindrical unit consisting of a fuel region assembly and an outer working fluid assembly. The two assemblies can be withdrawn from opposite ends of the reactor configuration for periodic maintenance and inspection. The fuel assembly consists of a plasma fuel zone with nuclear fuel injected in the form of UF_6. The uranium used in the UF_6 can be either highly enriched U-235 or U-233. Gaseous nuclear fuel is confined in the central region of the fuel zone by argon buffer gas. The mixture of nuclear fuel and argon buffer gas is withdrawn from one or both endwalls at the axial centerline for separation and recirculation.

A cross section of a breeder reactor version of a plasma core reactor is shown on the bottom of Fig. 2. Results of calculations of breeding ratios and doubling times for a plasma core breeder reactor are described in a subsequent section.

Plasma core reactors which have been discussed thus far have working fluid channels closely coupled neutronically to the reactor. Applications for plasma core reactors are under consideration for which it would be more advantageous to locate the working fluid channels at positions other than those adjacent to the fuel cavity, so that the neutron absorbing characteristics of material in the working fluid channels will be unimportant. Thus, a transmission cell must be provided so that thermal radiant energy fluxes can be transmitted from the nuclear fuel cavity, through the moderator and perhaps through the pressure vessel, to the working fluid channels.

A schematic diagram of two possible plasma core reactor configurations which make use of transmission cells is shown in Fig. 3. The configuration on the left shows an arrangement in which transmission cells are connected to working fluid channels within the pressure vessel, but outside of the beryllium oxide reflector-moderator, thus minimizing the neutronic coupling between the fuel cavity and working fluid channel. Potential applications for this configuration are principally terrestrial. The configuration shown on the right in Fig. 3 has a single centralized working fluid channel which receives thermal radiant energy from each of the surrounding six nuclear fuel cavities, and which is outside of the inner pressure vessel wall structure. This particular configuration can be employed in providing a high temperature gaseous propellant stream for space propulsion applications or for terrestrial power conversion applications. Further, radiant energy deposited in the reflective liner as well as neutron and gamma energy deposited in the moderator can be extracted to provide onboard power for the space vehicle.

The transmission cell employs series of fused-silica transparent walls with intermediate regions of gaseous hydrogen and/or deuterium gas to balance pressure between the fuel cavity region and the transmission cell. The hydrogen and/or deuterium gas provide a transparent light path for the thermal radiation emitted from the plasma. The gas also scatters neutrons effectively and, therefore, reduces leakage of fast and thermal neutrons from the system. The transmission cell supporting structure is cylindrical in shape and the inner cylindrical wall is lined with a highly reflective material such as aluminum. The reflective liner minimizes the loss of radiant energy to the walls of the transmission cell as it is transmitted from the fuel cavity to the working fluid channel. The fused-silica walls which are components of the transmission cells are not completely transparent to thermal radiant energy and absorption must be included in evaluating the transmission cell efficiency.

A summary of transmission cell performance is given in Table I. These results are calculated for an outward-directed thermal radiant energy flux corresponding to a black-body temperature of 4000 K. One component of transmissivity is related to the radiant energy absorbed by the fused silica and is a function of the wall thickness. This component varies from 0.941 to 0.85 for wall thicknesses of 0.25 and 3.5 cm, respectively. A second component of transmissivity is related to losses from the incident beam resulting from multiple wall reflections within the transmission cell along the path to the external working fluid channel. The transmissivity of a right circular, cylindrical transmission cell with aluminum reflecting walls was calculated as a function of the cell length-to-diameter ratio. Based on the Monte Carlo

technique developed in Ref. 7 in which the transmission of radiation from the diffuse source was calculated along a specular reflecting cylinder, the transmissivity at the exit of the cell varied from 0.92 to 0.56 as the length-to-diameter ratio varied from 0.5 to 4.0. The total transmissivity can be estimated, to a first approximation, by multiplying the two independent transmissivity components.

Fresnel reflection losses for fused silica and gas interfaces were not considered. The transmission cell must have a minimum of two fused-silica walls and thus four potentially reflecting surfaces. However, not all of the reflected energy is lost. Some of the energy will be reflected back into the fuel region to be reabsorbed and, subsequently, re-radiated by the plasma; some will be re-reflected within the transmission cell and find its way to the working fluid channel. Furthermore, reflection losses occurring at the interfaces of the fused silica can be reduced within given wavelength bands by depositing anti-reflection coatings on the surfaces. Further analyses or measurements are required to quantify the effects of interface reflections on overall transmission cell performance.

Criticality and Radiant Heat Transfer

Calculations of critical mass were performed using the one-dimensional neutron transport theory computer program, ANISN (Ref. 8), for the non-breeder reactor configuration shown in Fig. 2. The volume of each region was transformed into equivalent-volume spherical zones. A twenty group neutron energy structure was used in the calculation for which neutron cross sections were obtained from the HRG (Ref. 9), TEMPEST-II (Ref. 10), and SOPHIST-I (Ref. 11) computer programs. A critical mass of 86.4 kg of U-235 was calculated; 14.4 kg is in each of the six unit cells.

Nuclear fuel will be injected into the fuel region of plasma core reactors in the form of gaseous UF_6. Upon entering the plasma zone, the UF_6 will dissociate such that at high temperatures ($\sim$8000 K) the total pressure of the mixture will consist primarily of contributions from uranium atoms and ions, free fluorine atoms and ions, the corresponding electrons from ionized species, and some argon buffer gas which will mix into the plasma zone. The composition of UF_6 as a function of temperature and pressure were calculated using a UTRC computer code described in Ref. 12. The following species were included in the analyses: UF_6, UF_5, UF_4, UF_3, F, F^-, F_2, U^0, U^+, U^{+2}, U^{+3}, and electrons. A composite plot of the variation of the ratio of fluorine to uranium and uranium fluoride species is shown as a function of temperature for several total pressures in Fig. 4. The abrupt increase in fluorine partial pressure with temperature occurs with the onset of the dissociation of UF_6. A plasma core reactor must by definition be an ionized gas. If fueled by UF_6, the six fluorines and electron partial pressures add to those of the uranium species, resulting in operating pressures of several hundred atmospheres.

In calculating the temperature distribution for the fissioning plasma region for a given radiant heat flux at the plasma edge, the containment characteristics in the fuel and buffer-gas region must be considered. A reasonable constraint for containment is to require that from the edge-of-fuel location inward, the local density at any station be less than or equal to the density of the buffer gas at the edge-of-fuel location. With this constraint, and for constant total pressure, there exists an upper limit on the amount of uranium (which has a higher mass number) that can be confined with the fluorine and argon at a given local temperature. Calculations were performed to determine the ratios of uranium to fluorine and argon at local temperatures in the fuel region such that the total pressure is preserved and the total density of uranium, fluorine, and argon is equal to or less than that of the argon at the edge-of-fuel location. The compositions of fluorine, argon, and uranium as functions of temperature and pressure, including the effects of ionization at high temperatures, were taken from Refs. 13 and 14, and from the UF_6 decomposition calculations. By using UF_6 decomposition products and argon decomposition products in conjunction with the estimated spectral absorption cross sections, Rosseland mean opacities were calculated for the mixture of argon and UF_6 decomposition species in the fuel region. The estimates of the spectral characteristics of UF_6 and its dominant decomposition products over the range of pressure, temperature, and wavelength important to the plasma core reactor concept, were reported in Ref. 15. Results of current research on the experimental measurement of spectral emission and absorption characteristics by UF_6 and its decomposition products is reported in Ref. 16.

These mixture opacities were used in a radiation diffusion analysis to determine the temperature distribution required to deliver a net heat flux at radial boundaries, which are located at 110 cm intervals from the centerline of the fuel zone, equal to the total energy release due to the fissioning of the nuclear fuel within each boundary (local argon, fluorine, and uranium densities and partial pressures were calculated using the program discussed above). The calculation converges when the heat flux at the outer boundary corresponds to the net heat flux at the edge-of-fuel location and the contained uranium, based on the imposed density and total pressure constraints, equals the critical mass.

Radiant heat transfer calculations were performed for the unit cells in the reactor configuration shown in Fig. 2. Temperature distributions were calculated for edge-of-fuel temperatures of 2000 K, 3000 K, 4000 K, and 5000 K, and working channel duct to total cavity surface area ratios of 0.0, 0.1, 0.2, 0.3, and 1.0. The centerline

temperatures and total cavity pressures which include the resulting UF_6 and argon decomposition product partial pressures are given in Table II. The critical mass was held constant for the different operating conditions, so that the characteristic of the pressure increasing as the centerline temperature increases is indicative of the degree of UF_6 dissociation.

The reflective aluminum liner tends to trap photons in the fuel region. A portion of the reflected thermal radiation is reabsorbed by the nuclear fuel in the edge-of-fuel region which causes the local temperature to rise. The spectral heat flux incident on the aluminum liner was used to calculate an aluminum spectrum-weighted average reflectivity which at the liner surface was 0.909. The effective reflectivity is different from the spectrum-weighted average reflectivity of the aluminum liner because of geometrical factors. Diffusely reflected radiation from the liner would have a cosine distribution about the inward normal. Some of the reflected radiation, therefore, would not intercept the fuel cloud but would pass by the cloud and reflect off another portion of the liner.

The equations which describe the effective reflectivity for a given fuel region and reflective liner geometry are derived in Ref. 17. A given steady-state outward-directed heat flux and the reflected component of the thermal radiation which is absorbed by the fuel cloud, are related uniquely when the fuel cloud is assumed to be a cylindrical, optically-thick radiating fuel cloud. The radiant energy which is not reabsorbed by the fuel cloud is either absorbed by the reflective liner or is incident on the working channel duct where it represents energy available for an energy extraction cycle. The distribution of radiant energy absorbed by the working fluid channel and the reflective liner as a function of ratio of the area of the working fluid channel to the total cavity surface area is shown in Fig. 5. These energy deposition distributions were used to determine the radiant thermal powers deposited in the liner and duct for the parametric series of calculations. Calculations were also performed to estimate the convective removal of energy from the fuel cavity by the flowing gases as well as the energy deposited in the moderator by fission neutrons and gammas. The model used for the convective energy removal is similar to that described in Ref. 18. Using the temperature distributions calculated for each thermal heat flux condition and with a buffer gas residence time of 30 s and a ful residence time of 60 s, the total convective energy removal, Q_{CONV}, was calculated. In addition, the power deposited in the moderator, Q_{MOD}, was calculated to be equal to 0.125 times the total reactor power. The resulting energy balances for the cases calculated are given in Table III.

For the conditions at which the edge-of-fuel temperature is 4000 K and the working channel duct-to-cavity surface area ratio is 0.2, the calculated radial density distributions of the fuel, fluorine, and argon within the unit cell is shown in Fig. 6. The temperature variation was assumed to be linear with radius through the argon buffer region. This buffer gas region temperature variation and corresponding density variation was matched to the temperature and density radial distributions obtained from the radiation diffusion analysis of the fuel region. The actual temperature and density distributions in the buffer gas region are not as linear as shown in Fig. 6, but this approximation does indicate the expected steep density gradient which should result in a strong stable vortex flow for containing the hot fuel gas within an outer cool buffer gas layer.

Plasma Core Reactor Applications

The salient feature of the plasma core reactor applications investigated is the coupling of power to working fluids by radiant heat transfer. The applications studied include high-thrust, high-specific-impulse, space propulsion systems, electric power generators using closed-cycle helium gas turbines, an MHD power conversion concept, and photochemical/thermochemical processes for the production of hydrogen. In addition, Thorium-U-233 breeder configurations of plasma core reactors were analyzed to determine possible ranges of breeding ratios and doubling times.

High-Thrust, High-Specific-Impulse Space Propulsion

Historically, research on gaseous nuclear reactors was focused on high-performance space propulsion systems. Research was conducted on two major concepts of gaseous nuclear rockets: the open-cycle, coaxial flow concept and the closed-cycle nuclear light bulb concept. Comprehensive surveys of the ranges of performance of the open-cycle and nuclear light bulb rocket engines are discussed in Refs. 19 and 20, respectively. In addition, a version of the nuclear light bulb engine with size and critical mass reduced by use of cold beryllium reflector-moderators (less than 300 K) backed by cold deuterium-compound moderator materials and by use of axial propellant channels is described in Ref. 21. Table IV summarizes the performance characteristics of these propulsion systems.

The performance studies described below were done for closed-cycle gaseous nuclear rocket engines which employ gaseous UF_6 nuclear fuel and its decomposition products with radiating temperatures of 6000 K and lower and total pressures of a few hundred atmospheres. The resulting systems should be considered "first generation" plasma core reactor thrusters; the higher performance systems which should follow with technological improvements and growth having been thoroughly modeled and analyzed in earlier studies.

Engine performance characteristics were calculated for a derivative of the reference nuclear light bulb engine. Dimensional characteristics and component weights for this engine are given in Ref. 6. The assumptions employed to determine the performance of the engines over a range of fuel radiating temperatures from 4000 to 6000 K were as follows:

(1) Propellant exit temperature assumed to be 80% of fuel radiating temperature.

(2) Heat loads were assumed to be the same fraction of total power as those calculated for the reference nuclear light bulb engine in Ref. 6. Operating pressure and fuel and buffer gas heating were based on the calculations described in the preceding section.

(3) Specific impulse was reduced to 84% of the ideal value to allow for incomplete expansion, friction and recombination losses, nozzle transpiration coolant flow, and for the flow of tungsten seeds in the propellant to absorb thermal radiation.

(4) The total flow passing through the nozzle exit was increased by approximately 16% to include tungsten seed flow and transpiration coolant flow.

(5) Engine weight was determined by adding the reference nuclear light bulb moderator weight to the pressure vessel weight calculated using a weight factor given by $Z = W_{pv}/PV = 1.125$ kg/atm-m^3.

Performance characteristics for the cases considered are given in Table V. For the derivative of the nuclear light bulb reference engine with radiating temperatures from 4000 to 6000 K, the performance characteristics are: engine mass 32,700 to 42,900 kg; operating pressure 540 to 900 atm; Isp 880 to 1220 s; thrust-to-weight, 0.14 to 0.47.

For comparison purposes, preliminary analyses based on the techniques described in Ref. 22 were conducted of the performance of the engines described in Tables VI and V for a mission requiring a total V of approximately 853 m/s (i.e., low circular orbit to escape velocity, applicable to supply missions to synchronous orbit, for example). Comparisons were made in terms of initial mass required in earth orbit (IMEO) to a chemical rocket employing H_2/O_2 propellant with a specific impulse of 450 s, a weight of 1135 kg, and a thrust level of 890,000 N.

The missions comprised minimum energy Hohmann transfers from low circular earth orbit (100 nautical miles) to synchronous orbit and back using two rocket burns per transfer. Due to relatively low accelerations, gravity loss correction factors were included. The payload was assumed to be four space shuttle payloads, approximately 90,000 kg. Comparisons were made for two plasma core reactor rocket engines; a derivative of the nuclear light bulb reference engine with UF_6 fuel with an Isp of 1220 s and a thrust-to-weight ratio of 0.47 (see column 3 of Table V) and a small nuclear light bulb engine with an Isp of 1150 s and a thrust-to-weight ratio of 0.14.

For the cases calculated, the IMEO's for the plasma core rocket engines were about 40 to 60 percent of those for the chemical system. The performance advantage increases with increased payload also. These results indicate that the plasma core reactor engine with UF_6 nuclear fuel with "first generation" performance characteristics could be a desirable system for ferrying space shuttle payloads to selected earth orbits and possibly for other operations in cis-lunar space. The benefits of performance extension by technology growth and improvements to the high-thrust, high-specific-impulse systems described by the performance ranges quoted in Table V from earlier work are clear.

Closed-Cycle Helium Gas Turbine Electrical Generators

Basic performance analyses of closed-cycle gas turbine systems which could effectively utilize the high temperature capability of plasma core reactors were performed. The closed-cycle system uses a helium-driven gas turbine coupled to an electrical generator with a nominal output of 1000 MWe. Heat from the reactor can be transferred directly to the closed-cycle helium working fluid or can be transmitted through a secondary heat exchanger. The cycle under consideration would employ a multistage turbine connected to compressor spools. The working fluid leaving the main turbine would enter a second multistage turbine directly connected to the electric generator. Several heat exchangers would be incorporated in the system (i.e., a regenerator, precooler, intercooler) to increase the system performance. A schematic diagram of the closed cycle gas turbine system is shown in Fig. 7. Additional power generation is also possible by utilizing some of the heat from the working fluid at the regenerator and intercooler exhaust temperatures to operate supplementary steam or organic working fluid power systems to increasing the system overall efficiency. These additional systems were not investigated in this study.

The reactor configuration for electrical power generation was described in the preceding section. Sketches of the configuration and unit cells for power extraction are shown in Figs. 1 and 2. The mechanisms for extracting heat from the reactor can be either the system employing fused-silica U-tubes with graphite fins within the tubes to absorb thermal radiation, or the system with axial working fluid channels in which graphite fins absorb the thermal radiation without surrounding them with fused silica. The fused-silica U-tubes

permit a pressure differential between the operating pressure of the reactor and the operating pressure of the helium gas turbine loop. For example, fused-silica tubes under a compressive loading of 500 atm would require a ratio of OD to ID of 1.19 for a design point compressive stress of 1.38×10^8 N/m^2 (20,000 psi). Due to the temperature limitation on fused silica, the helium outlet temperature for the U-tube system is limited to approximately 1200 K. The alternate unit cell configuration with axial graphite fins would operate at working fluid pressures equal to those in the reactor fuel region. The working fluid would be conducted through a secondary heat exchanger across which a pressure drop could be sustained such that the helium gas turbine system could be operated at a desired cycle pressure. Helium outlet temperatures would be limited only by material limits in other system components. The latter unit cell would use less fused silica and structure in the reactor core and would be more adaptable to breeder reactor configurations where it is necessary to minimize parasitic neutron absorbers to maintain a desirable breeding ratio.

Performance was optimized by determining the system's overall efficiency, electrical power output divided by the total reactor thermal power, for a range of pressure ratios across the helium compressors and for three turbine inlet temperatures of 1098, 1506, and 1922 K. Efficiencies of the compressors, turbines and regenerator were assumed to be 0.9. The generator efficiency was assumed to be 0.98. Fractional pressure drops of $\Delta P/P = 0.02$ were assumed across all heat exchangers and through the reactor core. A compressor inlet temperature of 322 K was selected to permit use of a dry cooling tower for heat rejection (selection and evaluation of specific heat rejection systems was not included in the study, however). Based on the calculated results, a compressor pressure ratio of 1.75 was selected for cases with turbine inlet temperatures of 1089 and 1505 K and a compressor pressure ratio of 2.0 was selected for the case with a turbine inlet temperature of 1922 K. Three operating pressures were considered, 20, 51, and 153 atm. The overall cycle efficiency was found to be relatively insensitive to cycle pressure over the range from 20 to 150 atm. Thus, the principal impact of pressure selection would be on equipment size and cost.

The variation of overall cycle efficiency with turbine inlet temperature is shown in Fig. 8 with inlet temperatures noted for various blade materials and turbine blade cooling schemes. The progression of gas turbine technology into the 1980's is discussed in Ref. 23. With the use of cooled molybdenum alloy (TZM) blades and vanes, operation with turbine inlet temperatures of about 1900 K might be feasible by the mid 1980's. The cross-hatched region on the plot at working fluid temperatures of the order of 2500 K is indicated with an MHD label. The description of possible concepts which could be used for MHD system is given in the following section.

MHD Power Conversion Concepts

The high working fluid temperatures available from plasma core reactors make the use of MHD power extraction concepts attractive options. A comprehensive review of MHD power conversion systems based on gaseous nuclear reactor technology is given in Ref. 24. Plasma core reactors with fuel region radiating temperatures sufficiently high (4000 to 5000 K) to heat MHD working fluids to desired temperatures of 2000 to 2500 K have operating pressures on the order of 500 atm. Conductivity of MHD working fluid with alkali metal seeds decreases rapidly with increasing pressure ($\alpha P^{-\frac{1}{2}}$ for thermal ionization, αP^{-4} for nonequilibrium ionization). Therefore, MHD cycle performance for a given working fluid temperature tends to favor operation at a few atmospheres pressure. In the process of conceiving and evaluating configurations which might be used to couple MHD power extraction systems to plasma core reactors, two principal considerations are dominant; (1) the MHD duct operating pressure should be a few atmospheres while the reactor operating pressure is of the order of 500 atm; and (2) space occupied by MHD duct magnets and electrodes and parasitic neutron absorptions by the MHD duct materials should be small to minimize their impact on reactor criticality. The transmission cell concepts described in the preceding section provide a means to satisfy both constraints.

The configurations shown in Fig. 3 are both adaptable for use as MHD systems. In both cases, the MHD ducts would be located outside the nuclear fuel and moderator zones and essentially neutronically isolated. The transmission cells with series of fused-silica ports under compressive load would permit operation with the appropriate pressure differential between the PCR fuel region and the MHD duct. Two modes of operation would be possible. The MHD duct could be attached at the ends of the working fluid channels shown in Fig. 3. Power would be extracted after the fluid was heated as in most MHD concepts. A second option could be to install the MHD ducts with magnets and electrodes in the working fluid channels. Power would be extracted as the working fluid was heated, resulting in a very efficient cycle since the working fluid temperature and conductivity would be constant in the MHD duct. The latter constant temperature MHD power conversion system was first suggested in Ref. 25.

Preliminary investigations were made of possible MHD seeding materials. The most attractive working fluid and seeding materials identified for a PCR-MHD system were suspensions of thermionically emitting particles of barium oxide or mixed oxides of barium, calcium, and strontium in argon gas. The main theoretical advantages of an emitter suspension over an alkali metal seeded gas are its higher conductivity at temperatures up

to about 2000 K (especially at pressures of 10 atm and above) and its relatively small variation in conductivity with changes in pressure ($\alpha P^{-0.13}$). The latter property permits conceptual designs of MHD systems with operating pressures up to 50 atm with the resulting savings in component size. Discussions of theoretical and experimental investigations of the conductivities of gas borne suspensions of thermionic emitters are given in Refs. 26 and 27. Particle suspensions also tend to be broadband absorbers of radiant energy, making them ideally suited as PCR working fluids.

Related analyses of a closed-cycle nuclear MHD system using dust suspension described in Ref. 28 indicate that overall cycle efficiencies up to ~60 percent are theoretically possible with conventional nuclear reactors. Overall cycle analyses and identification of system components should be performed for a reference PCR-MHD power plant to evaluate its potential as an efficient power generation system.

Photodissociation of Halogens to Produce Hydrogen

Plasma core reactors have been proposed as a high power source of radiant energy for which efficient use of high intensity photon fluxes emitted from the radiating ionized fuel cloud can be employed in thermochemical and photochemical employing hydrogen as a fuel is attractive because it is nonpolluting. Hydrogen may be produced from energy sources such as nuclear reactors or solar radiation to the exclusion of production from fossil fuel sources. However, for hydrogen to become a viable fuel, satisfying significant future energy requirements, a means of producing vast quantities in an economic process must be identified and demonstrated.

Studies were conducted to evaluate methods for producing hydrogen using the intense photon fluxes emitted from plasma core reactors. A relatively simple concept proposed here for the photolytic decomposition of water in which the unique radiation emission characteristics of the plasma core reactor are utilized is shown in Fig. 9. Three successive working fluid channels are employed in the process. The first two channels provide a reaction site for the two-step, closed-cycle photolytic decomposition of water and the third channel is provided to absorb the residual thermal radiation either by flowing particle laden gases or by graphite finned rods which transfer the absorbed energy to a flowing gas stream by convection. The concept utilizes radiation and the chemical properties of halogens and hydrogen halides and the unique radiation characteristics of the plasma core reactor to circumvent the problems associated with the direct thermal or photolytic decomposition of water. The key to the concept depends upon the ability of halogens to react with water to form the corresponding hydrogen halide and oxygen species.

In the concept a series of relatively low temperature thermal or photolytic reactions are used to effect decomposition of water and to permit easy separation of reaction products. The combined overall reaction describing the process may be expressed as

$$Br_2(G) + 2I_2(G) + H_2O(G) \overset{h\nu}{\rightleftarrows} H_2(G) + Br_2(G) + 2I_2(G) + \tfrac{1}{2}O_2(G) \quad (1)$$

Results of composition calculations indicate that molecular bromine (Br_2) does not appreciably react with water. However, similar composition calculations with atomic bromine (Br) and water yield hydrogen bromide (HBr) and oxygen (O_2) as the principal products. Thermal dissociation of the halogens occurs to an appreciable degree (~50 percent) only at temperatures greater than 1500 K. In the concept, the radiant flux is used to induce photodissociation of the bromine and iodine molecular species and thermal dissociation is used for the hydrogen iodide and iodine monobromide species. Gaseous molecular bromine (Br_2) and water (H_2O) are allowed to react at approximately 450 K in the presence of radiation ($365 \leq \lambda \leq 535$ nm) to yield gaseous hydrogen bromide and oxygen. Since HBr is not appreciably dissociated at temperatures below approximately 1500 K, HBr is then allowed to react with iodine (I_2) at 456 K in the presence of radiation ($430 \leq \lambda \leq 740$ nm) to yield gaseous hydrogen iodine (HI) and iodine monobromide (IBr). Cooling the reaction mixture below the boiling point of IBr permits separation of liquid IBr from gaseous HI and HBr. Iodine (I_2) and bromine (Br_2) are regenerated from IBr at a temperature of about 700 K. The HI-HBr mixture is heated to about 700 K to thermally decompose HI to hydrogen (H_2) and I_2. Upon quenching to a temperature below 456 K, I_2 is liquefied and separated from the H_2 and HBr. Finally, the solubility of HBr in H_2O is utilized to separate H_2 from HBr.

For plasma core reactors with radiating temperatures between 4000 K and 6000 K, iodine absorbs over a larger fraction of the available spectra than bromine and overlaps portions of the spectra in which bromine also absorbs. To maximize bromine photodissociation to atomic bromine, the bromine region is positioned to intercept the incident thermal radiation first and is of sufficient thickness to reduce the spectral flux to less than one percent of its incident value. The iodine region is located behind the bromine region in the thermal radiation path and is also of sufficient thickness to absorb all but one percent of the spectral flux in its photodissociation wavelength range.

The fractions of radiant energy available to induce photodissociation of bromine and iodine are 0.25, 0.353, and 0.438 for black-body radiating temperatures of 4000 K, 5000 K, and 6000 K, respectively. The concept process also requires

two other dissociation reactions namely, HI and IBr into H_2, I_2, and Br_2. The dissociation of HI and IBr can be carried out thermally in a consecutive sequence of separation chambers. By considering these photodissociation and thermal dissociation reactions only, and assuming the higher heating value of water equal to 68.4 K-Cal/Mole of hydrogen consumed, a maximum thermal efficiency of 0.553 was calculated for the case where recombination and other thermal losses are neglected. The other thermal energy requirements considered were those related to heating the initial species of H_2O (liquid), bromine (liquid), and iodine (solid) from room temperature, to the gaseous state at a temperature of 456 K and at which the gaseous constituents enter the working fluid channels where they are exposed to the incident thermal radiant flux. Thermal efficiencies were calculated for each spectrum and were approximately 0.41. The calculated efficiencies are based on the assumption that there is no recombination of dissociated species and that there is no recovery either of the heats of reaction for the closed-cycle process or of the energy devoted to initial heating of the constituents. Thus in an actual process, the range of thermal efficiency would be expected to be between 0.41 and 0.55.

Because of the discriminatory manner by which the thermal radiant energy spectra are absorbed in the production of hydrogen for the photodissociation reactions of bromine and iodine, the residual energy in the spectra may be a considerable fraction of the total radiant energy available. This energy could be utilized for some other energy conversion system. The actual fraction of residual energy available depends upon the radiating temperature of the plasma and the spectral flux distribution emanating from the fuel region. For radiating temperatures between 4000 K and 6000 K, approximately 25 and 45 percent, respectively, of the spectral flux is available for use in bromine and iodine photodissociation reactions. For a plasma core reactor operating over this range of radiating temperature, this hydrogen production concept could be used as an auxiliary cycle to a primary energy conversion system such as the closed-cycle helium gas turbine system described in a previous section. The advantages of this dual energy extraction possibility is that the reactor can be operated at normal power during times when demand for electric power is not high and hydrogen may be produced. The hydrogen could be stored for subsequent usage. It is also possible to operate in a mode such that hydrogen production and the helium gas turbine system operate simultaneously. Here the hydrogen produced could either be consumed in fuel cells to aid in meeting the immediate power demand or stored for subsequent use.

Thorium--Uranium-233 Breeder Reactor

Plasma core reactors have several features which are of benefit in terrestrial applications in addition to increased thermodynamic cycle efficiency resulting from high temperature operation. One of these features involves use of the Thorium--U-233 breeding cycle. Studies were performed to estimate the operating characteristics of the plasma core reactor configuration shown on the right of Fig. 2 operating as a thermal breeder with the Thorium--U-233 cycle.

Fuel bred in a fertile blanket can be separated on-site and incorporated directly into the reactor fuel cycle flowing inventory or stored for use in other reactors. Such on-site reprocessing of the nuclear fuel would eliminate fuel element fabrication cost and avoid the necessity to transport expended fuel elements to remote locations. A thorough study of the safety of plasma core reactors has not been conducted; however, it is expected that the consequences of an accident in a plasma core reactor would be minimal because fission products are separated and removed continuously in the on-site reprocessing facility. The high pressure, power producing core region contains relatively small amounts of radioactive materials which potentially could be released from the reactor in the event of an accident. The breeder reactor concept could provide high temperature working fluids for efficient, closed-cycle gas turbine systems. In the breeder configuration shown in Fig. 2, structural neutron poisons are minimized by employing heavy-water as the reflector-moderator material and by encasing the working fluid and fuel region zones in Zircalloy tanks. A graphite-lined, fertile Thorium breeding blanket surrounds the heavy-water moderator. The complete assembly is contained within a pressure vessel. The reactor configuration consists of six 1-m-dia by 4.35-m-long cylindrical fuel cavities embedded in the heavy-water reflector-moderator. The fertile Thorium blanket is composed of a molten salt solution (ThF_4-BeF_2-LiF with mole fractions of 0.27, 0.02, and 0.71, respectively) similar to that employed in the molten salt breeder reactor concepts described in Ref. 29. The fissile nuclear fuel is U-233 which allows exploitation of the Th-232 and U-233 breeding cycle. The technology required for removing the U-233 produced in the molten salt fertile Thorium solution is well-developed and could be employed for a plasma core breeder reactor configuration. The unit cells of the breeder configuration are similar to those in the nonbreeder plasma core reactor configuration. However, in the breeder the graphite fins could not be enclosed in fused-silica tubes due to neutron absorption in the fused silica.

For the breeder reactor configuration described above, the breeding ratio was obtained from absorption rates obtained in one-dimensional transport theory critical mass search calculations using twenty neutron groups. Also, detailed analysis of the breeding ratio possibly achievable was performed. The reactor has a calculated critical mass of 84.4 kg of U-233, an operating fuel partial pressure of 498 atm, and a maximum

calculated breeding ratio of 1.080, assuming that all Th-232 absorptions in the fertile breeding blanket are converted to U-233 atoms. However, in an operating breeder reactor, the complete conversion and reclaimation of U-233 atoms from the Th-232 atoms which absorb neutrons is not possible and, hence, the actual achievable breeding ratio is somewhat reduced. Included in the model of the breeding chain, are the processes by which (1) uranium is reclaimed by fluoridation (UF_4+F_2 UF_6 gas) and removed from the molten fertile breeding blanket, and (2) protactinium is removed via a chemical process.

The particular leg of the U-233 production chain which would maximize the breeding ratio is

$$Th^{232} \xrightarrow{n\gamma} Th^{233} \xrightarrow[23.5\ m]{\beta^-} Pa^{233} \xrightarrow{\lambda_{CP}} Pa'^{233} \xrightarrow[27.4\ d]{\beta^-} U'^{233} \xrightarrow[1.62\times10^5 Y]{\alpha} \quad (2)$$

where λ'_{CP} is equivalent to a decay constant describing the removal rate of Pa from the fertile breeding blanket by chemical proeessing. In the presence of a neutron flux field, the isotopes of Th, Pa, and U undergo transmutation to other isotopes in the chain via (n,γ) absorption reactions or by fission reactions. The only desired neutron absorption reaction is the transmutation of Th^{232} to Th^{233} via the (n,γ) reaction. All other neutron absorption reactions and fission reactions are loss channels which diminish the breeding ratio. A computer program, ISOCRUNCH (Ref. 30), which solves the general differential equation describing the production and removal of an isotope in a reaction and decay scheme, has been modified and a procedure has been implemented to solve the differential equations which describe the production and removal of the isotopes in the Th-U-233 breeding cycle chain. The procedure makes use of the twenty neutron group flux distributions from one-dimensional spherical critical mass calculations to determine corresponding fission and absorption rates for each of the isotopes. The fission and absorption rates are used as input to the ISOCRUNCH computer program.

Breeding ratio results for the previously mentioned breeder reactor configuration were calculated for two different continuous chemical processing and fluoridation rates. The independent chemical processing and fluoridation rates were assumed to be equal for each of the cases. The chemical processing and fluoridation half-lives for the two cases are twelve hours and seven days (the half-lives are defined as the time required to remove half of the desired isotopes from the breeding blanket by the chemical or fluoridation processes). The calculated breeding ratios asymptotically approach 1.077 and 1.067 for the chemical processing and fluoridation half-lives of twelve hours and seven days, respectively. The concentration of Th-232 atoms in the breeding blanket was assumed to be constant with time for these calculations. For continuous chemical processing and fluoridation half-lives of twelve hours, the breeding ratio is greater than 1.06 after approximately seventy days. Similarly, for continuous chemical processing and fluoridation half-lives of seven days, the breeding ratio is not greater than 1.06 until approximately two years.

It has been calculated that a plasma core breeder reactor operating at a thermal power level of 2500 MW with a constant breeding ratio of 1.06, will have a doubling time of approximately five years for a total fuel inventory which includes fuel in the recirculation system equal to four times the critical mass. To achieve doubling times of approximately five years, it is necessary to have a time-averaged breeding ratio of 1.06, indicating that short chemical processing and fluoridation half-lives on the order of twelve hours to seven days are necessary to bring the system to secular equilibrium as quickly as possible and to minimize U-233 losses from the breeding blanket due to unwanted neutron reactions.

Concluding Remarks

The investigations described above have indicated that several space and terrestrial applications for plasma core reactors appear feasible and offer significant advances in performance and thermodynamic cycle efficiency. Progress reported in the other sessions of this conference on cavity reactor experiments, nuclear pumped laser demonstrations, uranium plasma experiments, and development of UF_6 handling technology is also very encouraging. Clearly, as soon as plasma core reactors with capability to provide intense radiant energy fluxes become available, the applications described above and many others as yet not considered will be coupled to them. In our judgment, it is most important to press forward with the planned cavity reactor experiments and the associated development of UF_6 handling technology and plasma confinement experiments to demonstrate the feasibility of plasma core reactors as a viable fission energy source for the 1980's and beyond.

References

1. Latham, T. S., F. R. Biancardi, and R. J. Rodgers: Applications of Plasma Core Reactors to Terrestrial Energy Systems. AIAA Paper No. 74-1074, AIAA/SAE 10th Propulsion Conference, San Diego, CA., October 21-23, 1974.

2. Helmick, H. H., G. A. Jarvis, J. S. Kendall, and T. S. Latham: Preliminary Study of Plasma Nuclear Reactor Feasibility. Los Alamos Scientific Laboratory Report LA-5679, prepared under NASA Contract W-13721, August 1974.

3. Thom, K., R. T. Schneider, and F. C. Schwenk: Physics and Potentials of Fissioning Plasmas for Space Power and Propulsion. International Astronautics Federation, XXVth Congress, Amsterdam, 30 Sept. - 5 Oct. 1974.

4. Bernard, W., H. H. Helmick, G. A. Jarvis, E. A. Plassmann, R. H. White: Research Program on Plasma Core Assembly. Los Alamos Scientific Laboratory Report LA-5971-MS, prepared under NASA Contract W-13755, May 1975.

5. Schneider, R. T., K. Thom, and H. H. Helmick: Lasers From Fission (Gaseous Core Reactors and Nuclear Pumped Lasers for Space Power Generation and Transmission). International Astronautics Federation, XXVIth Congress, Lisbon, 21-27 Sept. 1975.

6. Rodgers, R. J. and T. S. Latham: Analytical Design and Performance Studies of the Nuclear Light Bulb Engine. United Aircraft Research Laboratories Report Number L-910900-16, prepared under NASA Contract SNPC-70, September 1972.

7. Corlett, R. C.: Direct Monte Carlo Calculation of Radiative Heat Transfer in Vacuum. J. of Heat Transfer, Trans. ASME, Series C, Vol. 88, 1966, p. 376.

8. Engle, W. W., Jr.: A User's Manual for ANISN, A One-Dimensional Discrete Ordinates Transport Code With Anisotropic Scattering. Union Carbide Corporation Report K-1693, 1967.

9. Carter, J. L.: HRG3 - A Code for Calculating the Slowing-Down Spectrum in the P1 or B1 Approximations. Battelle-Northwest Laboratory Report BNWL-1432, June 1970.

10. Shudde, R. H. and J. Dyer: TEMPEST-II, A Neutron Thermalization Code. North American Aviation Report AMTD-111, September 1960.

11. Canfield, E. H., R. N. Stewart, R. P. Freis, and W. H. Collins: SOPHIST-I, An IBM 709/7090 Code Which Calculates Multigroup Transfer Coefficients for Gaseous Moderators. University of California, Lawrence Radiation Laboratory Report UCRL-5756, October 1961.

12. Roback, R.: Thermodynamic Properties of Coolant Fluids and Particle Seeds for Gaseous Nuclear Rockets. United Aircraft Research Laboratories Report C-910092-3, September 1964, prepared under NASA Contract NASw-847.

13. Krascella, N. L.: Theoretical Investigation of the Spectral Opacities of Hydrogen and Nuclear Fuel. Air Force Systems Command Report RTD-TDR-63-1101, prepared by United Aircraft Research Laboratories, November 1963.

14. Krascella, N. L.: Spectral Absorption Coefficients of Argon and Silicon and Spectral Reflectivity of Aluminum. United Aircraft Research Laboratories Report L-910904-3, prepared under Contract SNPC-70, September 1972.

15. Rodgers, R. J., T. S. Latham, and N. L. Krascella: Analyses of Low-Power and Plasma Core Cavity Reactor Experiments. United Technologies Research Center Report R75-911908-1, prepared under Contract XP4-54459-1, May 1975.

16. Krascella, N. L.: The Spectral Properties of UF_6 and Its Thermal Decomposition Products. United Technologies Research Center Report R76-912208, prepared under Contract NAS1-13291, Mod. 2, May 1976.

17. Rodgers, R. J., T. S. Latham, and N. L. Krascella: Investigation of Applications for High-Power, Self-Critical Fissioning Uranium Plasma Reactors. United Technologies Research Center Report R76-912204, prepared under Contract NAS1-13291, Mod. 2, May 1976.

18. Rodgers, R. J., T. S. Latham, and H. E. Bauer: Analytical Studies of Nuclear Light Bulb Engine Radiant Heat Transfer and Performance Characteristics. United Aircraft Research Laboratories Report K-910900-10, prepared under Contract SNPC-70, September 1971.

19. Ragsdale, R. G. and E. A. Willis: Gas-Core Rocket Reactors - A New Look. NASA TM X-67823, 1971.

20. Latham, T. S.: Summary of the Performance Characteristics of the Nuclear Light Bulb Engine. AIAA Paper 71-642, AIAA/SAE 7th Propulsion Joint Specialist Conference, June 1971.

21. Latham, T. S. and R. J. Rodgers: Small Nuclear Light Bulb Engines With Cold Beryllium Reflectors. AIAA Paper 72-1093, AIAA/SAE 8th Joint Propulsion Specialist Conference, Nov. 1972.

22. Titus, R. R.: Evaluation of NLB for Space Missions. United Aircraft Research Laboratories Report Number J-170817-1, February 1971.

23. Biancardi, F. R., G. T. Peters, and A. M. Landerman: Advanced Nonthermally Polluting Gas Turbines in Utility Applications. United Aircraft Research Laboratories Report J-970978-8, March 1971. Also issued as EPA Report 6130 DNE 0371.

24. Williams, J. R.: Nuclear Power From Space. Final Report prepared under NASA Grant NDR-11-002-181. Georgia Institute of Technology, November 1974.

25. McLafferty, G. H.: Nuclear Magnetohydroelectric Generator. U. S. Patent No. 3,140,410, July 7, 1964.

26. Sodha, M. S., C. J. Palumbo, and J. T. Daley: Enhancement of Gas Conductivity by Dust Suspensions and Its Application to Closed Cycle MHD Power Generation. Proceedings, International Symposium, MHD Electrical Power Generation, Paris, Vol. 2, 1964.

27. Waldie, B. and I. Fells: An Experimental Study of Gas Borne Suspensions of Thermionic Emitters as MHD Working Fluids. Philosophical Transactions, Royal Society of London, Series A, No. 261, July 1967.

28. Hooper, A. T., D. Newby, and A. H. Russel: Closed Cycle Nuclear MHD Studies Using Dust Suspensions. Proceedings of Symposium on Electricity from MHD. Salzburg, July 1966.

29. Kasten, P. R., et al.: Summary of Molten-Salt Breeder Reactor Design Studies: Thorium Fuel Cycle - Proceedings of 2nd International Thorium Fuel Cycel Symposium, Gatlinburg, Tenn., May 3-6, 1966, p. 41.

30. Friend, C. W. and J. R. Knight: ISOCRUNCH - Modifications to the CRUNCH Program for the IBM 7090. Oak Ridge National Laboratory Report ORNL-3689, January 1965.

List of Symbols

A_{WCD}/A_C	Ratio of working channel duct-to-total cavity surface area, dimensionless
P	Pressure, atm
$P_F/(P_U+P_{UF_X})$	Fluorine to uranium bearing species pressure ratio, dimensionless
P_{TOT}	Total pressure, atm
Q_{CONV}	Convective power removal by fuel and buffer flows, MW/Cell
Q_{MOD}	Power deposited in moderator, MW/Cell
Q_R or Q_{WCD}	Radiated thermal power, MW/Cell
Q_{RADD}	Radiated thermal power to duct, MW/Cell
Q_{RADL} or Q_L	Radiated thermal power to liner, MW/Cell
Q_{TOT}	Total power, MW/Cell
R	Radius, cm
R_{Al}	Aluminum reflectivity, dimensionless
T	Temperature, deg K
$(T^*_{BB})_{OUT}$ or T^+_{BB}	Black-body temperature corresponding to outward directed radiant flux at edge-of-fuel location, deg K
T_{CL}	Centerline temperature, deg K
λ	Wavelength, microns or nm
ρ	Density, g/cm^3

TABLE I

TRANSMISSION CELL PERFORMANCE

Spectral Weighted Al Reflectivity = 0.909
$(T^*_{BB})_{OUT}$ = 4000 K

Cell L/D	Cell Transmissivity Without SiO_2	Total SiO_2 Thickness, cm	Transmissivity of SiO_2
0.5	0.92	0.25	0.941
1.0	0.83	0.50	0.923
2.0	0.72	1.0	0.900
4.0	0.56	2.0	0.874
		3.5	0.850

TABLE II

PERFORMANCE CHARACTERISTICS FOR UF_6-FUELED GASEOUS NUCLEAR REACTORS

Cylindrical Reactor With Six Unit Cells -- See Fig. 2
Critical Mass = 86.4 kg of U-235
See Table III for Energy Balance

Black-Body Temperature For Outward Directed Radiant Flux, $(T^*_{BB})_{OUT}$, deg K	Duct-To-Cavity Area Ratio, A_{WCD}/A_C, Dimensionless	Black-Body Temperature For Net Radiant Flux, $(T^*_{BB})_{NET}$, deg K	Centerline Temperature T_{CL}, deg K	Cavity Pressure P_{TOT}, atm
2000	0.0	1170	5500	110
2000	0.1	1385	6300	95
2000	0.2	1520	6900	80
2000	0.3	1620	7300	85
2000	1.0	2000	8900	90
3000	0.0	1760	10,500	190
3000	0.1	2075	12,500	230
3000	0.2	2280	13,700	255
3000	0.3	2430	14,600	270
3000	1.0	3000	18,000	330
4000	0.0	2345	14,400	320
4000	0.1	2765	17,200	365
4000	0.2	3040	18,800	395
4000	0.3	3245	19,900	420
4000	1.0	4000	24,000	505
5000	0.0	2930	18,200	400
5000	0.1	3460	21,200	465
5000	0.2	3800	22,800	505
5000	0.3	4055	24,300	530
5000	1.0	5000	29,800	650

*Equivalent Black-Body Radiating Temperature

TABLE III

ENERGY BALANCE FOR UF_6-FUELED GASEOUS NUCLEAR REACTORS

See Table II For Associated Parameters

Black-Body Temperature For Outward Directed Radiant Flux, $(T^*_{BB})_{OUT}$, Deg K	Duct-To-Cavity, Area Ratio, A_{WCD}/A_C, Dimensionless	Total Power, Q_{TOT}, MW/Cell	Radiated Thermal Power To Duct Q_{RADD}, MW/Cell	Radiated Thermal Power To Liner Q_{RADL}, MW/Cell	Power Convected by Fuel and Buffer Flows, Q_{CONV}, MW/Cell	Power Deposited in Moderator Q_{MOD}, MW/Cell
2000	0.0	3.31	0.00	1.21	1.69	0.41
2000	0.1	4.71	1.29	1.06	1.77	0.59
2000	0.2	6.51	2.51	0.91	2.28	0.81
2000	0.3	8.21	3.66	0.78	2.74	1.03
2000	1.0	16.54	10.27	0.00	4.20	2.07
3000	0.0	13.24	0.00	6.13	5.46	1.65
3000	0.1	20.60	6.54	5.36	6.13	2.57
3000	0.2	27.29	12.72	4.63	6.53	3.41
3000	0.3	33.50	18.56	3.94	6.81	4.19
3000	1.0	68.70	52.02	0.00	8.09	8.59
4000	0.0	30.30	0.00	19.36	7.15	3.79
4000	0.1	52.28	20.67	16.93	8.15	6.53
4000	0.2	72.80	40.18	14.63	8.89	9.10
4000	0.3	92.03	58.65	12.45	9.43	11.50
4000	1.0	201.35	164.39	0.00	11.79	25.17
5000	0.0	64.30	0.00	47.26	9.00	8.04
5000	0.1	116.94	50.45	41.32	10.55	14.62
5000	0.2	166.21	98.11	35.71	11.62	20.77
5000	0.3	212.67	143.18	30.40	12.51	26.58
5000	1.0	479.28	401.35	0.00	18.02	59.91

*Equivalent Black-Body Radiating Temperature.

TABLE IV

PERFORMANCE CHARACTERISTICS OF GASEOUS NUCLEAR ROCKET ENGINES

Coaxial Flow, Open Cycle Performance From Ref. 19
Nuclear Light Bulb Performance From Ref. 20
Small Nuclear Light Bulb Performance From Ref. 21

	Coaxial Flow Open Cycle	Nuclear Light Bulb	Nuclear Light Bulb Reference Engine	Small Nuclear Light Bulb
Engine Mass, kg	40,000-210,000	29,500-45,500	31,750	15,000-26,000
Operating Pressure, atm	490-2000	400-900	500	500-650
Specific Impulse, s	2500-6000	1100-2500	1870	925-1550
Thrust-to-Weight	0.05-0.20	0.3-1.6	1.3	0.14-0.29

TABLE V

PERFORMANCE OF NUCLEAR LIGHT BULB ROCKET ENGINE WITH URANIUM HEXAFLUORIDE FUEL

Engine Parameter	Fuel Radiating Temperature		
	4000 K	5000 K	6000 K
Operating Pressure, atm	540	720	900
Uranium Partial Pressure, atm	60	80	100
Power, MW	244	596	1236
Propellant Exit Temperature, deg K	3200	4000	4800
Primary Propellant Weight Flow, kg/s	5.21	9.55	16.61
Corrected Specific Impulse, s	880	1030	1220
Thrust, N	45,000	96,500	198,800
Engine Mass, kg	32,700	37,900	42,900
Thrust-to-Weight Ratio	0.14	0.26	0.47

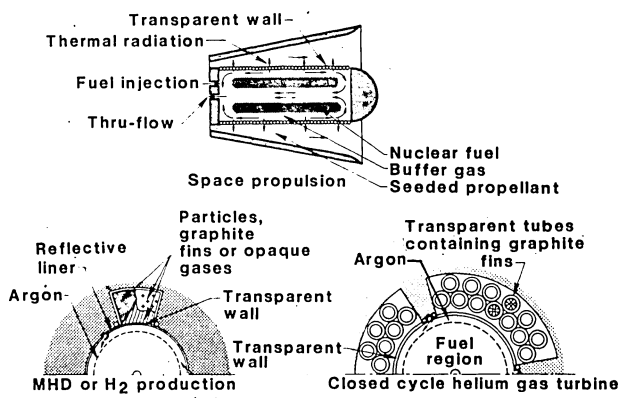

Fig. 1 Concepts for coupling thermal radiation to working fluids.

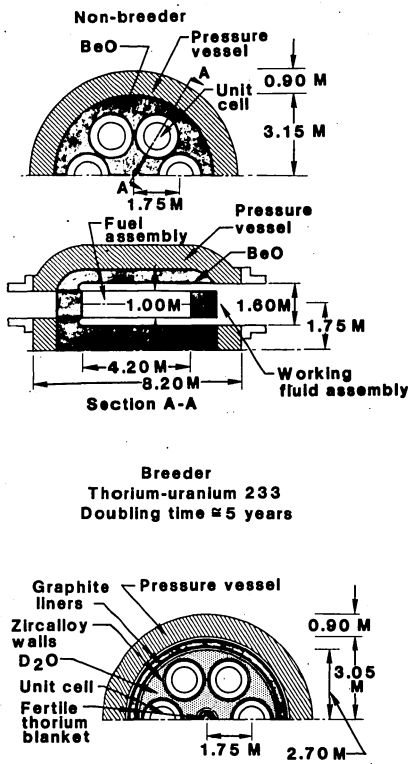

Fig. 2 Plasma core reactor configurations for electric power generation.

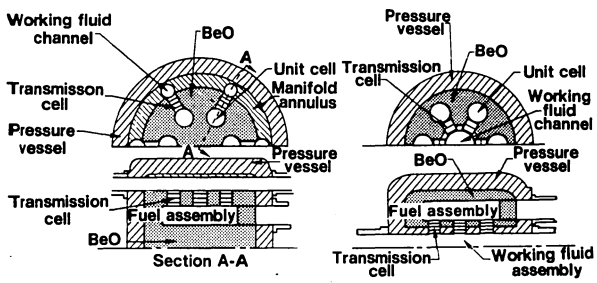

Fig. 3 Transmission cells in plasma core reactors.

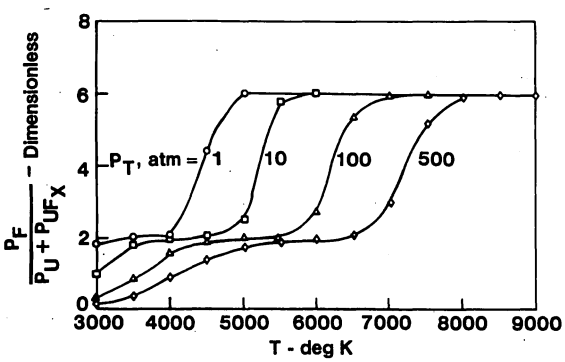

Fig. 4 Pressure ratios of fluorine to uranium and uranium fluoride species.

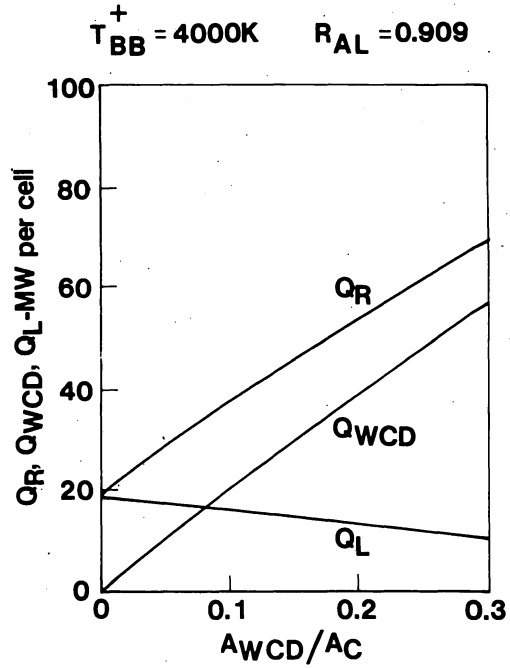

Fig. 5 Variations of thermal radiation power deposition for plasma core reactor unit cells with reflecting liners.

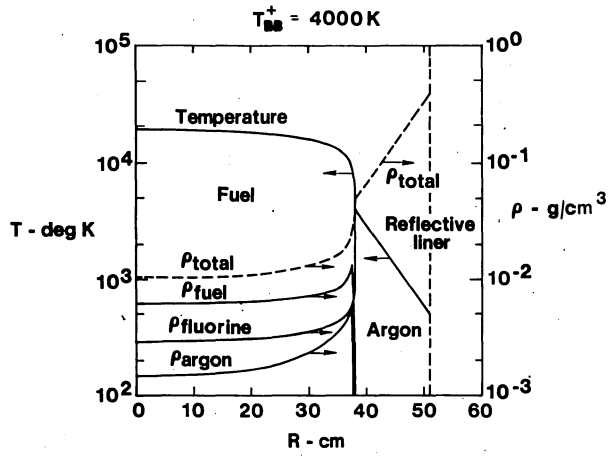

Fig. 6 Density and temperature distributions for plasma core reactor with edge-of-fuel temperature of 4000K.

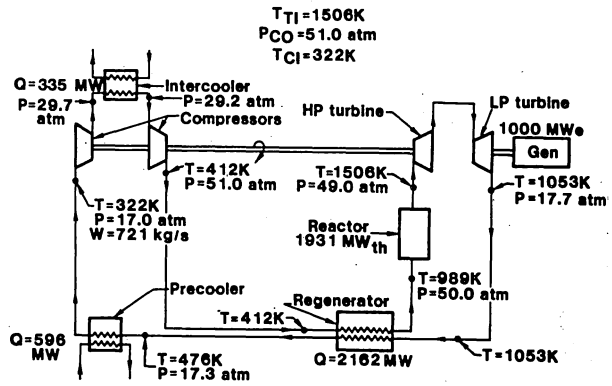

Fig. 7 Helium closed-cycle gas turbine system with plasma core reactor heat source.

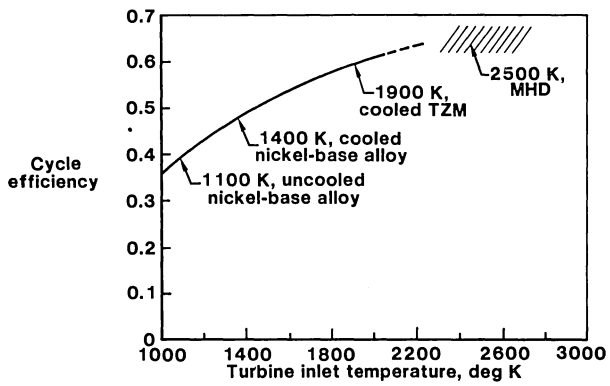

Fig. 8 Calculated cycle efficiency for helium closed-cycle gas turbine system with plasma core reactor heat source.

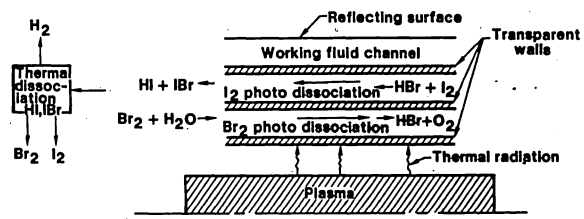

Fig. 9 Concept for photochemical/thermochemical hydrogen production using thermal radiation from plasma core reactor.

BROADBAND PHOTOEXCITATION OF LASERS

R. V. Hess
NASA, Langley Research Center, Hampton, VA 23665

A. Javan
Massachusetts Institute of Technology
Cambridge, MA 02139

P. Brockman
NASA, Langley Research Center, Hampton, VA 23665

Abstract

The purpose of this study is to review existing techniques and to discuss novel approaches for broadband photoexcitation of lasers. This subject is of interest because of the emergence of future intense near-equilibrium and blackbody sources, such as the gas-core reactor, and electric discharge plasma devices, which are the key to the development of intense broadband radiation sources. The possible use of radiation from solar concentrators in space also fits into this general area. The varied uses of photoexcitation of lasers are discussed ranging over direct optical pumping, photodissociation, and photopreionization. In addition, the new use of lasers for broadband photoexcitation of new laser transitions and chemical reactions is shown. This is accomplished through multiline operation of high-pressure tunable lasers which can use the broadband radiation for multiphoton excitation. Acknowledgment is made of helpful discussions with D. H. Phillips, R. S. Rogowski, and B. D. Sidney at the Langley Research Center, and J. Verdeyen (Illinois Univ.), D. L. Hess (Hughes Research Labs), C. Wittig (Southern Cal. Univ.), and T. Cool (Cornell Univ.).

I. Broadband Photoexcitation with Blackbody Sources

Photoexcitation of lasers requires that the spectral range of the radiation source overlap the absorption lines or bands of the laser and that the power density of the source in this range be sufficient for exceeding the threshold power density for lasing. For convenient analysis of these criteria Planck's law for the distribution of power/area/unit wavelength of blackbody radiation over various wavelengths is plotted in Figures 1 and 2 for 6000°K, 15,000°K, and 20,000°K vs wavelength.

Potential sources for broadband photoexcitation are the gas-core reactor which will be capable of radiating at temperatures from 6000°K to over 20,000°K, electric discharges which may even operate at higher temperatures and the Sun. Use of solar radiation requires concentration of the 1.4×10^{-1} W/cm^2 radiation intensity in Earth orbit. The maximum concentration of radiant energy is limited by the invariant N/n^2 where N is the radiance in power per unit area per steradian and n is the local index of refraction. In free space the maximum possible concentration of blackbody radiation will yield an irradiance equal to that found at the surface of the blackbody, which at 6000°K would be ~7000 Watts/cm^2. However, in a high index of refraction material this concentration is increased by a factor of n^2. The additional concentration due to the change in index of refraction does not change the radiation temperature, since by Planck's law

$$\frac{\partial(P/A)}{\partial\nu} \alpha \frac{hn^2}{c_0^2} \frac{\nu^3}{e^{h\nu/kT} - 1}$$

where c_0 is the velocity of light in free space. This additional concentration has been used for enhancement in photon counters behind high n material. Application to high index of refraction laser media would require special considerations. As indicated by the large concentration ratios, use of large lasing media would require large space structures. Use of solar concentrators for Nd:YAG lasers is discussed in references 2 and 3.

Broadband photoexcitation requires a combination of broadband absorption in the lasing medium and sufficiently low threshold power density to match the power density of the blackbody source in the spectral range of the absorption region. For example, both the solid-state Nd:YAG laser and the liquid dye laser absorb in the visible spectrum, but the Nd:YAG laser has orders of magnitude lower power density threshold. A threshold of less than 20 W/cm^3 is quoted in reference 4 for an Nd:YAG laser, whereas reference 5 gives a threshold of 20 kW/cm^3 for a dye laser. As a result, the Nd:YAG laser can be excited by 6000°K blackbody sources (Fig. 1), whereas, a dye laser would require a blackbody source somewhat in excess of 20,000°K (Fig. 2), to yield sufficient power density in the visible spectrum. Since a 20,000°K source has its peak power density in the near UV, such direct excitation of the dye laser is inefficient.

Broadband photoexcitation of gas lasers offers potential advantages over solid and liquid lasers because material limits are less severe, and large uniform lasing media are available. Two major categories of gas lasers are discussed: photodissociation lasers which have chemical reversibility through regeneration of the initial products, and are suited to continuous photoexcitation; and other lasers utilizing optical pumping of molecular vibrational states in the near infrared, which, when operated at high pressures, permit broadband pumping because of pressure broadening and overlapping of laser lines.

II. Broadband Photodissociation Lasers

$NOC\ell$ and IBr have been used to produce chemically reversible photodissociation lasers. For the $NOC\ell$ system, lasing occurs on the vibrational-rotational transitions of NO at 5.95-6.30 μm (Ref. 6). For the IBr photodissociation system electronic excitation of Br occurs with lasing at 2.714 μm (Ref. 7). Early flashlamp experiments indicate that the threshold for the $NOC\ell$ system may be low enough to allow solar pumping, however, further studies of $NOC\ell$ and IBr lasers are required. The photodissociation lasers using organic iodides CF_3I and C_3F_7I (Ref. 8) yield higher gain and power for analagous transitions of atomic iodine, I*, at 1.315 μm. These lasers have a broad absorption band from 2500-2900 Å which matches the peak intensity region of blackbody radiation at ∿20,000°K and could probably be excited by a gas-core reactor operating at that temperature.

Figure 3 shows a simplified diagram of an electronic-vibration (E-V) energy transfer Br^*-CO_2 laser. This type of photodissociation laser produces electronically excited Br^* from Br_2 molecules which have absorption bands from the near UV through the visible. The excited Br^* atoms are, however, not used directly for lasing, but for near resonant excitation of vibrational molecular states, e.g., CO_2, which lases in the infrared (Ref. 9). This type of system may be very important for pumping IR lasers with solar and other high-temperature blackbody sources, since absorption occurs near the peak of the blackbody spectrum (Fig. 1). Several molecules can be used in high efficiency IR lasers. These molecules should be investigated, to determine if their power density thresholds are sufficiently low to be pumped by these blackbody sources. Communications with C. Wittig (Southern Cal. Univ.) suggest that low thresholds may be possible. Since the conversion is from short-to-long wavelengths, the energy transfer efficiency is reduced by the ratio of the wavelengths.

More efficient transfer could be achieved in lasers which radiate at wavelengths shorter than the CO_2 laser. One such system has been demonstrated for HCN lasing at 3.85 μm (Ref. 10). This laser, however, requires intense excitation to maintain a steady-state population inversion due to the short lifetimes of the excited HCN states. For efficient E-V photodissociation lasers, molecular systems operating at short IR wavelengths and with long-lived excited states, such as CO, should be investigated.

Figure 4 shows a typical excimer laser; excimers, bound excited molecular states, form by the combining of electronically excited atoms with noble gas atoms. Such states have been obtained for noble gas-halides, noble gas-oxygen, and noble gas-alkali systems. The repulsive ground states encourage continuous lasing and reversibility. Broadband photodissociation can play a role, e.g., in the $(ArO)^*$ laser (Ref. 11); however, the production of O^* by broadband photodissociation occurs in the far UV. Photoexcitation, in the visible, of noble gas-alkali excimer lasers is being studied (Refs. 12 and 13). Recent communications with J. Verdeyen (Illinois Univ.) indicate that the absorption of tunable dye laser radiation by cesium in high-pressure xenon gas occurs over a broader spectral range than the width of Cs absorption lines. The lasing threshold was calculated to be 3.46 kW/cm^3. Communications with L. D. Hess (Hughes Research Labs.) indicate studies with flashlamp excitation which, however, did not attain the high efficiencies (up to 10%) theoretically projected for excimer lasers.

III. Broadband Optical Pumping of Vibrational Molecular Laser Transitions in the Infrared

For solar radiation the radiation intensity in the infrared is much smaller than at peak intensity (Fig. 1). The existence of many rotational-vibrational laser lines over a wide spectral band in the infrared combined with the broadening and overlapping of these lines at high pressures allows broadband absorption of the available radiation.

For the present preliminary study, optical pumping of the CO molecule was studied, because of its long V-T relaxation rates, $\sim 1.9 \times 10^{-3}$/sec/Torr, which facilitate buildup of steady-state population inversions even at high pressures. Since the CO molecule has a small anharmonic energy defect, the energy may shift to higher vibrational levels unless it is removed. This removal can take place either by cooling or by energy transfer to other molecules. The feasibility for optical pumping of the $0 \rightarrow 1$ CO vibrational-rotational band with subsequent near resonant V-V energy transfer to CO_2, OCS, N_2O, C_2H_2 (Fig. 5) was demonstrated in reference 14 using the second harmonic of the P(24) laser line of the 9.6 μm CO_2 band, which falls close to the CO $0 \rightarrow 1$, P(14) laser transition.

For 6000°K blackbody radiation ∿4 Watts per cm^2 are available over an integrated absorption bandwidth of ∿2000 Å (P&R branch) of the 5 μm $0 \rightarrow 1$ CO transition, corresponding to ∿0.2 watts per cm^2 per 100 Å at 5 μm (Fig. 1). The line absorption coefficients in this region are of the order of 10/cm, thus the total power would be absorbed over a distance of $\sim 10^{-1}$ cm, yielding a power density of ∿40 $watts/cm^3$.

Longer penetration depths may be achieved by direct optical pumping of the $0 \rightarrow 2$ CO transition using 2.4 μm radiation. The absorption coefficients are $\sim 7 \times 10^{-2}$/cm and at 2.4 μm concentrated solar radiation provides 4 $Watts/cm^2/100$ Å (Fig. 1), and 24 $Watts/cm^2$ across 600 Å integrated absorption bandwidth. The power density absorbed in the lasing medium will be ∿1.7 Watts per cm^3.

For transfer of the $v = 2$, CO vibrational energy to CO_2 and other molecules, V-V transfer first occurs to the $v = 1$, CO state. Calculations indicate that for several torr of CO_2 in atmospheric CO sufficient gain should occur in CO_2 to make this a potentially useful laser. The actual power output depends on the exact vibrational-rotational bandwidth available for absorption. More detailed calculations and experiments to determine the efficiency of energy transfer are required.

IV. Use of Multiline Lasers for Multiphoton Pumping of Lasers and Chemical Reactions

Two-photon pumped lasers have recently been demonstrated (Ref. 15) where simultaneous pumping with both P(12) and P(14) transitions of a CO_2 TEA laser were used to obtain lasing in SF_6 at 15.9 μm (Fig. 6). The desirability of better temporal and spatial coincidence, and increased power of the two laser pump lines is stated and the need for careful tuning is noted. In an article (Ref. 16) on stimulation of chemical reactions with laser radiation it is shown that the absorption of a large number of low-energy quanta rather than one high-energy quantum facilitates considerable deviation of resonance mode from the average temperature - and that this is very important for controlled stimulation of chemical reactions. A laser has been designed and operated by A. Javan, to achieve independent simultaneous operation of laser lines and broadband tunability (Fig. 7). The independent laser lines are obtained by spatially separating their production in a laser medium, which operates at low power to achieve optimum control of frequency and tunability. This multiline laser radiation passes co-linearly through another lasing medium which is forced to operate on these injected lines, thus maintaining the high frequency stability at considerably higher powers. Such injection locking has been demonstrated in the past for one injected laser line (e.g., Ref. 17), but is new for multiline operation. Furthermore, for high-pressure operation controlled continuous tuning over pressure broadened overlapping lines could be achieved. Rapid chirping over a wide spectral range could approach conditions of an intense broadband nonequilibrium source, in contrast to equilibrium blackbody sources.

V. Photopreionization for High Pressure Laser Plasmas

Photopreionization of high-pressure CO_2 electric discharge lasers and other lasers has been extensively studied in recent years to provide an alternative to electron beams in the production of uniform large volume high-pressure lasers, with highly efficient and stable operation. A novel technique involves the addition to the lasing medium of a small quantity of organic seed material (e.g., tripropylamine or trimethylamine) having lower ionization potential than the laser medium. Since the lasing media do not absorb at the wavelengths which preionize the seed and, since the seed density is low, an increased penetration depth is achieved. This technique was originally demonstrated by A. Javan* and J. S. Levine (Ref. 18) and additional studies have been reported in references 19 and 20. Figure 8 shows a high-pressure CO_2 photopreionized laser operating at the NASA Langley Research Center. The laser designed by A. Javan uses flashrods with open spark gaps, which avoid contamination buildup by the seed material such as might occur when using flashlamps.

References

1. Nicodemus, F. E.: Radiance. American J. of Physics, May 1963, pp. 368-377.

2. Young, C. G.: A Sun Pumped CW One-Watt Laser. Applied Optics, vol. 5, no. 6, June 1966, pp. 993-997.

3. Falk, Joel; Huff, L.; and Taynai, J. D.: GTE Sylvania: Solar-Pumped YAG, CLEA Paper 4.6, 1975.

4. Ross, D.: Lasers, Light Amplifiers, and Oscillators. Academic Press, Inc., New York, N.Y., 1969.

5. Bass, M.; Deutsch, T. F.; and Weber, M. J.: Dye Lasers. Chapt. 4, p. 301 in "Lasers a Series of Advances." Ed. Levine, A. K.; and De Maria, A. J., vol. 3, 1071.

6. Guilliano, C. R.; and Hess, L. D.: Chemical Reversibility and Solar Excitation Rates of the Nitrosyl Chloride Photodissociative Laser. J. of Appl. Physics, vol. 38, no. 11, Oct. 1967.

7. Guilliano, C. R.; and Hess, L. D.: Reversible Photodissociative Laser System. J. of Appl. Physics, vol. 40, no. 6, May 1969.

8. Hohla, K.; and Kompa, K. L.: Gigawatt Photochemical Iodine Laser. Appl. Phys. Lett., vol. 22, no. 2, January 15, 1973.

9. Petersen, A. B.; Wittig, C.; and Leone, S. R.: Electronic-to-Vibrational Pumped CO_2 Laser Operating at 4.3, 10.6, and 14.1 μm. J. of Appl. Physics, vol. 47, no. 3, March 1976.

10. Petersen, A. B.; Wittig, C.; and Leone, S. R.: Infrared Molecular Lasers Pumped by Electronic-Vibrational Energy Transfer from $Br(4^2P_{1/2}):CO_2$, N_2O, HCN, and C_2H_2. J. of Appl. Physics, vol. 47, no. 3, March 1976.

11. Hughes, W. M.: Experiments on 553-nm Argon Oxide Laser System. Appl. Phys. Lett., vol. 28, no. 2, January 15, 1976.

12. Tam, A. C.; Moe, G.; Bulos, B. R.; and Happer, W.: Excimer Radiation from Na-Noble Gas and K-Noble Gas Molecules. Optics Communications, vol. 16, no. 3, March 1976.

13. Cherrington, B. E.; Verdeyen, J. T.; Eden, J. G.; and Leslie: Studies of Discharge Mechanisms in High Pressure Gases - Application to High Efficiency High Power Lasers. Analysis of Excimer Systems by Combination of Excited $CS(7^2S,5^2D)$ and Xe. Semi-Annual Progress Report NASA Grant NCT 74-005-200, Univ. of Illinois, November 1, 1975.

14. Kildal, H.; and Deutsch: Optically Pumped Infrared V-V Transfer Lasers. Appl. Phys. Lett., vol. 27, no. 9, November 1, 1975.

15. Barch, W. E.; and Fetterman, H. R.: Optically Pumped 15.90 μm SF_6 Laser. Optics Communications, November/December 1975.

16. Basov, N. G.; Oraevsky, A. M.; and Pankratov, A. V.: Stimulation of Chemical Reactions with Laser Radiation. Chemical and Biochemical Applications of Lasers. Ed., Moore, C. B., vol. 1, p. 211, 1974.

* This work partially supported under NASA contract NAS1-14289.

17. Buczek, C.; and Freiberg, R. J.: Hybrid Injection Locking of High Power CO_2 Lasers. IEEE J. of Quantum Electronics, vol. QE-8, no. 7, 1972.

18. Levine, J. S.; and Javan, A.: Observation of Laser Oscillation in a 1 atm CO_2-N_2 He Laser Pumped by an Electrically Heated Plasma Generated via Photoionization. Appl. Phys. Lett., vol. 22, no. 2, January 15, 1973.

19. Judd, O. P.; and Warda, J. Y.: Investigations of UV Preionized Electric Discharge and CO_2 Laser. IEEE J. of Quantum Electronics, vol. QE-10, no. 1, January 1974.

20. Sequin, H. J.; Tulip, J.; and McKen, D. C.: Ultraviolet Photoionization in TEA Lasers. IEEE J. of Quantum Electronics, vol. QE-10, no. 3, March 1974.

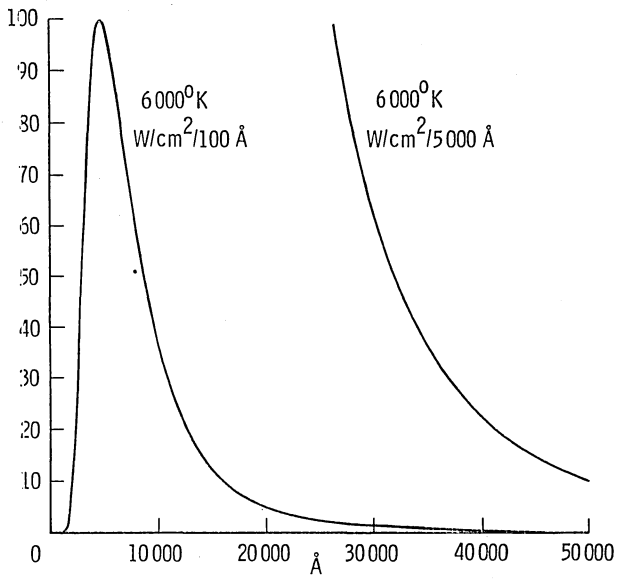

Figure 1. Blackbody radiation distribution at 6000°K

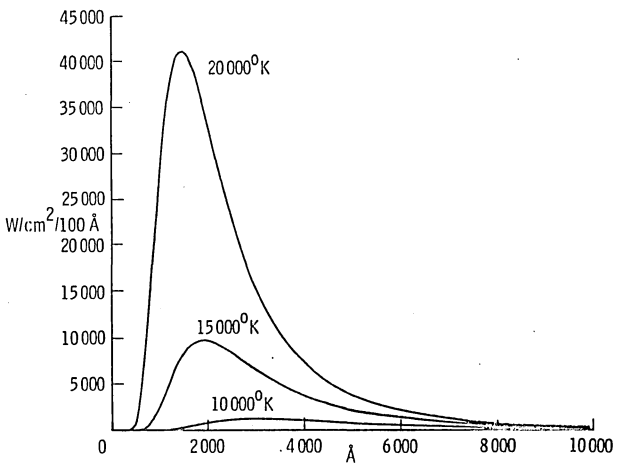

Figure 2. Blackbody radiation distribution up to 20,000°K

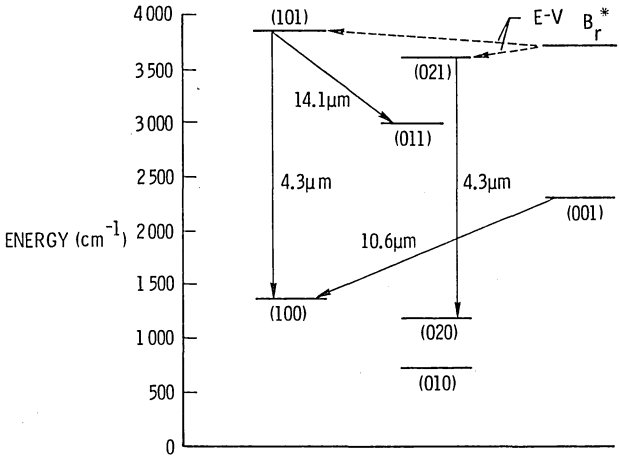

Figure 3. B_r^*-CO_2^+ E-V energy transfer laser

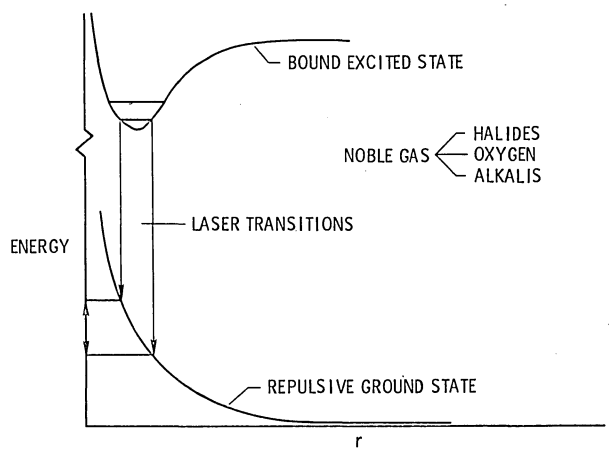

Figure 4. Typical excimer laser

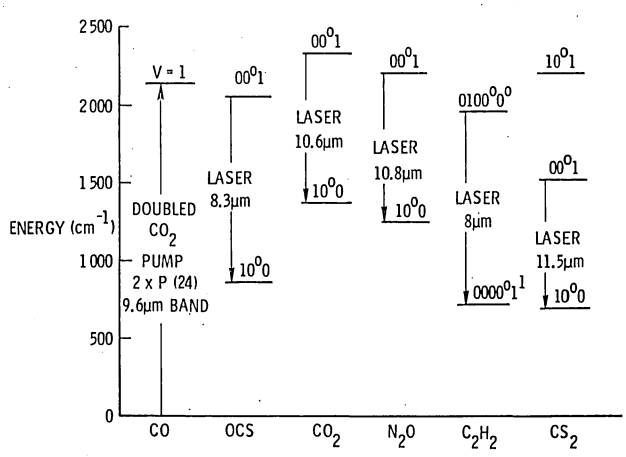

Figure 5. Molecules pumped by energy transfer from CO

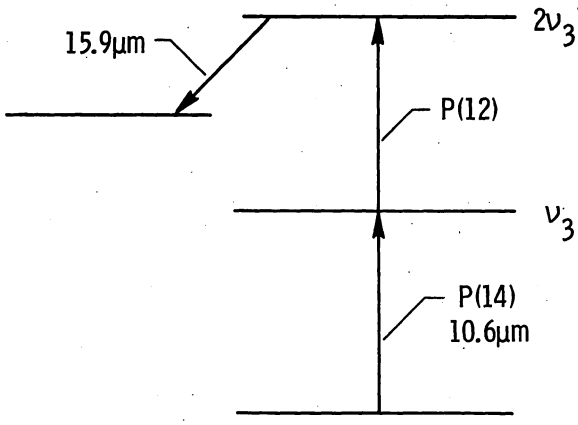

Figure 6. Two-photon pumping for SF_6 laser

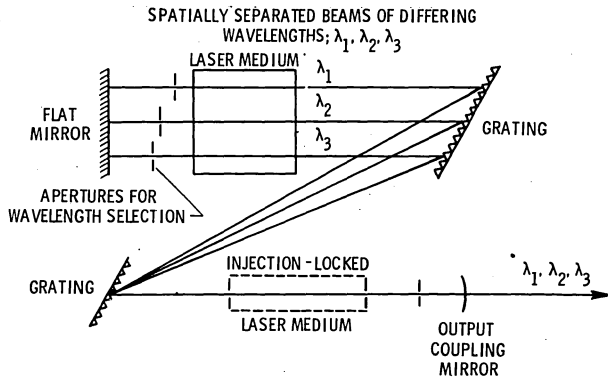

Figure 7. Independently controllable multiwavelength laser

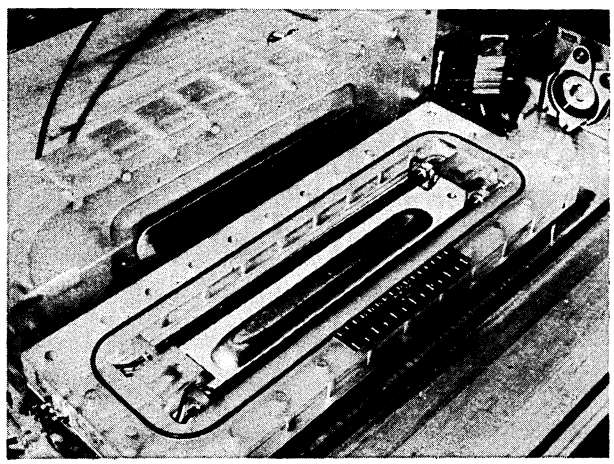

Figure 8. High-pressure photo-preionized CO_2 laser

DISCUSSION

F. HOHL: What sort of intensities do you need to pump an excimer laser?

R. V. HESS: It is very unlikely that one can pump excimer lasers by this method. Verdeyen calculated a threshold of 3.4 kilowatt per cubic cc for noble gas-alkali pumping which is too high. That would need flashlamp pumping. But some of the other lasers we mentioned - the photo dissociation lasers, NOCl, Iodine bromide and also the bromine molecule that has an e.v. transition, and also the CO which has long lifetimes and therefore low thresholds are potentials for pumping by this method.

K. THOM: What do you think about the possibility of using solar pumping for such lasers?

R. V. HESS: The Nd-Yag laser is being solar pumped but that is a solid state laser, being considered for communications. The best candidates for solar pumping seem to be NOCl, bromine molecules, IBR, and potentially CO because this displays broadband excitation and has a long lifetime and a relatively low threshold. We are looking more at these possibilities right now.

STATUS OF PHOTOELECTROCHEMICAL PRODUCTION OF HYDROGEN AND ELECTRICAL ENERGY

Charles E. Byvik and Gilbert H. Walker
NASA Langley Research Center
Hampton, Virginia

Abstract

The efficiency for conversion of electromagnetic energy to chemical and electrical energy utilizing semiconductor single crystals as photoanodes in electrochemical cells has been investigated. Efficiencies as high as 20 percent have been achieved for the conversion of 330 nm radiation to chemical energy in the form of hydrogen by the photoelectrolysis of water in a $SrTiO_3$ based cell. The $SrTiO_3$ photoanodes have been shown to be stable in 9.5 M NaOH solutions for periods up to 48 hours. Efficiencies of 9 percent have been measured for the conversion of broadband visible radiation to hydrogen using n-type GaAs crystals as photoanodes. Crystals of GaAs coated with 500 nm of gold, silver, or tin for surface passivation showed no significant change in efficiency. By suppressing the production of hydrogen in a CdSe-based photogalvanic cell, an efficiency of 9 percent has been obtained in conversion of 633 nm light to electrical energy. A CdS-based photogalvanic cell produced a conversion efficiency of 5 percent for 500 nm radiation.

I. Introduction

The utilization of broad band radiation from a fissioning plasma or of narrow band laser radiation in space[1] requires transformation into other energy forms. Ideally, this energy transformation should be performed by a device that is (a) efficient, (b) sensitive over a broad wavelength interval, (c) stable both thermally and chemically, and (d) intensity efficient (especially for the case of high photon energy densities characteristic of lasers and plasma reactors). Recent research has indicated that semiconductors used as photoanodes in an electrochemical cell with an aqueous electrolyte can be used to convert photon energy to both chemical energy[2-8] (in the form of molecular oxygen and molecular hydrogen) and electrical energy.[9,10] The purpose of this report is to present the status of recent research in the electrolysis of water and the production of electrical energy by photoelectrolytic cells and photogalvanic cells where semiconductors have been used as photoelectrodes.

II. Background

Electrochemical cells are in wide use today as batteries, fuel cells, catalytic reactors and many other applications. The photoelectrolytic and photogalvanic cells with semiconductor electrodes are of particular interest at NASA-Langley Research Center because they are promising techniques for converting photon energy to chemical and electrical energy.

Early work with semiconductors used as photoelectrodes in electrochemical cells indicated that electrolysis of water could be achieved and electrical energy could be produced at the expense of the semiconductor photoelectrode. It was found that photon energies greater than the bandgap of the semiconductor electrode could enhance the dissolution of the semiconductor.

Fujishima and Honda[3] reported results of a titanium dioxide-based photoelectrolytic cell which indicated that the TiO_2 photoanode might be stable. The photocell used by them is shown schematically in figure 1.

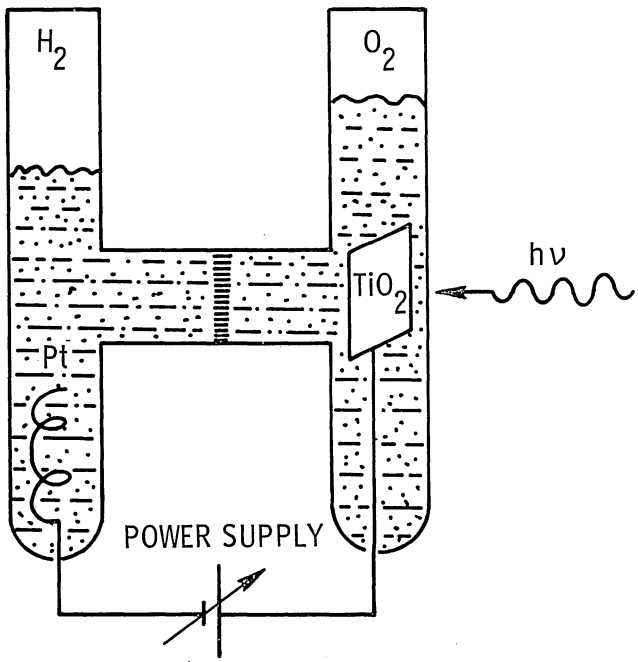

Fig. 1 Schematic of Photoelectrolytic Cell.

The overall reaction proposed to be taking place in the cell when light having energy greater than the bandgap of TiO_2 (3.0 eV) was

$$H_2O + 2\ h\nu \rightarrow 1/2\ O_2 + H_2 \qquad (1)$$

where the photon energy is converted to chemical energy stored as the free energy of hydrogen (68.3 kcal/mole).

A simple extension of this photon assisted electrolysis of water in a semiconductor-based electrochemical cell is to suppress the hydrogen and oxygen production by introducing into the electrolyte a suitable redox couple (an ionic couple which is oxidized at one electrode and reduced at the other without changing the composition of the electrolyte) and utilizing the electrical energy produced by placing a load in the external circuit. This is the principle of a photogalvanic cell.

The results reported for the TiO_2-based photochemical cell indicated that further research was needed to (1) establish the nature of the photon induced processes at the semiconductor-electrolyte interface; (2) determine the energy conversion efficiency of the semiconductor-based electrochemical cells; and (3) explore the use of other

semiconductors as photoelectrodes in both photogalvanic and photoelectrolytic cells. The results of the NASA sponsored work in this area is the subject of this paper.

III. Results

Photoelectrolysis Cells

A detailed study of the TiO_2-based photoelectrolysis cell was made by Wrighton, et al.[5] Their work concluded that, for a cell with a single electrolyte and UV radiation (351 nm, 364 nm): (1) oxygen is evolved at the photoanode (TiO_2) and hydrogen at the cathode (Pt) in the stochiometric ratio of two to one in agreement with equation (1); (2) a minimum external voltage of 0.25 volts is necessary for the photoelectrolysis to take place; (3) the photoelectrolysis reaction does not produce dissolution of the TiO_2 anode and is therefore a catalytic reaction; and (4) optical energy storage efficiency of the order of 1 percent can be achieved by the production of hydrogen.

This research was followed by studies of other semiconductors used as photoanodes in photoelectrolytic cells. Table I gives a listing of the semiconductors used as photoanodes in the work to date, as well as their efficiencies, the photon sources used, and the need for external power supplies.

Titanium dioxide, antamony doped tin oxide, the tentalates and strontium titanate have been shown to be photochemically stable as photoanodes in electrochemical cells. It should be noted that the semiconductor photoanodes TiO_2, Sb-SnO_2, and the tantalates need external power to electrolyse water but the strontium titanate- and the gallium arsenide-based cells do not. Maximum efficiency for the $SrTiO_3$-based cell is achieved when external power is added. This maximum conversion efficiency is measured to be 20 percent for 330 nm photons. The energy storage efficiency for the $SrTiO_3$ cell as well as the others cited in this section is determined by the formula

$$\text{Efficiency} = \frac{\text{Enthalpy } (H_2) - \text{Energy (Power Supply)}}{\text{Incident photon energy}}$$

Efficiencies lower than 20 percent result when the power supply is eliminated in the $SrTiO_3$-based cell.

Experiments with gallium arsenide crystals as photoanodes have shown that electrolysis proceeds with efficiencies as high as 9 percent when a broadband light source is focused on the crystal.[2] In an attempt to passivate the surface of the GaAs crystals, a sample with an efficiency of 6 percent to broadband radiation was coated with a gold layer approximately 5 nm thick. The efficiency of the coated sample was not significantly different from the uncoated sample. Similar coatings of tin and silver indicated no degradation of efficiency.

The spectral response curve for a GaAs photoelectrode in a photoelectrolytic cell is shown in figure 2. This cell has very broad response through the visible and into the near infra-red. The long wavelength cut-off corresponds to the bandgap of GaAs (1.43 eV or 867 nm). This response can be contrasted to the response of the other semiconductor-based cells listed in Table I which are sensitive to light in the UV only. Gallium Arsenide is, therefore, a good candidate photoanode material for sources such as the sun and other visible light sources.

TABLE I. SEMICONDUCTOR PHOTOANODES USED IN PHOTOELECTROLYSIS CELLS

PHOTO-ANODE	CHEMICAL STORAGE EFFICIENCY	PHOTO SOURCE	EXTERNAL POWER
TiO_2	1 %	ARGON ION LASER (UV)	YES
Sb-SnO_2	1 %	WATER FILTERED Xe - LAMP	YES
$KTaO_3$	6 %	300 nm LIGHT	YES
$KTa_{.77}Nb_{.23}O_3$	4 %		
$SrTiO_3$	20 %	WATER FILTERED Hg-SOURCE (330 nm)	YES NO
GaAs	9 %	TUNGSTEN FILAMENT LAMP	NO
GaAs - Au Ag Sn	6 %	TUNGSTEN FILAMENT LAMP	NO

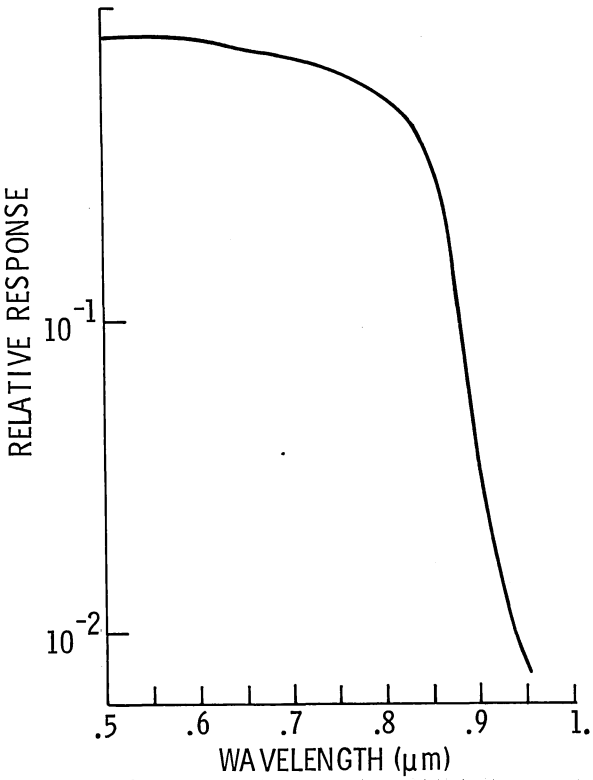

Fig. 2 Spectral response of GaAs-based photoelectrolytic cell.

Photogalvanic Cells

As was mentioned previously, the addition of a redox couple into the electrolyte can lead to the suppression of the photon assisted evolution of hydrogen and oxygen at the electrodes in the semiconductor-based photoelectrolysis cells. In the ideal case, only electrical energy is produced which may be utilized by connecting an electrical load in the external circuit. This cell is called a photogalvanic cell or an electrochemical photocell.

A recent paper by Gerischer[9] suggested that the bandgaps of CdS and CdSe lie in an optimum range (1.1 eV to 2.1 eV) for use as electrodes in solar energy converters. The principle limitations to the use of these semiconductors as photoanodes is the problem of photodissolution. Recently, however, Ellis, Kaiser, and Wrighton[10] reported that the addition of Na_2S and sulfur to a sodium hydroxide aqueous electrolyte suppresses the evolution of hydrogen at the platinum cathode and quenches the photodecomposition of both the CdS and CdSe electrodes. A schematic of their cell is shown in figure 3. They report an energy conversion efficiency of 5 percent for the CdS-based cell at 500 nm and 9 percent for the CdSe-based cell at 633 nm.

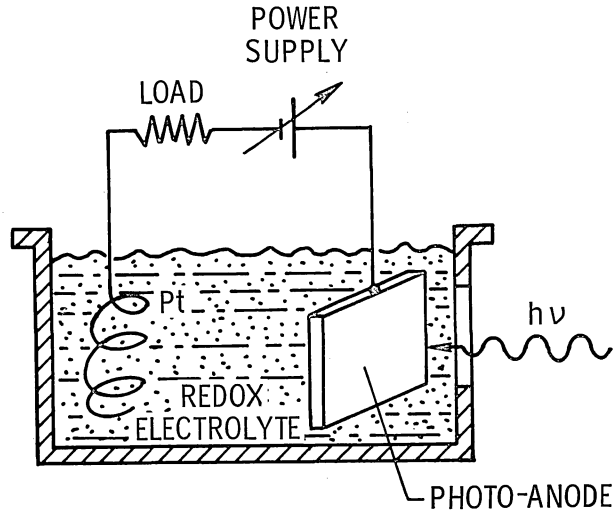

Fig. 3 Schematic of the photocell used in ref. 10.

IV. Conclusions

Titanium dioxide, strontium titanate, antimony doped tin oxide, and potassium tantalate have been shown to be chemically stable as photoanodes in photoelectrolysis cells. Of these, only $SrTiO_3$ has been shown to photodissociate water without the addition of electrical energy, but 20 percent energy conversion efficiencies for 330 nm light have been achieved with the addition of energy from a power supply. These semiconductor photoanodes are effective energy converters for photons in the ultraviolet. Gallium arsenide photoanodes have been shown to have a broad spectral response in the visible to near-IR and experiments with coatings of Au, Ag, and Sn suggests that the passivation of the surfaces of GaAs crystals can be achieved without degrading their energy conversion efficiency. Like $SrTiO_3$, GaAs-based photoelectrolysis cells dissociate water without the need of additional external energy.

Cadmium sulfide and cadmium selenide crystals used as anodes in photogalvanic cells have been shown to be photochemically stable with the addition of Na_2S and sulfur to aqueous solution of NaOH. Energy conversion efficiencies as high as 9 percent for 633 nm light have been measured in the CdSe-based photogalvanic cells.

A few semiconductors used as photoanodes in both photoelectrolytic cells and photogalvanic cells have been shown to be chemically stable and efficient for the conversion of electromagnetic radiation to chemical and electrical energy. Further research is necessary to determine the ultimate efficiencies of these two techniques using semiconductors as photoelectrodes as well as the effects of intensity of the incident photon energies on their performance.

V. References

1. Schneider, Richard T.; and Thom, Karlheinz: Fissioning Uranium Plasmas and Nuclear-Pumped Lasers. Nuclear Technology, vol. 27, 1975, pp. 34-50.
2. Byvik, Charles E.; and Walker, Gilbert H.: Photoelectrolytic Production of Hydrogen Using Semiconductor Electrodes. NASA TM X-72830, 1976.
3. Fujishima, A.; and Honda, K.: Electrochemical Photolysis of Water at a Semiconductor Electrode. Nature, vol. 238, 1972, pp. 37-38.
4. Fujishima, A.; Kohayakawa, K.; and Honda, K.: Hydrogen Production Under Sunlight with an Electrochemical Photocell. J. Electrochem. Soc., Electrochem. Science and Technology, vol. 122, 1975, pp. 1487-1489.
5. Wrighton, M. S.; Ginley, D. S.; Ellis, A. B.; Morse, D. L.; and Linz, A.: Photoassisted Electrolysis of Water by Irradiation of a Titanium Dioxide Electrode. Proc. Nat. Acad. Sci. U.S., vol. 72, 1975, pp. 1518-1522.
6. Wrighton, M. S.; Morse, D. L.; Ellis, A. B.; Ginley, D. S.; and Abrahamson, H. B.: Photoassisted Electrolysis of Water by Irradiation of an Antimony Doped Stannic Oxide Electrode. J. Amer. Chem. Soc., vol. 98, 1975, pp. 44-48.
7. Ellis, A. B.; Kaiser, S. W.; and Wrighton, M. S.: Semiconducting Potassium Tantalate Electrodes: Photoassistance Agents for the Efficient Electrolysis of Water. To be published.
8. Wrighton, M. S.; Ellis, A. B.; Wolczanski, P. T.; Morse, D. L.; Abrahamson, H. B.; and Ginley, D. S.: Strontium Titanate Photoelectrodes: Efficient Photoassisted Electrolysis of Water at Zero Applied Potential. J. Amer. Chem. Soc., vol. 98, 1976, pp. 0000.
9. Gerischer, H.: Electrochemical Photo and Solar Cell Principles and Some Experiments. Electroanalytical Chem. and Interfacial Electrochem., vol. 58, 1975, pp. 263-274.
10. Ellis, A. B.; Kaiser, S. W.; and Wrighton, M. S.: Visible Light to Electrical Energy Conversion. Stable Cadmium Sulfide and Cadmium Selenide Photoelectrodes in Aqueous Electrolytes. J. Amer. Chem. Soc., vol. 98, 1976, pp. 1635-1637.

DISCUSSION

ANON: Have you found that surface metal films are effective over a long period of time or short time?

C. BYVIK: This is a short duration experiment. We are looking into a little more detail now on this metal film idea at Langley.

F. C. SCHWENK: Have you done any analysis as to what levels of efficiency might be expected - for say a semiconductor like galium arsenide?

C. BYVIK: We haven't made those estimates. The literature points out the ultimate efficiency may be about 28%, but we haven't checked that. That was a guess made without any analysis.

F. C. SCHWENK: Mr. Tuck from Bell Labs who has been working with Indium Phosphide, says it has about the same kind of response as galium arsenide, but it has a lot more stability than galium arsenide: further, he was able to process it or heat it to fairly high temperatures without having it break down. So it might be an interesting lead to look into, and it is less expensive than galium arsenide.

J. H. LEE: You have a problem with corrosion of the anodes. Does the anode have to be immersed in water or can it be external to the electrolyte?

C. E. BYVIK: The only thing you have to have is an electrical conduction path between the anode and cathode, whether it be an aqueous electrolyte or solid electrolyte, it would work. As long as there is electrical conductivity between the two electrodes, the circuit would work.

UF_6 BREEDER REACTOR POWER PLANTS FOR ELECTRIC POWER GENERATION*

J. H. Rust and J. D. Clement
Georgia Institute of Technology
Atlanta, Georgia

F. Hohl
National Aeronautics and Space Administration
Langley, Virginia

Abstract

The concept of a UF_6 fueled gas core breeder reactor (GCBR) is attractive for electric power generation. Studies indicate that UF_6 fueled reactors can be quite versatile with respect to power, pressure, operating temperature, and modes of power extraction. Possible cycles include Brayton cycles, Rankine cycles, MHD generators, and thermionic diodes. Another potential application of the gas core reactor is its use for nuclear waste disposal by nuclear transmutation.

The reactor concept analyzed is a $^{233}UF_6$ core surrounded by a molten salt (Li^7F, BeF_2, ThF_4) blanket. Nuclear survey calculations were carried out for both spherical and cylindrical geometries. A maximum breeding ratio of 1.22 was found. Further neutronic calculations were made to assess the effect on critical mass, breeding ratio, and spectrum of substituting a moderator, Be or C, for part of the molten salt in the blanket.

Thermodynamic cycle calculations were performed for a variety of Rankine cycles. Optimization of a Rankine cycle for a gas core breeder reactor employing an intermediate heat exchanger gave a maximum efficiency of 37%.

A conceptual design is presented along with a system layout for a 1000 MW stationary power plant. The advantages of the GCBR are as follows: (1) high efficiency, (2) simplified on-line reprocessing, (3) inherent safety considerations, (4) high breeding ratio, (5) possibility of burning all or most of the long-lived nuclear waste actinides, and (6) possibility of extrapolating the technology to higher temperatures and MHD direct conversion.

I. Introduction

For about more than a decade, NASA has supported research on gas core reactors which consisted of cavity reactor criticality tests, fluid mechanics tests, investigations of uranium optical emissions spectra, radiant heat transfer, power plant studies, and related theoretical investigations.[1,2,3] These studies have shown that UF_6 fueled reactors can be quite versatile with respect to power, pressure, operating temperature, modes of power extraction, and the possibility of transmuting actinide waste products. Possible power conversion systems include Brayton cycles, Rankine cycles, MHD generators, and thermionic diodes. Additional research has shown the possibility of pumping lasers by fission fragment interactions with a laser gas mixture which leads to the possibility of power extraction in the form of coherent light.[4]

Gas core reactors have many advantages when compared to conventional solid fuel reactors in current use. Table 1 lists several advantages of gas core reactors.

Table 1 Advantages of gas core reactors

I.	Small Fuel Loadings
II.	Simplified On-Line Fuel Reprocessing
III.	Greater Safety due to Small Inventory of Fission Products
IV.	Require Less Structural Material
V.	Higher Breeding Ratios and Shorter Doubling Times
VI.	Potential for Higher Neutron Fluxes Which Makes Actinide Transmutation Practical
VII.	Operates at Higher Temperature with Increased Power Plant Efficiencies
VIII.	Possibility of Extrapolating Technology to Higher Temperatures and Use MHP Direct Conversion

One of the major advantages of UF_6 reactors for power generation is the simplified fuel reprocessing scheme which the gaseous fuel makes possible as shown in Fig. 1.

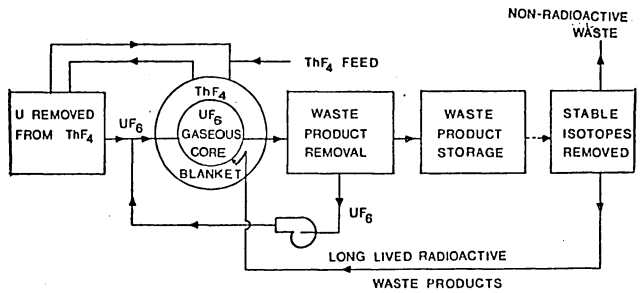

Fig. 1 Simplified diagram of UF_6 breeder reactor fuel cycle.

Part of the UF_6 can be extracted from the core continuously and sent to a fuel reprocessing facility for removal of waste products. The waste product removal can be accomplished by fractional distillation or cold trapping. After an appropriate waiting period, the waste products can be reprocessed for recovering long-lived fission products and actinides for return back to the reactor for transmutation to

*This research was supported by NASA Grants NSG-7068 and NSG-1168.

short-lived isotopes or fissioning of the actinides.

An additional advantage of gas core reactors is that they do not require the core structural materials that are necessary for solid fuel reactors. This lack of materials which undergo parasitic neutron capture enables higher breeding ratios for gas core reactors in comparison to conventional reactors. This paper reports a design study performed at Georgia Tech to evaluate the merits of gas core reactors for use as breeder reactors for electric power generation.

II. Materials

Materials selected for use for the gas core breeder reactor are listed in Table 2.

Table 2 Materials for UF_6 gas core breeder reactor

Core:	UF_6(U-233)
Blanket:	Molten Salt--LiF-BeF_2-ThF_4 (71.7-16-12.3 mole%)
Structure:	Modified Hastelloy-N
Secondary Coolant:	$NaBF_4$(92%) NaF(8%)

Uranium hexafluoride was chosen as the fuel because it exists in a gaseous state at low temperatures. U^{233} was selected as the fissionable isotope of the fuel because it enables use of the uranium-thorium fuel cycle which results in the direct production of U^{233} from breeding. An additional advantage is that the U^{233}-Th fuel cycle does not produce as great a buildup of actinides as fuel cycles employing U^{235}-U^{238} or Pu^{239}-U^{238}.

Several concepts were considered for the reactor blanket material. It was throught that a fluid blanket would be desirable so as to capitalize on the continuous reprocessing which is possible with the fluid fuel. The best material for use as the blanket is a molten salt similar to the type employed by the molten salt breeder reactor. This salt has a composition of LiF-BeF_2-ThF_4 which has a melting point of 500°C, has a low vapor pressure at the operating temperature, and is stable in the proposed range of application (540-970°C). In order to reduce parasitic neutron capture in lithium, the lithium is enriched to 99.995% in Li^7.

A modified Hastelloy-N was selected for the core liner, reactor pressure vessel, and primary piping. This material was developed for the molten salt breeder program and is quite compatible with the blanket salt and UF_6 over operating temperatures less than 900°C. Modified Hastelloy-N is very similar in composition and other related physical properties to standard Hastelloy-N; however, the modified version is superior because of its ability to resist helium embrittlement under neutron irradiation.

It was thought that it would be undesirable for UF_6 to interface with water which will be used as the working fluid for the power conversion cycle. Consequently, an intermediate coolant was selected for exchanging heat with the UF_6. This intermediate coolant is a molten salt which is composed of $NaBF_4$ and NaF and is quite compatible with UF_6.

III. Nuclear Analysis

Nuclear calculations were performed using the MACH-I one-dimensional, diffusion code[5] and the THERMOS transport code.[6] MACH-I employs 26 energy groups with the thermal neutron energy being 0.025 eV. Because of the high temperatures of the UF_6 and the blanket, it was thought that more accurate calculations could be performed by using THERMOS to supply thermal neutron cross sections.

The MACH-I code was used to calculate breeding ratios, critical masses, and reactor dimensions for a variety of reactor concepts. The lithium and beryllium contained in the blanket salt will act as a moderator for slowing down fission neutrons from the core. It was thought that additional moderation might be desirable and, consequently, carbon and beryllium were added in varying amounts to the blanket to evaluate the effects upon reactor parameters. Tables 3 and 4 show calculated breeding ratios, critical masses, and reactor dimensions for various percentages of carbon or beryllium in the blanket. As shown, additional moderation does increase breeding ratios and it appears that maximum breeding ratios occur when the blanket volume is about 25% carbon or beryllium. Additional studies showed that blanket thicknesses of 100 cm or greater behaved as though the blanket was of infinite thickness.

It is recognized that gas core reactors will undoubtedly be built in a cylindrical geometry. Since MACH-I is a one-dimensional code it was necessary to perform the survey calculations with a spherical reactor. In order to assess the effects of analyzing two-dimensional reactors with a one-dimensional diffusion code, some of the nuclear calculations were repeated using the EXTERMINATOR[7] diffusion code which is capable of doing calculations in an r-z geometry. The core capacity of the Georgia Tech CYBER-74 computer would not allow performing EXTERMINATOR calculations with more than 4-energy groups. Since the MACH-I calculations were performed with 26-energy groups, it was deemed desirable to collapse the 26-energy groups used in MACH-I down to 4-energy groups and repeat the MACH-I calculations. This enabled comparing the effects of using 4- or 26-energy groups for calculating breeding ratios, reactor dimensions, and critical masses. Table 5 illustrates the results of these calculations and, as seen, there are insignificant differences in using 4- or 26-energy groups with the MACH-I code. Therefore, it may be concluded that computations using 4-energy groups with the EXTERMINATOR code should yield valid results.

Table 5 also shows the results of the 4-energy group EXTERMINATOR calculations for a cylindrical reactor with a core height equal to the core diameter. As seen, the breeding ratio is slightly higher by going from a spherical geometry to a cylindrical geometry. This is to be expected because of the increased neutron leakage from a cylindrical core because of the increased surface-to-volume ratio of a cylinder compared to a sphere.

Table 3 Critical parameters vs volume percent of carbon in blanket (blanket thickness = 114 cm)

Percent of Carbon in Blanket	0	25	50	75	100
Breeding Ratio	1.183	1.196	1.190	1.133	0
Critical Radius (cm)	58.6	60.9	62.6	61.4	39.2
Critical Mass (kg U-233)	379	386	463	436	114

Table 4 Critical parameters vs volume percent of beryllium in blanket (blanket thickness = 114 cm)

Percent of Be in blanket	0	25	50	75	100
Breeding Ratio	1.183	1.223	1.203	1.065	0
Critical Radius (cm)	58.6	61.8	61.1	53.4	29.8
Critical Mass (kg U-233)	379	446	431	287	50

Table 5 Comparison of critical parameters

	Spherical Core (26 group)	Spherical Core (4 group)	Cylindrical Core (4 group)
Breeding Ratio	1.181	1.179	1.219
Critical Radius (cm)	58.6	60.9	54.8
Critical Core Volume	8.4×10^5 cm^3	9.5×10^5 cm^3	1.0×10^6 cm^3
Critical Mass (kg U-233)	379	426	496
Blanket Thickness (cm)	114	114	100

IV. Heat Transfer

Because of high power densities in gas core reactors, it is necessary to analyze the core heat transfer in order to assure that unacceptably high temperatures are not achieved in the UF_6. This requires solving the energy equation for UF_6 flowing through a cylindrical core. Equation 1 gives the energy equation for the UF_6.

$$\rho c_p U_z(r,z) \frac{\partial T}{\partial z} = \frac{1}{r} \frac{\partial}{\partial r} \left(r k_e \frac{\partial T}{\partial r} \right) + q'''(r,z) \quad (1)$$

where

ρ = density
c_p = specific heat at constant pressure
$U_z(r,z)$ = axial velocity
T = temperature
$k_e = k + \rho c_p \epsilon_H$, total conductivity
ϵ_H = eddy diffusivity for heat transfer
q''' = volumetric heat generation rate

Equation 1 is extremely complex because UF_6 physical properties are highly temperature dependent and the volumetric heat generation term is strongly spatially dependent due to the variable UF_6 density in the core and variable neutron flux distributions. Equation 1 was solved for two sets of boundary conditions: (Case 1)--an insulated liner wall in which no heat crosses the wall and (Case 2)--an insulated liner wall until the wall temperature reaches 920°K for the rest of the core length. Equation 1 was solved numerically by using finite difference representations for the partial derivatives and incorporating a MACH-I power distribution computation for the volumetric heat generation term. A marching technique was employed which required iteration at each axial step in order to incorporate the temperature dependence of the UF_6 physical properties. Reference 8 gives a detailed description of the heat transfer modeling and computational techniques.

It was estimated that 9.7% of the reactor power would be deposited in the blanket. Consequently, for a power level of 1000 MWth, 903 MWth would be generated in the reactor core. The UF_6 inlet temperature was specified as 558°K and mass flow rate at 6320 kg per second. The core geometry was a right cylinder with a 100 cm radius and 200 cm length.

Figure 2 illustrates the radial dependence of UF_6 temperatures for various axial positions for the insulated wall boundary condition (Case 1). Temperatures reach a peak at the wall because the volumetric heat generation term is a maximum at the wall and, in particular, the fluid velocity at the wall is zero which means heat is transferred at that location only through conduction. Figure 3 illustrates core liner wall temperatures and UF_6 fuel temperatures at the core axis as a function of core length. As shown by the calculations, after 50 cm down the channel length the liner wall temperatures exceed 920°K, which is considered unacceptably high.

Figure 4 illustrates the radial dependence of UF_6 temperatures for various axial locations for the boundary conditions that liner wall temperatures not exceed 920°K (Case 2). The maximum UF_6 temperature occurs at the core exit and is 1220°K, which is far below temperatures required for substantial UF_6 ionization. Figure 5 illustrates core liner wall temperatures and UF_6 temperatures at the core axis as a function of core length.

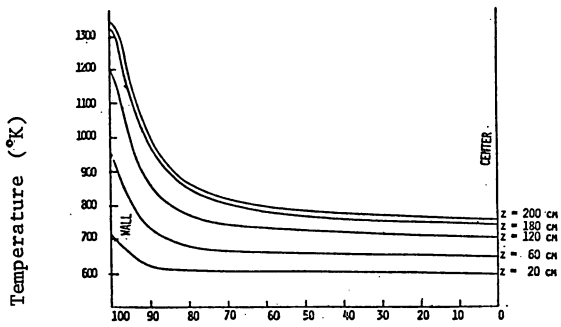

Fig. 2 Temperature vs radial distance (Case 1)

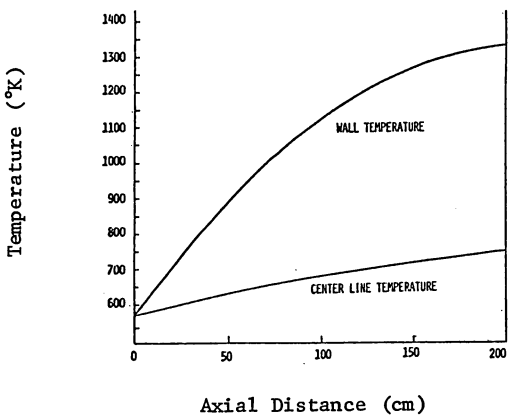

Fig. 3 Wall temperature vs axial distance (Case 1)

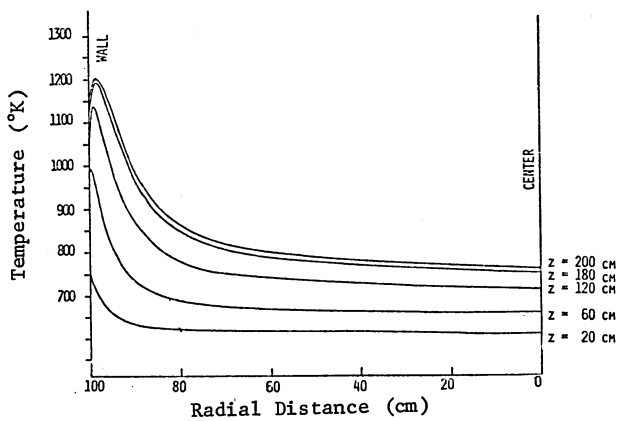

Fig. 4 Temperature vs radial distance (Case 2)

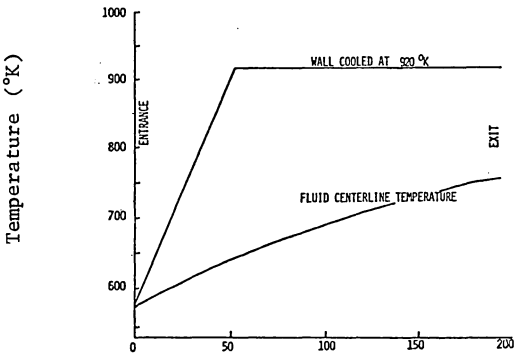

Fig. 5 Wall temperature vs axial distance (Case 2)

The boundary condition that the liner wall temperature not exceed 920°K requires wall cooling after about 40 cm down the core length. Consequently, it is necessary to examine wall heat fluxes in order to determine the extent of the wall cooling. Figure 6 illustrates calculated liner wall heat fluxes as a function of channel length. The maximum heat flux occurs at the channel exit and has a value of 0.205 watt per square centimeter which is a small heat flux for which it will be easy to provide wall cooling.

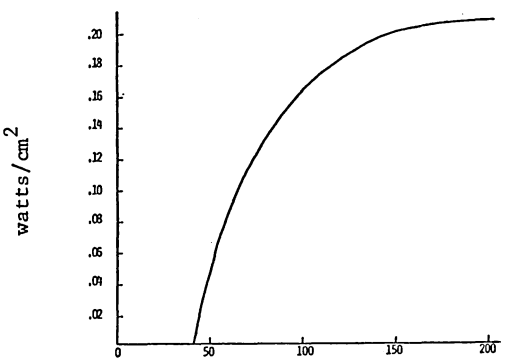

Fig. 6 Wall heat flux vs axial distance (Case 2)

V. System Analysis

It was thought that it would be desirable for the flow through the reactor core to be at a uniform velocity so as to simplify calculations and maximize reactor performance. In order to obtain an approximate uniform velocity distribution in the core it is necessary to employ numerous inlet and outlet nozzles for flow of UF_6 into and out of the core. Figure 7 illustrates the gas core reactor design. The reactor is a right cylinder with ellipsoidal heads and height equal to the diameter. It is easily fabricated and a good geometry to work with from both a practical and a calculational point of view.

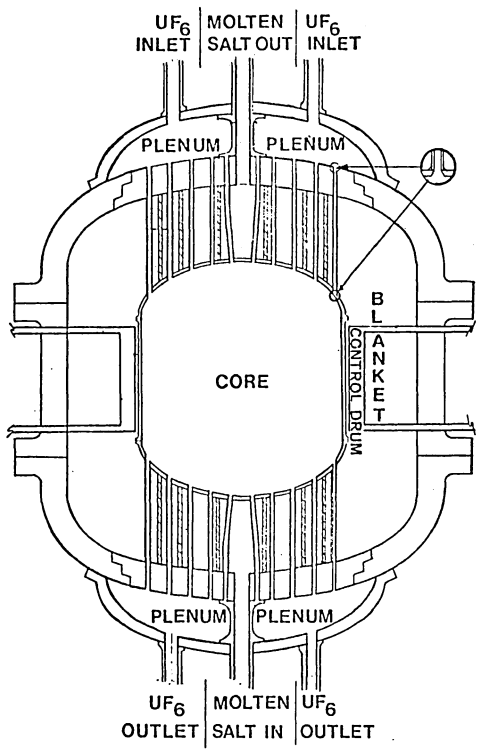

Fig. 7 Reactor configuration

The blanket will be pressurized to the same pressure as the core (on the order of 100 bars). The core liner is designed to withstand a pressure difference of only 15 bars. The outside pressure vessel will need to be capable of containing the 100 bar pressure plus a 20% safety margin, or 120 bar total. These pressures are not extreme and can be easily accommodated. The reactor pressure vessel was designed according to specifications from the ASME Boiler and Pressure Vessel Code; Section III--Rules for Construction of Nuclear Power Plant Components.[9] The core liner was selected at a thickness of 1.3 cm which is adequate for sustaining a 15 bar pressure difference at the reactor operating temperature for a 30-year lifetime. In case of a rapid depressurization of the blanket, the core liner can withstand a pressure difference of approximately 90 bars for a period of 6 minutes.

Many schemes were examined for energy conversion with gas core breeder reactors. The UF_6 can be used as a working fluid for either Brayton or Rankine cycles. However, in order to have reasonable efficiencies, a regenerator is necessary for either cycle. High efficiencies can be achieved using UF_6 in Rankine cycles for the operating temperatures selected for this study. For turbine inlet temperatures of 850°K and pressures of the order of 100 bars, Rankine cycle efficiencies will exceed 41%.

In order to reduce the inventory of UF_6 in the

power plant system, it is desirable to employ another fluid as the working fluid in the energy conversion device. Because of the adverse chemical reaction of UF_6 with water, in the event of a rupture of a boiler tube, it is not advisable for UF_6 to exchange heat directly with water in a boiler. Consequently, a molten salt $NaBF_4$-NaF was selected as an intermediate coolant for transferring heat from UF_6 to water in a boiler. The power plant schematic is shown in Fig. 8. The molten salt has heat transfer characteristics similar to those of water and an additional desirable feature is that it contains boron which is a control material used in conventional reactors and would thus prevent the possibility of criticality inside the intermediate heat exchanger.

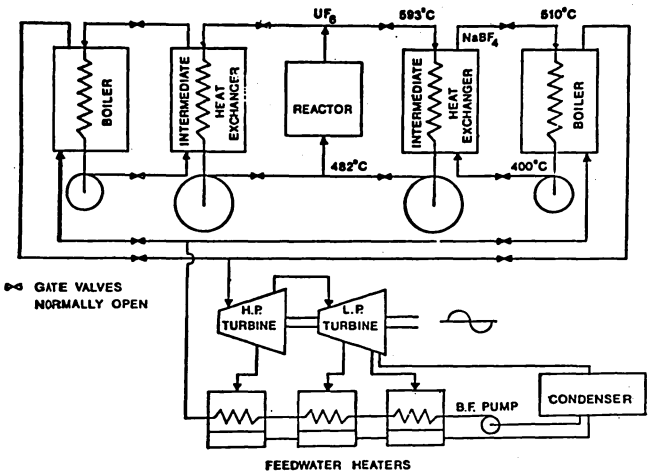

Fig. 8 UF_6 breeder power plant system schematic

The intermediate salt will be used to produce superheated steam at a temperature of 460°C and a pressure of 100 bars. The steam will be passed through high pressure and low pressure turbines for energy extraction. Three feedwater heaters are employed for extracting moisture from the turbines and heating the feedwater before it enters the boiler. By extracting steam at optimum pressures for each feedwater heater stage, the overall cycle efficiency will be 37%.

VI. Conclusions

The design study has shown that it is possible to construct a gas core breeder reactor with a high breeding ratio, of the order of 1.2 or higher, and an overall efficiency of 37%. The plant will not require excessive temperatures or pressures and will use much of the technology already developed for the molten salt breeder reactor program.

References

1. Thom, K., Schneider, R. T., and F. C. Schwenk, "Physics and Potentials of Fissioning Plasmas for Space Power and Propulsion," Paper No. 74-087, International Astronautical Federation 25th Congress, Amsterdam (October, 1974)

2. Williams, J. R., Clement, J. D., and J. H. Rust, "Analysis of UF_6 Breeder Reactor Power Plants," Progress Report No. 1, NASA Grant NSG-7067, Georgia Institute of Technology, Atlanta, Georgia (November, 1974)

3. Walters, R. A., and J. R. Williams, "High Efficiency Laser, MHD and Turbine Power Extraction from a Gas Core Nuclear Reactor," Proc. Southeastern IEEE Conf., Orlando, Florida (April, 1974)

4. Schneider, R. T., "Direct Conversion of Nuclear Energy into Laser Light," The 1976 IEEE International Conference on Plasma Science, Austin, Texas (May 24-26, 1976)

5. Meneley, D. A., et al., "MACH-I, A One-Dimensional Diffusion Theory Package," ANL-7223 (1966)

6. Toppel, B. J., and I. Baksys, "The Argonne-Revised THERMOS Code," ANL-7023 (1965)

7. Fowler, T. B., Tobias, M. L., and D. R. Nondy, "EXTERMINATOR-2; A Fortran IV Code for Solving Multigroup Neutron Diffusion Equations in Two Dimensions," ORNL-4078 (April, 1967)

8. Clement, J. D., and J. H. Rust, "Analysis of UF_6 Breeder Reactor Power Plants," Final Report, NASA Grant NSG-1168, Georgia Institute of Technology, Atlanta, Georgia (February, 1976)

9. "ASME Boiler and Pressure Vessel Code, Section III--Rules for Construction of Nuclear Power Plant Components," American Society of Mechanical Engineers, New York (July, 1971)

station. The axial component of the velocity measured in this way as a function of radial position is shown in Fig. 5. For both currents, the profiles are flat within experimental error out to 10 cm. Beyond this radius, the ion saturation current drawn by the probe drops rapidly to less than 10% of its centerline value, making velocity measurements impossible.

The observed axial and radial profiles thus indicate that a single measurement of centerline velocity 25 cm downstream of the anode should give a reasonable indication of trends in the average exhaust velocity, although any leakage of flow outside of the measureable 10 cm radius at lower velocities will clearly reduce the latter values somewhat.

Before presenting the results of the velocity vs current survey, it should be noted that the average exhaust velocity from an MPD discharge can also be expressed as the ratio of the total thrust to the propellant mass flow rate. The thrust is actually made up of two components, an electromagnetic component, as discussed in the introduction, and an electrothermal component derived from the arc chamber pressure. This electrothermal component was measured by Cory and found to be proportional to the current to the 1.5 power:[8]

$$T_{et} = cJ^{1.5} \qquad (4)$$

where c is an experimentally determined coefficient equal to 5.3×10^{-6} N·A$^{-1.5}$ for argon flow of 6 g/sec. Thus, this average exhaust velocity may be expressed in two terms:

$$\bar{u}_{em+et} = (bJ^2 + cJ^{1.5})/\dot{m} \qquad (5)$$

Average exhaust velocities calculated from this expression, and also from only the electromagnetic term are both shown in Figs. 6 and 7 along with the experimentally determined exhaust velocities for the 2.5 cm and for the 10 cm cathodes, respectively.

The data for both cathodes lie above the calculated values, reflecting the expected profile loss from outer flow leakage. As the current is increased, however, the data and the calculations converge, implying a significant decrease in this loss. Indeed, ion saturation currents measured with the time-of-flight velocity probe for the 2.5 cm cathode indicate that as the current increases from 8 to 25 kA, the outer flow leakage drops to a small fraction of the total mass flow. For a current of 15.3 kA, Boyle[5] performed a more detailed experimental analysis of the total exhaust velocity profile and after accounting for the profile losses, concluded that a good average value of the full experimental profile is provided by the velocity calculated from Eq. 5. To this extent, then, the discrepancy between the data and the calculated curves of Figs. 6 and 7 simply reflects the difference between centerline and average exhaust velocities of the flow.

Note also that while the velocity data for the 10 cm cathode rises smoothly with current and gradually meets the calculated average velocity line, the data for the 2.5 cm cathode display a discernible change in slope at the known onset current, J* of 16 kA. This fall-off beyond J* is believed related to a spurious increase in mass flow rate due to ablation, which, for given thrust lowers the average exhaust velocity from its pure argon value.[9] Since J* for the 10 cm cathode lies virtually at the end of the data line (23 kA), a similar change in slope is not discernible in this case.

Additional evidence for increased ablation at the onset current can be seen in the voltage-current characteristics for the two cathodes, as shown in Figs. 8 and 9. Here, the extrapolated value of the terminal voltage for zero current is taken to represent the electrode fall voltage and has been subtracted from the terminal voltage data shown in the figures. This quantity, the terminal voltage less the electrode fall, represents the potential drop over the discharge plasma body and is made up of contributions from ohmic losses, Lorentz terms and others. For an MPD thruster operating in an ideal electromagnetic mode, the Lorentz terms should dominate the plasma potential drop and scale with the exhaust velocity times the magnetic field. The self-magnetic field, in turn, scales with the current, and the exhaust velocity with the current squared, so that this component of plasma potential will be cubically dependent on the current. For a thruster operating in a pure electrothermal mode, in contrast, ohmic losses should dominate the plasma potential drop, which would then scale linearly with current. Any real thruster has both electromagnetic and electrothermal components to its thrust, so that the plasma potential drop should scale somewhere between a linear and a cubic dependence on current, according to the dominant process in any region. The data in Figs. 8 and 9 show this is indeed the case, with electromagnetic processes clearly favored over most of the regime studied.

The additional evidence for ablation beyond J* appears in the discernible change of slope for the 2.5 cm cathode just above its onset current of 16 kA. Since the exhaust velocity is inversely proportional to the total mass flow rate for a given thrust, as ablation increases, the velocity should decrease. This decrease will be reflected in a drop in the Lorentz voltage term and hence, in the terminal voltage. The decay in the $(V-V_o)$ vs J dependence beyond J* in Fig. 8 thus correlates well with the similar decay in the u vs J slope in Fig. 6.

GEORGIA INSTITUTE OF TECHNOLOGY RESEARCH ON THE GAS CORE ACTINIDE TRANSMUTATION REACTOR (GCATR)*

J. D. Clement, J. H. Rust, and A. Schneider
Georgia Institute of Technology
Atlanta, Georgia 30332

and

F. Hohl
National Aeronautics and Space Administration
Langley, Virginia 23665

Abstract

The Gas Core Actinide Transmutation Reactor (GCATR) offers several advantages including (1) the gaseous state of the fuel may reduce problems of processing and recycling fuel and wastes, (2) high neutron fluxes are achievable, (3) the possibility of using a molten salt in the blanket may also simplify the reprocessing problem and permit breeding, (4) the spectrum can be varied from fast to thermal by increasing the moderation in the blanket so that the trade-off of critical mass versus actinide and fission product burnup can be studied for optimization, and (5) the U^{233}-Th cycle, which can be used, appears superior to the U^{235}-Pu cycle in regard to actinide burnup.

The program at Georgia Tech is a study of the feasibility, design, and optimization of the GCATR. The program is designed to take advantage of initial results and to continue work carried out by Georgia Tech on the Gas Core Breeder Reactor under NASA Grant-1168. In addition, the program will complement NASA's program of developing UF_6-fueled cavity reactors for power, nuclear pumped lasers, and other advanced technology applications.

The program comprises:

(1) General Studies -- Parametric survey calculations will be performed to examine the effect of reactor spectrum and flux level on the actinide transmutation for GCATR conditions. The sensitivity of the results to neutron cross sections will be assessed. Specifically, the parametric calculations of the actinide transmutation will include the mass, isotope composition, fission and capture rates, reactivity effects, and neutron activity of the recycled actinides.

(2) GCATR Design Studies -- This task is a major thrust of the proposed research program. Several subtasks are considered: optimization criteria studies of the blanket and fuel reprocessing, the actinide insertion and recirculation system, and the system integration.

The total cost of the GCATR in a nuclear waste management system will be evaluated and compared to the cost of alternate strategies presently being considered.

This paper presents a brief review of the background of the GCATR and ongoing research which has just been initiated at the Georgia Institute of Technology.

*Research sponsored by N.A.S.A.

I. Introduction

The high level radioactive wastes generated in the operation of nuclear power plants contain both fission products and actinide elements produced by the non-fission capture of fissile and fertile isotopes. The fission products, atoms of medium atomic weight formed by the fission of uranium or plutonium, consist mainly of short term (30 years or less half-life) isotopes, including Sr^{90} and Cs^{137}. Tc^{99} and I^{129} are long-lived fission products. The actinide components of radioactive wastes, including isotopes of Np, Am, Cm, and Pu and others are all very toxic and most have extremely long half-lives. The amount of long-lived radioactive material expected to be produced is substantial. Smith[1] has estimated that in 1977, 150 kg of Am^{243}, 150 kg of Am^{241}, and 15 kg of Cm^{244} will be produced. The actinides cause waste management difficulties at two stages in the fuel cycle. Some are carried over with the fission products during fuel reprocessing, but also some dilute plutonium wastes will appear from fuel manufacturing plants. Thus at the entrance to the waste facility are found a mixture of transuranic actinides combined with shorter-lived and temporarily more hazardous fission products.

The safe disposition of the radioactive wastes is one of the most pressing problems of the nuclear industry. Any viable plan must meet the three requirements of

(1) technical soundness
(2) reasonable economics
(3) public acceptance.

II. Background

The strategies which have been suggested for high-level nuclear waste management encompass

(1) terrestrial disposal (geologic, seabed, ice sheet)
(2) extraterrestrial disposal, and
(3) nuclear transmutation,

or some combination of these methods, such as terrestrial burial of the short-lived fission products and extraterrestrial disposal or nuclear induced transmutation of the long-lived actinides. Papers discussing all of these methods were presented at the Waste Management Symposium in December 1974.[2] The technical soundness of terrestrial disposal is a controversial topic, and also public acceptance is questionable. Extraterrestrial disposal is costly. Hence, there is increasing interest in

nuclear transmutation as a potential solution to the nuclear waste disposal problem. Figure 1 summarizes the nuclear waste management schemes which are under consideration.

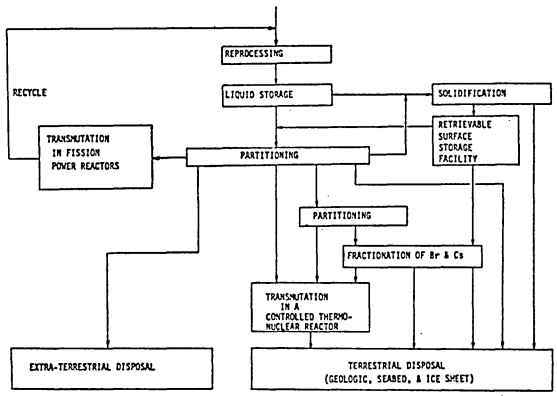

Fig. 1 Schematic representation of schemes for nuclear waste management

The first published suggestion for the use of neutron-induced transmutation of fission products was made in 1964 by Steinberg et al.,[3] who concerned themselves only with the transmutation of Kr^{85}, Sr^{90}, and Cs^{137}. Their calculations assumed that the krypton and cesium fission product wastes had been enriched to 90% in Kr^{85} and Cs^{137}. This was necessary due to the relatively small thermal neutron cross sections of these two nuclides and their small concentration with respect to their stable isotopes found in spent fuel. The Sr^{90} analysis was based on the presence of Sr^{90} and Sr^{89} which has a half-life of 53 days. If the strontium wastes are allowed to decay for one year before being returned to the reactor, then all the Sr^{89} portion will decay to Y^{89} (stable) which can be chemically separated from the Sr^{90}. However, even with these modifications to the waste isotopic composition, Steinberg et al, indicate that a thermal neutron flux of 10^{16} n/cm^2-sec is required before the halving time of Sr^{90} can be reduced from the normal half-life of 28.1 years to 1 year. A flux of 10^{17} n/cm^2-sec was indicated to be necessary before the halving time could be reduced from the natural half-life of 33 years to 1 year. The halving time describes the "total" time spent in a reactor for the inventory of a particular isotope to be reduced to half its value.

In another work, Steinberg and Gregory[4] considered the possibility of fission product burnup (specifically Cs^{137} and Sr^{90}) in a spallation reactor facility. In this scheme a nuclear power reactor is used to "drive" a high-energy proton accelerator with the resultant (p,xn) spallation reactions of the proton beam with the target producing the extreme fluxes of 10^{17} n/cm^2-sec necessary for fission product burnup. However, in addition to economic disadvantages this concept faces serious mechanical and material design problems.

Claiborne[5,6,7] was the first investigator to report detailed calculations of actinide recycling in light water reactors. Claiborne studied actinide recycling in light water reactors (LWR) operating on 3.3% U^{235}-U^{238} fuel cycle. He concluded that it was not practical to burn the fission products because the neutron fluxes were too low and "developing special burner reactors with required neutron fluxes of 10^{17} n/cm^2-sec or in thermonuclear nuclear reactor blankets is beyond the limits of current technology."[5]

For purposes of comparison, Claiborne[5] expressed radioactive waste hazards in terms of the total water required to dilute a nuclide or mixture of nuclides to its RCG (Radiation Concentration Guide Value, also known as the Maximum Permissible Concentration, MPC). Using this criterion, the waste from a PWR spent-fuel reprocessing plant is dominated by fission products for about the first 400 years. After the first 400 years the actinides and their daughters are the dominant factor. The americium and curium components of the actinide waste are the main hazards for the first 10,000 years, after which the long-lived Np^{237} and its daughters become the controlling factor. These data assume that 99.5% of the U and Pu has been removed from the waste.

Claiborne indicates that, if 99.5% of the U and Pu is extracted, then a significant reduction in the waste hazard can be achieved by also removing 99.5% of the other actinides, mainly americium, curium, and neptunium.

For the purpose of calculations, Claiborne assumes that recycling takes place in a typical PWR fueled with 3.3% enriched U and operated with a burnup of 33,000 MWd/metric tonne of uranium. The burnup was assumed continuous at a specific power of 30 MW/metric tonne over a three year period. The calculations also ignored intermittant operation and control rods and assumed that the neutron flux was uniform throughout a region. The recycled actinides were added uniformly to the 3.3% enriched fuel. The actual calculations were performed by a modified version of the nuclide generation and depletion code ORIGEN.[8] The calculations are based on three energy groups (thermal, 1/E energy distribution in the resonance region, and a fast group) with three principal regions in the reactor. Each region was in the reactor for three years while being cycled from the outside to the center so that the innermost region is removed each year.

The "standard" that was used for comparing the effect of the actinide recycle on the actinide waste hazard was the waste obtained after removing either 99.5% or 99.9% of the U and Pu at 150 days after discharge and sending the remaining quantities to waste along with all the other actinides, and all actinide daughters generated since discharge from the reactor. The results of Claiborne's calculations are presented in the form of a hazard reduction factor which he defines as "the ratio of the water required for dilution of the waste to the RCG for the standard case to that required to dilute the waste after each successive irradiation cycle."

The contributions of the actinides, fission products, and structural materials to the total waste hazard are shown in Table 1. Table 2 shows the effect of recycling the actinides in terms of the hazard reduction factor for two cases of actinide extraction efficiency. Note that the values decrease asymptotically with increasing recycles. This is due to the buildup of actinides in the system until decay and burnup equal production, after about 20 cycles. Figures 2 and 3 compare the effect of recycling in a LWR versus no-recycle for the short and long time hazards.

Table 1 Relative contribution of actinides and their daughters to the hazard measure of the waste and of each actinide and its daughters to actinide waste with 99.5% of U + Pu extracted[5]

Nuclides to Waste	Water required for dilution to the RCG[a] (% of total water required for the mixture) for decay times (yr) of: 10^2	5×10^2	10^4	10^5	10^6
	All Components of Waste:[b]				
Actinides	0.3	94	94	98	99
Fission Products	99+	5	6	2	1
Structural	0.04	1	0.2	0.03	4×10^{-4}
	Actinide Waste:[b]				
Americium	51	56	24	8	8
Curium	41	37	59	9	1
Neptunium	0.2	0.3	12	80	89
0.5% U + 0.5% Pu	8	7.7	5	3	1
Other	5×10^{-3}	1×10^{-3}	5×10^{-2}	6×10^{-3}	nil

[a]Using CFR RCGs and recommended default values for the unlisted nuclides.[8]

[b]Round-off may cause column not to total 100.

Table 2 Effect of recycle of actinides other than U and Pu on the hazard measure of waste from PWR spent fuel processing[5]

Recycle No.	Water required for dilution to RCG[a], ratio of standard to recycle[b] case (hazard reduction factor) for decay times (yr) of: 10^2	10^3	10^4	10^5	10^6
	Actinide Extraction Efficiency, 99.5%:				
0	12	15	18	28	52
1	9.3	12	13	20	46
2	8.2	10	11	18	44
3	7.6	8.4	9.3	17	43
4	7.2	7.4	8.3	17	42
5	6.8	6.6	7.5	17	42
10	5.8	4.7	5.8	17	42
20	5.1	3.8	4.9	17	42
30	5.0	3.6	4.6	17	42
	Actinide Extraction Efficiency, 99.9%:				
0	58	73	89	137	256
1	44	59	64	96	224
2	38	48	52	87	213
3	36	40	44	84	210
4	33	35	39	83	209
5	32	31	36	83	208
10	27	22	27	83	207
20	--	18	22	82	206
30	--	17	21	82	206

Using CFR RCGs and recommended default values for the unlisted nuclides.[8]

Chemical processing assumed at 150 days after reactor discharge; one cycle represents 3 years of reactor operation.

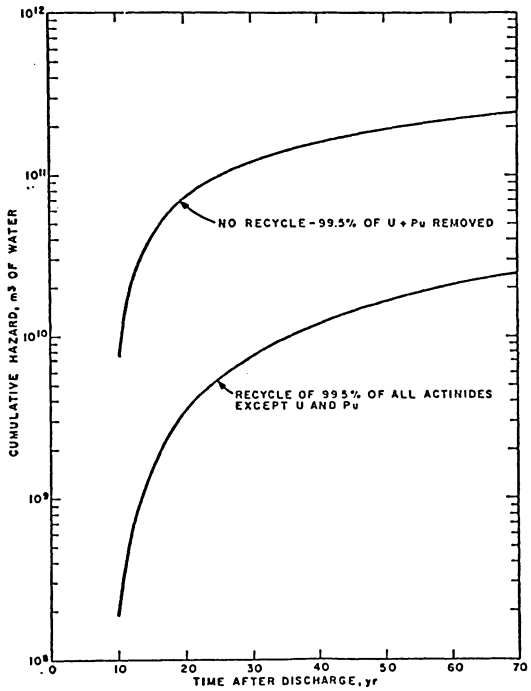

Fig. 2 Short-term cumulative hazard of actinide waste from 60-year operation of a typical PWR[5]

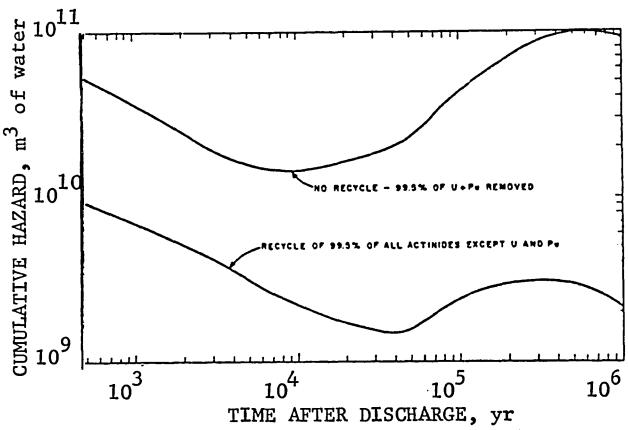

Fig. 3 Long-term cumulative hazard of actinide waste from 60-year operation of a typical PWR[5]

For the PWR examined, the decrease in the average neutron multiplication was only 0.8%. By increasing the fissile enrichment by only 2% (from 3.3 to 3.4% enrichment) the loss in reactivity can be compensated for.

The recycling of reactor actinide waste will increase radiation problems associated with chemical processing and fuel fabrication because of the increased radioactivity of the reactor feed and discharge streams. However, the increased actinide inventory in a reactor will probably have little effect on the potential danger in design basis accidents because the actinides are not volatile and, therefore, will not be significantly dispersed into the environment by any credible reactor accident.

Claiborne also states that the recycle of actinides in LMFBR's should produce even higher hazard reduction factors because of the better fission-to-capture ratio of the actinides in the presence of a fast flux. He also states that the recycling of actinides is well suited for fluid fuel reactors, such as the MSBR, because of the on-stream continuous reprocessing.

A technical group at Battelle Northwest Laboratories[9] extended Claiborne's work to provide a detailed review of the alternative method for long term radioactive waste management. Section 9 of their report was devoted to Transmutation Processing and covered four categories: (1) accelerators, (2) thermonuclear explosives, (3) fission reactors, and (4) fusion reactors. The study identified recycling in thermal power reactors as a promising method and went on to state, "consideration should also be given to evaluating the merit of having special purpose reactors optimized for destroying actinides."[9]

As reported in a review paper by Raman,[10] evaluations made by Raman, Nestor, and Dobbs[11] show that actinide inventories can be reduced further by recycling in a U^{233}-Th^{232} fueled reactor. This is made possible because neutron captures by the fertile Th^{232} produce the fissile U^{233}. Neutron capture by U^{233} results in higher U isotopes until U^{237} is reached. Plutonium and transplutonium isotopes are generated to a far lesser extent in a U^{233}-Th^{232} reactor than in a U^{235}-U^{238} reactor. Raman also stressed the need for more accurate cross section measurements.

The recycling of actinides in fast reactors has also been studied.[12,13,14,15] Greater actinide burnup is achievable in a fast reactor than in a thermal reactor because the fission-to-capture ratio is generally higher as shown in Table 3. In a 1973 review paper in Science, Kubo and Rose[16] suggested that recycling of actinides in an LMFBR has several advantages over recycling in a thermal reactor including the possibility that extreme chemical separations may not be required because fewer actinides are produced in a fast spectrum.

Paternoster, Ohanian, Schneider, Thom, and Schwenk[17,18,19] have studied the use of the gas core reactor for transmutation of fission products and actinide wastes. The fuel was UF_6 enriched to 6% in U^{235}. The four meter diameter core was surrounded by a reflector-moderator of D_2O with a thickness of 0.5 meter. The initial mass was 140 kg of $U^{235}F_6$. Adjustable control rods were located in the outer graphite reflector and the radioactive wastes were loaded in target ports. Figure 4 shows results of calculations, comparing both actinide and fission product waste in current LWR's with the gaseous fuel power reactor. Notice that after 800-1000 days, the actinide wastes in the gaseous core reactor are an order of magnitude less than those in a LWR.

In a study sponsored by NASA, Clement, Rust, and Williams[20,21] analyzed a gas core breeder reactor using a U^{233}-Th^{232} fuel cycle. One- and two-dimensional calculations were carried out for a UF_6 fueled core surrounded by a molten salt blanket. Figure 5 shows a diagram of the reactor. The medium fission energy in the core was found to be 300 keV, and there was some spectrum softening in the blanket.

Table 3 Fission-to-capture ratios of actinides in fast and thermal reactors[10]

Isotope	Half-Life Years	Fast Spectrum	Thermal Spectrum
Np^{237}	2.14×10^{6}	0.213	1.26×10^{-4}
Am^{241}	433	0.115	4.48×10^{-3}
Am^{242m}	152	4.85	1.12
Am^{243}	7370	0.309	4.87×10^{-4}
Cm^{244}	17.9	1.25	0.068

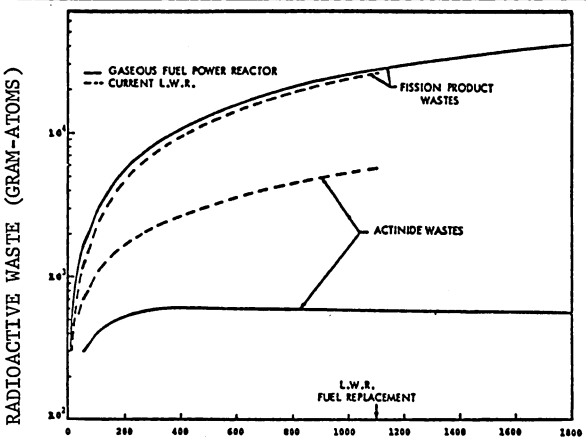

Fig. 4 Radioactive waste production of 3425 MW(t) fission power reactors[19]

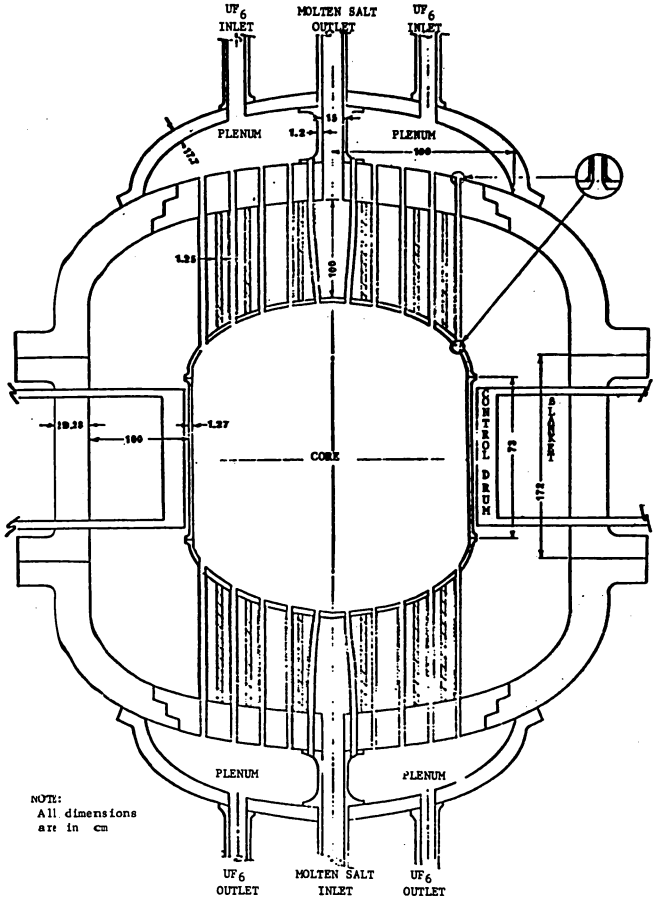

Fig. 5 UF_6 gas-core reactor

Table 4 is a brief summary of some important dates in the history of the GCATR. As previously stated, the burnup of fission products requires thermal neutron fluxes of the order of 10^{17} n/cm^2-sec. In the United States, the two reactors with the highest neutron fluxes are the ORNL High Flux Isotope Reactor (HFIR)[22] and the SRL High Flux Reactor (HFR)[23] which have maximum neutron fluxes of 3×10^{15} and 5×10^{15} n/cm^2-sec, respectively. Both of these reactors employ solid fuels and have essentially reached the upper limit in neutron fluxes because of heat transfer limitations. In addition, when operating at these neutron fluxes the refueling intervals are of the order of two weeks. The gas core reactor does not have the in-core heat transfer limitations posed by solid core reactors employing a coolant and, consequently, higher neutron fluxes should be achievable. In addition, reactor shutdown for refueling is not necessary because new fuel can be continuously added to the UF_6 during reactor operation. Therefore, a gas core reactor may be the only practical reactor for consideration of fission product burnup if such a scheme of waste disposal is considered desirable.

Table 4 Some dates in the history of GCATR

1960-73	- NASA sponsored research on gas-core reactor for rocket propulsion
1964	- Steinberg first suggests neutron-induced transmutation
1972	- Claiborne's studies of actinide recycling in LWR's
1973	- documentation of ORIGEN program
1974	- recycling studies in LWR's, LMFBR's, HTGR's by Croff, Raman, et al.
1974	- suggestion of GCATR by Paternoster, Ohanian, Schneider (University of Florida) and Thom (NASA)
1974-75	- UF_6 breeder reactor study at Georgia Tech sponsored by NASA
1976	- GCATR study at Georgia Tech sponsored by NASA

Table 5 summarizes some of the advantages of the GCATR which appear to make it an attractive candidate for actinide transmutation.

Table 5 Some advantages of the gas-core reactor

(1) The gaseous state of the fuel significantly reduces problems of processing and recycling fuel and wastes.

(2) High neutron fluxes are achievable.

(3) The possibility of using a molten salt in the blanket may also simplify the reprocessing problem and permit breeding.

(4) The spectrum can be varied from fast to thermal by increasing the moderation in the blanket so that the trade-off of critical mass versus actinide and fission product burnup can be studied for optimization.

(5) The U^{233}-Th cycle, which can be used, is superior to the U^{235}-Pu cycle in regard to actinide burnup.

III. GCATR Research Program

The overall objective of the NASA sponsored program is to study the feasibility, design, and optimization of a GCATR. The program involves three interrelated and concurrent tasks, as listed in Table 6.

Table 6 NASA sponsored GCATR research at Georgia Tech

General Studies
Update cross-sections
Sensitivity analysis
Parametric survey
Reactor and System Design
Design criteria
Reactor subsystem
(a) $^{233}UF_6$
(b) plasma core
Fuel and actinide insertion and recycling
Economic Analysis
Comparison of GCATR with other strategies

TASK 1 General Studies

Raman[9] has pointed out the need for more accurate cross section data and the necessity of assessing the sensitivity of the calculational results to the uncertainties in cross sections. This task will include the following subtasks:

A. Literature Survey and Cross Section Tabulation--A literature survey will be carried out and the best available cross sections of the fission products and actinides will be tabulated. Improved values will be used as they become available.

B. Implementation of a Versatile Depletion Program--ORIGEN[8] or a similar computer code will be implemented or developed. A depletion code which solves the equations of radioactive growth and decay and neutron transmutation for large numbers of isotopes is required. ORIGEN has been used previously for LWR's, LMFBR's, MSBR's, and HTGR's, and may also be suitable for the GCATR.

C. Parametric Survey Calculations--Parametric survey calculations will be performed to examine the effort of reactor spectrum, and flux level on the actinide transmutation for GCATR conditions. The sensitivity of the results to neutron cross sections will be assessed. These studies will be related to the nuclear analysis work of TASK 2. Specifically, the parametric calculations of the actinide transmutation will include the mass, isotope composition, fission and capture rates, reactivity effects, and neutron activity of the recycled actinides. Table 7 summarizes the most important parameters to te investigated.

Table 7 Most important parameters to be investigated

(1) The mass and composition of the actinides being recycled
(2) The rate at which the recycled actinides are fissioned and transmuted in the reactor
(3) The effect of the recycled actinides on fission reactor criticality and reactivity
(4) The effect of the recycled actinides on the out-of-reactor nuclear fuel cycle (i.e., fabrication, shipping, reprocessing, actinide inventory, etc.)

TASK 2 GCATR Design Studies

This task is a major thrust of the proposed research program. Four subtasks are considered:

A. Optimization Criteria Studies
B. Design Studies of the Reactor Subsystem
C. Design Studies of the Blanket and Fuel Reprocessing and Actinide Insertion and Recirculation System
D. System Integration

In subtask A, Optimization Criteria Studies, consideration will be given to understanding the trade-offs that are made to achieve a given result. For example, is the GCATR to be used only for actinide burnup? Should we also include breeding (U^{233}-Th) or fission product transmutation? If we reduce the mean neutron energy to achieve faster fission product burnup, how much do we sacrifice in actinide burnup? Should the reactor also be used to produce power? If so, how much power? What are the optimization criteria?

In subtask B, Design Studies of the Reactor Subsystem, a multidisciplinary approach similar to that in Refs. 20, 21 will be carried out involving:

(1) Materials
(2) Nuclear Analysis
(3) Thermodynamics and Heat Transfer
(4) Mechanical Design.

Results of this task will be used iteratively with the parametric study described in TASK 1. In previous work[20,21] one-dimensional and two-dimensional survey calculations were carried out for a UF_6-fueled core surrounded by a molten salt blanket, and a preliminary mechanical design was developed. This work will be extended to include the insertion of fission products and actinides in various locations in the reactor. The effect of other reactor component changes such as using different reflector materials (carbon, beryllium, deuterium oxide) or modifying the molten salt reflector by the addition of moderator will also be evaluated. Best available cross section data from TASK 1 will be utilized. A preliminary reactor design will be developed taking into account thermal and mechanical design considerations.

In subtask C, a preliminary design of the UF_6 and blanket reprocessing system (if molten salt) will be prepared and performance of the systems analyzed. Equilibrium fuel and blanket compositions including fission products and actinides will be computed. These results will provide necessary

information on equilibrium core and blanket compositions for use in the nuclear analyses.

Subtask D, System Integration, involves putting all the sub-components together in a workable system taking account of criticality, shielding, and economic considerations.

TASK 3 Comparison of the GCATR with Other Nuclear Waste Management Strategies

The cost of the GCATR shall be evaluated in terms of mills/kwhre. The cost can be broken down into the components:

(1) solid and liquid storage
(2) shipping
(3) interim retrievable storage separations
(4) separation
(5) disposal or elimination in GCATR

The total cost of the management system will be computed and compared to the cost of alternate strategies presently being considered.

As of June 1976, the research program has been underway for only two months. Table 8 summarizes the status of the program at this time.

Table 8 Summary of Georgia Tech GCATR research program to date

General Studies
1. Actinide cross sections have been updated
2. ORIGEN has been implemented and modified
3. Some sensitivity results and parametric studies have been obtained
Reactor Studies
1. Series of nuclear design codes have been implemented
2. Several configurations of $^{233}UF_6$ reactor are being analyzed

IV. References

1. Smith, J. A., "Proceedings of the Californium-252 Symposium," USAEC Report CONF-681032, p. 179 (1969)

2. "Waste Management Symposium," Nuclear Technology, 24 (December 1974)

3. Steinberg, M., Molzak, G., and Menovita, B., "Neutron Burning of Long-Lived Fission Products for Waste Disposal," BNL-8558, Brookhaven National Laboratory (September 1964)

4. Gregory, M. V. and Steinberg, M., "A Nuclear Transmutation System for Disposal of Long-Lived Fission Product Waste in an Expanding Nuclear Power Economy," BNL-1195 (November 1967)

5. Claiborne, H. C., "Neutron Induced Transmutation of High-Level Radioactive Wastes," ORNL-TM-3964 (December 1972)

6. Claiborne, H. C., "Effect of Actinide Removal on the Long-Term Hazard of High-Level Waste," ORNL Report TM-4724 (1975)

7. Bond, W. D., Claiborne, H. C., and Levze, R. E., "Methods for Removal of Actinides from High Level Wastes," Nuclear Technology, 24, 362-370 (December 1974)

8. Bell, M. J., "ORIGEN--The ORNL Isotope Generation and Depletion Code," ORNL-4628, Oak Ridge National Laboratory (May 1973)

9. Schneider, K. J. and Plat, A. M., "High-Level Radioactive Waste Management Alternatives," BNWL Report 1900 (1974)

10. Raman, S., "Some Activities in the United States Concerning the Physics Aspects of Actinide Waste Recycling," Review Paper from ORNL (1975)

11. Raman, S., Nestor, C. W., Jr., and Dabbs, J. W. T., "The U^{233}-Th^{232} Reactor as a Burner for Actinide Wastes," Proc. of the Conf. on Nuclear Cross Sections and Technology, Washington, D. C. (March 1975)

12. Breen, R., "Elimination of Actinides with LMFBR Recycle," Westinghouse Advanced Reactors Division, private communication reported in Ref. 10

13. Beaman, S. L., "Actinide Recycle Evaluations," General Electric Energy Systems and Technology Division, private communication reported in Ref. 10

14. Croff, A. G., "Parameter Studies Concerning Actinide Transmutation in Power Reactors," Transactions of the American Nuclear Society, 22, 345 (November 1975)

15. Davidson, J. W. and Draper, E. L., Jr., "Costs for Partitioning Strategies in High-Level Waste Management," Transactions of the American Nuclear Society, 22, 348 (November 1975)

16. Kubo, A. S. and Rose, D. J., "On Disposal of Nuclear Waste," Science, 182, No. 4118, 1205-1211 (December 1973)

17. Paternoster, R., Ohanian, M. J., Schneider, R. T. and Thom, K., "Nuclear Waste Disposal Utilizing a Gaseous Core Reactor," Transactions of the American Nuclear Society, 19, 203 (October 1974)

18. Paternoster, R. R., "Nuclear Waste Disposal Utilizing a Gaseous Core Reactor," Master's Thesis, University of Florida (1974)

19. Schwenk, F. C. and Thom, K. T., "Gaseous Fuel Nuclear Reactor Research," Paper presented at the Oklahoma State University Conference on Frontiers of Power Technology (October 1974)

20. Clement, J. D., Rust, J. H., and Williams, J. R., "Analysis of UF_6 Breeder Reactor Power Plants," Semi-annual Report NASA Grant NSG-1168 (October 1975)

21. Rust, J. H. and Clement, J. D., "UF_6 Breeder Reactor Power Plants for Electric Power Generation," Proc. Third Symposium on Uranium Plasmas, Princeton University Conference, June 10-12, 1976

22. Binford, F. T., et al., "The High-Flux Isotope Reactor," ORNL-3572 (Rev. 2) (May 1968)

23. Crandall, J. L., "The Savannah River High Flux Demonstration," USAEC Report DP-999 (1965)

APPLICATION OF GASEOUS CORE REACTORS FOR TRANSMUTATION OF NUCLEAR WASTE

B. G. Schnitzler, R. R. Paternoster*, and R. T. Schneider
University of Florida
Gainesville, Florida

Abstract

An acceptable management scheme for high-level radioactive waste is vital to the nuclear industry. The hazard potential of the trans-uranic actinides and of key fission products is high due to their nuclear activity and/or chemical toxicity. Of particular concern are the very long-lived nuclides whose hazard potential remains high for hundreds of thousands of years. Neutron induced transmutation offers a promising technique for the treatment of problem wastes. Transmutation is unique as a waste management scheme in that it offers the potential for "destruction" of the hazardous nuclides by conversion to non-hazardous or more manageable nuclides. The transmutation potential of a thermal spectrum uranium hexafluoride fueled cavity reactor was examined. Initial studies focused on a heavy water moderated cavity reactor fueled with 5% enriched U^{235}-F_6 and operating with an average thermal flux of 6×10^{14} neutrons/cm^2-sec. The isotopes considered for transmutation were I-129, Am-241, Am-242m, Am-243, Cm-243, Cm-244, Cm-245, and Cm-246.

Introduction

The proper management of high-level radioactive waste is an important issue with which the nuclear community must deal. In the face of rising social pressure, the identification of a satisfactory long-term management scheme is vital to the health of the industry.

A number of high-level, long-term waste management schemes have been proposed; none are entirely satisfactory. The ultimate standard against which any proposed management scheme must be judged is whether or not it will prevent any nuclear waste material from ever posing a threat to man's well-being. Management schemes are invariably aimed at accomplishing this goal by isolation of the waste material from man and from the environment for whatever period of time it remains hazardous. Transmutation is the only exception to the isolation rationale. Transmutation is unique in that it offers the potential of converting hazardous nuclides into non-hazardous forms by the same nuclear processes responsible for their creation.

Waste Characterization

Until recently, spent fuel reprocessing had been directed toward recovery of most of the uranium and plutonium present. Recovery fractions were governed by trade-offs between the value of the recovered metal and sharply increasing costs with higher recovery fractions. The remaining high-level waste was treated collectively by storage until future implementation of a long-term management scheme. With this technique, the entire high-level waste mass must be treated as though it had the half-life of the longest lived nuclide, the chemical toxicity of the most toxic nuclide, etc.

A recent study[1] on waste management alternatives examined the requirements and potential benefits of separating the high-level waste stream into two fractions based on half-life. The short-lived fraction would contain only those nuclides which would decay to radiologically non-toxic levels in 1000 years. At the end of the 1000-year decay period, this fraction of the high-level waste would require no more control than that necessary from a chemical standpoint. The long-lived fraction would contain the actinides and a few key fission products not meeting the "short-lived" criteria. Different management techniques might then be employed for the two fractions. Some options, such as transmutation, might require additional separation by element or chemical groups of elements.

Fission Products

The fission products are characterized by high specific activity and relatively low neutron absorption cross sections. They are generally short-lived compared to the actinide elements. They are neutron rich and decay toward a stable neutron-proton ratio by successive beta decays. Typical decay chains are illustrated in Figure 1. For thermal fission of U-235, there is slightly less than 1% fission yield into the 129 mass chain. There is negligible direct yield of xenon-129. The shorter-lived chain members rapidly decay into iodide-129 which has a half-life of 15.9 million years. Within the fission product group, a few long-lived nuclides, such as I-129, control the long-term waste hazard.

Actinides

The trans-uranic actinides are formed by those neutron absorption reactions in the fuel which do not result in fission. The most common such reaction competing with fission is radiative capture. The

* *Now at Los Alamos Scientific Laboratory*

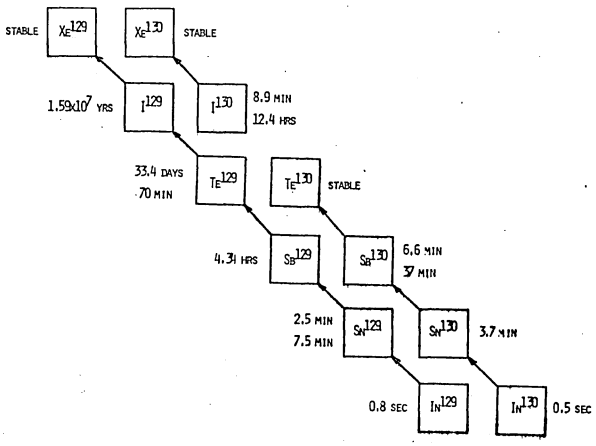

FIGURE 1. TYPICAL FISSION PRODUCT DECAY CHAINS

newly formed nuclide may then undergo spontaneous or neutron induced fission, decay by particle emission, or another neutron absorption reaction such as radiative capture may take place. In this manner, higher and higher mass number trans-uranics are built up in the fuel.

The heavy metals present the most severe long-term management problems. They are characterized by high chemical toxicity and very long half-lives. The waste hazard associated with the heavy metals remains high for hundreds of thousands of years. In general, the actinides possess substantial neutron reaction cross sections.

Transmutation

Transmutation is any process by which a nuclide is changed into another nuclide. The decay of a radioactive nuclide is a natural transmutation process, but it may not occur on a sufficiently short time scale to be useful for waste management. Transmutation may also be artificially induced by neutrons, photons, or charged particles. Of the known methods of artificially inducing transmutation, only neutron induced transmutation appears to offer near term technical and economic feasibility.

Transmutation of the long-lived waste fraction will involve treatment of the actinides and some key fission products. For the fission products, the motivation for treatment is illustrated by considering iodine-129. The I-129 decay bottleneck illustrated in Figure 1 may be relieved by irradiation. Radiative capture reactions in the I-129 will drive it to I-130. The short-lived (12.4 hours) I-130 will then beta decay to xenon-130 which is stable and non-hazardous. The very slowly decaying nuclides in a particular mass chain are shifted to a more rapidly decaying chain.

A number of competing reactions may also occur. The major reaction paths are indicated in Figure 2. Table 1 contains a symbol key for the figure. For I-130, radiative captures producing I-131 compete with the natural beta decay producing Xe-130. Similar competitive reaction paths may be readily observed for other nuclides. In general, the rate at which the transmutation proceeds will be governed by the magnitude of the neutron flux. The reaction rate may also be altered, sometimes substantially, by tailoring the neutron spectrum to exploit neutron absorption resonances. Particular reaction paths can be enhanced by altering the spectrum. The eventual distribution of nuclides is strongly dependent on the neutron spectrum.

The final nuclide distribution will be very significant from a waste management standpoint. The variety of possible reaction paths generally precludes prediction of the final distribution by observation. The effect of a spectral change must be evaluated by following the isotopic balance as a function of time during the irradiation and subsequent decay period. Nuclide concentrations, transmutation rates, and the waste hazard may then be calculated.

For the actinides, the transmutation rationale is different. Contrary to the fission products, there is little to be gained by radiative capture reactions in the actinides. To build even higher actinides from them is of questionable value. The ultimate objective is to induce fission. Actinide fission cross sections generally decrease with increasing energy, but at a faster rate for most actinides. Therefore, fission can be promoted over radiative capture by the employment of a harder neutron spectrum. As with the fission products, the optimum spectrum cannot be predicted by simple observation and detailed calculations must be performed.

A number of transmutation schemes have been proposed for waste management. Detailed transmutation calculations[6] indicate that actinide recycle in currently operating light water reactors (LWR) would be effective in reducing the long-term hazard associated with the actinide wastes. The liquid metal fast breeder reactor (LMFBR) may prove even more effective for actinide recycle.[1] Transmutation of most fission product wastes is not feasible for either the LWR or the LMFBR. Both the attainable fluxes and the fission product cross sections are too low for practical application. Neutrons produced in a CTR device would be most effective for transmutation of both actinides and fission products, but near term implementation is not possible.[7]

The requirements for very high neutron fluxes and the desirability of spectrum tailoring make the cavity reactor a logical candidate for transmutation of both fission product and actinide wastes. A uranium hexafluoride fueled heavy water moderated cavity reactor was considered in initial studies. The reactor was assumed

to operate at an average thermal flux of approximately 6.4 x 10^{14} neutrons/cm^2-sec for a five-year period. The assumed fuel enrichment was 5%. The transmutation rates of several waste isotopes present in the discharged fuel from currently operating light water reactors were studied using the isotopic generation and depletion code ORIGEN.[2]

The isotopes selected for evaluation of the gas core transmutation potential were I-129, Am-241, Am-242m, Am-243, Cm-243, Cm-244, Cm-245, and Cm-246. Americium and curium were chosen since they control the actinide waste hazard for very long decay times. The fission product iodine-129 was chosen since it is a major contributor to the long-term waste hazard. The amounts of the initial waste loading were determined by the composition of 20 typical light water reactor fuel loads stored for a decay interval of ten years. The waste quantities employed in the study are therefore approximately equivalent to that

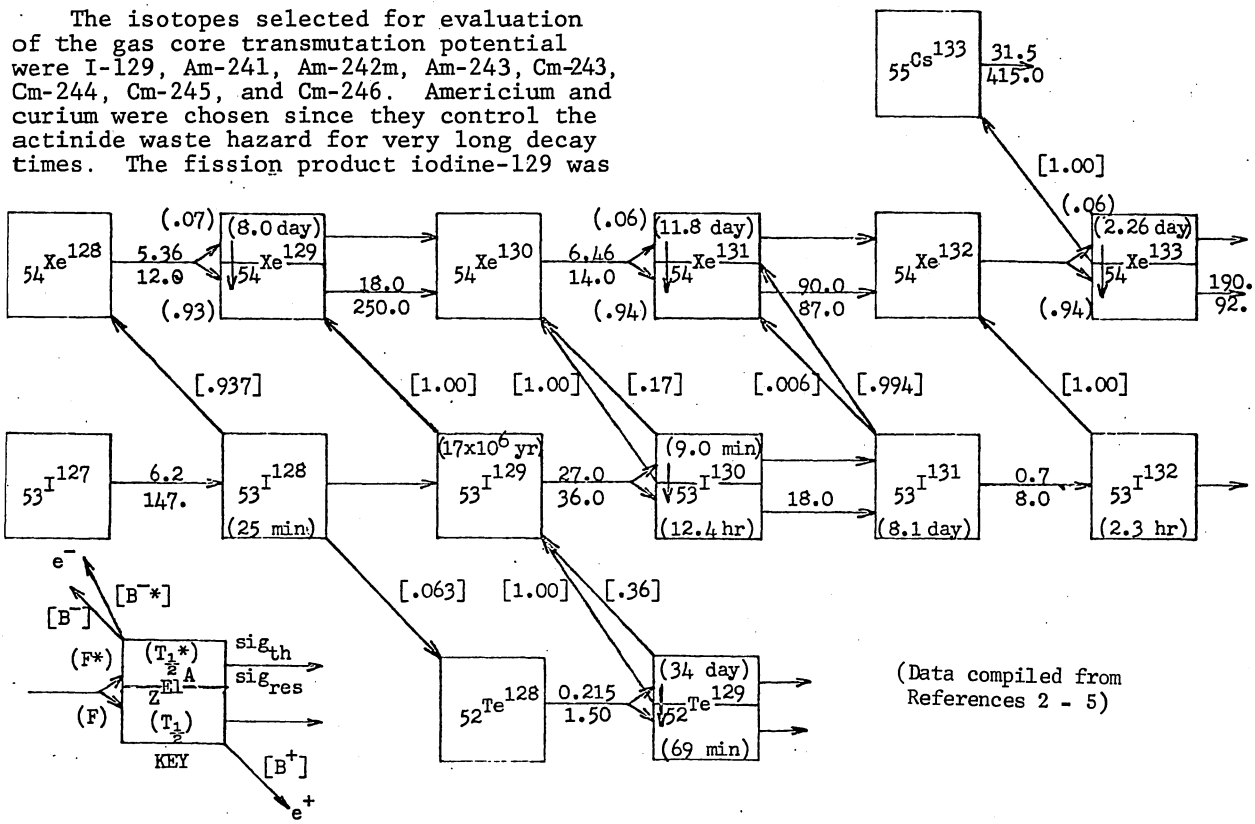

FIGURE 2. IODINE-129 TRANSMUTATION REACTION PATHS

TABLE 1: TRANSMUATION FIGURE SYMBOL KEY

El	element symbol	(F*)	fraction of (n,γ) transitions to an excited state of the product nuclide
A	mass number		
Z	atomic number	(F)	fraction of (n,γ) transitions to a ground state of product nuclide
e^-	electron emission		
e^+	positron emission	$[B^+]$	fractional decay by positron emission
$(T_{1/2}^*)$	excited state half-life	$[B^-]$	fractional decay by electron emission
$(T_{1/2})$	ground state half-life		
sig_{th}	thermal cross section for (n,γ) absorption	$[B^-*]$	fractional decay by electron emission to an excited state of the product nuclide
sig_{res}	resonance integral for (n,γ) absorption		

NOTE: designates an isomeric transition; the fraction of excited state decays by isomeric transition is 1 - $[B^+]$ - $[B^-]$ - $[B^-*]$

generated in 60 reactor years of operation.

As previously indicated, the transmutation rates and the final isotopic balances are strong functions of the neutron spectrum. For this study, three reference spectra were employed. A relatively hard spectrum typical of that expected in the core and a thermal spectrum typical of that present in the heavy water moderator were used. In addition, an intermediate spectrum typical of that found in light water reactors was used for comparison purposes It is emphasized that only the spectra is typical of the LWR; the magnitude of the flux in the gas core is substantially higher than that attainable in the light water reactor.

Gas Core Transmutation Results

Iodine-129

The initial loading of the I-129 was 400 kilograms. The mass of I-129 remaining as a function of irradiation time for the three reference spectra is shown in Figure 3. The curve labeled $\phi 3$ corresponds to irradiation in the core spectra and $\phi 1$ to irradiation in the moderator spectra.

Americium

Curves for the transmutation of the americium isotopes in the spectrum present in the reflector-moderator are shown in Figure 4. The initial loadings of the three americium isotopes considered are indicated. The Am-243 concentration approaches a steady state value after approximately two years. This behavior is due to Am-243 production by successive radiative captures and beta decays in the U^{238} present in the reactor fuel.

The effect of the neutron spectrum on the transmutation of Am-243 is illustrated in Figure 5. The reflector-moderator is indicated by the subscript 1 and the core by the subscript 3.

Curium

The curium transmutation calculations are illustrated in Figure 6. The significance of the neutron spectrum employed is most vividly illustrated in the case of

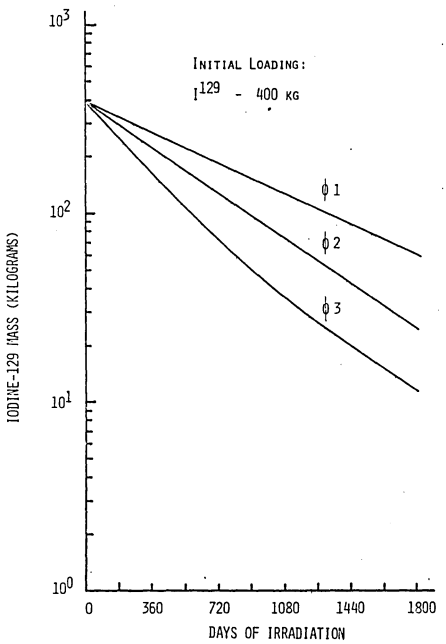

FIGURE 3. IODINE-129 TRANSMUTATION VERSUS IRRADIATION TIME

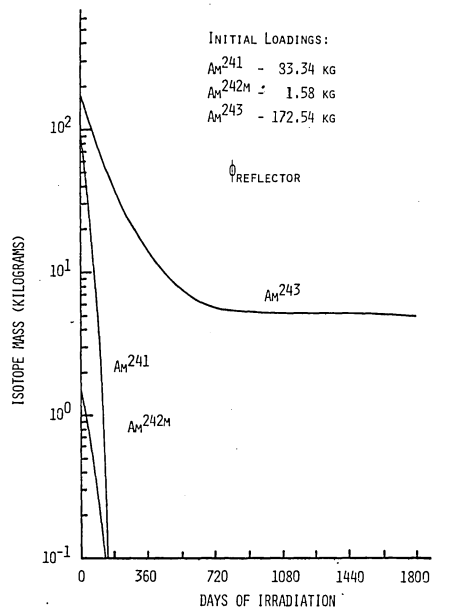

FIGURE 4. AMERICIUM TRANSMUTATION VERSUS IRRADIATION TIME

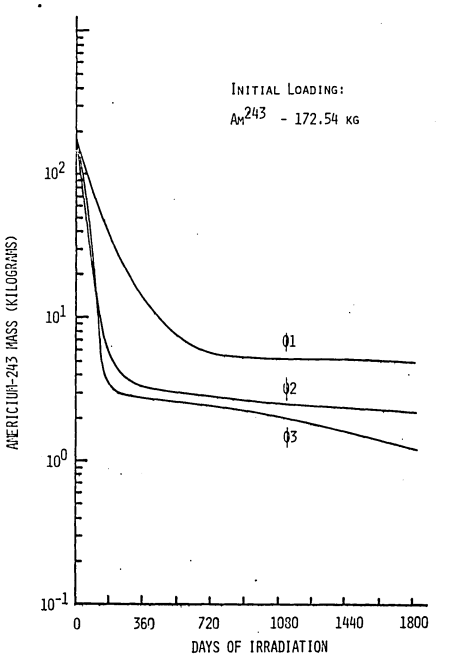

FIGURE 5. AMERICIUM-243 TRANSMUTATION VERSUS IRRADIATION TIME

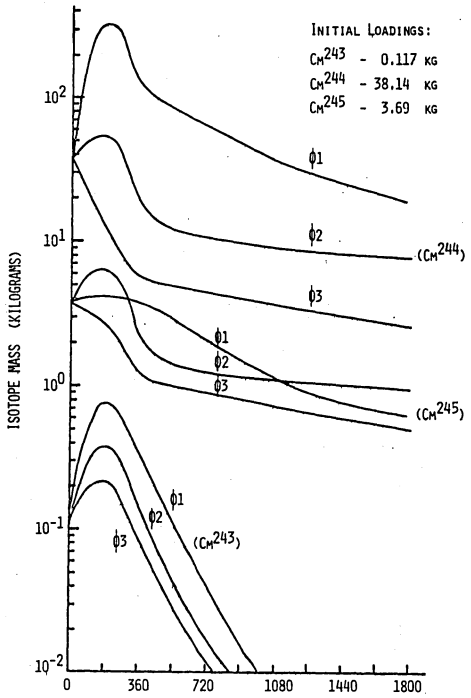

FIGURE 6. CURIUM TRANSMUTATION VERSUS IRRADIATION TIME

curium-244. After an irradiation period of approximately six months, the Cm-244 waste masses differ by a factor of 30 depending on whether the core or moderator spectrum is employed.

Higher Actinide Build-Up

Successive radiative captures and beta decays in both the reactor fuel and the isotopes to be transmuted can produce significant quantities of higher mass number actinides. The production curves for significant transmutation by-products are shown in Figure 7.

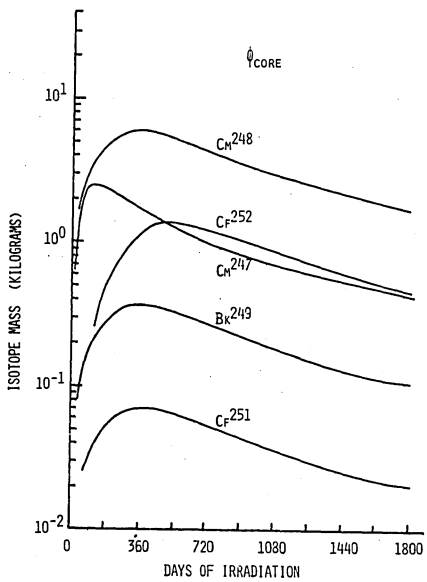

FIGURE 7. HIGHER ACTINIDE BUILD-UP VERSUS IRRADIATION TIME

Waste Hazard Reduction

The success of a particular transmutation scheme can be judged in terms of the overall reduction in the waste hazard. The relative inhalation hazard (RIHH) is defined as the volume of air (cubic meters) required to dilute the radioactivity in the waste to the Radiation Concentration Guide levels listed in Title 10 of the Code of Federal Regulations.[8] Similarly, the relative ingestion hazard (RIGH) is defined in terms of the volume of water required for dilution. The primary hazard associated with long-term waste disposal is the danger of dissolution in ground water or dispersal in the atmosphere and subsequent uptake by man. The quantity of air or water required to dilute the waste to a concentration low enough for unrestricted use can be used as a crude measure of the waste hazard.

The relative ingestion hazard associated with the americium and curium wastes is illustrated in Figure 8. The top curve represents the no irradiation case and the lower three curves, irradiation by the three reference spectra. The lower curves represent the hazard measure of the actinides to be transmuted, the by-products of the transmutation, and the new wastes generated by operation of the reactor for five years.

Conclusions

Transmutation of I-129 by a five-year exposure to a thermal neutron flux of 6.4×10^{14} n/cm^2-sec results in nearly order-of-magnitude reductions in the waste inventory of this nuclide. A five-year transmutation of americium and curium wastes produces order-of-magnitude decreases in the overall hazard potential of actinide wastes generated in 60 reactor years of LWR operation.

For this study, no attempt was made to optimize transmutation rates. Current studies are examining the transmutation potential of a fast spectrum cavity reactor. Other fuel cycles will be considered and an attempt made to optimize the irradiation time.

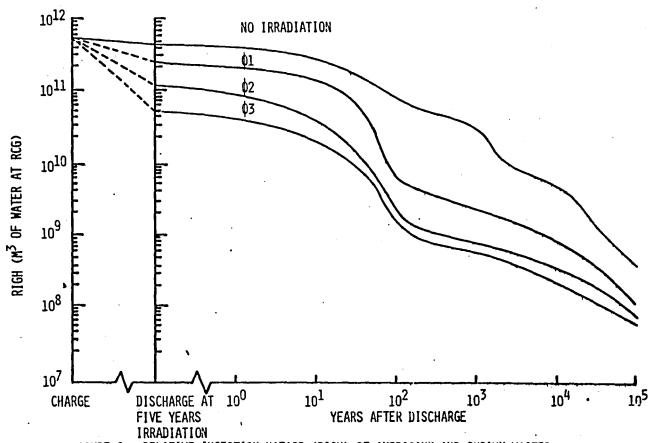

FIGURE 8. RELATIVE INGESTION HAZARD (RIGH) OF AMERICIUM AND CURIUM WASTES

References

1. K.J. Schneider and A.M. Platt, "High-Level Radioactive Waste Management Alternatives", BNWL-1900 (1974).
2. M.J. Bell, "ORIGEN - The ORNL Isotope Generation and Depletion Code", ORNL-4628 (May 1973).
3. ORYX-E, ORIGEN Yields and Cross Sections — Nuclear Transmutation and Decay Data from ENDF/B", Oak Ridge Radiation Shielding Information Center, DLC-38 (Sept. 1975).
4. N.E. Holden and F.W. Walker, "Chart of the Nuclides", 11th Edition, General Electric Company (April 1972).
5. Radiological Health Handbook, U.S. Department of Health, Education and Welfare (Jan. 1970)
6. H.C. Clairborne, "Neutron Induced Transmutation of High Level Radioactive Waste", ORNL-TM-3964 (1972).
7. W.C. Wolkenhauer, (ed.) "The Controlled Thermonuclear Reactor as a Fission Product Burner", BNWL-1685 (1972).
8. Code of Federal Regulations, Title 10, Part 20.

DISCUSSION

T. S. LATHAM: Have you looked at what the secular equilibrium buildup of actinide becomes as a function of the reprocessing time in the UF_6 itself? This suggests a class of reactor that may make most of the actinide problem go away.

B. G. SCHNITZLER: We did look at the actinide buildup in a typical light water reactor as opposed to the actinide buildup in the gas core. There is very little difference in the fission product buildup, but as for the actinides, they will level out, and we can only assume that the entire UF_6 mass was recirculated.

GAS CORE REACTORS FOR COAL GASIFICATION*

By

Herbert Weinstein
Illinois Institute of Technology
Chicago, IL 60616

Abstract

The use of nuclear process heat for coal gasification is a subject of considerable interest today. The concepts presently under study employ a process heat stream limited in temperature by the maximum allowable temperature of the reactor fuel elements. Because of this temperature limitation, the rates of the gasification reactions must be enhanced by the use of catalysts. The chemical plant associated with the production of either coal gas or hydrogen then becomes complex and expensive.

In this paper, the concept of using a gas core reactor to produce hydrogen directly from coal and water is presented. It is shown that the chemical equilibrium of the process is strongly in favor of the production of H_2 and CO in the reactor cavity, indicating a 98% conversion of water and coal at only 1500°K. At lower temperatures in the moderator-reflector cooling channels the equilibrium strongly favors the conversion of CO and additional H_2O to CO_2 and H_2. Furthermore, it is shown the H_2 obtained per pound of carbon has 23% greater heating value than the carbon so that some nuclear energy is also fixed. Finally, a gas core reactor plant floating in the ocean is conceptualized which produces H_2, fresh water and sea salts from coal.

Introduction

It has become apparent in recent years that the United States must utilize its coal resources more effectively to offset the problems caused by dwindling petroleum and natural gas resources. Some of the more attractive processes proposed for coal utilization are gasification—the production of synthetic natural gas—and hydrogen production. The problems associated with these processes are being worked on today. These problems include low efficiency and the complexities brought on by the use of very large scale catalytic reactors. It has been projected for gasification processes in which the coal is also used to generate process heat that the maximum possible efficiency is 67%, which means that one-third of the heating value of the coal is lost in processing and must be disposed of as waste heat.

The concept of utilizing nuclear energy for coal gasification can be traced back to the early 1960's.[1,2,3,4] Currently, this concept has seen renewed interest in Europe. Most of the related research is directed towards the utilization of process heat from high temperature gas cooled reactors (HTGCR). The maximum temperatures reached by the coolant gas in these reactors is less than 1500°K. Because of this temperature limitation, the chemical rates of the gasification reactions must still be enhanced by the use of catalysts.

* Work supported under NASA Grant NSG7039

It would appear that both coal gasification and hydrogen production could be done more directly and more efficiently in a gas core cavity reactor than in any indirect process heat application. There are several factors that make this approach seem promising. In the gas core reactor, the pulverized coal and steam would flow along together directly through the thermal radiation field from the fissioning plasma. In fact, the coal would provide the necessary shielding from thermal radiation required to protect the cavity walls. The resultant temperature of the steam-coal mixture can be high enough for the direct pyrolysis of water. The coal will combine with the oxygen as the mixture is cooled after leaving the reactor. However, the coal-steam mixture need be heated only to 1500°K to 2000°K at a 500 psi cavity pressure to effect the production of hydrogen and CO without the use of catalysts. The temperature of the mixture in the cavity should in fact be such as to obtain the most desirable mixture of H_2, CO, CO_2, H_2O and other organic compounds at the reactor exit.

The most straightforward application of this concept would be in the production of hydrogen. The idea of using hydrogen as a new type of clean fuel has been gaining acceptance. The potential of this process as discussed here is for producing fuel hydrogen in massive quantities. It should be noted that there also is potential for producing other valuable organic compounds directly in a gas core reactor.

The object of this work is to present the concept of using a gas core reactor to produce hydrogen from water and coal. The chemical equilibria is shown to be favorable for this reaction at modest gas core reactor temperatures. The chemical kinetics are not discussed because non-catalytic rate data is not readily available in the literature. An entire process is conceptualized in order to point out that the elements of the process appear feasible. The areas where intensive investigation is required are pointed out. The particular scheme chosen is one where the plant is floating in the ocean, using distilled sea water for the process and the ocean as a waste heat sink. The hydrogen and fresh water obtained from the waste heat are piped directly to the mainland. The sea salts obtained in the process can be returned to the mainland on the barges that bring coal to the plant.

Chemistry

The Heating Values of Products.

The resulting products of the water-coal reactions in the gas core reactor can be strongly influenced by the choice of temperature path for the reactant stream. The choice of products is based on the desirability of the fuel and the amount of nuclear energy that is chemically fixed in the fuel. It is desirable to fix as much nuclear energy as possible not only to increase our energy resources

TABLE I

Candidate Chemical Reactions

Reaction	Fuel	Lower heating value[5] per mole of fuel K cal	Fixed Nuclear energy per mole C	% Increase in HV of Coal
(1) $H_2O_{(\ell)} = H_2 + 1/2\ O_2$	H_2	57.8	--	--
(2) $C + 2H_2O_{(\ell)} = CH_4 + O_2$	CH_4	191.8	118.8	104%
(3) $2C + 2H_2O_{(\ell)} = CH_4 + CO_2$	CH_4	95.9(a)	12.4	2%
(4) $C + H_2O_{(\ell)} = CO + H_2$	$CO+H_2$	125.4	41.9	33%
(5) $C + 2H_2O_{(\ell)} = 2H_2 + CO_2$	H_2	115.6(b)	42.6	23%

(a) 191.8/2 (b) 2 x 57.8

but also to minimize the waste heat disposal problem. Candidate reactions are listed in Table 1 along with the fixed nuclear energy data. The fixed nuclear energy is expressed in two ways. First, as the number of kilocalories fixed per mole of carbon and second, as the resultant percentage increase in the heating value of carbon. The first two reactions are presented just to demonstrate the maximum possible fixed energy yields. The first of these is the pyrolysis of water without the use of coal to scavenge the oxygen. All of the fuel heating value is fixed nuclear energy. The second reaction is for the production of methane and oxygen from coal and water. Again coal is not used to scavenge O_2 and the increase in heating value of the coal is about 100%. However, this methane formation reaction is more truly represented by reaction 3. In this case the amount of fixed nuclear energy is negligible. Reaction 4 shows the production of a $CO+H_2$ fuel gas. The percent of nuclear energy fixed per pound of carbon heating value is 33%. While this is a significant increase, the problems associated with CO as a fuel make it an unlikely prospect as a final product. The last reaction is the production of H_2 and CO_2 and is the one used in this report because it represents a reasonable compromise of fuel utility and fixed nuclear energy. It will, however, occur as a two step process with reaction 4 being the first step. This is discussed in the next section.

Chemical Equilibrium Calculations

At elevated temperatures (>1500°K), the principal products in a C-H-O system are H_2, CO, CO_2. Methane formation is suppressed above 1000°K. Since the effects of nuclear radiation and the plasma field are neglected, only these products are considered. The overall reaction is:

1) $AH_2O + bC \rightarrow cH_2O + dC + eH_2 + fCO + gCO_2$ and the basic reaction steps are:

2) $CO + H_2O \rightleftharpoons CO_2 + H_2$

3) $C + H_2O \rightleftharpoons CO + H_2$

The equilibrium equations are:

$$K_3 = \frac{a_{CO}\, a_{H_2}}{a_C\, a_{H_2O}} \approx \frac{N_{CO}\, N_{H_2}\, P_T}{N_{H_2O}\, N_T}$$

and

$$K_2 \approx \frac{P_{CO_2} P_{H_2}}{P_{CO}\, P_{H_2O}} \approx \frac{N_{CO_2}\, N_{H_2}}{N_{CO}\, N_{H_2O}}$$

Here, a is chemical activity, N is number of moles, P is pressure and Subscript T stands for total. The activity of carbon is taken as one.

An H_2 balance and an O_2 balance complete the equation set

$$(N_{H_2O})\ \text{initial} = (N_{H_2O} + N_{H_2})\ \text{eq.}$$

$$(N_{H_2O})\ \text{initial} = (2\, N_{CO_2} + N_{H_2O} + N_{CO})\ \text{eq.}$$

Solving these equations with the K values of reference 6, and a total pressure of 500 psi yields the results shown in Figure 1. This value of pressure should be high enough for criticality and pressure level only affects in a small way the temperature at which conversion is completed. Equilibrium calculations below 900°K were not carried out because of the complexity of the calculations. Without these results it is impossible to determine the gas quenching paths required to yield the maximum value of the product stream. However, the reaction rates for the reverse reactions which would return the system to the initial reactant concentrations are certainly slow enough so that quenching is possible.

The results are presented for two cases. Figure 1a is for equimolar feed and Figure 1b is for a feed ratio of 2 moles H_2O/mole C. It is seen that for the equimolar case the equilibrium is such that conversion to CO and H_2 can be essentially complete above 1500°K. Chemical reaction rates at these temperatures are expected to be extremely large so that this equilibrium concentration should exist in the reactor cavity. For the case of molar feed ratio of 2, the coal is completely converted

to CO and CO_2 with about 57% of the water converted to hydrogen. It can be seen from the equilibrium constant data that as the percentage excess of steam is increased, the fraction of coal converted to CO_2 increases. The trade off becomes then, either separating large amounts of steam from the product stream or separating the CO and recycling it with a second steam feedstream. The chemical equilibrium of the latter case can be investigated:

$$CO + H_2O \rightleftharpoons CO_2 + H_2$$

and the equilibrium equation is:

$$K_4 = \frac{N_{H_2} N_{CO_2}}{N_{H_2O} N_{CO}}$$

The results of these calculations are shown in Figure 2 for molar feed ratios of steam to CO of 1 and 2. The equilibrium for this reaction is favored by lower temperatures, however, methane formation becomes significant below 900°K. It is apparent from the graph that between 900°K and 1000°K, conversions of 70% are readily attained. Again, increasing the steam-CO ratio favors the conversion but the same separations problem is involved. This temperature range is compatible with what would be expected in the moderator-reflector cooling channels close to the cavity. The second stage of the conversion process could be effected in passages next to the cooling channels. This reaction is exothermic however, and would add to the heat load on the cooling channels in this region of the reflector, but the problem should not be significant.

The Process Concept

The conceptual application of the process is described in this section. The fissioning plasma reactor station is fixed in the ocean, off shore of the continent. The off-shore location is chosen mainly for safety and environmental protection reasons. Coal is barged to the facility and sea water enters directly. The hydrogen and fresh water are piped directly to shore. Waste heat is disposed of to the ocean and sea salt resulting from the desalination is returned to shore in the barges. See Figure 3.

Figure 4 is a schematic of the various process elements which are described below. The choice of method for accomplishing the transformation in each element is not an optimal one but rather the one most obvious to the author.

Gas Core Reactor

The temperature field required for the chemical reactions is modest in the context of proposed gas core reactors. It should be readily achieved in either an open or closed cycle reactor. Therefore, both the coaxial flow GCR and the "light bulb" GCR are compatible concepts. Further, it does not appear that breeding of fuel or magnetohydrodynamic power generation are precluded from also being carried out along with the hydrogen production in the reactor facility.

The seeding of the working fluid in the cavity to make it opaque to thermal radiation is not an added complexity in this application. The pulverized coal reactant will be a very suitable seeding material. Because coal contains a large amount of volatile hydrocarbons, absorbing gases will be evolved at very low temperatures. In fact the steam itself will begin to strip some of them if the coal is soft enough. Furthermore, the coal in the large amounts present may have some neutron moderating effect, decreasing the critical mass requirements.

Water Supply and Cooling Requirements

No attempt has been made to estimate the energy generation rate in the GCR. There will, however, be a large excess of energy generated over that actually fixed chemically in the fuel. This excess will come from cooling of the moderator-reflector as well as the reaction products to suitable temperatures. It is expected that some of this waste heat will be used to obtain the process steam by distillation. Distillation is chosen rather than some less energy-expensive desalination process in order to keep the reactor cavity as free of salt as possible. The rest of the waste heat is used for desalination of sea water by some less expensive process. The final sink for waste heat after as much useful work as possible has been obtained is the ocean.

Process Elements

There are many process elements such as heat exchangers, and physical separations processes that make up the facility along with the reactor. They are described briefly according to alphabetic key on Figure 3. (a) Distillation of seawater for reactant steam. This should be a multiple distillation process in order to obtain a reactant stream which is as salt-free as possible. (b) Just downstream of the reactor is a heat exchanger in which fuel, and possibly some coal ash, is condensed. (c) A cyclone follows the condenser in which the spent fuel and coal ash are removed. (d) The product gases, still relatively hot, are cooled in a gas turbine. Electrical power for facility use is generated from the power derived. (e) The cold gases are filtered to remove any remaining solids. (f) The gases are cooled to room temperature in another heat exchanger and excess steam is condensed and passed to the CO stream. (g) The cool gases are passed through a refrigerated charcoal bed to remove radioactive gases such as iodine. Two beds, operating in flip-flop fashion, can be used. One operates in an adsorbing mode while the other is being regenerated. (h) The hydrogen is removed in a pair of molecular sieves operating in flip-flop fashion and piped to the mainland. (i) The CO stream from separator II meets the condensed water stream from (f) and a make up steam stream from the distillation unit and is piped to the reactor reflector. The product stream from the reflector goes to a heat exchanger where the gases are cooled and excess water condensed. (j) The hydrogen in the cooled gases is removed in separator III. This is another pair of molecular sieve units operating in flip-flop fashion. The CO_2 and CO remaining is then vented to the atmosphere.

Every element is not described in the above section. The heat removed in the heat exchangers along with heat removed in the reflector is used in the distillation column and an ancillary desalination plant.

Closure

The concept described in this paper is crudely formulated and presented. However, the basic idea is very sound.[7,8,9,10] The high temperatures of the gas core reactor can be used to effect valuable, endothermic chemical reactions in a non-catalytic manner. The example used here was chosen because of its great current interest. However, many other reactions for the production of a whole range of important organic compounds can be carried out instead of or along with the production of hydrogen.

References

1. Harder, H., Fischer, K., Nuclear Process Heat Programmes in Germany, Proceedings of the 1st National Topical Meeting on Nuclear Process Heat Applications, Nov. 1974 (Also Nuclear News; 4; No. 4, p. 56-62, May 1975).

2. Cohen, S., Nuclear Process Heat and Direct Coal Gasification, Proceedings of the 1st National Topical Meeting on Nuclear Process Heat Applications, Nov. 1974.

3. Schulten, R., Synthetic Natural Gas as a Nuclear Energy Carrier Over Long Distances, Umsch. Wiss. Tech., 73, No. 2, 53-54 (1973).

4. Schulten, R.; Kugeler, K., Coal Gasification & Other Nuclear Process Heat Applications, Proceedings of the 1st National Topical Meeting on Nuclear Process Heat Applications, Nov.,1974.

5. Hougen, O. A., Watson, K. M., and Ragatz, R. A. Chemical Process Principles, 2nd Ed., J. Wiley & Sons, Inc., New York, 1962.

6. Rossini, F. D., Pitzer, K. S., Arnett, R. L., Braun, R. M., and Pimental, G. C., Selected Values of Physical and Thermodynamic Properties of Hydrocarbons and Related Compounds. Carnegie Press, Pittsburgh, 1953.

7. Von Heek, K. H.; Juentgen, H., Reactions of Coal in High-Temperature Plasmas, Glueckauf Forschungsh, 33, No. 2, 45-47, (1972).

8. Sheer, Charles; Korman, Samuel, Arc Synthesis of Hydrocarbons, Advances in Chemistry Series. No. 131, Coal Gasification, 42-53, (1974).

9. Damo, Akibumi, Producing Hydrogen with Nuclear Fuel, Chem. Econ. and Eng. Rev., June, 1974.

10. Bal, S., Swierczek, R., and Musialski, A., Power-Coal Gasification in Plasmochemical Flow Reactors, Koks, Smola, Gaz. 1971 16(4) 96-100.

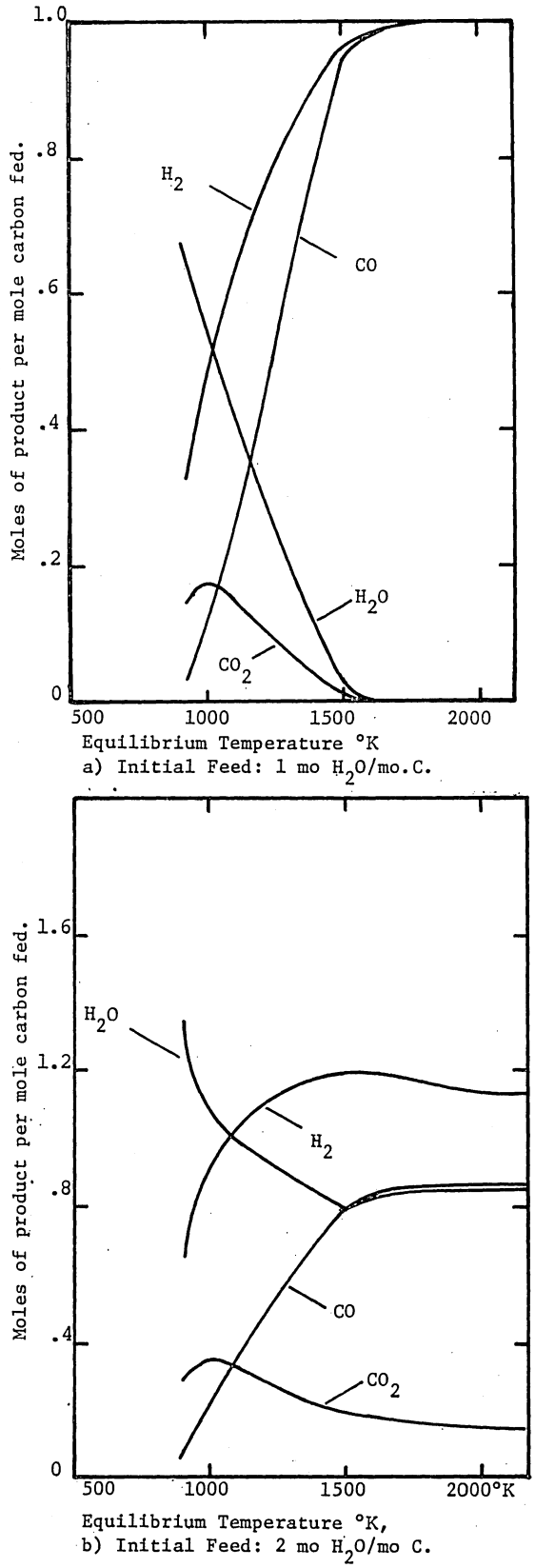

Figure 1. Equilibrium Conversion vs. Temperature for a C-H-O System at 500 psi.

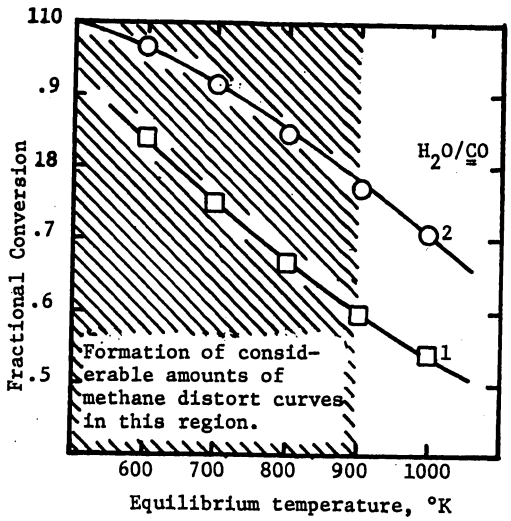

Figure 2. Equilibrium Conversion vs. Temperature for the reaction $CO + H_2O = CO_2 + H_2$.

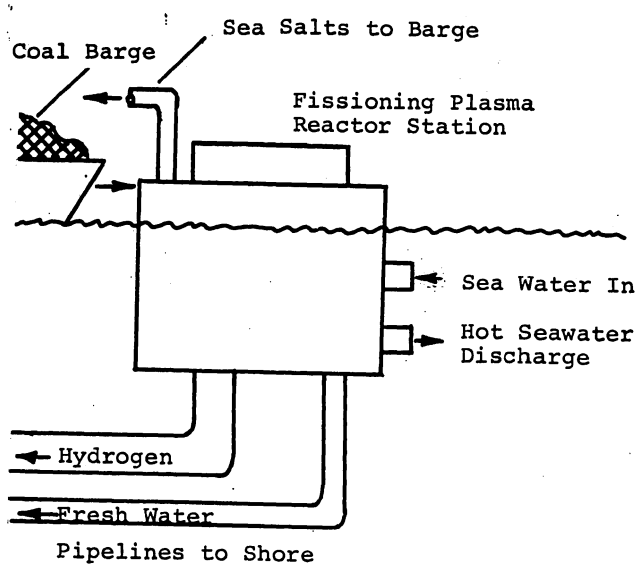

Figure 3. Gas Core Reactor Coal Gasification Facility

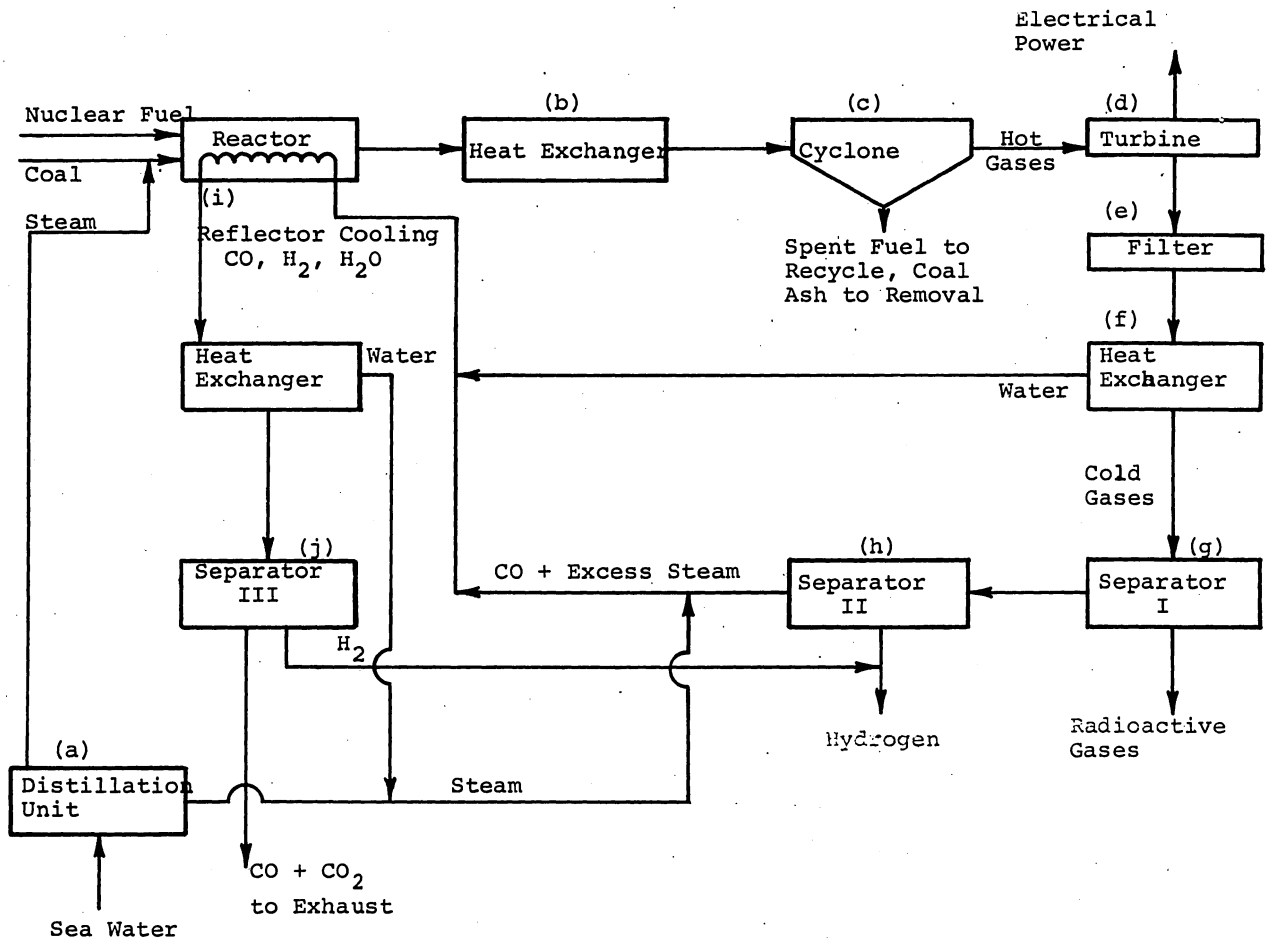

Figure 4. Schematic of Hydrogen Production Facility.

DISCUSSION

R. T. SCHNEIDER: In Europe last year, I saw an open peat lignite mine in Germany which had just been started. Forty five percent of German electricity is generated with lignite. The pits they have started at this rate will last them 500 years. The mining company was looking into gas cooled reactors to do what you have just said. Someone asked the question, "Why do you want to save 20% of the coal if you have that much?" That is the question they will want to ask you perhaps.

H. WEINSTEIN: That is not that damning a question. The environmental impact of burning peat and low grade coal is sizeable, and it would be easy to show that the hazards involved in large-scale power production around the world with coal is greater than with nuclear energy. The whole idea of producing important and expensive organics can be treated with a gas core very nicely. Hydrogen is the easiest thing to make.

CONSIDERATIONS TO ACHIEVE DIRECTIONALITY FOR GAMMA RAY LASERS

S. Jha* U. of Cincinnati, Cincinnati, OH
J. Blue, NASA-Lewis Research Center, Cleveland, OH

Abstract

This study concerns a method of alignment of nuclei for a gamma ray laser and a means of achieving preferential emission of radiation along the crystal axis. These considerations are important because it probably is not possible to achieve reflection of gamma radiation in order to have photons make multiple passes through an active region. Atomic alignment has been achieved by materials researchers who have made composite structures composed of needle-like single crystals all with the same orientation and all pointing in the same direction contained in a matrix of cobalt or nickel. The proposed method of preferential emission of radiation along the aligned needles is to have a symmetric field gradient at the nucleus and a sequence of excited levels of spin and parity 2^+ and 0^+. The proposed scheme will reduce the density of excited states required for lasing and reduce the linewidth due to inhomogenous broadening. Mossbauer absorption experiments intended to test these ideas are outlined.

I. Introduction

Historical Review

Recent review articles have indicated the substantial difficulties that exist in achieving a gamma ray laser.[1,2] The state of knowledge of the interactions of the nucleus and its surroundings was insufficient to allow those who conceived the concept of the gamma ray laser to foresee many of the problems.[3,4]

Perhaps the most difficult of the originally perceived problems, how to obtain a density of inverted states sufficient to have lasing, is still with us. There is, however, no known fundamental limitation to achieving high densities and man's continuing effort to make his power sources (fission reactors, fusion reactors and particle accelerators) more powerful may someday solve the intensity problem.[5]

An originally unappreciated problem, that fluctuating nuclear interactions with the surroundings that broaden nuclear levels to the extent that resonant absorption and stimulated emission are unlikely, is the subject of this paper. The static interaction of the nuclear quadrupole moment with an internal electric field gradient is considered as a means to achieve:

1) energy level splitting
2) desirable directivity of the emitted gamma radiation
3) a practical physical material with geometry suitable for a laser.

The conclusion of this paper unfortunately will not give a solution to all of these problems but is rather a suggestion as to what nuclear energy level configuration is desirable for a gamma ray laser. These considerations will serve to guide our future experimental research studies.

General Considerations for Population Inversion

To achieve population inversion of nuclear levels is not difficult if one takes advantage of beta decay and nuclear isomerism. This is illustrated with the decay of ^{113}Sn.

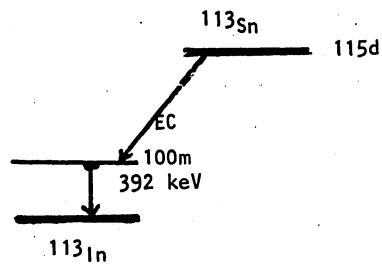

A freshly separated source of ^{113}Sn will decay into the isomeric level of ^{113}In and population inversion will exist for several hours; eventually the ground state population increases and exceeds that of the isomeric level.

Population inversion can be achieved by nuclear reactions as shown by the example:

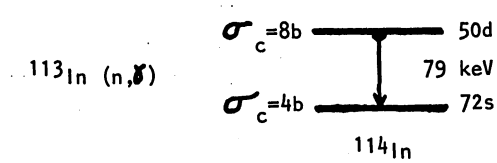

*supported by NASA Grant: NSG 3091

Energy Requirements

The energy of the isomeric level is a consideration since the parasitic absorption by atomic electrons is decreased for more energetic photons whereas the cross section for stimulated emission is proportional to λ^2 and therefore favors low energy transitions. Another consideration favoring low energies is that photon energies must not be decreased by the recoil of the emitting nucleus. The so-called recoilless fraction decreases exponentially with increasing energy, becoming negligible above 150 keV. In this note we are proposing the use of only certain kinds of nuclear levels because one can thereby achieve: 1) unidirectional transmission of gamma rays. 2) by removing level degeneracy, photons with less spread in energy than otherwise and 3) an energy matching of the photon with the levels that are to undergo stimulated emission.

II. Proposal

Electric Quadrupole Transitions

Gamma radiation emitted between nuclear levels of spin and parity 2^+ and 0^+ or 0^+ and 2^+ actually involves transitions to or from sublevels of the 2^+ state since that level splits into m = ± 2, ± 1 and 0. If there is an electric field gradient q which is axially symmetric with respect to the crystal axis then the sublevels split as shown in figure 1, and the three transitions Δm = ± 2, Δm = ± 1, and Δm = 0 are shifted in energy as shown.

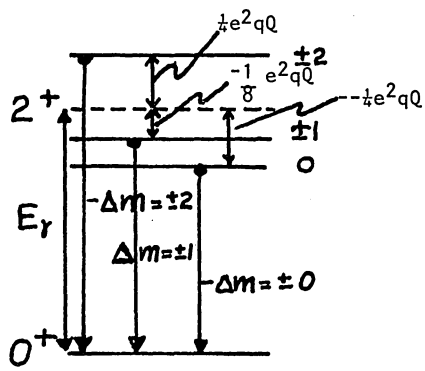

Fig. 1 Energy level splitting of 2^+ level in a field gradient and also showing the three transitions to a 0^+ level.

The angular distribution of the gamma radiation with respect to the symmetry axis is given by

$$W(\theta) = \frac{1}{2}(1 - \cos^4\theta) \text{ for } \Delta m = \pm 2$$

$$W(\theta) = \frac{1}{2}(1 - 3\cos^2\theta + 4\cos^4\theta) \text{ for } \Delta m = \pm 1$$

$$W(\theta) = 3(\cos^2\theta + 4\cos^4\theta) \text{ for } \Delta m = 0$$

These radiation patterns are shown in figure 2.

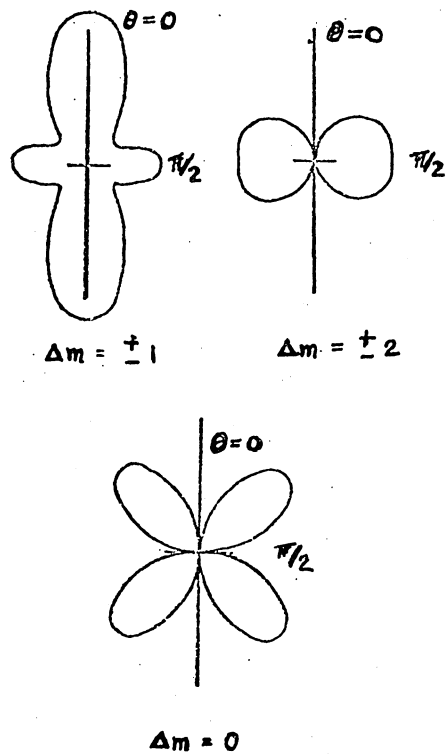

Fig.2 Electric quadrupole angular distributions for the three components of a 2^+ level.

Combining the information of the two figures shows that the Δm = ± 1 component is emitted along the crystal axis with an energy $E_\gamma - 1/8e^2qQ$. If the energy of the gamma ray is not too high and the Debye temperature of the solid is appropriate then there may exist a large fraction of recoilless photons. When one of these photons interacts with another nucleus in the isomeric state then stimulated emission will occur. However, only the Δm = ± 1 transition will have an energy match with the incident photon. The gamma rays arising from the other two transitions would emerge perpendicular to the symmetry axis.

These ideas have been tested by carrying out Mossbauer absorption experiments for the $2^+ \rightarrow 0^+$ transition. The absorption of the recoilless photon in a WS_2 single crystal (hexagonal close packed) which has an electric field gradient along the c axis at each tungsten nucleus gave the results shown in figure 3a.[6] Only a single component, Δm = ± 1, is resonantly absorbed when the incident photon is oriented along

c axis. A similar result is shown in figure 3b for the photon of the $2^+ \rightarrow 0^+$ transition in ^{178}Hf, which was absorbed in single crystal of hafnium metal.

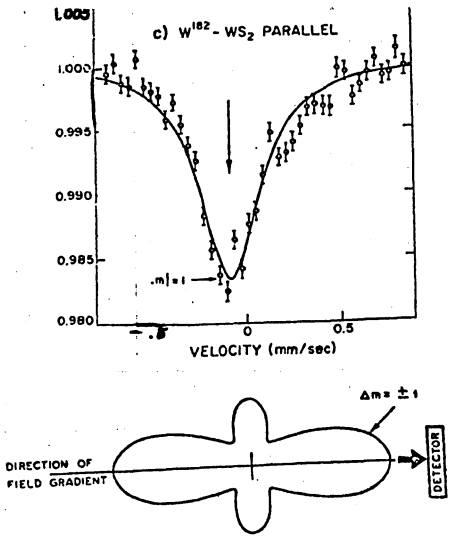

Fig.3a Mossbauer transmission experiment of the $2^+ \rightarrow 0^+$ transition in WS_2 for the case when the incident photon is aligned with c axis of the crystal.

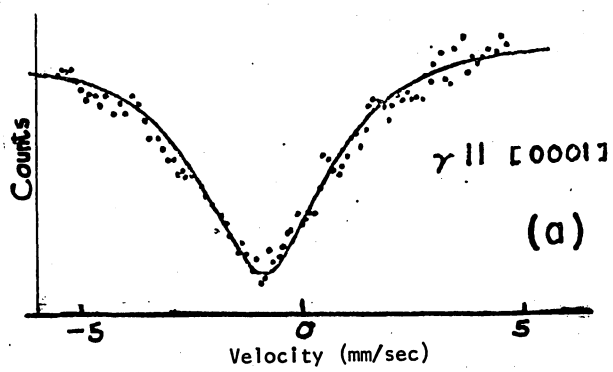

Fig.3b Same as 3a except the $2^+ \rightarrow 0^+$ transition is transmitted in Hf metal single crystal.

In both cases the results confirmed that the $\Delta m = \pm 1$ transition is absorbed parallel to the symmetry axis.

Filamentary Alignment of the Nuclear Isomers

It was recognized by the inventors of the gamma ray laser concept that the alignment of the active atoms on a single axis could solve the problem of the non-existance of mirrors with which to form a cavity. Whisker crystals were suggested as a possible materials configuration.[7]

The idea of the whisker configuration can be combined with the anisotropic distribution of the $\Delta m = \pm 1$ quadrupole transition. What is required to do this is an electric field gradient along the whisker filament and the crystal structure of the filament to be symmetric about the whisker axis. The concept is shown in figure 4.

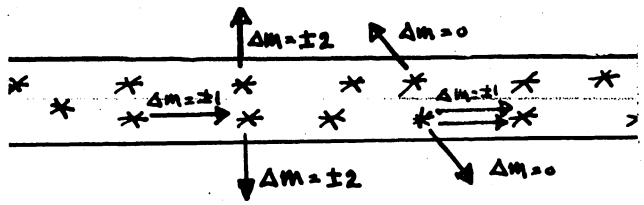

Fig.4 Schematic illustration of nuclei in isomeric states **, aligned in filaments and emitting quadrupole radiation when an electric field gradient is present and is in the filamentary direction.

Most of the photons from $\Delta m = \pm 2$ and $\Delta m = 0$ transitions will be emitted out of the whisker; those few emitted along the whisker axis will be shifted in energy from the $\Delta m = \pm 1$ photons. The axially directed, $\Delta m = \pm 1$ photons will have less energy spread than would photons from a degenerate 2^+ level.

Directionally Solidified Eutectics (DSE)

Materials scientists are working on the development of reinforced materials where the strengthening members are filaments or lamellae of a precipitated eutectic. The precipitates are single crystal and aligned and are often spaced in a rather regular array in the matrix alloy. Such a material is shown in figure 5, a SEM view of a directionally solidified rod of nominal composition Co-15 Cr-20 Ni-10.5 Hf -.7C; prepared by V. G. Kim of NASA's Lewis Research Center.[8] In this case the precipitate is HfC and the matrix material has been etched away to show the protruding HfC filaments.

Fig.5 Structure of directionally solidified TaC-15Cr-20Ni-Co alloy.

The DSE alloys offer an obvious solution to the gamma ray laser requirement for aligned nuclei. The requirement of symmetry and an electric field gradient along the filament can be achieved in either two ways:

1) the precipitate can have a crystal structure which has isotropy about a crystal axis and the crystal axis is parallel to the filament axis; an example of such a structure is tungsten disulfide, a hexagonal close packed crystal, or

2) the precipitate can have an isotropic structure, e.g., cubic, and be strained in the filamentary direction by differential expansion coefficients between the precipitate and the matrix. The strain of the crystal would be expected to destroy the symmetry in the strain direction and give rise to an electric field gradient.

Mossbauer absorber measurements will be made using the HfC reinforced composite as the absorber of the 93keV gamma from the $2^+ \rightarrow 0^+$ transition in ^{178}Hf. If the HfC has become noncubic, this should be detectable in the shape of the absorption line.

Preferred Level Arrangement

As we have indicated, a long-lived isomer having a spin sequence of levels $2^+ \rightarrow 0^+$ or $0^+ \rightarrow 2^+$ in a host having an axially symmetric field gradient will provide directed gamma radiation.

Additional considerations favor the $0^+ \rightarrow 2^+$ sequence, i.e., the isomeric state should be the 0^+ and the lower state 2^+ and both states should be above the ground state. With this arrangement, there will be no nuclear absorption of the recoilless gamma rays and there will be no broadening of the 0^+ level due to the stochastic field gradient or magnetic fields at the nucleus since a 0^+ state has no moment. The only factor then broadening the 0^+ level will be the inhomogenous isomer shift. We prefer the 2^+ level to be short-lived, then its natural width will be far larger than the isomer shift, thus an energy match between the recoilless gamma ray and the energy difference between $0^+ \rightarrow 2^+$ is assured and stimulated emission can occur.

The question as to whether the preferred nuclear level arrangement exists can only be answered by research studies in isomerism. A number of known $0^+ \rightarrow 2^+$ isomers are given below.

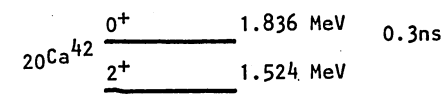

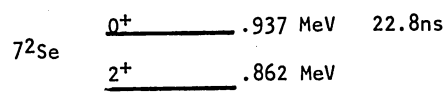

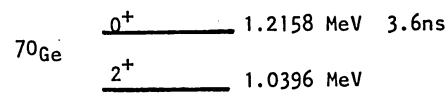

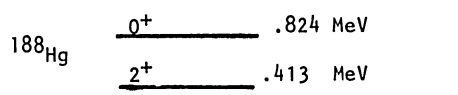

Isomeric states with longer lifetimes should be sought for the gamms ray laser. In addition to the traditional islands of isomerism, many quasiparticle states, bandheads of decoupled bands and nuclear levels with large changes in nuclear shape may provide the longer-lived isomeric state of the $0^+ \rightarrow 2^+$ type.

Conclusion

The rationale for searching for a nuclear isomer with a 0^+ spin and parity and decaying by means of a $0^+ \rightarrow 2^+$ transition has been given. At this point no suitable isomer is known. The directionality of emission which a laser requires can be achieved in filamentary structures with symmetry about the filamentary axis. Materials research in directionally solidified, precipitate reinforced, alloys should be watched for developments which may have the symmetry and electric field gradient required to achieve directional gamma ray emission.

References

1. V. A. Busheuv and R. N. Kuzmin Sov. Phys. Vsp., Vol. 17, 942, M. - Ju (1975)

2. G. C. Baldwin and R. V. Khokhlov, Phys. Today 28, 32 (1975)

3. B. V. Chirikov, Sov. Phys. - JETP 17 1355 (1963)

4. W. Vali, V. Vali, Proc. IEEE 51 182 (1963)

5. M. N. Yakimenko, Sov. Phys. Usp. 17 651 Mar-Apr (1975)

6. Y. W. Chow et al. Phys. Ltrs. 30B, 171 (1969)

7. G. C. Baldwin et al., Proc, IEFF 51, 1247 (1963)

8. Y. G. Kim, NASA TM X-71751

DISCUSSION

R. T. SCHNEIDER: It there such a thing as stimulated emission in a crystal?

S. JHA: In the nuclear case, stimulated emissinn has not been experimentally demonstrated. But there is no reason why there should not be stimulated emission. If the nucleus is so strongly bound that it excites without recoiling, the gamma ray leaves with full energy; if it now meets an atom which is so strongly bound that it can accept this gamma ray without recoiling, then stimulated emission should take place.

J. BLUE: Nuclear resonant absorption has been observed, and isn't it probable that spontaneous emission has happened but not been observed? If a nucleus is going to resonantly absorb a photon to an upper level, then we know the fraction of nuclei excited to that level, that should return emitting photons.

S. JHA: It is possible to create conditions, given appropriate energy and appropriate materials that will have 100% recoilless emissinn, such that all the gamma rays will be recoilless.

PRINCETON UNIVERSITY CONFERENCE ON PARTIALLY IONIZED PLASMAS
Including the THIRD SYMPOSIUM ON URANIUM PLASMAS
June 10, 11, and 12, 1976
WORKSHOP WORKING GROUP SUMMARY REPORT

GROUP I

PLASMA GENERATION AND CONFINEMENT

Chairman: J. S. Kendall
Group Members: J. Blue, P. W. Levy, M. Stoenescu, S. Sutherland, and A. Kazi

Status of the Field:

In the past several years, gas-core uranium plasma generation and confinement studies have centered on two major reactor schemes -- the vortex-stabilized uranium hexafluoride (UF_6) plasma contained in an argon buffer gas, which is a closed-cycle system, and the coaxial open-cycle gas core reactor. Significant progress has been made on vortex-stabilized confinement of UF_6 injected into an argon plasma. Long-term ($\tilde{\sim}$ 40 min) operation at high uranium particle densities has produced encouraging results with respect to the degree of deposition on the fused-silica walls of the container. However, considerable work remains in this area before a high-power closed-cycle plasma core reactor experiment is performed.

The advancement of both open- and closed-cycle gas core reactor research might be aided by more complete understanding of the complex fluid dynamics and its coupling with radiative transport phenomena in the reactor cavity.

Proposed Goals and Research Directions:

Major directions recommended for the proposed research on gas core plasma confinement are:

(1) The fissioning uranium plasma

(2) Transparent materials research

The Fissioning Plasma

Analytical and experimental research should be continued to determine the dominant physical processes relevant to the fluid dynamics and radiative heat transfer both within and at the edge of the fissioning plasma region. Development of a high-pressure vortex-stabilized optically-thick uranium plasma is a central feature to such an endeavor.

Priority in future research should be given to the vortex-stabilized concept over the coaxial concept for the following reasons:

(a) The virtual nonexistence of potentially attractive terrestrial applications for the coaxial flow concept; the coaxial concept being better suited to the design of a nuclear rocket for space missions requiring high thrust densities and high specific impulses.

(b) The higher levels of uranium confinement achieved using the vortex scheme.

(c) The apparent absence of a "restoring force" in the fuel region of the core for the coaxial scheme.

Reactor experiments should be complemented by concurrent experiments aimed at establishing empirical values of nonequilibrium transport coefficients for fissioning plasmas potentially suited to nuclear pumped laser applications.

Transparent Materials Research

Closed-cycle gas core reactors require use of transparent materials that remain optically-transparent over a wide spectral region and retain mechanical integrity at high temperatures while subjected to intense nuclear radiation. Currently most research has focused on very pure fused silica which appears to be a potentially attractive confinement material. Two areas of focus are suggested in future research:

(a) Radiation damage and color center formation studies should be extended to much higher temperatures, radiation levels, and neutron and electron fluxes appropriate to the highest power fissioning plasmas. Such studies should be aimed at predicting the absorption and mechanical properties of the confining material, as well as gauging its lifetime and reliability.

(b) The possibility of using materials other than fused silica such as single crystal beryllium oxide should be investigated.

New Concepts and Directions:

The National Aeronautics and Space Administration conducts and sponsors considerable research in fissioning plasma reactors. To complement this research, it is suggested that accelerator experiments be considered to evaluate UF_6 radiation decomposition by fission fragments, to obtain spectra of emitted radiation and to study materials problems. Accelerator experiments with heavy particles bombarding transparent windows may be useful for investigation of transparency under conditions analogous to reactor conditions where there are significant numbers of displaced atoms in the window material.

GROUP II

PLASMA CHARACTERISTICS

Chairman: J. H. Lee
Group Members: C. K. Choi, N. L. Krascella, D. Williams

Status of the Field:

At the present time, the available information on UF_6 and Uranium plasma characteristics under non-equilibrium conditions is limited (Ref. H. Helmick, LASL). The analytical investigation of the transport of radiation and the distribution of energy within reactor systems is hampered by a lack of accurate knowledge on such essentials as cross sections and radiative lifetimes for transitions involving electronic, vibrational and rotational excitation and also on the dissociation of (UF_6) molecules by fission fragment impact. While some elastic cross sections for electron-molecule (UF_6) collision processes are known (see the paper by S. Trajmar et. al. in this Proceedings), little work is done for inelastic cross sections, involving ionization exitation, etc.

Similarly, although a significant amount of data exists on spectral emission characteristics of fissioning uranium plasmas under equilibrium conditions, non-equilibrium radiation effects due to deposition of large quantities of fission fragment energy into the fissioning (UF_6) plasma have not been extensively examined on either a theoretical or an experimental basis. In addition, it is of paramount importance that the spatial and spectral content of radiation emitted by the fissioning plasma be known to aid the design of in-reactor experiments as well as the design and feasibility assessment of plasma core reactor applications. The above comments apply particularly strongly to nuclear pumped laser research, which cannot go forward as rapidly in the absence of detailed knowledge of non-equilibrium plasma characteristics.

In particular, more extensive work is required in the future regarding in-core measurements of density, temperature and neutron fluxes with both space and time resolution. At the present time, there are well established techniques for measuring all of these quantities but only in a spatially and temporally averaged form. Density measurements reported so far have tended to be confined to regions near the axis of the flowing (UF_6) system. Profiles of density do exist for unenriched (UF_6) but it is of some use to measure such profiles in a reacting system which includes the effect of a neutron flux on the density.

In summary, substantial data exists for low pressure, low temperature (UF_6) plasmas. However, such data lacks certain essential features of non-equilibrium plasmas and is also not compiled in a comprehensive manner. It would be of great benefit to the plasma core reactor research community to obtain a comprehensive compilation of all of the relevant data on (UF_6) plasma characteristics.

For the progress toward the ultimate goal of U-235 plasma-core reactor, basic studies on a metalic U-235 plasma are also necessary. The emission characteristics of metallic uranium plasma in UV and soft x-ray ranges have been reported (see the paper by M. D. Williams, et al. in this Proceedings). However, the effect of fissioning has not been observed due to the low reaction rate in the plasma. A study of metallic uranium plasma in a high-flux neutron field is desired.

Proposed Goals and Research Directions:

The proposed research on fissioning UF_6 and uranium plasma characteristics may be divided into four areas:

a) Measurement of inelastic cross-sections, vibrational and rotational energy levels, and dissociation by fission fragments for both (UF_6) and its decomposites.

b) Measurement of the Spectral Emission from fissioning (UF_6) plasmas. Initial Los Alamos Scientific Laboratory (LASL) reactor experiments will probably not operate at temperatures sufficient to produce appreciable emission in the fissioning (UF_6). Therefore, simulation experiments utilizing the GODIVA-Ballistic Piston combination should be accelerated to provide initial (UF_6) spectral emission data in a fissioning gas over a range of temperatures and pressures as well as neutron fluxes. These initial experiments would provide valuable baseline data for the design of similar subsequent experiments in various cavity reactor programs. Finally, the ultimate goal of this research should be to incorporate extensive radiation emission studies in the actual fissioning gaseous (UF_6) experimental series.

c) To complement the X-ray diagnostic techniques at United Technologies Research Center, in-core measurements should be made of density, temperature and neutron fluxes with space and time resolution. These measurements are essential to the

understanding of reactor start-up dynamics and to evaluate the effects on plasma parameters of neotron coupling. A good diagnostic would be a pulsed laser which can be focused down from a rather large aperture to spots throughout the volume of the (UF_6) tank. The back scattering of this coherent radiation yields temperatures and densities of various species throughout the plasma. The pulse shape will provide temporal resolution. Other diagnostics may also be readily applied to complement the above.

d) Study on a metallic uranium plasma, as a long-range program, should be continued. Especially the non-thermal effect of fissioning in the uranium plasma should be determined to obtain a reference data for reactor development and nuclear pumping of lasers in the plasma reactor.

e) Assignment of a special task group for the purpose of compilation and review of (UF_6) and U^{235} plasma data. The group will also conduct revisions using new data as it becomes available. The group may identify and recommend necessary measurements.

New Concepts and Directions:

The use of tunable dye lasers is suggested for determination of (UF_6) plasma characteristics, especially under reactor conditions. Electron beam probes may also complement the laser diagnostics.

GROUP III

NUCLEAR PUMPED LASERS

Chairman: F. Hohl
Group Members: G. Cooper, R. De Young, J. Early, D. Lorents, D. McArthur, S. Suckewer, P. Thiess, S. Trajmar, H. A. Hassan

Status of the Field:

The potential for achieving high power density, low wavelength lasers by direct nuclear pumping has been keeping the area of nuclear pumping active since about 1961. Several reviews of the field have appeared recently (Thom, K; and Schneider, R. T.: AIAA J. 10, 400 (1972); Schneider, R. T.; and Thom, K.: Nuclear Tech. 27, 34 (1975)). However, it has only been in the past 2 years that considerable progress has been made toward achieving high-power direct nuclear-pumped lasers. Present research uses neutrons from high flux reactors to induce nuclear reaction in either ^{235}U or B^{10} laser tube wall coatings, or in He^3 mixed with the lasing gas (see the paper by R. De Young, et al. in this Proceedings).

The first two nuclear pumped lasers using ^{235}U wall coatings were demonstrated in 1974 by researchers at Sandia Laboratories (McArthur, D. A.; and Tollefsrud, P. B.: Appl. Phys. Lett. 26, 187 (1975) and at the Los Alamos Scientific Laboratory (Helmick, H. H.; Fuller, J.; and Schneider, R. T.: Appl. Phys. Lett. 26, 327 (1975)). The Sandia group observed lasing of CO at the 5.24 and 5.6 μm vibrational bonds. At present they have achieved outputs of 100 watts at relatively high efficiencies. The Los Alamos group achieved lasing of a He-Xe laser at 3.5 μm. The lowest wavelength and lowest neutron threshold for a nuclear pumped laser has been achieved by the University of Illinois group (De Young, R. J.; Wells, W. E.; Miley, G. H.; and Verdeyen, J. T.: Appl. Phys. Lett. 28, 194 (1976)). They achieved lasing of a Ne-N_2 system at 8629 Å and 9393 Å. The first volume pumped laser was achieved only recently by the NASA-Langley Group (Jalufka, N. W., DeYoung, R. J.; Hohl, F.; and Williams, M. D.: Appl. Phys. Lett. 28, (1976)) who used the $He^3(n,P)^3H$ volumetric reaction to pump a He^3-Ar system which lased at 1.79 μm. Table I summarizes the nuclear-pumped laser results as of June 1976.

In addition to experimental work, considerable progress is being made in modelling nuclear pumping of lasers. Energy deposition, electron distribution, and excitation of various laser transitions are being predicted. Details of that work are given in the Proceedings.

It should be noted that all results achieved so far demonstrate only "proof of principle." What must be demonstrated next is that high-power nuclear-pumped laser can be competitive with more conventional lasers.

Proposed Goals and Research Directions:

Broadly speaking, the goals for Nuclear Pumped Laser Research fall into two categories:

1) To demonstrate the advantages of using nuclear pumping over other possible pumping mechanisms;

2) to determine what limitations, if any, are imposed on the lasing system by the characteristics of the pumping source, i.e., the fissioning plasma.

More specifically, the research goals may be summarized as follows:

a) To achieve high efficiency combined with high power CW laser output;

b) to extend the lasing wavelength range to shorter wavelengths such as the visible or even ultraviolet region of the spectrum;

c) to investigate the possibility of volumetric pumping using Uranium Hexafluoride (UF_6) - laser gas mixtures;

d) to investigate the compatibility of laser threshold flux requirements with the actual reactor flux levels.

Special recommendations for research aimed at achieving the above goals are as follows:

1) Identify laser media that are most amenable to nuclear pumping.

2) Conduct experiments to establish how well electron-beam pumping of a laser medium simulates nuclear pumping.

3) Obtain valuable kinetic data such as on radiative processes, electron collision processes and excitation and charge transfer processes. Use such data to model candidate laser systems. Analytical modelling should of course run concurrently with ongoing experimental research.

4) Investigate the relative merits of self-critical and externally driven neutron pumping schemes.

5) Identify the kinetics of the Carbon Monoxide nuclear pumped laser with a view to optimizing and scaling this laser to higher powers.

6) Investigate the advantages of nuclear pumping of noble gas-excimer laser media.

7) In a carefully diagnosed nuclear pumped laser system, compare volumetric versus surface-coated pumping sources for different laser media.

8) Conduct further detailed investigations of the effects of electric fields on the performance characteristics of nuclear pumped lasers.

New Concepts and Directions:

Nuclear pumped laser research has made significant progress in the past two years. The feasibility of producing a laser pumped by fission fragments has been clearly demonstrated. Spurred by these successes, nuclear pumped laser research may now continue in many potentially fruitful directions. A variety of concepts and innovative research directions may be actively pursued.

Whereas it is highly desirable to have a critical laser-reactor using UF_6 as a fuel, such a system is complicated by the low vapor pressure of UF_6 at temperatures appropriate for lasing. It is therefore of interest to study other possible fuels such as the transuranic elements whose nuclei offer much higher fission cross sections, or liquids which contain the transuranic elements. Since fusion reactors are potential sources of neutron and charged particle fluxes, their application to nuclear pumped lasers should be investigated.

Nuclear radiation enhancement of an electrically pumped laser has been experimentally demonstrated. Preliminary studies at Los Alamos Scientific Laboratories on the effects of an electric field on a nuclear pumped laser indicate the potential for substantial enhancement of the laser output at a minimal cost of electrical energy. It is therefore of great interest to investigate further the physics and economics of electric field enhancement of nuclear pumped lasers.

Finally, nuclear pumped flowing gas and gas dynamic lasers are also worthy of further research. While such laser systems do suffer the inefficiencies of foil excitation, they do offer the possibility of making very large lasers for which there are many potential applications.

Table 1. Summary of Nuclear-Pumped Laser Results

NUCLEAR PUMPED LASERS (May 1976)	WAVELENGTH	PRESSURE (TORR)	THERMAL FLUX THRESHOLD (n/cm^2-sec)	ENERGY DEPOSITED (J/ℓ) TIME PERIOD	DURATION OF LASER OUTPUT	PEAK POWER DEPOSITED (W/ℓ)	PEAK LASER OUTPUT (WATTS) (J/ℓ)
γ-Pumped HF laser Los Alamos		1.3		≈ 923 12 nsec	12 nsec	8×10^{10}	5×10^{8} 92.3
γ-Pumped Xe Amplified spontaneous emission Livermore	~ 1700 Å	5,200 7,800 10,500 13,000 15,700		5×10^{3} to 15×10^{3} 17 sec	31-10 nsec A.S.E.	2.7×10^{11} to 9×10^{11}	
Fission Fragment CO Laser Sandia Labs	5.1-5.6 μm	100	$\sim 5 \times 10^{16}$	200 150 μsec	50 μsec	1.3×10^{6}	2 - 6 0.2
Fission Fragment He-Xe Laser Los Alamos	3.0-4.2 μm	200	3×10^{15}	50 150 μsec	235 μsec	3.3×10^{5}	> .01 2.8×10^{-5}
$B^{10}(n,\alpha)\ Li^{7}$ Ne-N_2 Laser Univ. of Illinois	8629 Å and 9393 Å	75-400	1×10^{15}	313 to 1000 10 msec	6 msec	3×10^{4} to 1×10^{5}	1.5×10^{-3} 2.4×10^{-5}
$He^{3}(n,p)H^{3}$ He-Ar Laser NASA-Langley	1.79 μ	200-700	1.4×10^{16}	24 to 270 150 μs	550 μsec	1.6×10^{5} to 1.8×10^{6}	0.05

GROUP IV

REACTOR CONCEPTS, SYSTEMS, AND APPLICATIONS

Chairman: H. Weinstein
Group Members: T. S. Latham, M. Suo, E. Maceda, S. Chow, H. Helmick

Status of the Field:

Plasma-Core Nuclear Reactor concepts may be conveniently divided into closed cycle and open cycle systems. Open cycle systems are predominantly of the coaxial flow type in which wall jet injection of propellant keeps the fissioning plasma in the central region of the cavity surrounded by a moderator-reflector shell and high pressure buffer gas. Closed cycle systems, such as the Nuclear Light Bulb, confine the fissioning fuel by means of a tangentially injected swirl flow of a buffer gas. In both cases the transfer of power from the fissioning fuel to the propellant or buffer gas is by radiative heat transfer. Obviously, in the coaxial system, such transfer can go unimpeded, whereas, in the closed cycle system, limited transparency of the confining cell limits radiative energy fluxes. On the other hand, the closed cycle concept offers complete fuel confinement, while in the coaxial open flow system, flow mixing can lead to fuel losses and furthermore, the efflux from the reactor of radioactive material relegates this concept to solely space power application with no realistic terrestrial power applications.

The fuel used in these reactors may be a pure fissionable fuel, a compound such as Uranium Hexafluoride (UF_6) or perhaps a hybrid composed of a solid fuel-UF_6 combination.

At the present time there are few enough concepts and no well established basis for ordering them in terms of probability of success. Consequently, all concepts should be vigorously investigated. The real basis of priority for a given concept derives from its applicability to a particular mission, be it ground-based or space-based.

The applications for plasma-core nuclear reactor systems are numerous. They fall into three major categories:

a) Space propulsion and power

b) Terrestrial power concepts

c) Indirect applications

Space Propulsion and Power

The gas-core nuclear reactor is rather versatile in that it can provide (for example in a coaxial flow configuration) direct propulsion for a spacecraft by acceleration of propellant to high velocities resulting in thrust levels and specific impulses for exceeding those attainable by conventional chemical rockets. Simultaneously the nuclear power plant can also supply electrical power for the maintenance of spacecraft functions. Alternatively, a closed cycle system may be used to generate electrical power for use in ion thrusters or magnetoplasmadynamic gas accelerators or even to generate a high power laser beam which may then be used either to transmit power to other regions in space or else to provide thrust via a laser-heated thrust chamber.

Terrestrial Power Concepts

The closed cycle reactor system is best suited to ground-based power needs. Gas-core nuclear reactors offer a new technology for the use of high temperature (~4000 K) working fluids. There is also the attractive possibility of direct coupling of the radiant energy in the reactor to output laser radiation and other direct conversion schemes. The compactness of feasible gas-core fissioning reactor systems combined with their efficient operation at temperatures of order 4000 K make them viable alternatives to fusion reactor systems which are necessarily burdened by mammoth dimensions and plasma temperatures in excess of 10^6 K.

Indirect Applications

The gas-core nuclear reactor system is an excellent source for indirect power conversion such as radiochemical, thermochemical, and photochemical schemes, since it produces radiant power over a very wide and easily tunable bandwidth of the electromagnetic spectrum. Not necessarily being restricted to power conversion schemes, the gas-core reactor is also an excellent source of high temperature process heat for metallurigal uses and also for photochemical production processes.

An Ideal Fission Power Reactor must satisfy the following requirements:[1]

a) Low Critical Mass $\tilde{}$ 10kg

b) Small Units Possible (MW range)

c) Fuel Circulation and On-Site Processing

d) Burnup of Transuranium Actinides and Certain Fission Fragments

e) Increased Fuel Utilization

[1] Karlheinz Thom, "Gaseous Fuel Nuclear Reactor Research" invited paper at 1976 IEEE International Conference on Plasma Science, May 24-26, 1976, held at Austin, Texas.

f) High Efficiency Power Generation

g) Breeding of U-233 from Thorium

h) Low Fission Fragment Inventory

i) High Temperatures for Process Heat (coal gasification, steel and hydrogen production, etc.)

j) Non-equilibrium Radiation for Photochemistry and Hydrogen Production

k) Nuclear Pumped Lasers

l) Advanced Propulsion in Space

m) Nuclear Safeguards - Non proliferation of Atomic Weapons

The Gaseous Fuel Reactor is ideally suited to all of these requirements and is worthy of considerable attention in the future. Figures 1 and 2 summarize the essential features of Conventional Nuclear Power Plants and Gaseous Fuel Reactors and highlight the advantages of developing Gaseous Fuel Reactors in preference to present day nuclear power plants.

Proposed Goals and Research Directions:

In planning a well balanced program of research into cavity reactor systems, the basis of priority should be on the most suitable system concept for a particular application. There are few enough concepts at the present time and no well established basis for ordering them in terms of probability of success, so that all concepts should be vigorously investigated. The priorities for program planning may be classified as follows:

a) Maintenance of a program of research in baseline technology such as cavity reactor experiments, fluid mechanics, fuel handling, laser pumping aspects, and plasma experiments of fundamental nature on, for example, plasma characteristics etc.

b) Choice of a set of reference systems that are competitive with other systems for particular applications.

c) Maintenance of an effort into the development of a broad spectrum of innovative reactor concepts to supplement current ideas.

d) Maintenance of a program to develop supporting technology such as in materials, handling, fuel recycling, etc.

e) Total benefit evaluation of different concepts. Such an evaluation must take into account the following considerations:

(i) minimal environmental impact

(ii) nuclear safeguards

(iii) efficient energy resource utilization

(iv) exploitation of low grade nuclear fuels and breeding possibilities.

Based on these priorities and program goals, research should revolve around five key areas as outlined below:

a) Materials

b) Plasma Confinement and Radiative Heat Transfer

c) Fuel Recycling and Processing

d) System Confinement and Radioactive Material Separation

e) Integrity of the boundary of the reactor flow system -- Mechanical Design Features.

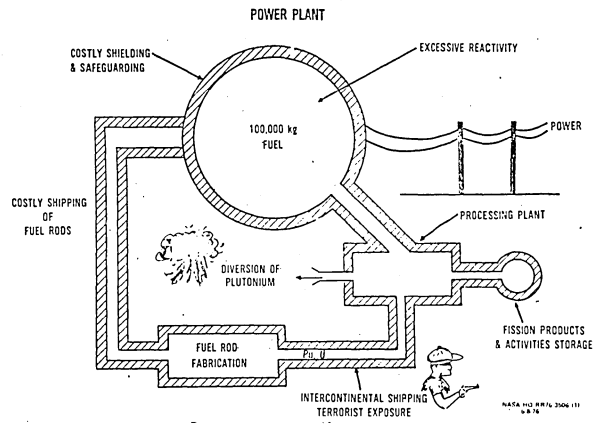

Figure 1 Conventional Nuclear Power Plant

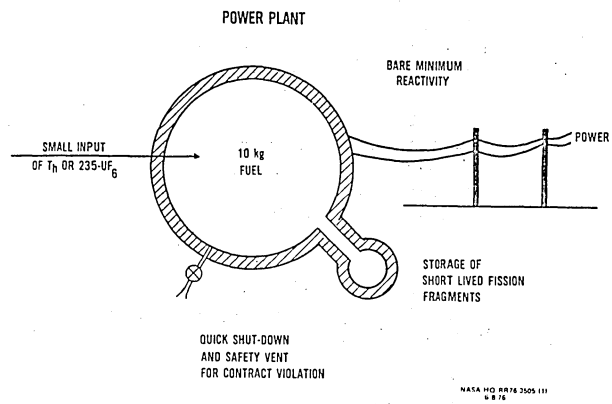

Figure 2 Gaseous Fuel Reactor

PRINCETON UNIVERSITY CONFERENCE ON PARTIALLY IONIZED PLASMAS
Including the THIRD SYMPOSIUM ON URANIUM PLASMAS

June 10, 11 and 12, 1976

List of Participants

M. A. Akerman
Nuclear Engineering Program
University of Illinois
Urbana, IL 61801

J. H. Anderson
Nuclear Engineering Program
University of Illinois
Urbana, IL 61801

Michael J. Antal
Department of Aerospace &
Mechanical Sciences
Princeton University
Princeton, NJ 08540

C. Bathke
Plasma Physics Laboratory
Princeton University
Princeton, NJ 08540

G. K. Bienkowski
Department of Aerospace &
Mechanical Sciences
Princeton University
Princeton, NJ 08540

J. Blue
NASA Lewis Research Center
21000 Brookpark Road
Cleveland, OH 44135

S. M. Bogdonoff
Department of Aerospace &
Mechanical Sciences
Princeton University
Princeton, NJ 08540

C. Byvik
Mail Stop 231A
NASA Langley Research Center
Hampton, VA 23669

S. I. Cheng
Department of Aerospace &
Mechanical Sciences
Princeton University
Princeton, NJ 08540

C. Choi
University of Illinois
214 Nuclear Engineering Laboratory
Urbana, IL 61801

S. Chow
75 Montgomery Street, Apt. 18A
New York, NY 10002

K. E. Clark
Department of Aerospace &
Mechanical Sciences
EQ D309
Princeton University
Princeton, NJ 08540

J. D. Clement
School of Nuclear Engineering
Georgia Institute ot Technology
Georgia, GA 30332

G. W. Cooper
Gaseous Electronics Laboratory
University of Illinois
607 East Healey Street
Champaign, IL 61820

J. F. Davis
Department of Nuclear Engineering
& Science
University of Florida
Gainesville, FL 32611

R. De Young
NASA Langley Research Center
Hampton, VA 23365

D. H. Douglas-Hamilton
AVCO Everett Research Laboratory
201 Lowell Street
Wilmington, MA 01887

J. T. Early
Lawrence Livermore Laboratory
University of California
Livermore, CA

J. Grey
American Institute of Aeronautics
& Astronautics
1290 Avenue of the Americas
New York, NY 10019

H. A. Hassan
Department of Aerospace &
Mechanical Sciences
University of North Carolina
P. O. Box 5246
Raleigh, NC 27607

H. H. Helmick
P. O. Box 1663, Group A5
Los Alamos Scientific Laboratory
Los Alamos, NM 87544

R. V. Hess
Laser Molecular Physics Branch
NASA Langley Research Center
Mail Stop 160
Hampton, VA 23360

F. Hohl
Mail Stop 160
NASA Langley Research Center
Hampton, VA 23660

R. G. Jahn
School of Engineering & Applied Science
Princeton University
Princeton, NJ 08540

J. F. Jaminet
United Technologies Research Center
Silver Lane
East Hartford, CT 06108

S. Jha
Department of Physics
University of Cincinnati
Cincinnati, OH 45221

A. H. Kazi
Army Post Radiation Facility
Bldg. 860
Aberdeen Proving Ground, MD 21005

J. S. Kendall
United Technologies Research Center
Silver Lane
East Hartford, CT 06108

N. L. Krascella
United Technologies Research Center
400 Main Street
Hartford, CT 06108

M. Krishnan
Department of Aerospace & Mechanical Sciences
Princeton University
Princeton, NJ 08540

S. H. Lam
Department of Aerospace & Mechanical Sciences
Princeton University
Princeton, NJ 08540

T. S. Latham
United Technologies Research Center
Silver Lane
East Hartford, CT 06108

J. Laudenslager
Jet Propulsion Laboratory
4800 Oak Grove Drive
Pasadena, CA 91103

J. P. Layton
The Aerospace Systems Laboratory
Princeton University
Princeton, NJ 08540

J. H. Lee
Box 1807
Department of Physics & Astronomy
Vanderbilt University
Nashville, TN 37235

P. W. Levy
Brookhaven National Laboratory
Upton, Long Island, NY 11973

G. Lewicki
Jet Propulsion Laboratory
4800 Oak Grove Drive
Pasadena, CA 91103

D. C. Lorents
Molecular Physics Center
Stanford Research Institute
Menlo Park, CA 94025

E. Maceda
Nuclear Engineering Laboratory
University of Illinois
Urbana, IL 61801

T. C. Maguire
Department of Nuclear Engineering
University of Florida
Gainesville, FL 32611

J. L. Mason
The Garrett Corporation
9851 Sepulveda Blvd.
Los Angeles, CA 90009

D. A. McArthur
Division 5423
Sandia Laboratories
Albuquerque, NM 87115

R. B. Miles
Department of Aerospace & Mechanical Sciences
Princeton University
Princeton, NJ 08540

G. H. Miley
214 Nuclear Engineering Laboratory
University of Illinois
Urbana, IL 61801

T. G. Miller
High Energy Laser Laboratory
Redstone Arsenal, AL 35809

D. M. Monson
Mail Code N230-3
NASA Ames Research Center
Moffett Field, CA 94035

E. V. Pawlik
Jet Propulsion Laboratory
4800 Oak Grove Drive
Pasadena, CA 91103

R. J. Rodgers
United Technologies Research Center
400 Main Street
East Hartford, CT 06108

W. C. Roman
United Technologies Research Center
Silver Lane
East Hartford, CT 06108

G. R. Russell
Mail Code 122-123
Jet Propulsion Laboratory
4800 Oak Grove Drive
Pasadena, CA 91103

J. H. Rust
School of Nuclear Engineering
Georgia Institute of Technology
Atlanta, GA 30332

R. T. Schneider
Department of Nuclear Engineering
University of Florida
Gainesville, FL 32611

B. G. Schnitzler
202 Nuclear Sciences Building
University of Florida
Gainesville, FL 32611

F. C. Schwenk
Code RR
NASA Headquarters
Washington, DC 20546

W. A. Sirignano
Department of Aerospace &
Mechanical Sciences
Princeton University
Princeton, NJ 08540

D. E. Smith
Sayre Hall, Forrestal Campus
Princeton Univeristy
Princeton, NJ 08540

T. M. Smith
Sayre Hall, Forrestal Campus
Princeton University
Princeton, NJ 08540

D. E. Sterritt
Tennessee Valley Authority
216 Haney Building
Chattanooga, TN 37401

R. C. Stoeffler
United Technologies Research Center
Silver Lane
East Hartford, CT 06108

M. L. Stoenescu
Sayre Hall, Forrestal Campus
Princeton University
Princeton, NJ 08540

S. Suckewer
Forrestal Campus
Princeton University
Princeton, NJ 08540

M. Suo
Power System Technology
United Technologies Research Center
Silver Lane
East Hartford, CT 06108

S. Sutherland
University of Illinois
214 Nuclear Engineering Laboratory
Urbana, IL 61801

T. B. Taylor
International Research & Technology Corp.
1501 Wilson Boulevard
Arlington, VA 22209

P. E. Thiess
University of Illinois
Champaign, IL 61801

K. Thom
Code RR
NASA Headquarters
Washington, DC 20546

L. Toburen
Battelle Northwest Laboratory
Box 999
Richland, WA 99352

S. Trajmar
Mail Code 183-401
Jet Propulsion Laboratory
4800 Oak Grove Drive
Pasadena, CA 91103

W. F. von Jaskowsky
Department of Aerospace &
Mechanical Sciences
Princeton University
Princeton, NJ 08540

H. Weinstein
Illinois Institute of Technology
Chicago, IL 60616

P. J. Wilbur
Mechanical Engineering Department
Engineering Center
Colorado State University
Fort Collins, CO 80521

M. D. Williams
NASA Langley Research Center
Hampton, VA 23365

J. R. Williams
College of Engineering
Georgia Institute of Technology
Atlanta, GA 30332

H. P. Yockey
Aberdeen Proving Ground, MD 21005